FOSSIL ENERGY

DOE/BC/14657-15
(DE94000129)

MEASURING AND PREDICTING RESERVOIR HETEROGENEITY IN COMPLEX DEPOSYSTEMS

The Fluvial-Deltaic Big Injun Sandstone in West Virginia

Final Report
September 20, 1991-October 31, 1993

By
Michael Ed. Hohn
Douglas G. Patchen
Milton Heald
Khashayar Aminian
Alan Donaldson
Robert Shumaker
Thomas Wilson

May 1994

Performed Under Contract No. DE-AC22-90BC14657

West Virginia University
Appalachian Oil and Natural Gas Research Consortium
Morgantown, West Virginia

Bartlesville Project Office
U. S. DEPARTMENT OF ENERGY
Bartlesville, Oklahoma

DISCLAIMER

This report was prepared as an account of work sponsored by an agency of the United States Government. Neither the United States Government nor any agency thereof, nor any of their employees, makes any warranty, expressed or implied, or assumes any legal liability or responsibility for the accuracy, completeness, or usefulness of any information, apparatus, product, or process disclosed, or represents that its use would not infringe privately owned rights. Reference herein to any specific commercial product, process, or service by trade name, trademark, manufacturer, or otherwise does not necessarily constitute or imply its endorsement, recommendation, or favoring by the United States Government or any agency thereof. The views and opinions of authors expressed herein do not necessarily state or reflect those of the United States Government or any agency thereof.

This report has been reproduced directly from the best available copy.

Available to DOE and DOE contractors from the Office of Scientific and Technical Information, P.O. Box 62, Oak Ridge, TN 37831; prices available from (615) 576-8401.

Available to the public from the National Technical Information Service, U.S. Department of Commerce, 5285 Port Royal Rd., Springfield VA 22161

DOE/BC/14657-15
Distribution Category UC-122

Measuring and Predicting Reservoir Heterogeneity in Complex Deposystems

The Fluvial-Deltaic Big Injun Sandstone in West Virginia

Final Report
September 20, 1991-October 31, 1993

By
Michael Ed. Hohn
Douglas G. Patchen
Milton Heald
Khashayar Aminian
Alan Donaldson
Robert Shumaker
Thomas Wilson

May 1994

Work Performed Under Contract No. DE-AC22-90BC14657

Prepared for
U.S. Department of Energy
Assistant Secretary for Fossil Energy

Edith C. Allison, Project Manager
Bartlesville Project Office
P.O. Box 1398
Bartlesville, OK 74005

Prepared by
West Virginia University
Appalachian Oil and Gas Research Consortium
P.O. Box 6064
Morgantown, WV 26506-6064

TABLE OF CONTENTS

ABSTRACT 1

EXECUTIVE SUMMARY 4
- TECHNICAL PERSPECTIVE 4
- RESULTS 4
- APPROACH 5

INTRODUCTION 7
- RESEARCH METHODS AND OBJECTIVES 7
- ACKNOWLEDGEMENTS 8

EVIDENCE OF HETEROGENEITY IN THE BIG INJUN RESERVOIR 9
- REGIONAL HETEROGENEITY 9
- FIELD-SCALE HETEROGENEITY 9
- DRILLING HISTORY 9
- WATER-FLOODING PERFORMANCE 10

STRUCTURAL CONTROL OF REGIONAL HETEROGENEITY 12
- INTRODUCTION 12
- BASEMENT STRUCTURE 12
- DETACHED STRUCTURE 13
- FRACTURES 13
- RELATION OF STRUCTURAL POSITION TO PRODUCTION 14

STRATIGRAPHIC CONTROL OF REGIONAL HETEROGENEITY 15
- INTRODUCTION 15
- CORRELATION 15
- HETEROGENEITY 16

FIELD-SCALE HETEROGENEITY 18
- INTRODUCTION 18
- STRUCTURAL CONTROLS - GRANNY CREEK FIELD 19
- STRUCTURAL CONTROLS - ROCK CREEK FIELD 19

FIELD-SCALE HETEROGENEITY INTERPRETED FROM SEISMIC STUDIES 20
- INTRODUCTION 20
- BASEMENT FAULTS 21
- SMALL-SCALE FOLDS 22
- FRACTURE ZONES AND FAULTS 24
- VSP OBSERVATIONS 25

STRATIGRAPHIC CONTROLS ON INTERWELL HETEROGENEITY 27

SUBDIVISIONS AND DEPOSITIONAL ENVIRONMENTS IN GRANNY CREEK FIELD 27
SEDIMENTOLOGICAL AND DIAGENETIC HETEROGENEITIES IN GRANNY CREEK FIELD 28
SUBDIVISIONS AND DEPOSITIONAL ENVIRONMENTS IN ROCK CREEK FIELD 28
SEDIMENTOLOGICAL AND DIAGENETIC HETEROGENEITIES IN ROCK CREEK FIELD 29
COMPUTER MODELING OF SEDIMENTARY FACIES 30
STRATIGRAPHIC DISTRIBUTION OF POROSITY 31
PETROLOGY OF THE POCONO AND "MACCRADY" BIG INJUN SANDSTONE 32

RESERVOIR CHARACTERIZATION 37
CORE ANALYSIS 37
WELL LOGS 37
PRESSURE TRANSIENT TESTS 38
PRODUCTION AND INJECTION DATA 39

HETEROGENEITY RELATED TO OIL PRODUCTION 40
SPATIAL TRENDS 40
INDICATOR KRIGING 40
GRANNY CREEK FIELD 41
ROCK CREEK FIELD 41
STRATIGRAPHIC AND DIAGENETIC EFFECTS ON PRODUCTION 42
EFFECTS OF STRUCTURE, DEPOSITION, DIAGENESIS, AND PRODUCTION 43
DEFINITION OF PRODUCTION AREAS WITH SEISMIC DATA 44
ROCK CREEK FIELD 45
FRACTURE POROSITY AND COMMUNICATION BETWEEN WELLS 45

CONCLUSIONS AND RECOMMENDATIONS 48
STRATIGRAPHY 48
DIAGENESIS 48
RESERVOIR CHARACTERIZATION 49
TRAP 49
OIL PRODUCTION 49
REGIONAL IMPLICATIONS 50
RECOMMENDATIONS FOR INFILL DRILLING 50
SECONDARY RECOVERY 50
RESERVOIR CHARACTERIZATION METHODOLOGY 51
SEISMIC STUDY METHODOLOGY 52

REFERENCES CITED 54

APPENDIX A: THE EFFECTS OF FRACTURES AND BARRIERS ON

SECONDARY OIL A1
INTRODUCTION A1
MODELING MEGA-HETEROGENEITIES A1
SIMULATION STUDY A2
APPLICATION TO GRANNY CREEK A3
CONCLUSIONS A3
REFERENCES CITED A4

APPENDIX B: PRESSURE FALL-OFF TEST ANALYSIS B1

APPENDIX C: MICRO-HETEROGENEITY CHARACTERIZATION OF THE BIG INJUN SANDSTONE C1
INTRODUCTION C1
METHODOLOGY C1
RESULTS C2

APPENDIX D: MICROSCOPIC MODELING OF POROUS MEDIA D1
INTRODUCTION D1
DEFINITIONS D1
ANALYSIS D2
FLUID FLOW PATH D2
FLOW BLOCKAGE D7
SKIN MODEL D8
MEASUREMENT METHODS D9

APPENDIX E: SEISMIC DATA PROCESSING AND SMALL FAULTS E1
REFERENCES CITED E3

APPENDIX F: VSP GUIDED POST-STACK DECONVOLUTION AND MODELING IN THE GRANNY CREEK FIELD F1
INTRODUCTION F1
VIBROSEIS DECONVOLUTION F1
MODEL STUDY F1
POST-STACK FREQUENCY DOMAIN INVERSION F2
NONSTATIONARITY F2
CONCLUSIONS F3
ACKNOWLEDGEMENTS F3
REFERENCES CITED F3

APPENDIX G: SEISMIC MODEL STUDIES OF THE GRANNY CREEK FIELD G1
SEISMIC RESOLUTION IN GRANNY CREEK G1
SEISMIC MODELS G3
STARTING MODELS G3
STRATIGRAPHIC VARIABILITY G3
DISCRETE VERTICAL FAULTS G4
FRACTURE ZONE WITH NO FAULT OFFSET G5

VERTICAL FAULT WITH VELOCITY REDUCTION G6
VELOCITY ANOMALIES G7
CONCLUSIONS G8
ACKNOWLEDGEMENTS G9
REFERENCES CITED G9

APPENDIX H: PETROGRAPHIC DATA FOR GRANNY AND ROCK CREEK H1

APPENDIX I: 2D GIS I1
RASTER VERSUS VECTOR GIS I1
RASTER IMAGES I1
VECTOR FILES I2
SPATIAL QUERY I2
IDRISI VIDEO IMAGES I3
GRANNY CREEK SPATIAL ANALYSIS I3
SUMMARY AND CONCLUSIONS I14
REFERENCES CITED I15

ABSTRACT

Evidence for heterogeneity in the Big Injun reservoir-forming sandstones on a regional scale is found in the distribution of hydrocarbons into distinct fields across the basin. The easternmost fields traditionally are considered to be updip unconformity traps; those to the west appear to be regionally downdip from the truncated margin of the reservoir.

Drilling history for Granny Creek suggests reservoir heterogeneity as drillers first developed the northern and central part of the field in the 1920's and 30's, then the southern-most part. There was sporadic infill drilling throughout the field since initial development. In contrast, Rock Creek field was developed in two stages, first within the shallower part of this synclinal field, then deeper when drillers accepted higher water saturations.

Evaluation of waterflood performance revealed the non-uniform pressure and production behavior in several patterns in Granny Creek field. A novel approach was employed to model a fracture between a well that exhibited low injection pressures and a production well that experienced early water breakthrough. This led to successful simulation of waterflood production performance for two adjacent patterns with substantially different behaviors. The results of simulation studies also revealed that the communication path must be through a separate zone, most probably the overlying Greenbrier Limestone.

Waterflooding simulation analysis of injection pressure/rate data across the field, and results of fall-off tests revealed that the permeability around the injection wells has experienced a severe reduction after water injection was initiated. High injection pressures experienced as result of permeability reduction around injection wells could be responsible in part for establishing communication between the Big Injun and Greenbrier Limestone.

Regional distribution of hydrocarbons suggests that both basement and detached structures have in part determined the locations of Big Injun oil fields. Primary migration pathways resulted in oil accumulations above basement structures; secondary migration (re-migration) occurred later into Alleghenian detached structures. Stratigraphic controls also are important at the regional scale. Big Injun sandstones were deposited in fluvial-deltaic systems that prograded into the study area from both the east and west. Although Big Injun sandstones nearly blanket the study area, regional correlations show that the western Big Injun is younger than the eastern Big Injun sandstones. Both Big Injun sandstones can be subdivided into upper coarse-grained channel facies and lower fine-grained distributary mouth bar facies. Distribution of sandstone facies and thicknesses suggests control by structural features such as the Waverly Arch, Cambridge Arch, Warfield anticline, and Rome trough. These patterns were modified later by pre-Greenbrier erosion associated with growth of the West Virginia Dome. Thus, at the regional scale, there are three causes for stratigraphic discontinuities: lateral discontinuities resulting from pre-Greenbrier and pre-Pottsville erosion; lateral discontinuities due to facies changes from sandstones to shales at the distal margins of deltaic-river-mouth bars and channels; and vertical discontinuities resulting from shales separating Big Injun reservoir sandstones of different ages. Granny Creek field produces oil from the older Big Injun, whereas Rock Creek field exemplifies production from the younger unit.

At the field scale, Big Injun structure mapped from well data suggests a number of small wave-length, low-relief folds that plunge northeast on the flank of the large syncline in which Granny Creek field is located. Some, but not all, of the these folds appear to correlate with

folds mapped using seismic data. Variations in interval travel-time through major stratigraphic subdivisions of the Paleozoic sedimentary sequence recognized in seismic data reveal a complex history of basement fault reactivation within the field. Coincidence of thickening in the Big Injun to Huron Shale interval beneath small folds indicate these folds are detached. In some cases thickening may in part be the result of syndepositional reactivation of basement faults.

Structural, stratigraphic, and diagenetic controls of heterogeneity all are present in Granny Creek field. The lower, fine-grained, distributary mouth-bar facies comprises three subfacies with differing porosity and permeability characteristics. Highest porosity occurs in the marine-influenced proximal bar, and lowest in the distal mouth bar as well as between prograding tongues of the bar sandstones. Permeable facies generally correspond to the distribution of porosity facies; thus, porosity and permeability can be related to depositional environments. However, high permeability accompanying average porosity in cores from the southern part of the field suggests local fractured zones.

Original porosity in the lower fluvial channel sandstones was low due to poor sorting. Lack of chlorite coatings resulted in quartz cementation, further reducing the original low porosity and permeability. In contrast, porosity and permeability were preserved in the lower proximal bar facies by well-formed chlorite coatings that restricted quartz cementation. Original sedimentary conditions apparently set the stage for later diagenetic variations in porosity and permeability, again emphasizing the importance of depositional environments in predicting favorable porosity-permeability trends.

The reservoir in Rock Creek field is largely a fine-grained sandstone deposited as river mouth bars. Heterogeneities include thin shales near the base, and high density zones similar to those in Granny Creek field. Analysis of porosity variation in Rock Creek field shows that zones of relatively high porosity tend to be larger in Rock Creek field compared with Granny Creek field.

Distribution of key reservoir parameters such as permeability and porosity was determined from core, well log, pressure fall-off tests, and production/injection data from Granny Creek field. Results generally confirmed the geological description of the reservoir, including the conclusion that the major pay zone in Granny Creek field consists of sandstones of a westward-prograding, mouth bar complex. Permeability computed from geophysical logs showed the importance of conventional core (plug) analysis and knowledge of depositional environments to develop useful estimates.

A south-east trend in initial potential in the northern part of Granny Creek field reflects truncation of the reservoir sandstone to the northeast, but a distinct north-south trend in cumulative production is divided mid-field by a discontinuity, and the trend is broad in the north and very narrow in the south. Maps of cumulative production in Rock Creek field indicate heterogeneity at the same scale as Granny Creek. Analyses in Granny Creek field indicate a positive correlation between high initial oil production and preservation of subfacies of the distributary mouth-bar and channel facies in the northern half of the field. High production occurs where the upper distal and marine-influenced proximal mouth-bar subfacies pinch out against the overlying channel facies and where at least a few feet of the relatively impermeable channel facies are present. Low production is associated with: thin areas of proximal mouth-bar subfacies; a change from marine to fluvial dominance of the mouth-bar subfacies, accompanied by reduction of porosity and permeability; and loss of overlying channel subfacies, a possible seal.

High density zones interpreted from logs, cores and petrographic analysis of thin sections

are due to both shale (depositional barriers) and cementation (diagenetic barriers). Shale breaks between sandstone tongues at the base of the distal bar parallel bedding and facies boundaries, whereas diagenetic breaks appear to cut across bedding and sandstone tongues. Thus, these interpreted permeability barriers, recognized as high-density intervals on logs, form thin tabular to lens-shaped intervals of impermeable sandstone that occur slightly below and approximately parallel to the pre-Greenbrier unconformity, and probably alter fluid flow paths and apparently divide the reservoir into compartments. Subtle folds and faults coincide in location and orientation with these high diversity zones, suggesting that carbonate cementation of the reservoir occurred in areas that fractured during deformation.

Time-structural highs on seismic profiles show some correlation with areas of high primary and 10-year cumulative production. The most productive areas of the field lie in an area where reactivation of basement faults was most intense. Small folds over basement structures appear to be more productive than those which are not.

EXECUTIVE SUMMARY

Technical Perspective

Non-uniform composition and permeability of a reservoir, commonly referred to as reservoir heterogeneity, is recognized as a major factor in the efficient recovery of oil during primary production and enhanced recovery operations. Heterogeneities are present at various scales and are caused by various factors, including folding and faulting, fractures, diagenesis and depositional environments. Thus, a reservoir consists of a complex flow system, or series of flow systems, dependent on lithology, sandstone genesis, and structural and thermal history. Ultimately, however, fundamental flow units are controlled by the distribution and type of depositional environments.

Reservoir heterogeneity is difficult to measure and predict, especially in more complex reservoirs such as fluvial-deltaic sandstones. The Appalachian Oil and Natural Gas Research Consortium (AONGRC), a partnership of Appalachian basin state geological surveys in Kentucky, Ohio, Pennsylvania, and West Virginia, and West Virginia University, studied the Lower Mississippian Big Injun sandstone in West Virginia. The Big Injun research was multi-disciplinary and designed to measure and map heterogeneity at various scales, and to develop tools and techniques to predict heterogeneity in existing fields and undrilled areas. The main goal was to develop an understanding of the reservoir sufficient to predict, in a given reservoir, optimum drilling locations versus high-risk locations for infill, outpost, or deeper-pool tests.

Results

Several lines of evidence substantiate the presence of heterogeneity in the Big Injun reservoir in Granny Creek field, West Virginia. These include the patterns of initial open flow and cumulative production, and the non-uniform behavior of injection pressures and rates during water-flood operations. An integrated analysis of stratigraphic, structural, seismic, petrographic, and engineering data has led to the conclusion that heterogeneity within the field is due to the interplay of both structural and stratigraphic controls. At the regional scale, geologic controls include the distribution of basement-related and detached structures, the distribution of sandstone facies and thickness patterns, and a pre-Greenbrier erosional event, the Greenbrier unconformity, that modified these patterns of sedimentation.

Depositional facies of the Big Injun sandstone in Granny Creek field are westward prograding river-mouth bars that comprise three more-or-less distinct tongues, which form the principal pay zone. Coarse-grained sandstones and conglomerates overlie the fine-grained river-mouth bars. Post-depositional diagenetic events include extensive quartz-cementation of the lower channel-fill sandstones; coating of sand grains with chlorite, leading to preservation of permeability where pore-throats were large in the proximal mouth-bar facies, or reduced permeability where pore-throats were small in the distal mouth-bar facies; and squashing of argillaceous clasts into pseudomatrix. Presumed barriers or baffles to oil movement within the reservoir are identified on geophysical logs and in cores, and include both shale breaks and zones of diagenetic cementation. The combination of several depositional units and diagenesis means that zones of high porosity and permeability are limited areally.

In Rock Creek field, maps and cross sections of porosity show large continuous zones of

relatively high porosity that correspond with facies identified from geophysical logs. These high-porosity zones are larger in areal extent than those in Granny Creek field.

Trends in cumulative production strike north-south in Granny Creek field. The largest single area of high production is in the northern half of the field, and corresponds in location with a north-south trending unit of the river mouth-bar facies. The north-south zone of high oil-producing wells is discontinuous in the central part of the field, and is much narrower in the southern half, where presence of faults or folds apparently affects production. Maps of porosity and permeability suggest presence of local fracture zones.

Within Granny Creek field, seismic data reveal a variety of structural interrelationships with areas of high primary and 10-year cumulative production. These include small-scale seismic structures, hinge areas between active basement blocks, areas marked by syndepositional growth over subsiding basement blocks, and an interplay between these structural elements. Small structures generally correlate with subsurface structures. In some cases these structures are interpreted to be detached. The interaction of shallow detached structures with basement-related structures is observed in the more productive northern part of the field.

In addition to these structural controls, stratigraphic and petrographic controls also have been documented. The cementation barriers of diagenetic origin commonly cut across bedding and facies and apparently subdivide the reservoir into compartments.

The combination of stratigraphic, structural, and diagenetic factors resulted in reservoir heterogeneity which significantly influenced the primary production performance of Granny Creek field. The evaluation and interpretation of the injection pressure data, pressure transient data, and the water flooding simulation results indicate significant permeability reduction around injection wells. The evaluation of the water flood performance and tracer tests indicate communication between the wells through low angle isolated fractures in overlying Greenbrier Limestone. The fracture responsible for well communication can be identified from the seismic interpretations. The communication problems were created by a combination of natural fractures in rocks above the reservoir and reduced permeability zones.

Approach

Regional stratigraphic cross-sections of the interval between the Greenbrier Limestone and the Sunbury Shale were constructed, and data from correlated logs were used to construct isopach and isolith maps of the Big Injun sandstones. Sandstones within the study area were divided into genetic types (channel versus bar) using gamma-ray log character. Within Granny Creek field these genetic types were further subdivided using both core and log data. Displays of porosity and permeability were prepared and correlated with initial potential and cumulative production trends. Cluster analysis was used to define electrofacies based on digitized geophysical logs; results were studied as a series of cross-sections. All available cores were cut and described, and thin sections were made and examined. Subcrop maps were prepared for both Granny Creek and Rock Creek fields, and surface fracture patterns were mapped over parts of both fields. Vibroseis seismic data were obtained over Granny Creek field, interpreted, and reprocessed. High resolution weight-drop seismic data were collected in order to image the Big Injun and overlying intervals and to document post depositional structural activity and evaluate its possible influence on the reservoir interval. A vertical seismic profile along one of the seismic profiles was used to design deconvolution

operators and improve seismic resolution.

Cores, well logs, and initial potential (IP) data were used to draw distribution maps of petrophysical rock properties including porosity, permeability, and fluid saturations for different zones. An approach for estimating permeability from well log data was developed. Injection pressure data, pressure transient data, and reservoir simulation results were used to confirm the significant reduction of permeability around injection wells.

A realistic model of porous media using "textural transforms" was developed and turned into a mathematical model (network model). The mathematical model was utilized to investigate fluid flow paths and flow blockage by particles. In addition, novel methods of quantifying key model parameters were developed.

Data collection efforts were focused on obtaining production data for both Granny Creek and Rock Creek fields. All data were verified and entered into a common computer account accessible by all project researchers. Computer programs were written to generate graphs, statistics, panel diagrams and maps. Analysis of lithofacies continuity and detailed analysis of well performance versus date of completion and well location were performed. Variograms of porosity, permeability and production data were computed and used with indicator kriging to map the probability that cumulative production exceeded particular cutoffs. These maps were compared with maps showing structure, presence of high-density zones and shales, and thickness maps of units within the Big Injun. Thickness, water saturation, and log-calculated porosity were used for estimating oil in place at each well location.

INTRODUCTION

The purpose of this research was to develop techniques to measure and predict heterogeneities in oil reservoirs that are the products of complex deposystems. The unit chosen for study was the Lower Mississippian Big Injun sandstone, a prolific oil producer from nearly 60 fields in West Virginia. The Big Injun is a drillers' term and generally refers to the first sandstone penetrated below the Greenbrier Limestone (Big Lime of the driller). In most cases, the first sandstone in this stratigraphic portion will be within the Pocono (Price) Formation. However, the pre-Greenbrier unconformity, which represents an erosion event that removed varying amounts of Pocono rock, is present throughout the productive area, so different Pocono-age sandstones pinch out against the overlying Greenbrier Limestone across the basin (Figure 1). Furthermore, recognition of red beds below the Big Injun reservoir in several fields under study has led to the realization that the sandstones above the red beds may be in the Maccrady Formation, which is strati-graphically above the Pocono Formation. Therefore, within the regional study area (Figure 2) it is important to know which Big Injun sandstone (Figure 1) forms the reservoir in the various fields of interest. Stratigraphic correlation through several of these fields suggests that the Pocono Big Injun is the only reservoir in Granny Creek field and the "Maccrady" Big Injun is the only reservoir in Rock Creek field. Other fields, however, contain reservoir sandstones in both formations.

Because of the discontinuous nature of the Big Injun sandstone, it was studied at various scales, including regional scale (23 counties), and field scale. The Granny Creek field in Clay and Roane counties, West Virginia, and the Rock Creek field in Roane County (Figure 2) were chosen for detailed study. However, Granny Creek field has been the main focus for analyzing geologic controls on heterogeneity in an oil producing area. Available data included geophysical logs, cores, seismic data, and a vertical seismic profile run as part of this research (Figure 3). The field has been developed by two companies that have contributed data for this research: Pennzoil (northern part) and Columbia Natural Resources (southern part). Analysis of these and other data has led to the conclusion that heterogeneities in the Big Injun reservoir sandstone are due to the complex interplay of stratigraphic, structural, and diagenetic factors, present at various scales. In this report, these heterogeneities and their geologic controls will be discussed in order of diminishing scale, from regional to inter-well.

Research Methods and Objectives

This research effort was designed and implemented as an integrated effort involving stratigraphy, structural geology, petrology, reflection seismology, petroleum engineering, modeling and geostatistics. Sandstone bodies were mapped within their regional depositional systems, then sandstone bodies were classified in a scheme of relative heterogeneity to determine heterogeneity across depositional systems. Facies changes were mapped within given reservoirs, and the environments of deposition responsible for each facies were interpreted to predict the inherent relative heterogeneity of each facies. Structural variations were correlated both with production, where the availability of production data permitted, and with variations in geologic and engineering parameters that affect production. Pore types were described and related to permeability, fluid flow and diagenesis, and petrographic data

were integrated with facies and depositional environments to develop a technique to use diagenesis as a predictive tool in future reservoir development.

Another objective in the Big Injun study was to determine the effect of heterogeneity on fluid flow and efficient hydrocarbon recovery in order to improve reservoir management. Graphical methods were applied to Big Injun production data and geostatistical methods were used to detect regional trends in heterogeneity. Geologic and engineering data on Big Injun reservoirs were used to construct facies maps.

Acknowledgements

The Consortium would like to acknowledge the assistance of scientists and engineers of the Columbia Natural Resources, Pennzoil, Quaker State, and Eastern American Energy companies. Specific thanks are due to Richard Beardsley, John Buurman, Joe Lemon, and Mian Ahmad of Columbia; Greg Morrison, Bill Toomey, Paul King, Roger Heldman and John Hagar of Pennzoil; Mike Brannock of Quaker State; and Scot Rodeheaver and Kent Schamp of Eastern American Energy for their advice and assistance throughout this project, particularly during the beginning phase of the research when they were often bothered on a daily basis for basic data. The cumulative production and initial flow maps used in this report came directly from Pennzoil and Columbia. Appreciation is expressed to Richard Larese of Amoco Production Co. for furnishing materials and important advice and to Samuel Hannah for supplying some of the data on a core from a Clay County well.

The Program Manager and Principal and Key Investigators were responsible for producing this report and wrote much of it. However, significant contributions were made by other members of the integrated research team. These researchers and their area of contribution are: Ron McDowell, Ana Vargo, and David Matchen (Geostatistical Studies); K. Lee Avary and Paul Londeree (Geology); Kim Timberlake (Computer Programming); Ilkin Bilgesu, Samuel Ameri, Thomas P. Meloy, Shahab Mohaghegh, Ashim Das, Wigo Dascalescu, Jason Garner, Qamer Malik, Darwin Molnar, and Ujjal Chatterjee (Petroleum Engineering); James Britton (Petrology); Xiangdong Zou (Stratigraphy); Kurt Donaldson, (Expert Systems, GIS, and Stratigraphy); and Li Zheng (Structural Geology and Seismic Studies); Guoqi He (computer applications and seismic studies), Dave Hunter (seismic modeling), and Richard Guiler (regional structural framework).

EVIDENCE OF HETEROGENEITY IN THE BIG INJUN RESERVOIR

Regional Heterogeneity

Evidence for heterogeneity in the Big Injun on a regional scale is shown by the distribution of hydrocarbon production in distinct fields across central West Virginia. Of the six fields studied (Figure 2), the easternmost of these fields traditionally have been considered to be fairly simple updip unconformity traps. Those on the west, such as Blue Creek and Rock Creek fields, have not been studied in detail and little has been published concerning their relationship to the eastern fields. However, the western fields appear to be regionally downdip from the truncated margin of the reservoir, and thus it is presumed that the trapping mechanism is different than that for fields to the east.

Field-scale Heterogeneity

At the field scale, shallow oil reservoirs like the Big Injun sandstone have been developed as if they were homogeneous units enclosed by thick lateral and top seals. Well spacing has commonly been based on optimum spacing dictated by owned acreage rather than any precise knowledge of reservoir heterogeneity. Most secondary recovery projects in these fields have been undertaken with little more knowledge or foresight beyond that used to initially develop the field. In part, this is because secondary recovery projects generally incorporate wells that were drilled on regular spacing for primary production. Such is the case with Granny Creek field. The five-spot pattern (Figure 4) used for secondary recovery is a modification of well spacing utilized during primary recovery. Even though Columbia's secondary recovery project has been a commercial success (John Buurman, 1992, personal communication), it still has had a number of problems related to reservoir heterogeneity.

Reservoir heterogeneity in Granny Creek field is indicated by patterns of primary production shown by two maps of the field. Specifically, high initial volumes of oil (Figure 5) occur in two trends; one that trends slightly east of north on the west edge of the field and another trending slightly west of north through the center of the field. The large contrast in values across these two trends indicates internal heterogeneity within the Big Injun reservoir. The map of cumulative production (Figure 6) has an appearance that is similar, but not identical to, that of initial flows (Figure 5). Reliable data on field pressure are difficult to find in this old field.

Drilling History

Historical production data for Granny Creek and Rock Creek fields are limited and possibly unreliable due to the age of the fields (Granny Creek discovered in 1924; Rock Creek discovered in 1906). Information that is available and verifiable for the entire life of both fields is the location and date of completion of producing oil wells. In an attempt to get a preliminary assessment of field-scale reservoir heterogeneity, the distribution of dates of completion and geographic location of producing oil wells were analyzed (McDowell, et al., 1992).

Completion data for both fields are not distributed uniformly in time (Figures 7a and 7b). Rather, well completions are clustered into groups of variable size separated in time by periods of no successful drilling activity. To determine if clusters of completions in time represent the discovery of new production within a field or merely offsets from existing production, locations of all wells completed during each time period were plotted on a map of the appropriate field (Figures 8a-f and 9a-f). Each map generally contains two distinct sets of wells: (1) those scattered throughout the field, obviously adjacent to existing wells (offset), and (2) those more tightly grouped in parts of the field where previous well completions are sparse or lacking (discovery). Comparison of the completion distribution maps for Granny Creek and Rock Creek reveals distinctly different patterns of development. After the discovery period (1924 - 1930), Granny Creek completions (Figure 8a-f) show a fairly constant mix of a few offset wells and one or more tight well groupings representing areas of new production. On the other hand, Rock Creek (Figure 9a-f) is dominated by two major periods of completions (1906 - 1924 and 1961 - 1976) and minor offset drilling throughout the rest of the life of the field. Distribution of production appears "patchy" for Granny Creek, but much more continuous for Rock Creek, implying that the probability of discovering additional new production is greater in Granny Creek than in Rock Creek.

Water-Flooding Performance

Modeling and simulation studies in Granny Creek field were focused on performance predictions during waterflooding phase of the production because sufficient primary production data were not available. The primary purpose was to investigate the validity of geological model, core analysis and log interpretation results. Two areas, one in the northern part and one in the southern part of the Granny Creek Filed, were selected for modeling and simulation studies (Figure 4).

Three adjoining waterflood patterns in the south show non-uniform injection pressure behavior. For example, one injection well exhibited a pressure nearly half as much as the other wells, whereas injection rates were quite similar. Furthermore, water breakthrough took place almost immediately in one of the patterns (P2), whereas the other patterns (P1 and P3) produced oil for several years without water breakthrough, resulting in significantly different oil and water production for the three patterns (Figure 10a and 10b). Direct communication between the injection and production wells, possibly through fractures, must exist in this area. A number of wells in the field have exhibited direct communication in a southwest to northeast orientation (Figure 4). Lines drawn between wells on this map indicate communication between wells as indicated by rapid breakthrough, pressure or pumping and tracer tests. This map suggests a linear trend in reservoir heterogeneity within the field that is distinctly different in characteristics and orientation from that indicated by primary production.

To understand and quantify the effects of fractures (or channels) and obstacles (barriers) on the waterflooding performance, a novel approach (transmissibility modifications) was developed and utilized to simulate isolated fractures and barriers in the southern study area. This modeling approach allowed accurate prediction of waterflood production performance in the three adjacent patterns (Figure 10a and 10b; details in Appendix A). Simulation studies also revealed that communication between injection and production wells did not take place through the producing horizon (Big Injun), but rather most likely the Greenbrier Limestone

(Big Lime). This conclusion is consistent with the results of the oriented core study and observations by down-hole televiewer run in one of the injection wells in the northern part of the field.

The study area in the north also consisted of three adjoining five-spot patterns. Oil production from the three patterns exhibit only minor differences (Figure 11a). The injection rates and pressures also exhibit a more or less uniform behavior in this area (Figure 11b). Waterflood production performance in this area can be satisfactorily predicted (Figures 11a) based on the reservoir description obtained from the geological interpretations, core analysis, well log interpretation, and injection rate histories. These observations suggest that heterogeneities in this area are confined to changes of rock properties (porosity, permeability, and thickness) in the waterflood patterns.

Although waterflood production performances in both study areas were simulated successfully, injection pressures could not be simulated satisfactorily. Simulated injection pressures in both areas are consistently lower than actual field values. Simulated injection pressures compared favorably to field injection pressures only after the introduction of localized low-permeability zones. Analysis of injection pressure/rate data across the field as well as results of the fall-off tests on two injection wells (see Appendix B for details) generally confirmed the presence of an area of reduced permeability around injection wells. The mechanism responsible for this permeability reduction is not well understood, but possibilities include clay swelling/migration, wax deposition, or sludge formation. Clay swelling or migration due to the heterogeneities in pore surface mineralogy was investigated as a possibility for permeability reduction during water injection (Appendix C). Influence of particle movement (clay migration) on permeability reduction has been also studied and documented in Appendix D.

High injection pressures commonly exceeded original formation pressures, and may be responsible in part for establishing communication between the Big Injun and Greenbrier Limestone. The high injection pressure are necessary because of the severe permeability reduction around injection wells. Therefore, the combination of natural fractures in brittle rocks above the reservoir and reduced permeability zones created many of the communication problems.

STRUCTURAL CONTROL OF REGIONAL HETEROGENEITY

Introduction

Regional distribution of both detached and basement structures has directly and indirectly influenced regional distribution of oil production from Big Injun reservoirs. Basement structure will be discussed first inasmuch as the configuration and movement of basement blocks influenced the deposition of sands that have become the Big Injun reservoirs. Detached structures in the region were formed later by the late Paleozoic Alleghenian orogeny, probably well after the Big Injun sands were lithified.

Most basement structure formed as the result of two deforming events. The older of the two, called the Grenville orogeny, formed the continental crust (basement) under the Appalachian foreland (Beardsley and Cable, 1983). Radiometric dates of samples taken from the basement date at approximately one billion years before present (bp). The second deforming event relates to the post-Grenville breakup of the North American continent. This second deformation, dated at approximately 550-600 million years bp (Shumaker, 1986a), formed the Interior Graben System that includes normal and strike-slip faults of the Rome trough in the study area. Most basement faults and arches (Figure 12) that affected Paleozoic sedimentation in the outer foreland appear to be reactivated basement structures formed by these two deformations. Lack of precise data concerning structure of the Precambrian basement forces simplification of what must have been a more complex history, and likewise, it forces speculation on the time of formation of many of the basement structures which have been mapped. Assignment of an age and origin to a particular basement structure largely rests on the physical relationships between basement and adjacent Paleozoic sediments and the dip of intra-basement seismic reflections. Basement structure can be considered to have been formed by extensional deformation associated with formation of the Interior Graben System if bedded sediments lie adjacent to vertically offset basement, whereas low-angle, east-dipping seismic events within the basement are considered to be thrusts formed by the Grenville orogeny (Beardsley and Cable, 1983). It is likely, however, that many normal faults considered part of the Interior Graben System are, in reality, Grenville structures that were reactivated or modified during Cambrian extension.

Basement Structure

Regional distribution of Paleozoic lithofacies and thicknesses (Donaldson and Shumaker, 1981; Shumaker, 1986a) indicates the locations of large basement blocks that differentially subsided during the Paleozoic (Figure 12). The regional study area largely lies within the Ohio-West Virginia block, the Rome Graben, and the horst block along the east margin of the trough which Kulander, et al. (1980) called the Central West Virginia arch. Granny Creek field lies on a northeast-striking cross-fault zone at the eastern margin of the Rome Graben. The absence of deep drilling and seismic data in the Rock Creek area does not allow definition of basement structure there.

The West Virginia dome, also called the Pocono dome or the Beverly uplift, is another regional feature important in the sedimentary and structural development of the study area. That this dome was high-standing during the mid-Mississippian is indicated by pre-Greenbrier

erosion of sediments as old as the Upper Devonian Hampshire (Catskill) red beds near the center of the dome. That it was a structure, at least a west-plunging nose, is indicated by low-angle dip of subcropping (pre-Greenbrier) units away from the dome on its north, west, and south flanks. The origin of the dome is uncertain, but it is presumed to have been a basement feature that grew during Mississippian time to influence the extent and depth of erosion that occurred prior to deposition of carbonates and sands of the Greenbrier Group. The eastern extent of Big Injun reservoirs and hydrocarbon production associated with them are limited by erosion that occurred during this time interval.

Detached Structure

The study area is located at the outer margin of detached deformation in the Appalachian foreland. These structures were formed by the Allegheny Orogeny of Permian age, and did not affect Paleozoic sedimentation. A number of authors have proposed early (mid-Paleozoic) growth of certain detached structures in the Appalachian foreland. However, a strong interrelationship between the position and trend of basement structure and overlying detached structure (Shumaker, 1986b) in the outer foreland suggests that any reported growth may relate to underlying basement structure rather than pre-Alleghenian growth of detachment.

Several horizons were zones of regional detachment within the Appalachian foreland, including the Cambrian Rome Formation, the Ordovician Martinsburg Formation, Silurian salt beds, Devonian shales, the Mississippian Mauch Chunk Formation, and Pennsylvanian coals. The difference in structural configuration between the Pittsburgh coal (Figure 13) and the Greenbrier Group (Figure 14), that lies directly above the Big Injun reservoir, demonstrates structural disharmony in the Granny Creek-Rock Creek area. This contrast is greatest at the southeastern margin of these regional maps. Evidence of disharmonic deformation is also seen at outcrop scale in the field and on seismic within this area.

This disharmony indicates the presence of either a major or many minor horizons of detachment above the Big Injun reservoir. Seismic studies suggest that the Upper Devonian Huron Shale is the major detachment horizon below the Big Injun reservoir within the Granny Creek-Rock Creek study area.

Fractures

Joints within surface rocks at the Granny Creek and Rock Creek fields are vertical to high dipping and have complex strike patterns (Table 1). The trend of face cleats in surface coals (Kulander, et al., 1980) is approximately east-west in the Rock Creek-Granny Creek area, but there is an abrupt change in strike to west-northwest along the western margin of the study area in Kanawha County.

Small thrust faults mapped at the surface in the Devonian shale section (Gas Research Institute, 1991) and in basal limestones of the Greenbrier Group (Dowell Schlumberger, 1986) strike southwest parallel to the trend of surface folds. Production of gas from small thrust faults and their attendant cross faults (Gas Research Institute, 1991) within the otherwise tight Devonian shale suggests that small faults may be an important source of secondary porosity in other brittle reservoirs such as the Big Injun in the study area. The occurrence of very small thrusts in areas traditionally considered to be beyond the margin of detachment in the

Appalachian foreland suggests the necessity of reassessing the role of very small thrusts in creating fracture porosity in rocks at the periphery of other foreland fold belts. Such small thrusts may not affect primary production, but they may cause serious problems during secondary recovery, as will be discussed later.

Oriented cores from three wells within the Rock Creek-Granny Creek area have been analyzed for induced fractures that reflect the trend of regional in-situ stress. All three cores, two in limestones of the Greenbrier Group in Granny Creek field, and one in the Devonian shale at the northeastern margin of Figure 13, indicate that principal in-situ stress direction for the region is N75°E to east (Table 1).

Relation of Structural Position to Production

Big Injun oil fields are found in synclines and on the flanks of anticlines (Figure 14). The synclinal nature of the oil traps in the Big Injun sandstone is apparent on the map of Greenbrier structure as compared with the map of the Pittsburgh coal because of the disharmony between structure of these two units. Oil accumulations occur at the northern end of the basement-cored Warfield anticline, but the synclines in which the oil occurs may, in part, be detached at the Devonian shale level. Analysis of basin subsidence and the time of growth of structures in the Rock Creek-Granny Creek area has led to a better understanding of pathways and timing of hydrocarbon migration in this part of the basin. The likely source rocks, upper Devonian and lower Mississippian shales, for Big Injun oil entered the oil window during the Pennsylvanian before the Allegheny orogeny. Basement structures grew throughout the Paleozoic; thus primary migration of hydrocarbons occurred into several fields above basement structures. In the case of Granny Creek and Rock Creek fields, the adjacent basement anticline was the ancestral Warfield-Queen Shoals-Minnora anticlinal trend. Secondary (re)migration may have occurred during the Allegheny (Permian) Orogeny into detached structures formed by that terminal orogeny. The area between these eastern fields at Rouzer and Granny Creek and the western fields at Rock Creek is structurally high and produces only gas from the cap.

Thus, the eastern fields that include Rouzer, Granny Creek, and Tariff (Figure 14) along the unconformity occur above the structural level of the regional oil-water contact, which has only been established in the "Maccrady" Big Injun sandstone in the western field at Rock Creek between -1140 and -1170 feet. The western fields, as typified by Rock Creek, have a water leg, whereas the eastern fields, as at Granny Creek, have no water leg. Slight differences in elevation of the gas/oil contact at Granny Creek, Rouzer, Blue Creek and Tariff is thought to be a function of: (1) the distribution of the various reservoir quality sands in the Pocono and "Maccrady" Big Injuns; (2) by-passing of oil in closed synclines as the gas cap of the large ancient field has expanded with erosion of overburden, and possibly; (3) late-paleozoic elevation of synclines along the southeastern margin of the study area by detached deformation. The long-standing question concerning the absence of water in certain Appalachian oil fields (Davis and Stephenson, 1929), at least in the case of the Big Injun reservoir, is not considered to be unusual once details of the regional geology and the timing of subsidence and deformation are known. Other reservoirs in the Appalachians, noted for their absence of down-dip (bottom) water, may have been created under similar conditions.

STRATIGRAPHIC CONTROL OF REGIONAL HETEROGENEITY

Introduction

A regional stratigraphic framework of the Pocono (Price) Formation was established in order to determine the correct correlation and continuity of Big Injun sandstones on a regional scale. Six oil fields producing from "Big Injun" sandstones, including Rock Creek, Tariff, Blue Creek, Granny Creek, Clendenin and Pond Fork fields, in Roane, Kanawha and Clay Counties of West Virginia (Figure 2) were selected for stratigraphic comparison and are distributed within a 20 x 30 mile area. Among these fields, reservoir heterogeneity within the Granny Creek field is best understood.

Correlation

The uppermost Sunbury Shale of Early Mississippian age represents the maximum flooding surface of a sequence bounded by the pre-Berea unconformity at its base and the pre-Greenbrier unconformity at its top. This highly radioactive shale is laterally extensive and was used as the datum in the regional study of 23 counties in western West Virginia. Where this shale loses its radioactivity in the eastern part of the area (Riddlesburg Shale - Bjerstedt, 1986; Boswell, Donaldson, and Lewis, 1987), multilateral sandstones that overlie this shale at a uniform interval also serve as a secondary datum and confirmation of the correlation. The Maccrady Formation, a red shale with sandstone interbeds between the Pocono and Greenbrier formations in the outcrop of southeastern West Virginia, is recognized in the subsurface in southwestern West Virginia and its presence separates the Big Injun into the Pocono Big Injun below and the "Maccrady" Big Injun above these redbeds. This distinction supports the correlations based on interval thickness above the Sunbury Shale in the six selected oil fields.

Several sandstones in the Lower Mississippian pinch out against the pre-Greenbrier unconformity (Figure 1). Blue Creek, Clendenin and Granny Creek fields all mainly produce oil from the first sandstones named "Big Injun" underneath the unconformity. Redbeds underlie the Big Injun sandstones in Blue Creek field and the laterally equivalent sandstones of the Rock Creek field define its oil reservoir as "Maccrady" rather than Pocono (Figure 15).

The subcrop map of the pre-Greenbrier Limestone (Figure 16) shows the different Lower Mississippian sandstones immediately underlying the Greenbrier Limestone in the regional study area. The map indicates that the reservoir rock immediately underlying the Greenbrier Limestone is (1) Pocono Big Injun for Granny Creek and Tariff fields, (2) "Maccrady" Big Injun for Rock Creek and Blue Creek fields, and (3) "Maccrady" and/or Pocono Big Injun for Clendenin and Pond Fork fields. Within Rock Creek field, the major oil reservoir is the "Maccrady" Big Injun sandstone, whereas minor production is from the overlying basal oolitic unit of Greenbrier Limestone. The Tariff field consists only of a reservoir in the Pocono Big Injun sandstones. Within Blue Creek field, the major reservoirs are the "Maccrady" Big Injun, upper Weir and middle Weir sandstones, whereas the basal unit of the Greenbrier Limestone is its minor reservoir. Within Granny Creek field, the major reservoir is the Pocono Big Injun sandstones, and its minor reservoir is the so-called Squaw sandstone, time-equivalent to the upper Weir sandstone. Within Clendenin and Pond Fork fields, major

reservoirs include "Maccrady" Big Injun, Pocono Big Injun, upper Weir and middle Weir sandstones.

Heterogeneity Between Oil Fields

Stratigraphic heterogeneities between oil fields seem to be related to the control of basement structures (Figure 17) on sedimentation of the Big Injun sandstone, or conversely, its erosion as a result of uplift of the West Virginia dome. The thickness map of the Pocono Big Injun (Figure 18) shows it rimming the West Virginia dome in a narrow belt with its eastern edge truncated by the pre-Greenbrier unconformity. In the regional study area, this narrow belt of sandstone is 5 to 18 miles wide from Fayette to Roane counties, at least 20 feet thick, oriented N10°W, which is also the trend of its eroded edge, and exhibits a facies change to shale along its western margin. This facies change to shale occurs between Granny Creek and Rock Creek fields. The Pocono Big Injun sandstones are thickest within the eastern margin of the Rome trough. Maximum sandstone thickness of about 60 feet occurs in two separate pods along this belt, one in Fayette County and the other in Granny Creek field. Core and geophysical log data from the Granny Creek field indicate this sandstone was deposited as distributary-mouth bars and channel fill of a bed-load fluvial delta. The thick sandstone accumulations along this narrow belt probably represent two locations where ancient rivers of separate drainage basins deposited deltaic sediments at the shoreline. Probably, lateral switching of delta lobes by these two river systems, other small streams, and littoral drift account for the sandstone thicknesses along other segments of this narrow belt.

Pocono Big Injun sandstones occur in Wirt and Ritchie counties in a southwest-northeast trending belt, which is about 20 to 30 miles wide, with eroded margins as a result of the pre-Greenbrier unconformity to the east and the pre-Pennsylvanian unconformity along the southern (Wirt and Wood counties) and western (Wood and Pleasants counties) margins. This belt of sandstone in the study area is generally 60 to 120 feet thick, thickening northward, bifurcating southwestward, and exhibiting a facies change to shale to the south in Roane County where it merges with the previously mentioned northwest-trending belt of Pocono Big Injun. This thicker belt of sandstone is interpreted to represent southwesterly prograded fluvial-deltaic deposits in the study area probably supplied by an ancient river from the eastern orogenic mountains that flowed around the northern part of the West Virginia dome, and thins and ends in the area of the pre-Pennsylvanian unconformity west of the Burning Springs structure.

The "Maccrady" Big Injun sandstones are thickest in Mason and Cabell counties and continue as a thick trend northward into Ohio (Figure 19). These sandstones thin into West Virginia and show lobes mainly to the east and south where facies change to shales occurs. One such lobe extends into the Rock Creek field, where truncation by the pre-Greenbrier unconformity also affects the thinning of the sandstones. The "Maccrady" Big Injun sandstones are concentrated along the western edge of the Rome trough and spread within the trough with thinning along the axis of the Warfield anticline. Both Pocono and "Maccrady" Big Injun sandstones are recognized in the thick sandstone trend of southeastern Ohio that extends into southwest West Virginia south of the Burning Springs anticline. These Big Injun sandstones represent fluvial-deltaic deposits of a very large river system (Figure 20) that developed with the merging of orogenically derived rivers from the east with cratonic-derived

rivers from the north and northwest (ancient Ontario River drainage system). The large drainage basin was structurally controlled (Zou and Donaldson, 1992b).

Basement structures apparently controlled the paleoflow directions of Big Injun rivers as well as the distribution patterns of erosion associated with the West Virginia dome. This relationship is evident at the regional scale between oil fields, and the local scale within fields such as the Granny Creek field. Lateral discontinuities are located where basement structures were active during Early Mississippian sedimentation and erosion.

In summary, all six selected oil fields claim the Big Injun sandstone as their reservoir rock, but detailed correlations recognize discontinuities that establish stratigraphic heterogeneities at the regional scale in the following three ways:

1. lateral discontinuities result from total or partial erosion of the Big Injun sandstones by the pre-Greenbrier unconformity and/or the pre-Pennsylvanian unconformity.

2. lateral discontinuities result from facies changes of the sandstones to shales at the distal margins of the deltaic river-mouth bars and/or fluvial channels.

3. vertical discontinuities result from shales separating Pocono Big Injun sandstone from younger "Maccrady" Big Injun sandstone.

FIELD-SCALE HETEROGENEITY

Introduction

This part of the report describes reservoir heterogeneity within the Granny Creek and Rock Creek fields. Heterogeneities in structure, porosity, permeability, and petrographic characteristics of the reservoir rock are present and can be related to spatial patterns in initial potential and production.

The section on structural geology describes northeast-trending, low-relief folds of small areal extent, and presence of fractures oriented in the same direction. Seismic work shows that major basement faults created blocks under Granny Creek field. These blocks subsided and rotated during the Paleozoic and possibly during deposition of the Big Injun sandstone. Small-scale features placed on structure maps represent detached folds. Local disruptions in reflections from the Big Injun and surrounding intervals appear to be in response to fracture zones or faults. In some cases, these zones lie near wells found by operators to experience rapid water breakthrough during secondary recovery.

The Big Injun in Granny Creek field consists of a relatively fine-grained sandstone representing deposition in distributary mouth bars, and an overlying, coarser-grained sandstone deposited in point bars and channels. Heterogeneities include: thin shales; variability in grain size; and calcite, siderite and quartz cement. Depositional bodies within this reservoir are aligned north-south. The Big Injun within Rock Creek field is mainly a fine-grained sandstone deposited as distributary mouth bars, with shale and carbonate zones. Discriminant function analysis of geophysical logs delineated four electrofacies: channel, fluvial mouth bar, marine mouth bar, and distal bar. Oil production in both fields is largely limited to marine or fluvial bar facies. Cross-sections of porosity computed from logs shows zones of low porosity within the Big Injun separating better reservoir sandstones. Zones of relatively high porosity appear two to five times larger in Rock Creek than Granny Creek field. Both primary depositional and diagenetic heterogeneities exist in both fields. The best porosity and permeability are present most consistently within the proximal mouth bar facies. The main factor in preservation of porosity is chlorite coatings restricting quartz concentration.

Maps of average porosity and permeability measured from cores in Granny Creek field show similar north-south trends paralleling isopach maps of facies of the Big Injun. Estimating permeability from log-calculated porosity is most successful when regression equations are computed for each facies. Both pressure transient tests and analysis of initial potentials show that water flooding significantly reduced permeability around the well bores.

North-south trends are also evident on a map of cumulative oil production in Granny Creek field, especially maps generated by indicator kriging. Highest values occur in the northern half of the field. The main north-south trend in oil production occurs between two parallel trends in shale depositional barriers defining units within the lower, finer-grained portion of the Big Injun. The upper coarser unit within the Big Injun may act as a reservoir seal where it is highly quartz cemented. Irregularly tabular, diagenetic high density zones within the Big Injun cut across bedding at low angles, and may act as barriers to oil movement. Subtle folds and faults coincide in location and orientation with presence of the high density zones, suggesting that carbonate cementation of the Big Injun occurred in areas fractured during deformation. Some success was experienced in locating above-average oil

production within Granny Creek field by seismic methods. Study of Rock Creek field shows a correspondence of production trends with presence and thickness of high density zones.

Problems experienced during secondary recovery included early water breakthrough for some wells. This well-to-well communication was probably caused by fracture porosity in the reservoir and the overlying Greenbrier Limestone.

Structural Controls - Granny Creek Field

The structure of Granny Creek oil field (Figure 21) was mapped on the Big Injun reservoir based on geophysical logs from 642 wells. As noted in the first annual report (Donaldson, et al., 1992), the quality of well data in West Virginia always is suspect in regard to well locations, datums, and depths to reference horizons and requires checking for accuracy. This was accomplished in Granny Creek field by carefully comparing data printed on geophysical logs with the original driller's logs, company documents, and a large-scale topographic map provided by Columbia Natural Resources, Inc. Well locations were cross checked using topographic and company field maps. The datums of 20 logs were corrected and used in the study. A few logs were dropped from consideration because of a missing well number, no log datum, or poor log quality. Logs in the northern and central parts of the field generally are of good quality and have reliable datums because these wells were completed in the 1960's and later. Data from older wells were found to be less reliable and commonly more difficult to check because original well records were lost. The general shape of the structure (Figure 21) compares well with structure mapped using seismic data and as mapped on surface coals (Figure 13).

The map suggests that a number of small wave-length, low-relief folds are present in the field. Folds appear to be caused both by basement and by deformation above the Devonian shale detachment horizon.

Structural Controls - Rock Creek

The position of Rock Creek field is controlled by structure. Rock Creek lies in the Jarrett syncline and wraps around the nose of the Milliken anticline to the west. The eastern portion of the field lies along the western flank of the Arches Fork anticline. Oil collected in the Big Injun sandstone around the trough of the Jarrett syncline as shown by the close relation of structure to the field outlines (Figure 22). A map of initial production reports (Figure 23) shows that wells completed during the initial drilling phase (1906 - 1924) produced oil, with a gas component in the southern part of the field.

Drilling reports from the later episode (1961 - 1976) indicate concurrent oil and water production (Figure 23). A simple structural cross section (Figure 24) shows the relationship between the presence of water and the structural low to the north of the field. Estimates for the elevation of the up-dip limit of water production, roughly equivalent to the oil-water contact, based upon the relationship between water reports and structure, indicate that the limit may lie between -1100 and -1150 feet. Core analysis from two Quaker State wells position the oil-water contact at -1140 and -1169 feet, respectively.

FIELD-SCALE HETEROGENEITY INTERPRETED FROM SEISMIC STUDIES

Introduction

The main objective of this portion of the study was to determine whether heterogeneity within the reservoir and surrounding intervals can be identified seismically. Surface seismic data was collected at two different times during the project. The initial surveys of the field were conducted using a conventional Vibroseis source. Six Vibroseis lines representing a total of approximately 28 miles of common midpoint coverage were initially obtained for this study (Figure 25, lines 1-6). Two of these lines (lines 5 and 6), representing a total of 14 miles of data, were collected in 1988 and provided to us for interpretation by Columbia Natural Resources, Inc. The fold of the Vibroseis data is generally around 30, with 110 foot group interval, and input frequency range from 20 to 120 Hz. Following the interpretation and reprocessing of the Vibroseis lines, 13.5 miles of additional high resolution seismic data were collected over selected areas within the field (lines 12 through 18 on Figure 25). The source used in the high resolution survey was an accelerated weight drop. Bandwidth of the weight drop data is approximately 40-140 Hz. The fold of the weight drop data is optimally 48 with a group interval of 45 feet. Seismic surveys conducted for this study included three vertical seismic profiles (VSP). The source used to generate the VSP's was also Vibroseis. The source characteristics of the surface and VSP data sets were matched. Three additional weight-drop lines, each 1500 feet long, were collected using a 22.5 foot group interval. Bandwidth of these data was approximately 40-250Hz.

A typical Vibroseis seismic line through the field is shown in Figure 26. This line (Line 2; Figure 25) cuts through the middle of the field. Prominent reflection events along the line were identified using synthetic seismograms compiled from density and sonic logs from the field and surrounding area. Synthetics compiled from sonic logs outside the field were used to identify prominent reflection events from the organic-rich Huron Shale, the Onondaga Limestone, the Newburg and Keefer sandstones, the Trenton Limestone, and deeper intervals.

In Clay 2509, sonic and density logs were collected along with the three vertical seismic profiles. Clay 2509 is noted as the VSP well in Figure 26. This well extends several feet below the Big Injun. A synthetic seismogram (Figure 27) was calculated using an average wavelet extracted from the downgoing wavefield measured in the vicinity of the Big Injun sandstone from the VSP. The match between the synthetic seismogram and seismic data near the well forms the basis for relating individual reflection events in the zone of interest to subsurface stratigraphic intervals. The Big Injun sandstone is marked by a large amplitude negative cycle at 0.31 seconds produced by the large negative impedance contrast between the overlying Greenbrier Limestone and Big Injun sandstone. This reflection event is easily followed across Line 2 and throughout the field.

As noted in earlier discussions, the field lies in the Appalachian Plateau province of the central Appalachians along the eastern margin of a Cambrian-aged, failed-rift complex known as the Rome Trough. A slight drop of the pre-Cambrian basement reflector into the trough is noticeable on Line 2 (Figure 26).

An example of the weight drop data is shown in Figure 28. These data are from Line 17 which parallels the central part of Line 2 (Figure 25). The resolution of shallow reflectors by the weight drop source is better than that obtained with Vibroseis. The weight-drop lines were concentrated in areas of high cumulative production where extensive secondary recovery

(water-flooding) operations have been undertaken. One of the objectives to be achieved with the high resolutions weight-drop data was to determine whether these basement faults were active following the deposition of the Big Injun sandstone.

In the following sections, seismic evaluations reveal some relationship between heterogeneity within the structural framework of the reservoir and oil production. While seismic data do not resolve each of the numerous stratigraphic and petrographic controls on production within Granny Creek, analysis indicates that seismic studies can play an important role during exploration, in-field development, and secondary recovery operations within heterogeneous reservoirs.

Basement Faults

The basement isotime map (Figure 29) shows that major basement faults subdivide the basement into blocks, which (actively) subsided or rotated into the Rome Trough along a hinge or high area east of the field. Approximate locations of these hinge lines at different periods of time throughout the Paleozoic is shown in Figure 30. Fault block subsidence and rotation were consistently into the Trough. Subsidence and rotation occurred at different rates from the Early Cambrian through Mississippian time, as revealed from an analysis of travel time differences through successive stratigraphic intervals (Figure 31). In Figure 31, 1 and 2 refer to subdivisions southeast of the hinge areas and in the southeastern part of the field, 3 refers to the basement block bounded by faults A and B, and 4 refers to the basement block northwest of Fault B. Subsidence in meters/million years (not compensated for compaction) is measured relative to the southeastern edge of the line. Southeastern basement blocks 1 and 2 on Figure 31 remained structurally high throughout the Paleozoic. The southeastern margin of the field lies over this basement block.

The western limb of the syncline and margin of the field appear to be controlled in part by periodic reactivation of a deeper basement fault (basement fault B and AB of Figure 29). The displacements have not always been downward relative to the eastern margin of the field into the Rome Trough. Inversion or relative uplift of the northwestern basement block along fault B and AB to the south occurred during the late Ordovician, Devonian, and Pennsylvanian periods of the Paleozoic, resulting in the present day structural high along the western margin of the field.

Correlation of basement fault patterns observed in the seismic data reveals the presence of a basement fault (basement fault A in Figures 26 and 29) that cuts across the field. Correlation of the fault from line to line across the field suggests the presence of a pronounced "right-lateral" bend in the fault trace. This bend is observed in the travel time and isochron maps of all overlying intervals. Whether variation in the trend of the fault is simply due to an irregularity in shape occurring during normal fault offset or is due in part to strike-slip or transtensional offset, is not known.

Across the northern half of the field, patterns of growth from the overlying Lower Cambrian through Mississippian intervals consistently reveal an imprint of basement fault A, indicating active growth of this structure during Paleozoic sedimentation. Maximum subsidence trends during successive periods of time through the Paleozoic (Figure 32) are concentrated in the northern part of the field between faults A and B (Figure 29). To the south, the basement fault extends along the western margin of the field, but is poorly defined because it lies at the edge of data coverage. The isochron map of the Middle Cambrian

Rome Shale indicates that thickening to the west of Fault AB (Figure 29) is much less than that observed across Faults A and B through the center and northwestern margins of the field respectively. This suggests that fault blocks northwest of faults A and B rotated downwards to the north and dropped to the west.

Indications of post Big Injun fault reactivation are observed in the Vibroseis data, however, these observations are limited. The isochron map from the Big Injun to a shallow Pennsylvanian reflection event (Figure 33), compiled from weight-drop data, reveals some thinning from south-to-north within the field. This thinning occurs southeast of basement fault A and forms a trend that is parallel to it. The relative uplift of the fault block north of fault A is atypical, since this central block has generally subsided relative to southeastern block. The possibility that uplift of the central block occurred during deposition of the Big Injun is suggested by thinning of the Big Injun observed along Line 6 (Figure 34) south of Fault A (located approximately at CMP 620). Local thinning and thickening of this interval is observed within the field. Although there is no clear relationship between patterns in the isochron and production variability, the most highly productive areas of the field are located north of this structural hinge, which is parallel and southeast of underlying basement fault A.

The weight-drop lines provide additional detailed information about the Big Injun-to-Onondaga interval. The Big Injun-to-Onondaga isochron (Figure 35), which was compiled from both the weight-drop and Vibroseis data, also reveals the influence of faults A and B during deposition of this interval. A pattern of thickening over the central block shows that the central block moved down relative to the southeastern and northwestern blocks during this period of time. Subsidence of the central block was already defined by the earlier Vibroseis survey. However, weight-drop data provide additional detail concerning thickness variation of this interval in the northern more highly productive areas of the field.

Small-Scale Folds

Arrival time variations for the Big Injun reflection event reveal that the reservoir interval is disrupted internally by small-scale folds. These time structures are believed to be detached folds based on the disharmony between the travel times to the Big Injun and lower Huron or Onondaga. In places isopach thickening is greater than the structural relief along the Big Injun reflector. The low in the Huron over the central basement block suggests that some of the disharmony between the configuration of the Big Injun and the Huron reflectors (Figure 36) is, in part, the result of basement growth as noted earlier.

Although shallow detachment of the section appears to be the source of disharmony between the Big Injun and the organic-rich Huron Shale, lack of reflection continuity in this interval makes it difficult to locate a specific decollement zone(s). Weak continuity of reflectors within the Huron-to-Big Injun interval, when visible, suggests that this disharmony extends almost to the Huron. Vertical disharmony between these "noisy" reflectors is also observed, indicating that these folds may be the result of incremental growth of detached structures at various levels above the lower Huron.

The possibility that travel time variations to the Big Injun are simply due to relief on the unconformity is ruled out because of a general lack of correlation between seismic travel time variation to the unconformity and thickness variations of Big Injun intervals exposed beneath the unconformity. This conclusion is also consistent with the observation that these small folds are observed in reflectors above and below the Big Injun/Greenbrier reflector rather

confined to it. Although net relief along this reflector must be the result of both post-unconformity deformation and erosion, the contribution of erosional relief to arrival time variation is relatively minor and not resolvable.

Time-structural features with wavelengths of a half-mile or less generally correlate with folds on the structure map of the Big Injun. The possibility that these time-structure are due to static and velocity errors is ruled out since: (1) the arrival-time variations of the Big Injun reflection event do not correlate with surface topographic features; (2) the arrival time variations are not superimposed on later reflection events; and (3) arrival-time variations of earlier (overlying) seismic events do not coincide with those from the Big Injun. Long wavelength static errors, on the other hand, are present and are significant. Surface consistent static corrections cannot solve for the long-wavelength static component, but has to be modeled as part of the structure term (Yilmez, 1987).

Travel times to the Big Injun event observed in both data sets were converted to depths and plotted for comparison to the well-log-derived structural relief near lines 17 and 2 (Figure 37). Weight-drop Line 17 coincides with part of Vibroseis Line 2 across the central part of the field (Figure 25). Seismic derived depths are tied to well-log depths at a point near the VSP well. Well-log depths were taken from the Big Injun structure map (Figure 21). Weight-drop derived depths diverge from the well-log structure and rise steadily to the west of midpoint 350. The Vibroseis structure drops below the well-log structure west of midpoint 450. Neither of these differences between seismic and well-log structure correlate to topographic relief along the line and thus are not attributable to errors in the elevation correction.

To the east of midpoint 460, the weight-drop and well log structure are similar. The Vibroseis and weight-drop profiles do not coincide on the east end of the figure (Figure 37). The structure is taken along the weight-drop profile and is not expected to coincide with that along the Vibroseis line where depth to the top of the Big Injun is about 15 feet above that along the weight-drop line.

In addition to anticipated long wavelength variability, discrepancies between the seismic structure and well-log structure exist at the short wavelength. Comparison of the two seismic data sets (Figure 37), however, reveals similar small scale structures A, B, C, D, and E, west to east along the profile. These five structural highs, perhaps with the exception of D, also appear on the structural profile.

The structural profile is taken from a contour map of the well data. Along the profile minimum spacing between wells is about 400 feet, and can be as large as 1000 feet. Control points are sparsest between midpoints 360 to 480 where the correlation to small structures observed on the seismic lines is poorest. In the Vibroseis data the sampling interval (midpoint spacing) is 55 feet and in the weight-drop data the sampling interval is 22.5 feet.

During our seismic surveys, elevations of 50 wells were resurveyed. The standard deviation of the difference between the resurveyed elevations and those reported by the operators is approximately 5 feet. When this error is combined with errors in the pick of the Big Injun top, and deviations of the well from vertical, it seems likely that the accuracy of the well log depths must be roughly ± 10 feet or so. Combining this error with the coarser sampling of the well-log data base, it is not surprising that differences between seismic and well-log structure exist.

Fracture Zones and Faults

Seismic data reprocessing is discussed by Zheng and Wilson (1992) and in Appendices E and F. Comparison of original data for Line 2 (Figure 38) to reprocessed data (Figure 39) reveals some improvement of temporal resolution with reprocessing and the presence of local disruptions in the reflections from the Big Injun and surrounding intervals. Small folds discussed in the previous section are observable in both the original and reprocessed versions of the data; however, local disruptions of the interval are introduced by reprocessing (compare Figures 39 and 40). Disruptions are particularly noticeable in the positive (black) cycle immediately above the Big Injun event. Weak patterns of disruption can also be followed into the intervals above and below the Big Injun along with the small time structures. Disrupted zones identified on the reprocessed data are noted across the base of Figure 40. Disruption in the vicinity of the VSP well near midpoint 300 is supported by interpretations of the offset VSP's recorded in the well. This disruption occurs along the southeast flank of a small fold and takes the form of abrupt time-offsets with little amplitude variation.

Direct communication between wells identified during waterflooding was observed near reflector disruptions at midpoints 395, 408, and 417 (Figure 40). A local map of the area along this part of the line (Figure 41) shows the locations of the wells between which direct communication has been identified by operators in the field. The coincidence of so-called problem wells with the seismic disruptions suggests that these seismic features may be associated with faults and/or fracture zones. However, amplitude and waveform character changes similar to those discussed here are observed elsewhere in the seismic data and are not always associated with problem wells in the waterflood program.

Additional seismic data were collected across communicating wells shown in Figure 41 in the later part of the project to determine if these areas could be imaged more clearly. The weight-drop data from this area along Line 17 are compared to the Vibroseis data along Line 2 across the same area (Figure 41) after Berkhout deconvolution (Figure 42b). Midpoints in the weight-drop data (Figure 42a) are spaced at 22.5 foot intervals while those in the Vibroseis data (Figure 42b) are spaced 55 foot intervals, hence there are 2.44 times as many traces in the weight-drop data set as in the Vibroseis data. Lateral and vertical resolution are much better in the weight-drop data.

The presence of character changes noted above for the reprocessed data (Figure 40) are less noticeable when plotted at this scale (Figure 42b). Because lines 17 and 2 do not coincide on their west end, there is a slight difference in the inferred location of the western-most well communication zone (WCZ) on the Vibroseis and weight-drop lines (Figure 42). Although numerous character and amplitude changes occur in the weight-drop data (Figure 42a), small time-offsets observed on the Vibroseis data and other changes of character in the vicinity of well communication zones are not observed in the weight-drop data. The most significant change of reflection character and amplitude in weight-drop data (observed between shot points 280-290) is not associated with any well communication problems in the area.

The abrupt character changes noted above in the tightly grouped plot of the Vibroseis data after Berkhout deconvolution (Figure 40) appear to be associated with changes of amplitude and phase in cycles 1, 2, and 3 (Figures 40 and 42b), and also to a general decrease of signal-to-noise ratio in these areas. Cycles 1, 2, and 3 are associated with the overlying Big and Little Lime carbonate intervals. TV logs in wells with communications problems reveal water passing through fractures in the overlying Big Lime (Morrison, personal communication,

1993), and breakthrough is generally believed to occur along fracture zones in the overlying Big Lime rather than in the Big Injun. Model studies (Appendix G) indicate that faults extending through the Big and Little Lime, with little or no velocity reduction, offer a possible explanation for the changes in seismic character observed near well communications zones. The response is the result of scattering or diffraction from the fault edge. Waveform changes observed in the data extend through the Big and Little Lime, and their presence in areas associated with well communication problems supports the possibility of a fault origin. Reprocessing of the seismic data at Granny Creek to enhance diffraction events (Appendix E) increases waveform disruptions observed near communication wells. This also supports a diffraction origin for the disruptions observed in the data. Further analysis of recently collected weight-drop data is needed to evaluate the nature and significance of the differences between weight-drop and Vibroseis images.

VSP Observations

Three VSP's were surveyed by Schlumberger in Clay 2509 (Figure 43) Source locations for each VSP included one near-well offset, 390 ft to the southwest (S52°W) of the well, and two long offsets, one at 1395 ft southwest (S82°W) of the well, and a third 1600 ft to the northeast (N48.5°E) of the well. Displays of the 1395 and 1600 ft affects were prepared after normal moveout correction and waveshape deconvolution of the upgoing waves (Figures 44 and 45). Contour lines crossing the data represent lines of constant reflection point offset from the well. For instance, a vertical fault would actually lie along one of these contours, while a vertical line on this type of display would represent a feature that dips into the northwest or southwest quadrants on the west offset, and a feature dipping into the north or east quadrants for the northeast offset. Migration eliminates this distortion but introduces additional ones including frequency reduction and smearing.

Near-vertical interruptions of reflection patterns are observed in the 1395 and 1600 ft offset VSP's. These features are of interest because of their proximity to the small time structure in this area (Figure 37) and because of the indications of possible structural disruption observed in the reprocessed version of the data (Figure 40). These features are located on a detailed map of the area surrounding the VSP. Thief zones encountered in this area during waterflooding lend additional weight to the possibility that these features may have fault or fracture zone origin, and to an association of faults and fracture zones with the small scale folds observed elsewhere along this and other lines throughout the field.

Because disruptions of reflection events are enhanced if they dip away from the borehole toward the location of the source, VSP's to the northeast and west reveal the presence of disruptions dipping in both directions away from the well. Calculated dips are less than 12 degrees from the vertical. Their presence on a small fold, in an area marked by well communication problems, suggests they have tectonic origins.

The location of the VSP projects onto the southeast-dipping flank of the small fold noted above near CMP 300 of Vibroseis Line 2 and CMP 515 on weight-drop Line 17 (Figure 37). On the other hand, moveout corrected reflection events in the VSP appear to dip slightly to the west. An eastward dip, however, is confirmed by well-log-derived structure in this area. A low moveout-correction velocity could produce the anomalous reflector dip observed in the VSP. Moveout corrections made by Schlumberger assuming a flat velocity model may introduce some error since layers are actually dipping.

VSP also played a critical role in the reprocessing and modeling of the seismic data (Appendix F). Direct arrivals observed in the VSP revealed that the downgoing wavefield was not zero-phase as is usually assumed for Vibroseis data, but mixed-phase. Computation of the synthetics using the mixed-phase wavelet observed at the level of the Big Injun sandstone in the borehole led to a good match between synthetic and actual data. The mixed-phase wavelet observed in the VSP served as the basis for conversion of the Vibroseis data to zero-phase in the vicinity of the borehole. Conversion to zero-phase increases resolution and definition of impedance variations along Line 2 near the VSP well. More complete discussions of the use of the VSP in the design of the deconvolution operator is presented in Appendix F.

While the cause of these features cannot be definitively identified, they cannot be discounted, for instance, as simple noise related artifacts of the data. It is recommended that areas of similar signal disruption and attenuation be avoided in water flood recovery operations.

STRATIGRAPHIC CONTROLS ON INTERWELL HETEROGENEITY

Subdivisions and Depositional Environments in Granny Creek Field

The Pocono Big Injun sandstone within Granny Creek field has been subdivided into informal members, tongues, and subfacies in stratigraphic cross section GB-GB' (Figure 46) constructed from cores and geophysical log data, with the underlying Squaw sandstone as the datum. Three informal members of the Big Injun sandstone were recognized using signatures on gamma-ray logs that correspond to grain-size distribution and deflections in the bulk density log that relate to high and low density: (1) a basal fine-grained sandstone of the C member (low density); (2) an overlying coarse-grained sandstone and conglomerate of the B member, (high density); and (3) the uppermost coarse-grained sandstone and conglomerate of the A member (low density). The cross section illustrates that pre-Greenbrier erosion removed increasing amounts of Big Injun sandstone toward the east. A sharp erosional contact separates the fine-grained sandstone of the C member from the overlying coarse-grained B and A members, whereas the basal contact of the C member is gradational into shales. Laterally, the C member consists of westward-prograding tongues, numbered from oldest to youngest, respectively, as C1, C2, and C3 within Granny Creek field. Subfacies within tongues of the C member are characterized by composition, texture, fossils, sedimentary structures, porosity and permeability (where available), geophysical log signatures (caliper, gamma ray, density) and nature of contacts. The subfacies are named according to the depositional environment that they suggest. Therefore, the C member and its tongues represent a facies deposited in a deltaic river-mouth bar environment and the subfacies are distal and proximal parts of bar, further distinguished by whether dominated by marine or fluvial processes. Importantly, the distal river-mouth bar subfacies intertongues with shale, which also is a permeability barrier to fluid flow. The textures, fossils, and sedimentary structures are similar between the B and A members, but pore-filling minerals due to diagenesis are sufficiently different to affect the porosity and permeability of the units, and thereby warrant their separation.

In general, fine-grained sandstone of the C member is a coarsening upward facies with shale drapes bounding the tongues. Interbedding of basal sandstone and shale beds probably is due to sediment supply shifts (autocyclic sedimentation) that caused local transgression of the sea, periodically interrupting an otherwise steady westward progradation of a deltaic shoreline. Subfacies of the C member along GB-GB' are shown diagrammatically in Figure 47 and keyed to three cored wells (permits Clay 1126, 1108, and 1134). The C2 mouth bar (Figure 48) shows a thick trend oriented north-south (depositional strike trend locally), although regionally the reservoir sandstone of the Big Injun mouth-bar sandstone facies exhibits a depositional dip trend (classified as DS2 sandstone reservoir by Donaldson and Boswell, 1990). In Granny Creek field, paleoflow direction seems to have changed from mostly westward during Pocono C member time, to southwest paleoflow during Pocono B and A member time, probably reflecting emergence of the West Virginia dome.

Detailed examination of the Big Injun A and B members in two Clay County cores allowed the interpretation of minor channel and bar fill of a bedload paleostream (Figures 49 and 50). Probably, the initial porosity and permeability of this river-channel fill was high, based on petrographic data, but cementation of the lower part of the unit during burial produced a diagenetic facies called the B member.

Sedimentological and Diagenetic Heterogeneities in Granny Creek Field

Heterogeneities found in the coarse-grained sandstone (A and B members) of the Granny Creek field include: (1) thin shale, (2) high variability in grain size and bedform creating vertical heterogeneities, (3) calcite cement, and (4) quartz cement. The shales are usually waxy green and only a couple of inches thick; therefore, they may not be identified on wireline logs because they are too thin for resolution. Several feet below the unconformity, calcite cement commonly occurs as nodules or may follow bedforms. Quartz cement causes a decrease in density and appears as a high bulk density zone on density log. The coarse-grained sandstone contains as many as three zones of high bulk density, creating probable impediments to fluid migration. Most wells contain at least one high density zone (Figure 51). However, in the southern part of the field, wells may contain one to three high-density zones creating additional compartments.

Heterogeneities found in the fine-grained sandstone (C member) of the Granny Creek field include: (1) shale or siltstone at the bottom of the reservoir which cause pinchout of porosity at the bottom of the reservoir, and (2) calcite, siderite, or quartz cement creating zones of high density. These heterogeneities may be recognized on wireline log: (1) shales are identified by deflections in gamma-ray and density logs whereas (2) the cement zones are identified by deflections in only the density logs.

An increase in the amount of shale and siltstone at the bottom of the reservoir causes an interfingered basal contact (Figure 52). These shales and siltstones form north-south trending belts in the eastern and western portions of the field (Figure 53).

Sandstone zones with high bulk density and normal ("clean-sand") gamma-ray response are caused by an increase in calcite, siderite, or quartz cement with a corresponding decrease in porosity. These high density zones form horizontal, inclined (Figure 52), and irregular pods of impermeable sandstone. Pods may be confined to a single well or encompass as many as 25 wells (Figure 51), creating linear or irregularly shaped barriers to fluid migration which may divide the reservoir into discrete compartments.

Subdivisions and Depositional Environments in Rock Creek Field

Within Rock Creek field, the Big Injun is predominantly a fine-grained, quartz sandstone with localized interbeds of shale and very fine to coarse sandstone. Rare, ripple-scale crossbeds and single-grain layers of white quartz and chert granules and pebbles occur in the upper portion of the Big Injun; indistinct burrows and pyrite are also present locally. Mud rip-up clasts may occur above interbedded shale or in isolated layers. These features indicate that the depositional environment for the Big Injun sandstone in Rock Creek may have been a distributary mouth bar within a deltaic system similar to that for the Granny Creek.

The Big Injun in Rock Creek contains shales and carbonate-cemented zones that are similar in geophysical properties to those encountered in Granny Creek. The primary difference between the Big Injun in the two fields is the reduced thickness or absence of an upper, coarse-grained sandstone in Rock Creek. The only evidence of an upper, coarse-grained sandstone in Rock Creek is found in core chips from three wells from the southwestern portion of the field; the chips indicate that 0.5 to 8 feet of coarse material may be present. However, six Big Injun cores taken two miles to the east show only stringers of

coarse material at the top of the Big Injun interval. The fine-grained portion of the Big Injun in Rock Creek appears very similar to that in Granny Creek except that it may be twice as thick.

Sedimentological and Diagenetic Heterogeneities in Rock Creek Field

Heterogeneity within the Rock Creek field is stratigraphic and diagenetic, as shown in core analysis. In the Rock Creek field, nine of the eleven cores are associated with a single CO_2-flood project (Figure 54), limiting the distribution of the cores to a small area in the southeastern part of the field. Additionally, two complete cores and core chips from three wells outside the CO_2-flood area were examined. Big Injun cores from Rock Creek differ from those from Granny Creek in that coarse-grained sandstone is reduced in thickness or absent. Chips from Roane 1021, 1052, and 2854 suggest the presence of 3 to 7 feet of coarse-grained sandstone at the top of the core. The core from Roane 1051, shows stringers of coarse material interbedded with fine-grained sandstone in the upper 3 feet of the interval.

The Big Injun sandstone in Rock Creek field looks like the fine-grained sandstone in Granny Creek field: a relatively homogeneous, fine to very fine-grained sandstone with local coarse-grained stringers. Faint horizontal laminae and siderite specks (< .05 in. diameter) are common throughout the core. The cores show two features that may contribute to heterogeneity within the reservoir: (1) thin shales (2 inches to 2.5 feet thick), and (2) zones of increased siderite and/or calcite cement (0.5 inches to 4 feet thick). The high density zones differ from those in Granny Creek field in that they show a sharp red boundary with unaffected rock (Figure 55), and are made up of mostly siderite; whereas Granny Creek contains high density zones of siderite and minor quartz cement as well as carbonate. These cemented zones contain increased rock density and reduce porosity.

Unlike Granny Creek field, the basal Big Lime in Rock Creek includes a discontinuous, porous member. The basal Big Lime near the CO_2-flood project (Figure 54) is mostly are crystallized ooid-quartz wackestone to grainstone sometimes interbedded with quartzose dolomicrite, i.e., while 1.25 miles to the west of the CO_2 project area (Roane 1021) the Big Lime is a recrystallized ooid packstone-grainstone with small solution voids. These solution voids decrease the bulk density of the carbonate, causing the basal Big Lime to be more porous locally and to mimic the signature of the upper Big Injun. This can create problems when identifying the unconformity between the Big Injun and Big Lime. Analysis has shown that using the gamma ray wireline logs alone gives more consistent results when identifying the unconformity.

Using log data and core analysis, Rock Creek field can be divided into three domains (Figure 54). The basis for this division is the presence or absence of porosity in the basal Big Lime. In the eastern domain, basal Big Lime porosity is thin with low porosities, 8%-10% (Figure 56d). The Big Injun averages 40 feet in thickness and displays a blocky log signature. Porosity in this domain lies between 15%-18%. The Big Injun is removed to the northeast by the unconformity. The Big Injun of the central domain also averages 40 feet in thickness and displays a blocky log signature (Figure 56c). The few porosity breaks present are attributed to both carbonate cements and shales. The overlying Big Lime in the central domain is tight. The Big Injun in the western domain may reach 60 feet in thickness. However, the pay zone may be restricted to 15 feet of 15%-18% porosity. The log signature in this domain (Figure 56a) displays many small breaks interpreted as interbedded shale units

(particularly near the base of the unit) and cemented zones (particularly near the top of the unit). The Big Lime signature in this domain (Figure 56b) displays an extensive porosity unit (up to 35 feet) with porosities that occasional exceed 12%. Little or no production has been reported in any of the Big Lime porosity within the field.

Within each domain, the presence of interbedded shales (Figure 57a) and density zones (Figure 57b) decrease the thickness of available reservoir. Individual wells locally may show the reservoir being separated into several discrete units due to these shale and diagenetic zones. Isopachs of the Big Injun show the effects of different heterogeneities on the sandstone. Thinning of the Big Injun in the central and eastern parts of the field indicates truncation by the pre-Greenbrier unconformity (Figure 58a). Thickening of the Big Injun in the west can be related to interbedded shales near the base of the sandstone (Figure 58a). The effect of cemented zones and shale units on available reservoir can be seen in the isopach of Big Injun reservoir, which thins to the west (Figure 58b).

Cross section A to A' (Figure 59) shows the association of a thick cement zone (high zone) to the overlying carbonate. The combination of cemented zones and interbedded shales results in reduced reservoir sandstone in the western part of the field. Cross section B to B' (Figure 59) shows a similar porous unit in the Greenbrier in the northeastern part of the field. Shales are thinner and do not reduce the reservoir in this part of the field.

Computer Modeling of Sedimentary Facies

Geophysical logs for ten, "type" Big Injun cores chosen previously for study (Smosna and Bruner, 1991) from Granny Creek were compared to core descriptions and lithofacies picks so that each proposed lithofacies had representative gamma ray and density values. Discriminant statistical analysis was then performed on the log data to determine the reproducibility of a classification scheme when based on gamma ray, density, gamma ray and density, or other combinations of the two log variables. Through this process, a six-fold facies classification scheme (Smosna and Bruner, 1991) was eliminated from consideration (McDowell, 1992) because it could not successfully classify the type wells more than 50% of the time.

Two other classification schemes: (1) a two-fold subdivision based on grain size (Coarse and Fine lithofacies) and (2) a four-fold subdivision based on depositional environment (Channel, Fluvial Mouth Bar, Marine Mouth Bar, and Distal Bar facies) were analyzed statistically. Both were determined to be reproducible with a $\geq$ 70% success rate when a linear combination of gamma ray and density variables was used. To test the utility of these schemes at the field scale, a set of linear discriminant function coefficients - Fisher's coefficients (Norusis, 1992) - was determined based on gamma ray and density values from the ten type wells. These coefficients were then used on all correlated gamma ray and density logs for Granny Creek and Rock Creek.

Log response at each depth interval was classified as either coarse or fine lithofacies or, alternatively, into one of the four depositional environments. A series of facies cross sections were then produced along the same lines of section as used for porosity modeling (in the next section). Each facies identified in log was color-coded and displayed at its appropriate position along the line of cross section. Figure 60a is an example from Granny Creek using the four depositional environments to classify the Big Injun interval - the channel facies is restricted to the upper Big Injun (dominantly coarse-grained in core) whereas the remaining three facies are restricted to the lower Big Injun (dominantly fine-grained in core). The

presence of inclined, prograding sand bodies is suggested by this modeling process in Granny Creek.

A facies cross section from Rock Creek based on the same four depositional environments (Figure 60b) shows the predominance of the marine bar facies at the southern end of the cross section. Compared with the rest of the field, this area is anomalous in the expression of this facies. Coincidentally, the majority of core information for the field comes from the same area. Also apparent from the cross section is the predominance of more distal (marine) facies in the west and northeast and more proximal (fluvial) facies in the center and south.

Rock Creek cross sections show the presence of a thin veneer of channel facies at the top of the Big Injun. In Granny Creek this facies is associated with coarse-grain size. Although in the majority of Rock Creek cores, coarse-grained material is volumetrically insignificant, these cores come from an anomalous part of the field (CO_2 flood area, Figure 54). In fact, core cuttings from three wells only 1 mile to the east indicate 1 to 6 ft. of coarse, pebbly sandstone at the top of the Big Injun. However, in the absence of further core evidence, the channel facies in Rock Creek cannot be unequivocally tied to coarse-grained sediment. Rather its presence merely indicates similar gamma ray and density signatures as seen for the upper Big Injun in Granny Creek and, by inference, fluvial deposition.

Finally, Big Injun pay intervals were compared against the facies sequences shown in cross section for both fields. This information is poorly reported and poorly constrained by depth for Granny Creek; Rock Creek data is more complete and analysis indicates that the producing horizon within the Big Injun is generally restricted to or includes either the marine or fluvial bar facies. If the facies based on four depositional environments is truly applicable on a regional scale, this information may be significant in other Big Injun fields.

Stratigraphic Distribution of Porosity

All available gamma ray and density logs for Granny Creek and Rock Creek were scanned and digitized into ASCII files. The log database for each field was restricted to only those wells for which both gamma ray and density logs were available. Additional wells were excluded from the database because of unacceptable caliper logs (enlarged well bore due to explosive fracturing with nitroglycerin) in the Big Injun interval. Finally, the Big Injun interval for remaining logs was extracted. Those wells for which raw density counts had been recorded instead of API density values were singled out and converted to density (Alger, et al., 1971; Schlumberger, 1989) for the given well bore diameter and fluid in hole. Density values computed by this method were systematically lower (by 15%) than API density values logged in adjacent wells - appropriate corrections were made to compensate for this effect.

Granny Creek and Rock Creek were subdivided into adjoining cells ("quadrats") of uniform size. The optimum cell size for each field was chosen to maximize the total number of cells while minimizing the number of cells containing fewer than three well locations - this size was 1180 ft. x 1310 ft. for Granny Creek and 2360 ft. x 2620 ft. for Rock Creek. Cells with fewer than three wells were merged with their nearest neighbors. A central or reference well was chosen for each cell. Automated log correlation was performed using the cross-correlation algorithm proposed by Davis (1973). Within each cell, the gamma ray response for individual wells was correlated to that for the reference well and the log elevations of the correlated wells were adjusted to sea level.

Gamma-ray logs for each reference well were correlated against all other reference wells

and the relative "shifts" in log elevation associated with each correlation were placed in a matrix. This matrix of relative elevation shifts was analyzed using multidimensional scaling (Kruskal, 1964) to produce a set of coefficients necessary to adjust the elevations of each quadrat until all were at the same elevation (with respect to sea level). This process removes the effects of structural deformation from the reservoir data and aligns it horizontally at a uniform elevation (with respect to sea level); therefore
correlation is no longer tied to any particular stratigraphic datum.

Density values for all correlated well logs were converted to porosity using the formula:

$$\text{Porosity } (\phi) = (\rho_{ma} - \rho_{log})/(\rho_{ma} - \rho_{H2O})$$

Where: ρ_{ma} = "typical" rock density for the reservoir (2.68)
ρ_{log} = density value from the log
ρ_{H2O} = density of formation water (1.00).

A number of cross section lines were chosen for each field in order to transect assumed depositional strike and dip for the Big Injun. Wells immediately adjacent (within one cell spacing) to each leg of a cross section were projected into the plane of the vertical cross sections and distance-weighted gridding techniques were then used to produce a series of porosity cross section for each field. Figures 61a and 61b shows typical cross sections for Granny Creek and Rock Creek fields. Examination of the two figures points out a common feature of both - presence of zones of low porosity, 150 ft. to 650 ft. in cross-sectional width, separating zones of high porosity. These low porosity zones appear spherical to oval in cross section (Figures 61a and 61b) due the vertical exaggeration associated with each (75:1). In reality, low porosity zones are ovoid or "pancake-like" in three dimensions because their thickness is restricted to the thickness of the Big Injun interval. The low porosity zones displayed in cross section are directly analogous to the high density zones discussed elsewhere in this report. Zones of continuous, relatively high porosity ($\geq$ 17%) occur in both fields but those in Rock Creek may be two to five times larger in width than those in Granny Creek. This leads to the conclusion that production in Granny Creek is more compartmentalized than that for Rock Creek due to increased horizontal and vertical continuity of reservoir porosity (and, by implication, permeability) within the latter field.

Petrology of the Pocono and "Maccrady" Big Injun Sandstone

Petrographic study of the Big Injun sandstone indicated that diagenetic processes had significant effects on reservoir character. Inasmuch as diagenetic effects were influenced by initial conditions of deposition, the environment of deposition was particularly important in determining variations in porosity and permeability.

Four hundred and fifty thin sections of the Big Injun sandstone taken from cores and chips from 26 wells were studied. Samples for the thin sections were collected generally at 2 to 4 foot intervals where the sandstone was uniform. Finer sampling was carried out where significant lithologic changes occurred. Mineral percentages for the most part were determined by counting 300 points in each thin section; compositional information for all thin sections is given in Appendix H. In a few cases where a small part of the sample was unsuitably impregnated because of unusually low permeability, counting was limited to 100 or

200 points. Grain size in thin section was measured along the long axis of the grains.

The Big Injun sandstone in Granny Creek and Rock Creek fields is mainly a sublitharenite. Chief components are monocrystalline and polycrystalline quartz in which constituent grains range from coarse to cryptocrystalline chert. Lithic grains are the next most abundant constituent. These grains which are rich in illite, mica and chlorite are referred as predominantly phyllosilicate grains. They represent fragments of shale or mud rip-ups, slate, phyllite, fine-grained schist and highly micaceous quartzite. A few grains appear to be altered volcanic fragments. Feldspar is a minor constituent and consists of the varieties plagioclase, microcline, and orthoclase including microperthite. Mica occurs in small amounts mainly as muscovite with some biotite, commonly partly altered to chlorite. In addition to illite in lithic grains, primary illite occurs in some laminations and microstylolite seams. Accessory minerals include zircon, tourmaline, leucoxene, rutile, sphene and glauconite.

Detritus was supplied from a variety of source rocks. A plutonic igneous source is indicated by K-feldspar, a metamorphic source by quartzite and schist grains and a sedimentary source by grains of chert and shale.

Authigenic minerals were important in causing heterogeneity in the Big Injun sandstone. Illite was the first mineral to form in the sandstone after deposition and occurred as coatings on the detrital grains (Figures 62a and 63). Small feldspar overgrowths formed in some parts of the sandstone. This was followed by the development of chlorite coatings on the grains (Figure 62b) mainly in the mouth bar facies. A period of calcite formation ensued, with calcite filling pores and replacing other minerals, particularly illite. Most calcite formed in small patches a few millimeters in diameter, but some extended across the width of the 10 cm cores. Syntaxial overgrowth of quartz formed where illite and chlorite coatings were not well developed or pores were not filled by calcite. A second period of calcite formation occurred with most of the calcite developing in small patches, filling pores and replacing detrital grains, especially feldspar. A small amount of dolomite occurs with the calcite. Siderite formed late in the sequence, generally occurring in small patches filling pores and replacing grains. Siderite is much more common in the lower Big Injun. A small amount of secondary quartz formed in association with the siderite. In some parts of the Rock Creek field, siderite occurs in larger patches extending across the width of the core. Small amounts of kaolinite formed as a late pore filling and replacement of feldspar. Accessory secondary minerals included barite and pyrite. Feldspar underwent partial dissolution (Figure 62b) and alteration to clay minerals late in the diagenetic sequence. The extent of alteration of feldspar varies greatly, some grains are totally dissolved (Figure 63) whereas others appear perfectly fresh. A limited number of very small voids developed in calcite and siderite as a result of leaching.

Significant differences in the petrology of the sandstone occurs in the different facies. Illitic laminations are more common in the fluvial channel deposits and are composed mainly of intraclasts with some separate flakes of illite. Although the intraclasts have formed a pseudomatrix as a result of compaction, the cellular appearance and heterogeneous nature of the lamination material indicate that it represents accumulations of clasts. Presence of argillaceous intraclasts in the channel system apparently resulted from fluctuation in flow rate with attending rip-up of mud flats on floodplains and deposits in the braided streams.

The upper A member of the fluvial channel facies is a well-sorted, largely medium-grained sandstone with generally good porosity and permeability. Typically, grains are well coated with illite, which may have resulted from redistribution of some of the illite which had accumulated along laminae or from early infiltration of muddy waters. Downward flow is

definitely indicated in some places by geopetal features. The source of some of the illite may have been from soils developed at the unconformity at the top of the Big Injun. These illite coatings were instrumental in preserving porosity by preventing detrital quartz grains from serving as suitable seed crystals for quartz cement. Some layers have chlorite coated grains, particularly near the base of the A member.

Calcite is particularly abundant in the upper few feet of the Big Injun. The calcite partially replaced illite in the sandstone and filled pores, particularly in the coarse sandstone, producing tight zones which otherwise would have retained high permeability.

The lower part of the channel facies, the B member, is markedly different from the upper A member. Original porosity was only fair in some layers because of poor sorting (Figure 64a) resulting from strong fluctuations in flow, whereas original porosity in the A member was good. Quartz cementation was a major factor in the drastic reduction of porosity and permeability in the B member. Dissolution of feldspar increased porosity, but there was little change in permeability where the feldspar had been isolated by secondary quartz. Quartz growth was more common in the B member because clay coatings were generally either absent or poorly developed. If coatings had been present to interfere with secondary quartz formation, prismatic and eccentric growths would have developed instead of the observed euhedral normal growths (Heald and Larese, 1974).

In parts of the sandstone, normal quartz overgrowths formed on those grains which were poorly coated. Originally, grains rimmed with material such as iron oxide may have been deposited along with grains free of rims. Subsequently, grains with rims would have been favorable sites for formation of well-developed chlorite coatings which would have retarded quartz overgrowth (Dixon, et al., 1989, p. 720). On the other hand, chlorite was much less likely to form on the grains devoid of pre-existing rims, so normal quartz would have been free to grow on these grains. Irregular distribution of early hydrocarbon could be another reason for the patchy development of secondary quartz. Chlorite does not form in pores occupied by early hydrocarbon. Where hydrocarbon later moves out, secondary quartz is able to form on the uncoated grains surrounding these pores (Pittman, et al., 1992).

Illite also was instrumental in reducing porosity in the lower fluvial channel. During periods of slack water, illite laminae formed which later caused formation of microstylolite seams. Sandstones adjacent to these laminae contained illite which promoted pressure solution (Heald, 1959) that reduced or eliminated intergranular porosity (Figure 64b).

Pressure solution along microstylolites and between quartz grains in the illitic areas yielded much silica in solution. This may have been the source of the relatively high quartz cement in the B member of the channel facies.

Porosity and permeability of the fluvial channel sandstone are particularly variable for a number of reasons. Fluctuation in stream flow resulted in marked differences in sorting and in the distribution of illite which aided porosity preservation in some places, but promoted pressure solution in other places. Erratic distribution of calcite cement near the overlying Greenbrier Limestone contributed to local impermeable zones. Lack of coatings in the lower fluvial channel sandstone resulted in quartz cementation and low porosity and permeability.

Core analyses and geophysical log data indicate that the best porosity and permeability in Granny Creek field occur more consistently in the proximal mouth-bar facies of the Big Injun (Figures 65 and 66). Well-sorted, fine- to very fine-grained, high quartz sand was deposited in this interval. The main factor in porosity preservation appears to have been the development of well-formed chlorite coatings. These restricted quartz cementation, unlike the heavily cemented, uncoated sandstone above. Chlorite flakes in the coatings are loosely

packed so the coatings apparently have a microporosity of 75%-85%. Thus, overall porosity is little reduced by the coatings, and they are not thick enough to seriously reduce pore throat size in this interval, ensuring that good permeability was maintained.

Although some workers (Paxton, et al., 1990) question the importance of coatings in retarding quartz growth, several features indicate they were a significant factor affecting cementation in the Big Injun sandstone. In general, the least secondary quartz is where the best coatings occur. Where coatings were fractured during compaction so that detrital quartz was exposed, secondary overgrowths formed only where the quartz was uncovered. Quartz commonly grew where chlorite was replaced by siderite apparently because the protective coating of chlorite was not present to retard quartz growth. In some places, clean, uncoated grains occur in burrows surrounded by coated grains. Normally, secondary quartz formed on the uncoated grains in the burrows but not on the surrounding coated grains. These examples indicate that silica was available in the system and conditions were favorable for quartz growth, yet quartz formed selectively only on the sites that were least coated.

The origin of the chlorite coatings is important because of their role in porosity preservation, but unfortunately their origin is difficult to determine. Feldspars do not seem to be the local source because their alteration occurred after chlorite formation. Volcanic materials would be a good source but only in a few samples is there any hint of a volcanic contribution. The fact that the boundary between the coated and uncoated zones seems to follow stratigraphic layers suggests more of a control by sedimentary conditions. Studies in other areas (Fuchtbauer, 1974, and Longstaffe, 1986) have led to the idea that mixing of fresh and saline waters produces conditions favorable for later diagenetic development of chlorite. A certain amount of mixing of fresh and saline waters would have been expected in the environment where distributary mouth bars formed and this may account for the well developed chlorite coatings in the bar facies. Formation of chlorite was not favored in the higher energy fluvial channel sandstones (B member).

Although some of the distal mouth-bar facies is a suitable reservoir sandstone, much of it is unsatisfactory for a number of reasons. Some of the sandstone has an above average content of argillaceous ductile grains which compacted and were squeezed into adjacent pores, thereby reducing porosity and permeability. Some of the sandstone is very fine grained, with corresponding small throat cross sections, so coatings of normal thickness block the pore throats, leading to very low permeability, even though porosity (including microporosity in the coatings) is still high. The decrease in permeability with decreasing grain size for Clay 1126 (Figure 67) is typical of much of the Big Injun. In some cases the sandstones are not unusually fine, but the coatings are thicker, so that throats are blocked with attending loss of permeability. In addition, several percent siderite occurs as a pore filling in this facies. Commonly a combination of these factors came into play to lower porosity to some extent and drastically reduce permeability.

In all of the sandstone units, secondary porosity generally ranging from 1-5% has resulted from partial to complete dissolution of both K-feldspar and plagioclase.

Major factors affecting intergranular porosity and hence permeability are shown in the triangular diagrams for cement, packing-density, and intergranular porosity (Figures 68). In order to show variations more clearly, the portion of the diagram for wells in Granny Creek field was enlarged. Some facies were absent in some wells, so the number of points for each facies is not the same for all wells.

In Figure 68, points for the B member of the fluvial channel facies fall in the lower part of the diagram, indicating lower intergranular porosity which largely accounts for the low

permeability in this zone. Points falling nearer the lower left corner of the diagram have a higher packing density from compaction or poor sorting or a combination of the two factors. In the B member, the cement which is indicated is mainly secondary quartz.

Compared to the wells in the B member, most points representing the proximal bar fall higher in the diagram, indicating that the more favorable porosity is due to lower packing density and in some wells a smaller amount of cement.

Porosity of most samples from the distal bar is slightly less than the proximal bar because of somewhat more cement (carbonate and chlorite) as indicated by more points nearer the lower right corner of the diagram.

The influence of cementation and packing on porosity within the different facies of a given well are given in the bar graph diagram for Clay 1109 (Figure 69). In this figure the relative amounts of the different cements and grain coatings which tend to reduce porosity and permeability are plotted on bars extending to the left. Intergranular volume and intergranular porosity that are favorable for permeability are plotted on bars extending to the right. Except where other factors are more important, permeability generally increases with grain size. However, in a few parts of the core, such as in the interval near 1898', permeability is good, yet the sandstone is fairly fine. This is due to the fact that there are some thin layers of coarser permeable sandstone which are not well represented in the thin sections. Relationships are reasonably consistent in most of the bar facies. Note that the permeability of the distal bar is much lower than in marine influenced bar, yet the porosity of the distal bar is fairly good. In both facies, chlorite coatings reduced the size of the throat openings but the effect is much greater in the small throats of the finer grained distal bar.

In summary, diagenesis played an especially important role in contributing to the heterogeneity of the Big Injun reservoir in the Granny Creek and Rock Creek fields, particularly in terms of porosity and permeability. Original sedimentary conditions apparently set the stage for later diagenetic variations in porosity and permeability. This emphasizes the importance of considering the environment of deposition in prospecting for favorable porosity trends.

RESERVOIR CHARACTERIZATION

Distribution of key reservoir parameters such as permeability and porosity are essential for reservoir characterization. These reservoir parameters can be evaluated from different sources including core analysis, geophysical well logs, pressure transient well tests, and production and injection data. This section considers the geographic distribution of porosity, permeability and other formation properties from available data in Granny Creek field.

Core Analysis

Figure 70 shows the location of the wells in Granny Creek field that have core analysis or core samples available. The available core samples were analyzed to establish core analysis for all the wells. The core analysis results were then utilized to determine average porosity and permeability values for zones (A, B, C3, C2, C1) in each well (Tables 2 and 3). Thickness-weighted average porosity and permeability properties were mapped for each zone (Figures 71-75).

Permeability maps show permeability increasing toward the south for A (Figure 71b); low permeability in the center of the field for zone B (Figure 72b); and north-south trends within C tongues (Figures 73b, 74b, and 75b). Generally, porosity maps for the various zones have appearances that are similar, but not identical to that of the permeability maps. An area of high permeability for zones A, B, and C3 is observed in the southern part of the field where the CO_2 pilot project was conducted. However, porosity distributions did not indicate a high porosity trend in this area for the same zones. Therefore, high permeability value in this area may be attributed to the presence of fractures. In cross section, permeability from core analyzes can be related to depositional environments (Figure 76).

Well Logs

Density and induction logs from a number of wells in Granny Creek field (Figures 70) were used to determine porosity and water saturation values for each zone (Tables 4 and 5). The Archie equation was employed assuming a matrix density of 2.68 grams/cc, fluid density of 1.0 grams/cc, and formation water resistivity of 0.05 ohm-meter. The distribution of thickness (Figures 77-81) shows the absence of A and B members in the eastern part of the field due to erosion (Figures 77a and 78a); westward progradation of C members with pinch outs of C-1 and C-2 (Figures 79a and 80a); and the conclusion that C2 is the major pay. The maps also show a westward thickening trend for zone A (Figure 77a); a southward thickening trend for zone B, reaching the maximum in the center of the field (Figure 78a); and a thick trend oriented north-south in center of the field for C2 (Figure 80a).

Porosity and water saturation values determined from core and log analysis were also compared using cross plots. In general, most of the cross plots showed scattered data points indicating the difficulty in correlating core and log results. Comparisons were extended to core permeability and log porosity values. Based on the regression analysis of each zone, most of the correlations were found to be poor. The evaluation of permeability in heterogenous formation from well log data represents a difficult problem because a simple

correlation between permeability and porosity cannot be developed. An attempt was made to integrate data from various well logs with depositional, lithological and sedimentological interpretations to correlate permeability with well log responses.

The inability to find a correlation between the permeability and log data was attributed to inaccuracies in the whole core analysis. The full diameter core analysis results represent the average rock properties over the interval of study and tend to ignore the rapid changes in rock properties that are common to heterogeneous formations. In order to study the averaging problem in whole core analysis, two wells were selected for detailed plug (or conventional) core analysis. The two wells, as shown in Figure 70, are located on the eastern (Clay 1110) and the western (Clay 1134) boundaries of the field. The core elevation was moved up or down to provide a good match between porosity values determined from the core and log analysis. Figure 82a shows the comparison of core and log determined porosity values for Clay 1110. Measured permeability values for Clay 1110 and the log response values of bulk density, resistivity, and gamma ray are illustrated in Figure 82b. Actual log response values were selected in order to minimize any assumptions that are needed for determining porosity and water saturation from the well log data. Although a general trend might exist between permeability and bulk density, the scatter in data points was significant enough to preclude any possibility of developing a correlation. This failure to develop correlations can be attributed mainly to the qualitative nature of geological interpretations relative to depositional environments, grain-size and stratigraphy, and lithology. Figure 83 illustrates the stratigraphic and lithologic interpretations for Clay 1110 and 1134.

It is necessary to integrate the geological descriptions of the various zones, geophysical well log responses and the trend of the permeability variations in order to define the zones quantitatively. Comparison of log responses and permeability values on the two investigated wells indicated similarities in permeability variation and the responses in density, induction, and gamma ray logs from well to well. As a result, several zones were delineated in terms of log responses and annotated as G.I.D. (Gamma Ray-Induction-Density) zones "1", "Transition", and "2". Zones 1 and 2 were further subdivided into 1A ,1B, 2A and 2B as illustrated in Figures 82b. Figure 83 compares the G.I.D zones, as defined here, for the two wells with other geological interpretations. Figure 84 illustrates the permeability variation as function of the bulk density for G.I.D. zones 1, Transition, and 2 for the two investigated wells. Although there are few data points in zone 1, a trend can be observed. The data in the Transition zone demonstrate a lack of permeability-bulk density correlation. A well defined relationship between permeability and bulk density for zone 2 is apparent.

The data available from the seven wells with whole core analysis located between the two investigation wells were utilized to evaluate G.I.D. correlations. G.I.D. zones were first delineated utilizing the log responses from each well (Figure 85), whole core analysis data have the same general trend (slope) as the G.I.D. regression lines for zone 1 and 2, but data points are shifted toward higher permeability values.

Pressure Transient Tests

There were limited well test data available from Granny Creek field. Pressure fall-off and step rate tests were performed on wells located in the southern half of the field. Upon analyzing the test data, effective permeability, skin factor, and radius of investigation for each well were determined (data, analysis procedures, and results are provided in Appendix B).

Computed values of permeability (0.40 md and 0.31) were much less than permeability values determined from core analysis. This indicates a major reduction in permeability must have occurred after water injection was initiated. Negative values for skin factors (-3.1 and -2.5) indicate that the wells had been stimulated prior to the tests. The skin factors and radii of investigations determined from the test indicate that the permeability reduction is not caused by completion (skin effects), but rather is due to permeability alteration.

Production and Injection Data

Permeability was also estimated from production or injection data using Darcy's radial flow equation, and initial oil potential data available from the unstimulated wells drilled between 1924 and 1944 in Granny Creek field. Permeability values determined in this manner should be only viewed in qualitative manner due to inherent inaccuracies involved in the measurements as well as the assumptions. The assumptions included virgin formation pressure, open flow, wellbore filled with fluid, negligible frictional pressure losses, and an isotropic, continuous reservoir without permeability barriers within the radius of investigation. In addition, water injection rate data available from the wells in the southern part of the Granny Creek field were utilized to estimate permeability. Due to lack of accurate pressure data prior to water injection, pressures were estimated based on the experiences in the field. Permeability values were then calculated utilizing January 1983 injection rate data and assuming a reservoir pressures of 75 psia.

Permeability estimated from initial potential represents the average permeability of all zones contributing to the production. Maps of estimated permeability (Figure 86) and core permeability (Figure 82b) show two north-south trends corresponding with permeability trend C2 (the central trend) and C3 (the western trend). This conclusion is in agreement with the geological interpretation that the marine-influenced proximal bar subfacies of the C member is the primary pay zone, and that permeability variations can be attributed to compartmentalization of the reservoir. Initial potential permeability values are one to two orders of magnitude higher then the injection rate-based permeability values, (Figure 86a) suggesting that permeability has been significantly reduced as result of water injection. Permeability values obtained from injection data are in agreement with permeability values obtained from the well test data. This confirms the presence of low-permeability areas around the injection wells as was concluded from the waterflooding performance evaluations.

HETEROGENEITY RELATED TO OIL PRODUCTION

Spatial Trends

Maps of primary cumulative oil production were drawn from data obtained from operations in Granny Creek and Rock Creek fields. For some wells, missing annual volumes were estimated from available data, and for other wells annual production reported on a lease basis, individual well production was estimated from the date production began for each well by dividing the total lease production for the year by the number of producing wells.

The resulting contour map shows north-south trends within Granny Creek fields that are broad in the northern part of the field, and narrow in the southern part (Figure 87). In the rest of the field, especially the east, production appears patchy with no clearly defined trends. The production map for Rock Creek shows a small area of high production in the southwest and several, narrow bands of relatively high production trending NW-SE in the south, central, and northeast portions of the field (Figure 88). The rest of the Rock Creek field shows a scattering of high-volume wells similar to Granny Creek that appear to reflect a non-uniform distribution of oil volumes and make interpretation of the map difficult. The next section describes the method of indicator kriging for mapping trends in spatial data. This method is applied to both the Granny Creek and Rock Creek fields.

Indicator Kriging

Linear estimation methods such as distance-weighted gridding or ordinary kriging are designed to delineate large-scale trends in data, but tend to smooth out variations between individual data points in the process of generating estimated values for the entire area of interest. If the target of the analysis is reservoir heterogeneity, maps of gridded or ordinary kriged estimates have little usefulness. On the other hand, When data are non-normal, or outliers are present, linear estimation either creates a number of isolated "hotspots" where spatial continuity of the high values is low, or large areas of overly optimistic estimates where high values lie in poorly sampled areas.

Indicator kriging is a method for handling data that contain outliers, represent a mixture of populations, or are not normally distributed (Journel, 1983; Hohn, 1988). Define z(x), to be value of a variable at a location x. z_c is a cutoff value of the regionalized variable; and $i(x;z_c)$ is the indicator variable calculated through the indicator transform:

$$i(x;z_c) = 1 \text{ if } z(x) < z_c \qquad \textbf{(1)}$$
$$\text{else} \quad = 0.$$

The indicator transformation converts the original, continuous variable into one that takes on the values of 0 and 1. For each indicator variable created, directional variograms were calculated and modeled.

Estimated probability that the regionalized variable exceeds a given cutoff at a location equals:

$$1 - P^*(x;z_c) = 1 - \Sigma w_k \, i(x_k;z_c) \qquad \textbf{(2)}$$

where k is the number of wells in the neighborhood of location x. Weights w_k were calculated by ordinary kriging. For a subset of locations on a grid, problems in order relations can occur, i.e.:

$$P^*(x;z_i) < P^*(x;z_{i+1}), \qquad (3)$$

where cutoff z_i is less than cutoff z_{i+1}. This relationship is inconsistent with the definition of the indicator variables, for the probability of exceeding the higher cutoff can never exceed that of exceeding the lower cutoff. Order relations were checked for all grid cells for pairs of cutoffs, and resolved using the procedure of Journel (1987) as implemented in the GSLIB package of geostatistical software (Deutsch and Journel, 1992).

Granny Creek Field

Cutoffs chosen in computing indicator variables were 12,335, 18,244, and 25,000 barrels of oil, corresponding to the 50th, 75th, and 90th percentiles. Directional variograms reflected the spatial anisotropy at all cutoffs, and in particular, at the highest percentile. Kriged maps of the three indicator variables show a number of north-south trends. At the lowest cutoff (Figure 89), three trends are apparent: a broad swath of elevated probabilities in the north-western part of the field ("A"); "B" to the east; and a narrow band of elevated probabilities in the southern part of the field ("C"). Localized highs ("D") are separated from the main north-south trend by a west-southwest to east-northeast band of depressed probabilities.

At the 75th percentile, the broad swath of high probabilities remains (Figure 90), but all other trends disappear. The contrast between the northern and southern halves of the field becomes most apparent at higher cutoffs; no wells produced more than 25,000 barrels of oil in the southern portion of the field (Figure 91).

Comparison of Figures 89, 90, and 91 to Figure 87 demonstrates the ability of indicator kriging to emphasize spatial trends and to reduce the number of "hotspots". Notice that the 50th percentile map (Figure 89) is the most similar to the cumulative production map (Figure 87); north-south high production trends are greatly enhanced and the discontinuity between the two halves of the field is clear.

Rock Creek Field

Variograms calculated from 10-year cumulative production showed little directional anisotropy, and were used to fit omnidirectional, exponential models for each of three cutoffs: the median (12,914 BO), 75th percentile (17,069 BO), and the 90th percentile (22,048 BO).

Probability maps for each cutoff (Figures 92, 93, and 94) display low cumulative production in the western part of the field, and the highest concentration of wells that produced above the 75th percentile in the southeastern part. A band of high probabilities extends along the northwestern boundary of the field, oriented northeast-southwest (Figure 93). The same map shows reduced probabilities in the extreme northeastern part of the field.

Stratigraphic and Diagenetic Effects on Production

Within Granny Creek field, pods of relatively high initial oil production appear to align in a northwest direction in the northern 60 percent of the field approximately parallel to the pre-Greenbrier unconformity (Figure 5). A positive correlation exists between high initial oil potential and those areas where the upper distal and marine-influenced proximal mouth-bar subfacies of the C member "pinch out" against the base of the B member and where the C member is capped by at least a few feet of the relatively impermeable B member. These stratigraphic relationships are illustrated with initial oil production on two different cross sections: P1-P1' (Figure 95) oriented SW-NE across the field nearly normal to the erosional margin of the coarse-grained B member of the Big Injun; and P4-P4' (Figure 96) oriented parallel and near this same erosional margin where the upper part of the Big Injun reservoir is truncated by the pre-Greenbrier unconformity. The smooth curves were established from wells used in the cross sections, supplemented by projecting values from nearby wells into the lines of section.

Initial oil production averages about 46 barrels per day where the marine proximal river-mouth-bar subfacies is thick and pinches out against the overlying well-cemented, coarse-grained B member. Where the marine proximal river-mouth bar is thick but is some distance from its pinch out against the B member, average initial oil production drops to about 24 barrels per day. Relatively low initial oil production (11 to 15 barrels per day) occurs where: 1) the permeable/porous marine proximal mouth-bar subfacies is thin near its pinch out; 2) the mouth-bar subfacies changes from marine to fluvial dominated and is less porous and permeable, although it pinches out against the B member; and 3) the B member is absent.

Where the A and B members are absent and the Big Lime (Greenbrier Limestone) directly overlies the C member, oil possibly was lost into the "thief" Big Lime during lateral migration, or was blocked by a postulated gas cap prior to the Allegheny orogeny for wells northeastward of the eroded B member. Apparently, the B member does not need to be very thick to serve as a possible seal.

Cross sections (Figures 96 and 97) constructed NW-SE through the generally high initial oil production trend in the "pinch-out" belt affected by the pre-Greenbrier unconformity show wells with relatively low initial oil production along this trend, suggesting compartments within the oil reservoir. The zero isopach contour for the B member indicates "embayments" oriented southwestward for approximately 2000 feet, and these areas of thin to absent B member occur where the low initial oil production wells are located. These localized southwest trends probably developed where ancient rivers eroded and reduced the thickness of the possible seal above the pay zone in the C member of the Big Injun. The interpreted southwest trend of paleoflow of ancient rivers is based on thickness maps of these members, and portends emergence of the West Virginia dome (or Pocono dome, Donaldson and Shumaker, 1981), which apparently influenced the erosional patterns of the pre-Greenbrier unconformity for this combination oil trap. Compartments of oil production, therefore, can be attributed to occurrence of high permeability/porosity facies (marine-dominant proximal mouth-bar subfacies) of different C member tongues capped by a less permeable B member, which exhibits discontinuities because of either the pattern of pre-Greenbrier erosion near the "pinch-out" margin, or diagenetic controls.

The distribution of diagenetic density breaks in two stratigraphic cross sections (P1-P1', Figure 98 and P2-P2', Figure 99) indicates further compartmentalization of the reservoir and isolated areas that correlate with initial oil production and cumulative oil production. High

initial oil production appears to occur within the proximal subfacies where it is bounded by relatively impermeable, thin intervals separating tongues of the C member; the "diagenetic high density zone"; and the B member capping the high permeability pod. The combination of a permeable subfacies enclosed by lower permeability barriers in the vicinity of the "pinch out" zone of the B member shows a positive correlation with both initial oil production and cumulative oil production. Rock pressure data across these compartments or cells is presently unavailable.

Considering Granny Creek fields as a whole, high oil production occurs in a north-south belt about midway from west to east across the field (Figure 91; area "A" in Figure 89). Lack of high oil production in the northernmost part of the field corresponds with the absence of the B member of the Big Injun sandstone (Figure 78a), which presumably served as a seal for the oil accumulated in the proximal mouth-bar facies of the C member. The north-south belt of highest primary oil production occurs between two bracketing belts of lower oil production: 1) the eastern north-south belt is where the C1 sandstone is overlapped by the C2 sandstone, the location of the shale depositional barrier (Figure 53); and 2) the western north-south belt is where the C2 sandstone is overlapped by the C3 sandstone, the location of the shale depositional barrier. The north-south belt of highest primary oil production occurs within the proximal bar facies (pay zone) of the C2 sandstone of the Pocono Big Injun. This highest belt of production parallels the structure contours for the Granny Creek field, thereby indicating an important influence of structure. Within the belt of highest primary oil production, the best production occurs in 12 patches (compartments) ranging in size from 1 to 29 acres and averaging 12 acres (Appendix I). Diagenetic density barriers (Figure 51) are irregularly tabular, cut across the bedding at a low angle, and occur nearly parallel to the overlying pre-Greenbrier unconformity. These diagenetic barriers occur where the primary oil production is 2 to 8 times less than the "sweet spots" of highest production, a condition that attests to their lower permeability and value as partial barriers to fluid migration.

Effects of Structure, Deposition, Diagenesis, and Production

As the previous section shows, observed spatial patterns in shales, siltstones, and diagenetic features support the conceptual model of the reservoir as a prograding deltaic sequence, comprised of several lenticular units oriented north-to-south, offlapping from east to west, the source of sediments being to the east or northeast (Zou and Donaldson, 1992a, 1992b). Maps of both permeability and average reservoir porosity describe north-south trends, although with many small-scale, east-west trends. These features do not fully explain the sharp contrast between the northern and southern halves of the field, particularly the discontinuity in production separating areas C and D from A to the north. It seems clear that depositional and diagenetic features play a major role in controlling accumulations of oil in the field. This section shows that structural features coincide with specific sedimentological and production trends.

Several north-south folds or faults (Zheng, et al, 1993) in both the northern and southern halves of the field coincide or lie adjacent to the areas of highest production (Figures 21, 89, and 100). These folds or faults are offset between northern and southern halves by a zone of east-west faults occurring in the area of discontinuity in oil production and potential (Zheng, et al., 1993). A remarkable coincidence occurs between the locations of these structural features and presence of high-density zones (Figure 100), and shales and siltstones (Figure

101). In the northern half of the field, the north-south features and the east-west discontinuity to the south define a geographic area that includes both the highest oil production, and the thickest, most extensive high-density zones. In the southern half, the north-south trending folds or faults and the discontinuity to the north lie adjacent to a group of wells that contained shale breaks near the base of the Big Injun, the distinct north-south trend in production, and a thickening in the upper, coarse part of the Big Injun (Figure 102).

These observations suggest that post-depositional deformation or faulting resulted in fracturing of the Big Injun and movement of carbonate-laden fluids into the sandstones to create the high-density zones that subsequently blocked movement of oil. In addition, fractures might provide porosity and an increase in apparent permeability to fluids. The fact that areas with observed shale breaks are bounded in part by folds or faults in the southern part of the field, and that portions of the Big Injun are thickened in the same area suggest that a north-south fault in this part of the field was active during deposition of the Big Injun.

In summary, structure plays an important part in determining the volume of oil obtained from the Big Injun in Granny Creek. Structure might have affected deposition of the Big Injun, but more significantly, carbonate cementation of the Big Injun appears to have occurred most heavily in areas fractured as a result of deformation.

Definition of Production Areas With Seismic Data

One of the most noticeable characteristics of production within the field is its division into a highly productive northern part and a less productive southern part (Figure 87). The effects of reactivation of basement fault after deposition of the Big Injun sandstone appears to influence this subdivision. Big Injun arrival time and Big Injun-to-Onondaga isochron plotted relative to each other along weight-drop Line 14 (Figure 103a) reveal that considerable thickening of the Big Injun-to-Onondaga interval coincides with significant increases of primary, 10 year primary, and 10 year secondary production along the line (Figure 103b). Lines 2 and 17 cross the southern end of this thickened Big Injun-to-Onondaga area. Big Injun-to-Onondaga Isochron and Big Injun arrival time along Vibroseis Line 2 (Figure 104a) where the line coincides with weight-drop Line 17 (Figure 25) reveals that high production (Figure 104b) on the west end of the line coincides with a time-structure and thickening of the Big Injun-to-Onondaga interval.

Line 18 provides a view of this feature, along its strike, north-to-south (Figures 25 and 105). The Big Injun-to-Onondaga isochron and Big Injun arrival time plot reveals interrelationships that are different from those observed across strike. Thickening of the Big Injun-Onondaga interval increases significantly toward the center of the line from both north and south directions. However, along the strike of this feature, production variability is unrelated to thickening of the Big Injun-to-Onondaga interval or to variations of Big Injun arrival time. The highest production along this line (both primary and 10 year primary) occurs on the south end of the line and coincides with the hinge across which thickening of the Big Injun-to-Onondaga section occurs. Although this strike line (Line 18) reveals little in the way of significant structural relief, dip lines 2, 17, and 14 suggest that the feature is folded. This fold is considerably larger along Line 14 to the north than along Lines 17 and 2 to the south. As noted, production along Line 14 (Figure 103) rises significantly with westward thickening of the Big Injun-to-Onondaga interval. Extension over the shallow depositional hinge on the southern end of Line 18, which developed during reactivation of the underlying basement

fault combined with late-stage detachment could enhance fracture porosity in this area resulting in the higher production.

Correlation between primary production and structural relief determined from Vibroseis lines varies between 0.4 and 0.84 and averages 0.64. Correlation with the 10 year cumulative production data varies between 0.33 and 0.91 with an average of 0.55. It is difficult to evaluate this relationship more precisely. Although cumulative production data is not available on all wells from the field, data are available at intervals of 500 to 1000 feet throughout the area. Nevertheless seismic coverage is comparably more detailed. Both seismic and well log data reveal the presence of considerable structural variability over distances of 500 to 1000 feet. Hence, although correlations between structure determined from Vibroseis lines and production are not high, the correlations do suggest that structural compartmentalization of the reservoir may, in part, control the distribution of oil within the reservoir.

Rock Creek Field

Geologic controls on production appear simpler for Rock Creek field compared with Granny Creek. The earlier discussion on structure within Rock Creek field showed that the shape and location of the field is controlled by the syncline in which it occurs. The western part of the field is defined by the thinning of the reservoir as it interfingers with shales westward. The same is true in the extreme northeastern part of the field.

In the east-central part of the field, Figure 106 shows a north-south trending, elliptical region, with porosity-feet thickness ranging from 6 to 9 feet, that coincides with the most favorable production in the field (Figure 93). On the other hand, the northeast-trending high in production seen in Figure 93 does not correspond with trends in reservoir thickness or porosity, but rather with the presence and thickness of strongly cemented sandstones (Figure 57b). This suggests that the same factors control production locally within both fields. Because no seismic data are available for the Rock Creek field, these factors cannot be identified with the same degree of confidence as in the Granny Creek field.

Fracture Porosity and Communication Between Wells

Several lines of evidence suggest that communication is caused by fracture porosity in the reservoir and in the overlying Greenbrier Limestone: (1) pumping tests from wells adjacent to mapped breaks in seismic continuity; (2) possible minor stratigraphic repetition noted on several logs within the field that suggests the presence of small reverse faults; (3) presence of slickensided, inclined fractures in the Greenbrier Limestone of two oriented cores taken in the heart of the field (Dowell Schlumberger, 1986); (4) presence of northeast-trending, small, detached fold and reverse faults within Pennsylvanian surface sediments; and (5) the narrow, geometry, consistent northeast trend, and the rapid speed of communication between wells (Figure 4); (6) occurrence of faults as mapped on seismic data; and (7) flow simulation studies that predict flow in fractures outside of the reservoir.

Critical to the understanding of the cause for the rapid inter-well communication of injected water is a study made by Pennzoil (Dowell Schlumberger, 1986) on two oriented cores (Clay 2253 and 2255, Figures 4 and 107) drilled through the basal Greenbrier

Limestone in the heart of the field. Prior to that study, a down-hole televiewer run in Clay 1248 (Figure 4) showed that injected water entered the Greenbrier at about 30 feet above the Keener sandstone horizon. Study of the oriented cores (Dowell Schlumberger, 1986) suggested that northeast-trending communication was probably through low-angle, slickensided fractures (small reverse faults) found in the Greenbrier Limestone. Cores taken from the several wells described in our study (Figure 3) failed to show fractures in the Big Injun sand, let alone the numerous low-angle fractures reported in the Greenbrier (Figure 108). It is not certain if fractures seen in the teleview were induced by drilling or if they represent a more highly fractured area of the reservoir. However, bedding parallel slickensides noted in shales of the Big Injun cores suggest interbed slip in response to deforming stress rather than by internal shear as seen in the more competent and brittle Greenbrier Limestone. Thus it is likely that the Greenbrier is more highly fractured than the Big Injun sandstone and deformed in a different manner.

Shear fractures within the Greenbrier strike parallel to regional folds formed by Alleghenian (Permian) deformation, and concludes that the Greenbrier fractures formed by stress associated with that deformation (Dowell Schlumberger, 1986). In addition, small detached structures in Pennsylvanian coals at the surface correspond closely to the trend of the small faults in the Greenbrier (Table 1).

Narrow zones of abnormally-high primary production with a northeast trend are not apparent on either the initial open-flow or 10-year cumulative production maps (Figures 5 and 6), which suggests that this particular heterogeneity was enhanced after primary production. One might suspect that induced fractures associated with well completion formed the pathways for fluid communication during secondary production. However, analysis of the oriented cores by load and sonic tests (Figure 108) indicated that the principal horizonal in situ stress, which is usually sigma one, is oriented in an east-west direction, and thus communication along induced fractures should be along east-west lines (Table 1). This is not the case (Figure 4).

Even though communication appears to be at least in part along natural fractures in the Greenbrier, there is still the question of how the water penetrates the upper, coarser sandstone within the Big Injun to enter the overlying Greenbrier. Nearly instantaneous communication of injected water between certain wells in the field suggests that the brittle seal was broken during stimulation in the communicating wells, and that water immediately penetrated the seal to the Greenbrier. However, communication can be delayed, occurring abruptly along similar northeast trends well after the water flood had been initiated in the communicating wells. In such cases, it is presumed (Paul King and Roger Heldman, 1993 personal communication) that communication occurred when the flood front had gone beyond the stimulated zone and reached a natural fracture in the Big Injun. In such instances, injected water communicated either along a natural fracture in the Big Injun or, more likely, it penetrated a natural fracture in the seal to link through the more numerous fractures in the Greenbrier Limestone. Theoretical studies of depleted reservoirs (Teufel, 1993) indicate that low-angle shear surfaces, such as those found in the Greenbrier, are more likely to open than high-angle fractures during repressuring of depleted reservoirs.

To further explore the origins of well communication, discussions were held with field engineers of the operating companies and a map was made which showed the method of completion used for each well in the field. According to completion records, communication has occurred in both shot wells (explosively fractured with nitroglycerin), usually those drilled for primary production, and in wells fractured and propped with sand, usually those drilled for

secondary recovery. It was pointed out by operating engineers that initial injection pressures (1000-1500 lbs/in) commonly exceeded original formation pressures (± 800-900 lbs/in.). The combination of natural fractures in brittle rocks above the reservoir, completion techniques and high injection pressures may have created many of the communication problems encountered during secondary recovery.

Suggestions for remediation of communication problems during secondary recovery come from the interpretation developed above and from actual field experience (King, Heldman and Hagar, 1993 personal communication). Suggestions for remedial actions that also may apply to other reservoirs with similar characteristics, and specifically to those reservoirs with thin, brittle seals, include: (1) reduction of injection pressure, (2) reduction in the size and severity of well stimulation design, (3) cementing cavities associated with old shot wells and recompletion through pipe, and (4) drilling offset wells to communicating wells. Because of the presumed size of fractures, gel polymer treatment would not be practical for remediation.

CONCLUSIONS AND RECOMMENDATIONS

Stratigraphy

The Pocono Big Injun sandstone (Lower Mississippian) is the reservoir rock in Granny Creek field. The Big Injun is bounded by marine shales at the base and the pre-Greenbrier unconformity at the top. Depositional facies of the Big Injun sandstone are westward prograding river-mouth bars (fine-grained sandstone), which were transgressed periodically by thin marine shale beds that separate the mouth-bar facies into several tongues within the field. Subfacies of the mouth bar are the (1) distal bar, (2) marine-influenced proximal bar, and (3) fluvial-influenced proximal bar.

Coarse-grained sandstones and conglomerates overlie the mouth-bar sandstones. These coarse deposits are channel-fill deposits of bedload fluvial/deltaic rivers. An increase in secondary quartz cementation in the lower part of this unit can be recognized as a higher density zone on the geophysical logs and may serve as a seal.

Diagenesis

Diagenetic facies are post-depositional in origin and developed during burial history, but were dependent on conditions at the time of sedimentation, such as in the case of:

- quartz-cemented B member, which contained small amounts of illite in laminae that apparently promoted pressure solution of quartz and the source of silica for the cement;

- fresh water-marine mixing zone of the marine-influenced proximal mouth bar environment that produced water chemistry that caused chlorite to coat detrital sand grains and maintain good permeability of this pay-zone subfacies;

- distal mouth-bar subfacies where the combination of chlorite coatings on detrital sand grains and small pore throats effectively reduced permeability, (further reduced by squashing of argillaceous clasts into pseudo-matrix); and

- compaction and mineralization of the shaly and argillaceous intercalations creating low permeability in these thin beds, particularly in the lower half of the fine-grained sandstone tongues to form barriers to fluid flow.

A second type of stratigraphically controlled diagenetic facies formed slightly below and sub-parallel to the pre-Greenbrier unconformity, possibly where a fossil water table had existed, is marked by mineralization and pore plugging by siderite. This diagenetic cementation zone cuts across the bedding at a low angle and both reduces porosity for oil storage and establishes another low permeability barrier to lateral fluid flow.

Reservoir Characterization

Simulated injection pressures did not correlate with actual injection pressures in Granny Creek field: calculated (or simulated) injection pressures were consistently lower than actual field data. To account for this discrepancy, localized low-permeability zones around the injection wells were introduced in the simulations.

Permeability values calculated from initial potential data are one or two orders of magnitude higher than permeability values calculated from injection data. This indicates that formation damage occurred during water flooding.

In comparing permeability distributions derived from initial potential data for the case with all wells and for the case which does not include stimulated wells, it can be inferred that high permeability zones (i.e. heterogeneous zones) have a natural occurrence in the reservoir and also an induced occurrence generated during well stimulation. Prevention of permeability reduction in injection wells should significantly enhance waterflood performance in Granny Creek field.

Trap

The distribution of formation water in Big Injun oil fields in southern West Virginia can be explained on the basis of a developing gas cap and the expulsion of formation oil and water down-dip and down-plunge north and westward by an expanding gas cap above a large basement high, now called the Warfield and Queen-Shoals-Minnora anticlinal trend.

Oil Production

Within Granny Creek field, Cumulative oil production displays above-average values within a north-south trend along the western margin of the field. This trend is broader in the northern half of the field, and is separated from the narrower trend in the southern half by an east-west discontinuity. Less geographically-extensive trends in other parts of the field have the same north-south orientation.

Trends in oil production correlate with depositional subfacies, diagenetic facies, reservoir characteristics, and structure, suggesting presence of relatively high oil-producing compartments enclosed by low oil-producing areas. Continuity of the pay zone appears best along depositional strike, north-south. Stratigraphic heterogeneity of the reservoir reflects the depositional and diagenetic history of the lower, fluvial mouth bar facies of the Big Injun: 1) oil accumulated in the thickest portions along depositional strike; 2) the upper, coarser channel facies caps the reservoir in most places; 3) shaly intertongues occur within the fluvial mouth bar facies; 4) diagenetic zones oriented north-south within the fluvial mouth bar facies cut across depositional units, thereby reducing permeability and retarding fluid flow. A map of ten-year cumulative production for wells completed during water flooding suggests poorer yield across the middle of the field where diagenetic cementation barriers are thickest, and best yield to the north, where these barriers thin and the marine-influenced proximal mouth-bar facies are thickest under the river channel facies.

Based on vibroseis and weight-drop seismic data, areas affected by reactivation of basement faults coincide roughly with trends in above-average oil production. Some

correlation exists between structures within the field and local high cumulative production. In the southern part of the field, permeability data and structure maps support the thesis that the narrow trend of high production results from enhancement of permeability and possibly porosity by fracturing and faulting.

Within Rock Creek field, production appears to be mainly controlled by structure. Fluids are stratified within the reservoir, with gas updip, and water downdip. Porosity modeling of the reservoir in this field suggests the presence of large, continuous zones of porosity, correlating with features identified in facies models.

Regional Implications

Stratigraphic cross sections recognized distinction between Pocono Big Injun (Granny Creek, Tariff, Clendenin fields) and "Maccrady" Big Injun (Rock Creek, Blue Creek, Pond Fork fields). Shales separate the Pocono from the "Maccrady" Big Injun sandstones. A subcrop map shows some sandstone reservoirs which are not Big Injun, but older Weir sandstones.

Basement structures were active during and after Big Injun sedimentation, influencing the: (1) paleoslopes for rivers; (2) vertical stacking of units over Rome trough border faults; (3) erosion and preservation resulting from pre-Greenbrier unconformity in response to movement of the West Virginia dome; (4) deposition of "Maccrady" Big Injun sandstones along the western block outside of Rome trough and the fluvial-deltaic complexes within Rome trough, skirting the Warfield anticline which was a growing structure; and (5) drainage basins affecting Big Injun sedimentation.

Comparison of other oil fields with Big Injun reservoirs show the importance of the river-mouth bar facies, capped by the coarser grained, trailing, fluvial channel-fill deposits.

Recommendations For Infill Drilling

Continue to infill along trends of good oil production in C2 tongue, and C1 and C3 tongues where thick marine-influenced proximal mouth-bar subfacies occur along a northwest-southeast trend within belt of influence south and near B member pinch out. Concentrate efforts on the flanks of basement structures developed after deposition of the reservoir interval. The western boundary of Granny Creek field is controlled by late-stage uplift of a basement fault. Locate small time-structures within the field where cumulative production is often higher. Identify interplay between detached and basement structures. Production from small folds tends to be highest over reactivated basement structures.

Care should be taken in well-stimulation design in areas where thin, brittle top seals are present. Thus, care and planning should be implemented during completion and stimulation design from the drilling of the first during the initial recovery stage so as not to impede future secondary recovery projects.

Secondary Recovery

Over-stimulation and relatively high injection pressures at Granny Creek field have

imposed a heterogeneity on the reservoir not visible during the primary production phase of field development. Additional reservoir heterogeneity at Granny Creek field was caused well stimulation and high injection pressures that breach the reservoir seal and bypass the reservoir through natural fractures that are, in part, small, low-angle faults in overlying tight limestones of the Greenbrier Group. In view of these conclusions, a reassessment should be made of the unsuccessful, experimental CO_2 flood in Granny Creek field.

In secondary recovery of oil by water flooding: (1) keep water injection pressures below 900-950 psi to avoid developing communication between wells; (2) perforate above and below diagenetic cementation zones in pay zone; (3) expect flow paths to be preferentially north-south where diagenetic cementation barriers cut across the pay zone; and (4) expect areas of reduced recovery where the shaly intertongues and/or diagenetic cementation barriers proportionally increase in thickness at the expense of the pay-zone thickness. Where five-spot well configuration straddles permeability barriers, engineering practices need to recognize this condition for optimum oil recovery. There is potentially recoverable oil in areas where communication between the wells has occurred. The re-arrangement of flooding patterns in these areas should lead to additional recovery.

Care should be taken in planning secondary recovery projects in basins that have had a history of compression. In brittle rocks, low-angle shear fractures can extend beyond the recognized margin of deformation. In such basins, it may be important to recover oriented core in adjacent brittle units for structural data as well as planning core recovery from the reservoir to document its characteristics.

Remediation of wells communicating through fractures should include:

- careful well-stimulation design;
- low-pressure injection;
- cementing previously over-stimulated wells;
- gentle recompletion through pipe and offset well drilling.

Reservoir Characterization Methodology

Permeability can be predicted from well log data in heterogeneous reservoirs if conventional core plug analyses and geological interpretations are available.

Indicator kriging is a sensitive tool for mapping data such as cumulative production, which displays considerable variability over short distances. Maps of indicator variables defined a number of trends that were not obvious on conventional contour maps of production. A recommended procedure for using the method is to begin with examination of a histogram of the raw data, and determining at least the median, 25^{th} percentile, 75^{th} percentile, and the 90^{th} or 95^{th} percentiles for use as cutoffs. The median can be considered a "typical" value, such that one can speak of a typical well with respect to production. The high percentiles highlight the unusual, presumably very profitable wells. At high cutoffs, the small number of wells exceeding the value means that variograms become irregular, and model-fitting becomes difficult.

For each cutoff selected, perform the indicator transform and compute directional variograms. Here one can learn about the presence and degree of directional anisotropies as reflected in the different ranges, relative degree of discontinuity at small scales as reflected in the apparent y-intercept ("nugget effect"), and changes in spatial continuity with increased cutoff value.

The final step is to use the variogram models and kriging to calculate the probability surfaces, check and correct order relations, and plot maps. Products may be used for economic assessments, for siting new wells in favorable areas, and for comparing with geologic maps. Probabilities calculated for low cutoff values can be used to calculate the probability of falling below each cutoff; such a map highlights areas of problem wells to be avoided in future drilling.

Seismic Study Methodology

The seismic time-structural relationships to oil production observed in some instances within the Granny Creek field suggest a possible seismic exploration rationale.

1. Concentrate exploration efforts on the flanks of basement structures developed after deposition of the reservoir interval: Seismic interpretations suggest that tectonic development of the field involves an interplay between basement and detached styles of deformation.

The reactivation of basement Fault A and its continuation to the south as Fault AB form the western boundary of the field. These faults were reactivated after deposition of the Big Injun sandstone, lifting the structure to the west with respect to Granny Creek field. The highest producing areas in the field are roughly confined to the reservoir interval affected by late stage uplift of the basement block between Faults A and B in the northern part of the field. Internal segmentation of the field by Fault A is suggested. Maximum subsidence trends are concentrated over the central basement block in the northern half of the field. With the exception of the Lower Cambrian, the block west of Fault B always subsided more slowly with respect to the block beneath the northern part of the field.

2. Locate small structures: Low relief folds within the reservoir are interpreted to be detached above decollements in the Upper Devonian shale section. Also, in some cases there appears to be an interplay between folds in the Big Injun and basement structures which were active during the deposition of the Big Injun to Huron (or Onondaga) interval. These folds are not readily visible using standard reflection arrival time contouring and isochroning. They are, in general, only about 4 milliseconds in relief.

Identification can be aided simply by displaying seismic data in the form of expanded-time-scale Big Injun arrival-time plots, and by noting interval travel time maxima (thickened areas) in the Big Injun-to-Huron travel time-difference plots.

3. Identify interplay between detached and basement structures: Although a detailed analysis of time differences may be impossible within the time frame and economics of exploration and field development efforts, several events on a seismic section can be digitized by hand and plotted in two to three hours. From an exploration and development viewpoint, it is critical to locate and determine the distribution of basement faults within a field. Structures above basement faults, active prior to, during and after deposition of the reservoir interval may have enhanced fracture porosity and be more highly productive than other areas within the reservoir.

4. Compute the *stack*-wavelet: Because the process of stack does not significantly change the phase of the seismic wavelet observed in a short-offset VSP (Appendix F), the zero-offset

VSP or near-hole VSP provides an accurate measurement of the seismic wavelet present in a stacked seismic data set. Determining the *stack*-wavelet provides the basis for subsequent deconvolution and model studies.

Because of the similarity between the *stack*-wavelet and the downgoing wavefield measured in the near-hole VSP, the VSP measurement could be used directly to deconvolve the data, yielding a 20 % increase of bandwidth and peak-frequency in the data. If the *stack*-wavelet were significantly different from that measured by the VSP, the deconvolution operator should be designed using the *stack*-wavelet rather than the VSP measurement.

Although long-offset VSP's were recorded in this study, measurements of the downgoing wavefield were distorted significantly by critical refractions along a shale/carbonate interface above the reservoir. Hence, modeling offset response may be a more effective and less costly way to determine whether offset variations of phase and amplitude are significant and whether stacking produces significant alteration of the wavelet measured in the VSP.

Computation of synthetic seismograms depends upon accurate definition of the seismic wavelet. The seismic wavefield can be significantly nonstationary, and the assumption of zero-phase for Vibroseis data can be wrong.

5. Identify reflector disruptions (small time offsets and amplitude anomalies): Small abrupt reflection-time offsets and local amplitude reductions were observed in seismic reflections from the reservoir and adjacent intervals near wells found to be problematic during water flood sweeping. These disruptions might indicate faulting and fracturing within the reservoir.

If reflector disruptions are encountered in the seismic data, they should be weighed by their association with other aspects of the data. In general, these disruptions of amplitude and phase are observed across folds in the reservoir interval. This interrelationship implies a structural origin, and increased probability of encountering fracture zones or faults in such areas. Where amplitude disruptions are not associated with significant structures in the seismic data, fracture and fault zone origins seem less probable.

These features are generally not observed in routinely processed seismic data and the approach to processing can significantly enhance these disruptions (Appendix E). Reduced stacking velocities can enhance diffraction associated with small faults. Deconvolution procedures produce considerable differences in seismic character, and careful design of the first break mute can enhance resolution of detail. Significance of reflector disruptions depends upon their association with other features such as folds.

Based on the results to date, it is recommended that locations of amplitude anomalies, phase changes, small folds and abrupt reflection time-offsets should be mapped. Their areal distribution should be examined for patterns, which might provide a distinction between randomly distributed features or ones that have stratigraphic or structural trends. When localized disruptions of the seismic signal appear along with other structural features in the reservoir, there may be an increased probability that these features represent highly fractured areas which might serve as thief zones during waterflooding of the reservoir.

REFERENCES CITED

Alger, R., Raymer, L., Hoyle, W., and Tixier, M., 1971, "Formation density log applications in liquid-filled holes": *in* Well Logging, Society of Petroleum Engineers Reprint Series No. 1, p. 185-196.

Bagnall, W., 1975, A Geological Investigation of the Granny's Creek Field, Clay County, West Virginia: unpublished intercompany report for Columbia Gas Transmission Company, Charleston, WV, 20 p.

Beardsley, R., and Cable, D., 1983, "Overview of the evolution of the Appalachian basin": Northeastern Geology, v. 5, p. 137-145.

Bjerstedt, T., 1986, "Stratigraphy and deltaic deposystems of the Price Formation (Upper Devonian-Lower Mississippian) in West Virginia: unpublished PhD Thesis, West Virginia University, Morgantown, WV, 730 p.

Boswell, R., Donaldson, A., and Lewis, J., 1987, "Subsurface stratigraphy of the Upper Devonian and Lower Mississippian of northern West Virginia": Southeastern Geology, v. 28, no. 2, p. 105-131.

Davis, J., 1973, Statistics and Data Analysis in Geology: John Wiley and Sons, New York, 550 p.

Davis, R. and Stephenson, E., 1929, "Synclinal oil fields in southern West Virginia": *in* Structure of Typical American Oil Fields, v. 2, p. 571-576.

Deutsch, C. and Journel, A., 1992, GSLIB: Geostatistical Software Library and User's Guide: Oxford University Press, New York.

Dixon, S., Summers D., and Surdam, R., 1989, "Diagenesis and preservation of porosity in Norphlet Formation (Upper Jurassic) Southern Alabama": American Association Petroleum Geologists Bulletin, v. 73, p. 707-728.

Donaldson, A., and Boswell, R., 1990, "Regional stratigraphy of Upper Devonian and Lower Mississippian sandstones of the Appalachians and their classification as hydrocarbon reservoirs using basin analysis": *in* 21st Annual Appalachian Petroleum Geology Symposium - Program and Abstracts, p. 10-21, abstract.

_____ and Shumaker, R., 1981, "Late Paleozoic molasse of the central Appalachians": *in* Sedimentation and Tectonics, edited by A.D. Miall, Geological Association of Canada, Special Paper no. 23, p. 99-124.

_____, Shumaker, R., Laughrey, C., Aminian, K., and Hohn, M., 1992, Measuring and Predicting Reservoir Heterogeneity in Complex Deposystems: Annual Report for Fiscal Year 1991, DOE/BC/14657-7, U.S. Department of Energy.

Dowell Schlumberger, 1986, "Formation evaluation of the J. B. Casto 133 and J. B. Casto 134 wells": Dowell Schlumberger Formation Analysis Laboratory (report to Pennzoil), p. 1-88.

Fuchtbauer, H., 1974, "Diagenesis of fluvial sandstones": Geologiche Rundschau, v. 63, p. 404-925.

Gas Research Institute, 1991, "Devonian (Ohio) gas shales workshop": Workshop handout, Gas Research Institute.

Heald, M., 1959, "Significance of stylolites in permeable sandstones": Journal Sedimentary Petrology, v. 29, p. 251-253.

_____, and Larese, R., 1974, "Influence of coatings on quartz cementation": Journal Sedimentary Petrology, v. 44, p. 1269-1274.

Hohn, M., 1988, Geostatistics and Petroleum Geology: Van Nostrand Reinhold, New York, 264 p.

Journel, A., 1983, "Nonparametric estimation of spatial distributions": Mathematical Geology, v. 15, no. 3, p. 445-468.

Journel, A., 1987, Geostatistics for the Environmental Sciences: U.S. Environmental Protection Agency, Project No. CR 811893, Las Vegas, 135 p.

Kruskal, J. 1964, "Non-metric multidimensional scaling: a numerical method": Psychometrika, v. 29, p. 115-129.

Kulander, B., Dean, S., and Williams, R., 1980, "Fracture trends in the Allegheny Plateau of West Virginia": West Virginia Geological and Economic Survey, map WV-11, scale 1:250,000.

Longstaffe, F., 1986, "Oxygen isotope studies of diagenesis in The Basal Belly River Sandstone, Pembina I-Pool, Alberta": Journal Sedimentary Petrology, v. 56, p. 77-88.

McDowell, R., 1992, "Discriminant analysis of Big Injun data classified by lithofacies and depositional environments": unpublished report to D. Patchen, West Virginia Geological and Economic Survey, Morgantown, 58 p.

McDowell, R., Avary, L., Matchen, D., and Vargo, A., 1992, "Evaluation of two techniques for the initial quantification of reservoir heterogeneity - Examples from the Appalachian Basin": American Association of Petroleum Geologists Bulletin, v. 76, No. 8, p. 1282, abstract.

Miall, A. 1977, "A review of the braided river depositional environment": Earth Science Reviews, v. 13, p. 1-62.

Norusis, M., 1992, SPSS for Windows - Professional Statistics, Release 5: SPSS Inc., Chicago, 348 p.

Paxton, S., Szabo, J., Calvert, C., and Ajdukiewicz, J., 1990, "Preservation of primary porosity in deeply buried sandstone: a new play concept from the Cretaceous Tuscaloosa Sandstone of Louisiana": American Association of Petroleum Geologists Bulletin, v. 74, p. 737, abstract.

Pittman, E., Larese, R., and Heald, M., 1992, "Clay coats; occurrence and relevance to preservation of porosity in sandstones": Society of Economic Petrologists and Mineralogists, Special Publication no. 47, p. 241-255.

Schlumberger, 1989, Log Interpretation - Principles/Applications: Schlumberger Educational Services, Houston.

Shumaker, R., 1980, "The importance of regional and local structure to the Devonian shale gas production from the Appalachian basin": 26th International Congress, Fossil Fuels Volume, Editions Technic, Paris France, p. 147-174.

_____, 1986a, "Structural development of paleozoic continental basins of eastern North America": Sixth International Conference on Basement Tectonics, Proceedings, p. 82-95.

_____, 1986b, "The effect of basement structure on sedimentation and detached structural trends within the Appalachian basin": *in* the Lowrey Volume; Studies in Appalachian Geology, Virginia Polytechnical Institute and State University, Dept. of Geology, Blacksburg, VA, p. 67-81.

Smosna, R., and Bruner, L., 1991, "Reservoir sedimentology of the Mississippian Big Injun in West Virginia": unpublished report to D. Patchen, West Virginia Geological and Economic Survey, Morgantown, 26 p.

Teufel, L., 1993, "Pressure-induced changes in reservoir stress state: applications to reservoir management": American Association of Petroleum Geologists Annual Convention Program, p. 189, abstract.

Yilmez, O., 1987, Seismic Data Processing: Society of Exploration Geophysicists, Investigations in Geophysics, v. 2, 526 p.

Zheng, L. and Wilson, T., 1992, "Vibroseis deconvolution: A case study in the Granny Creek oil field, West Virginia": *in* Proceedings, 60th International Meeting of the Society of Exploration Geophysicists, Proceedings, p. 281-283.

_____, Shumaker, R., and Donaldson, A., 1993, "A seismic interpretation of the structural development of the Granny Creek oil field": *in* 24th Annual Appalachian Petroleum Geology Symposium - Program and Abstracts, p. 125-126, abstract.

Zou, X. and Donaldson, A., 1991, "Regional stratigraphic analysis of the Big Injun sandstones (Mississippian) of West Virginia": American Association of Petroleum Geologists Bulletin, v. 75, no. 8, p. 1391, abstract.

_____ and Donaldson, A., 1992a, "Regional Big Injun (Price/Pocono) subsurface stratigraphy of West Virginia": Geological Society of America Abstracts, v. 27, no. 7, p. 309.

_____ and Donaldson, A., 1992b, "Reservoir sedimentology of the Big Injun sandstone in Granny Creek field, West Virginia": *in* 23rd Annual Appalachian Petroleum Geology Symposium - Programs and Abstracts, p. 80-86, abstract.

APPENDIX A
THE EFFECTS OF FRACTURES AND BARRIERS ON SECONDARY OIL PRODUCTION

Introduction

This study is a aimed at addressing the effects of the of heterogeneities on production performance. Hydrocarbon reservoirs are highly complex arrangements of porous media and heterogeneity is always present in these systems. Typical variations in absolute permeability, porosity, and fluid saturations that are caused by stratigraphic variations can be determined adequately by interpretation of well log and core data. It is not uncommon, however, to find large-scale heterogeneities such as fractures or sealed faults in these systems. This type heterogeneity (mega-heterogeneity) usually changes the flow patterns in a large area and affects the recovery of the fluid from the reservoir. Statistical approaches that are employed in modeling typical variations of reservoir parameters are inadequate in representing a fracture or barrier because they generally occur in a random fashion.

The objectives of this study were to find a simple and easy method of simulating isolated mega-heterogeneity (fractures and barriers) in a finite difference simulator and to determine the effects of heterogeneities on production performance during waterflooding. The results of this study will be also utilized to model the waterflooding performance of the Granny Creek field where communication between production and injection wells has been observed.

Modeling Mega-Heterogeneities

In an attempts to characterize naturally fractured systems, Warren and Root (1963) introduced the double-porosity model. Figure A1a portrays the idealization of a double porosity systems. The model has a primary porosity (matrix) which is high in volume but low in permeability; and a secondary porosity which is low in volume but high in permeability. On a macroscopic scale, this system could be considered homogeneous due to the relatively large size of the matrix blocks to the fracture blocks. However, on a microscopic scale, fluid flow occurs primarily within the fracture "network". Originally, the Warren and Root technique was created for pressure transient data analysis. Today, Warren and Root type simulation grids had been used to define most problems involving the characterization of fractured reservoirs. It is cumbersome and wasteful to create an elaborate system of matrix and fracture/barrier blocks only to model isolated natural fractures and barriers.

Fractures are characterized by very small volumes and high conductivity. Conversely, barriers or sealed faults have no volume and no conductivity. Altering conventional parameters to model the behavior of the mega-heterogeneities will generally lead to numerical instability. Grid refinement is another approach (Figure A1b) that uses very small blocks in a section of the model to represent the fracture or barrier. However, the size of the blocks representing the heterogeneity often needs to be extremely reduced or the parameters (porosity, permeability) need to be altered significantly. Large changes in block sizes and permeability values normally lead to the numerical instability. The numerical instability problems can be resolved by greatly reducing the time step which often renders the simulation impractical.

Transmissibility modification is an alternative approach for representing a fracture or barrier. Transmissibility determines the rate of fluid flow between two adjacent blocks in the numerical simulator (Figure A2a). As a result, the flow between the two adjacent blocks can be boosted, to model a fracture, or prevented, to model a barrier, simply by multiplying the simulator calculated transmissibility value explicitly by a constant. The advantage of transmissibility modification is that it is simple and practical for modeling isolated heterogeneities and since it makes no changes to block size or permeability, the numerical stability is not compromised. While for modeling barrier the transmissibility is usually multiplied by zero, an order of magnitude increase in transmissibility is typically sufficient for modeling fracture. Larger changes in transmissibility can, however, be made without sacrificing numerical stability.

Simulation Study

One of the objectives of this study to determine the effects of mega-heterogeneities on production performance during secondary (waterflooding). Previous studies on the effects of natural fractures and barriers on sweep efficiency and conductivity used an analog model (Aziz and Settari, 1929; Fanchi, et al., 1987) to allow visual inspection of the frontal advance. The results showed that impermeable barriers generally had small negative effects upon sweep and conductivity. The effect of a barrier is not critical because, as time proceeds, the injected fluid eventually moves around the restriction. But, the effects may be magnified if the barrier is long enough to reach the boundary, essentially sealing off a portion of the reservoir. In the case of a fracture, when placed parallel to the streamlines, the most profound effect is seen. This is due to a "conduit" effect created between the injector and the producer. To study the effects of mega-heterogeneity during the secondary recovery, a normal five-spot waterflood project was modeled. Four cases were simulated utilizing transmissibility modification approach. They were: parallel barrier, parallel fracture, orthogonal barrier, and orthogonal fracture. A base case with no heterogeneity was also simulated for comparison. Figure A2b shows the orientation of barriers and fractures used in this study. When When the heterogeneities are oriented orthogonal to the streamlines, their overall effects are not very significant. Figures A3 and A4 show that oil production is almost unaffected by fractures while it is slightly reduced in presence of barriers. The reason is that streamlines are almost unaffected by the existence of fractures. Barriers will distort the streamlines significantly but fluid will eventually find its way around the barrier. The effects on water production in either case are insignificant. When the barrier is parallel to streamlines, the cumulative oil production is reduced but not significantly. This is due to the fact that the barrier will not alter the sweep efficiency, although it may disturb the streamlines and cause fluids to travel through a longer path between the injection and production wells. The presence of barriers parallel to streamlines makes relatively little difference in water production.

The most significant effects was observed in the case of fracture parallel to streamlines as can be seen in Figures A3 and A4. The effects are due to existence of only one fracture. As can be seen in Figure A4, the water production in the fracture case is much higher than the base case. This can easily be explained since water is the injected fluid and will flow through the fracture into the production well. Early water break-through is usually a good indicator for the presence of the presence of natural fractures in parallel orientation with streamlines in

the field. Another indicator is a relatively lower injection pressure at the well nearby the fracture because water faces less resistance to flow.

Application to Granny Creek

For the purpose of implementing the methodology presented here, two adjacent five-spots were studied (Figure A5). These patterns are named P1 and P2 for referral purposes in this study. Waterflooding operations on the two five-spots have been in progress for approximately six years. The injection wells have been constrained by constant wellhead pressure, nearly 900 psi for all but the I-4 injector (Figures A6 and A7) which is approximately 400 psi. Initial average reservoir properties as well as the properties prior to waterflooding are given in Tables A1 and A2. Although the injected water volumes, reservoir rock parameters, and the sizes of these two patterns are similar, the oil and water production from these patterns is very different. While P1 behaves like a typical five-spot waterflood pattern (given all the field dependant parameters), P2 exhibits very low sweep as essentially no oil is produced. The inspection of the injection pressure data revealed that the pressure at I-4 is 50% less than that of the other injection wells. In addition, seismic data shows that a fracture may be present, oriented NE-SW through the pattern. Figures A8 and A9 show oil and water production from these two waterflood patterns. The behavior of the P2 pattern is characteristic of a system possibly containing a natural fracture extending from near I-4 to the production well P2 (Figure A5).

The modeling and simulation studies revealed that existence of a natural fracture connecting I-4 and P-2 within the Big Injun to be improbable. Careful evaluations showed that the injection from the I-5 well would interfere with a fracture having such orientation. A pressure distribution of the fracture area showed that I-5 created pressure interference at the midpoint of the fracture. This interference created a greater pressure drop between the fracture and P-1 than along the entire length between the fracture and P-2. Therefore, another zone was added above the "A" member. This layer was implemented to account for the fractured zone and corresponds to the Big Lime formation which lies directly above the Big Injun (Figure A10). Figures A11 and A12 show the comparison between field production history and the simulated results for P1 and P2. It should be noted that without implementation of findings from this study, matching the oil and water production for P2 would have been misleading. Once the presence of a natural fracture parallel to the streamlines was considered, the production history for P2 was matched. Geological studies and seismic interpretations confirm the presence and orientation of natural fractures in that area.

Conclusions

1. The effects of mega-heterogeneities in hydrocarbon reservoirs can be modeled successfully by altering the inter-block transmissibilities. This will allow the use of black-oil simulators with slight modification. The results are comparable to those achieved by using a Warren & Root type grid. Also, the method has proven easier to apply than a Warren & Root approach. It is believed that this method is also economical for smaller,

independent companies to utilize when faced with modeling a fracture or fault in a reservoir.

2. The most significant effects of mega-heterogeneities are seen in secondary production (waterflooding), when a fracture is oriented parallel to injection-production streamlines.

3. The future waterflooding projects in reservoirs in which mega-heterogeneities are thought to exist, may be optimized by orienting injector-producer pairs so that optimum sweep can be achieved.

4. The above method was used to simulate two Granny Creek five spot pattern production behavior initially with an in-zone fracture that provided poor results as compared to the field history. However, when fracture was modeled through the Big Lime, good agreement with the production history was obtained.

References Cited

Aziz, K. and Settari, A., 1929, Petroleum Reservoir Simulation: Applied Science Publishers Limited, London, England.

Fanchi, J., Kennedy, J., and Dauden, D., 1987, BOAST II: A Three-Dimensional, Three-Phase, Black Oil Applied Simulation Tool: Department of Energy, Bartlesville, OK.

Warren, J. and Root, P., 1963, "The Behavior of Naturally Fractured Reservoirs": Society of Petroleum Engineers Journal, p. 244-245.

APPENDIX B
PRESSURE FALL-OFF TEST ANALYSIS

Pressure fall-off tests were performed on Clay 891 in September of 1988 for 200 hours, and Clay 2499 in June of 1991 for 455 hours. The pressure fall-off data are shown in Table B1 . Upon analyzing the test data, effective permeability, skin factor, and radius of investigation for each of the wells were determined. The data in Table B2 were used for test analysis.

First, the presence of wellbore storage effects was investigated. The bottomhole pressure log was plotted versus the log of $[(t_p+\Delta t)/\Delta t]$ (Figures B1a and B1b). A line with a slope of one was then drawn. If any of the early time data matched a slope of one, the data would be affected by wellbore storage. If any wellbore storage is present, the slope from the Horner plot would be taken one and a half log cycles away from the affected data. This process will ensure the integrity of the analysis. The wellbore storage plots are found in Figures B1a and B1b. It was determined that no wellbore storage effects were present.

It should be mentioned that the following procedure assumes a mobility ratio of one between oil and water, which seems to be a valid assumption in this case. The second step was to plot bottomhole pressure versus the log of $[(t_p+\Delta t)/\Delta t]$ for each injection well. Figures B2a and B2b demonstrate the pressure fall-off test analysis. A best straight line was drawn through the late time data points and the slopes were determined to be 309 psi/cycle and 629 psi/cycle for Clay 891 and 2499, respectively. Also, $p_{1\ hr}$ was determined to be 2054 psi (Clay 891) and 1940 psi (Clay 2499) from the plots. This was accomplished by finding the intersection of Δt equal to one hour, and the straight line. The slopes were then used in the following Equation to determine the effective permeability of the formation.

$$k = \frac{162.6*q*\mu_w*B_w}{m*h} \qquad (1)$$

The computed values of permeability were determined to be 0.40 md for Clay 891 and 0.31 md for Clay 2499. Note that, for the permeability calculation, the viscosity and formation volume factor of water is used and not that of oil. This is because the flowing fluid in the well is water and not oil.

Next, the skin factor for each well was computed. This was accomplished using the following Equation.

$$s' = 1.1513\ \left(\frac{p_{1\ hr} - p_{wf}}{m} - \log \frac{k}{\phi\ \mu_w\ C_t\ r_w^2} + 3.2275\right) \qquad (2)$$

When the appropriate variables are substituted into Equation 2, the skin factors were determined to be -3.1 for Clay 891 and -2.5 for Clay 2499. A negative value for skin factor

indicates that the well has been stimulated sometime prior to the test. This is an interesting finding since the low permeability calculated from Equation 1 is in spite of the prior stimulation of the wells.

Finally, the radius of investigation was computed for the time-pressure test using Equation 3. Note that the time of tests were 200 hours for Clay 891 and 455 hours for Clay 2499. This value indicates the radius beyond the wellbore that was covered by this test.

$$r_{inv} = \sqrt{\frac{0.00105 * k * t_s}{\phi * \mu_w * C_t}} \qquad (3)$$

When computed, the radius of investigation was determined to be 243 feet for Clay 891 and 312 feet for Clay 2499 (Note: t_s is the time of the fall-off test).

The step rate testing was conducted in conjunction with the pressure fall-off testing of Clay 891 and 2499 and was used to determine the minimum injection rates and pressures which will fracture the formation.

The methodology used was to plot flow rate versus stabilized bottomhole pressure and determine the trend of the points. As the flow rates and pressure are increased, the data would reach a point where each new point lies on a new and different trend. This is the point where a fracture has opened within the formation. Here, only a few more data points are to be taken to ensure no damage to the formation. The last step is to determine two distinct trends within the data and their intersection is the maximum injection pressure and injection rate for the well.

It is important to note that when this test was conducted, surrounding wells were not shut in to ensure test integrity. Also, the testing on Clay 891 was terminated after six time steps because of an injection line leak. The trends for this well seem to yield slightly larger values of injection pressure and rate and this may be due to completely avoiding the lower pressures (300 to 1000 psi) experienced at the low flow rates (15 to 25 bpd) in Clay 2499. Table B2 presents the data and solutions of the step rate test.

APPENDIX C
MICRO-HETEROGENEITY CHARACTERIZATION OF THE BIG INJUN SANDSTONE

Introduction

This study is an attempt understand the higher than expected injection pressures encountered during waterflooding in the Granny Creek field. A detailed reservoir simulation study using core analysis permeability values (cores were taken prior to primary production) was performed. Numerically calculated injection pressures were found to be considerably lower than the field values. The analysis of injection pressure/rate data across the field as well as the results of the fall-off tests on two injection wells generally indicated that effective permeability was significantly lower than the permeability values determined from the core analysis. The modeling studies revealed that the introduction of a low permeability area around the injection wells (localized low-permeability area) produced successful simulation of both production and pressure behavior during waterflooding in Granny Creek field. Clay swelling/migration is the most common phenomenon responsible for formation damage in waterflooding operations. Thin sections taken from many of the cores showed that there was indeed a small amount of clay present in the rock matrix. However, the amount of clay in the rock matrix was not enough to justify the such drastic formation damage. It should be noted that optical microscopy cannot always make a distinction in mineralogy between the coatings on walls of the pores and the grains making up the rock. This suggested a need for characterization of the pore wall mineralogy, where fluids come into direct contact with the rock. This lies in the domain of micro-heterogeneity.

Methodology

This study is concentrated on characterizing the spatial distribution of clay minerals within the rock. Clay minerals distributed on the surface of grains where they come into direct contact with injected water, may explain the damage/high injection pressure in the wells. Scanning electron microscopy (SEM) was utilized to examine reservoir rock grains by bombarding them with electrons under varying accelerating voltages (units of kilo-electron volts, keV). This causes electrons located within the k-orbital of various minerals to be excited and emit a photon of energy. The SEM can detect this type of energy as a characteristic property of each element present within the grains. As the voltage is varied, the depth of penetration into the grain becomes proportional to the accelerating voltage (Figure C1). As seen in the figure, penetration depth becomes meaningful when comparing homogeneous and heterogeneous grains. In a heterogeneous grain, the mineralogy and elemental composition is unevenly distributed throughout the grain. This could cause the grain to have a different composition at its surface (point of contact with fluid) than that of the grain as a whole.

The laboratory setup included a scanning electron microscope equipped with a viewing monitor and adjustment controls. Data passed from the scanning electron microscope to a KEVEX machine which displayed the composition of each element over the time interval in the form of spikes. The height of each data spike is proportional to the amount of each

element present in the grain. Elemental composition data is then stored in the KEVEX computer in binary form, converted into ASCII format, and transferred to an IBM computer.

It should also be noted that the testing interval for each accelerating voltage was changed only once. When testing at 5 keV, the time interval was 40 seconds. When testing at any other voltage, 20 seconds was used. This is due to the amount of "dead time" (the amount of time the machine spends idle) the SEM encounters since it is much more difficult to control the dead time at 5 keV.

At first, testing was made at 5, 7, 9, 11, 13, and 15 keV. Then, a voltage sensitivity analysis was performed to see what voltage would allow complete penetration of a 1-3 microns grain. The results showed that eleven keV would completely penetrate each grain. Thus, the final testing voltages were 5, 8, and 11 keV.

Results

The results from Clay 1132 (1988.5 feet) and Clay 1110 (1917 feet) show that the Big Injun formation is indeed made up of grains of heterogenous mineral and elemental composition. It should be noted that the well depths from which samples were taken were located within the injection interval. The best way to represent this heterogeneity is by creating a silicon signal fraction chart.

The silicon signal fraction is simply the silicon signal count (Isi) obtained from SEM analysis divided by the addition of the aluminum signal count and the silicon signal count (Ial + Isi). When plotted versus accelerating voltage, the shape of the curve is flat from 20 to 11 keV (penetrating the entire grain) then decreases steadily from 11 to 5 keV (penetrating only the cement on the surface of the grain). Figures C2a and C2b show typical silicon signal fractions for Clay 1132 and 1110.

The results obtained from Clay 1132 show a decrease in silicon signal fraction as the depth of penetration - or accelerating electron voltage - decreases. Similarly, Clay 1110 exhibits the same increase in percentages of aluminum with decreasing accelerating voltage as does Clay 1132. Therefore, this suggests that the majority of aluminum (in the form of clay) is concentrated primarily on the surface of the grain (where it comes into direct contact with fluid).

APPENDIX D
MICROSCOPIC MODELING OF POROUS MEDIA

Introduction

How fluids flow through rocks and unconsolidated sediments is of technical and economical importance. The mechanism and flow path of the fluids in permeable solids must be understood if more effective recovery of hydrocarbon reserves is to be realized. The purpose of this research is to relate the structure of porous media on a microscopic level to the macroscopic properties including permeability. Permeability in rocks is not a well understood phenomenon. While simple porosity and permeability measurements are currently made on cores, the fluid flow in the reservoir depends on a detailed understanding of how porosity and permeability are affected by the structure of the porous media. This understanding depends on a detailed knowledge of the porous structure, size, interconnections and shape of the individual pores.

To obtain the detailed information on the shape and size distribution of pores and their intersections, the mathematical approach of "textural transforms" is used. Textural transforms provide a foundation for predicting pore size, shape and opening size distribution through a sophisticated analysis of surface area, line segment length, boundary curvature and boundary intersection. Should this be successful, then the flow properties may be predicted for a variety of petroleum bearing strata of different lithological properties.

Definitions

Porous rock generally consists of a deposit of particles that has consolidated over time. In this type of porous media there is a number of interconnected voids or large spaces called pores. Pores are connected by smaller spaces or constriction that are called throats or more precisely, ostioles. Each connected pore may have one or more ostioles. Pores and pore size may be critical to the amount of fluid that is stored in a porous media, but they are irrelevant to the flow of fluids in a porous media. What influences the flow is the narrowest part of the pore system that connects the pores. For clarity, this narrowest opening is called an ostiole.

Coordination number is defined as the average number of ostioles connected to each pore and is a measure of connectivity of the system. If a pore has four ostioles, then it has a coordination number of four. Similarly, if a pore has six ostioles, then it has a coordination number of six. Pores with four and six coordination numbers may be seen in Figure D1a. One can reason that if the medium is formed by spherical particles of similar size, then the expected coordination number would be six. No other model leads to arguable different coordination number.

A textural transform is physical model of a real world solid in which the key physical parameters are conserved. In porous media, the void space are pores connected through ostioles to other pores. Essentially this is a network wherein the pores are the nodes and the ostioles are the connections between the nodes. Therefore, a porous medium with a an average coordination number of four can be transformed into a rectangular array wherein each pore has coordination number of four. Ostiole size is a measure of the flow resistance

between the pores. In this case the textural transform is a regular network replacing the random network of the porous media.

Analysis

A realistic model of a porous medium was developed. Coordination number and ostiole size distribution were found to be the key parameters in the model. From this model a textural transform was developed. The textural transform is a regularized net work where the key parameters are the coordination number of the porous medium and the size distribution of the ostioles. Using the these parameters the textural transform was turned into a mathematical model.

In a porous rock there will be pores with a variety of coordination numbers. For the sake of modeling, however, it is simpler if one assumes that all pores have the same coordination number. To model a porous rock with all the pores having the same coordination number, one sets up an orderly three dimensional array of interconnected pores. In a real world porous rock the pores are not connected in an orderly array, but this spacial distortion is not relevant, because the governing factor is the resistance to flow in the ostioles. Two extended studies were made of the mathematical model:

1) the effect of ostiole size on fluid flow path;

2) the effect of particle size on flow blockage.

Additionally, novel methods for quantifying both the coordination number and the ostiole size distribution were also developed.

Fluid Flow Path

In this part of analysis, the fluid flow path characteristics in the permeable media was investigated. When possible, simple equations were developed to facilitate physical-mathematical insight into flow behavior. The porous medium is modeled as a network of interconnected pores with only two sizes of ostioles. A typical array may be seen in Figure D1b. Because it is difficult to represent a three dimensional array in a two dimensional drawing, all further drawings of networks will show a two dimensional network. Figure D2a is such a two dimensional array, with the understanding that each pore in the plane is connected to a similar two-dimensional array in front of the drawing and one behind the drawing. Note that in Figure D2 there are two different sizes of ostioles large and small.

In this simple model, it is assumed that the flow through an ostioles is proportional to the square of the ostiole's diameter times the difference in pressure between the two pores connected by the ostioles. In other words the pore diameter is much larger than the ostiole's diameter and thus all the resistance to flow occurs in the ostioles and none in the pores. This means that the pore is a juncture of six different flow resistances connecting the six nearest neighbor pores or junctures. Moreover, flow through the ostioles is linear with respect to the pressure gradient between the two pores.

If at the top of the permeable rock the fluid is under high pressure, while at the bottom the fluid pressure is at ambient pressure, flow through the rock will progress from the top of the rock to the bottom through the ramulus network. While some flow may be straight down any one column of pores, most flow will be through a complex path. For any given pore, the major part of the flow through that pore can either be down or lateral, through the four side ostioles, depending on the relative sizes of the ostioles in that pore and the pressure in adjacent pores. Figure D2b shows two paths: "a" and "b". If the flow is straight down as it is in "b", then, while the path is short - 8 steps - but the flow must pass through 4 small ostioles to reach the bottom. On the other hand, if the flow takes the longer path of "a" it takes 13 steps but only through 2 small ostioles. Thus the path "a" has a lower resistance than the path "b". Consequently, more flow will go through "a" than "b".

Let p_l be the probability that a given ostiole is large and p_s the probability that a given ostiole is small, then:

$$p_s = (1-p_l) \qquad (1)$$

In the proposed model, if the bottom ostiole is large, then the fluid will flow down - Figure D3a - "a"). Thus the probability of the fluid flowing down depends only on the probability that the bottom ostiole is large - p_l. However, for the fluid to flow laterally, two conditions must be met:

1) the bottom ostiole must be small - p_s;

2) at least one of lateral ostioles is large (Figure D3a - "b").

The probability that all four of the lateral ostioles are not small is "1 - p_s^4" Therefore, the probability of flow in a given pore being lateral is, p_{lf}, is:

$$p_{lf} = p_s (1 - p_s^4) = p_s (1 - p_s^2)(1 + p_s) (1 - p_s) \qquad (2)$$

As the fluid traverses the slab, the ratio of side steps to down steps is:

$$r = \frac{p_s(1+p_s^2)(1+p_s)(1-p_s)}{(1-p_s)} = p_s(1+p_s^2)(1+p_s) \qquad (3)$$

Note that as p_l goes to zero or conversely p_s goes to 1, r goes to 4 - as one might expect. If the number of pores in a vertical pore column is "n", then by definition, the total number of down steps is n. Therefore, the number of side steps is:

$$S_s = n\, p_s (1 + p_s^2) (1 + p_s) \qquad (4)$$

If one adds the number of side steps, S_s, to the number of steps down, n, one obtains the total number of expected steps, S_t, the fluid would take if it traversed the rock by going through only the larger ostioles. Thus S_t *is:*

$$S_t = n [1 + p_s (1 + p_s^2) (1 + p_s)] \quad (5)$$

Consider now the case of the flow resistance in two separate paths:

1) straight down a pore column (Figure D2b - "a");

2) through the much longer path of larger ostioles only (Figure D2b - "b").

Moreover, assume the flow resistance in both paths is the same. Define the variable r_s as the ratio of the resistance in the smaller ostioles to that in the larger ostioles. For simplicity assume that the resistance through the larger ostioles is unity. To equate the resistance in the two different paths, one must determine the number of large and small ostioles in each path. In the large ostioles' path all the ostioles are of the large size, but, remember in the straight down path of n steps there are $n(1-p_s)$ large ostioles and np_s small ostioles. Equating the resistance of the two paths as equal, one obtains the following equation:

$$n\ [1+p_s(1+p_s)(1+p_s)] = n\ [(1-p_s)+r_s p_s] \quad (6)$$

where:

$$r_s=1+(1+p_s)(1+p_s^2) \quad 2\le r_s\le 5 \quad (7)$$

There are four solutions for p_s: two are imaginary, one is trivial ($p_s = 0$) and the fourth exists in a narrow range of r_s values. Since p_s is a probability function, the values of r_s range from a low of 2 to a high of 5. From a physical point of view, this narrow range of resistances is unrealistic because one would expect ostioles diameters to vary by at least a thousandfold and thus ostioles resistances, by a million fold.

To explain the restriction on resistance values one must examine the hidden assumption in the model. It was assumed that if flow could not proceed down through a large ostioles, then it would proceed laterally through large ostioles until the flow could find a pore with a large down ostiole. Consider the model from a second point of view. Since the model is a rectangular array, it consists of n horizontal plates. The question asked is: "What is the probability of a flow that enters a pore in one level, be able to find a path of all large ostioles such that it moves to one layer below - Figure D3a - "c" and "d". This function, p_d, is the sum of a geometric series: the

probability of it moving down immediately, the probability of 1 step laterally and then down, 2 steps laterally then down, 3 steps laterally and so forth.

$$p_d = (1-p_s)(1+\frac{p_s(1-p_s^4)}{1-p_s(1-p_s^4)}) \quad (8)$$

If one sets the probability of a small ostiole occurring equal to 0.5, 0.2, 0.1, 0.01, 0.001, then the probability of the flow moving through large ostioles is respectively 0.72, 0.84, 0.91, 0.99, 0.999. Thus even with half the ostioles being large, there is less than 3/4 of a chance the flow will move down in just one step. Even with 99 percent of the ostioles being large, there is only 0.99 chance of the flow moving down one level. The inescapable conclusion is that flow cannot traverse porous rock via large ostioles only.

Still using the same model, consider now two paths of fluid flow:

1) flow directly down a column;

2) flow through large ostioles.

In this exercise, the objective is to compare the number of small ostioles in the two flow paths. As calculated earlier, the expected number of small ostioles in the column is np_s. Since p_d is the probability of traversing one layer by flowing through larger ostioles, then 1 - p_d is the probability that the flow will traverse small ostioles when going from one layer to the next layer. Thus, in the second flow path, the expected number of small ostioles is $n(1 - p_d)$. Since the straight column path should have the largest number of small ostioles, the difference in small ostioles in the two paths is:

$$\Delta n = n\,(1-p_d-p_s) \quad (9)$$

While the lateral path always has fewer small ostioles to traverse, the difference is not spectacular. As illustrated in Figure D3b, when the percentage of large ostioles is high the difference is low because few small ostioles are encountered in the columnar path. At the other extreme, when the percent of large ostioles is low, under 10%, the difference is again low because the likelihood of finding a lateral path that leads down through n large ostiole is low. Even at the peak which occurs at 53% small ostioles, the difference is 26% fewer small ostioles or 43% reduction in the small ostioles traversed in the lateral path. While this is a significant reduction in the flow resistance and indicates that complex multichannel flow does occur, it is not an order of magnitude, in fact, it is not even a factor of two reduction.

Using the same model of pore network as above, for all the paths to contain at least one small ostiole the fluid must either start though a small ostiole or all the channels of connected large ostioles must be lined with small ostioles. (One can expect that all the large-ostiole

channels will eventually end in a pore with only small ostioles exits.) If the number of ostioles, small and large, intersecting surface (layer) A is N, then the number of small ostioles is: Np_s.

To evaluate the number of small ostioles lining the large-ostiole channels one must calculate the number of large-ostiole channels that run from the layer A and then the number of small ostioles that line each of these large-ostiole channels. When only the large and small ostioles are being considered, the number of large-ostiole channels that run from surface A is the same as the number of large ostioles that are at the surface A which is: $N(1- p_s)$.

Next, the length (m), or the number of pores, that large-ostiole channels extend must be estimated. Since the fluid is entering a pore via a large ostiole and the probability of a pore having one or more of its ostiole exits be large is: $(1 - p_s^5)$. Then, the probability of having a large-ostiole channel of length 2 is $(1 - p_s^5)^2$ and of length m is $(1 - p_s^5)^m$. To estimate the average length of the large-ostiole channels, it is assumed that there is probability of 1/4th that the channel will terminates in a "blind end" pore . . (One uses 1/4 rather than 1/2 for two reasons: (a) to be conservative and (b) some of the large-ostiole channels will branch.). Therefore the length m (number of pores) is:

$$m = \frac{\log(1/4)}{\log(1-p_s^5)} \quad \textbf{(10)}$$

To calculate the number of small ostioles that associated with the large-ostiole channels, one multiplies the number of said channels, by the length of each channel (in pores) by 4 (the number small ostioles associated with each pore). At the end of each large-ostioles channel there is a "blind end" pore with 5 small ostioles. Thus the total number of small ostioles associated with each of the large-ostioles channels, N_p, is:

$$N_p = N(1-p_s^5)[\frac{\log/(1/4)}{\log(1-p_s^5)}]+5 \quad \textbf{(11)}$$

Equation 11 above is an approximation of the total number of small ostioles that are associated with the large-ostiole channels. Combining the number of small ostioles in a layer with the number of small ostioles in the large ostiole channels, one obtains the total number of small ostioles needed to impede the flow. Namely:

$$N_t = Np_s+N(1-p_s^5)[\frac{\log(1/4)}{\log(1-p_s^5)}]+5 \quad \textbf{(12)}$$

The above equation is only a reasonable approximation under restricted conditions. If the number of large ostioles is relatively small then large ostiole channel length will tend to be short. In addition, there is less likelihood of branching to occur in any given large ostiole channel.

While the proposed porous rock model is simple, the analysis of all possible flow paths through an infinite slab of rock is a complex process, beyond the scope of this study. Nevertheless, a set of simple equations has been developed from the uncomplicated model that yield an insight into (predicts) how the flow of a fluid in a porous rock will behave as a function of the percent of large and small ostioles. From Equation 3, it is clear that even for a small percentage of small ostioles, e.g. 20%, the flow rate is sensitive to the presence of small ostioles. Moreover, flow is seldom straight down the network, rather it is a complex path unless either the percentage of large or small ostioles is very small - 5%. From Figure D2b one can see that the more complicated lateral flow yield less flow through small ostioles.

Because the flow of fluids in porous rocks almost always goes through a narrow ostiole, clogging of these small ostioles is almost inevitable if the fluid carries any type of small particles or emulsions. Moreover, because it is the small ostiole carrying the greatest flow load that is most likely to be clogged or infarcted by an entrained particle, the rate of blockage or rate of flow resistance mounts rapidly with just a few entrained particles.

Flow blockage in a porous medium is an area, not a volume phenomenon. This means that it takes a relatively small volume of entrained particles to completely block the flow in a porous rock. In other words the blockage is almost a skin effect that is permanent unless the rock is fractured perpendicular to the blocked skin thus permitting the fluid to penetrate through the blocked skin.From this study two important conclusions may be drawn:

1) If effective modeling work of porous media is to be done, then the size distribution of ostioles must be measured.

2) Porous media, whose flow is from pore to pore via ostioles, is easily blocked by fine particles clogging the smaller ostioles. The greater the flow through a given small ostiole, the more likely it is to be blocked.

Flow Blockage

A model based on a two-dimensional array with varying size ostioles and coordination number of four was developed to simulate ostiole blockage. A single particle of a given size was introduced into the system at a random point on the porous medium surface. It flowed through the porous medium until it entered an ostiole smaller than the particle. Complete ostiole blockage was assumed. Again a single particle of a given size was introduced into the system at a random point on the porous medium surface. This second particle was followed until it entered and thus blocked an ostiole smaller that the particle. Particle flow out of a pore was probabilistically calculated based on a random number and the rate of flow through the exit ostioles from the pore.

This results of investigations based on the developed computational method showed that blockage was an area phenomenon. Almost all the blockage took place within the first ten layers and almost all the significant blockage took place within the first five layers. As the percent of ostioles blocked increased there was a slow decrease in the permeability, followed

by a rapid permeability decline after the percent of ostioles blocked exceeded the threshold. This threshold increased with increasing coordination number. The results of this study have been presented in previous reports.

Additional studies of pore array investigated the effect of coordination number on ostiole blockage and permeability reduction. Coordination numbers of two, four, six and eight were evaluated. Simulation of the odd coordination numbers, three, five and seven lead to complex arrays and were not considered for evaluation. The results of this study show that the higher the coordination number the greater the number of ostioles that must be blocked to significantly diminish the permeability. However, the influence of coordination number diminishes as it exceeds 6 (for two-dimensional array).

Skin Model

The above studies involved linear flow. Flow entered an essentially infinitely wide slab and exited an infinitely wide slab. While flow velocities through any given size ostiole might vary widely, average velocities throughout the slab were independent of position in the slab. In this model, the porous medium behaves as a filter for entrained particles in the fluid. The particles are filtered out near the up stream surface of the porous medium. This model simulates flow through a porous media in a laboratory. These two mathematical models are also effective in predicting fluid away from the wellbore. Linear flow in a rectangular networks is not a satisfactory model for ostiole blockage near the wellbore.

A different model for flow into a well was developed. This model involved increasing flow velocities as the fluid approached the well. Since there are literally no reliable data on the coordination number, ostiole size distribution, particle generation, and particle size distribution in the literature, the model requires too many assumptions about the nature of porous media to accurately be developed .

Ostiole blockage as a result of fluid flow into the wellbore is a complex problem. Not only the flow velocity increases as the fluid approaches the wellbore, but the problem of particle arises. Two potential sources of particles can be postulated:

1) the particles lying loose in the pores and entrained by the fluid;

2) the particles created in the pores and breaking loose from the pore surface due to the fluid velocity.

From our earlier study, it is clear that particles are rapidly filtered from the fluid. This means that entrained particles from a distance are not going to block ostioles near the wellbore. Similarly, if the created particles arise a distance from the wellbore, they too will be filtered out long before they get to the well. Thus the particles that block the wellbore must be created near the wellbore. If the created particle is the cause of blockage, the blockage will occur within a very short period of time. This is unlikely. If the entrained and created particles are not the source of ostiole blockage near the wellbore, then what causes blockage of flow? Two possible phenomena are suggested:

1) agglomeration of fine particles;

2) narrowing of the ostioles.

If these suppositions are true, then increasing fluid velocity should aid the agglomeration and/or narrowing of the ostioles. Agglomeration of fine particles with increasing velocity appears unlikely. If the agglomeration phenomena were velocity sensitive then all the wells would have been plugged at the critical velocity. Moreover, as the well plugs, the velocity changes and so would the critical agglomeration velocity. However, narrowing of the ostioles is a possibility. With the change in pressure, temperature, or pH near the wellbore, material normally soluble might become less soluble or solids can be formed as a results of chemical reactions. This material would precipitate out in the region close to the wellbore clogging the ostioles. Thus if a well were pumped slowly (lower pressure drop), then more total oil could be removed before the near well ostioles were plugged.

Measurement Methods

The lack of reliable experimental data on the ostiole size distribution and the coordination number cripple even simple understanding of how porous media are blocked by particles. It is therefore necessary to develop a method for measuring both the coordination number and the ostiole size distribution. The proposed two theoretical measurement methods need to be developed if the behavior of porous media is to be predicted. While developing these measurements will take time and effort, these key physical properties of porous media characterize the media. For progress, eventually these parameters must be measured.

This section describes possible methods for experimentally measuring the ostiole size distribution and coordination number of porous solids. While the ostiole size distribution measurement would appear the most difficult task experimentally, it is the coordination number that is the more complex. Simpler methods may be found, but, presented below are experimental methods for making each measurement.

Coordination number measurement method requires counting the number of pores in a solid and the number of ostioles. If N_p is the number of pores and N_o is the number of ostioles, then the coordination, C_N, is:

$$C_N = \frac{2N_o}{N_p} \quad (13)$$

To count the pores and ostioles one must reverse the solid and void spaces. To do this hot liquid wax is forced into the porous media in a vacuum. After the wax hardens, the solid is dissolved in hydrofluoric acid. Left behind is the void space modeled in solid wax (the wax mold is impermeable to the acid). Once the original solid is dissolved, one can count the pores, the large cavities, and the number of arms associated with each pore, the ostioles. While tedious, this method will quantify the coordination number for a given porous solid. As far as is known, no such data exists.

Measuring the ostiole size distribution may be done by a step procedure using mono-sized spherical particles. Take a porous medium disk. Flow a liquid containing a known number of

mono-sized spherical particles through that disk. Cycle the fluid through the disk until the change in pressure drop is negligible. All the (blockable) ostioles equal to or smaller than the particles are blocked. Repeat the process with a larger set of mono-sized particles. Again all blockable ostioles equal to or smaller than the larger spheres are blocked. The number of larger spheres stored in the porous media are the number of blockable ostioles which have a size smaller than the spheres. Repeat this procedure for larger set of mono-sized spheres to obtain the ostiole size distribution.

While the above method for quantifying the ostiole size distribution using steps of mono-sized spheres, should yield reproducible results, it is not the true ostiole size distribution. A small percent of the ostioles will not be blocked because particles will block the flow path containing the different size ostioles, thereby preventing all ostioles in a given size range from being blocked. If the coordination number for a given porous media is known, then a correction factor can be estimated.

APPENDIX E
SEISMIC DATA PROCESSING AND SMALL FAULTS

Well log interpretation suggests that small faults may be the cause of well communication problems. Well log structure in the areas where communication wells are reported indicates that fault offsets of 15 to 20 feet are possible. Computer simulations suggest that abrupt faults with relatively restricted fractures zones bracketing them could produce some of the changes in seismic character observed near problem wells. Table E1 lists the presence or absence of time-offset and waveform changes in seismic data observed near reported problem wells identified by pumping tests. The tabulation indicates that in most instances, some change of seismic characters can be found near wells where communication problems have been reported.

Seismic expression of the features found near problem wells in the water-flooding project vary with the seismic source and data processing parameters. For example, weight-drop Line 17 was shot along part of Vibroseis Line 2. As listed in Table E1 above, areas near communicating wells along these two lines are marked by different time offsets and character changes. The weight drop source generates wider bandwidth than the Vibroseis data. Comparison of weight drop with Vibroseis data in Table E1 (line 17 and line 2; line 11 (brute stack) and line 6) suggests that sometimes, the former may show more detailed waveform changes than later in the vicinity of communicating wells.

Considerable seismic data reprocessing was undertaken as part of this study. Data processing tests suggest that different processes and processing parameters will produce significantly different changes of seismic character in the vicinity of communicating (or problem) wells. Much of the reprocessing was focuses on improving the resolution of the seismic data. Figures E1 and E2 show that the regular vibroseis deconvolution (Ristow and Jurczyk, 1975) used in the original data processing (Figure E1) does not significantly compress the seismic wavelet compared to the seismic section without the deconvolution (Figure E2). Faults or fracture zones (if present) may be poorly resolved in the original seismic sections (Lines 2 and 6). Therefore, the data reprocessing was focused on how to enhance seismic characters found in areas where well communication problems were reported. If resolution of seismic features in these areas could be improved their presence might become more obvious in other parts of the data.

Deconvolution is a standard data process used to increase seismic resolution. However, there are a variety of different deconvolution methods that can be used. Numerous deconvolution tests suggested that the Berkhout (1977) deconvolution designed on the Klauder wavelet derived from the 20 to 120 Hz sweep used in the Vibroseis survey improves resolution of character changes in the vicinity of problem wells (Figure E3). Apparent frequency of the Big Injun reflection (at about 0.3 seconds) has been increased from 48 Hz achieved by regular vibroseis deconvolution (Figure E2, Ristow and Jurczyk, 1975) and the Berkhout deconvolution using the zero phase equivalent of VSP derived wavelet (Figure E4) to 60 Hz. Reduction in amplitude and/or 2-4 ms time offsets near problem wells on the reprocessed section (Figure E3).

The processing sequence also influences the quality of the stack section. Gibson and Larner (1984) suggested to apply the zero-phase vibroseis deconvolution after application of an earth attenuation filter. This sequence may improve the phase treatment for zero-phase data, because vibroseis wavelet is nearly symmetrical after gain recovery. Figure E3 displays

the result of first applying gain recovery and then deconvolution. This processing sequence increases low amplitude events, especially, the event below the Big Injun, which pinches onto the Big Injun reflection (Figure E3). This processing sequence also reduces processing noise. Figure E5 shows the same seismic section, but processed with deconvolution before gain recovery. The noise observed at the interpreted fault locations is believed to be the result of deconvolution process rather than statistics since these vertical zones are less noisy without deconvolution (Figure E2). In the reprocessing, the window length selected to calculate gain recovery curve is 0.3 seconds. A short window may also help to enhance weak events and reduce noise spikes before deconvolution.

As noted above structural relief of 15 feet or so is often observed between wells in the field. Relief differences of 15 feet or so are associated with wells in the vicinity of problem wells, and have been interpreted to result from faulting. Seismic model studies discussed in Appendix G indicate that a small fault with 15 feet of vertical offset and no associated fracture (low-velocity) zone will produce only minor changes of seismic amplitude, and no unusual waveform character changes. The presence of waveform changes in these areas suggests that other factors influence fault appearance on the seismic section. As noted in Appendix G, changes of waveform character similar to those observed near reported problem wells can be simulated by introducing low-velocity zones across the faults. In addition, time-delays observed in these areas are greater than expected based on structural relief between wells in these areas. As noted in Appendix G enhanced time-delays are produced by the velocity reduction in the vicinity of the fault.

Stacking velocity tests reveal that the appearance of the anomalous seismic features also vary with stacking velocity. Figures E6 and E7 show stack sections of line 2 using, respectively, 400 ft/s above and 400 ft/sec below the optimal stacking velocity used in Figure E3. In general, if the stacking velocity is increased, waveform changes are reduced. Table E2 gives the relationship between stacking velocity and the time delay observed at Station Nos. 155 and 210 on Vibroseis Line 2.

Observation on Table E2 indicates that time offset of the Big Injun reflection associated increases with decreasing stacking velocity. Stacking velocities that are slightly lower (e.g. 200-400 ft/sec.) than the final one may enhance seismic features related to small faults. If stacking velocity is too low, it will decrease the signal-to-noise ratio.

Increase of time offset may also, in part, be related to interference of diffractions. As noted in Appendix G diffractions at points of impedance contrast such as those associated with low-velocity fracture zones or small faults produce noticeable changes of seismic phase and amplitude. Apparent faults are also produced by diffraction events in areas not actually offset (see Figure E17b for example). Lower stacking velocity enhances diffractions, because moveout of the diffraction is greater than that of reflections at the same time. Interference of enhanced diffractions may result in apparent time offset of the Big Injun reflection at these small fault zones. Obviously, apparent time offset may not represent true offset of the fault. Seismic and well log interpretations suggest that equivalent time offset of faults at Station Nos. 155 and 210 are 1.5 to 3 ms. Therefore, 100 ft/s higher than the final stacking velocity probably is optimal to show the real time offsets on the seismic section. Since seismic sample rate is 2 ms, time offsets will appear as multiples of the sample rate.

Variations in the application of first break mute will also significantly change apparent frequency and waveform characteristics in a stack section. Figures E3, E8, and E9 were processed using different first break mute parameters (20%, 30% and 40 % normal moveout (NMO) stretch respectively). The best fault interpretation is made on the seismic section using

20 % NMO stretch. Larger allowable NMO stretch yields phase and amplitude distortion in after stack and reduces bandwidth and therefore seismic resolution.

In summary, seismic data processing can enhance the amplitude and waveform changes observed in the vicinity of problem wells in the waterflood project at Granny Creek. These features are interpreted to be associated with small faults or fracture zones. Processing studies indicate that changes in the processing parameters may produce significant changes in the seismic waveforms and apparent time offsets observed in the data. Therefore, apparent time-offset may not represent true time-offset.

Additional faults interpreted from the seismic section (Figure E3),such as those observed at station nos. 160, 180, are not related to well communication problems. These seismic features do not resemble the seismic response predicted by the model studies of Appendix G and probably are not fault related. Pumping tests indicate that in the Granny Creek field, the trend of almost all communicating wells is in a northeast-southwest direction. Operators in the field report that well communication appears to occur through the overlying carbonate intervals in natural fracture systems.

The interpretations made in this study suggest that these inter-well fracture zones may be seismically detectable. However, the presence of these anomalies in areas not associated with communicating wells, and the absence of similar features in the weight-drop data, leave the significance of these features in question.

References Cited

Berkhout, A., 1977, "Least square inverse filtering and wavelet deconvolution": Geophysics, 42, no. 7, p. 1369-1383.

Gibson, B. and Larner, K., 1984, "Predictive deconvolution and the zero-phase source": Geophysics, 49, no. 4, p. 379-397.

Ristow, D., and Jurczyk, D., 1975, "Vibroseis deconvolution": Geophysical Prospecting,.23, p. 363-379.

APPENDIX F
VSP GUIDED POST-STACK DECONVOLUTION AND MODELING IN THE GRANNY CREEK FIELD

Introduction

Changes of reflection amplitude and waveform shape associated with reflection events from the reservoir and surrounding intervals in the seismic data over Granny Creek (Figure F1) are rather subtle. For the most part, they result from changes of acoustic impedance associated with intervals that are too thin to be resolved.

Waveform variability is also a function of the shape of the effective seismic wavelet in the data. The assumption that the seismic wavelet is either zero- or minimum-phase, if incorrect, introduces additional error into geological interpretations of the data. As an alternative, direct measurement of the wavefront with a vertical seismic profile helps eliminate some of this uncertainty. Even this, however, does not accurately define the seismic wavelet, since: the seismic section is a mixture of traces collected over several different offsets and directions; several processes have been applied to the data; the wavelet from one place to another along the length of the line may undergo additional changes related to changing near-surface conditions and source-coupling; and the downgoing wavefield at any given point may be significantly non-stationary.

At Granny Creek, direct measurements of the downgoing wavefield were made at several levels beneath the surface with a vertical seismic profile. The primary wave just below the reservoir interval was used as the design wavelet for post-stack frequency domain inversion. The issue of wavelet distortions resulting from CMP stack and amplitude variations with offset (AVO) is also addressed.

Vibroseis Deconvolution

The standard approach to the processing of Vibroseis seismic data employs a surface consistent deconvolution approach designed for Vibroseis data (Gibson and Larner, 1984). The technique effectively eliminates phase shifts produced by the deconvolution filter leaving the phase of the output wavelet nearly identical to that of the input. Hence, if the input wavelet is zero-phase, the output wavelet will also be zero-phase (Gibson and Larner, 1984).

A synthetic seismogram computed at the VSP well ties with the data near the well (Figure F1), and suggests that the output phase of the *stack*-wavelet must be similar to that observed in the VSP, and that Vibroseis deconvolution has not altered the phase (or changed the shape) of the wavelet by very much.

Model study

The effect of amplitude variations with offset and stacking can be evaluated by generating the synthetic seismic response for a CMP gather. The computed gather includes offset

variations of phase and amplitude using Poisson's ratios derived from a full-waveform log of the VSP well.

The seismic response of reflection events from the top and bottom of the Big Injun sandstone in a CMP gather (after moveout correction) are shown in Figure F2. A significant drop-off of reflection amplitude occurs with offset, however, there is little change in the shape of the reflection, which in this case is just the isolated mixed-phase wavelet measured in the VSP. The effect of stacking the offset response is shown at right. The stacked trace represents a "stack" wavelet. The stack-wavelet would be the effective shape of the seismic wavelet imbedded in the stacked seismic data. The experiment supports the inference made above that the *stack*-wavelet is almost identical to the VSP-wavelet.

Computation of the offset reflection response for the entire series of reflectors in this intervals is shown in Figure F3. The need for careful design of the first-break mute as discussed in Appendix E is highlighted by the significant difference in appearance of the stack traces at right in Figure F3. Failure to eliminate the long offsets in the top part of the figure produces a stack response much different from what is observed in the data. Attempts to model such a data set would be impossible given the wavelet measurements at the VSP well.

Post-stack frequency domain inversion

The mixed-phase wavelet observed in the vertical seismic profile can be used to design a deconvolution filter to convert the effective wavelet in the data to zero-phase in the vicinity of the well. The filter is designed in the frequency domain (Rabiner and Gold, 1975; Berkhout, 1977; Press, et al., 1992), and does not require random reflectivity distribution.

The results of frequency domain inversion are shown in Figure F4. Amplitude spectra of the data before and after inversion (Figure F5) reveal an increase of bandwidth from 20-85 Hz (Figure F5a) to 20-98 Hz (Figure F5b). Comparison of Figures F1 and F4 indicate that additional detail is resolvable in the interval associated with reflection events 4 and 5. Reflection event 5 can be followed to the east where it appears to "pinch out" near the VSP well. Events 2 and 3, which tend to merge together at several points along the profile in Figure F1 are resolved as separate events in most instances.

After inversion, the effective wavelet in the neighborhood of the VSP well should now be zero-phase. Recomputation of the synthetic using the zero-phase equivalent of the VSP wavelet yields a good match (Figure F6).

Nonstationarity

Changes of wavelet phase and bandwidth occur as the seismic wavelet propagates through the earth. These changes are referred to as nonstationarity. Wilson (1990) presented model studies to show that frequency domain inversion of surface data designed on the average downgoing wavefield can be ineffective if significant nonstationarity exists in the downgoing wavefield. This may be the case even if the design is based on the downgoing wavefield measured near the zone of interest, since the deconvolution operator is stationary while the response over any given time interval is a composite one comprised of a superposition of nonstationary wavelets.

Nonstationarity does not appear to be significant within the current data set. Over the length of the borehole only minor variability in the shape of the primary wave is observed.

We have no information about the nature and degree of variability in the wavefield, which may occur along the length of the line.

Conclusions

The example presented here is a special case. Model studies suggest that the effective wavelet in the stacked seismic data is similar to that measured in the near-well VSP. The VSP data from Granny Creek reveal that the downgoing wavefield is nearly stationary. Differences between the synthetic and actual data remain (Figure F6), and if the above estimation of the stack-wavelet is correct, these differences may be due largely to Fresnel zone effects.

Within the context of *resolution* limitations several possible explanations for seismic variability observed within the reservoir and surrounding intervals were evaluated in Appendix G.

Acknowledgements

Synthetic seismograms are computed using GeoQuest Technology Corporations' AIMS package. We thank Columbia Natural Resources, Inc. for allowing us to run a VSP in one of their wells, and Tom McGovern of Lauren Geophysical Processing Services for handling the initial processing of the seismic data over Granny Creek.

References Cited

Berkhout, A., 1977, "Least squares inverse filtering and wavelet deconvolution", Geophysics, v. 42, no. 7, p. 1369-1383.

Gibson, B., and Larner, K., 1984, "Predictive deconvolution and the zero-phase source": Geophysics, v. 49, no. 4, p. 379-397.

Press, W., Teukolsky, S., Vetterling, W., and Flannery, B., 1992, Numerical Recipes: The Art of Scientific Computing: Cambridge University Press, 963 p.

Rabiner, L., and Gold, B., 1975, Theory and Application of Digital Signal Processing: Englewood Cliffs, N. J.: Prentice Hall.

Wilson, T., 1990, "Nonstationarity in Seismic Data: A VSP Case Study": *in* Proceedings, 58th Annual International Meeting of the Society of Exploration Geophysicists, p.1683-1686.

APPENDIX G
SEISMIC MODEL STUDIES OF THE GRANNY CREEK FIELD

The Big Injun sandstone has a thickness that varies from zero to approximately 50 feet within the field, and lies approximately 1900 feet beneath the surface. Seismic travel time to the Big Injun is just over 3/10ths of a second.

The Vibroseis seismic response of the Big Injun and surrounding intervals is illustrated by events 1 through 5 along Line 2 (Figure G1). A post-stack deconvolution process discussed in Appendix F was used to prepare the data for modeling. A synthetic seismogram (Figure G2) was computed using sonic and density logs for Clay 2908 near midpoint 300 (Figure G1). The synthetic traces are inserted for comparison near the projection of the location of Clay 2509 onto the seismic line. A good tie is obtained.

The synthetic was generated using a zero-phase wavelet (Figure G2). This wavelet was computed from the mixed-phase wavelet measured just beneath the Big Injun sandstone by the vertical seismic profile of Clay 2908. The preparation of the data shown in Figure G1 along with synthetic comparisons are discussed in Appendix F. The seismic data (Figures G1 and G2) were deconvolved using a frequency domain inversion approach, which converts the data to zero-phase (Appendix F) using the wavefield measurement from the VSP as the desired wavelet. The similarity between the synthetic and seismic data provide a reliable basis for making general correlations of stratigraphic intervals to individual acoustic events.

Seismic Resolution at Granny Creek

Peak frequencies associated with reflections observed in the Vibroseis data from the zone of interest (.27 to 0.33 s) range from about 65 to 90 Hz. The Big Injun sandstone lies in the negative cycle between events 3 and 4 (Figures G1 and G2). This negative cycle is the lowest frequency event in the package. While frequency content of the data has been improved by deconvolution, discrete resolution of the top and bottom of the Big Injun sandstone is generally not possible, even for the ideal case where such an interval is considered to be bounded by homogeneous intervals.

The response of an isolated thinning layer is modeled in Figure G3. An isolated layer with a velocity of 11300 f/s is thinned, right to left, from 100 feet on the right, to 0 feet on the left. The synthetic seismic response of the thinning layer is shown in Figure G3a. A zero-phase wavelet derived from a Butterworth spectrum with 20 and 90 Hz half-amplitude points was used to approximate the seismic wavelet shown in Figure G2. This is a *conservative* estimate of the bandwidth of the wavelet in the data. Separate reflections from the top (negative cycle) and bottom (positive cycle) of the interval appear on the right. As the layer thins to the left, the reflections from the top and the bottom of the layer begin to overlap or interfere with one another.

This interference is constructive over about a thirty foot range of thicknesses from about 60 feet to 30 feet. This constructive interference is represented by a plot of the amplitude difference (Figure G3b) between the negative cycle associated with the reflection from the top of the layer and the positive cycle reflected from the base. The resolution limit is often associated with the "tuning point" or the maximum in the amplitude difference plot (Sheriff,

1976). As the layer thins beyond this point, the amplitude difference drops to zero at zero-thickness.

The ability to measure actual differences of two-way transit time through the layer (i.e. to resolve the top and bottom of the layer) is complicated by reflection interference. This complication is illustrated by plotting actual versus apparent travel time through the layer (Figure G4a) or thickness versus apparent travel time (Figure G4b). These plots indicate that a one-to-one relationship between measured interval transit time and layer thickness is gradually lost as the layer thins below 50 feet. The function flattens out around 45 feet. For thicknesses less than 40 feet, the apparent two-way interval transit time remains at about 7 milliseconds (40 feet). Beyond this point, changes in the thickness of the layer can be inferred only from changes of reflection amplitude (Figure G3).

The possibility of accurately resolving the upper and lower contacts of the sandstone are further complicated since its response is partially masked by reflections from the overlying Greenbrier Limestone. The synthetic seismic response computed in Figure G5a incorporates reflection events from several of the overlying intervals including the Little Lime and Big Lime carbonate intervals. Since the impedance contrast between the Big Lime and the Big Injun sandstone is very large (Figure G2), the reflection from the top of the Big Injun tends to mask the reflection from the base.

The amplitude difference between the reflection from the top and base of the Big Injun is plotted for the composite multilayer response (Figure G5b). The Big Injun is thinned over a smaller range (70 to 0 feet). Constructive interference occurs in much the same way as in the previous example, but the amplitude-difference continues to increase beyond the tuning-point predicted for the single-layer case. This happens because the negative cycle associated with the *top* of the Big Injun includes a portion of the reflection response from the top of the Big Lime. The side lobes and peak of the reflection event from the base of the Big Injun also interfere with the shallower reflection event producing an additional build-up of reflection amplitude with thinning.

This condition also appears in plots of apparent versus actual travel time differences through the Big Injun (Figure G6). The bend in the curve occurs at smaller thickness, because the cycles between which interval transit times are being measured are not due solely to the top and bottom of the Big Injun, but include a superposition of overlying reflections.

This effect might be viewed as a beneficial one. The combined effect allows one to *see* smaller variations of thickness than expected based on the theoretical response of an isolated layer. If the thickness of the Big Injun sandstone were the only variable, then this would be the case; however, because of the large velocities of the overlying carbonate intervals, even small changes of impedance in the Big and Little Lime could influence the amplitude and time-difference measurements between the negative and positive cycle within which the reflection from the Big Injun is embedded. The effect of shallower reflection events on the response of the interval containing reflections from the Big Injun appears to be significant, given that the amplitude variations in this interval do not correlate directly with thickness variations of the Big Injun.

This non-uniqueness precludes the possibility of deriving unique interrelationships between amplitude and impedance variations of stratigraphic or structural origin that are confined to the reservoir interval.

Within the context of these *resolution* limitations we evaluate several possible explanations for seismic variability observed within the reservoir and surrounding intervals. Models presented include simple fault, fault with bounding low-velocity fracture zone (both

penetrative and stratigraphically restricted), stratigraphic variability within the Mauch Chunk across the top of the Little Lime, thinning and elimination of the Blue Monday and Pencil Cave intervals between the Big and Little Limes. Within the context of these models, possible interrelationship of production to reflection amplitude and waveform variability within the seismic data will be evaluated, including possible seismic detection of "thief zones" or high permeability pathways observed in the water-flooding projects currently underway within the field. All computations include Fresnel zone effects.

Seismic Models

On either side of the VSP well along Line 2 (Figures G1 and G2), considerable variability can be observed in the pattern of reflections associated with the Big Injun and surrounding intervals. Possible origins of this variability are examined using two-dimensional seismic models. Wave theory calculations are used to compute the synthetic seismic response of all models so that Fresnel zone effects will be portrayed. The use of a zero-offset wave-theory approach to modeling is supported by the tie shown in Figure G2, and by the similarity of a synthetic stack trace (Appendix F, Figure F3) obtained from a synthetic common midpoint gather.

The possibility of discriminating between the effects of stratigraphic variability and the influence of small faults or fracture zones is evaluated in the following studies. As discussed in Appendices E and F, the seismic response along line 2 may vary significantly depending on the approach used to process the data. Based on the arguments of Appendix F, the model studies presented here attempt to explain features observed in the post-stack frequency domain inversion section (Figure G1). Appendix F also includes discussions of the use of the VSP as a guide to the deconvolution of Line 2.

Starting Model

The initial synthetic model of Line 2 (Figure G7) is based on gamma ray and density logs from several wells along Line 2. Velocities for these units are taken from the VSP well. The general appearance of the three cycles 2, 3, and 4 of Figure G1) are represented in the synthetic. However, subtler waveform variations observed in the actual data are not present in the synthetic seismic response. Arrival time variations related to the long wavelength static errors mentioned in the main text are also apparent. Reflection events shown in the synthetic (Figure G7) come in earlier on the west end than they do in the actual data. Well control is concentrated in the central two-thirds of the line. Impedance variations on the ends of the line were extrapolated from the nearest control point. Spline fitting between control points produces an anomalous structure between Clay 2493 and 2500.

Stratigraphic Variability

The origins of some of the subtler waveform variability observed along Line 2 were examined by varying the thickness of individual units and recomputing the synthetic response until a match was obtained. The Blue Monday sandstone and Pencil Cave shale between the Big and Little Lime vary from 0 to 100 feet within the field. Examination of density and gamma ray logs along

the line reveals significant variability in the thickness of a low velocity interval at the base of the Mauch Chunk (overlying the Little Lime). Variations of the interval velocity and thickness of the Big and Little Lime were also introduced into the models.

Synthetic seismograms (Figures G8, G9, and G10) indicate that waveform variation along Line 2 can be explained by confining velocity variations to individual stratigraphic horizons. The corresponding velocity models are shown below each synthetic. Whether these variations of impedance are simply a function of stratigraphic variability within the section or stratigraphically confined impedance variations induced by deformation is a matter of speculation. The presence of considerable variability over small folds and reflector offsets suggests they may be primarily of structural origin. These individual models have been combined to form a synthetic seismic model of Line 2 (Figure G11), which duplicates a larger percentage of the variability of seismic response observed in the actual data.

The differences between the initial model (derived from the wells along the line) and the individual models (derived to simulate the observed seismic response) suggest that impedance variability observed in a given well may not be representative of the *bulk* properties or *average* characteristics of a given interval away from the well location. This is related to what are known as Fresnel Zone effects. Basically, subsurface impedance variations will not produce a noticeable seismic response unless they span horizontal distances, which are the size of a Fresnel zone or larger. This horizontal distance is a function of the dominant frequency of the seismic wavefield, and the depth of the target interval. At the depth of the Big Injun, the Fresnel Zone radius is approximately 450 feet. So continuous reflections events in a seismic section must arise from impedance contrasts that are roughly 450 feet or greater in extent.

Discrete Vertical Fault

The impedance models used to simulate the seismic response of Line 2 leave several questions unanswered. Faults and fracture zones, for example, have been suggested to have significant influence on production and secondary recovery operations within the Granny Creek field. The possibility that these fracture zones are detectable seismically is suggested by Zheng and Wilson (1992) (see also Appendix E). Possible zones of fracturing (and/or faulting) are suspected to be associated with the waveform character changes observed near midpoints 390, 415, and 454. The frequency domain inverse (Appendix F) is being modeled because of the tie achieved between the synthetic seismogram computed near the VSP well and the surface seismic near the well. The approach to deconvolution used to enhance waveform variability in the vicinity of known well communication zones increases the relative percentage of noise in the data. The increase of noise and phase distortion makes this version of the data difficult to model.

The questions concerning the expected seismic response of a fracture and/or fault zone begin by computing the response of a simple vertical fault with no associated velocity variation. Models are shown for vertical offsets of 10 feet, 15 feet, and 20 feet (Figure G12a, b, and c respectively). The fault is located halfway between traces 20 and 21. Ten feet of vertical offset (Figure G12a) produces a traveltime delay of about 1.5 milliseconds, and less than the 2 millisecond sample rate of the Vibroseis data. Subtle amplitude reduction and phase changes can be observed out to about 300 feet on either side of the fault. The most visible effect of this offset is a reduction of amplitude in cycles 3 and 4. Fifteen feet offset (Figure G12b) yields a more noticeable delay across the fault (approximately 2.5 milliseconds). Amplitude reduction is observed in cycles 2, 3, and 4 across the fault, and cycles 2 and 3 start to merge together. Amplitude and phase

changes can be observed to varying degrees out to about 300 feet from the fault. A fault with 20 feet offset produces additional merging and amplitude reduction of cycles 2 and 3. The amplitude changes are more pronounced and consistent across the fault (Figure G12c). The 3 and 1/3 millisecond offset is easily identifiable. The seismic delay occurs transitionally across traces 18 to 20. Again the changes of amplitude and phase extend at least 300 feet on either side of the fault.

If offsets are sufficiently large (15 to 20 feet), a fault with no associated velocity reduction will appear on a seismic data set as a set of about 4 traces marked by reduced amplitude on cycles 2, 3, and 4, and slight merging together of cycles 2 and 3. The amplitude reduction predicted by the models corresponds to amplitude reduction of cycles 2, 3, and 4 in Figure G1. Examination of Figure G1 reveals that this or similar patterns are found in the data at midpoints 417, 435, 450, and 475. At these midpoints the amplitudes of cycles 2 and 3 decrease, and merge together. A delay in arrival time and drop in amplitude of cycles 2,3 and 4 is observable on three traces near the VSP well around midpoint 305 (Figure G1). Further comparison with the data, however, reveals that the changes observed in the actual data occur gradually over distances of a few hundred feet.

Fracture Zone With No Fault Offset

Several impedance models could be proposed to represent the possible seismic response of fracturing within the reservoir and surrounding intervals. However, in the following evaluation, *fracture zones* are simulated as low impedance intervals restricted to the more brittle limestones (the Big and Little Lime) above the Big Injun as shown in Figure G13. Velocity within these zones was reduced from 19,000 f/s or 20,000 f/s (Little or Big Lime respectively) to 15,000 f/s. The magnitude of the velocity reduction is arbitrary, but intentionally large. The effect is modeled simply as a basis for comparison. The widths of the *fracture zones* (or low velocity zones) are varied as a fraction (0.22, 0.44, .9, 1.3, and 2.2) of the Fresnel Zone radius (approximately 450 feet).

Examination of the models (Figure G14a) suggest that a 100 foot wide low-velocity *(fracture)* zone (traces 20 to 21) produces no delay in the arrival time of the positive cycle above the Big Injun (see synthetic seismic response) and the Big Injun negative cycle itself. Apparent delay does occur on either side of the fracture zone as a result of diffraction interference. The synthetic computations are made at intervals of 55 feet, corresponding to the midpoint separation present in the Vibroseis data collected along Line 2. Amplitude variations are generally subtle and would likely be obscured by background noise. Most of the amplitude and phase changes are attributable to diffraction from the edge of the fracture zone. The effects of the narrow fracture zone are observable over a distance of more than 800 feet at the level of cycle 4 just beneath the Big Injun negative cycle.

Increasing the width of the fracture (or *low-velocity*) zone to 200 feet (traces 18.5 to 22.5 in Figure G14b) produces noticeable delay in cycles 3 and 4. The amplitude drop associated with velocity reduction extends nearly 300 feet beyond the edges of the fracture zone into the normal section. The amplitude drop on cycle 3 is greatest at the edges of the fracture zone. The amplitude of this cycle increases beneath and toward the middle of the fractures area. Cycle 4 beneath the Big Injun is delayed and broadened. The effects extend about 300 feet beyond the edges of the fracture zone. Diffraction interference is most noticeable on cycle 4.

Increasing fracture zone width duplicates and enhances the effects observed above. The models shown in Figure G14c and G15a and G15b represent 400 foot (traces 17 to 24), 800 foot (traces 8 to 28) and 1000 foot wide (traces 11.5 to 29.5) fracture zones respectively. In all cases travel time delays are observed beneath the fracture zones along with significant loss of amplitude in cycle 3. Cycle 4 on the other hand shows numerous increases and decreases of amplitude along with cycle duration and shape changes in general.

Note that for the wider zones, the amplitude variations are clearly transitional. This is particularly evident in the 1000 foot fracture-zone model. Subtle variations of amplitude can be observed in some cases out to as much as 380 feet from the edges of the fracture zone (a distance approximately equal to the Fresnel Zone radius).

Features similar to those associated with the simple low-velocity zone representation of a fracture zone are seen throughout the data, however they don't occur in the combinations represented by the models. The models suggest that for simple velocity reduction restricted to the carbonate intervals, the upper cycle remains unaffected. The middle cycle is delayed and drops significantly in amplitude, while the lower cycle also delayed, reveals a variety of phase and amplitude changes. The area between traces 350 and 370 along Line 2 (Figure G1) might be a possibility, but the features observed near problem wells in the waterflood recovery program (near midpoints 417 and 452) do no fit this description. Also as noted above, the features observed in the data develop in a transitional rather than abrupt fashion.

The influence of diffractions is very obvious in these models. In the unmigrated seismic data, however, diffractions are not observed. While the synthetic data are noise free, the field data are not. It is likely that the low amplitude of the diffractions observed beneath the reflection events in the model are obscured by the background noise or overprinted by deeper reflection events. The data shown being modeled (Figure G1) is migrated. Since the low amplitude diffraction events are generally obscured in the data, it is assumed that interference in the vicinity of the diffraction apex remains after migration. Comparison of migrated and unmigrated versions of the lines from the field reveal little difference in amplitude and phase of the events in the nearly horizontally layered sequence.

Vertical Fault With Velocity Reduction

The possibility that the region bounding a fault might experience some reduction of velocity because of rock-fracturing in the vicinity of the fault has also been modeled. As noted in the structural discussions, in the main body of this report, analysis of the core from Clay 2253 and 2255 revealed the presence of numerous fractures within the Greenbrier Limestone intervals above the Big Injun. Operators in the field also note that communication between problem wells in the field appears to occur through fracture zones within the overlying limestone interval.

In the model studies presented here, the possible effect of faulting is modeled as zones of reduced velocity restricted to the carbonate intervals above the Big Injun sandstone in much the same way as for the low velocity fracture zones. The depth section of Figure G16 highlights the low velocity intervals in the Big and Little Lime along with the fault offset. The widths of these low velocity zones were varied. The results for 100, 200, and 400 foot wide low velocity zones centered across the fault are shown in Figure G17. The fault in these examples has a constant 15 foot offset and is located half-way between traces 20 and 21 in each display.

For a 100 foot wide fracture zone centered about a vertical fault with 15 feet of offset, the effects on the seismic response are very subtle. A 2.5 millisecond delay occurs from the high-to-

low side across the fault. A decrease of cycle width occurs out to a couple hundred feet on either side of the fault in cycle 2. The effects on cycles 3 and 4 extends out to more than 350 feet on either side of the fault.

The 200 foot wide velocity reduction zone extends from about trace 18 to 23. A reduction of amplitude occurs in cycles 2, 3, and 4 across the fault. In addition, cycles 2 and 3 merge together near the fault. The amplitude of cycle 4 increases at distances greater than a Fresnel Zone radius due to the interference of diffractions from the fault. The delay associated with the fault offset is easily identifiable at the expanded plot scale. The effects away from the fault are subtle and extend out to distances corresponding to the Fresnel Zone radius.

Amplitude reduction associated with the 400 foot wide velocity reduction zone is more significant than in either of the above models. The low velocity zone extends approximately from trace 17 to trace 24. Although cycles 2 and 3 on the high side of the fault do not merge together, the amplitude of cycle 3 drops almost to zero. Diffraction interference produces apparent offsets in cycle 4. directly beneath the fault zone cycle 4 has almost a normal appearance.

The 1000 foot wide low velocity zone shown on Figure G16 extends approximately from trace 11.5 to trace 29.5. The response of such a broad low velocity region is very systematic compared with the above examples. The amplitudes of cycles 2 and 3 have decreased across the fault in the middle of the low velocity zone. Left-to-right across the base of the model, cycle 4 decreases in amplitude, increases, and decreases again. As with the simple low-velocity zone, the high amplitude of cycle 4 occurs across the central part of the low velocity zone and beneath the fault itself.

Comparison of the synthetics to the data along Line 2 reveal at least one area where a case can be made for a fault bounded by a low velocity fracture zone. The seismic response near midpoint 415 has characteristics similar to those observed in the 200 foot model (Figure G17). Simple fault (Figure G12) and velocity reduction with no offset (Figures G14 and G15) do not produce the merging together of cycles 2 and 3 observed in the data near this midpoint and in the model. In fact, the character changes observed near midpoints 417, 435, 450 and 475 may, in general, be more like the character changes associated the combination of fault and low-velocity zone, than without the fault. However, the fracture zones associated with these areas must be relatively narrow. Since merging together of cycles 2 and 3 occurs only for the 200 foot wide zone across the fault, it may be that the area near trace 415 (and others like it) consists of multiple small faults with associated low velocity fracture zones covering a considerable distance.

Velocity Anomalies

The above model studies are based on a zero-offset wave-theory approach to simulation of the seismic response. This approach has been used because computations of the offset response followed by stacking yield similar results to the zero-offset approach. The velocity anomaly associated with the stratigraphically restricted low-velocity zones that might be isolated or bound a fault, is addressed using both zero-offset wave-theory computations and non-zero offset models of common midpoint gathers, which are then stacked.

Zero-offset wave-theory computations are shown in Figure G18. The reflection response is computed for a reflector located at 3500 feet beneath the surface shown in Figure G19. The width of the low-velocity zone varies from 100 feet, 200 feet, and 400 feet (Figure G18a, b, and c, respectively) corresponding to the cases modeled in Figure G14. The interval is unfaulted. The

response of the 100 foot wide fracture (or low-velocity) zone reveals anomalous cycles 200 feet to either side of the center of the zone. A delay of about 1/2 millisecond is observed across the intervening interval. This delay is much less than the sample rate and would be unnoticeable in real data.

The effect of the 200 foot wide low-velocity zone produces a delay of a little over 1 millisecond. This delay might be noticeable in real data but given even minor levels of noise is seems unlikely. The delay associated with a 400 foot wide fracture zone reaches 3 milliseconds. The delay develops gradually over a distance of about 250 feet. The feature spans about 500 feet or 9 traces and should be observable in the actual data.

Ray-paths in a common midpoint gather are shown for the deeper reflector in Figure G19. Common midpoint gathers were computed across 100 foot, 200 foot, and 400 foot wide low-velocity zones and stacked to give the synthetic seismic response shown in Figure G20. The layers were unfaulted. The response is quite different from that shown in the wave-theory solutions. The difference can be characterized as noisy. Numerous small fluctuations of arrival time and changes of phase occur across the low-velocity zones. These features are probably the result of the discrete nature of the low-velocity zone boundary, and to the phase changes which occur as rays are refracted and delayed through the low-velocity zone.

Despite the significant differences between the wave-theory and offset models, similar conclusions can be drawn. The 100 foot wide low-velocity zone is basically undetectable. The 200 foot wide low-velocity zone produces some delay, which spans a somewhat greater distance than in the wave-theory solution, and would probably be at the threshold of detection, given the small delay and increased noise in the data. The 400 foot wide low-velocity zone produces more noticeable delay, which spans about 9 traces, and would probably be detectable in the actual data.

As mentioned earlier, the wave-theory models yield results which are similar to those observed in the actual data (Figure G1). Common midpoint gathers were modeled as a test. The applicability of this approach to modeling is questionable in the present case. The method employs ray tracing and doesn't accurately represent Fresnel Zone effects. The wave-theory option for computing common midpoint gathers did not function properly and could not be used. It is anticipated that wave-theory modeling of common midpoint gathers would smooth out some of the differences observed in the synthetics of Figure G20.

Regardless, the model studies of the effect of a low-velocity zone on a deeper reflector suggest, in either case, that narrow low-velocity zones 200 feet wide or less, will produce an undetectable delay in deeper reflectors. Traveltime delays are not observed beneath the features interpreted to be faults or fracture zones in the data. The model studies suggest that if velocity reduction is associated with fracture zones bounding faults, the widths of these zones must be less than 200 feet.

Conclusions

The model studies presented here indicate that simple variation in thickness of the Big Injun and surrounding intervals predicted by individual wells along the seismic profile produce only minor variability in seismic response along Line 2. Models indicate that much of the waveform variability which is observed along Line 2 can be explained by introducing impedance variations confined to stratigraphic subdivisions of the section. The synthetics also suggest that features

observed in any given well may not extend very far from the wellbore, and therefore, are not representative of the bulk (or Fresnel zone scale) properties of these intervals.

The interpretation of faults in the seismic section receives only minor support from the model studies. Some of the characteristics of the seismic response observed near reported interwell communication zones are simulated in the synthetic seismic response of a simple fault or fault with adjacent fracture zone. However, it is difficult to explain the broad transitional development of these seismic characteristics using isolated faults and velocity reduction zones.

In summary, it is possible to offer both stratigraphic and structural features as the origin of waveform variability observed along Line 2 (and hence within the field as a whole). The models cannot uniquely specify the origins of waveform and amplitude changes observed in the data.

Acknowledgements

Synthetic seismograms are computed using GeoQuest Technology Corporations' AIMS package. We thank Tom McGovern of Lauren Geophysical Processing Services for handling the initial processing of the seismic data over Granny Creek.

References Cited

Sheriff, R., 1976, "Limitations on resolution of seismic reflections and geologic detail derivable from them": *in* American Association of Petroleum Geologists Memoir 26, Seismic Stratigraphy-Applications to Hydrocarbon Exploration, p. 3-14.

Zheng, L. and Wilson, T, 1992, "Vibroseis deconvolution: A case history in the Granny Creek oil field, West Virginia": *in* Proceedings Volume, 60th Annual International Meeting of the Society of Exploration Geophysicists, p. 281-283.

APPENDIX H
PETROGRAPHIC DATA FOR GRANNY AND ROCK CREEK

CLAY 1107 POINT COUNT PERCENTAGES

SECT #	WELL #	DEPTH	FACIES	GS mm	GS	Core	Core	TSpor+	Qtz	Qtite	PsG	Chl	Ill	Mix	Kaol	Ppor	Fpor	Feld	Chrt	SecQ	Ccem	Crep	Sidr	Mica	Opaq	Misc
					phi	K	por	COATS																		
41	1107	2119.50	A	0.12	3.0	0.1	8.1		57.0	4.7	21.3	0.3	13.0[1]	0.7	tr	0.0	0.0	0.0	1.3	0.0	0.3	0.0	0.0	0.0	0.0	1.3
301	1107	2120.80	A	0.23	2.1	11.0	13.1	15.3	58.3	7.3	7.7	4.0	0.3	0.7	tr	9.3	1.0	2.3	0.3	2.0	1.3	5.0	0.0	0.0	0.3	0.0
359	1107	2124.30	B	0.18	2.5	9.7	17.5	17.0	52.3	8.7	6.3	7.0	1.0	0.0	tr	7.7	1.3	2.7	0.3	3.0	3.3	3.7	0.0	1.7	1.0	0.0
42	1107	2125.80	B	0.14	2.8	0.9	9.8	10.3	60.0	6.7	9.3	0.7	0.0	0.3	tr	6.7	2.7	2.0	1.7	4.7	4.0	0.3	0.0	0.0	0.0	1.0
78	1107	2127.40	B	0.53	0.9	0.2	5.6	7.7	68.0	5.0	3.0	1.3	0.0	0.3	2.3	0.7	3.0	3.0	1.0	10.7	1.3	0.3	0.0	0.0	0.0	0.0
360	1107	2129.60	B	0.39	1.4	0.3	4.0	8.0	61.0	10.7	0.0	1.0	1.3	0.0	1.3	0.7	3.7	3.7	0.3	13.3	1.7	0.7	0.0	0.3	0.3	0.0
79	1107	2132.50	B	0.34	1.6	5.4	10.7	10.7	64.0	8.0	5.3	2.3	0.3	1.7	tr	3.0	3.3	2.7	2.0	5.0	0.0	0.3	0.0	1.7	0.0	0.3
80	1107	2134.50	3	0.19	2.4	19.0	22.4	24.3	56.7	5.7	8.0	3.3	0.3	1.7	0.0	16.3	2.7	2.3	1.3	0.3	0.3	0.3	0.0	0.3	0.0	0.3
362	1107	2138.10	3	0.18	2.5	18.0	21.6	25.7	50.7	9.3	3.0	8.7	0.0	0.7	0.0	13.3	3.0	3.3	1.7	0.3	0.7	1.0	1.7	1.0	1.7	0.0
81	1107	2138.80	3	0.18	2.5	18.0	22.0	22.7	54.0	6.7	8.3	10.3	0.0	0.0	0.0	10.0	2.3	3.3	0.7	0.3	0.0	0.0	2.0	0.7	0.0	1.3
43	1107	2140.00	3	0.15	2.7	0.1	15.8	3.3	47.7	7.0	22.7	1.0	0.0	0.0	0.0	0.7	1.7	4.0	2.0	0.0	0.0	0.0	11.7	0.3	1.3	0.0
82	1107	2146.50	3	0.15	2.7	2.9	21.3	22.3	54.3	6.7	10.0	11.7	0.0	0.0	0.0	9.7	1.0	1.3	0.7	1.0	0.0	0.0	0.0	2.0	0.0	1.7
44	1107	2148.50	3	0.14	2.9	11.0	21.8	24.0	57.3	7.0	8.3	6.7	0.0	0.0	0.0	13.7	3.7	1.3	1.0	0.3	0.0	0.0	0.0	0.3	0.0	0.3
45	1107	2151.40	3	0.16	2.7	4.6	21.0	26.0	56.3	5.0	3.0	16.7	0.3	0.7	0.0	8.0	0.3	2.3	2.0	1.3	2.3	0.0	0.0	1.0	0.0	0.7
46	1107	2153.80	4	0.14	2.8	4.2	21.7	28.3	52.7	4.7	10.0	9.3	0.7	0.3	0.0	14.0	4.0	1.7	0.0	0.0	0.7	0.0	0.3	0.3	1.7	0.0
47	1107	2157.50	4	0.14	2.8	0.3	23.9	18.3	51.0	5.0	10.7	14.3	0.0	0.3	0.0	3.3	0.3	0.7	3.7	0.0	3.7	0.0	4.0	1.0	0.0	2.0

[1] **Total interstitial illite. Illite coatings could not be distinguished from pseudomatrix because of intense pressure solution.**

GRANNY CREEK FIELD, CLAY 1108 PETROLOGY DATA

SECT #	WELL #	DEPTH	FACIES	GS mm	GS	Core	Core	TSpor+	Qtz	Qtite	PsG	Chl	Ill	Mix	Kaol	Ppor	Fpor	Feld	Chrt	SecQ	Ccem	Crep	Sidr	Mica	Opaq	Misc
					phi	K	por	COATS																		
83	1108	2063.40	B	0.29	1.78	3.70	9.0	3.7	62.0	6.7	5.3	0.3	0.7	0.7	tr	1.3	0.7	1.3	0.3	0.3	17.0	1.7	tr	0.3	tr	1.3
48	1108	2065.90	B	0.16	2.67	0.80	8.2	0.0	71.3	3.3	12.3	tr	7.0[1]	tr	0.3	0.7	tr	tr	2.0	tr	0.7	tr	tr	1.7	tr	0.7
49	1108	2069.00	B	0.36	1.49	0.10	11.3	13.7	61.3	7.3	4.3	0.3	0.3	tr	tr	6.0	6.0	5.3	1.3	5.3	0.0	0.3	0.3	tr	1.3	0.3
50	1108	2070.00	B	0.27	1.90	0.20	9.8	12.7	63.7	6.3	3.0	2.0	tr	tr	1.0	4.7	5.0	5.7	1.0	7.3	0.3	tr	tr	tr	tr	0.0
84	1108	2071.90	B	0.47	1.08	3.30	9.7	14.0	66.7	8.0	2.7	3.3	tr	0.7	2.0	5.3	2.7	2.3	1.7	3.7	1.0	tr	tr	tr	tr	0.0
51	1108	2073.30	2	0.21	2.22	13.00	18.0	21.7	61.0	4.3	6.3	2.7	0.3	0.3	tr	16.0	2.3	2.3	0.7	1.7	0.7	tr	tr	0.7	tr	0.7
52	1108	2075.50	2	0.16	2.68	12.00	16.1	16.3	65.7	7.0	5.0	5.7	0.3	0.0	tr	7.7	2.7	1.0	2.3	tr	1.0	tr	tr	1.0	tr	0.7
364	1108	2076.20	2	0.14	2.85	7.50	17.2	20.3	58.3	11.7	4.3	11.3	1.0	0.3	tr	4.0	3.7	2.3	0.7	0.7	0.7	tr	tr	0.3	0.3	0.3
53	1108	2077.50	2	0.12	3.08	18.00	21.2	20.3	59.7	5.0	9.0	11.0	1.3	0.3	0.0	6.7	1.0	1.7	3.3	tr	0.0	tr	tr	1.0	tr	0.0
1	1108	2080.80	3	0.14	2.85	3.40	21.4	26.7	55.0	5.3	6.3	3.3	0.0	0.7	0.0	21.0	1.7	3.3	0.3	0.7	0.0	tr	1.3	tr	1.0	0.0
85	1108	2081.60	3	0.12	3.08	3.40	21.3	18.0	55.0	4.3	11.3	7.7	2.3	0.7	0.0	7.3	2.3	2.0	3.0	0.3	0.0	tr	tr	2.0	tr	1.7
2	1108	2083.50	3	0.13	2.93	11.00	21.7	21.7	54.7	6.0	9.0	4.0	tr	0.3	0.0	15.0	2.3	3.7	2.3	0.7	0.0	tr	tr	1.3	tr	0.7
86	1108	2084.70	3	0.15	2.70	15.00	21.4	23.0	53.7	8.3	7.0	7.7	tr	0.3	0.0	12.3	2.7	3.0	1.3	tr	0.7	tr	1.0	0.7	1.3	0.0
54	1108	2085.50	3	0.11	3.16	0.53	18.9	24.0	55.3	4.0	8.7	9.7	1.3	2.3	0.0	9.0	1.7	2.0	1.7	tr	0.7	tr	1.3	1.3	1.0	0.0
3	1108	2087.00	3	0.13	2.97	3.60	20.4	23.7	52.0	3.3	12.7	3.7	0.7	1.0	0.0	14.0	4.3	3.0	3.0	tr	tr	tr	tr	1.7	tr	0.7
55	1108	2089.90	3	0.12	3.11	2.50	20.5	24.3	52.0	6.7	12.7	5.7	0.3	0.7	0.0	16.7	1.0	2.0	0.7	0.3	0.3	tr	tr	0.7	tr	0.3
56	1108	2091.40	3	0.13	2.97	6.10	22.3	21.3	52.3	5.0	13.0	6.3	tr	0.7	0.0	12.7	1.7	3.3	2.0	1.0	1.3	tr	tr	0.3	tr	0.3
4	1108	2093.00	3	0.14	2.88	8.10	23.4	26.7	50.3	5.0	8.0	4.0	tr	tr	0.0	20.0	2.7	4.0	1.7	tr	1.0	tr	1.0	1.3	tr	1.0
57	1108	2094.80	3	0.15	2.72	7.80	19.7	18.3	49.0	5.0	9.3	4.0	tr	1.0	0.0	8.7	4.7	5.0	2.3	0.7	0.7	0.0	7.3	1.0	1.3	0.0
365	1108	2097.00	4	0.15	2.78	1.00	17.6	17.3	53.0	10.0	4.3	13.0	0.3	0.3	0.0	3.0	0.7	1.0	2.7	0.3	4.0	2.7	3.0	0.7	1.0	0.0
5	1108	2097.40	4	0.13	2.99	1.00	17.6	19.0	46.3	6.7	11.7	8.3	tr	0.7	0.0	9.0	1.0	3.0	2.7	tr	8.0	1.3	tr	tr	tr	1.3
58	1108	2099.40	4	0.14	2.84	0.38	13.3	18.3	48.3	8.0	8.0	13.0	0.3	0.3	0.0	4.3	0.3	1.7	2.3	0.3	6.3	0.7	4.0	tr	tr	2.0

[1] Illite mostly in partings.

GRANNY CREEK FIELD, CLAY 1109 PETROLOGY DATA

SECT #	WELL #	DEPTH	FACIES	GS mm	GS	Core	Core	TSpor+	Qtz	Qtite	PsG	Chl	Ill	Mix	Kaol	Ppor	Fpor	Feld	Chrt	SecQ	Ccem	Crep	Sidr	Mica	Opaq	Misc
					phi	K	por	COATS																		
366	1109	1880.00	A	0.21	2.25	19.0	11.7	9.3	55.7	12.7	1.7	3.7	tr	0.3	0.3	2.7	2.3	4.3	2.3	13.7	0.0	0.3	tr	tr	tr	0.0
367	1109	1880.33	A	0.16	2.61	19.0	11.7	17.7	55.3	12.7	12.0	8.7	0.3	0.7	tr	6.3	1.7	tr	tr	1.0	0.3	tr	tr	1.0	tr	0.0
16	1109	1881.10	B	0.47	1.08	19.0	11.7	11.0	69.0	9.3	3.0	2.0	1.0	0.0	tr	7.7	0.3	1.7	0.7	2.3	1.0	1.0	tr	0.3	tr	0.7
17	1109	1881.80	B	0.29	1.80	0.1	6.4	8.3	61.7	5.3	11.0	2.3	1.7	2.3	tr	1.0	2.7	2.3	2.3	5.3	tr	tr	tr	1.3	tr	0.7
368	1109	1883.20	B	0.34	1.54	0.1	6.0	7.3	57.3	9.0	0.3	1.0	tr	tr	0.7	0.3	5.3	4.0	1.0	19.7	tr	0.7	tr	0.7	tr	0.0
369	1109	1885.00	B	0.20	2.32	0.4	6.2	9.0	59.7	13.3	1.3	3.3	2.0	0.3	0.3	1.3	1.7	3.3	0.3	9.7	0.3	tr	tr	0.7	2.3	0.0
370	1109	1888.20	B	0.23	2.10	0.3	6.2	7.0	62.0	10.7	1.3	2.3	0.3	tr	tr	0.7	3.7	5.3	0.7	11.3	tr	1.3	tr	tr	0.3	0.0
18	1109	1890.30	B	0.19	2.43	0.2	6.0	4.0	59.3	7.7	8.7	1.0	tr	1.3	tr	0.7	1.0	3.0	9.3	6.0	tr	tr	tr	2.0	tr	0.0
371	1109	1892.50	B	0.47	1.10	10.0	7.2	14.7	69.3	12.0	1.0	4.7	tr	tr	1.7	5.7	2.7	1.7	tr	1.0	tr	tr	tr	0.3	tr	0.0
87	1109	1894.50	B	0.62	0.68	1.8	4.8	3.7	71.7	13.0	1.7	1.3	tr	0.7	1.0	0.3	0.3	2.3	2.3	5.0	tr	0.3	tr	tr	tr	0.0
88	1109	1895.80	B	0.59	0.76	17.0	7.7	9.7	67.3	8.3	3.0	3.0	0.3	tr	tr	5.0	1.3	1.3	1.0	2.7	2.7	4.0	tr	tr	tr	0.0
89	1109	1896.80	B	0.12	3.08	8.8	16.4	6.0	58.3	7.7	10.3	2.0	0.3	0.7	tr	2.3	0.7	0.3	1.0	0.3	13.3	0.3	1.0	1.0	tr	0.3
19	1109	1897.30	B	0.13	2.95	8.8	16.4	15.3	59.0	6.3	9.0	3.3	0.7	1.0	tr	9.0	1.3	2.0	3.7	0.7	1.0	tr	tr	1.0	tr	2.0
20	1109	1898.50	3	0.11	3.13	24.0	22.1	19.7	54.0	10.3	4.3	10.7	tr	0.7	0.0	6.7	1.7	2.0	2.0	0.7	tr	2.3	3.3	0.3	0.7	0.3
21	1109	1901.80	3	0.14	2.83	21.0	17.4	16.7	53.3	10.3	4.7	7.3	0.3	tr	0.0	6.7	2.3	0.7	1.7	tr	tr	1.7	8.7	0.7	1.7	0.0
90	1109	1902.90	3	0.16	2.66	2.4	21.1	20.3	53.3	7.0	5.7	10.0	0.3	tr	0.0	8.3	1.7	2.0	1.3	0.7	4.3	0.3	3.0	0.3	tr	1.7
372	1109	1903.70	3	0.15	2.71	15.0	21.5	19.3	60.3	10.3	2.7	11.3	1.0	0.7	0.0	5.0	1.3	3.3	0.3	0.7	0.7	0.3	0.7	0.7	0.7	0.0
91	1109	1905.00	3	0.25	1.99	0.6	13.8	21.0	54.0	10.0	6.7	9.7	tr	1.0	0.0	9.7	0.7	1.3	0.7	1.0	tr	tr	3.7	tr	1.3	0.3
92	1109	1906.10	3	0.15	2.77	8.9	20.4	17.0	60.0	9.3	6.3	6.3	tr	2.0	0.0	6.0	2.7	2.7	2.3	0.3	tr	0.3	0.7	0.3	0.7	0.0
22	1109	1908.30	3	0.16	2.62	4.2	20.4	23.0	59.0	4.0	1.7	12.7	tr	0.3	0.0	6.7	2.0	5.0	2.0	1.0	3.3	0.3	tr	0.7	tr	1.3
93	1109	1910.80	3	0.16	2.61	0.1	16.5	16.7	51.3	9.7	10.0	11.0	tr	0.3	0.0	5.0	0.3	2.7	2.0	tr	0.0	tr	6.0	0.3	1.3	0.0
373	1109	1912.00	3	0.13	2.91	2.4	19.5	24.0	53.0	8.3	4.7	17.7	0.3	tr	0.0	4.0	2.0	0.3	3.7	0.3	0.7	1.0	1.3	0.7	2.0	0.0
325	1109	1915.60	3	0.11	3.24	0.3	14.8	21.7	50.3	12.7	5.7	18.0	tr	0.3	0.3	2.7	0.7	2.7	2.3	0.7	0.7	1.0	0.7	tr	1.3	0.0
326	1109	1917.25	4	0.11	3.17	0.2	16.7	18.0	54.3	9.7	7.7	12.3	1.0	1.3	0.0	3.0	0.3	1.3	1.0	0.3	tr	1.3	3.0	3.0	0.3	0.0
328	1109	1921.70	4	0.11	3.20	0.1	14.7	14.3	58.7	11.3	6.0	9.3	0.3	1.7	0.0	3.0	tr	0.3	1.3	tr	tr	1.7	5.0	tr	1.0	0.3
95	1109	1923.00	4	0.10	3.29	0.1	15.8	16.7	54.7	6.3	7.7	8.3	0.3	0.7	0.0	5.3	2.0	2.3	0.7	0.7	tr	1.3	7.7	0.7	1.3	0.0
329	1109	1924.40	4	0.11	3.20	0.1	15.1	18.7	53.3	10.3	8.0	12.3	tr	3.0	0.0	3.0	0.3	0.3	0.7	tr	0.3	2.0	4.7	0.7	tr	1.0
330	1109	1926.90	4	0.09	3.44	0.1	9.6	12.7	56.7	5.7	6.7	5.3	0.3	1.0	0.0	5.7	0.3	2.3	1.7	tr	1.0	1.7	10.0	tr	1.3	0.3

GRANNY CREEK FIELD, CLAY 1110 PETROLOGY DATA

SECT #	WELL #	DEPTH	FACIES	GS mm	GS	Core	Core	TSpor+	Qtz	Qtite	PsG	Chl	Ill	Mix	Kaol	Ppor	Fpor	Feld	Chrt	SecQ	Ccem	Crep	Sidr	Mica	Opaq	Misc
					phi	K	por	COATS																		
23	1110	1887.00	A	0.253	1.98	*	*	16.3	61.3	3.3	8.0	1.0	4.7	tr	tr	9.0	1.7	1.7	3.3	2.7	3.3	tr	tr	tr	tr	0.0
24	1110	1888.30	A	0.476	1.07	*	*	4.3	70.0	5.7	2.3	0.3	1.0	0.3	tr	2.0	0.7	0.7	2.3	1.0	12.7	0.7	tr	tr	tr	0.3
25	1110	1888.60	A	0.176	2.51	*	*	11.7	62.0	4.0	15.0	1.0	5.3	1.0	tr	5.3	1.0	0.3	1.3	1.7	tr	tr	0.7	tr	tr	1.3
26	1110	1890.30	A	0.240	2.06	*	*	9.3	60.7	4.3	7.0	1.0	1.3	0.3	tr	1.3	5.3	5.0	3.7	6.3	tr	tr	1.7	0.3	tr	1.7
27	1110	1894.50	B	0.324	1.63	*	*	6.3	63.7	7.0	7.7	3.7	0.3	0.3	tr	0.7	1.3	3.7	2.3	6.7	0.7	0.3	tr	0.3	tr	1.3
28	1110	1899.20	B	0.277	1.85	*	*	8.0	59.0	6.3	3.7	1.7	0.3	0.3	tr	2.0	3.7	4.3	3.3	11.7	2.0	0.3	tr	tr	tr	1.3
29	1110	1900.80	B	0.348	1.52	*	*	2.0	57.0	6.0	2.0	0.7	0.3	0.0	tr	tr	1.0	5.3	1.7	4.3	18.7[1]	2.7[1]	tr	0.3	tr	0.0
30	1110	1902.20	B	0.630	0.67	*	*	4.0	61.0	10.7	3.0	0.3	tr	0.3	tr	3.0	0.3	2.0	2.0	3.7	8.7	2.3	tr	0.7	tr	2.0
32	1110	1904.00	2	0.113	3.15	*	*	12.7	58.0	5.3	13.0	2.3	tr	0.3	0.0	8.3	1.7	3.0	0.7	0.7	2.7	0.3	2.0	0.3	tr	1.3
31	1110	1905.80	2	0.670	0.58	*	*	7.0	63.3	6.7	2.0	2.3	tr	0.7	0.0	3.3	0.7	2.0	1.7	2.7	11.3	2.7	tr	tr	tr	0.7
33	1110	1906.90	2	0.146	2.78	*	*	18.0	53.3	6.0	11.3	5.3	tr	0.7	0.0	8.7	3.3	6.3	0.7	0.7	0.7	tr	2.7	tr	0.3	0.0
34	1110	1910.30	3	0.160	2.64	*	*	15.3	61.0	3.7	8.7	3.3	tr	tr	0.0	9.3	2.7	2.7	3.3	2.0	1.0	tr	tr	0.3	tr	2.0
97	1110	1913.00	3	0.145	2.79	*	*	25.0	56.3	6.3	8.0	6.0	0.3	0.3	0.0	15.0	3.3	1.0	0.7	0.7	1.0	tr	tr	0.3	tr	0.7
35	1110	1917.50	3	0.125	3.00	*	*	7.3	46.0	6.0	12.3	1.0	tr	tr	0.0	4.7	1.7	1.7	4.0	1.0	14.0	0.7	5.0	0.7	1.0	0.3
36	1110	1920.30	3	0.154	2.70	*	*	21.0	58.3	5.0	8.3	3.0	tr	tr	0.0	13.0	5.0	1.3	1.7	0.7	0.3	0.7	tr	tr	tr	2.7
98	1110	1924.00	4	0.144	2.80	*	*	15.7	59.3	6.0	10.3	3.7	1.0	tr	0.0	10.3	0.7	1.3	1.7	tr	2.0	tr	2.0	0.3	1.0	0.3
37	1110	1925.40	4	0.142	2.82	*	*	14.3	52.0	5.3	12.3	6.0	tr	tr	0.0	5.0	4.0	2.0	1.3	1.0	2.3	2.0	4.3	0.3	2.0	7.0
38	1110	1928.80	4	0.130	2.94	*	*	11.3	50.0	5.3	11.7	4.3	tr	0.3	0.0	4.3	2.3	4.0	3.7	0.7	3.0	1.0	7.7	0.3	1.3	0.0
39	1110	1930.30	4	0.131	2.93	*	*	5.3	46.0	5.3	10.0	2.0	tr	tr	0.0	2.7	0.7	1.7	2.7	0.3	8.0	7.0	12.3	0.3	1.0	0.3
40	1110	1930.70	4	0.109	3.20	*	*	10.0	50.0	2.3	21.7	5.0	tr	tr	0.0	3.0	2.0	1.3	2.7	tr	2.0	1.0	6.0	0.7	2.0	0.3

[1] **Approximate values. Carbonate cement could not always be distingulshed from replacement carbonate.**

GRANNY CREEK FIELD, CLAY 1126 PETROLOGY DATA

SECT #	WELL #	DEPTH	FACIES	GS mm	GS PHI	CORE K	Core Por	Qtz	Qtite	PsG	Chl	Ill	Mix	Kaol	Ppor	Fpor	Feld	Chrt	SecQ	Ccem	Crep	Fcarb	Mica	Opaq	Misc
*	1126	1775.90	A	0.35	1.51	23.3	13.8	43.0	26.5	2.3	tr	6.7	*	tr	7.0	1.0	1.3	1.7	tr	6.0	3.7	tr	*	*	0.8
*	1126	1776.60	A	0.40	1.32	73.6	14.5	43.7	29.1	2.3	0.9	3.1	*	tr	10.1	0.6	1.6	2.0	tr	2.7	3.0	tr	*	*	0.9
*	1126	1777.90	A	0.30	1.74	2.5	13.1	48.8	26.0	2.7	0.5	2.5	*	tr	8.7	0.7	3.0	2.3	tr	2.0	2.0	tr	*	*	0.8
*	1126	1778.50	A	0.30	1.74	27.8	20.8	39.7	29.9	4.3	5.0	0.4	*	tr	7.0	3.0	5.0	3.9	tr	0.7	tr	tr	*	*	1.1
*	1126	1779.50	A	0.28	1.84	33.6	17.9	49.7	24.7	2.3	2.8	1.5	*	tr	9.0	0.7	0.3	2.3	tr	3.0	3.3	tr	*	*	0.4
*	1126	1780.50	A	0.20	2.32	21.3	17.0	50.0	24.1	2.5	6.7	tr	*	0.2	5.3	2.5	2.7	1.2	tr	3.2	1.1	tr	*	*	0.5
*	1126	1781.50	A	0.40	1.32	15.2	18.4	45.9	17.8	5.7	4.0	tr	*	tr	10.0	2.7	3.0	5.0	tr	2.3	3.3	tr	*	*	0.3
*	1126	1782.20	A	0.50	1.00	16.1	11.6	50.4	30.2	1.3	5.7	tr	*	tr	3.7	2.3	0.7	3.3	tr	1.3	0.7	tr	*	*	0.4
*	1126	1783.50	A	0.18	2.47	1.5	15.2	41.0	31.0	4.3	6.8	0.2	*	0.3	4.3	3.1	4.4	1.7	tr	tr	tr	2.3	*	*	0.6
*	1126	1784.50	B	0.25	2.00	0.7	14.9	36.3	38.1	3.0	3.2	tr	*	tr	4.3	2.0	5.0	2.0	4.5	tr	0.3	1.0	*	*	0.3
*	1126	1785.50	B	0.31	1.69	0.7	9.8	34.6	39.4	2.1	1.5	tr	*	0.7	2.0	3.0	1.9	3.1	6.8	2.1	1.4	0.7	*	*	0.7
*	1126	1786.50	B	0.38	1.40	0.2	9.0	26.3	44.5	1.0	2.0	tr	*	2.0	1.7	4.0	3.0	2.7	11.0	0.5	0.2	0.3	*	*	0.8
*	1126	1787.40	B	0.22	2.18	0.3	11.4	41.0	29.5	2.7	3.3	tr	*	1.0	1.7	2.7	1.3	2.0	12.8	0.4	0.3	0.3	*	*	1.0
*	1126	1788.50	B	0.20	2.32	0.5	12.7	42.8	27.3	0.7	4.0	tr	*	1.0	6.0	4.0	5.3	1.0	7.3	0.3	tr	tr	*	*	0.3
*	1126	1789.50	B	0.35	1.51	0.1	6.2	34.3	51.2	0.3	0.0	tr	*	0.8	0.7	3.0	3.0	1.3	[1]	1.0	3.7	0.3	*	*	0.4
*	1126	1790.50	B	0.18	2.47	0.0	8.0	51.4	19.3	6.0	1.7	5.3	*	0.6	0.7	2.3	4.4	0.9	4.0	0.3	0.9	1.2	*	*	1.0
*	1126	1791.50	B	0.17	2.56	1.3	5.2	40.3	35.1	1.8	0.3	tr	*	0.3	0.7	2.3	4.3	1.7	10.5	1.0	1.0	tr	*	*	0.7
*	1126	1792.50	B	0.18	2.47	4.9	18.7	42.8	17.6	5.0	7.7	tr	*	0.0	8.5	3.7	7.3	3.0	0.9	0.8	1.5	0.3	*	*	0.9
*	1126	1793.50	B	0.16	2.64	0.0	4.4	42.0	23.3	14.5	tr	11.5	*	0.0	0.7	tr	3.3	2.3	tr	0.5	0.8	0.3	*	*	0.8
*	1126	1795.50	B	0.40	1.32	13.6	9.0	41.0	40.6	tr	3.2	tr	*	0.0	9.0	2.0	1.4	1.0	tr	0.9	0.4	tr	*	*	0.5
*	1126	1796.40	B	0.65	0.62	14.8	8.0	55.0	29.3	1.0	1.7	tr	*	0.0	2.0	tr	0.7	0.3	tr	6.3	2.8	tr	*	*	0.9
*	1126	1797.50	2	0.20	2.32	3.0	18.6	50.6	24.4	3.0	8.0	tr	*	0.0	7.7	0.3	1.7	3.0	tr	tr	tr	0.3	*	*	1.0
*	1126	1798.50	2	0.18	2.47	1.4	17.6	43.0	29.5	4.3	7.8	tr	*	0.0	6.2	1.0	1.4	4.5	tr	tr	0.4	0.8	*	*	1.1
*	1126	1799.50	2	0.20	2.32	1.9	18.9	44.7	25.8	4.0	7.6	tr	*	0.0	8.8	1.0	2.2	3.8	tr	tr	tr	0.8	*	*	1.3
*	1126	1800.50	3	0.16	2.64	2.4	18.6	44.5	24.3	5.0	7.8	tr	*	0.0	7.0	2.0	4.8	2.3	tr	tr	tr	1.4	*	*	0.9
*	1126	1801.50	3	0.16	2.64	21.2	21.0	44.3	29.0	1.0	7.0	tr	*	0.0	10.4	1.9	1.8	2.7	tr	tr	tr	0.9	*	*	1.0
*	1126	1802.50	3	0.16	2.64	20.0	20.4	49.0	20.7	4.5	5.0	tr	*	0.0	9.7	0.8	3.8	3.8	tr	tr	tr	1.6	*	*	1.0
*	1126	1803.50	3	0.12	3.06	1.1	18.2	38.5	30.4	6.0	6.5	tr	*	0.0	7.0	3.8	1.7	3.8	tr	tr	tr	1.0	*	*	1.3
*	1126	1804.50	3	0.30	1.74	7.5	20.1	49.7	21.3	3.3	7.7	tr	*	0.0	9.3	1.7	2.3	3.7	tr	tr	tr	0.3	*	*	0.7
*	1126	1805.50	3	0.29	1.79	12.4	20.9	58.2	18.6	3.2	7.0	tr	*	0.0	8.5	2.2	0.3	0.7	tr	tr	tr	0.3	*	*	1.0
*	1126	1806.50	3	0.12	3.06	0.0	3.2	53.8	17.0	3.3	1.0	tr	*	0.0	tr	tr	1.7	2.0	tr	14.7	5.3	tr	*	*	1.0
*	1126	1807.60	3	0.29	1.79	12.1	20.0	54.2	21.6	2.4	7.0	tr	*	0.0	8.1	1.2	2.8	1.4	tr	tr	tr	tr	*	*	1.3
*	1126	1808.50	3	0.28	1.84	10.5	20.4	47.0	18.0	6.3	7.0	tr	*	0.0	11.3	2.0	2.0	4.7	tr	tr	tr	1.0	*	*	0.7
*	1126	1809.50	3	0.13	2.94	0.0	2.7	53.0	13.3	7.0	0.0	tr	*	0.0	tr	tr	3.0	2.7	tr	20.0[2]		tr	*	*	1.0
*	1126	1810.50	3	0.23	2.12	7.0	19.2	53.3	20.7	2.7	7.7	tr	*	0.0	7.0	2.0	2.3	2.0	tr	tr	tr	1.3	*	*	1.0
*	1126	1811.50	4	0.11	3.18	4.2	16.6	59.5	17.3	3.7	3.8	tr	*	0.0	6.0	1.5	2.3	0.7	tr	2.0	1.5	0.7	*	*	1.0
*	1126	1812.50	4	0.10	3.32	3.0	18.7	56.9	18.1	4.0	6.6	tr	*	0.0	7.2	1.2	0.8	2.5	tr	tr	tr	1.9	*	*	0.8
*	1126	1813.40	4	0.15	2.74	4.5	19.0	52.9	21.0	4.0	5.0	tr	*	0.0	9.0	0.7	2.1	3.2	tr	tr	tr	1.4	*	*	0.7

[1] **Abundant secondary quartz but dust rings too vague for measurement.**
[2] **Total carbonate.**

GRANNY CREEK FIELD, CLAY 1126 PETROLOGY DATA

SECT #	WELL #	DEPTH	FACIES	GS mm	GS PHI	CORE K	Core Por	Qtz	Qtite	PsG	Chl	Ill	Mix	Kaol	Ppor	Fpor	Feld	Chrt	SecQ	Ccem	Crep	Fcarb	Mica	Opaq	Misc
*	1126	1814.40	4	0.16	2.64	4.5	19.2	52.6	17.2	6.8	5.0	tr	*	0.0	10.3	1.0	1.4	3.6	tr	tr	tr	1.4	*	*	0.7
*	1126	1816.60	4	0.13	2.94	1.0	16.3	44.3	21.7	8.0	7.0	tr	*	0.0	8.7	0.3	1.3	1.0	tr	3.0	3.3	0.7	*	*	0.7
*	1126	1817.50	4	0.12	3.06	0.3	17.0	50.7	24.1	5.5	9.3	tr	*	0.0	3.5	1.5	1.0	1.0	tr	0.6	0.4	1.7	*	*	0.7
*	1126	1818.50	4	0.13	2.94	0.2	16.1	54.7	18.7	8.2	6.3	tr	*	0.0	4.5	0.3	0.3	0.3	tr	0.7	0.3	3.7	*	*	2.0
*	1126	1819.40	4	0.12	3.06	0.1	13.5	53.1	15.5	4.8	8.1	tr	*	0.0	2.1	1.5	1.9	1.9	tr	3.0	1.7	4.5	*	*	1.9
*	1126	1821.90	4	0.11	3.18	0.3	13.8	46.0	32.5	5.7	6.5	tr	*	0.0	2.6	0.7	0.8	1.9	tr	tr	tr	2.2	*	*	1.1
*	1126	1822.60	4	0.11	3.18	0.1	14.8	55.4	12.5	15.0	6.8	tr	*	0.0	3.7	0.8	0.3	1.1	tr	0.9	0.9	1.5	*	*	1.1
*	1126	1823.50	4	0.12	3.06	0.1	14.4	49.3	28.7	4.0	6.5	tr	*	0.0	6.0	tr	tr	1.3	tr	tr	tr	3.0	*	*	1.2
*	1126	1824.50	4	0.11	3.18	0.1	14.5	51.6	24.0	4.0	4.6	tr	*	0.0	6.4	1.0	0.3	2.7	tr	0.6	0.6	3.1	*	*	1.0
*	1126	1825.50	4	0.11	3.18	0.2	16.3	50.0	38.2	2.0	3.6	tr	*	0.0	1.9	tr	0.7	1.0	tr	0.3	0.3	1.3	*	*	0.7
*	1126	1826.50	4	0.12	3.06	0.1	16.1	50.3	31.0	2.0	6.8	tr	*	0.0	5.2	0.4	tr	1.3	tr	tr	tr	2.0	*	*	1.0
*	1126	1827.60	4	0.09	3.47	0.1	15.4	52.1	24.9	6.4	6.0	tr	*	0.0	5.2	1.4	1.0	1.0	tr	tr	tr	1.2	*	*	0.7

GRANNY CREEK FIELD, CLAY 1128 PETROLOGY DATA

SECT #	WELL	DEPTH	FACIES	GS mm	GS phi	Core K	Core por	TSpor+ COATS	Qtz	Qtite	PsG	Chl	Ill	Mix	Kaol	Ppor	Fpor	Feld	Chrt	SecQ	Ccem	Crep	Sidr	Mica	Opaq	Misc
99	1128	1997.30	B	0.28	1.85	0.47	10.2	15.3	66.7	5.0	3.7	0.7	2.3	1.0	tr	10.7	1.3	2.0	2.0	0.3	3.0	tr	tr	tr	tr	1.3
375	1128	2000.40	B	0.40	1.33	0.58	5.4	8.3	66.0	8.7	tr	4.0	0.3	0.0	0.7	0.3	3.0	3.0	tr	12.7	0.3	1.0	tr	tr	tr	0.0
59	1128	2002.90	B	0.39	1.34	0.10	5.4	4.3	70.3	6.7	3.0	1.0	0.3	0.3	tr	2.0	0.7	2.7	1.3	10.0	0.3	1.0	tr	tr	tr	0.3
100	1128	2003.80	B	0.24	2.06	0.10	6.2	2.0	72.3	7.0	4.3	tr	1.7	tr	tr	0.3	1.0	tr	1.0	tr	11.3	tr	tr	tr	tr	0.7
60	1128	2004.70	B	0.26	1.92	0.10	6.2	4.3	70.7	2.7	3.7	tr	0.3	0.3	tr	1.7	2.0	2.0	1.0	13.3	2.3	tr	tr	tr	tr	0.0
61	1128	2007.20	B	0.21	2.25	0.10	7.9	8.7	67.0	4.3	4.3	2.3	tr	0.3	tr	2.0	4.0	3.0	1.7	8.0	1.3	0.3	tr	tr	tr	1.0
6	1128	2009.60	B	0.41	1.28	1.30	6.3	4.0	77.3	5.3	1.7	0.0	0.3	0.7	tr	0.7	2.3	2.3	1.3	7.0	0.7	0.3	tr	tr	tr	0.0
62	1128	2011.40	B	0.38	1.41	1.30	9.4	16.7	64.3	8.0	2.3	6.3	2.3	tr	0.3	7.7	2.7	2.7	0.7	2.0	tr	0.3	tr	tr	0.3	0.0
376	1128	2013.00	B	0.67	0.58	1.60	5.3	4.0	67.3	12.7	1.3	1.0	0.7	tr	0.3	1.7	0.3	0.3	tr	11.7	1.7	0.7	tr	tr	0.3	0.0
7	1128	2014.80	B	0.63	0.67	1.20	8.8	12.7	61.0	7.7	0.7	1.7	1.3	tr	tr	9.7	1.0	3.0	0.7	1.3	4.7	1.3	tr	tr	5.7	0.0
63	1128	2015.90	3	0.15	2.74	2.50	19.8	15.0	55.3	5.7	11.7	4.7	0.7	0.3	tr	8.0	1.3	2.0	2.0	1.0	1.3	tr	4.3	0.3	1.3	0.0
377	1128	2016.40	3	0.16	2.65	2.50	19.8	18.0	52.3	11.7	9.7	14.0	tr	0.3	tr	2.3	1.3	1.7	1.7	0.7	tr	tr	1.7	1.3	1.3	0.0
378	1128	2018.90	3	0.15	2.75	1.10	19.9	20.0	53.0	10.0	8.0	10.7	0.3	tr	tr	6.3	2.7	2.0	1.3	0.3	tr	tr	2.7	1.3	1.3	0.0
64	1128	2024.10	3	0.15	2.78	0.80	20.2	21.3	55.3	8.7	5.0	10.7	0.3	0.3	tr	7.3	2.7	3.0	2.3	0.7	2.0	tr	0.0	0.7	tr	1.0
65	1128	2027.20	3	0.15	2.72	3.10	16.0	17.7	51.3	7.0	12.3	12.3	tr	0.7	tr	3.3	1.3	2.3	3.0	0.3	2.0	tr	2.3	1.3	0.3	0.0
66	1128	2032.30	4	0.12	3.08	0.38	19.8	18.7	54.3	6.3	5.7	11.0	tr	0.3	tr	5.3	2.0	6.0	1.7	0.3	5.0	tr	tr	0.3	tr	1.7
379	1128	2037.00	4	0.15	2.73	0.42	19.6	18.7	48.3	11.0	15.3	13.3	tr	0.3	tr	4.0	1.3	0.7	0.7	0.3	tr	0.3	1.7	tr	2.7	0.0
380	1128	2045.10	4	0.10	3.40	0.10	8.8	9.3	34.0	8.7	12.0	9.0	0.3	tr	tr	tr	tr	0.7	2.3	tr	5.3	4.7	20.0	0.3	2.3	0.3

GRANNY CREEK FIELD, CLAY 1130 PETROLOGY DATA

SECT #	WELL	DEPTH	FACIES	GS mm	GS	Core	Core	TSpor+	Qtz	Qtite	PsG	Chl	Ill	Mix	Kaol	Ppor	Fpor	Feld	Chrt	SecQ	Ccem	Crep	Sidr	Mica	Opaq	Misc
					phi	K	por	COATS																		
69	1130	1864.50	A	0.22	2.19	0.16	14.0	1.0	55.0	8.0	30.7	tr	3.7[1]	0.7	tr	0.3	tr	0.7	0.7	tr	tr	tr	tr	0.3	tr	0.0
302	1130	1865.10	A	0.29	1.79	0.16	12.0	18.7	62.7	6.7	4.3	tr	7.7	1.7	tr	7.7	1.7	1.0	1.3	tr	1.7	3.0	0.3	tr	0.3	0.0
303	1130	1866.50	A	0.38	1.38	13.00	14.9	17.7	60.0	8.3	3.7	tr	5.7	3.0	tr	7.3	1.7	4.7	1.0	tr	1.7	3.0	tr	tr	tr	0.0
304	1130	1867.80	A	0.22	2.20	11.00	17.0	19.3	64.7	6.0	2.3	1.0	2.7	2.3	tr	8.7	4.7	3.3	0.7	0.3	1.3	1.3	0.3	tr	0.3	0.0
70	1130	1870.70	A	0.33	1.60	0.16	13.6	9.3	61.7	9.3	3.0	1.0	tr	0.3	tr	4.7	3.3	4.0	2.0	9.3	0.3	0.3	tr	0.3	tr	0.3
71	1130	1874.50	B	0.33	1.59	1.30	14.2	10.0	62.7	4.0	1.3	5.0	tr	tr	tr	4.0	1.0	4.3	1.7	4.3	10.7	0.3	tr	0.3	tr	0.3
381	1130	1876.50	B	0.70	0.51	1.50	5.3	5.7	64.3	14.0	0.7	1.7	0.7	0.3	1.3	0.7	1.0	2.3	0.7	8.7	3.0	0.7	tr	tr	tr	0.0
382	1130	1878.70	B	0.59	0.76	0.20	7.8	5.0	55.7	19.0	1.7	3.0	1.0	tr	0.0	0.3	0.7	1.0	1.0	5.0	8.7	3.0	tr	tr	tr	0.0
8	1130	1879.80	3	0.17	2.57	28.00	17.3	23.0	55.7	8.0	9.3	1.7	0.3	tr	0.0	17.0	4.0	1.7	0.3	tr	0.7	tr	tr	0.7	tr	0.7
9	1130	1881.90	3	0.12	3.04	0.29	16.0	19.3	55.0	5.7	10.0	3.7	0.3	tr	0.0	14.7	0.7	3.3	2.0	0.3	2.3	tr	tr	0.7	tr	1.3
383	1130	1883.30	3	0.13	2.98	2.10	19.5	24.0	52.0	9.0	5.0	15.0	0.3	1.0	0.0	5.7	2.0	3.7	1.7	1.7	tr	0.3	1.3	0.3	1.0	0.0
384	1130	1884.90	3	0.11	3.20	0.52	21.0	23.0	47.7	13.7	7.3	18.3	tr	tr	0.0	3.3	1.3	3.3	2.3	tr	tr	tr	0.3	1.3	1.0	0.0
385	1130	1887.00	3	0.17	2.56	11.00	22.2	21.7	48.3	10.0	12.0	10.3	tr	tr	0.0	7.3	4.0	3.7	0.3	0.7	0.7	tr	0.7	1.0	1.0	0.0
386	1130	1891.90	3	0.15	2.76	6.00	22.2	26.3	47.7	11.7	6.3	15.3	tr	0.3	0.0	8.7	2.0	3.3	1.7	1.0	0.3	tr	tr	0.3	1.3	0.0
10	1130	1895.30	3	0.15	2.79	5.70	22.4	23.3	54.3	6.3	9.0	6.3	tr	tr	0.0	14.7	2.3	4.0	0.3	tr	1.0	0.3	tr	tr	tr	1.3
72	1130	1897.10	4	0.16	2.63	8.20	22.6	20.0	54.0	8.0	8.0	11.0	0.3	tr	0.0	8.0	0.7	3.7	1.7	0.7	1.0	tr	0.3	0.7	2.0	0.3
387	1130	1901.00	4	0.15	2.72	3.80	21.9	28.7	43.3	12.3	7.0	16.7	tr	0.7	0.0	8.7	2.7	3.3	1.0	0.3	1.0	0.3	1.0	1.0	0.7	0.0
73	1130	1906.90	4	0.13	2.93	0.96	18.9	19.7	49.3	7.0	12.3	9.7	tr	0.3	0.0	7.0	2.7	2.0	1.0	tr	4.7	tr	3.0	0.7	0.3	0.0

[1] Illite in partings as well as in grain coatings.

GRANNY CREEK FIELD, CLAY 1132 PETROLOGY DATA

SECT #	WELL #	DEPTH	FACIES	GS mm	GS	Core	Core	TSpor+	Qtz	Qtite	PsG	Chl	Ill	Mix	Kaol	Ppor	Fpor	Feld	Chrt	SecQ	Ccem	Crep	Sidr	Mica	Opaq	Misc
					phi	K	por	COATS																		
388	1132	1967.00	A	0.41	1.30	6.70	11.3	7.7	59.7	14.7	tr	tr	6.0	0.7	tr	1.0	tr	1.7	1.0	2.7	7.0	5.3	0.3	tr	tr	0.0
389	1132	1969.00	A	0.23	2.15	6.70	13.5	13.0	53.7	14.0	8.3	2.0	8.7	0.7	tr	2.0	1.3	4.0	0.3	tr	2.3	2.0	tr	tr	0.7	0.0
11	1132	1970.10	A	0.27	1.90	6.70	15.4	15.0	59.7	7.0	5.7	0.3	0.3	0.7	tr	11.0	2.7	3.7	0.3	4.7	2.0	1.3	tr	tr	tr	0.7
12	1132	1972.30	A	0.21	2.26	9.70	18.2	21.7	59.0	4.7	7.0	4.0	1.0	0.3	tr	13.7	2.7	3.0	1.3	2.7	tr	tr	tr	0.7	tr	0.0
74	1132	1974.30	A	0.20	2.31	1.20	12.0	16.3	64.0	5.0	6.3	4.7	tr	0.3	tr	9.0	2.3	1.3	2.3	3.7	0.3	tr	tr	0.3	tr	0.3
390	1132	1976.25	B	0.27	1.92	0.38	8.6	13.0	55.0	9.3	4.0	5.3	1.3	0.3	0.3	2.0	3.7	3.3	tr	14.0	tr	0.7	0.3	tr	0.3	0.0
391	1132	1977.80	B	0.48	1.07	0.21	7.2	8.3	61.7	11.7	2.3	4.7	tr	tr	1.0	1.3	1.3	2.7	tr	11.7	0.7	0.3	0.3	tr	tr	0.3
392	1132	1980.60	B	0.53	0.91	1.30	6.2	6.0	61.7	11.0	1.0	2.3	0.7	0.3	0.7	0.7	1.3	4.7	tr	12.7	tr	2.0	1.0	tr	tr	0.0
13	1132	1981.90	B	0.81	0.30	1.30	5.3	3.0	66.0	12.7	2.0	1.7	tr	tr	tr	0.7	0.7	2.3	tr	4.7	6.0	2.3	tr	tr	tr	1.0
393	1132	1983.10	2	0.16	2.69	0.10	6.8	11.3	51.3	11.3	4.3	4.7	tr	0.3	tr	1.3	5.0	6.0	tr	14.3	tr	tr	tr	1.0	0.3	0.0
394	1132	1985.90	3	0.16	2.68	0.20	13.0	16.7	51.3	10.7	5.0	9.7	0.7	0.3	tr	2.0	4.0	2.7	0.7	10.0	0.3	1.0	0.7	0.7	0.3	0.0
395	1132	1989.00	3	0.14	2.83	7.50	21.8	26.3	48.3	12.7	8.0	15.3	1.3	1.0	0.0	6.7	2.0	1.7	1.3	1.0	tr	tr	tr	tr	0.7	0.0
396	1132	1990.00	3	0.13	3.00	7.50	18.8	26.3	46.0	14.3	5.0	17.0	0.3	0.7	0.0	6.3	2.0	4.0	0.3	1.3	tr	tr	1.3	tr	1.3	0.0
14	1132	1991.20	3	0.17	2.56	9.30	14.3	9.3	55.3	3.0	9.7	2.3	0.3	tr	0.0	5.7	1.0	2.3	1.7	0.3	15.0	0.7	tr	0.3	2.3	0.0
75	1132	1994.90	3	0.15	2.75	3.80	21.8	21.3	52.0	5.7	9.3	12.7	tr	tr	0.0	7.0	1.7	3.7	4.3	tr	1.3	tr	tr	0.7	tr	1.7
397	1132	1997.40	3	0.16	2.66	5.40	22.3	23.7	51.0	13.3	5.0	14.7	tr	0.3	0.0	7.3	1.3	2.3	2.0	1.0	tr	0.7	0.3	tr	0.7	0.0
398	1132	1999.90	3	0.15	2.74	7.50	22.0	26.0	44.7	15.0	6.0	12.3	1.7	1.0	0.0	8.0	3.0	3.3	1.7	1.0	tr	tr	tr	0.3	2.0	0.0
399	1132	2002.30	3	0.14	2.86	5.40	22.7	26.3	45.7	15.0	6.7	16.7	0.3	tr	0.0	7.3	2.0	2.7	1.0	tr	tr	1.0	tr	1.0	0.7	0.0
400	1132	2005.00	3	0.14	2.83	2.20	21.7	24.3	44.3	16.0	8.3	15.7	0.7	tr	0.0	5.3	2.7	2.7	1.3	0.3	tr	1.0	0.7	0.7	0.3	0.0
401	1132	2007.10	4	0.13	2.92	1.50	21.9	26.3	45.3	10.3	8.0	17.3	tr	0.3	0.0	8.0	0.7	3.0	1.7	0.7	tr	1.3	2.0	0.7	0.3	0.3
76	1132	2009.30	4	0.13	2.94	1.00	20.9	22.0	48.0	8.0	10.7	13.3	tr	tr	0.0	6.3	2.3	1.3	2.0	tr	2.3	0.3	4.0	0.3	1.0	0.0
77	1132	2011.10	4	0.10	3.38	0.10	15.8	17.7	54.3	4.0	7.7	13.3	tr	tr	0.0	1.7	2.7	2.0	1.3	tr	2.7	0.3	8.0	1.0	1.0	0.0

GRANNY CREEK FIELD, CLAY 1133 PETROLOGY DATA

SECT #	WELL #	FACIES	ZONE	GS mm	GS	Core	Core	TSpor+	Qtz	Qtite	PsG	Chl	Ill	Mix	Kaol	Ppor	Fpor	Feld	Chrt	SecQ	Ccem	Crep	Sidr	Mica	Opaq	Misc
					phi	K	por	COATS																		
305	1133	2081.80	B	0.45	1.16	*	*	1.7	62.0	9.7	1.7	tr	1.3	0.3	tr	tr	tr	0.3	0.7	1.7	9.3	12.0	tr	0.3	0.7	0.0
306	1133	2082.60	B	0.50	1.01	*	*	1.7	62.3	10.0	0.3	1.0	0.7	tr	tr	tr	tr	2.3	1.3	tr	17.0	4.0	0.3	tr	0.7	0.0
101	1133	2084.00	B	0.50	0.99	*	*	7.7	66.7	9.3	1.3	1.3	0.3	0.3	2.7	0.7	2.3	1.7	1.7	1.0	7.7	2.7	tr	tr	tr	0.3
102	1133	2086.40	B	0.31	1.70	*	*	8.0	64.7	7.3	6.0	0.3	0.7	1.7	1.7	1.3	2.3	2.0	1.3	2.0	6.7	0.7	tr	0.7	tr	0.7
103	1133	2089.80	B	0.14	2.81	*	*	13.3	52.0	4.7	9.0	2.7	0.7	0.7	0.0	9.0	0.3	1.0	tr	2.0	15.3	tr	tr	1.0	tr	1.7
104	1133	2096.80	3	0.14	2.86	*	*	24.3	49.3	8.7	11.3	7.0	0.7	0.3	0.0	15.0	1.3	2.0	3.3	tr	0.7	tr	tr	tr	tr	0.3
105	1133	2098.90	3	0.14	2.86	*	*	14.7	66.7	6.7	6.7	7.0	tr	0.3	0.0	5.3	2.0	1.3	0.7	tr	tr	0.3	tr	1.7	1.0	0.3
106	1133	2103.60	3	0.13	2.91	*	*	18.7	58.3	5.7	10.3	4.0	1.0	0.3	0.0	11.3	2.0	2.3	1.7	0.3	tr	0.3	tr	0.7	tr	1.7
107	1133	2107.40	3	0.14	2.81	*	*	8.0	55.0	10.3	20.7	3.7	0.3	tr	0.0	3.0	1.0	1.7	1.7	0.0	0.3	tr	tr	0.3	tr	2.0
108	1133	2109.30	3	0.16	2.68	*	*	20.7	57.7	5.3	6.0	11.7	0.3	0.3	0.0	5.7	2.7	1.7	1.3	0.3	1.0	2.3	1.3	1.7	0.3	0.3
109	1133	2113.80	4	0.10	3.28	*	*	17.0	49.3	6.0	10.3	15.0	tr	tr	0.0	1.3	0.7	1.7	0.7	tr	3.7	tr	8.3	0.7	2.0	0.3

GRANNY CREEK FIELD, CLAY 1134 PETROLOGY DATA

SECT #	WELL #	DEPTH	FACIES	GS mm	GS	Core	Core	TSpor+	Qtz	Qtite	PsG	Chl	Ill	Mix	Kaol	Ppor	Fpor	Feld	Chrt	SecQ	Ccem	Crep	Sidr	Mica	Opaq	Misc
					phi	K	por	COATS																		
307	1134	2195.00	B	0.552	0.86	*	*	7.33	73.33	6.33	0.67	tr	0.67	tr	2.00	2.00	2.67	3.33	0.67	7.67	tr	0.33	tr	tr	0.33	0.00
110	1134	2203.10	2	0.109	3.20	*	*	6.00	59.00	11.00	14.00	6.00	3.00[1]	tr	tr	tr	tr	tr	tr	tr	tr	tr	2.00	5.00	tr	0.00
15	1134	2204.00	3	0.138	2.86	*	*	18.33	57.00	5.67	11.33	5.33	tr	0.67	0.33	9.00	3.00	2.67	1.67	0.67	0.33	tr	tr	0.33	tr	2.00
111	1134	2206.30	3	0.122	3.04	*	*	16.67	60.33	6.67	9.67	9.33	0.33	2.33	tr	3.67	1.00	1.67	1.33	tr	0.67	tr	tr	1.33	1.33	0.33
112	1134	2208.60	3	0.151	2.73	*	*	18.33	55.67	10.33	6.33	10.33	tr	tr	0.00	5.67	2.33	1.67	2.33	0.33	2.00	tr	0.33	0.33	2.33	0.00
113	1134	2212.60	3	0.156	2.68	*	*	23.00	55.67	6.67	6.33	8.67	1.00	0.33	0.00	10.33	2.67	3.00	2.33	0.33	0.33	0.33	0.33	1.00	0.67	0.00
114	1134	2216.80	3	0.138	2.86	*	*	13.67	52.67	8.00	10.67	7.33	tr	0.67	0.00	3.33	2.33	2.00	2.00	0.67	tr	tr	8.00	0.33	2.00	0.00
115	1134	2218.70	4	0.152	2.72	*	*	16.00	51.00	11.67	12.67	7.67	0.33	0.67	0.00	6.00	1.33	1.67	1.33	0.33	3.00	tr	0.33	tr	2.00	0.00
116	1134	2225.10	4	0.143	2.81	*	*	12.00	56.33	12.67	8.67	8.00	tr	0.33	0.33	1.33	2.00	0.67	1.00	tr	0.33	3.33	1.67	1.00	2.00	0.33

[1] **Interstitial illite could not be distinguished from deformed argillaceous grains.**

GRANNY CREEK FIELD, CLAY 1222 PETROLOGY DATA

SECT #	WELL #	DEPTH	FACIES	GS mm	GS	Core	Core	TSpor+	Qtz	Qtite	PsG	Chl	Ill	Mix	Kaol	Ppor	Fpor	Feld	Chrt	SecQ	Ccem	Crep	Sidr	Mica	Opaq	Misc
					phi	K	por	COATS																		
257	1222	2250.00		0.28	1.84	*	*	1.3	61.7	7.3	1.0	0.7	tr	0.7	0.0	tr	tr	1.3	1.0	tr	13.7	7.7	3.3	1.0	0.3	0.3
258	1222	2255.80		0.23	2.13	*	*	4.7	66.3	10.7	2.3	2.3	tr	1.3	0.0	1.0	tr	0.3	1.0	0.3	10.0	2.3	1.3	tr	0.3	0.3
259	1222	2256.50		0.13	2.95	*	*	9.0	54.0	7.0	7.0	4.0	1.0	3.0	0.0	1.0	tr	0.7	1.7	0.0	12.3	2.3	1.3	0.3	4.3	0.0
A 260	1222	2256.90		0.42	1.24	*	*	5.0	70.3	9.3	1.0	3.3	tr	0.7	0.0	0.7	0.3	2.7	0.7	0.3	4.7	tr	4.7	tr	1.3	0.0
260	1222	2257.50		0.33	1.60	*	*	7.3	59.7	7.3	4.0	4.0	tr	0.7	0.0	2.7	tr	tr	0.3	tr	11.0	2.3	6.0	tr	2.0	0.0
261	1222	2258.50		0.16	2.66	*	*	14.0	60.3	12.0	5.7	7.3	tr	1.0	0.0	4.7	1.0	1.7	2.3	0.7	1.0	0.7	0.3	0.7	0.3	0.3
262	1222	2259.50		0.11	3.13	*	*	11.3	68.3	7.0	7.0	2.7	1.0	0.3	0.0	4.0	3.3	3.0	0.7	0.3	tr	0.7	0.3	0.7	0.7	0.0
263	1222	2263.00		0.15	2.79	*	*	12.0	55.3	6.7	16.3	3.7	tr	0.7	0.0	6.7	1.0	3.0	1.3	0.3	tr	tr	0.3	0.3	3.3	1.0
264	1222	2264.80		0.12	3.08	*	*	20.3	53.7	10.0	6.7	12.0	tr	0.3	0.0	6.0	2.0	3.0	0.7	0.3	1.3	tr	tr	1.7	2.3	0.0
265	1222	2265.80		0.16	2.63	*	*	1.0	51.3	9.3	4.3	0.7	0.3	tr	0.0	tr	tr	0.3	1.7	0.3	23.7	6.3	tr	0.7	1.0	0.0
266	1222	2266.90		0.15	2.70	*	*	20.3	56.7	8.7	6.3	8.7	tr	2.3	0.0	7.0	2.3	5.7	1.3	0.7	0.3	tr	tr	tr	tr	0.0
267	1222	2269.80		0.17	2.55	*	*	19.0	57.0	11.3	6.0	8.3	0.7	1.3	0.0	6.7	2.0	2.0	1.3	1.0	tr	0.3	tr	1.0	1.0	0.0
268	1222	2275.10		0.15	2.77	*	*	10.0	48.0	9.7	7.0	10.0	tr	tr	0.0	tr	tr	2.3	5.0	tr	6.0	4.7	5.3	1.0	1.0	0.0
269	1222	2275.80		0.14	2.80	*	*	3.0	41.7	11.0	4.3	2.3	0.3	0.3	0.0	tr	tr	1.0	0.7	tr	24.0	9.7	2.3	0.3	1.7	0.3

GRANNY CREEK FIELD, CLAY 1598 PETROLOGY DATA

SECT #	WELL #	FACIES	ZONE	GS mm	GS	Core	Core	TSpor+	Qtz	Qtite	PsG	Chl	Ill	Mix	Kaol	Ppor	Fpor	Feld	Chrt	SecQ	Ccem	Crep	Sidr	Mica	Opaq	Misc
					phi	K	por	COATS																		
213	1598	1957.25		0.29	1.81	*	*	3.0	66.3	6.7	7.7	1.0	3.0[1]	1.7	tr	0.3	tr	0.7	2.7	tr	9.3	0.7	tr	tr	tr	0.0
214	1598	1959.50		0.32	1.64	*	*	8.0	68.7	5.0	4.0	0.7	2.0	1.7	tr	3.7	tr	3.3	0.3	1.0	7.3	1.0	tr	1.3	tr	0.0
254	1598	1960.00		0.30	1.74	*	*	9.7	58.7	17.0	1.7	tr	5.3	0.3	tr	4.0	tr	1.7	1.7	1.3	4.0	4.0	tr	tr	0.3	0.0
215	1598	1961.50		0.15	2.78	*	*	16.0	56.3	9.0	7.0	2.0	1.3	4.0	tr	5.7	3.0	4.3	0.7	1.0	0.7	3.3	0.3	1.3	tr	0.0
216	1598	1962.20		0.18	2.48	*	*	9.3	62.0	6.7	10.7	0.3	tr	3.7	0.3	2.3	2.7	1.3	0.7	8.3	tr	1.0	tr	tr	tr	0.0
217	1598	1963.50		0.28	1.86	*	*	9.0	67.7	8.3	1.7	1.7	1.0	1.3	tr	0.7	4.3	2.3	1.7	9.0	tr	tr	0.3	tr	tr	0.0
255	1598	1963.80		0.28	1.85	*	*	6.0	73.0	6.7	3.7	tr	tr	0.3	1.0	tr	4.7	4.7	tr	2.0	0.3	1.0	0.7	1.3	0.3	0.3
256	1598	1964.80		0.31	1.71	*	*	7.0	68.7	16.3	0.7	1.0	tr	1.7	1.0	0.7	2.7	1.7	tr	3.0	1.3	1.0	tr	tr	0.3	0.0
218	1598	1965.75		0.32	1.66	*	*	4.3	67.3	11.7	4.3	0.7	tr	0.7	0.0	1.0	2.0	2.3	1.3	6.0	tr	1.7	tr	0.3	0.7	0.0
219	1598	1966.00		0.67	0.58	*	*	3.3	78.0	7.3	0.7	1.0	0.3	tr	0.0	1.0	1.0	1.0	7.7	tr	1.0	0.3	tr	tr	tr	0.7
220	1598	1967.16		0.65	0.63	*	*	6.0	70.0	7.0	2.3	1.3	tr	tr	0.3	3.3	1.0	1.3	0.7	0.3	11.7	0.3	tr	tr	tr	0.3
221	1598	1967.50		0.11	3.17	*	*	8.3	54.3	12.3	13.0	6.7	0.3	1.3	0.0	tr	tr	0.3	1.3	1.7	1.3	tr	5.7	1.3	0.3	0.0
222	1598	1968.83		0.19	2.39	*	*	1.7	55.3	5.3	3.3	0.3	tr	tr	0.0	0.7	0.7	1.0	3.0	2.0	25.3	0.7	tr	1.7	tr	0.7
223	1598	1970.30		0.16	2.65	*	*	9.0	49.3	8.0	3.7	6.7	tr	1.0	0.0	1.0	0.3	1.3	3.3	0.3	0.7	0.7	21.0	1.3	1.3	0.0
224	1598	1976.50		0.21	2.26	*	*	19.3	52.7	7.7	11.3	10.0	0.3	1.3	0.0	6.0	1.7	4.3	2.7	tr	tr	0.3	0.7	0.3	0.3	0.3
225	1598	1981.50		0.19	2.39	*	*	19.0	60.3	4.7	6.0	11.0	tr	tr	0.0	7.3	0.7	3.0	1.7	0.3	2.3	0.3	tr	0.3	tr	2.0
226	1598	1984.50		0.18	2.44	*	*	21.0	57.0	6.7	6.0	11.0	0.7	tr	0.0	8.0	1.3	1.7	2.0	0.7	1.0	tr	tr	1.0	tr	3.0
227	1598	1991.50		0.14	2.89	*	*	17.7	59.0	5.0	10.3	10.3	tr	0.3	0.0	6.3	0.7	2.0	1.7	0.3	2.3	tr	tr	0.3	tr	1.3

[1] Illite mostly in partings.

GRANNY CREEK FIELD, CLAY 1726 PETROLOGY DATA

SECT #	WELL #	FACIES	ZONE	GS mm	GS	Core	Core	TSpor+	Qtz	Qtite	PsG	Chl	Ill	Mix	Kaol	Ppor	Fpor	Feld	Chrt	SecQ	Ccem	Crep	Sidr	Mica	Opaq	Misc
					phi	K	por	COATS																		
294	1726	2083.16		0.23	2.09	*	*	2.3	63.0	16.7	7.0	0.3	3.7[1]	1.3	0.0	0.7	tr	1.3	1.0	0.3	0.7	3.7	tr	0.3	tr	0.0
295	1726	2083.90		0.53	0.91	*	*	3.7	63.7	15.0	2.0	0.7	2.0[1]	2.3	0.0	0.7	tr	1.0	1.0	1.7	6.0	2.7	0.7	tr	0.7	0.0
296	1726	2084.40		0.14	2.80	*	*	15.0	57.7	10.0	7.7	6.7	1.7	2.0	0.0	4.0	0.7	2.3	2.0	1.0	0.7	2.0	tr	0.3	1.3	0.0
297	1726	2085.00		0.41	1.29	*	*	10.0	64.3	12.7	3.0	4.0	0.3	1.0	0.0	4.3	0.3	1.0	1.7	0.7	1.7	4.0	tr	tr	1.0	0.0
298	1726	2085.50		0.43	1.23	*	*	5.7	65.0	14.7	1.7	2.7	0.3	0.3	0.0	2.3	tr	1.0	1.3	tr	6.7	2.7	tr	0.3	0.7	0.3
299	1726	2086.50		0.15	2.71	*	*	10.0	44.3	12.0	6.3	5.3	0.3	1.3	0.0	2.7	0.3	0.7	1.0	tr	17.0	1.3	0.7	2.0	4.3	0.3
300	1726	2088.16		0.12	3.08	*	*	16.0	58.3	10.0	8.3	6.0	tr	tr	0.0	8.0	2.0	2.7	0.7	0.7	tr	1.0	0.3	tr	1.3	0.7

GRANNY CREEK FIELD, ROANE 2410 PETROLOGY DATA

SECT #	WELL #	FACIES	ZONE	GS mm	GS	Core	Core	TSpor+	Qtz	Qtite	PsG	Chl	Ill	Mix	Kaol	Ppor	Fpor	Feld	Chrt	SecQ	Ccem	Crep	Sidr	Mica	Opaq	Misc
					phi	K	por	COATS																		
290	R 2410	1878.50	B	0.54	0.90	0.10	4.5	0.3	60.3	9.0	5.0	tr	2.3[1]	0.3	tr	tr	tr	0.3	tr	0.7	13.3	8.7	tr	tr	tr	0.0
291	R 2410	1879.00	B	0.37	1.45	0.10	4.0	1.3	69.3	8.0	4.0	tr	8.7[1]	0.3	tr	0.7	0.3	1.0	2.0	1.0	1.3	3.3	tr	tr	tr	0.0
292	R 2410	1879.90	B	0.42	1.24	0.10	4.0	6.0	66.3	11.0	0.7	0.3	2.0	1.0	tr	2.7	tr	2.7	tr	6.0	1.3	5.7	tr	tr	0.3	0.0
293	R 2410	1880.08	B	0.42	1.24	0.40	3.9	7.3	68.7	10.0	0.3	tr	5.7	0.7	tr	0.7	0.3	1.0	0.3	6.0	2.3	4.0	tr	tr	tr	0.0
270	R 2410	1880.30	B	0.49	1.04	0.40	3.9	11.3	66.7	11.7	tr	1.7	2.3	0.7	tr	4.7	2.0	2.3	1.0	2.3	2.3	1.7	tr	tr	0.3	0.3
271	R 2410	1881.50	B	0.65	0.62	8.90	6.5	4.3	75.0	12.3	1.0	tr	1.3	0.3	0.3	2.3	tr	1.0	tr	4.3	1.3	0.7	tr	tr	tr	0.0
272	R 2410	1882.10	B	0.18	2.45	0.20	9.8	2.0	51.7	15.0	2.0	tr	3.3	1.7	0.0	0.3	tr	tr	tr	tr	23.0	1.3	0.7	tr	0.7	0.3
273	R 2410	1882.80	3	0.13	2.90	0.20	9.8	12.0	67.7	8.0	6.0	1.7	3.0	1.0	0.0	5.0	1.3	3.7	0.3	0.3	tr	0.3	tr	0.7	1.0	0.0
274	R 2410	1883.40	3	0.13	2.99	6.00	14.7	15.0	55.0	10.7	12.3	2.7	1.3	3.7	0.0	6.3	1.0	3.0	2.0	0.3	tr	tr	tr	1.0	0.7	0.0
275	R 2410	1884.00	3	0.12	3.05	2.00	15.9	18.3	59.7	8.3	9.0	3.7	0.7	2.0	0.0	9.3	2.7	3.0	tr	tr	tr	0.3	tr	0.3	1.0	0.0
276	R 2410	1885.75	3	0.12	3.04	9.50	19.1	20.7	46.0	8.3	16.0	4.0	1.0	4.0	0.0	9.3	2.3	3.3	1.0	0.7	tr	tr	2.0	0.7	1.3	0.0
277	R 2410	1887.20	3	0.16	2.66	36.00	22.1	25.3	54.0	8.3	4.7	11.3	tr	0.3	0.0	11.0	2.7	3.7	1.0	1.0	0.3	0.7	tr	0.7	0.3	0.0
278	R 2410	1890.50	3	0.17	2.56	42.00	20.1	25.3	49.0	5.0	5.7	12.0	1.0	1.0	0.3	8.0	3.3	3.0	0.7	0.7	0.7	1.7	1.3	0.3	1.0	5.3
279	R 2410	1890.80	3	0.19	2.37	42.00	20.1	23.7	52.7	5.7	5.3	12.7	0.3	2.7	0.0	5.7	2.3	2.3	2.0	0.7	1.0	tr	tr	0.3	1.3	5.0
280	R 2410	1891.75	3	0.17	2.52	34.00	15.0	20.0	52.0	12.3	4.3	9.0	tr	0.7	0.0	8.3	2.0	3.0	2.3	4.0	0.3	0.7	tr	0.7	0.0	0.3
281	R 2410	1893.00	3	0.16	2.61	15.00	16.6	24.3	53.7	8.7	6.7	9.7	tr	tr	0.0	10.0	4.7	1.7	1.3	2.3	tr	0.3	tr	0.3	0.7	0.0
282	R 2410	1895.20	3	0.16	2.69	20.00	16.6	18.3	54.3	10.3	7.0	6.3	0.3	1.0	0.0	8.7	2.0	1.7	1.3	4.0	0.7	0.3	tr	0.7	0.3	1.0
283	R 2410	1898.25	3	0.13	2.95	11.00	20.4	24.7	51.0	9.3	7.7	9.3	tr	1.3	0.0	10.3	3.7	3.0	1.3	tr	0.7	1.0	tr	0.3	1.0	0.0
284	R 2410	1899.40	3	0.14	2.87	16.00	20.4	24.0	51.0	12.0	6.7	14.3	0.7	0.3	0.0	6.3	2.3	0.7	3.7	tr	1.3	0.3	tr	0.3	tr	0.0
285	R 2410	1902.70	3	0.14	2.85	10.00	19.7	20.3	56.3	11.0	4.3	9.7	tr	0.3	0.0	9.0	1.3	3.3	2.0	2.0	tr	tr	0.7	tr	tr	0.0
286	R 2410	1907.50	4	0.14	2.89	2.00	15.8	15.7	46.7	13.3	4.7	10.0	tr	0.3	0.0	4.3	1.0	1.7	1.3	0.3	1.3	1.0	13.3	0.3	0.3	0.0
287	R 2410	1909.80	4	0.10	3.29	0.40	17.5	10.7	50.0	14.0	9.0	10.0	0.3	0.3	0.0	tr	tr	1.0	5.0	tr	0.3	tr	2.7	3.7	3.7	0.0
288	R 2410	1910.50	4	0.10	3.27	1.00	17.6	21.0	45.0	9.0	6.0	14.0	tr	3.0	0.0	2.0	2.0	tr	tr	tr	tr	2.0	10.0	5.0	1.0	1.0

[1] Illite mostly in partings.

ROCK CREEK FIELD, ROANE 1020 PETROLOGY DATA

SECT #	WELL #	DEPTH	GS PHI	CORE K	Core	TSpor +	Qtz	Qtite	Pag	Chl	Ill	Mix	Kaol	Ppor	Fpor	Feld	Chrt	SecQ	Ccem	Crep	Sidr	Mica	Opaq	Misc
					Por	coats																		
146	R 1020	2029 - 30	1.85	*	*	1.7	73.7	9.3	tr	tr	1.3	0.3	0.0	tr	tr	0.3	0.7	1.7	5.0	7.7	tr	tr	tr	0.0
308	R 1020	2034 - 36	1.67	*	*	9.3	68.0	6.3	1.7	0.3	0.3	tr	1.0	1.7	6.0	3.3	1.0	8.7	tr	0.3	tr	0.7	0.3	0.3
147	R 1020	2037 - 38	2.37	*	*	2.3	70.0	13.0	5.3	1.3	0.7	tr	0.0	tr	0.3	2.0	1.7	3.7	0.3	0.7	tr	1.0	tr	0.0
148	R 1020	2041 - 42	2.74	*	*	20.7	57.3	4.7	6.0	7.3	0.7	tr	0.0	8.0	4.7	2.7	0.7	0.3	tr	tr	6.0	1.0	0.7	0.0
149	R 1020	2044 - 45	2.79	*	*	12.0	48.0	10.3	7.0	5.7	0.3	0.3	0.0	2.7	3.0	2.0	1.0	tr	tr	tr	17.0	1.0	1.7	0.0
150	R 1020	2046 - 47	2.72	*	*	22.0	64.3	6.7	1.7	4.3	tr	tr	0.3	14.0	3.3	1.7	tr	1.0	tr	tr	1.0	0.7	0.7	0.3
151	R 1020	2052 - 53	2.85	*	*	19.0	53.7	9.7	7.3	6.7	tr	tr	0.0	9.7	2.7	2.0	tr	1.3	tr	tr	4.7	0.3	2.0	0.0
152	R 1020	2055 - 56	2.58	*	*	18.3	51.7	11.0	7.3	9.7	0.3	tr	0.0	5.3	3.0	3.0	0.3	2.3	tr	1.3	2.0	1.0	1.3	0.3
153	R 1020	2059 - 60	2.60	*	*	18.0	55.0	10.3	6.3	4.3	tr	0.7	0.0	8.7	4.3	2.7	2.3	1.0	0.3	0.3	2.0	0.3	0.7	0.7
154	R 1020	2064 - 65	2.74	*	*	23.3	53.7	6.7	7.7	7.3	0.3	0.3	0.3	10.3	4.7	3.7	0.7	1.3	tr	tr	2.0	0.7	0.3	0.0
155	R 1020	2067 - 68	2.74	*	*	19.0	57.0	11.3	4.0	7.3	tr	tr	0.0	8.7	3.0	3.0	1.3	1.3	0.7	0.3	tr	1.0	0.7	0.3
156	R 1020	2069 - 70	2.81	*	*	3.7	46.0	11.0	2.7	3.7	tr	tr	0.0	tr	tr	0.3	1.7	0.7	26.3	1.0	3.3	2.0	0.7	0.7
157	R 1020	2073 - 74	2.61	*	*	4.7	65.3	14.0	6.3	3.3	1.0	tr	0.0	tr	0.3	1.3	1.0	4.0	tr	tr	tr	2.0	1.0	0.3
158	R 1020	2080 - 81	2.94	*	*	16.7	47.3	18.7	7.7	13.3	0.7	1.3	0.0	tr	1.3	3.0	5.0	0.3	tr	tr	0.3	0.3	0.7	0.0
159	R 1020	2082 - 83	2.85	*	*	21.7	58.3	7.7	5.7	11.3	1.7	tr	0.0	6.3	2.3	1.3	1.3	tr	0.3	tr	1.3	1.3	0.7	0.3
160	R 1020	2092 - 93	3.00	*	*	14.7	63.7	6.7	6.3	11.7	tr	0.3	0.0	2.7	tr	2.7	0.7	0.7	tr	tr	3.0	tr	1.3	0.3

ROCK CREEK FIELD, ROANE 1021 PETROLOGY DATA

SECT #	WELL #	DEPTH	GS PHI	CORE K	Core	TSpor	Qtz	Qtite	Pag	Chl	Ill	Mix	Kaol	Ppor	Fpor	Feld	Chrt	SecQ	Ccem	Crep	Sidr	Mica	Opaq	Misc
					Por	coats																		
309	R 1021	2113 - 14	1.06	*	*	3.7	74.0	6.0	tr	tr	0.3	tr	1.0	1.0	1.3	2.7	tr	6.0	2.3	5.3	tr	tr	tr	0.0
162	R 1021	2117 - 18	1.45	*	*	5.3	69.7	10.7	tr	0.3	tr	tr	1.3	1.3	2.3	1.7	1.3	10.0	0.7	0.3	tr	tr	0.3	0.0
161	R 1021	2118 - 19	2.29	*	*	6.0	59.8	15.5	9.7	tr	2.7	0.3	tr	0.5	2.5	0.3	2.7	3.7	tr	tr	tr	1.3	0.7	0.3
163	R 1021	2119 - 20	1.84	*	*	6.0	76.0	6.0	0.7	0.3	1.0	1.0	1.0	0.7	2.0	3.7	2.0	5.3	0.3	1.0	tr	tr	tr	0.0
164	R 1021	2121 - 22	2.68	*	*	7.5	65.2	11.6	10.7	0.7	4.0	0.3	tr	0.5	2.0	1.7	1.7	1.0	tr	tr	tr	0.3	0.3	tr
165	R 1021	2122 - 23	1.45	*	*	7.7	70.3	6.7	3.0	tr	0.3	tr	0.7	2.0	4.7	3.0	0.3	7.0	0.7	1.0	tr	0.3	tr	0.0
310	R 1021	2124 - 25	2.37	*	*	17.3	59.0	9.0	6.0	2.0	0.3	tr	0.0	10.3	4.7	3.7	0.3	1.3	0.7	tr	0.7	tr	1.3	0.7
166	R 1021	2130 - 31	2.59	*	*	19.0	58.7	7.7	2.0	6.0	tr	0.3	0.0	9.3	3.3	3.3	1.7	1.0	0.7	1.7	3.3	0.3	0.7	0.0
167	R 1021	2131 - 32	2.68	*	*	18.3	53.7	10.0	7.0	11.0	tr	0.3	0.0	6.0	1.0	2.7	1.0	0.3	tr	tr	2.7	0.3	3.7	0.3
168	R 1021	2134 - 35	2.83	*	*	14.3	54.7	13.7	4.3	5.3	0.7	0.7	0.0	6.7	1.0	4.0	2.3	1.0	tr	tr	4.7	0.3	0.3	0.3
169	R 1021	2137 - 38	2.57	*	*	13.7	53.0	13.0	5.0	4.7	tr	1.0	0.3	6.0	1.7	1.3	1.7	4.0	3.3	0.7	3.0	0.3	1.0	0.0
170	R 1021	2143 - 44	2.54	*	*	21.7	56.0	9.3	3.7	6.3	tr	tr	0.0	12.3	3.0	2.3	2.7	0.7	0.3	tr	1.7	tr	1.0	0.7
171	R 1021	2148 - 49	2.68	*	*	16.0	59.3	11.3	2.7	6.7	0.3	0.7	0.0	5.3	3.0	2.3	2.0	1.0	tr	tr	3.3	1.3	0.7	0.0
172	R 1021	2155 - 56	2.84	*	*	19.7	57.0	11.3	4.3	11.0	0.3	tr	0.0	6.3	2.0	2.3	1.7	0.7	tr	tr	1.0	0.7	1.0	0.3
173	R 1021	2157 - 58	2.84	*	*	20.7	56.0	9.0	5.7	9.0	tr	tr	0.0	7.3	4.3	1.3	2.7	tr	0.3	0.3	2.3	0.3	1.3	0.0
174	R 1021	2160 - 61	2.90	*	*	18.7	55.0	11.0	4.3	10.0	0.7	tr	0.0	6.3	1.7	2.7	2.3	0.7	tr	tr	3.7	0.7	1.0	0.0
175	R 1021	2164 - 65	2.69	*	*	23.7	54.3	7.3	6.3	11.0	0.3	0.3	0.0	11.0	1.0	2.0	0.7	1.3	0.3	tr	2.3	0.3	1.0	0.3
176	R 1021	2167 - 68	2.78	*	*	24.7	58.0	9.7	2.7	12.7	0.3	tr	0.0	8.0	3.7	3.3	1.0	0.3	tr	tr	tr	tr	0.3	0.0
177	R 1021	2172 - 73	2.90	*	*	14.3	55.3	5.3	7.3	8.3	0.3	0.3	0.0	5.3	tr	0.3	2.0	tr	7.3	6.3	0.3	0.7	0.7	0.0

ROCK CREEK FIELD, ROANE 1051 PETROLOGY DATA

SECT #	WELL #	DEPTH	GS PHI	CORE K	Core	TSpor +	Qtz	Qtite	Pag	Chl	Ill	Mix	Kaol	Ppor	Fpor	Feld	Chrt	SecQ	Ccem	Crep	Sidr	Mica	Opaq	Misc
					Por	coats																		
311	R 1051	1983.50	1.90	*	*	4.7	48.7	6.0	9.0	0.3	4.0	tr	0.0	0.3	tr	0.7	1.0	0.3	22.7	5.7	tr	0.7	0.7	0.0
178	R 1051	1984 - 85	1.41	*	*	4.0	70.0	7.3	0.3	0.0	tr	tr	0.3	2.3	1.3	1.0	0.7	4.3	10.3	2.0	tr	tr	tr	0.0
179	R 1051	1986 - 89	1.99	*	*	8.3	55.0	12.7	5.0	0.0	tr	tr	1.7	1.0	5.7	5.7	2.3	2.0	0.3	4.7	2.7	1.0	0.3	0.0
180	R 1051	1989 - 90	2.55	*	*	13.0	59.0	7.0	7.0	7.0	tr	1.0	0.0	tr	5.0	2.0	1.0	tr	tr	1.0	9.0	1.0	tr	0.0
181	R 1051	1991 - 92	2.72	*	*	19.0	57.3	7.0	5.3	8.7	tr	tr	0.0	9.7	0.7	2.0	1.0	tr	3.7	1.3	2.7	0.7	tr	0.0
182	R 1051	1992 - 93	2.70	*	*	13.3	56.0	15.0	6.3	9.0	tr	tr	0.0	3.7	0.7	2.7	1.3	tr	0.7	0.3	1.0	1.3	2.0	0.0
183	R 1051	1993 - 94	2.60	*	*	21.3	58.7	6.3	4.0	8.3	tr	tr	0.0	10.0	3.0	1.3	1.0	1.0	2.0	1.0	2.0	0.3	0.7	0.3
184	R 1051	1996 - 97	2.83	*	*	20.7	51.7	10.3	7.0	9.7	0.3	1.0	0.0	7.7	2.0	2.0	1.3	0.7	1.0	tr	2.3	1.7	1.3	0.0
185	R 1051	2000 - 01	2.74	*	*	18.7	55.7	11.7	4.3	8.7	tr	0.3	0.0	8.7	1.0	1.3	0.7	0.3	1.3	1.7	2.0	1.3	1.0	0.0
186	R 1051	2003 - 04	2.74	*	*	19.3	51.3	11.7	8.3	8.0	tr	0.3	0.0	8.0	3.0	2.0	1.3	tr	0.3	0.7	3.0	0.3	1.7	0.0
188	R 1051	2017 - 18	2.79	*	*	22.3	47.7	14.0	5.3	7.7	tr	1.0	0.0	10.3	3.3	3.7	1.0	tr	1.0	0.3	1.3	2.0	1.3	0.0
189	R 1051	2024 - 25	2.87	*	*	22.7	58.7	6.3	5.7	10.7	tr	0.3	0.0	7.7	4.0	2.3	1.3	tr	0.3	tr	0.7	1.7	0.3	0.0
190	R 1051	2026 - 27	2.87	*	*	23.7	51.3	10.0	5.7	10.0	0.7	0.3	0.0	10.3	2.3	1.3	2.3	tr	0.3	tr	2.0	2.0	1.3	0.0

ROCK CREEK FIELD, ROANE 1052 PETROLOGY DATA

SECT #	WELL #	DEPTH	GS PHI	CORE K	Core	TSpor +	Qtz	Qtite	Pag	Chl	Ill	Mix	Kaol	Ppor	Fpor	Feld	Chrt	SecQ	Ccem	Crep	Sidr	Mica	Opaq	Misc
					Por	coats																		
191	R 1052	1966 .5- 68	0.70	*	*	14.0	56.0	18.3	1.7	1.3	0.3	tr	8.7	1.0	2.7	3.0	1.7	tr	0.7	2.3	tr	1.7	0.3	0.3
192	R 1052	1968 - 70	2.42	*	*	4.7	67.3	12.0	1.3	0.3	tr	0.3	1.0	0.3	2.7	3.7	1.0	4.0	0.7	3.3	tr	2.0	tr	0.0
193	R 1052	1975 - 77	2.51	*	*	16.7	57.7	10.0	3.3	6.7	trtr	tr	0.0	8.0	2.0	3.3	2.0	tr	2.3	0.3	2.7	0.3	1.3	0.0
194	R 1052	1981 - 85	2.75	*	*	17.0	57.0	12.7	6.3	8.7	0.3	tr	0.0	7.0	1.0	2.0	1.7	tr	0.3	tr	1.3	1.7	tr	0.0
195	R 1052	2019 - 20	2.88	*	*	24.0	53.0	12.0	3.3	17.0	tr	0.3	0.0	3.0	3.7	1.3	2.7	tr	tr	0.3	0.7	2.0	0.7	0.0

ROCK CREEK FIELD, ROANE 2053 PETROLOGY DATA

SECT #	WELL #	DEPTH	GS PHI	CORE K	Core	TSpor +	Qtz	Qtite	Pag	Chl	Ill	Mix	Kaol	Ppor	Fpor	Feld	Chrt	SecQ	Ccem	Crep	Sidr	Mica	Opaq	Misc
					Por	coats																		
117	R 2053	2084.25	3.13	*	*	21.0	48.0	9.0	5.3	8.7	0.3	1.7	0.7	6.3	3.3	3.0	1.3	2.0	0.3	0.3	6.0	1.7	1.7	0.3
118	R 2053	2087.00	2.81	*	*	22.0	53.0	14.0	7.0	6.7	0.3	0.7	1.0	12.0	1.3	1.0	1.0	tr	tr	tr	1.3	tr	0.7	0.0
119	R 2053	2089.00	3.00	*	*	17.0	53.3	11.0	7.0	7.7	tr	0.7	0.0	8.0	0.7	1.7	1.3	tr	tr	tr	4.7	2.0	2.0	0.0
120	R 2053	2093.00	2.67	*	*	23.3	55.3	6.7	8.0	12.0	0.7	tr	0.0	8.3	2.3	2.3	2.0	1.0	tr	tr	0.3	0.3	0.7	0.0
121	R 2053	2094.00	2.87	*	*	4.0	37.7	9.3	1.0	1.0	tr	tr	0.0	2.7	0.3	2.7	1.7	tr	3.7	9.0	28.0	1.7	1.3	0.0
122	R 2053	2095.33	2.83	*	*	27.0	48.0	9.0	8.7	14.3	tr	0.3	0.0	9.7	2.7	3.3	1.7	0.7	tr	tr	0.3	0.7	0.7	0.0
123	R 2053	2095.50	2.83	*	*	20.0	54.3	9.3	9.7	9.7	0.3	0.7	0.0	7.3	2.0	1.3	3.7	tr	tr	tr	tr	0.3	1.3	0.0
124	R 2053	2097.00	2.55	*	*	27.3	50.7	7.0	9.0	13.3	0.3	1.0	0.0	9.0	3.7	2.3	0.7	0.3	0.3	tr	tr	1.0	1.3	0.0
125	R 2053	2098.00	2.72	*	*	20.7	56.0	10.0	5.7	8.7	tr	0.7	0.0	9.7	1.7	2.7	0.3	0.3	0.7	0.3	0.3	1.0	2.0	0.0
126	R 2053	2098.75	2.82	*	*	25.3	51.3	6.3	6.7	12.7	tr	tr	0.3	9.7	2.7	2.7	2.7	0.7	1.7	1.0	tr	0.3	1.3	0.0
127	R 2053	2103.00	2.89	*	*	16.0	39.7	5.7	4.7	8.3	tr	tr	0.0	7.7	tr	1.7	1.7	tr	23.0	4.7	2.7	tr	0.3	0.0
128	R 2053	2104.00	2.92	*	*	25.0	48.0	10.0	9.0	14.3	tr	tr	0.0	9.3	1.3	2.7	1.0	1.0	tr	0.7	tr	1.7	1.0	0.0
129	R 2053	2107.00	3.06	*	*	25.0	54.3	10.3	5.0	14.3	tr	tr	0.0	8.0	2.7	1.0	0.3	0.3	0.3	tr	0.3	2.0	1.0	0.0
130	R 2053	2108.00	2.92	*	*	25.7	51.7	11.3	5.7	13.7	tr	tr	0.0	8.7	3.3	2.0	1.3	0.3	tr	tr	tr	1.0	1.0	0.0
131	R 2053	2110.00	2.82	*	*	25.3	50.7	9.7	8.0	13.3	tr	1.0	0.0	9.0	2.0	1.7	0.7	0.7	tr	tr	1.3	1.7	0.3	0.0
132	R 2053	2112.50	2.76	*	*	26.0	44.7	9.7	8.7	13.0	tr	0.3	0.0	8.7	4.0	1.0	tr	1.7	1.0	1.0	3.0	1.3	2.0	0.0
133	R 2053	2114.00	2.98	*	*	21.3	49.3	9.7	10.3	9.7	tr	tr	0.0	8.7	3.0	1.7	1.3	0.3	0.7	tr	2.7	1.7	1.0	0.0
134	R 2053	2115.00	3.02	*	*	22.3	48.0	8.0	11.3	12.0	tr	0.3	0.0	7.3	2.7	2.3	1.3	0.3	0.7	tr	1.7	2.0	2.0	0.0
135	R 2053	2118.40	2.94	*	*	19.0	55.0	12.0	5.3	14.0	tr	0.3	0.0	4.0	0.7	1.0	1.3	tr	tr	tr	3.7	1.7	1.0	0.0
136	R 2053	2120.40	0.46	*	*	18.0	52.7	10.7	8.7	14.7	tr	tr	0.0	3.0	0.3	1.3	0.7	0.3	0.7	0.3	4.3	1.7	0.7	0.0
137	R 2053	2122.00	3.12	*	*	19.0	52.0	13.3	7.7	12.3	tr	0.7	0.0	6.0	tr	1.0	2.0	0.3	0.3	tr	2.0	1.3	1.0	0.0
138	R 2053	2123.75	3.08	*	*	6.3	58.0	8.7	18.0	6.0	tr	0.3	0.0	tr	tr	0.3	1.7	2.0	tr	tr	0.3	1.7	3.0	0.0
139	R 2053	2124.90	3.25	*	*	23.7	47.0	11.0	7.7	14.3	0.7	tr	0.0	7.0	1.7	0.3	1.0	0.3	0.3	tr	4.7	tr	4.0	0.0
140	R 2053	2126.67	3.13	*	*	0.3	46.3	6.0	8.0	0.3	tr	tr	0.0	tr	tr	0.0	1.7	tr	0.3	tr	34.3	1.0	1.0	1.0
141	R 2053	2127.00	3.12	*	*	18.0	48.0	9.7	10.3	11.0	tr	1.0	0.0	4.7	1.3	2.0	1.0	1.3	1.0	4.0	0.3	1.3	3.0	0.0
142	R 2053	2128.50	3.27	*	*	19.0	45.7	7.7	6.3	15.0	tr	tr	0.0	3.0	1.0	1.3	0.3	tr	1.7	1.7	12.3	tr	4.0	0.0
143	R 2053	2130.00	3.37	*	*	17.0	53.7	10.7	6.3	11.0	tr	tr	0.0	3.0	3.0	3.0	1.0	tr	2.0	2.0	0.7	0.7	2.7	0.3
144	R 2053	2131.50	3.31	*	*	24.3	55.0	11.0	3.0	7.0	tr	1.0	0.0	9.0	7.3	2.3	1.0	tr	tr	tr	0.7	2.0	0.7	0.0
145	R 2053	2134.50	3.37	*	*	8.0	50.0	19.0	13.0	7.0	tr	1.0	0.0	tr	tr	tr	1.0	tr	tr	tr	2.0	2.0	5.0	0.0

ROCK CREEK FIELD, ROANE 2054 PETROLOGY DATA

SECT #	WELL #	DEPTH	GS PHI	CORE K	Core	TSpor +	Qtz	Qtite	Psg	Chl	Ill	Mix	Kaol	Ppor	Fpor	Feld	Chrt	SecQ	Ccem	Crep	Sidr	Mica	Opaq	Misc
					Por	coats																		
402	R 2054	1882.80	2.76	9.70	23.50	2.3	35.0	6.3	2.3	1.0	tr	tr	0.0	0.7	0.7	2.7	1.0	tr	6.0	22.3	20.7	0.7	0.7	0.0
403	R 2054	1883.25	2.46	9.70	23.50	27.7	45.7	13.7	7.7	12.3	1.3	tr	0.0	10.0	4.0	2.0	0.7	1.0	0.3	0.3	tr	0.3	0.7	0.0
404	R 2054	1884.50	2.76	< 0.1	8.90	14.3	43.7	6.7	4.0	7.3	tr	tr	0.0	5.3	1.7	4.0	0.7	tr	6.3	5.7	12.7	0.3	1.7	0.0
405	R 2054	1887.00	2.77	5.10	20.30	27.3	47.0	11.3	7.0	15.7	tr	0.7	0.0	6.7	4.3	3.7	1.0	0.3	tr	0.7	tr	1.0	0.7	0.0

ROCK CREEK FIELD, ROANE 2055 PETROLOGY DATA

SECT #	WELL #	DEPTH	GS PHI	CORE K	Core	TSpor +	Qtz	Qtite	Psg	Chl	Ill	Mix	Kaol	Ppor	Fpor	Feld	Chrt	SecQ	Ccem	Crep	Sidr	Mica	Opaq	Misc
					Por	coats																		
409	R 2055	1964.25	2.71	0.47	14.10	0.3	35.7	12.3	3.0	0.3	tr	tr	0.0	tr	tr	2.3	0.7	tr	22.0	13.7	8.7	0.7	0.7	0.0
410	R 2055	1964.90	2.94	0.47	14.10	24.7	49.3	10.7	8.7	11.3	tr	tr	0.0	11.7	1.7	2.7	1.0	0.3	tr	tr	tr	0.7	2.0	0.0
411	R 2055	1966.50	2.87	11.00	18.40	0.7	35.3	10.3	2.7	0.0	tr	tr	0.0	0.3	0.3	3.0	1.0	tr	21.7	15.7	9.7	tr	tr	0.0

ROCK CREEK FIELD, ROANE 2056 PETROLOGY DATA

SECT #	WELL #	DEPTH	GS PHI	CORE K	Core	TSpor +	Qtz	Qtite	Psg	Chl	Ill	Mix	Kaol	Ppor	Fpor	Feld	Chrt	SecQ	Ccem	Crep	Sidr	Mica	Opaq	Misc
					Por	coats																		
347	R 2056	1914.83	2.69	47.00	21.70	27.3	48.3	11.0	6.0	12.3	tr	0.7	0.0	11.0	3.3	2.0	1.3	0.3	1.0	tr	1.3	0.3	1.0	0.0
348	R 2056	1917.92	2.82	40.00	23.10	28.3	48.7	8.7	5.3	9.3	1.3	tr	0.0	15.3	2.3	0.7	0.7	1.0	0.3	0.7	2.0	1.3	1.7	0.7
349	R 2056	1918.58	2.83	28.00	22.90	19.0	51.0	12.3	6.7	10.3	0.3	tr	0.0	7.3	1.0	1.3	2.0	0.3	tr	tr	4.0	2.3	1.0	0.0
350	R 2056	1923.08	2.66	23.00	22.10	24.0	52.3	8.0	7.3	13.0	tr	0.3	0.0	8.0	2.7	2.0	0.3	1.3	tr	tr	1.7	2.0	1.0	0.0
351	R 2056	1925.67	2.89	46.00	23.30	28.7	46.3	10.7	6.3	16.3	0.7	tr	0.0	8.0	3.7	2.7	1.3	0.3	0.3	tr	tr	2.0	1.3	0.0
352	R 2056	1928.75	2.69	62.00	23.20	27.7	52.3	6.0	4.7	13.0	tr	0.7	0.0	10.7	3.3	3.3	0.7	1.7	tr	0.3	0.7	1.3	1.3	0.0
353	R 2056	1934.75	2.85	8.20	20.60	22.0	51.3	10.7	6.7	10.0	1.0	tr	0.0	8.7	2.3	2.7	1.0	tr	tr	tr	1.0	3.7	0.7	0.3
354	R 2056	1942.58	3.06	4.60	20.20	21.0	53.7	8.0	9.7	10.0	0.7	tr	0.0	7.7	2.7	1.0	0.7	1.0	tr	tr	1.0	2.0	2.0	0.0
355	R 2056	1947.58	2.92	2.60	5.70	21.7	41.7	14.7	5.3	13.7	0.7	tr	0.0	6.0	1.3	0.7	2.0	1.3	7.0	2.3	2.3	0.7	0.3	0.0
356	R 2056	1951.42	3.15	< 0.1	14.20	14.7	31.0	11.0	5.0	9.0	tr	tr	0.0	4.0	1.7	2.0	0.3	0.3	5.7	4.0	23.3	2.0	0.7	0.0
357	R 2056	1952.92	3.04	0.66	17.60	18.3	54.3	14.0	7.7	12.7	1.0	0.3	0.0	2.7	1.7	1.3	1.7	0.3	tr	tr	0.3	0.7	1.0	0.3
358	R 2056	1958.92	3.00	< 0.1	16.40	21.0	53.3	11.3	7.3	15.7	1.3	tr	0.0	2.7	1.3	2.7	1.3	0.7	tr	0.7	tr	1.0	0.7	0.0

ROCK CREEK FIELD, ROANE 2057 PETROLOGY DATA

SECT #	WELL #	DEPTH	GS PHI	CORE K	Core Por	TSpor + coats	Qtz	Qtite	Psg	Chl	Ill	Mix	Kaol	Ppor	Fpor	Feld	Chrt	SecQ	Ccem	Crep	Sidr	Mica	Opaq	Misc
331	R 2057	1967.00	2.76	23.00	16.80	23.0	49.7	6.3	6.7	7.0	0.3	0.7	0.0	12.7	2.3	2.0	1.7	3.0	2.7	tr	2.7	0.3	2.0	0.0
332	R 2057	1969.16	2.86	14.00	20.40	15.3	51.3	9.3	11.0	5.0	2.7	tr	0.3	6.0	1.3	1.3	2.0	2.0	tr	tr	2.3	2.3	2.7	0.3
333	R 2057	1971.25	2.90	31.00	23.70	26.0	57.0	6.7	4.3	13.0	tr	tr	0.0	11.0	2.0	2.7	1.0	tr	tr	tr	tr	1.3	1.0	0.0
334	R 2057	1975.00	2.62	25.00	23.70	27.0	52.7	6.0	8.0	11.3	0.7	0.3	0.0	13.7	1.0	1.7	1.0	0.7	0.3	tr	0.3	1.0	1.3	0.0
335	R 2057	1976.08	2.58	25.00	24.00	22.7	48.0	10.7	9.0	10.7	0.3	tr	0.0	8.7	3.0	3.7	0.7	1.0	0.7	1.3	0.7	1.3	0.3	0.0
336	R 2057	1980.75	2.85	26.00	24.60	25.0	49.7	11.3	8.0	12.3	0.7	tr	0.0	9.7	2.3	2.7	0.7	0.7	0.7	tr	tr	0.7	0.7	0.0
337a	R 2057	1983.83	3.18	21.00	22.60	16.0	50.0	17.0	3.0	11.0	1.0	tr	0.0	2.0	2.0	1.0	tr	tr	tr	tr	9.0	3.0	1.0	0.0
337b	R2057	1983.83	2.95			0.3	34.3	2.7	0.3	0.3	tr	tr	0.0	tr	tr	0.7	1.7	tr	25.7	13.3	19.3	0.7	tr	tr
406	R 2057	1984.50	3.02	0.05	4.10	12.7	42.7	9.7	4.0	9.3	tr	tr	0.0	1.7	1.7	3.0	1.0	tr	tr	2.3	24.0	tr	0.7	0.0
407	R 2057	1990.50	2.93	15.00	20.20	18.3	40.4	9.3	8.0	7.3	tr	tr	0.0	11.0	1.0	2.0	0.7	0.3	2.0	3.0	14.0	0.7	0.3	tr
338	R 2057	1990.58	2.97	15.00	20.20	21.7	55.7	11.0	7.0	10.3	2.0	1.0	0.0	7.0	1.3	0.3	2.7	tr	0.7	tr	tr	tr	1.0	0.0
408	R 2057	1991.60	2.97	30.00	23.20	22.0	47.3	13.0	9.0	13.7	0.7	tr	0.0	7.0	0.7	3.0	1.7	tr	0.3	1.7	tr	0.7	1.3	0.0
339	R 2057	1992.33	2.99	30.00	23.20	26.3	50.7	11.3	6.0	12.3	1.0	tr	0.0	10.3	2.7	1.3	1.7	0.7	tr	tr	tr	1.7	0.3	0.0
340	R 2057	1995.75	3.06	22.00	22.60	23.7	49.7	9.0	9.3	9.3	0.3	tr	0.0	11.0	3.0	2.0	0.7	0.7	1.0	tr	1.0	1.7	1.3	0.0
341	R 2057	2000.08	2.48	23.00	20.60	21.7	50.3	9.7	7.3	9.3	0.3	tr	0.0	10.3	1.7	2.0	0.7	0.7	0.3	0.7	4.3	0.3	1.7	0.3
342	R 2057	2003.17	3.04	4.20	20.40	23.3	52.3	8.3	9.3	14.3	0.7	tr	0.0	6.3	2.0	1.3	1.0	0.3	tr	tr	tr	2.0	1.7	0.3
343[1]	R2057	2004.00																						
344	R 2057	2004.58	2.98	6.80	21.00	26.0	43.7	14.3	8.7	13.3	tr	1.0	0.0	8.7	3.0	2.0	1.3	0.7	tr	0.3	tr	0.7	2.3	0.0
345a	R 2057	2006.17	2.95	1.90	13.30	22.0	52.0	14.0	6.0	11.7	tr	0.3	0.0	9.0	1.0	1.0	1.0	tr	tr	tr	tr	3.0	0.7	0.3
345b	R2057	2006.17	3.05			tr	34.5	8.5	3.0	tr	tr	tr	0.0	tr	tr	tr	3.0	tr	3.5	2.5	45.0	1.0	0.5	tr
346	R 2057	2009.50	3.12	< 0.1	13.80	7.0	60.7	9.7	7.0	4.3	1.3	tr	0.0	1.0	0.3	1.0	1.7	tr	6.0	2.0	4.0	0.7	0.3	0.0

[1] Calcareous Shale
[a] Part of thin section outside of carbonate-rich portion
[b] Within carbonate-rich portion.

ROCK CREEK FIELD, ROANE 2067 PETROLOGY DATA

SECT #	WELL #	DEPTH	GS PHI	CORE K	Core	TSpor +	Qtz	Qtite	Pag	Chl	Ill	Mix	Kaol	Ppor	Fpor	Feld	Chrt	SecQ	Ccem	Crep	Sidr	Mica	Opaq	Misc
					Por	coats																		
196	R 2067	1930.00	3.12	*	*	1.7	49.7	10.3	4.3	1.7	tr	tr	0.0	tr	tr	1.3	0.7	tr	24.7	5.7	tr	1.3	tr	0.3
312	R 2067	1930.40	2.93	*	*	22.3	47.7	13.0	6.7	13.7	1.0	1.0	0.0	4.7	2.0	4.7	1.0	0.3	tr	0.3	0.3	3.0	0.7	0.0
313	R 2067	1931.00	2.92	*	*	23.3	54.3	6.3	6.3	11.7	0.3	0.7	0.0	5.0	5.7	4.0	tr	tr	0.7	2.3	1.0	1.3	0.3	0.0
197	R 2067	1931.50	2.63	*	*	17.7	52.3	13.3	7.7	10.0	tr	tr	0.0	4.0	3.7	4.0	0.3	0.7	tr	1.7	0.3	0.7	1.0	0.3
198	R 2067	1934.00	2.50	*	*	21.3	51.0	11.3	6.0	7.0	tr	tr	0.0	12.3	2.0	2.3	2.0	0.7	tr	1.3	2.3	0.7	0.7	0.3
199	R 2067	1935.00	3.06	*	*	22.7	50.7	11.0	7.3	7.0	0.3	1.0	0.0	9.7	4.7	2.7	0.7	0.3	tr	0.3	1.0	2.7	0.7	0.0
201	R 2067	1937.25	2.11	*	*	21.7	56.7	7.7	5.0	8.7	tr	0.3	0.0	10.3	2.3	2.0	3.0	0.3	tr	0.7	tr	0.7	2.0	0.3
200	R 2067	1937.50	2.71	*	*	20.7	54.3	10.3	9.0	8.7	0.3	2.0	0.0	8.7	1.0	1.0	tr	tr	0.3	1.3	tr	1.7	1.3	0.0
202	R 2067	1938.00	2.81	*	*	9.0	39.7	13.3	3.0	5.3	tr	tr	0.0	3.0	0.7	1.0	2.0	tr	10.3	3.3	16.3	0.7	1.3	0.0
203	R 2067	1939.50	2.63	*	*	20.0	45.7	7.7	4.7	8.3	tr	tr	0.0	10.7	1.0	1.3	1.7	tr	10.7	4.3	2.7	0.7	0.7	0.0
204	R 2067	1943.00	2.76	*	*	22.7	55.3	10.0	6.7	11.0	tr	tr	0.0	9.7	2.0	0.7	0.7	tr	0.7	0.3	tr	1.3	1.7	0.0
205	R 2067	1944.00	2.72	*	*	27.7	48.0	16.0	4.7	13.0	tr	0.3	0.0	11.0	3.3	1.3	0.3	0.3	tr	0.3	0.3	tr	1.0	0.0
206	R 2067	1948.00	2.78	*	*	24.7	49.3	12.0	7.0	12.3	tr	0.3	0.0	9.0	3.0	2.7	0.3	tr	tr	0.7	1.3	1.3	0.7	0.0
207	R 2067	1950.00	2.85	*	*	23.7	49.7	10.7	7.0	10.0	tr	0.3	0.0	9.0	4.3	2.3	2.0	tr	tr	tr	1.0	3.0	0.7	0.0
208	R 2067	1954.00	2.73	*	*	21.3	50.0	12.7	8.3	8.7	tr	0.3	0.0	9.0	3.3	3.0	1.7	0.7	tr	tr	1.7	tr	0.3	0.3
209	R 2067	1959.00	2.72	*	*	18.7	51.0	13.3	6.3	10.3	0.3	0.7	0.0	5.7	1.7	1.3	3.0	0.7	0.3	0.3	3.3	1.3	0.3	0.0
210	R 2067	1961.00	2.70	*	*	18.7	54.0	14.0	6.0	10.7	tr	0.7	0.0	5.7	1.7	2.3	2.0	tr	tr	0.3	1.0	1.3	0.3	0.0
211	R 2067	1974.00	3.05	*	*	18.0	54.0	11.0	5.0	11.0	tr	tr	0.0	7.0	tr	tr	tr	tr	2.0	tr	9.0	tr	1.0	0.0

APPENDIX I
2D GIS

A geographic information system (GIS) is a computer-assisted system that acquires, stores, processes and displays spatial data. GIS extends the capabilities of a traditional database query by performing analyses based on geographic position. To accelerate the analysis and presentation of 2D spatial data for Granny Creek oil field, a primarily raster-based GIS was used.

Raster Versus Vector GIS

In GIS there are two fundamental representation techniques for storing geographical data: raster and vector. Raster data are encoded as a regular array of cells while vector data entities (points, lines, and polygons) are defined by employing relational database tables (Figure I1). Since both raster and vector systems have their special strengths, GIS systems commonly incorporate elements from both representational techniques. Most GIS systems, however, usually specialize in either raster or vector methods.

For this project, a primarily raster-based GIS software, IDRISI, was chosen because of its quick and easy map overlay and spatial analysis functions. In addition to raster systems having substantially more analytical power than their vector counterparts, raster-based methods are ideally suited to geological and engineering data that continuously change over space. Because most of the Granny Creek spatial data like structure and production maps consist of continuously gridded values, a raster GIS was chosen.

A disadvantage of using a raster GIS instead of a vector GIS is cruder maps. For instance, a line in a raster data format would be represented by tiny grid cells (pixels) whereas as in a vector GIS the same object would be portrayed to its true dimensions (Figure I2). As the object is enlarged, the grid cells become larger. If the enlargement is great enough, the object may become distorted or jagged-looking in appearance. Another disadvantage is the precision loss that occurs if continuous vector data is quantized into gridded cells. Because gridded cells are used to represent vector data, the precise depiction of points, lines, and polygons does not occur. Figure I2 illustrates the precision loss from converting vector data to raster cells. In this example, a fifteen meter wide communication path (line) is converted to a raster image that has a cell resolution of 60 by 60 meters. Although the conversion procedure erroneously increases the path width, the general outline of the path is still clearly discernable (Figure I2).

Raster Images

IDRISI uses a simple raster structure to represent spatial data. In a raster structure a rectangular grid is divided by rows and columns to create a two-dimensional array of cells. The 0,0 cell (row 0, column 0) of simple raster structures is located in the top left-hand corner (Figure I2). Each grid cell is indexed by a row and column number and contains an attribute for that map location. Thickness, initial open flow, and permeability values are examples of attributes stored as numbers in grid cells. When the raster format with numeric attribute codes is applied to some rectangular portion of space, it is commonly called an image. Images, which form maps from a series of dots or pixels, are often called bitmaps or raster-graphics files.

Sixteen raster images (Table I1) provided the foundation for the spatial analysis of Granny Creek. These images or data layers were derived from structure, stratigraphic, engineering, and production data. Twelve of these images are shown in Figure I3. Each image represents spatial variations of a single phenomenon (e.g., cumulative oil production, mean porosity, thickness). In contrast, conventional maps, such as topographic quadrangles, represent many types of information on a single map: roads, streams, relief, etc.

For the Granny Creek study, new images were created whenever the original images were processed by GIS operations like the reclassify and overlay functions. For example, original data values of the cumulative production image were reclassified into a new image showing oil producing areas either greater or less than 25,000 barrels. During the spatial processing and analysis of Granny Creek, over 100 images (equivalent to 100 different maps) were generated from the initial sixteen images.

Most of the sixteen images listed in Table I1 originated from grids of scattered well data. A grid interval of 60 by 60 meters was established by dividing the rectangular viewing area (north-south orientation) of the map into 160 rows and 100 columns. Consequently, every grid was composed of 1600 different cells; each cell was georeferenced by a unique row and column number.

Grids were first created by the contouring package Surface III and subsequently transferred to IDRISI. Thus, the same grid utilized to display a contour map in Surface III was also employed to portray an IDRISI raster image. For instance, the grid of the pre-Greenbrier Unconformity could be used to display the structure contour lines in Surface III or a raster image in IDRISI. Both the contour map and raster image of the unconformity are equivalent; they only differ in how the grid is represented.

Some images, however, resulted from vector-to-raster conversion. The bottom row of Figure I3 shows four vector files converted to raster images. Each mouth bar image, for example, was first digitized into a vector polygon and then converted to a raster image. Likewise, the stratigraphic density breaks within the C zone were converted from vector points to rasterized cells.

Vector Files

Although most of the Granny Creek data had to be converted to raster form for geographical and spatial analysis, vector files were necessary too. Vector files (Figure I4) were important because they could be overlaid onto raster images to georeference landmarks or to analyze raster and vector data together. Vector files were created three ways: (1) map digitizing, (2) computer screen digitizing, and (3) raster-to-vector conversion. Some examples of vector files for Granny Creek are the field boundary (polygon), seismic lines (lines), well locations (points), etc. Table I2 is a listing of vector files for Granny Creek.

Spatial Query

After all the raster images or data layers (cumulative oil production, mean porosity, isolith, etc.) are constructed, the user can query spatial data from any data layer combination. Extracted information is then displayed as a single map.

In a spatial query two fundamental GIS operations, the **RECLASS** and **OVERLAY** functions, are executed. Figure I5 shows how a final image is created to satisfy the following conditions:

(1) oil production > 30 b/day, (2) seal present, (3) reservoir thickness > 20 ft., and (4) mean porosity > 14 percent. First, each image that represents a geological/engineering parameter is RECLASSified into a new image or data layer. For instance, initial oil production is RECLASSified into a binary grid (0/1 values) so that a grid cell contains either a 1 (true) if oil production is greater than 30 b/day or 0 (false) if it is not. Using the OVERLAY operation, the four data layers then are combined to form a final image that satisfies all the above conditions.

To assist in analyzing the newly derived data, a series of traditional statistical procedures and specialized routines for the statistical description of spatial data exists as well. Table I3 describes some geographical and statistical analysis operations used for the investigation of reservoir heterogeneities within the Big Injun.

IDRISI Video Images

Although many images of Granny Creek are illustrated in this paper, it is recommended that the reader also utilize the interface software (Figure I6) created by the author to access the display modules of IDRISI. By accessing the display modules one can view on a VGA monitor most of the raster images and vector files created for Granny Creek. All the video images are in color, not black and white. Besides viewing images, the interface software allows one to execute the useful interactive commands (query by X/Y position, zoom in or out of image, etc.) of the COLOR function. The customized interface was created so that anyone can view the images and do their own spatial analysis without having any experience using GIS software.

Granny Creek Spatial Analysis

Various spatial analysis and statistical methods were applied to better understand heterogeneity within the Big Injun sandstone. Most of the Granny Creek spatial data examined by the author using GIS can be grouped into one of the following categories: primary oil production; optimal oil production; variables affecting oil production; pre-Greenbrier unconformity analyses; and Granny Creek regional analyses. Table I4 is an overview of twenty specific topics investigated using GIS. Each topic (Table I4) and its contribution to the study of Granny Creek oil field will be discussed in the remainder of this chapter.

1. Image Enhancement of Primary Production

   a. *Purpose*: Visually enhance images to identify oil production trends.

   b. *Operation*: Stretch

   c. *Discussion*: A contrast stretch utility is used to visually enhance both the initial open flow (IOF) and ten year cumulative oil production (COP) images (Figure I7). A linear stretch is applied to force high values for each production image to a lower maximum value. The new image is then rescaled, allowing for enhanced visualization of the best and worst production areas. Solid black areas of the enhanced image represent the highest oil producing regions.

d. *Analysis*: The best primary production occurs in the northern half of the field. Higher production also appears to follow a north-south trend.

2. Reclassification of Oil Production

a. *Purpose*: To analyze the spatial distribution of oil production.

b. *Operation*: Reclass

c. *Discussion*: Initial open flow (IOF) and the 10-year cumulative oil production (COP) are reclassified into new images (Figure I8) to illustrate the spatial distribution of oil production. Solid black areas portray oil production that satisfy the specified conditions.

d. *Analysis*: Generally, the highest level of production for both IOF & COP occurs in the interior and in the northern half of the field.

3. Spatial Query of Best Oil Production

a. *Purpose*: Combine initial open flow and 10-year cumulative oil production to locate best oil producing areas.

b. *Operations*: Reclass, Overlay (multiply), Group, Area, Vector Overlay

c. *Discussion*: Cutoff values of 25 b/day and 25,000 barrels are chosen by analyzing the histogram of each image. The initial open flow and cumulative oil production images are then reclassified to greater than 25 b/day and 25,000 barrels, respectively. Next, using map algebra, both images are multiplied together, creating a new image that represents the best oil producing regions (solid black areas of Figure I9a). Areas of best production are then classified into contiguous groups and the acreage subsequently calculated for each group. This image is reclassified again to show areas of best production greater than ten acres (Figure I9b). The last step is to overlay field boundaries, petrographic well locations, and basement faults.

d. *Analysis*: Thirteen areas were identified that met the following conditions: initial open flow > 25 b/day and cumulative oil production > 25,000 barrels. Seven of the thirteen best oil producing areas are greater than ten acres, ranging from eleven to twenty-nine acres. The largest area of production (29 acres) is approximately in the center of the field (UTM coordinates 486460, 4265040 meters). Although seismic Line 2 and the stratigraphic profile P1-P1' are not shown on the figures below, they also cross the 29-acre area.

Thirteen wells that had petrographic studies are overlaid onto the greatest oil producing areas to determine if any of these wells are located where best production is found (Figure I9a). Unfortunately, only one cored well with petrographic analysis - Roane 2410 located in the northern part of the field - is in one of the highest oil producing areas.

A second example examines whether a relationship exits between a basement fault and best production (Figure I9B). Basement Fault "A" is also overlaid onto best production to figure out if it divides Granny Creek oil field into a higher producing northern half and a lower producing southern half. However, the fault is located in the middle of the highest producing areas (Figure I9b), and thus it does not segregate the field into good and poor producing areas.

Instead, the Columbia-Pennzoil company boundary seems to be a more accurate dividing line between the best and worst oil producing areas. It is unknown whether this is a coincidence or manifestation of two oil companies reporting production data differently.

4. Comparison of Northern and Southern Granny Creek field

a. *Purpose*: To compare the northern and southern regions of Granny Creek.

b. *Operation*: Extract

c. *Discussion*: Granny Creek field is divided by the company line into two regions, the northern (Pennzoil) and southern (Columbia) areas (Figure I10). Before computing summary statistics to compare both regions, the Granny Creek field boundary first is redefined so that no extrapolated values at the field's margins are incorporated into any calculations. This is necessary to prevent errors resulting from edge effects. The newly defined field boundary is then partitioned into a northern (1379 acres) and southern half (1159 acres).

d. *Analysis*: Of the seven properties analyzed (Table I5) to compare the northern and southern regions of Granny Creek field, average permeability, initial open flow, 10-year cumulative, and best production have higher mean values in northern Granny Creek field. The C zone thickness and average porosity are the same for the entire field. The parameter total thickness of the Big Injun sandstone is greater in the southern part of the field because the fluvial channel or AB zone is the thickest there. Thus the total mean thicknesses of the Big Injun sandstone are different for both regions. The comparative analysis also showed that 96% of the best oil production occurs in the northern half.

5. Crosstabulation of Two Oil Production Images

a. *Purpose*: To compare initial open flow (IOF) and cumulative oil production (COP).

b. *Operations*: Crosstabulation, Reclass, Overlay (cover)

c. *Discussion*: Crosstabulation compares the qualitative data of initial open flow and cumulative production. Table I6 is a crosstabulation table that lists the frequency (in acres) for each possible category combination of each image. In addition to the crosstabulation table, a cross-classification image is created from the IOF and COP images to show all possible combinations of the IOF & COP categories. All categories of the cross-classification image are then reclassified into a new image shown in Figure I11.

d. *Analysis*: Crosstabulating the two production images reveals that 66% of Granny Creek field has initial open flow and cumulative oil production less than 20 b/day and 20,000 barrels, respectively. (These percentages, however, are probably slightly inflated due to grid extrapolation at the field margins.) Also, according to the table, the largest acreage (937 acres) occurs when IOF is between 1-10 b/day and COP is between 500-10000 barrels.

6. Linear Regression between IOF & COP Images

a. *Purpose*: To determine similarity between initial open flow (IOF) and 10-year cumulative oil production (COP).

b. *Operation*: Regression

c. *Discussion*: Regression compares the quantitative data of initial open flow and cumulative oil production to determine if they are similar. To prevent an erroneous regression analysis, it is necessary to create a binary mask that defines the field boundaries of Granny Creek.

d. *Analysis*: Results of the linear regression (Figure I12) show a positive sloping trend line and a correlation coefficient (R) of 0.59. This suggests that initial open flow and cumulative production do not correlate very well between each other.

7. Spatial Query of Six Geologic/Engineering Variables

a. *Purpose*: To locate optimal oil producing areas in Granny Creek field and to determine how each geologic/engineering variable affects oil production.

b. *Operations*: Reclass, Histogram, Distance, Overlay (multiply, add)

c. *Discussion*: Three steps (Figure I13) are executed to determine which geologic/engineering variables affect primary production. First, histograms are produced for each of the six geologic/engineering parameters to determine their spatial distribution. Every histogram is then examined to help decide the reclassification scheme for each parameter or data layer. For example, Step 1 of Figure I13 shows histograms for the mean porosity and reservoir thickness parameters. Cutoff values are calculated by dropping the lower one-third range of values or by estimating favorable reservoir conditions for that particular parameter. After studying the porosity and reservoir thickness data, cutoff values of 12% for porosity and 20 feet for reservoir thickness are selected. The remaining parameters are evaluated the same way to identify reclassification criteria for each layer.

The second step (Step 2) is to reclassify the six different map layers or images. Every image is reclassified according to its cutoff value into a new binary image (true/false image) so that grid cells with values of 1 represent favorable reservoir conditions whereas cells with 0 values unfavorable. For instance, after the porosity image is reclassified, areas that satisfy the condition "> 12% porosity" contain 1 (true) values while regions that meet the reverse condition "< 12% porosity" contain 0 values (false).

The last step (Step 3) is to overlay or combine all six reclassified images. Using map algebra, all six reclassified images or data layers are multiplied together (same as a logical AND) to create a final image, *Optimal Production*. This image (Figure I14) summarizes the results of the spatial query, or where the best oil producing areas within the reservoir should be located, assuming that all the variables that control production have been identified. To determine how well the best primary production compares to optimal production, *Best Production* is added to *Optimal Production* (Figure I15).

d. *Analysis*: The final image, *Optimal Production*, depicts the results of the spatial query, or where the greatest amount of oil within the reservoir should be located. Figure I14 shows that ideal production should be located in the middle part of the field.

To compare *Best Production* to *Optimal Production* (Figure I15), both images are added together, resulting in the image shown in Figure I15c. Spatial statistics computed for this image reveal that there is a 60% match where best production covers optimal production. Accounting for the 40% that does not match, however, requires a more detailed investigation. One factor precluding a 100% relationship between best production and optimal production could be that some variables are not as important as others in affecting production. Therefore, to better understand the relationship between optimal production and best production, an evaluation of each geologic/engineering variable and how it compares to high oil producing areas is required.

Figures I16a-d shows that the first four reclassified images - *Seal*, *Reservoir Thickness*, *Porosity*, and *Water Saturation* - are all located in areas where best production occurs. On the other hand, the reclassified images of *Permeability* and *No Barriers* (Figure I16e-f) reveal a lesser match with best production. A poor correlation could exist because these two parameters are not as important as the other variables in affecting production, or because of the inaccuracy of the permeability and barrier variables. The latter is discussed in more detail below.

The permeability image (Figure I3), for example, was created from averaged permeability values at each well location, and, consequently, may not absolutely reflect true subsurface conditions. Besides averaged permeability values, the original permeability was computed from initial open flow, a data source that may be untrustworthy.

As for the density breaks, these diagenetic zones are identified within the C zone at certain well locations. Figure I17a is a map showing the locations of 71 density breaks. A quadrat analysis is performed to describe the pattern of wells with density breaks. Results of the quadrat analysis suggest the density breaks follow a clustered pattern. The mean center of the density break locations falls in column 42, row 69 (UTM 486561, 4265419) of the 100 column, 160 row grid.

To estimate the extent of the diagenetic zones, the computer calculates a 100 meter buffer around each 60 by 60 meter grid cell containing a density break well. Expanding each density break well location to cover a larger area requires several steps. The first step is to convert well locations that are vector points to raster cells (Figure I17b). However, remember that converting vector points to 60 meter resolution grid cells results in a loss of precision.

The next step is to compute the distance of each cell to the nearest density break. Euclidean distances are calculated between each cell and the nearest density break cell using the DISTANCE operation. This operation creates a new grid or image whose cell attributes contain the measured distances to the nearest density break well (Figure I17c). Therefore, a value of 0 meters signifies the location of a well with a density break in that cell. Because of the 60 meter grid resolution, grid cells orthogonal to a density break cell are divisible by 60 meters. Therefore, a cell next to a density break cell represents a distance of 60 meters; a cell two grid cells away is a distance of 120 meters.

The last step is to RECLASSify all distance values less than or greater than 100 meters into a binary image. After RECLASSifying the image, grid cells with values of 1 represent the newly defined density break zones, whereas grid cells with values of 0 indicate areas where no density breaks occur. (Figure I17d). By creating a 100 meter buffer around each well, the original density break cell is expanded to a 3 by 3 grid cell square. Likewise, the area covered by each density break also increases from 60 to 180 square meters (8 acres).

In summary, because the boundary limits may vary for each density break, a 8-acre area may not accurately define the extent of some density breaks and thus result in error. Incorrect dimensions of each density break can lead to a wrong correlation value between best production and the expanded density zones.

8. Crosstabulation of Primary Production & Unconformity Surface

a. *Purpose*: To compare primary production with unconformity surface.

b. *Operation*: Crosstabulation

c. *Discussion*: Primary production is crosstabulated with the elevations of the unconformity surface to decide if a relationship exists.

d. *Analysis*: The best primary production (Table I7) occurs in the middle of the field or at approximately -875 feet. In Table I7 both initial open flow and cumulative production show a similar pattern of increasing oil production as up dip and down dip elevations converge towards the interior part of the field. Figure I8 shows this same phenomenon spatially. The higher producing interior regions of Granny Creek may be attributed to stratigraphy, structure, or a combination of both.

9. Dip Angles and Directions of Unconformity

a. *Purpose*: Determine dips angles and dip directions of pre-Greenbrier Unconformity.

b. *Operations*: Slope, Aspect

c. *Discussion*: The slope and aspect of each grid cell also can be thought of as the dip angle and dip direction of the unconformity surface. Dips of the unconformity surface are determined by calculating the maximum slope around each cell from the local slopes in X and Y. The aspect, or direction the maximum slope is facing, is then computed. Figure I18 shows graph plots derived from the dip angle and dip direction images.

d. *Analysis*: Dips calculated for each grid cell range from 0 to 6 degrees, of which 96% of all slopes are 2 degrees or less. Therefore, the dips of the unconformity surface are very gentle. The highest dips are found in the southern part of the field where production is poor.

As for which way the unconformity surface is dipping, the computer calculated that the highest number of slopes dip in a 40 to 140 degree direction. A 91 degree dip direction had the highest probability. Although it appears that the beds dip gently to the east, there also appear to be small undulations along the unconformity that cause the beds to dip in other directions. Perhaps, since the dip is very gently, it takes only take small irregularities in the surface to change the dip directions. However, it should be noted that if any well elevations are incorrect, then erroneous dip directions will result.

10. Trend Surface of Unconformity

a. *Purpose*: To create a trend surface of the unconformity surface.

b. *Operation*: Trend

c. *Discussion*: Trend surface analysis is used to reveal if any significant spatial trend can be computed from the elevation data.

d. *Analysis*: Figure I19 shows the linear, quadratic, and cubic trend surfaces calculated for the unconformity surface. All three trend surfaces reveal a strong regional dip to the east. Table I8 summarizes the trend surface statistics for all three trends. Each correlation coefficient (R) is higher than 0.7, suggesting the original elevation values conform closely to the trend surfaces (Davis, 1986). The table also shows that the goodness of fit values for the first, second and third-degree surfaces are 85%, 91%, and 93%, respectively. To test whether the goodness of fit for all three trends is significantly greater than zero, the F ratio and associated degrees of freedom are evaluated. In all cases the F ratio exceeds the critical F-value, thereby rejecting the hypothesis that the variance about the regression line is no different than the variance in the observations. Finally, the significance of the improvement in the goodness of fit derived from moving to a higher order polynomial is tested. Results of the statistical test show that the quadratic trend surface significantly improves the fit over the linear trend.

11. Trend Surface Residuals

a. *Purpose*: To create local relief residual maps of the unconformity surface.

b. *Operations*: Overlay (subtract, add)

c. *Discussion*: Another use of trend surface analysis is "to interpret residuals from a trend to delineate local structures that otherwise would be concealed by a strong regional dip" (Davis, 1992). A second-degree trend surface is chosen to "filter out" the regional eastern dip of the unconformity surface (Figure I20). This trend surface provides a very good approximation of the surface, with almost 97% of the elevation variances accounted. The remaining 3%, however, represent elevation lows or highs of the regional trend.

d. *Analysis*: Figure I20 shows a second-degree residual map calculated by subtracting the trend surface from the unconformity map. Positive residuals define areas locally higher then the trend surface while negative residuals are locally lower. If areas of best oil production are overlaid onto the trend residuals, then local elevations higher than the regional trend of the unconformity surface correlate 67% with the best oil producing areas. Therefore, the local highs in elevation do probably affect production.

12. Local High-Pass 3 by 3 Filter of Unconformity Surface

a. *Purpose*: To locate elevation changes of unconformity surface.

b. *Operation*: Filter

c. *Discussion*: In raster graphics, a filter is a mathematically defined operation for removing long-range (high-pass) or short range (low-pass) spatial variations. A high-pass filter emphasizes areas where there is change, whereas a low-pass filter smooths out "noisy data" that vary from

the local trend. For Granny Creek field, a local high-pass filter was used to extract areas of elevation change along a surface versus those of gradual change. When applied to the unconformity surface, the high-pass filter operation modifies the original elevation value of every grid cell so that the new value reflects the degree of change in local relief. The new values do not represent actual elevations, but measure the abruptness of change between target cells and their cell neighbors.

Both trend surface and local high-pass filters can be utilized to detect changes in local relief. Though both procedures are employed to delineate the same phenomenon, their results require different interpretations. Figure I21a illustrates the distinction between trend surface and local high-pass filter. Positive trend surface residuals reflect areas of relief above the regional trend surface, whereas positive local filter values characterize an abrupt change from lower to higher elevations.

Since the Granny Creek grid is 100 columns by 160 rows, each grid cell represents 60 meters (200 feet). So, a 3 by 3 grid cell filter encompasses a 180 square meter area or 8 acres. Figure I21b shows a 3 by 3 filter used to assign each cell a new value based on the center cell's original value and its eight nearest numbers. This example (Figure I21b) shows how the boldfaced center cell (-891 ft) and the elevations of its eight neighbors (which are 60 meters from the target cell) are multiplied by the 3 by 3 filter and then summed together; the new center cell value is ten feet.

For Granny Creek field, a positive value such as ten feet indicates an abrupt increase in elevation, while a negative value of the same magnitude signifies a sharp decrease in elevation. This procedure is repeated for each grid cell, beginning at the first row, then progressing from left to right along each row.

d. *Analysis*: Figure I22 shows a map of values generated from using a local high-pass filter. Most of the values range between -2 and 2 feet, indicating that a majority (over 90%) of the unconformity surface has a gradual slope. A scattered, random pattern of extreme negative and positive values, however, does dot the central part of the image, suggesting that numerous, small undulations also occur along the unconformity surface. This is especially evident where large negative and positive value cells are juxtaposed together. These "small hills and valleys" along the unconformity surface may have formed from small faults or detached folds.

One of the highest positive values calculated by the high-pass filter for Granny Creek was 10 feet. This value, located (Figure I22) on the eastern margin of the field (UTM 487750, 4265361), represents an abrupt change from low to high elevations for an 8-acre area. In this case, the greatest difference in elevation between this center cell and neighboring cell (-891 and -914) is approximately 23 feet (Figure I21b).

13. Oil Production Draped onto Perspective Display of Unconformity

a. *Purpose*: To superimpose oil production data onto a three-dimensional perspective of a structural surface.

b. *Operation*: Orthograph (Perspective)

c. *Discussion*: Pseudo three-dimensional displays (Figure I23) improve the visualization of two-dimensional images. Images having continuous surfaces can display dense sets of parallel profile lines to yield three-dimensional views. A second image also can be draped on the top of the surface displayed.

Changes in the local relief of the unconformity surface (reservoir top) are easier to discern with three-dimensional perspective displays than with two-dimensional images. Two dimensional images, such as trend surface and high-pass filter, were also employed to detect local "lows" and "highs" of the unconformity; but the resulting images could be difficult to visualize. Therefore, perspective displays are helpful in showing irregularities that occur and in supporting the conclusions of the trend surface and high-pass filter analysis.

Production data, in this case initial open flow greater than 25 b/day, is superimposed on the perspective display of the pre-Greenbrier Unconformity to evaluate the spatial relationship between oil production and structural relief. The view direction of the orthographic display is northward, the viewing angle (inclination of the eye to the image plane) 50 degrees, and the vertical exaggeration 1.5.

d. *Analysis*: It has been postulated that better oil producing areas may be associated with detached folds represented by local "highs" of the unconformity surface (Donaldson, et al., 1992). When areas of high oil production (represented by white lines) are draped onto to the perspective display of the unconformity surface, certain locations of Granny Creek field show a correlation between high oil producing areas and local highs of the structural surface, but not always.

14. Communication Paths Compared to Initial Open Flow

a. *Purpose*: To determine if the communication paths correlate with initial open flow.

b. *Operations*: Overlay (multiply, cover)

c. *Discussion*: Well communication paths, which may represent fracture zones (Donaldson, et al.) are overlaid onto initial open flow to determine if a relationship exists (Figure I24).

d. *Analysis*: The well communication paths appear not to correlate with high initial open flows, suggesting that the paths or fracture zones may have formed or widened as a result of waterflooding. This assumption is incorrect, however, if the first producing wells encountering fracture zones drained these zones, and this information was not properly recorded. Wells drilled into the drained fracture later would be depressed in volume and pressure.

15. Spatial Query of Stratigraphy

a. *Purpose*: To determine if mouth bar overlap and density breaks affect primary oil production.

b. *Operations*: Overlay (multiply, add), Vector Overlay

c. *Discussion*: It has been postulated that where two mouth bar tongues overlap, possible lateral stratigraphic barriers exist that may impede the flow of oil. Other possible barriers are diagenetic density zones identified at certain wells within the fine-grain horizon (C zone) of the Big Injun.

The mouth bar tongue C2 is overlaid with tongues C1 and C3 to create a new image depicting where the mouth bar tongues overlap. This image is then covered by the best production. Using

vector overlay files, the density break wells and the northern limit of the B member are superimposed onto the final image.

d. *Analysis*: The stratigraphic image (Figure I25) shows that the best primary production is in the C2 tongue and in areas where the mouth bar tongues do not overlap. Secondly, most of the density breaks are located where production is marginal. Table I9 lists the corresponding percentages between the 71 density break wells and oil production. The best match (90%) occurs when the density breaks wells are compared to the worst oil producing areas. It seems likely that the overlapping tongues and high density zones may form barriers that impede the movement of oil.

16. Cross-classification of Mouth Bars and Seal

a. *Purpose*: To determine how two stratigraphic images affect oil production.

b. *Operations*: Crosstabulation, extract

c. *Discussion*: First, the diagenetic seal (A & B zone) is divided into two regions (Figure I26a) whereas the depositional mouth bars (C zone) are divided into four (Figure I26b). The classified areas are then crosstabulated into seven new zones (Figure I26c). Summary statistics (Table I10) are calculated to compare the new cross-classified zones to production data.

d. *Analysis*: If best oil production (initial open flow > 25 b/day OR cumulative production > 20,000 barrels) is superimposed on the cross-classification image, then areas of high oil production occur in 46% of the C2 belt (Zone 3) where the seal is present (Figure I27b). In this zone the average initial open flow and average 10-year cumulative production are 19 b/day and 17,000 barrels respectively. This region encompasses approximately 25% of the field.

17. Oil Production Draped onto a Stratigraphic Zone

a. *Purpose*: To produce stratigraphic perspective displays draped with oil production images.

b. *Operations*: Transpose, Orthograph (Perspective)

c. *Discussion*: It has been suggested that the fluvial unit (A & B zone) of the Big Injun is the reservoir seal (Zou, et al.,1992). Figure I28 shows a perspective display of this coarse-grained unit that is superimposed with cumulative oil production greater than 25,000 barrels (white circled areas). The view direction of the stratigraphic channel display is 270 degrees, the viewing angle (inclination of the eye to the image plane) 45 degrees.

d. *Analysis*: Notice that the northeastern part of the A & B zone is eroded away by the pre-Greenbrier Unconformity (Figure I28). Since the best oil production (cumulative oil production > 25,000 barrels) occurs where this unit is present, the A & B zone may serve as an important seal for the reservoir.

18. Spatial Query of Injection Pressure Rates

a. *Purpose*: To compare high injection pressure rates and low permeability to cumulative oil production for the southern part of Granny Creek.

b. *Operations*: Reclass, Overlay (multiply, add)

c. *Discussion*: To locate possible barriers, an image is created to portray low permeability (< 5 md) and high injection pressures (> 900 p.s.i.). This image is then combined with cumulative production. The yellow color of the final image (see "Secondary Recovery" of video images, Figure I6) represents possible barriers, defined by a positive correlation between low production, low permeability, and high injection pressures. In contrast, the rusty orange color suggests no correlation between low production and possible barriers.

d. *Analysis*: After a low permeability/high pressure image was generated for the southern part of Granny Creek field, it was found that 62% of the low permeability/high pressure zones correlated with cumulative oil production less than 10,000 barrels. It is possible that some lower production areas may characterize low permeability/high pressure zones within the reservoir.

19. Reservoir Volume

a. *Purpose*: To compute the reservoir volume of the Big Injun.

b. *Operations*: Scalar, extract

c. *Discussion*: Although IDRISI lacks specific procedures for calculating the volume of a property, it still can be done. To compute the reservoir volume of the Big Injun, the thickness value of each grid cell is multiplied by its cell area and then all the cells are summed together.

d. *Analysis*: The Big Injun reservoir volume is estimated to be 200,714 acre-ft.

20. Profile of Seven Raster Images

a. *Purpose*: To construct a profile from seven raster images.

b. *Operation*: Profile

c. *Discussion*: Figure I29 shows an east-west profile constructed along P1-P1' for the following properties: (1) A & B zone thickness, (2) C zone thickness, (3) mean porosity of C zone, (4) initial open flow, (5) cumulative oil production, (6) unconformity elevations, and (7) well permit numbers. To create the profile, cell attributes along the profile line for each of the seven raster images are extracted to a text file. A total of 46 cells is exported from each image to an attribute text file and then imported into a spreadsheet. By using the combination and overlay spreadsheet functions, a single graph is created to portray every geological parameter.

d. *Analysis*: The thickness and mean porosity of the C zone are fairly static and do not seem to vary much. The A & B zone (Fluvial Channel), which may be the reservoir seal, is missing on the eastern side of the profile. The seal first appears in Clay 1383 (Figure I29) and then

progressively thickens westward. Best production occurs in the middle of the field on the western flank of the syncline or between the unconformity elevations -885 to -855. In summary, probably the best production is controlled by both structure and stratigraphy.

Summary and Conclusions

GIS provided important processing and display operations for analyzing the large amounts of spatial data associated with Granny Creek field. Once the base images, such as reservoir thickness and mean porosity, were created, various GIS operations were applied to better characterize the reservoir. To determine locations of optimal oil production, for example, a spatial query of six geologic and engineering variables was made utilizing the RECLASS and OVERLAY operations. Other valuable GIS operations not usually found in other spatial analysis software were vector overlay, image enhancement, image cross-classification, draped images onto perspective displays, and spatial statistics. These and other GIS operations facilitated the integration, analyses and presentation of two-dimensional spatial data. Below are some conclusions resulting from the GIS analyses of Granny Creek field:

1. Generally, primary oil production was found to be the highest in the interior and in the northern half of the field. When primary production was crosstabulated with the elevations of the pre-Greenbrier unconformity surface, it was discovered that best production for both initial open flow and cumulative production occurs in the middle of the field or at approximately -875 feet.

2. Thirteen separate areas in Granny Creek field were identified that met the following conditions: initial open flow greater than 25 b/day and 10-year cumulative production greater than 25,000 barrels. Seven of these thirteen best oil producing areas are greater than ten acres, ranging from eleven to twenty-nine acres.

3. Two stratigraphic images (mouth bar and seal) were cross-classified to form a new image showing the combinations of the categories of the original images. Of the seven new zones created, best oil production occurs in 46% (the highest percentage) of the region where the C2 belt and seal are present. This region encompasses approximately 25% of the field. In this main pay zone the average initial open flow and 10-year cumulative production are 19 b/day and 17,000 barrels. Oil production probably would be higher in this area of Granny Creek field if it were not for high density zones within the reservoir that affect oil production.

4. Crosstabulating two production images revealed that for two-thirds of Granny Creek field initial open flow and 10-year cumulative oil production are less than 20 bbls/day and 20,000 barrels, respectively.

5. A linear regression analysis of initial open flow and cumulative production showed that the two production images do not correlate ($R = 0.59$) very well.

6. A spatial query of six geological and engineering variables revealed that ideal production should be located in the middle part of the field. Images of the six variables, including the reservoir seal, reservoir thickness, mean porosity, mean permeability, water saturation, and high

density zones, were first reclassified to represent favorable reservoir conditions for oil. All six reclassified images then were combined into a final image depicting the results of the spatial query, or where the best oil producing areas within the reservoir should be located.

7. No apparent relationship was found between well communication paths and areas of high oil production.

8. The dip angles of the pre-Greenbrier Unconformity surface range from zero to six degrees, of which 96% of all slopes are two degrees or less. The highest dips are in the southern part of the field where production is poor. Although the computer calculated that most of the beds dip gently towards the east, there also appear to be small undulations along the unconformity surface that cause beds to dip in other directions.

9. A local high-pass filter was applied to the unconformity surface to detect abrupt elevation changes. Results of the filtered image confirmed that a majority of the surface has a gradual slope. A scattered, random pattern of extreme negative and positive values, however, dotted the image, suggesting that numerous, small undulations also occur along the unconformity surface. These "small hills and valleys" along the unconformity surface could have formed from small faults or detached folds (Donaldson, et al.,1992).

10. A residual map showing the local relief of the unconformity surface was calculated by subtracting the second-degree trend surface from the pre-Greenbrier unconformity map. Positive residuals defined areas locally higher then the trend surface while negative residuals represented those areas lower. If areas of best oil production are overlaid onto the trend residuals, then elevations above than the regional trend of the unconformity surface correlate 67% with the best oil producing areas. Therefore, the local highs in elevation do probably affect production.

11. Of seven properties analyzed to compare northern and southern Granny Creek field, average permeability, initial open flow, 10-year cumulative, and best production have higher mean values in the northern half of Granny Creek field. This comparative analysis also showed that the C zone thickness and average porosity are the same for the entire field; while the total thickness of the Big Injun sandstone is greater in the southern part of the field because the fluvial channel or AB zone is the thickest there.

References Cited

Davis, J., 1986, Statistical and Data Analysis in Geology: John Wiley & Sons, New York, 646 p.

Davis, J., 1992, "Trend-surface analysis: early computer technique remains popular, useful": Geobyte, v. 7, n. 4, p. 38-41.

Donaldson, A., Shumaker, R., Laughrey, C., Aminian, K., and Hohn, M., 1992, Measuring and predicting reservoir heterogeneity in complex deposystems: Annual Fiscal Report for Year 1991 - Department of Energy Contract Number DOE/BC/14657-7, 62 p.

Zou, X., Donaldson, A., Smosna, R., and Bruner, K., 1992, "Reservoir Sedimentology and Petrophysical Heterogeneity of Big Injun Sandstone of West Virginia": American Association of Petroleum Geologists, Eastern Section Meeting and Illinois Geological Society 1992 Symposium, p. 26-28, abstract.

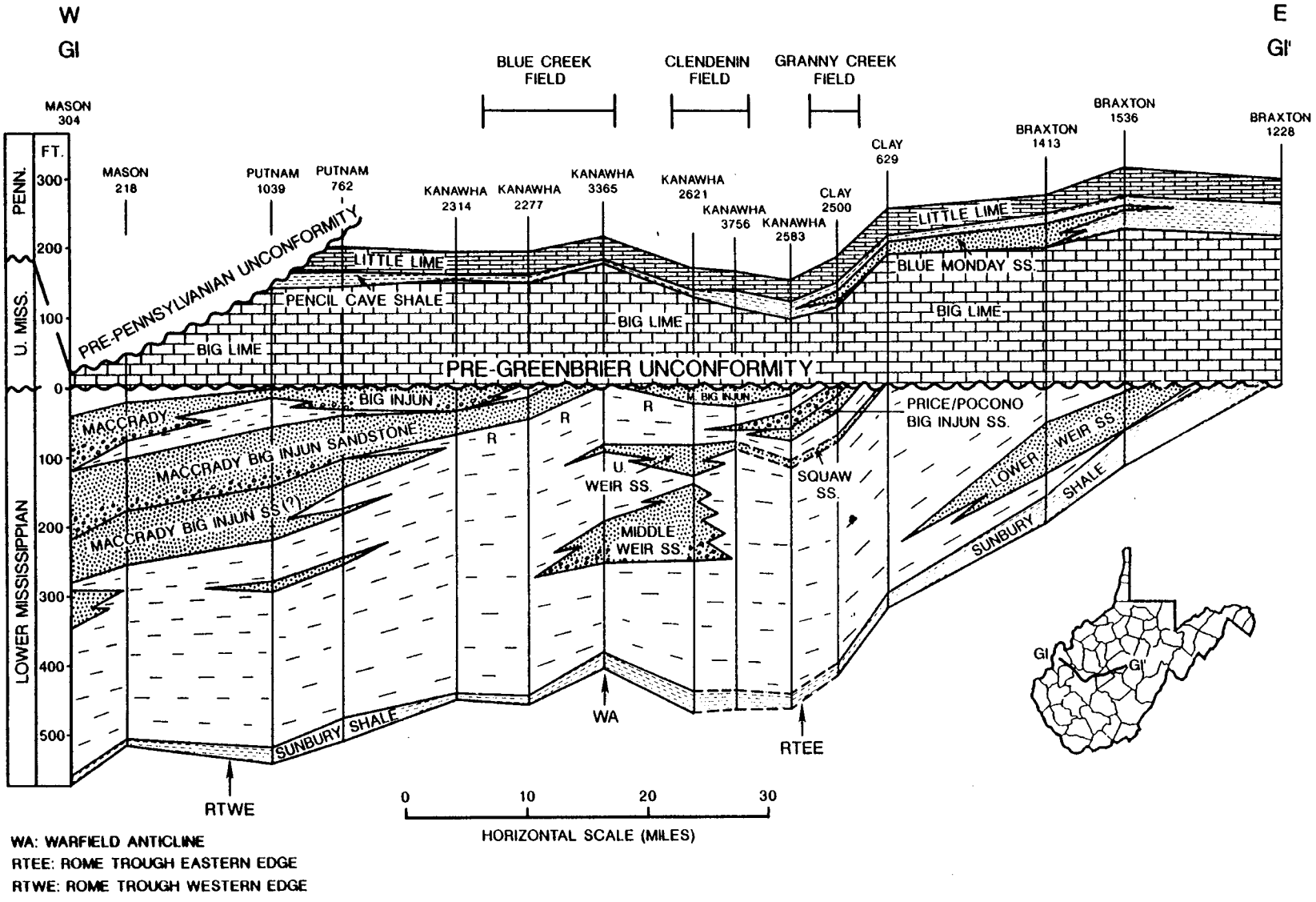

FIGURE 1. Generalized stratigraphic profile (GI-GI') in western West Virginia. Pre-Greenbrier unconformity (datum) shows increased eastward erosion of the Lower Mississippian rocks, resulting in angular contacts with different reservoir sandstones along the profile (modified from Zou and Donaldson, 1991).

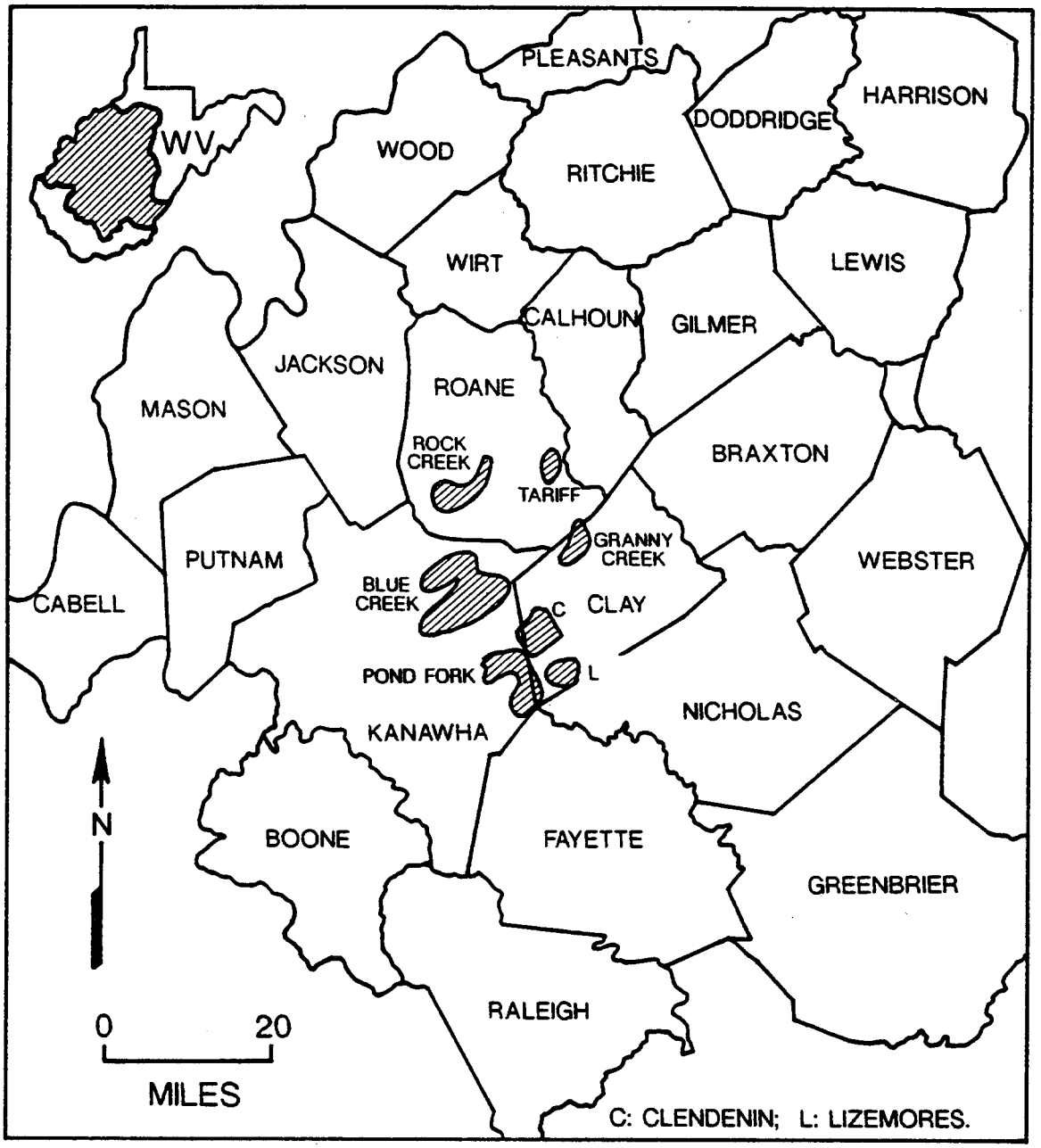

FIGURE 2. Location map of six West Virginia oil fields within the regional study area that produce from Big Injun sandstones. C = Clendenin; L = Lizemores.

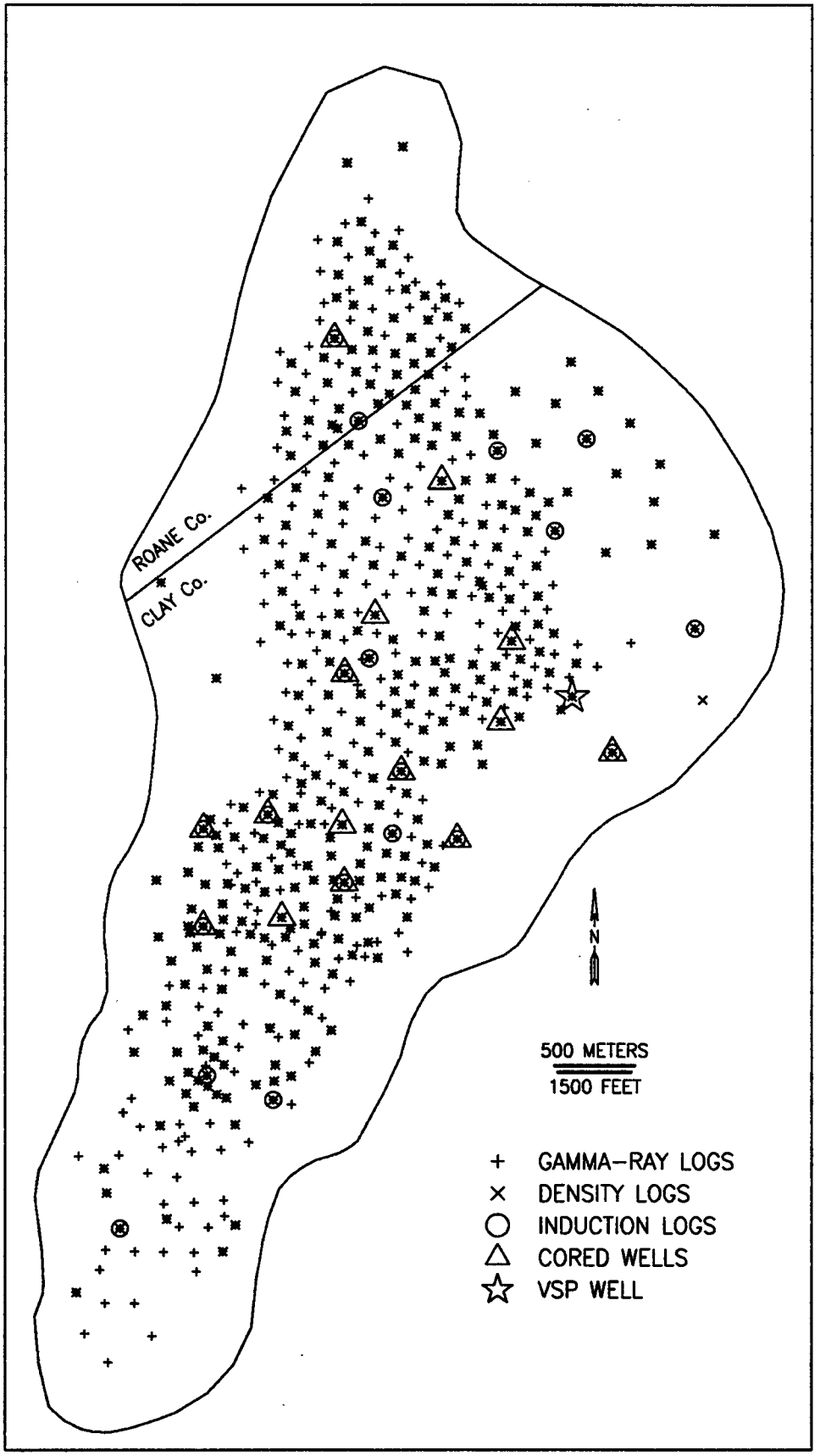

FIGURE 3. Control points and types of data available in Granny Creek field.

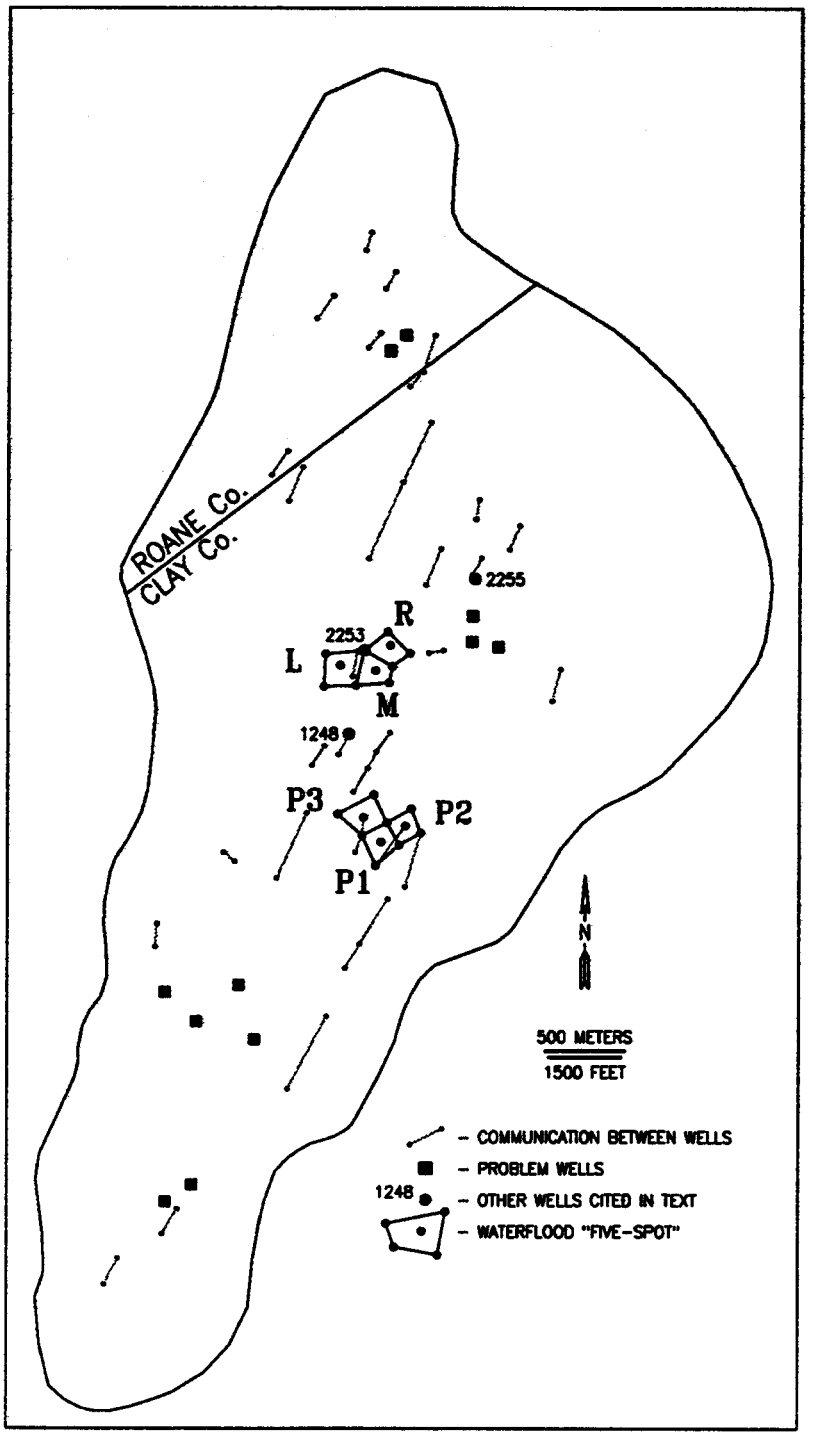

FIGURE 4. Map of Granny Creek showing the locations of two waterflooding projects discussed in the text. Also shown are lines of communication between wells in the field.

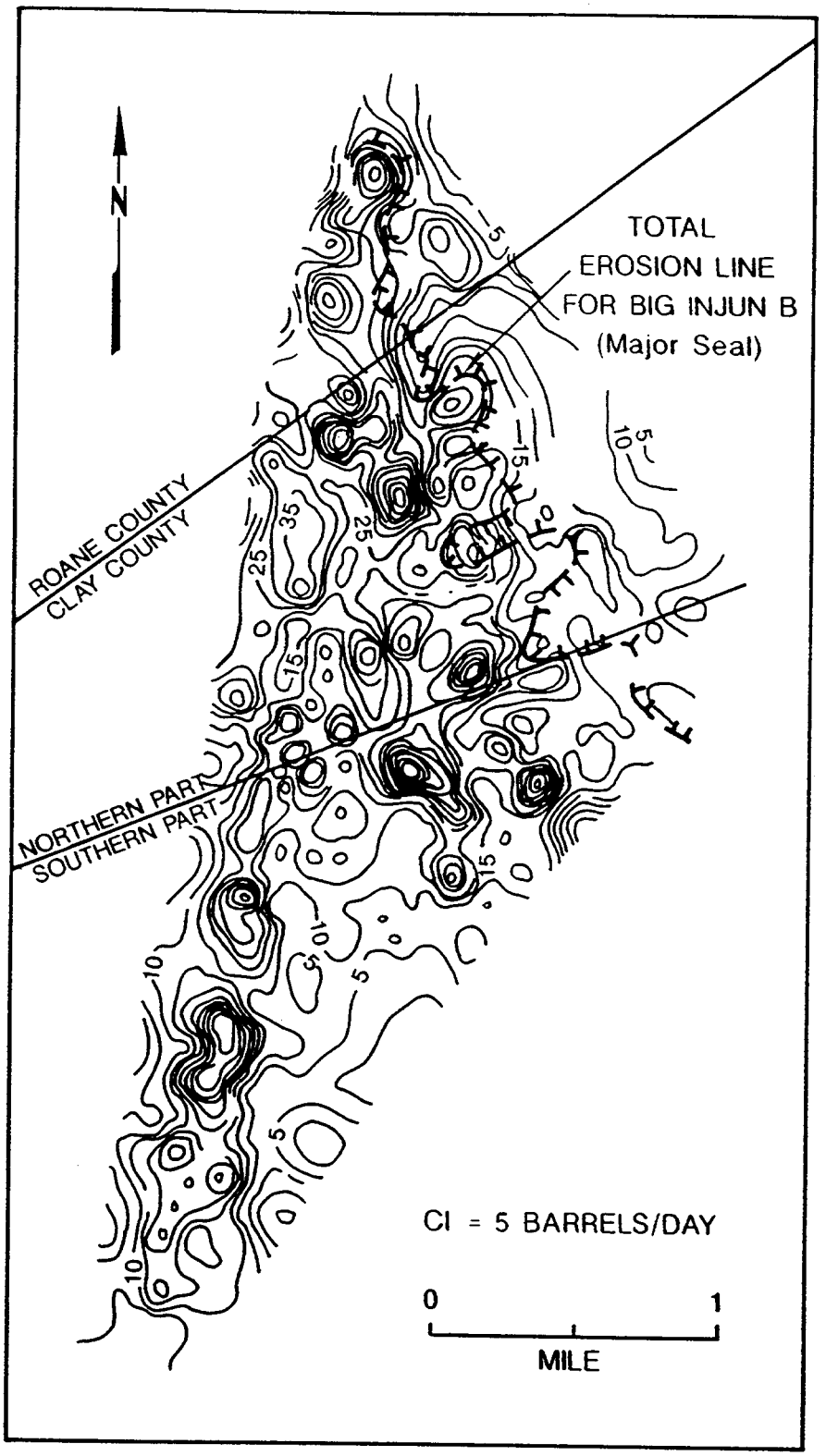

FIGURE 5. Map showing Initial Oil Potential (IP) for Granny Creek field. Contour interval is 5 barrels/day.

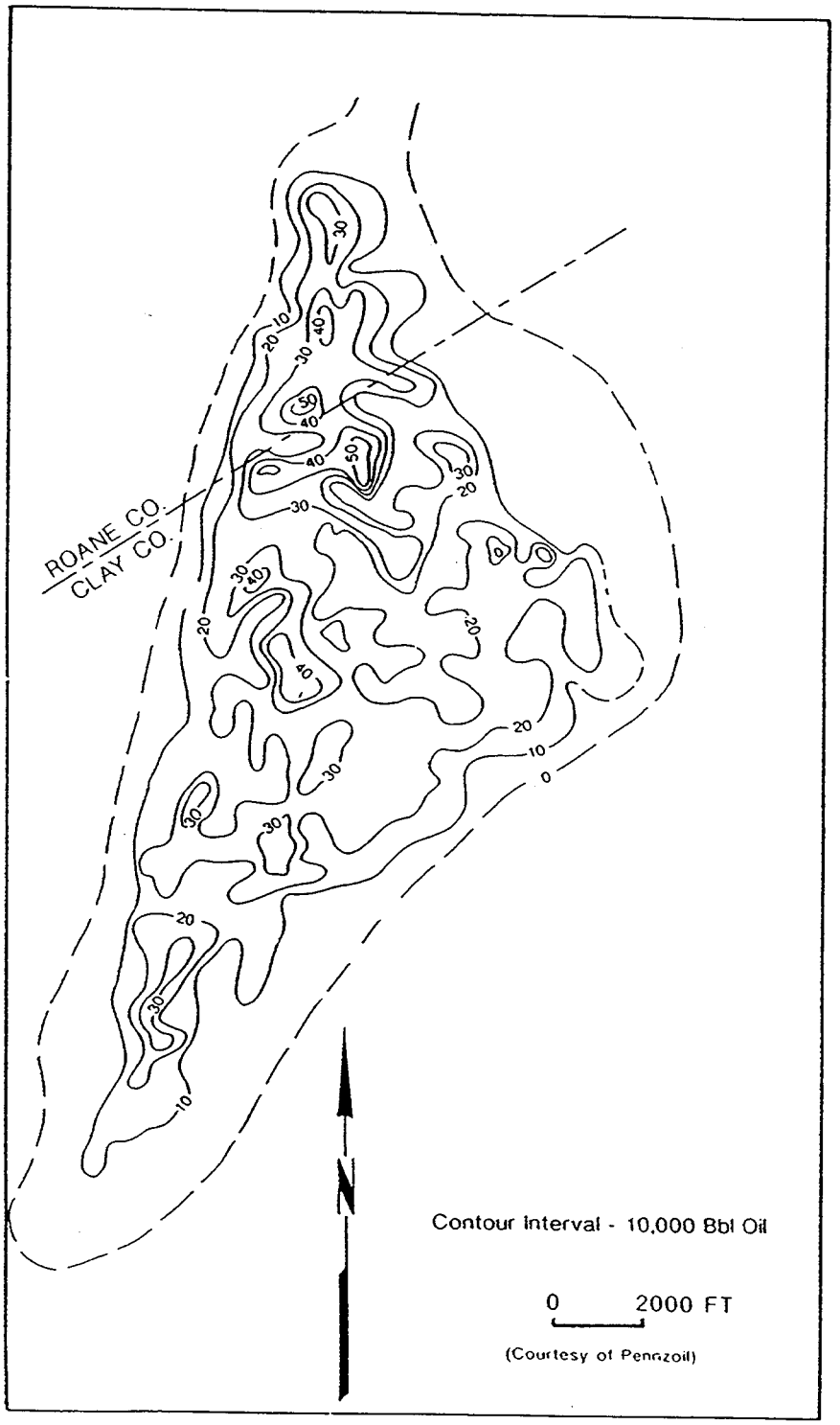

FIGURE 6. Map of cumulative oil production during first ten years of primary production, Granny Creek field. Figure courtesy of Pennzoil. Contour interval is 10,000 barrels.

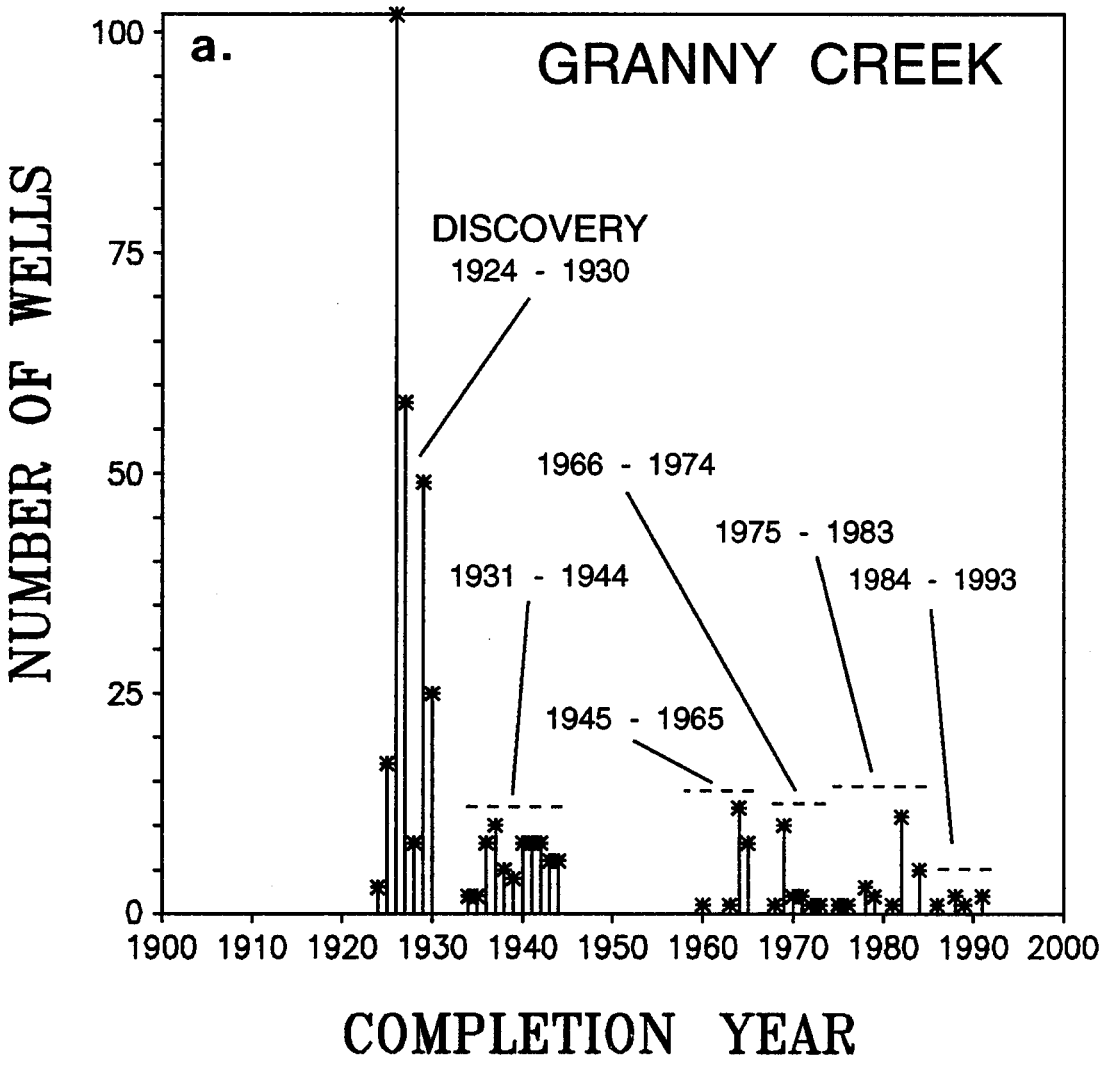

FIGURE 7a. Frequency spectrum showing numbers of wells completed versus year of completion for producing oil wells in Granny Creek field. Six periods of drilling activity are identified.

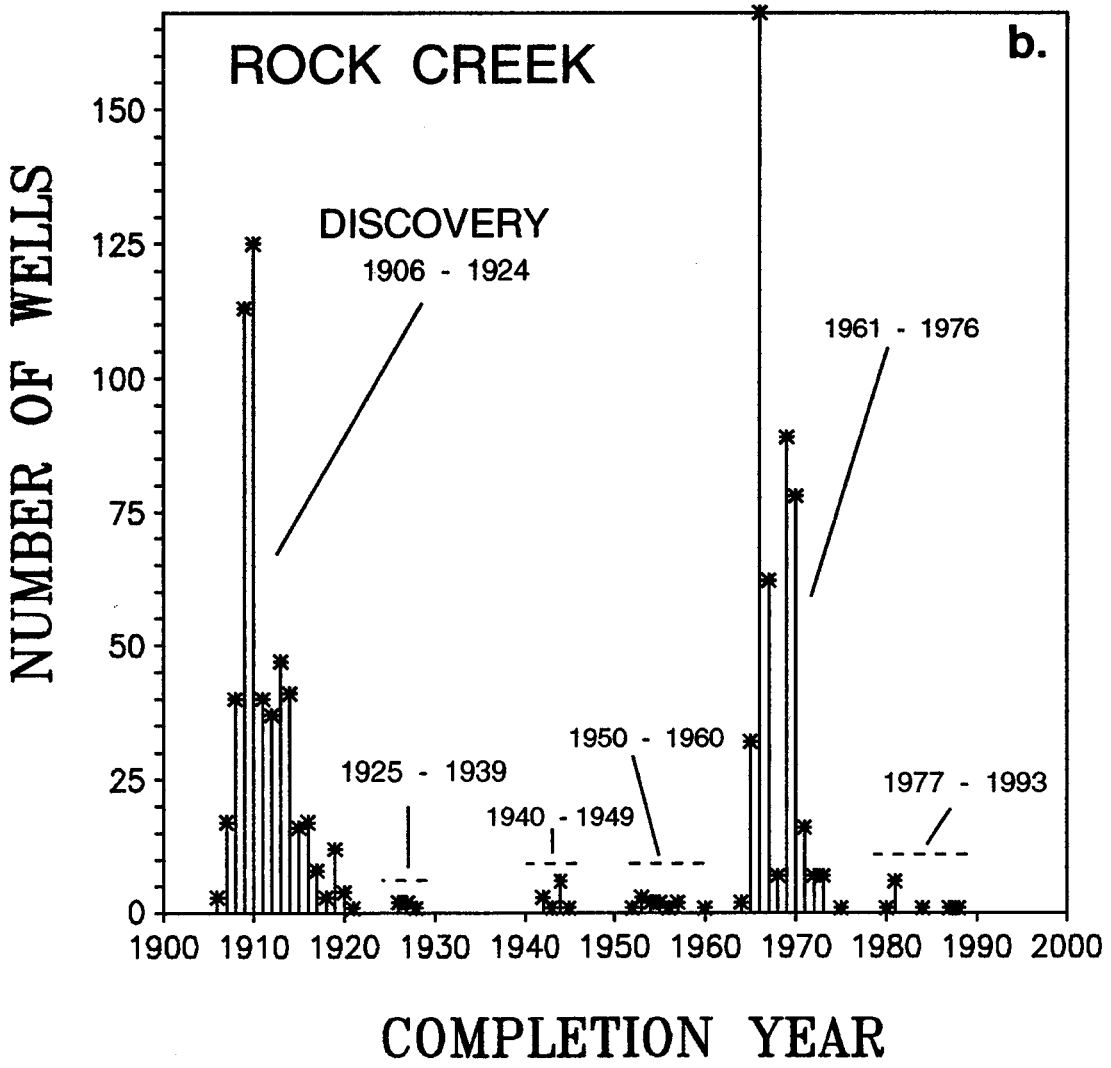

FIGURE 7b. Frequency spectrum showing numbers of wells completed versus year of completion for producing oil wells in Rock Creek field. Six periods of drilling activity are identified.

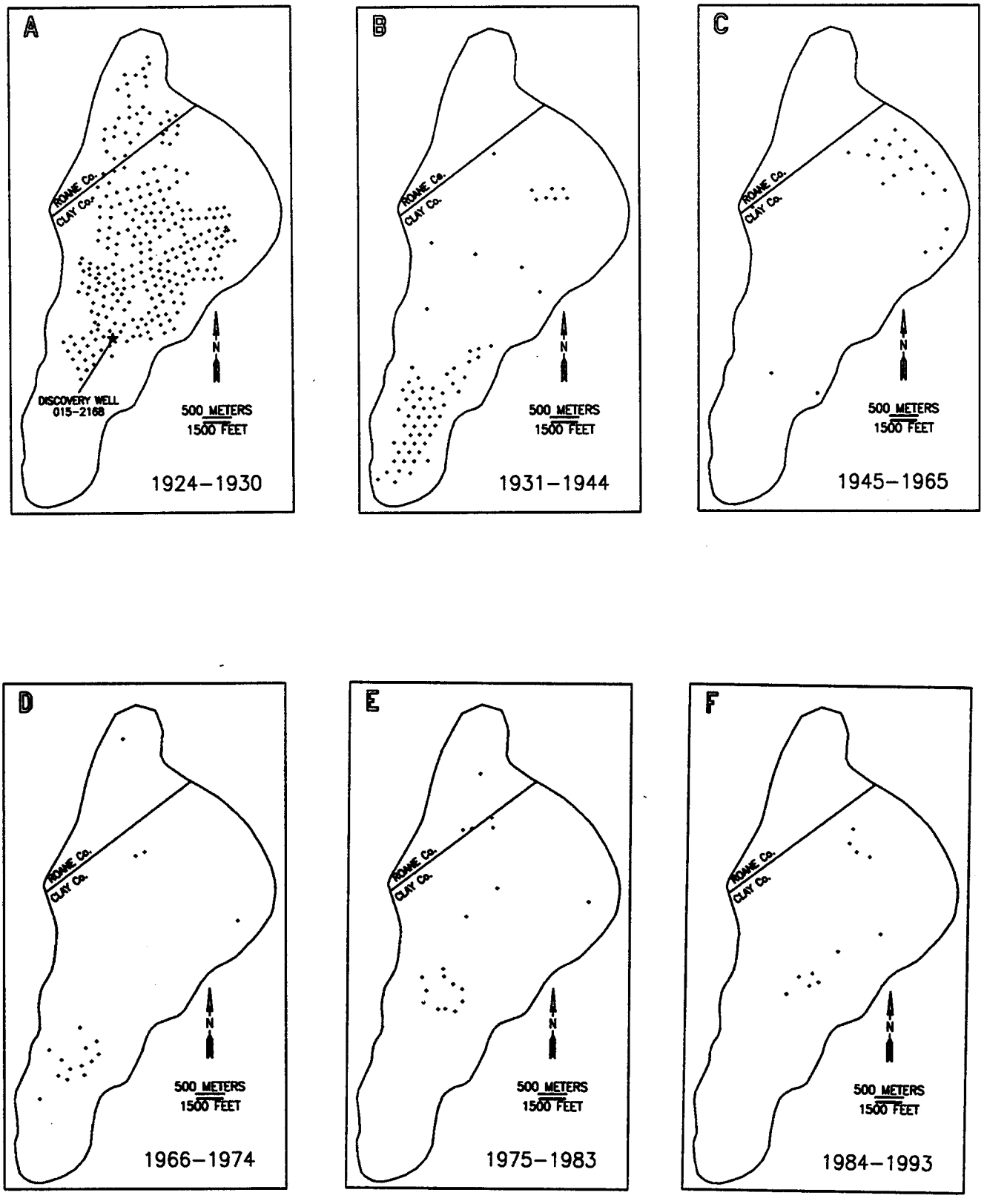

FIGURE 8. Geographic distribution of Granny Creek oil wells completed in each of the six period of drilling activity identified in Figure 7a.

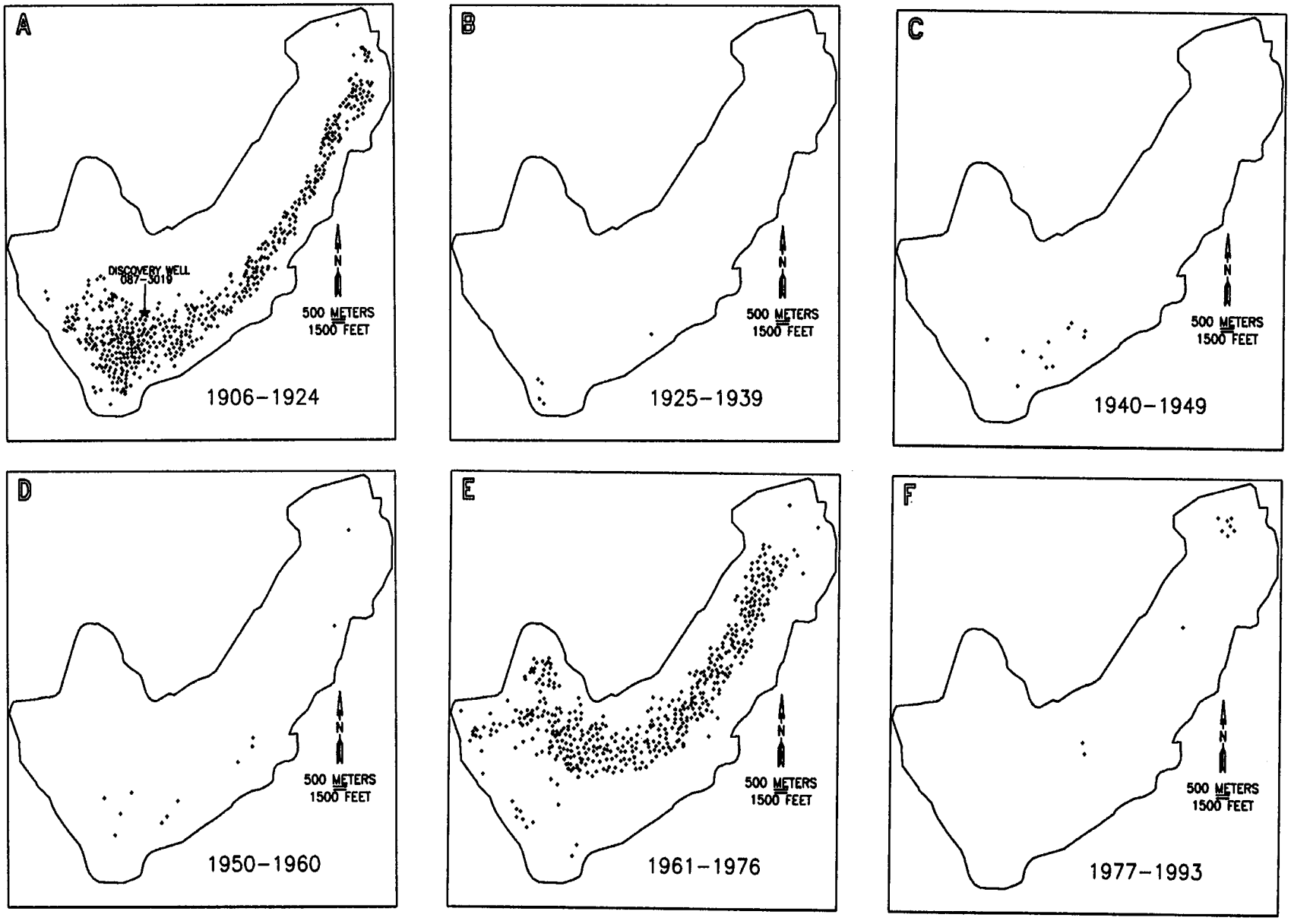

FIGURE 9. Geographic distribution of Rock Creek oil wells completed in each of the six periods of drilling activity identified in Figure 7b.

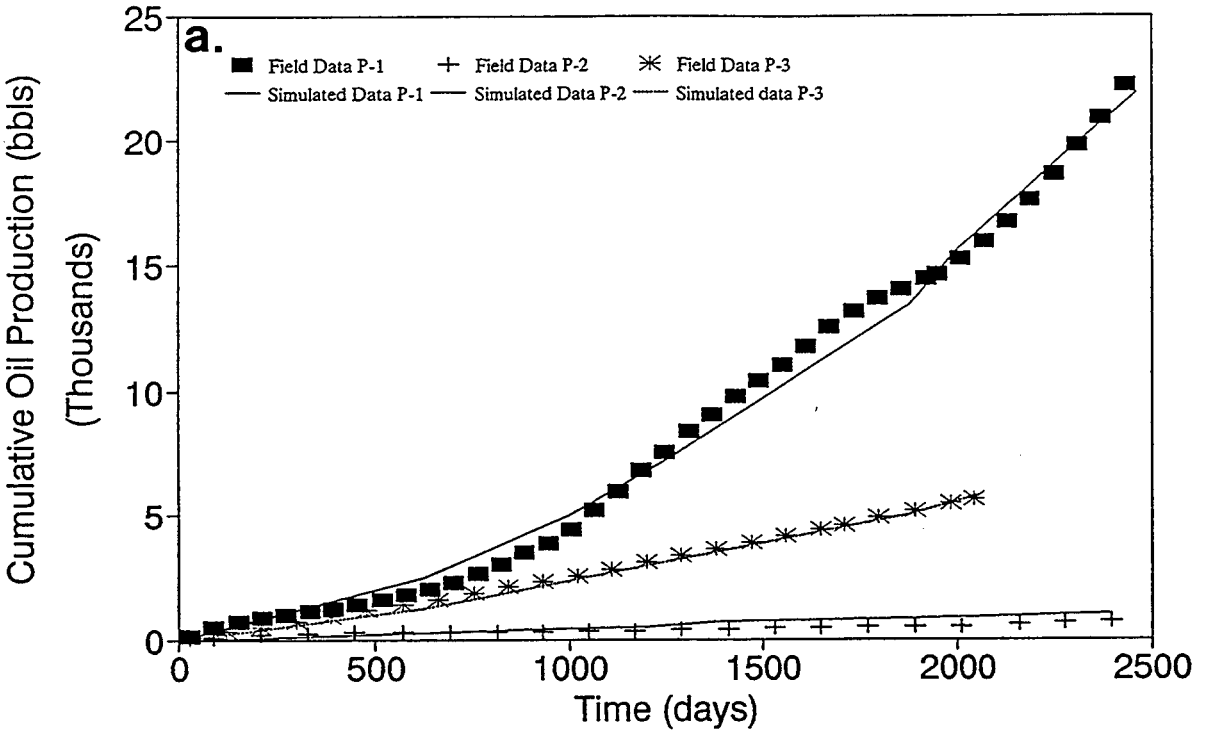

FIGURE 10a. Actual and simulated oil production for the southern waterflood area, Granny Creek field.

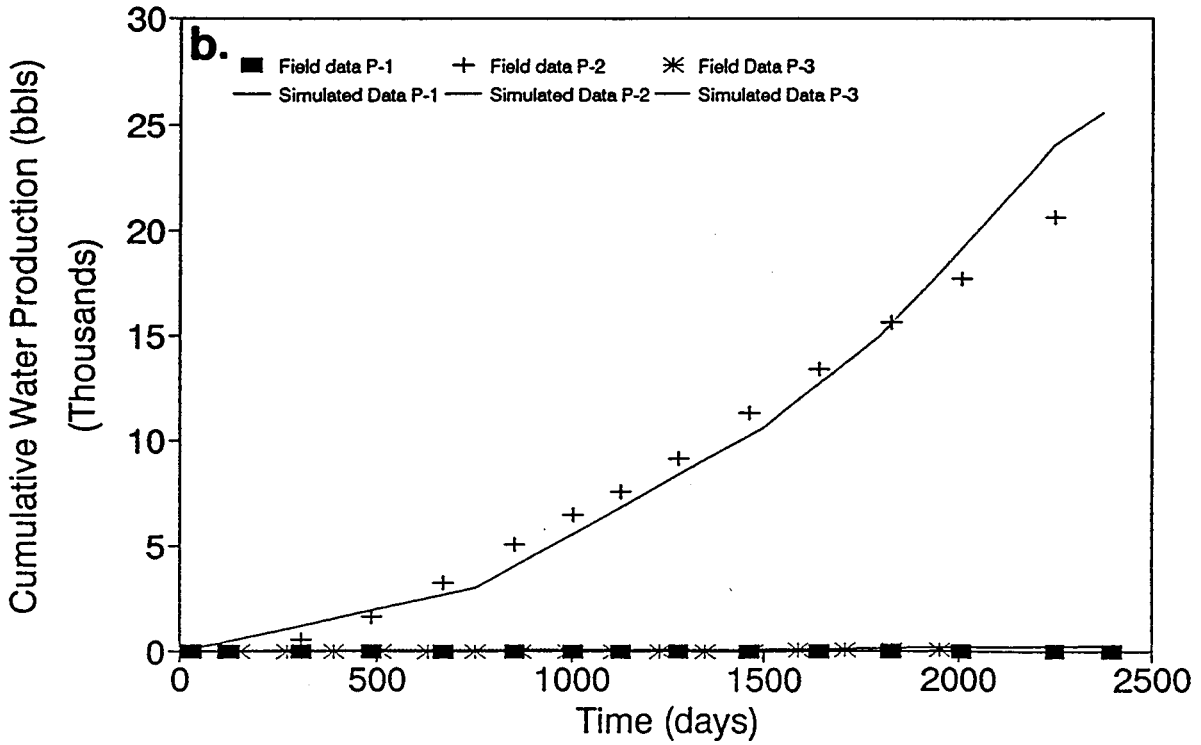

FIGURE 10b. Actual and simulated water production for the southern waterflood area, Granny Creek field.

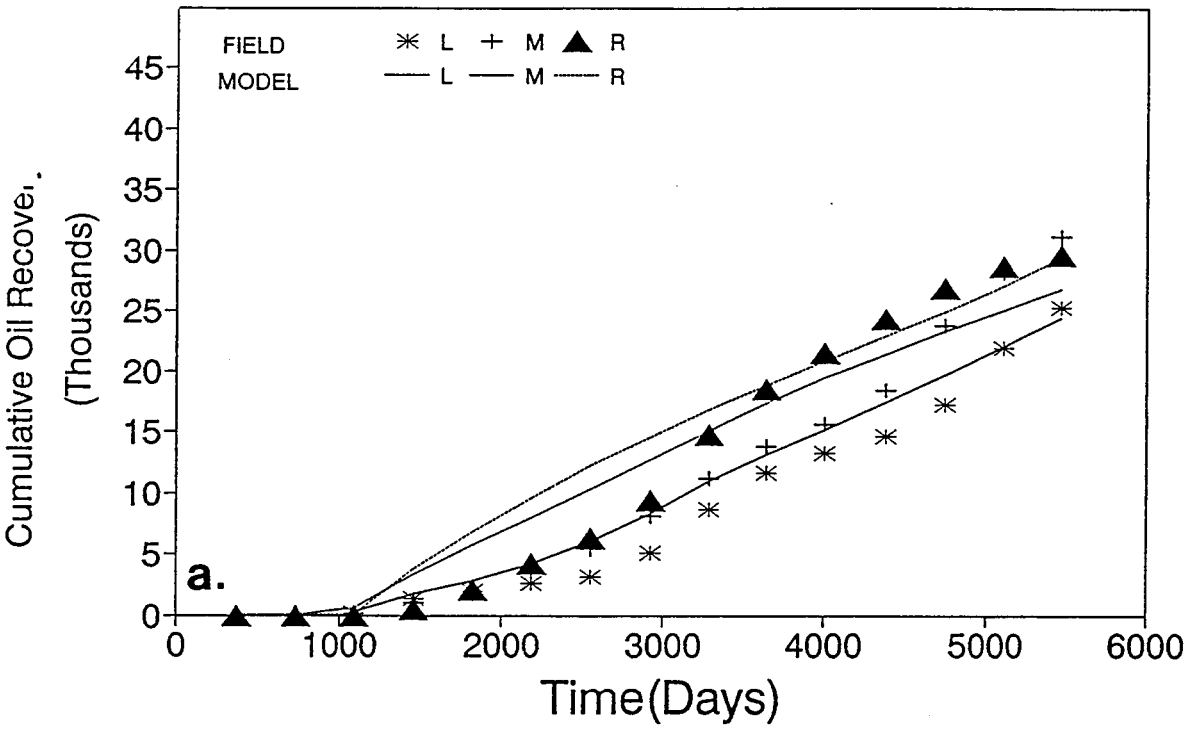

FIGURE 11a. Actual and simulated oil production for the northern waterflood area, Granny Creek field.

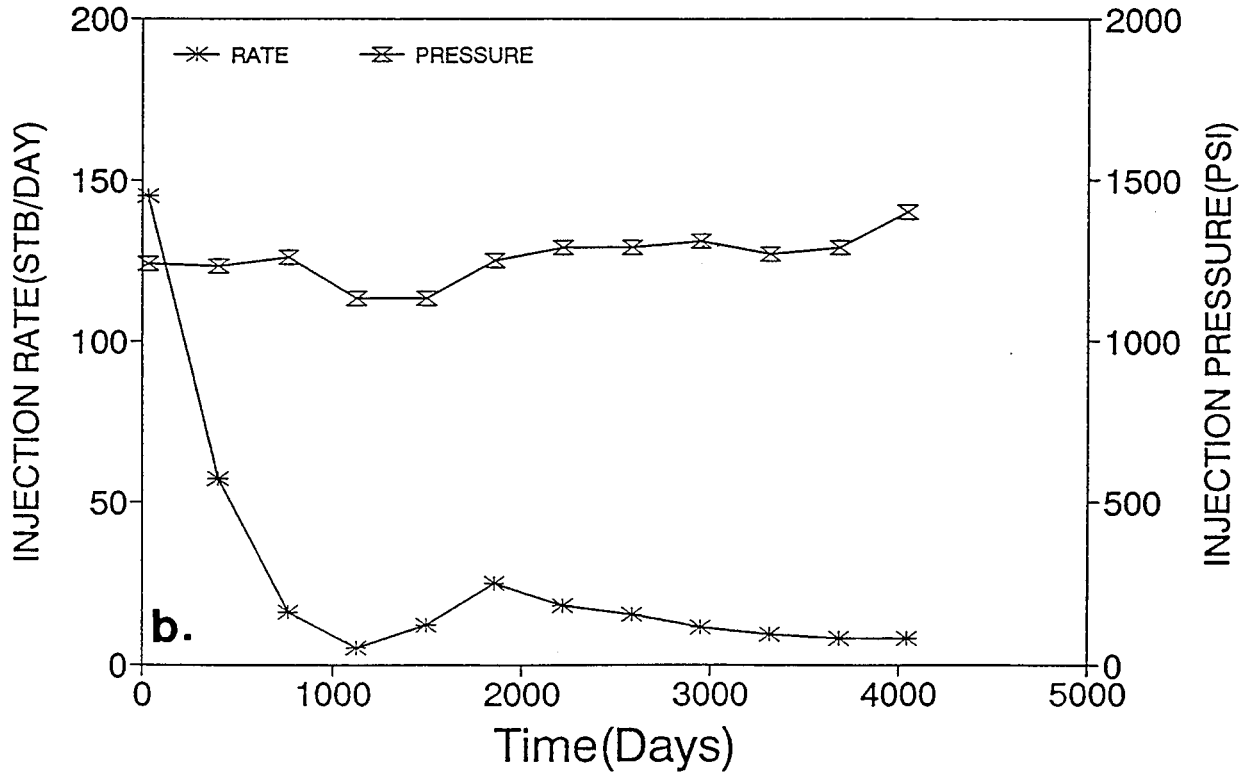

FIGURE 11b. Typical water injection rates and pressures for the northern water flood area, Granny Creek field.

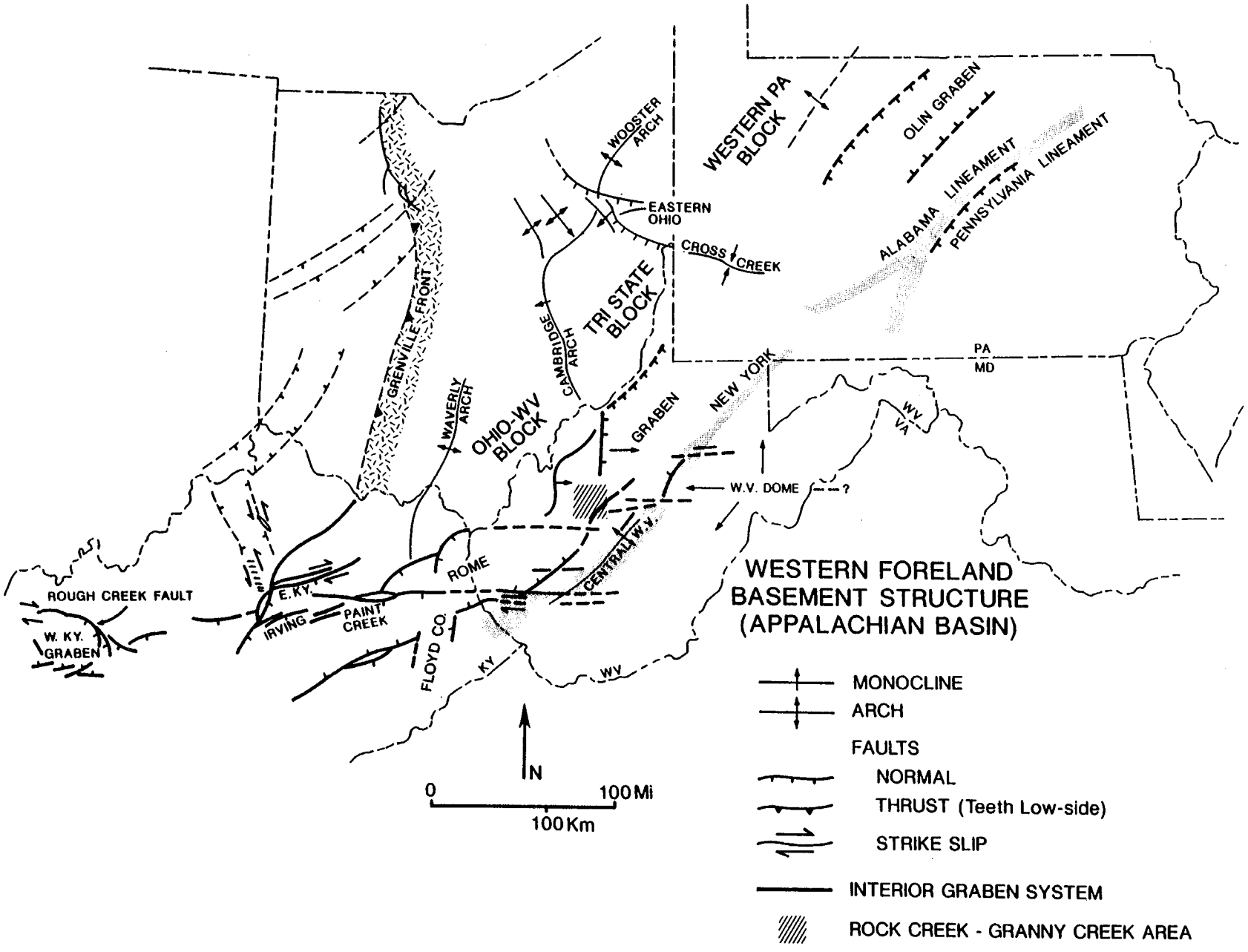

FIGURE 12. Basement structure map of the Appalachian basin.

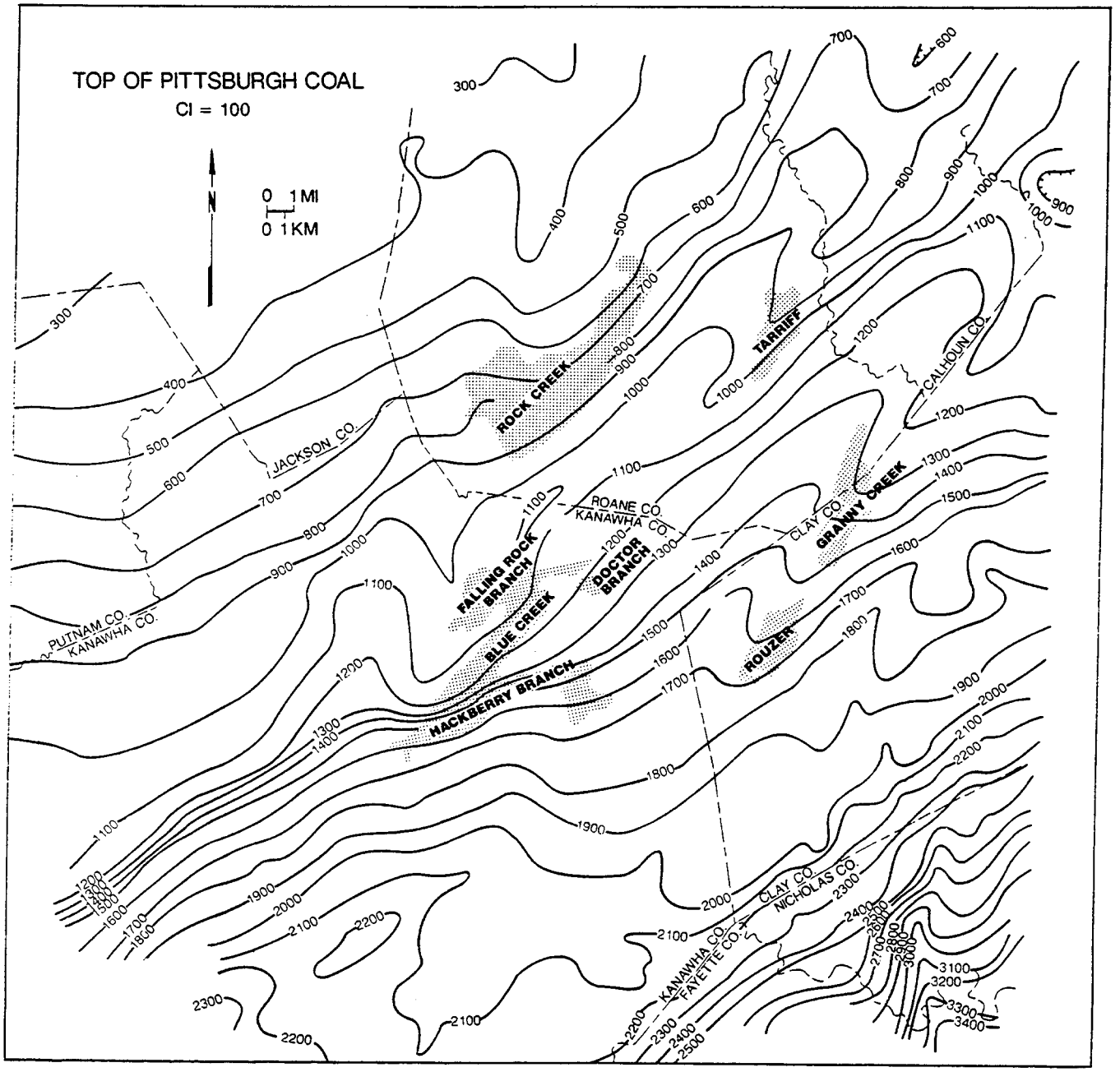

FIGURE 13. Structure on top of the Pennsylvanian Pittsburgh coal in the Rock Creek-Granny Creek area. Contour interval is 100 feet.

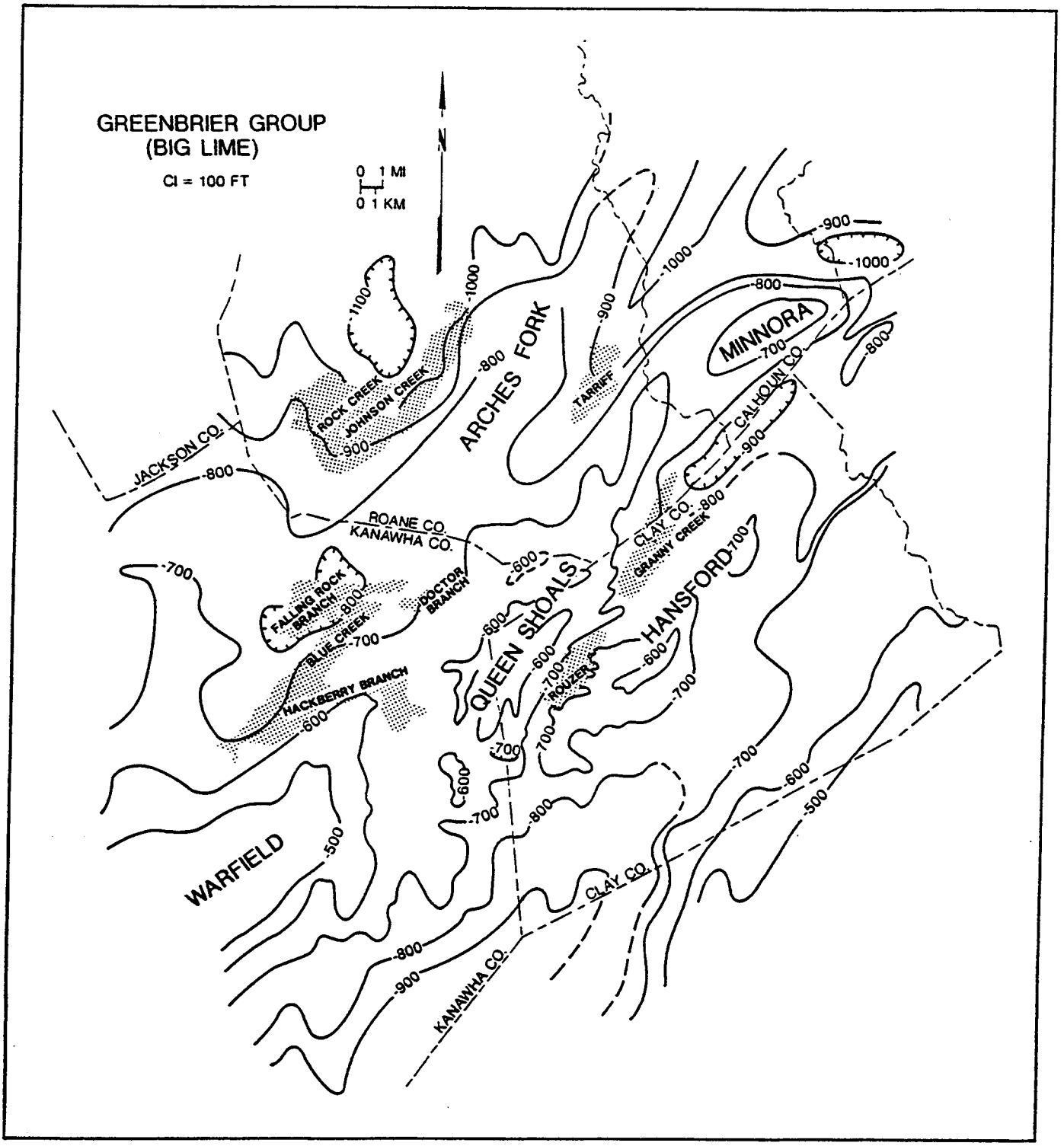

FIGURE 14. Structure on top of the Mississippian Greenbrier Group (Big Lime) in the Rock Creek-Granny Creek area. Contour interval is 100 feet.

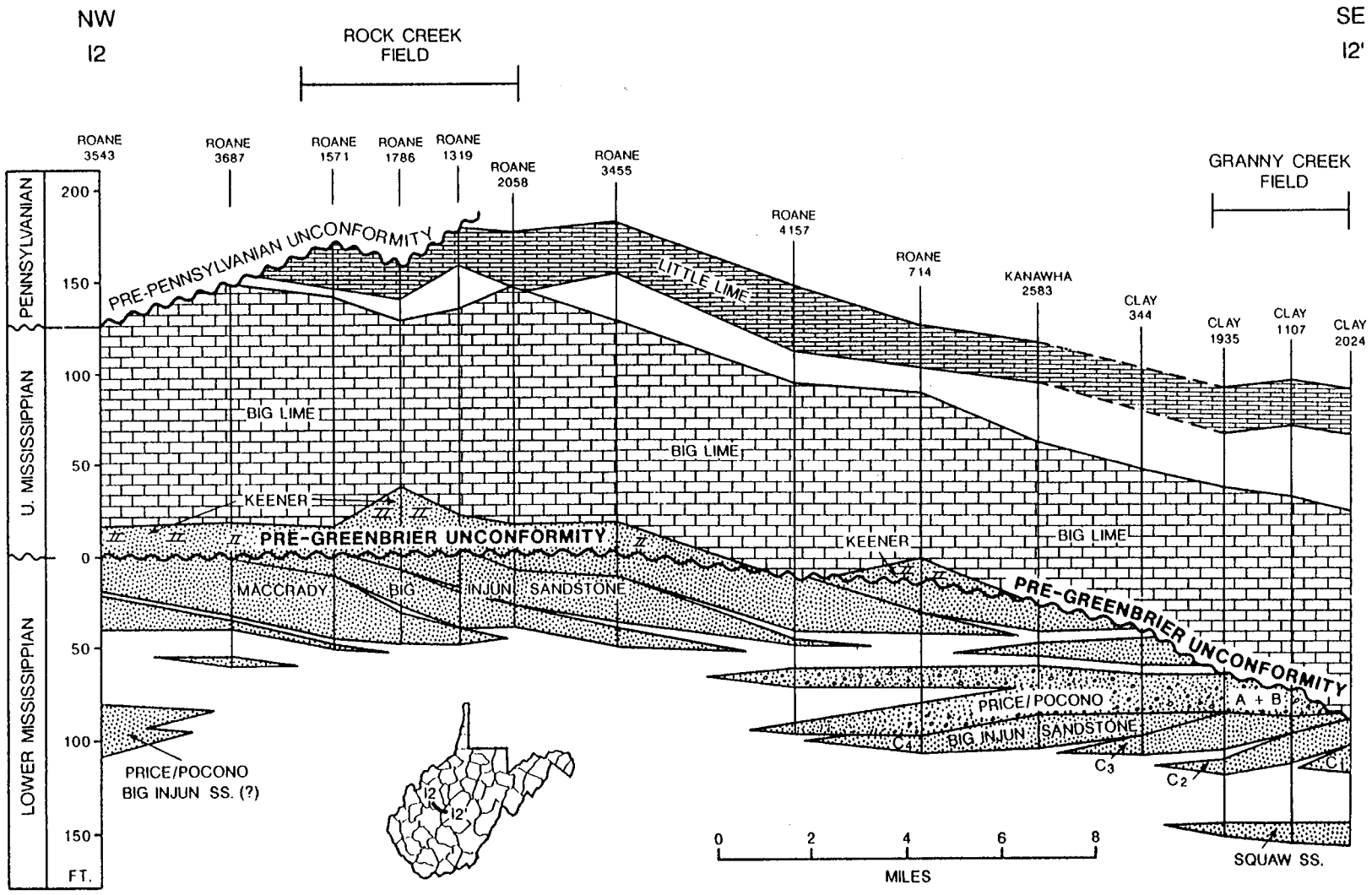

FIGURE 15. Stratigraphic cross section showing the "Maccrady" Big Injun sandstone in Rock Creek field to be separated by shales from the slightly older Pocono Big Injun sandstone of Granny Creek field. Fine-grained sandstones of the lower part of the Pocono Big Injun occur as westward prograding tongues (C1, C2, C3, and C4), capped by the coarse-grained upper unit, except where eroded by pre-Greenbrier erosion.

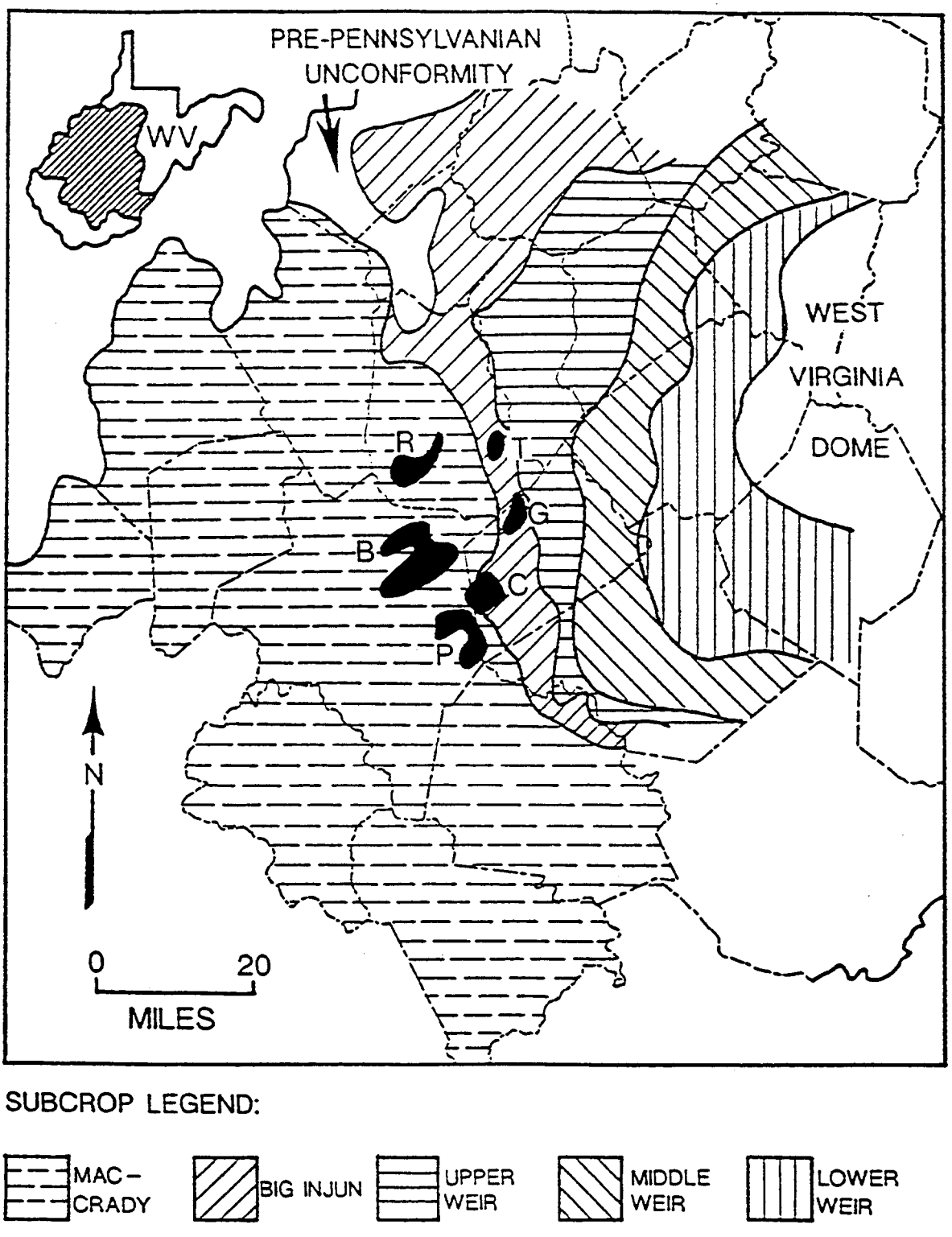

FIGURE 16. Subcrop map of pre-Greenbrier unconformity, the boundary between the Lower and Upper Mississippian strata in western West Virginia. Location of the six oil fields on map also indicates whether the Big Injun is "Maccrady" and/or Price/Pocono sandstones. (B: Blue Creek field, C: Clendenin field, G: Granny Creek field, P: Pond Fork field, R: Rock Creek field, T: Tariff field).

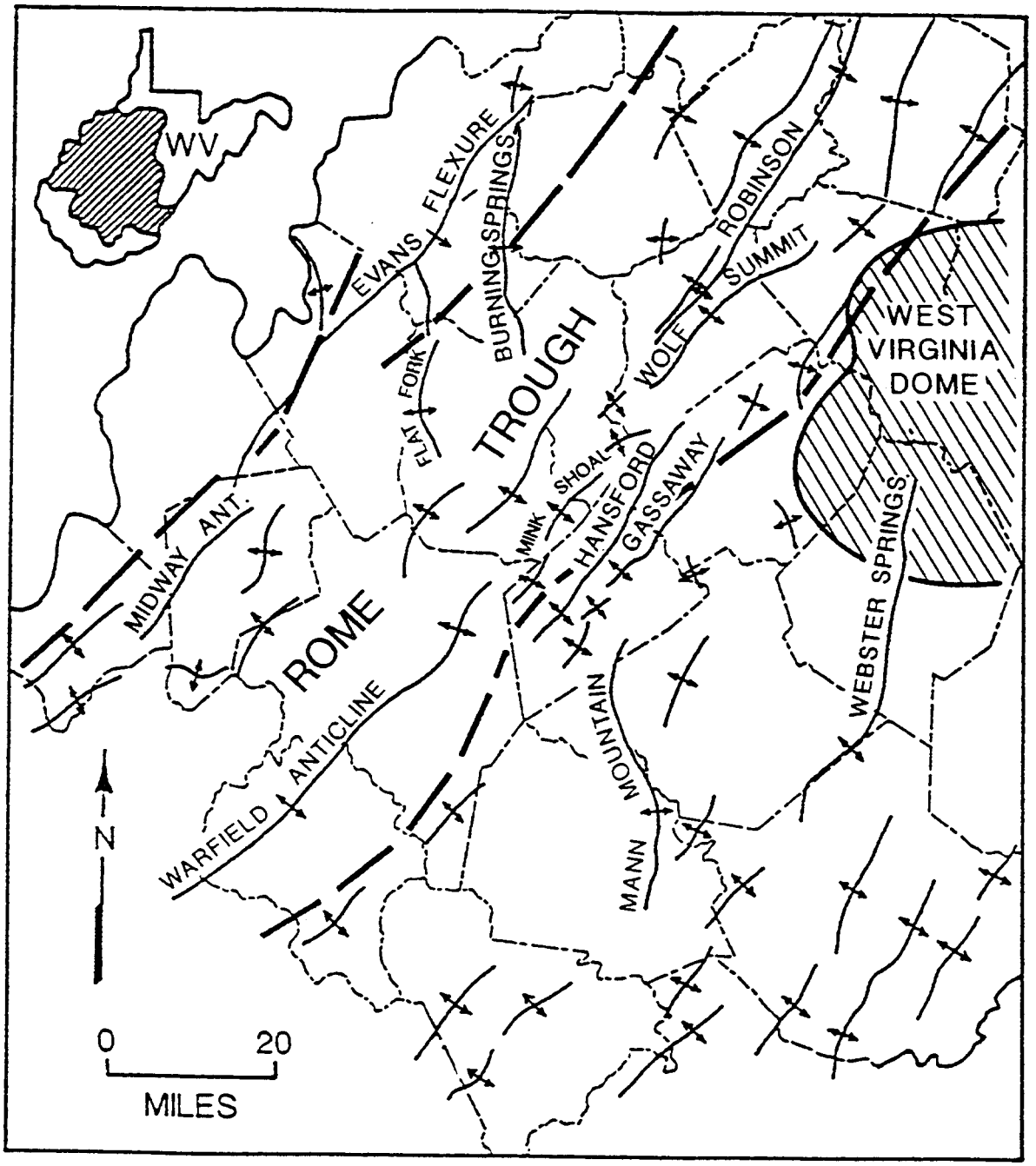

FIGURE 17. Structural map of western West Virginia.

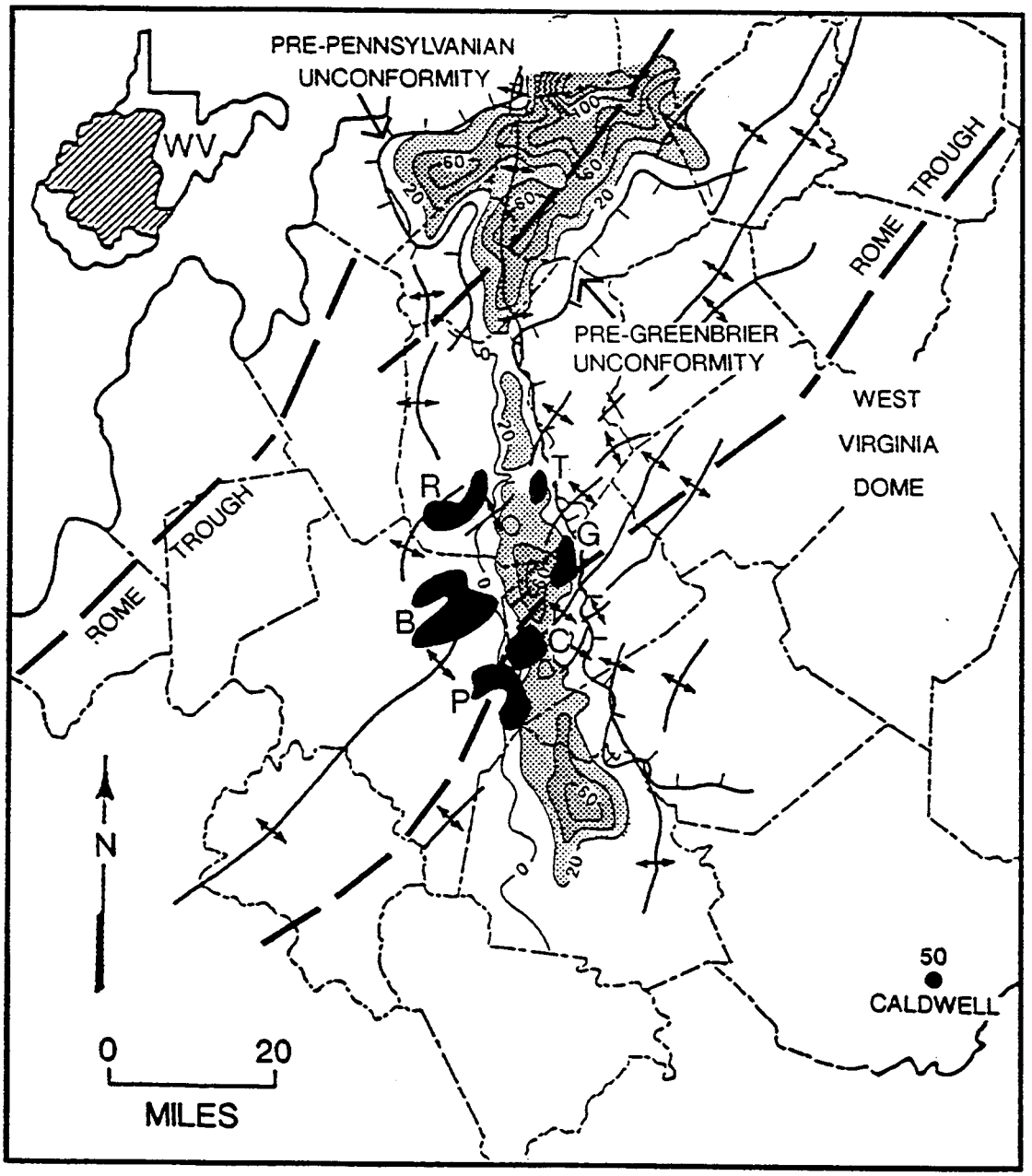

FIGURE 18. Isolith map of the Price/Pocono Big Injun sandstones, superimposed with some major structures, in western West Virginia (modified from Zou and Donaldson, 1991). (B: Blue Creek field, C: Clendenin field, G: Granny Creek field, P: Pond Fork field, R: Rock Creek field, T: Tariff field). Contour interval is 20 feet.

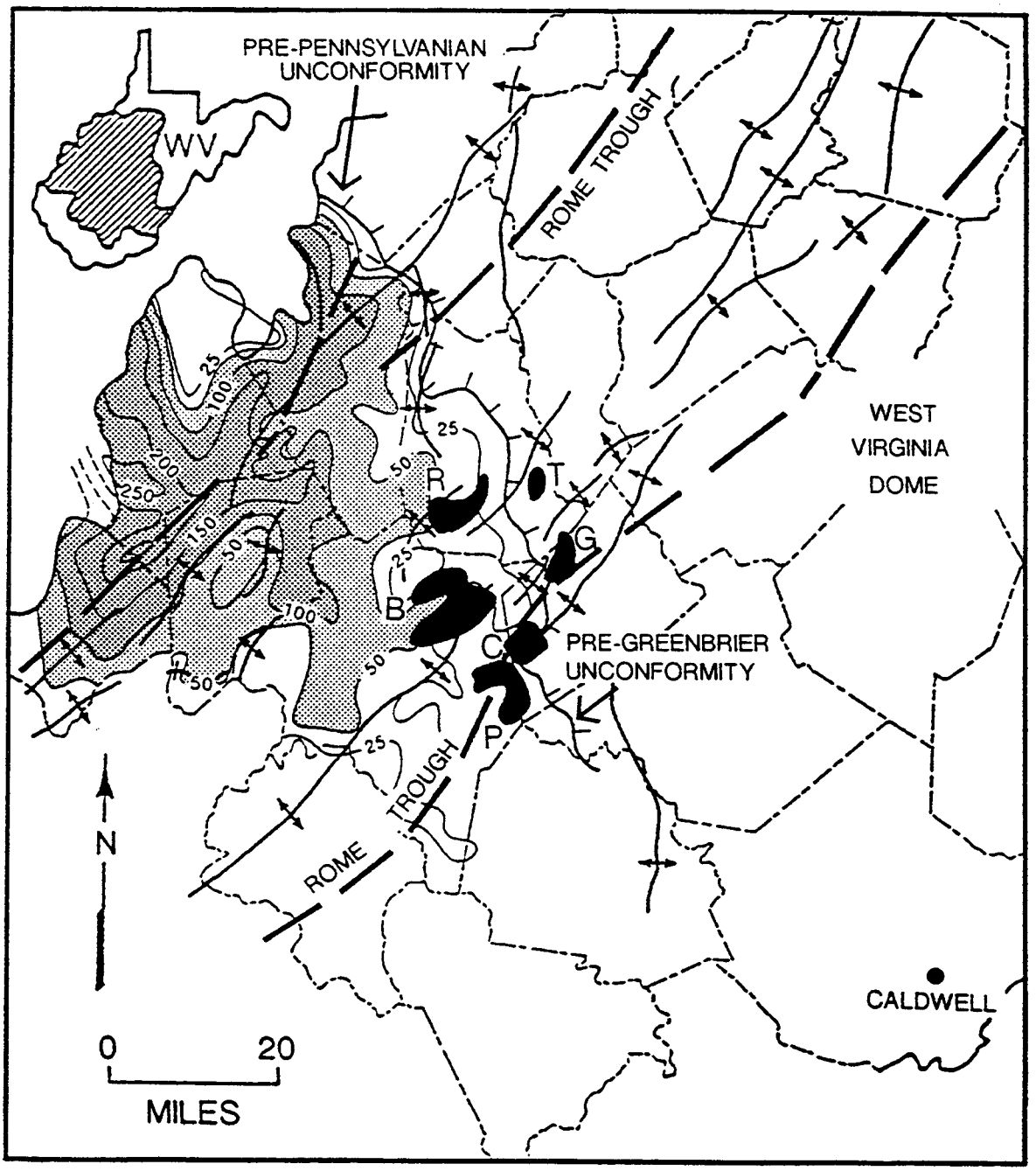

FIGURE 19. Isolith map of the "Maccrady" Big Injun sandstones, superimposed with some major structures, in western West Virginia (modified from Zou and Donaldson, 1991). (B: Blue Creek field, C: Clendenin field, G: Granny Creek field, P: Pond Fork field, R: Rock Creek field, T: Tariff field). Units are feet.

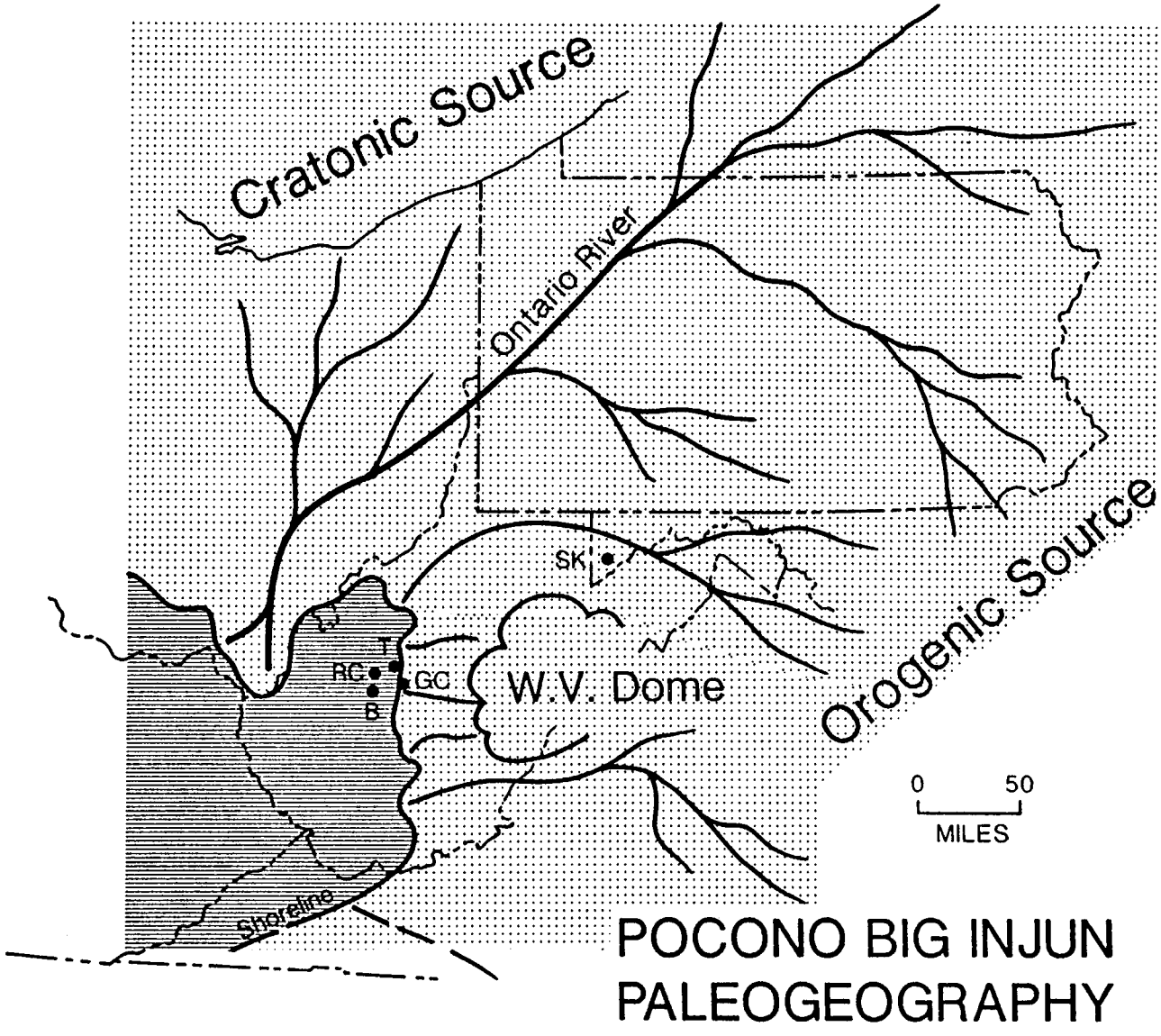

FIGURE 20. Paleogeographic map for Pocono Big Injun time showing ancient river systems and shoreline positions relative to locations of four oil fields. (T: Tariff field, RC: Rock Creek field, GC: Granny Creek field, B: Blue Creek field, SK: Big Injun outcrop in Oakland, MD).

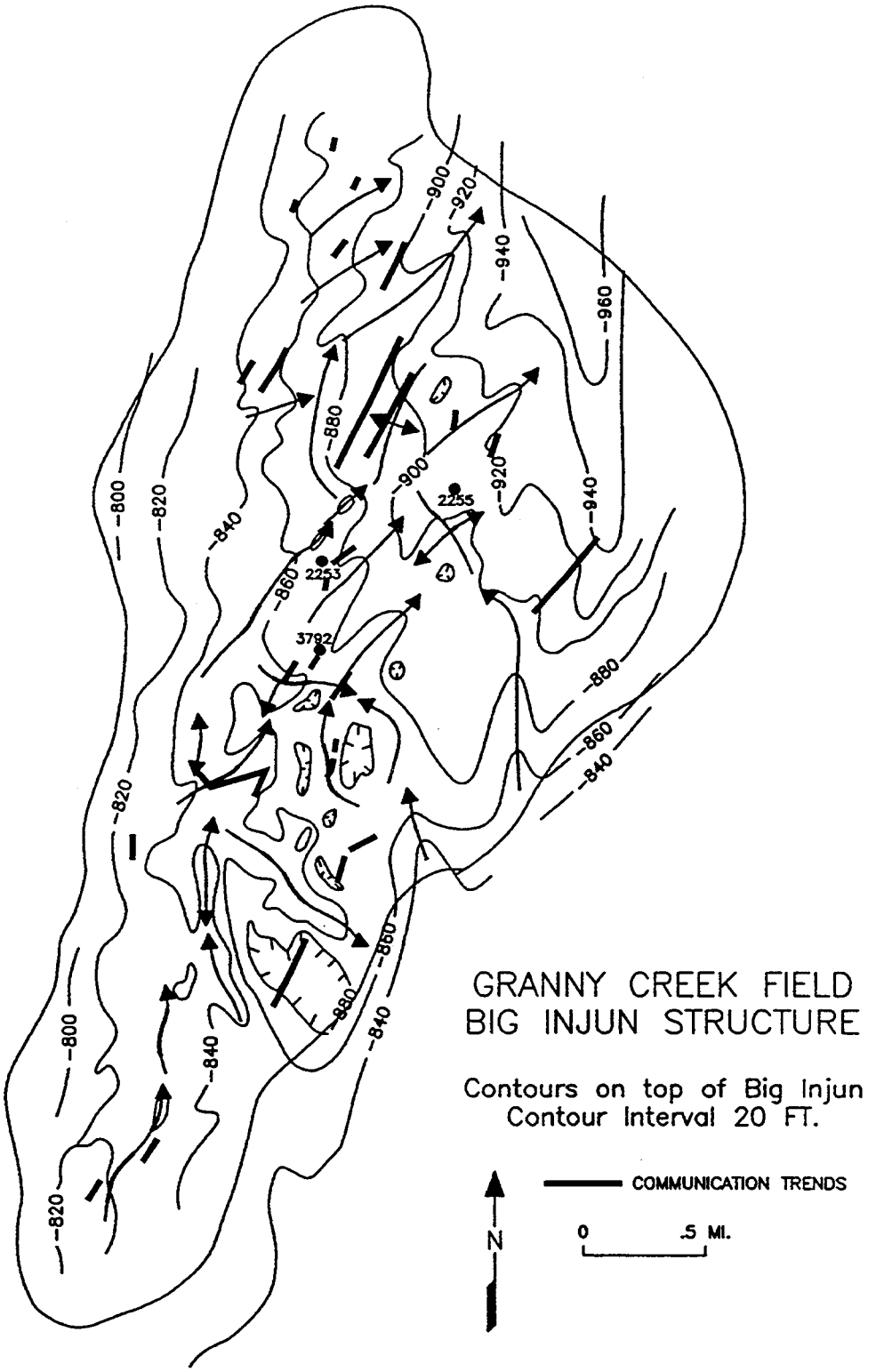

FIGURE 21. Granny Creek structure contour map drawn on the top of the Big Injun sandstone. Axes of interpreted folds (arrows) and traces of interpreted faults (thick lines) are superimposed. Contour interval is 20 feet.

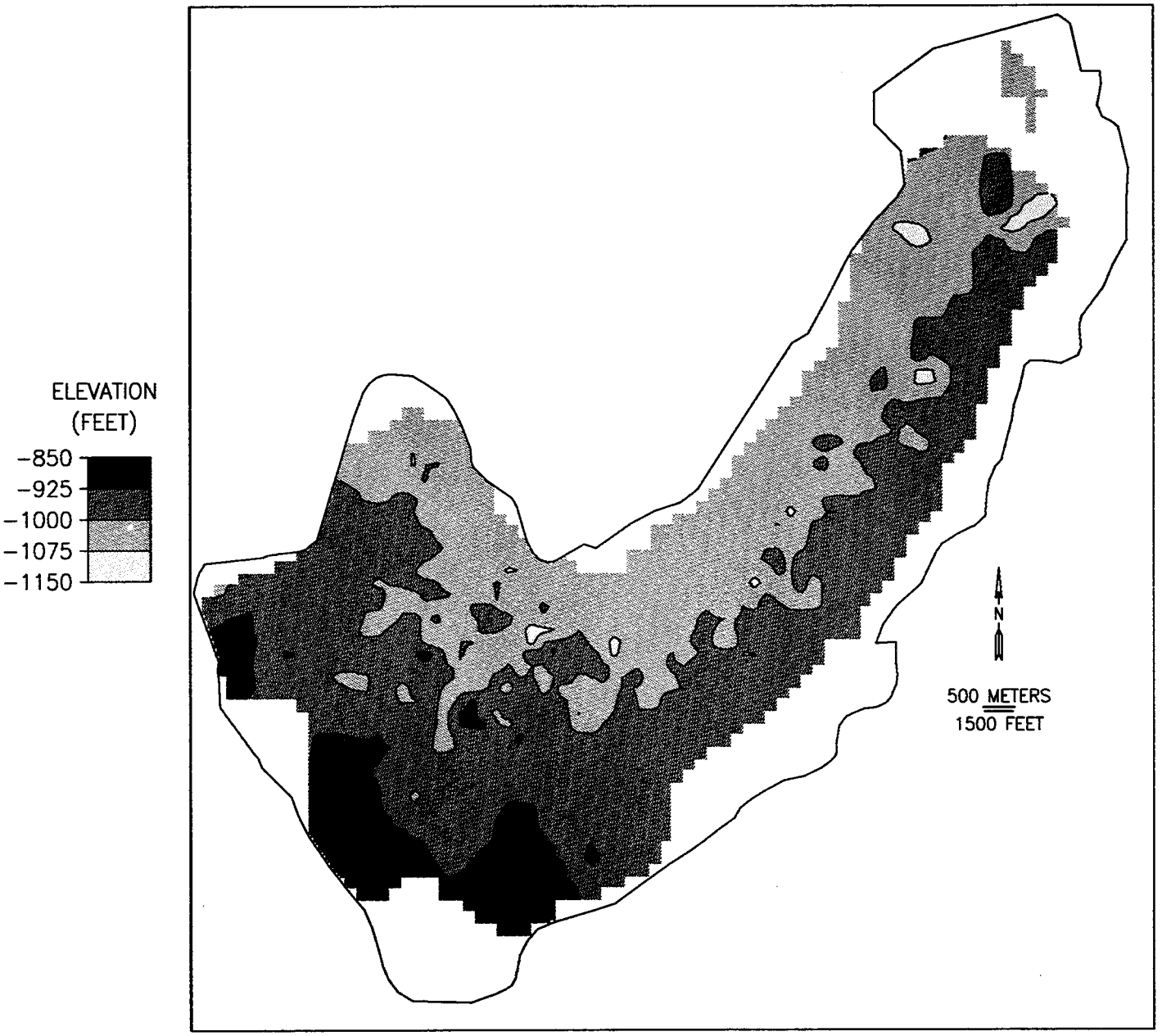

FIGURE 22. Rock Creek structure contour map drawn on the top of the Loyalhanna limestone (as identified by drillers). Contour interval is 75 feet.

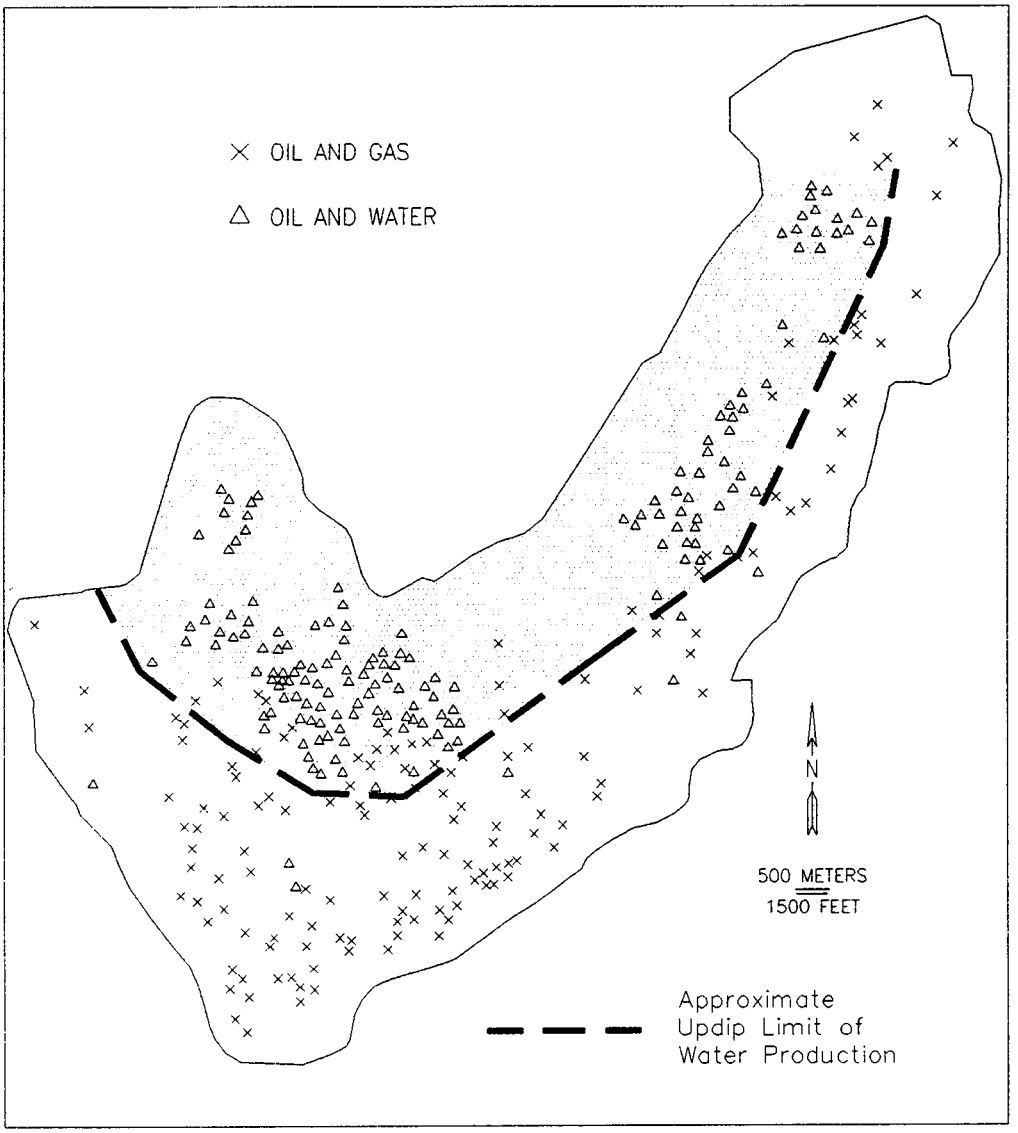

FIGURE 23. Distribution map showing Rock Creek wells reporting initial production of oil-water and oil-gas fluid.

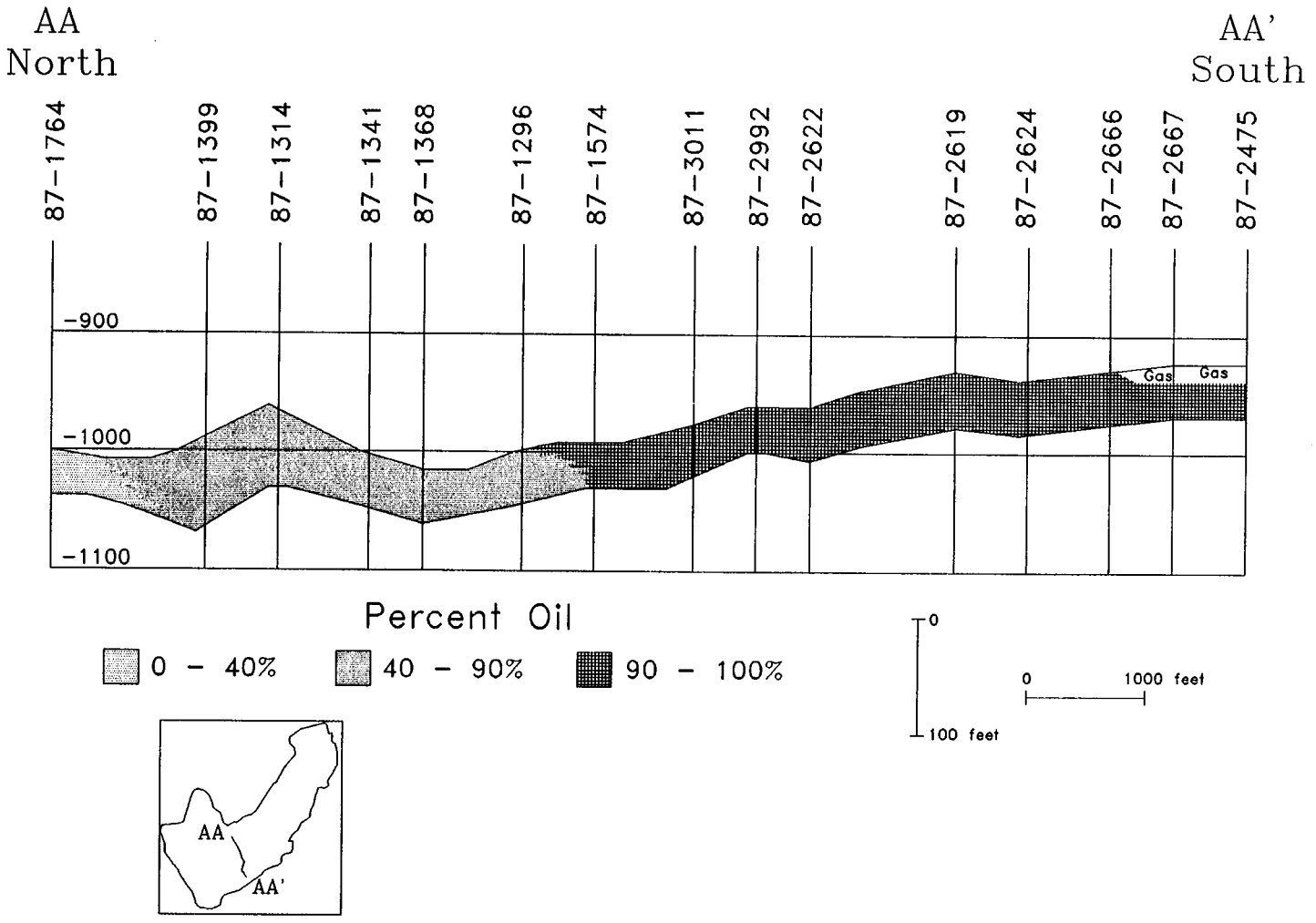

FIGURE 24. Structural cross section for Rock Creek. Superimposed shading shows oil as percentage of total initial fluid produced.

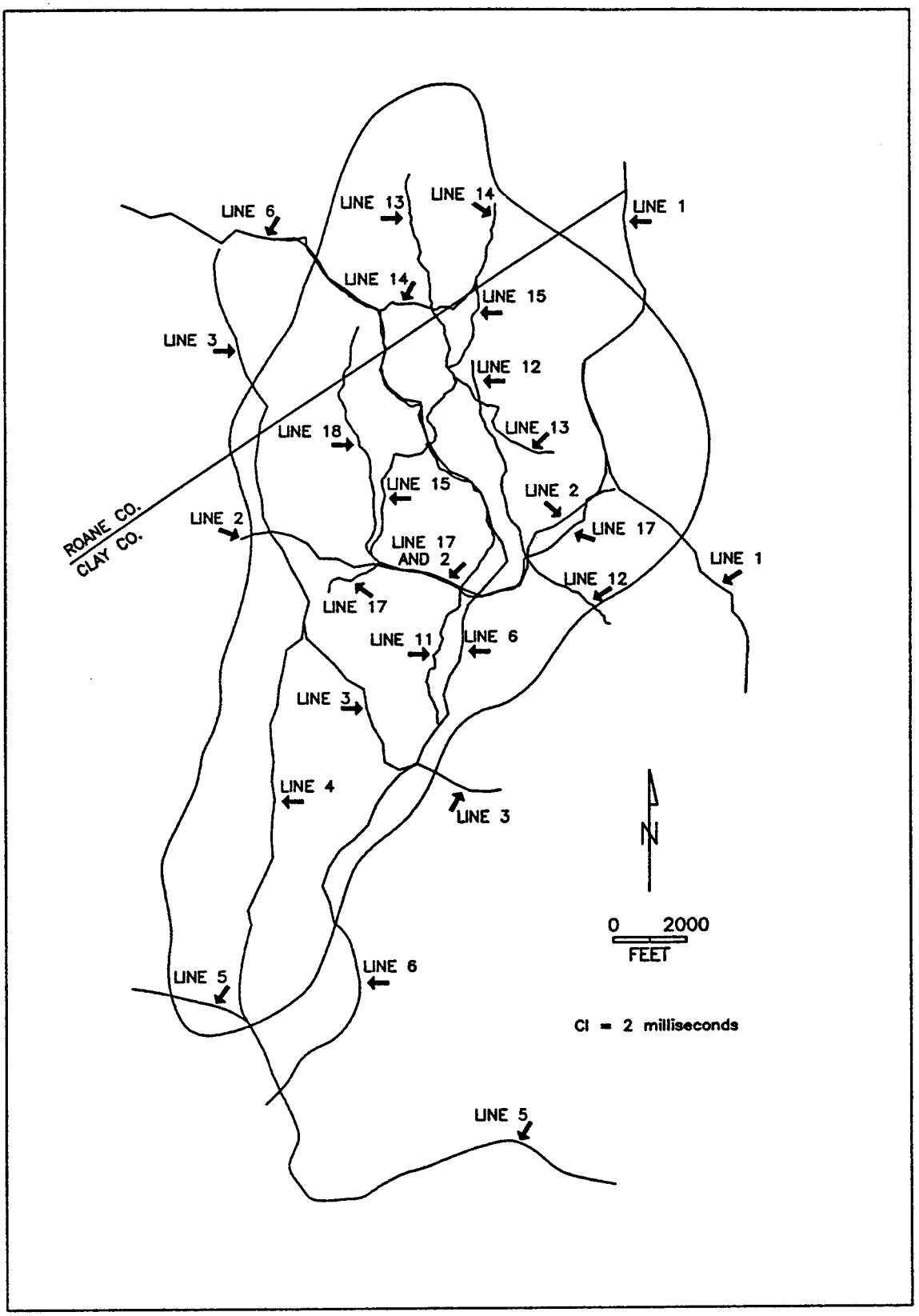

FIGURE 25. Seismic line location for Granny Creek field.

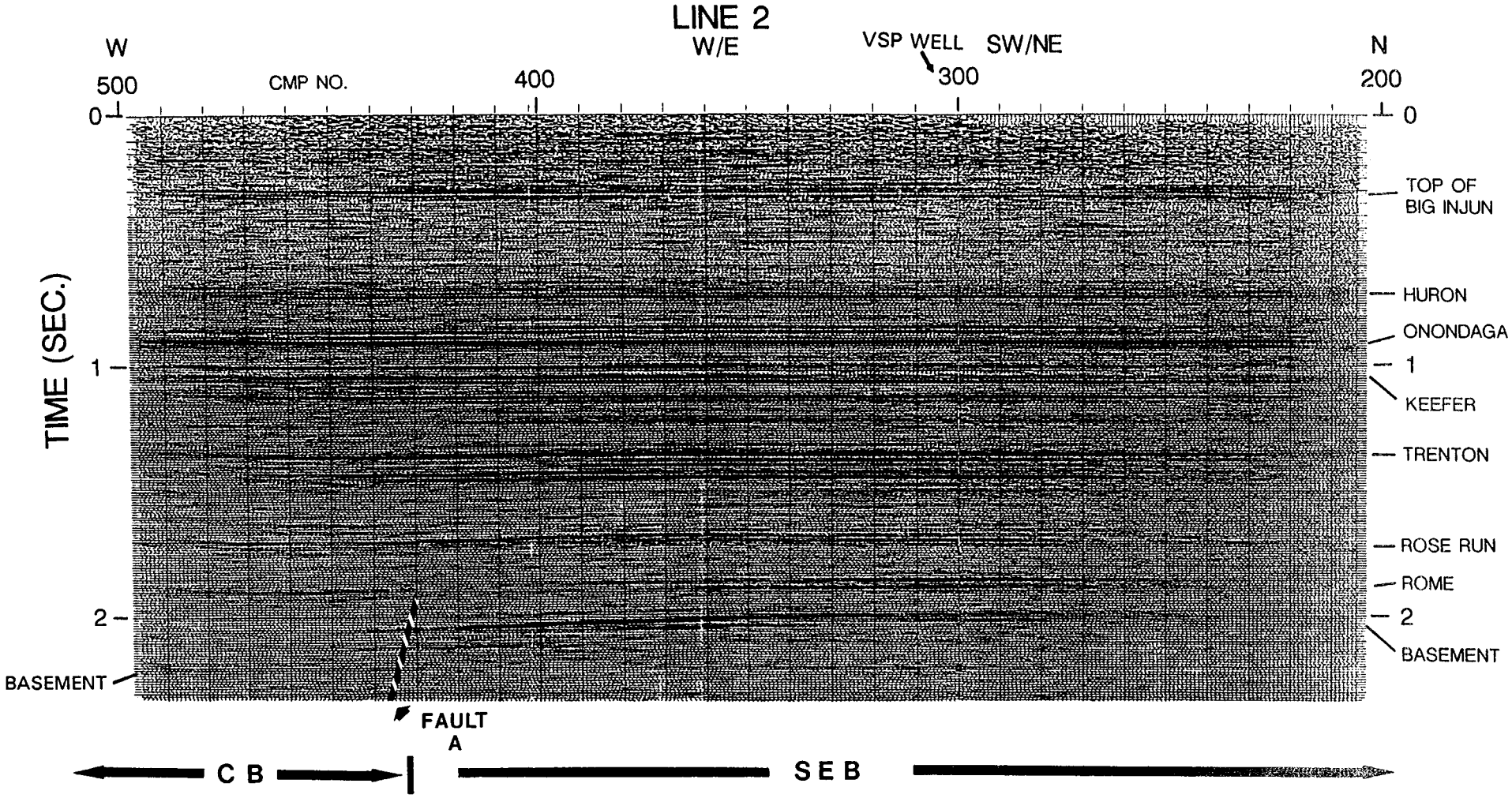

FIGURE 26. Reflection events, basement block and major basement fault (A) are identified on seismic Line 2 across Granny Creek field.

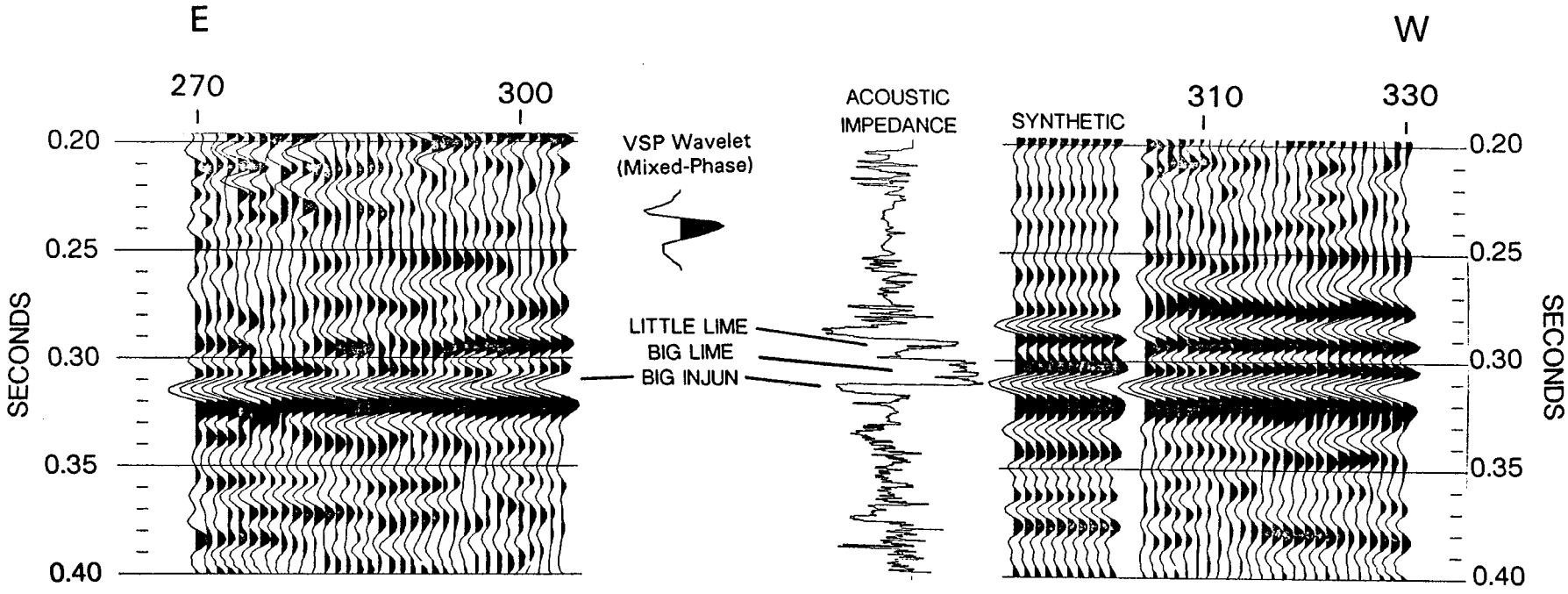

FIGURE 27. Synthetic seismogram compiled from sonic and density logs from Clay 2509 and then inserted into Vibroseis data (Line 2) near the well.

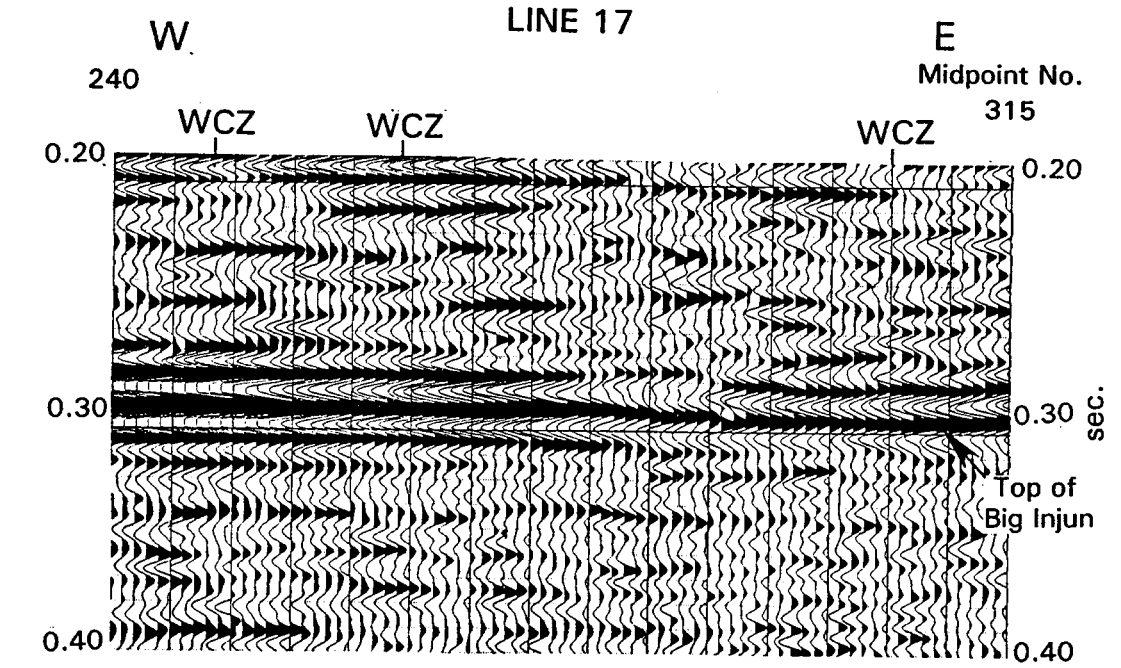

A. Weight Drop

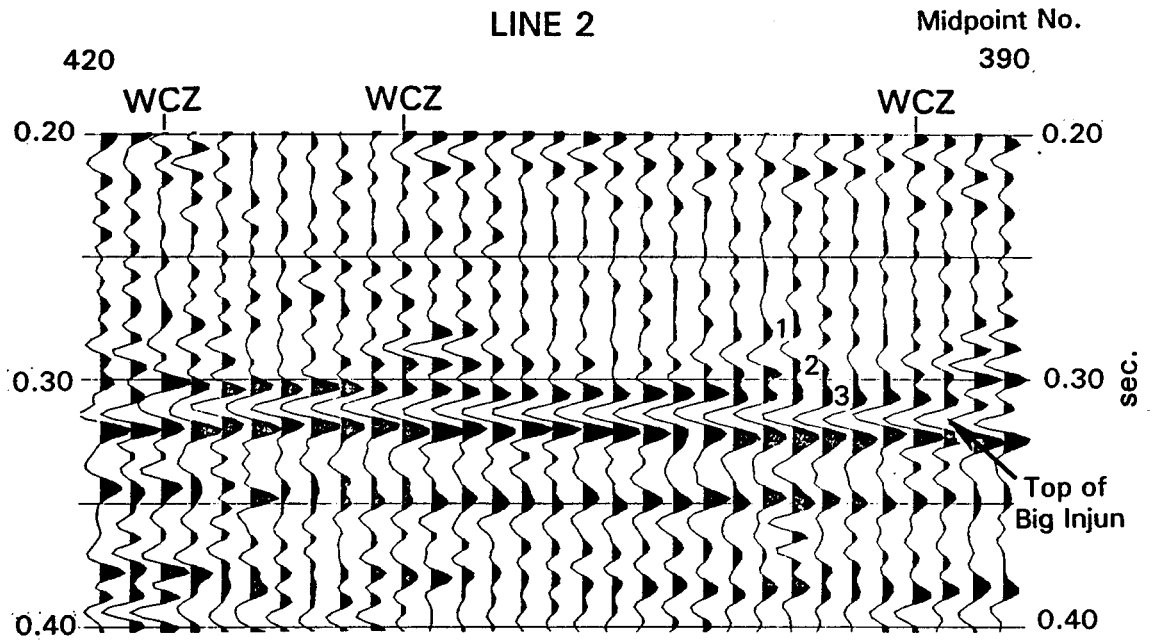

B. Vibroseis

FIGURE 28. Seismic data for coincident parts of seismic Lines 17 and 2, Granny Creek field. (a) Segment of weight-drop data from Line 17; (b) Segment of Vibroseis Line 2 after Berkhout Klauder wavelet deconvolution (see Appendix E).

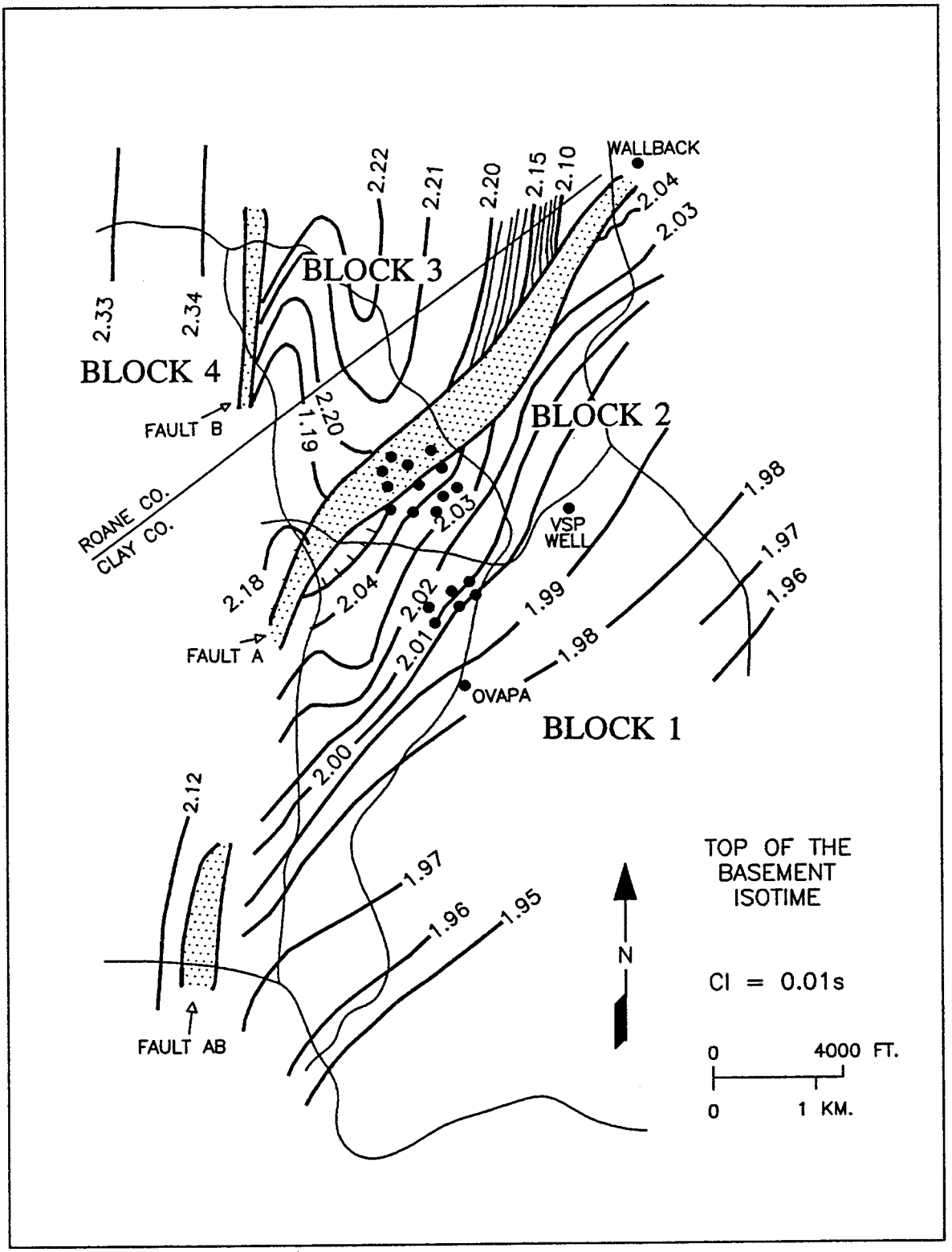

FIGURE 29. Basement isotime map. Fault gaps represent the edges of the blocks as observed in the seismic data. Locations of the Vibroseis lines are also shown. Contour interval is 0.01 seconds.

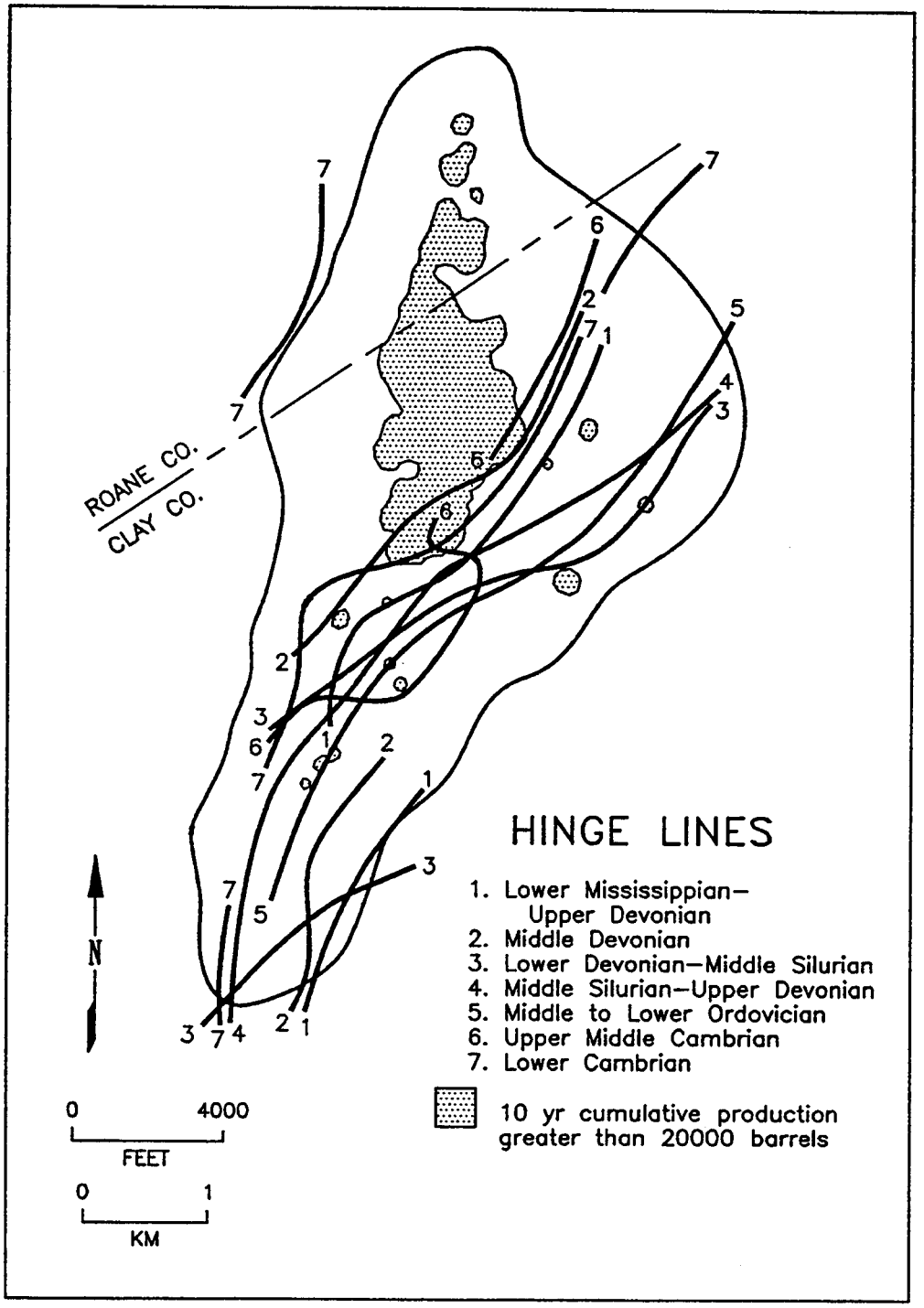

FIGURE 30. Hinge lines about which basement blocks A and AB subsided to the northwest and west, respectively, Hinge lines are plotted for various periods of time throughout the Paleozoic.

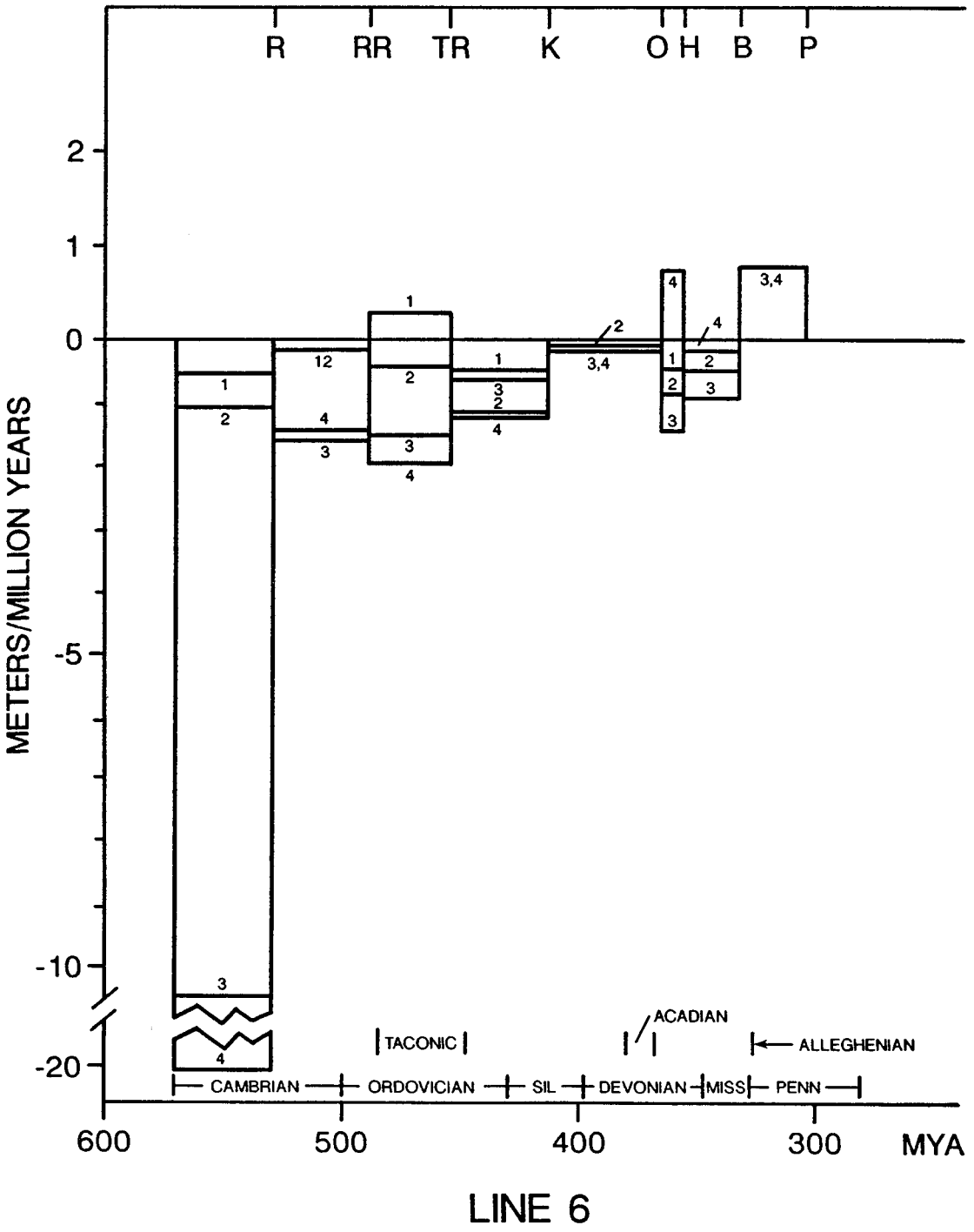

FIGURE 31. Basement subsidence rates are plotted against time throughout the Paleozoic. The basement is subdivided into areas 1 through 4 (southeast to northwest) along Line 6. Subsidence was measured relative to the southeastern end of the line.

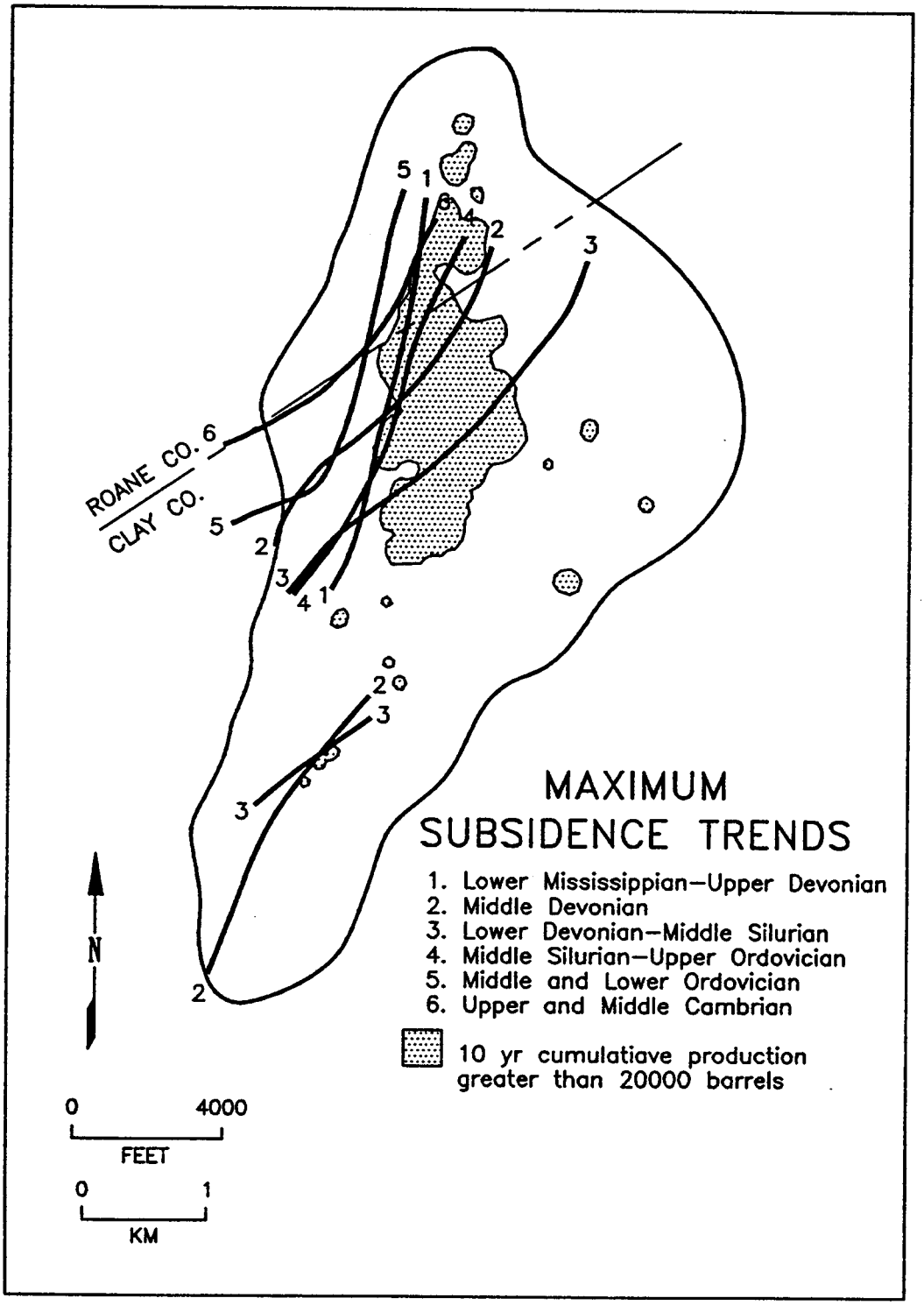

FIGURE 32. Distribution of maximum subsidence trends inferred from seismic isochron maps for Granny Creek field.

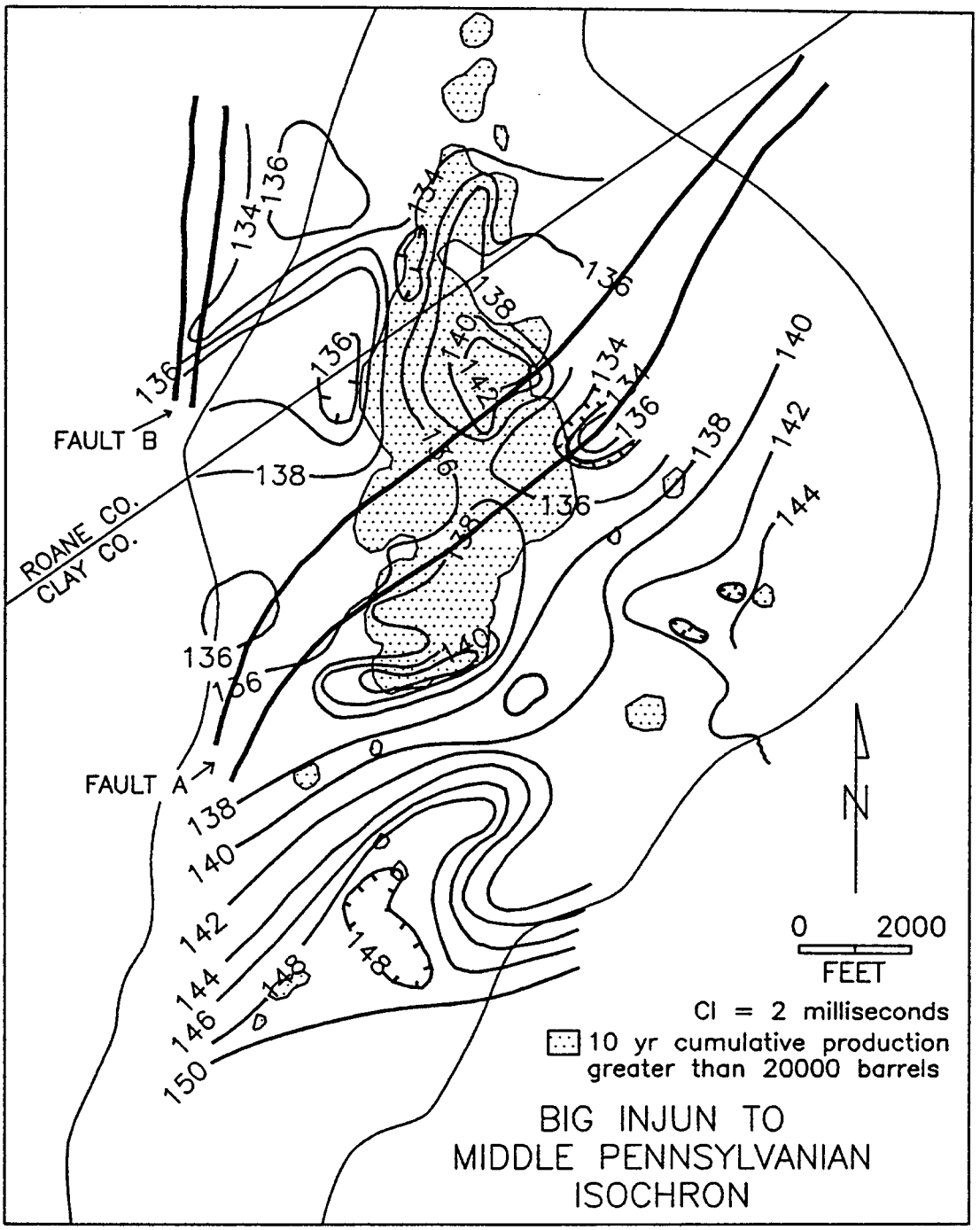

FIGURE 33. Big Injun-to-shallow Pennsylvanian isochron map for Granny Creek field with Faults A and B superimposed. Contour interval is 2 milliseconds.

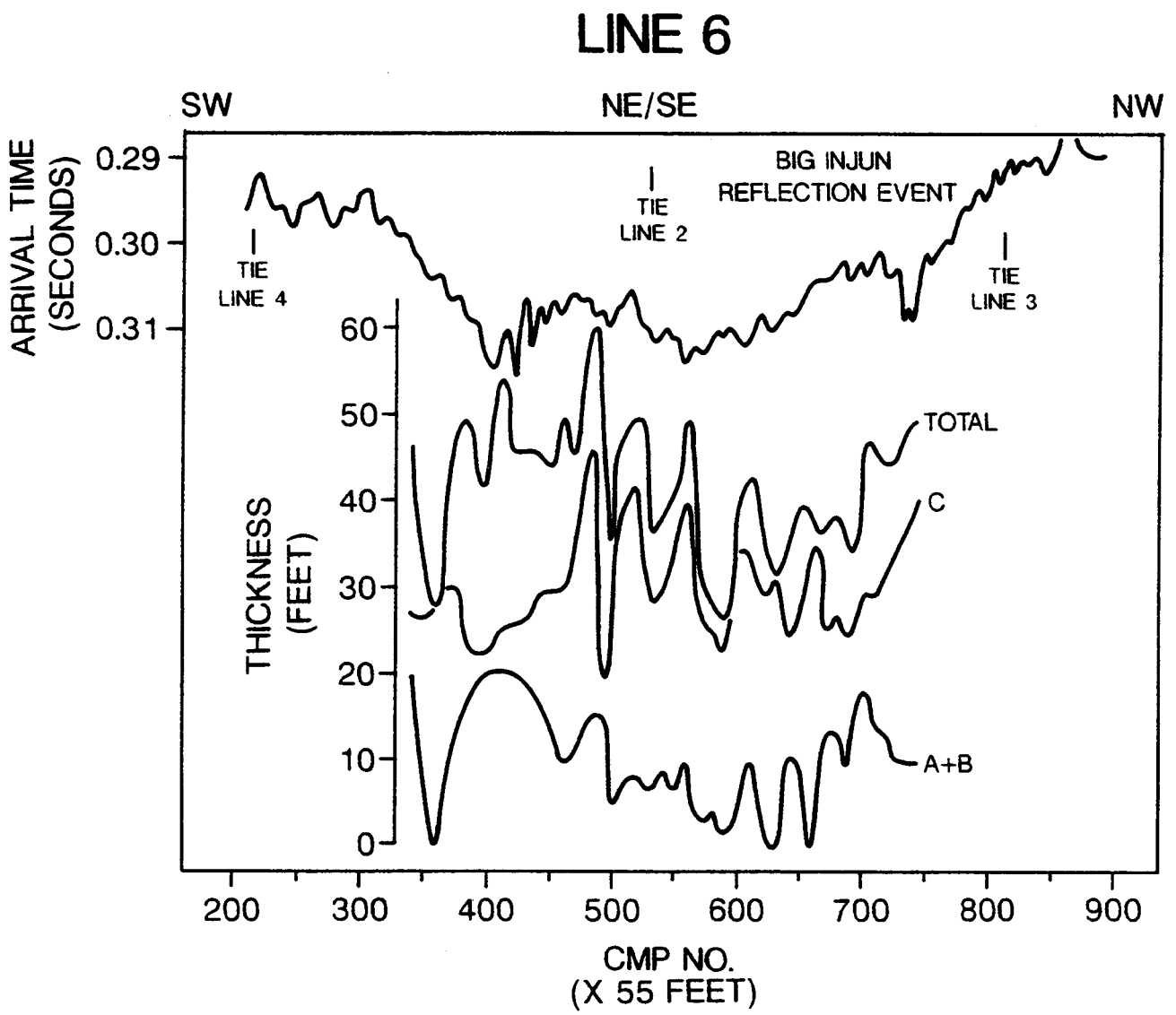

FIGURE 34. Thickness of the A, B, and C subdivisions of the Big Injun sandstone (Bagnall, 1975) along with total thickness plotted for comparison to reflections arrival time variations for the top-of-Big Injun event along Line 6.

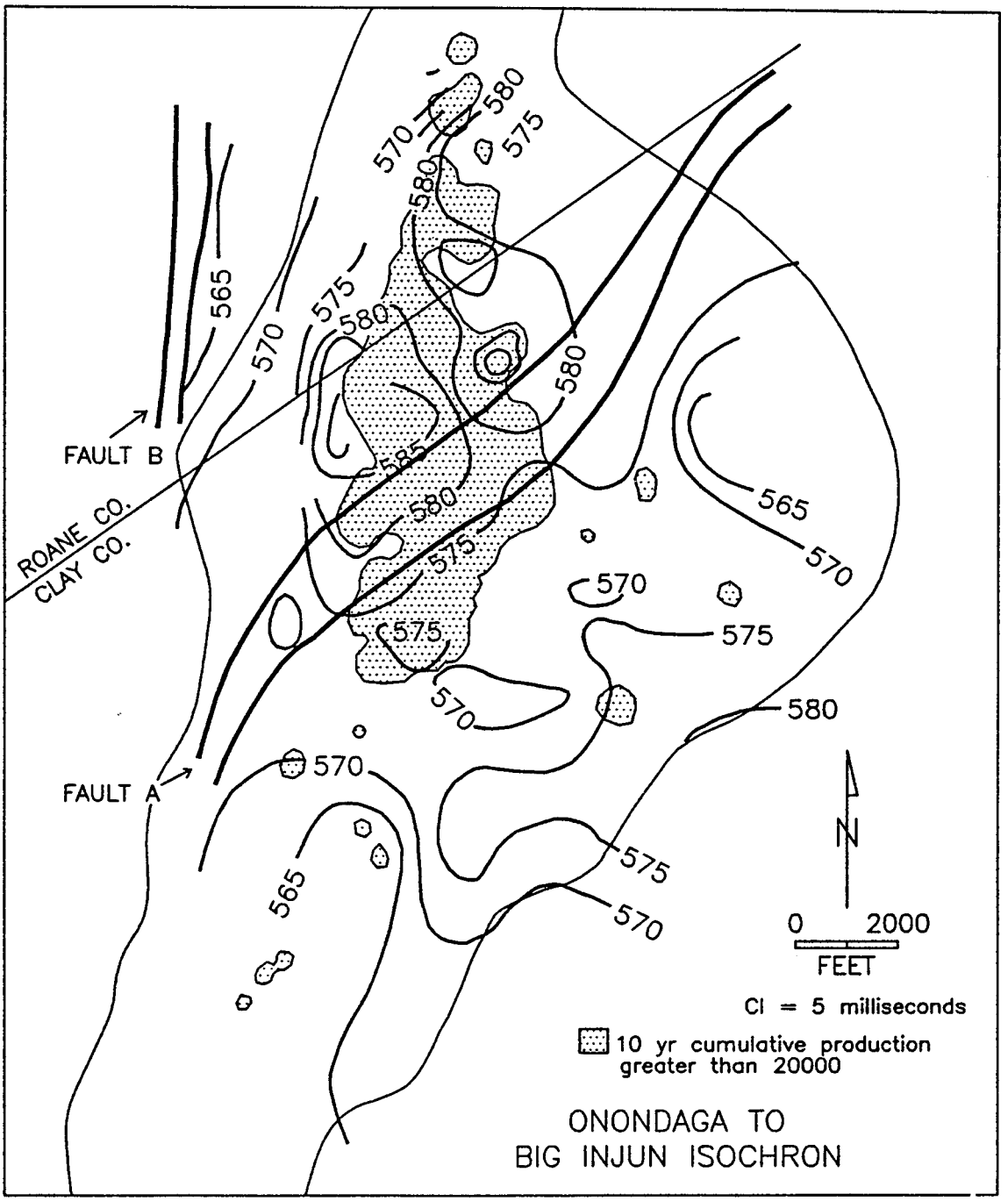

FIGURE 35. Big Injun-to-Onondaga isochron map for Granny Creek field with Faults A and B superimposed. Contour interval is 5 milliseconds.

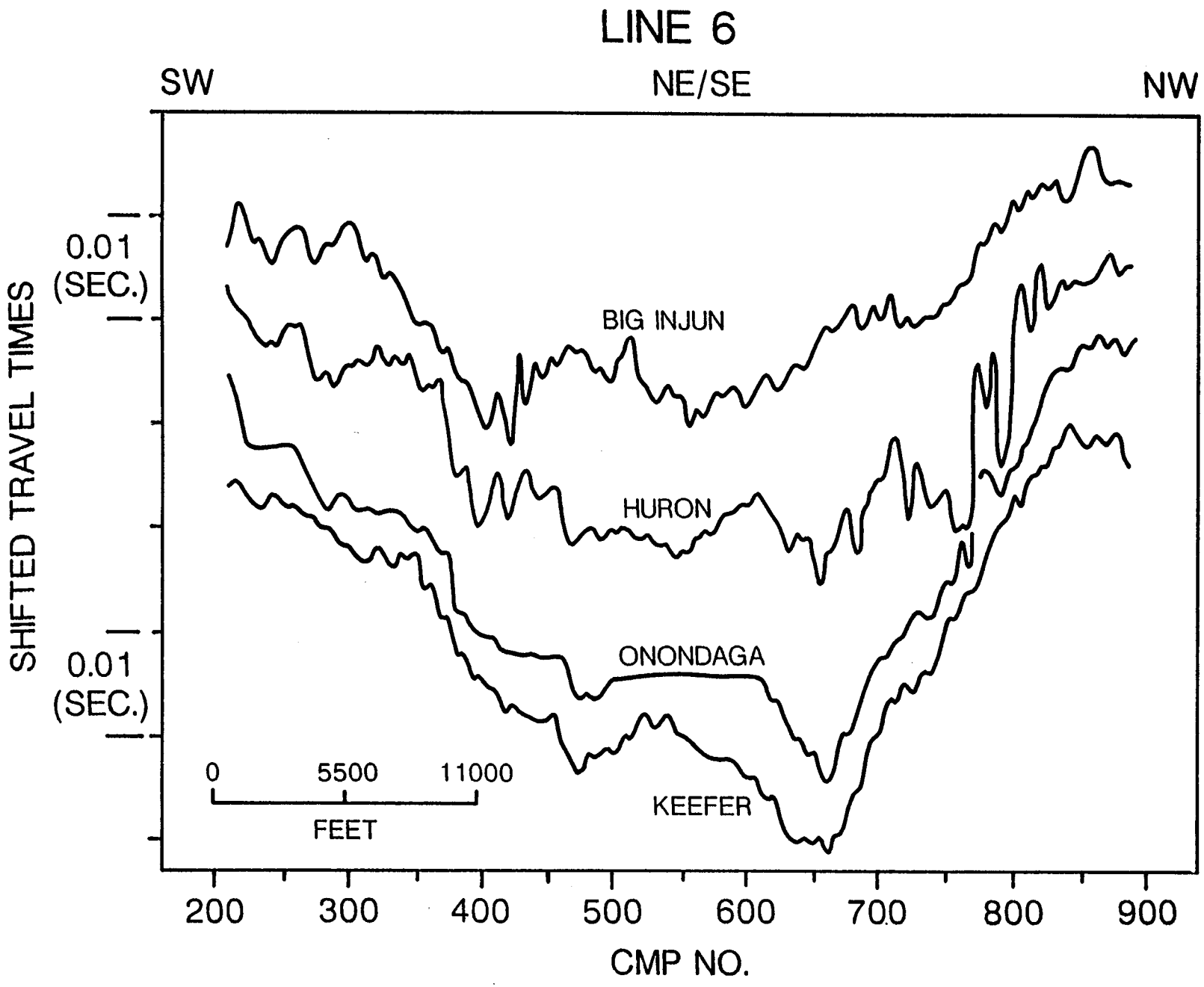

FIGURE 36. Travel times to reflectors observed on Line 6 shifted relative to each other and plotted for comparison.

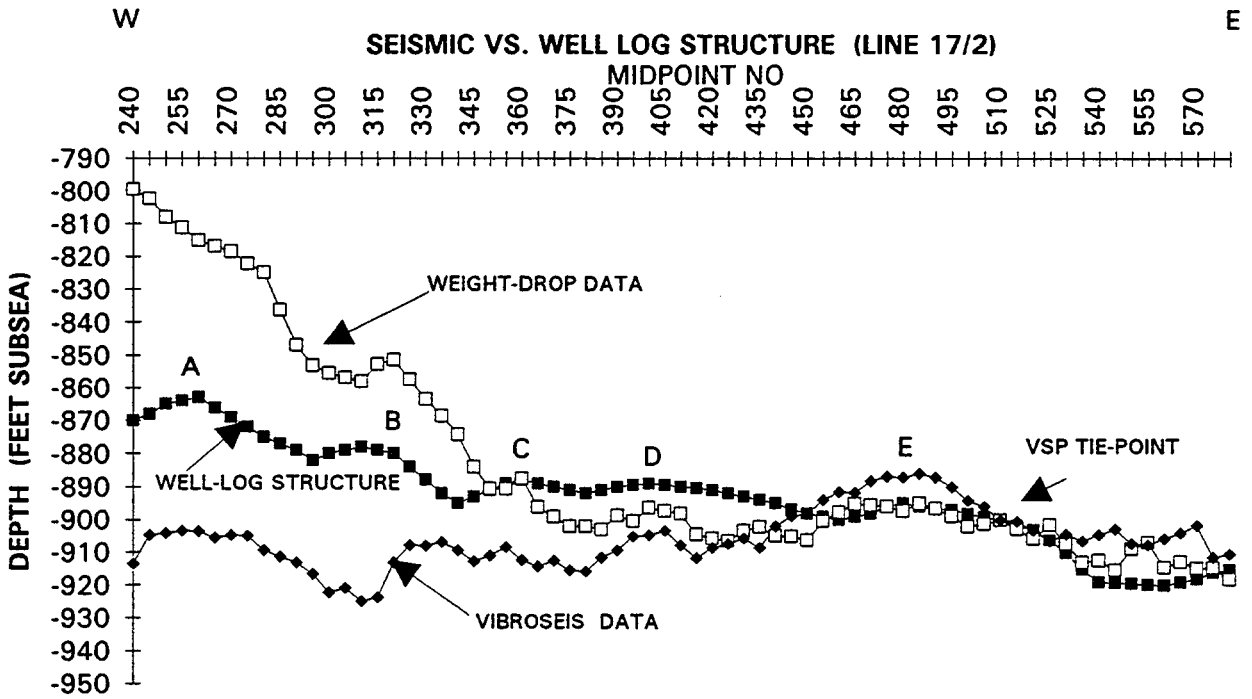

FIGURE 37. Well-log structure along seismic Lines 2 and 17 compared with depth to the top of the Big Injun as computed from seismic travel times.

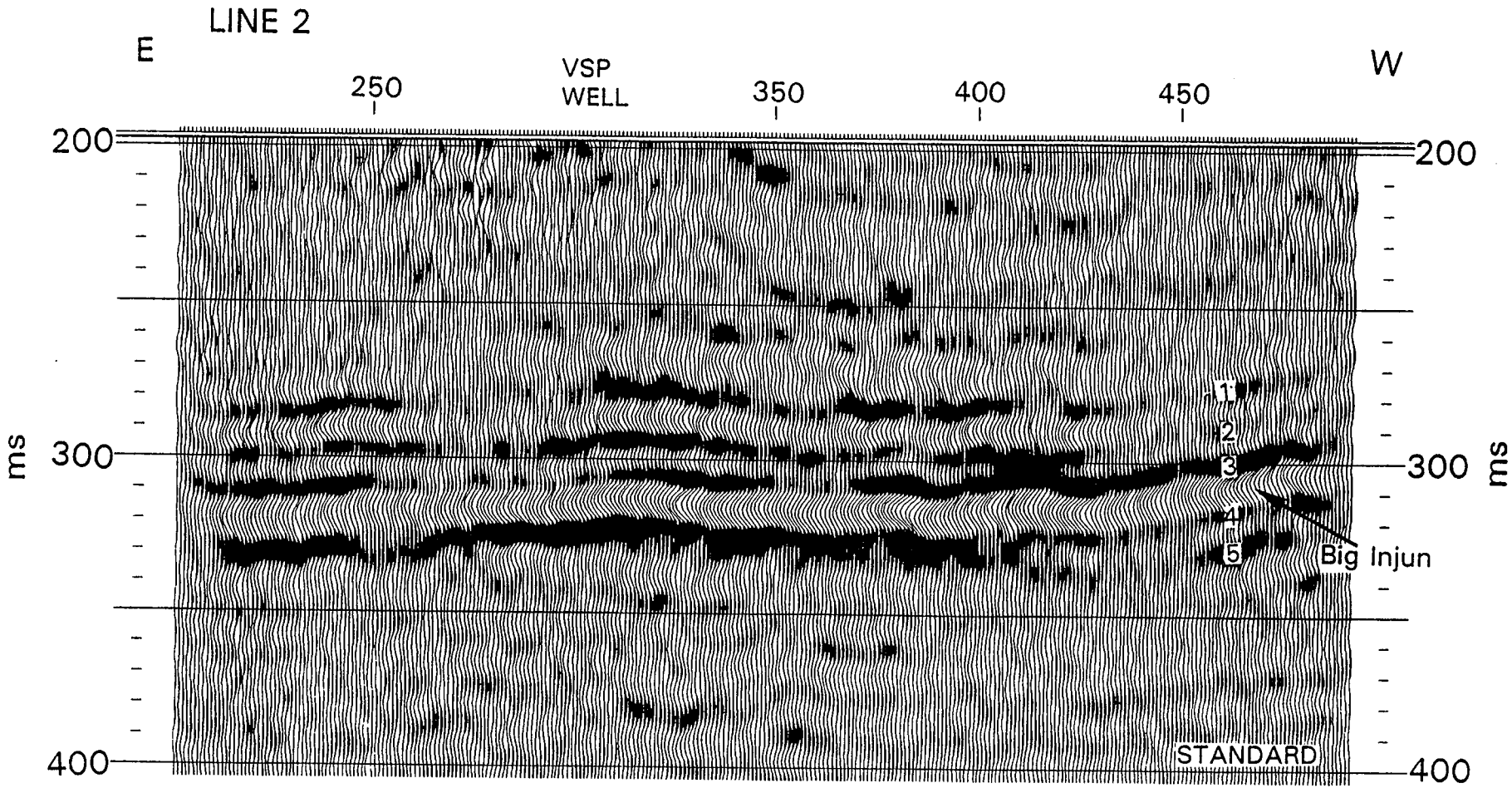

FIGURE 38. Window of data along Line 2 including the Big Injun reflection event at approximately 0.31 seconds shown after the initial processing of the line.

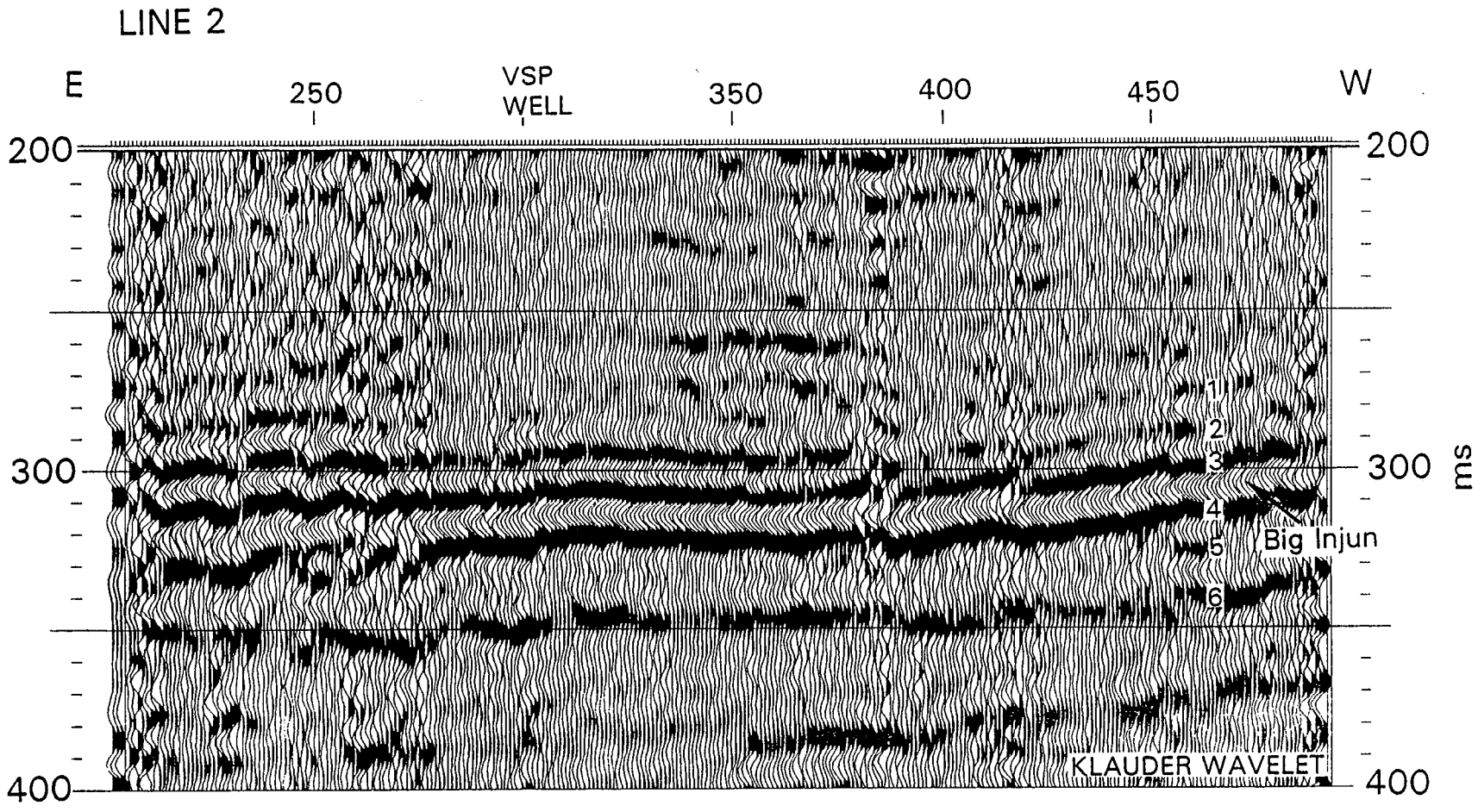

FIGURE 39. Same window of data shown in Figure 38 after reprocessing.

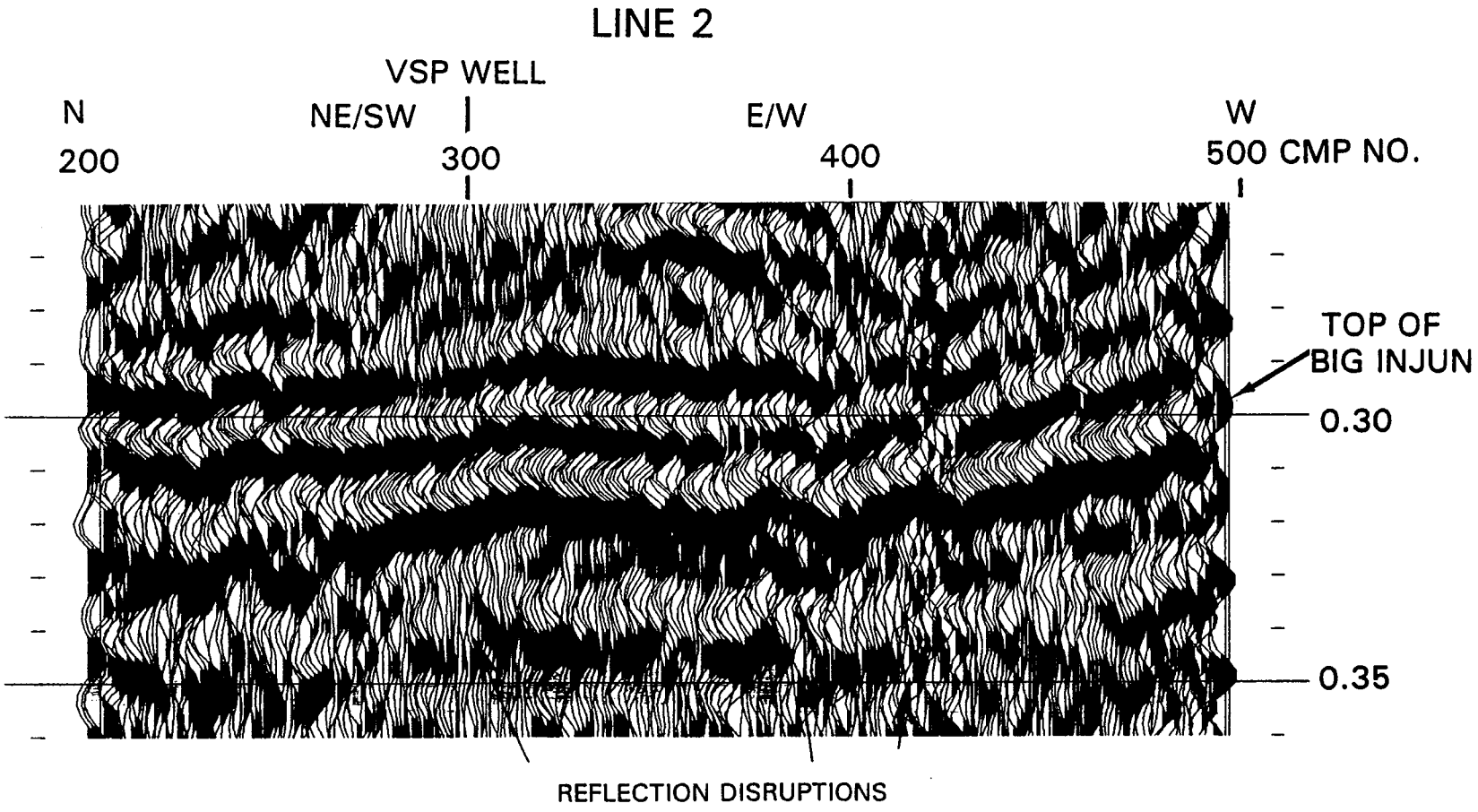

FIGURE 40. Enlargement of reprocessed seismic data from Figure 39.

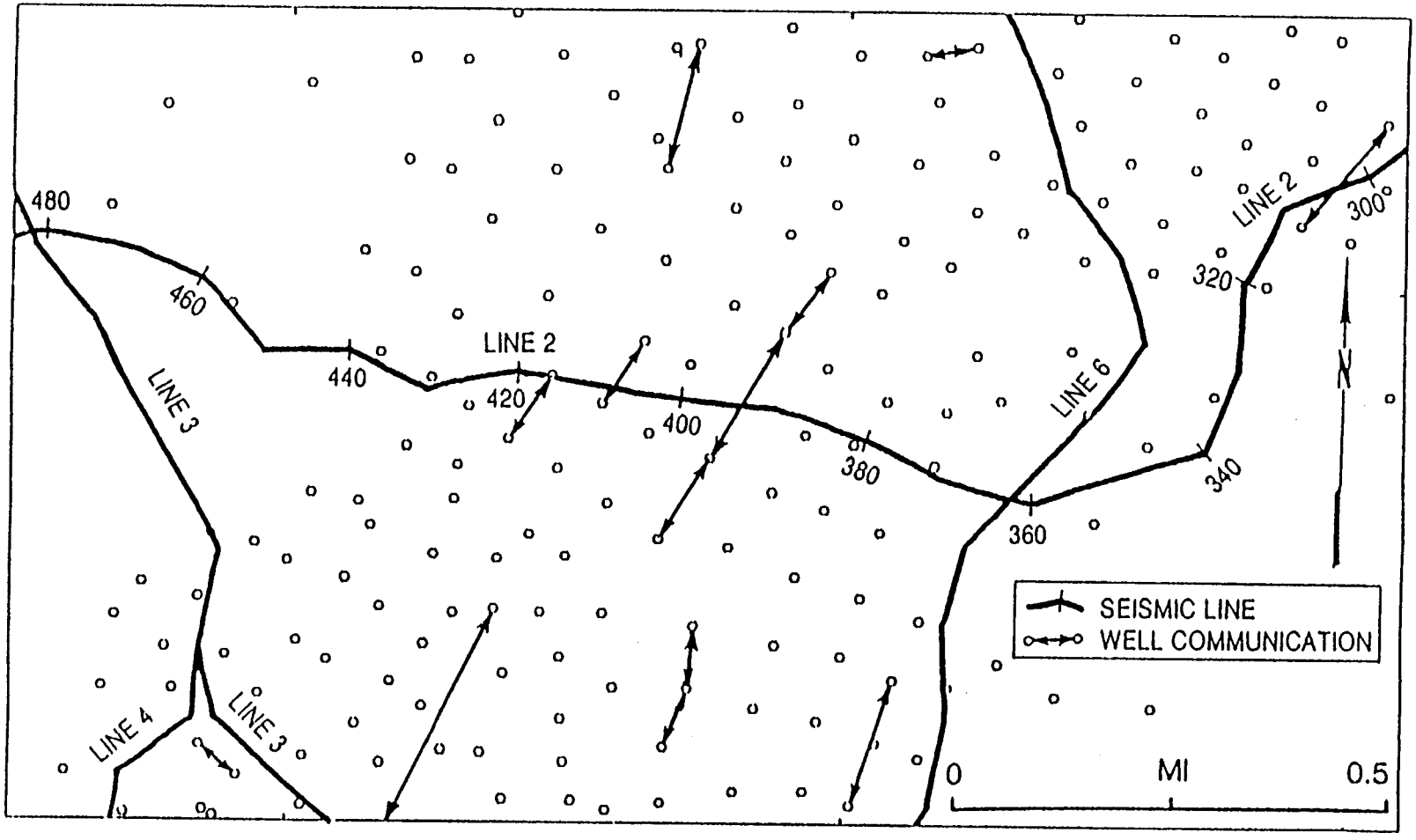

FIGURE 41. Midpoint map for Line 2 along its western end showing the location of wells where communication problems were encountered. Communication near Line 2 midpoints 395 and 417 coincides closely with reflection disruptions and a small fold in the composite Big Injun reflection event. NOTE: Line 17 coincides with Line 2 in this area.

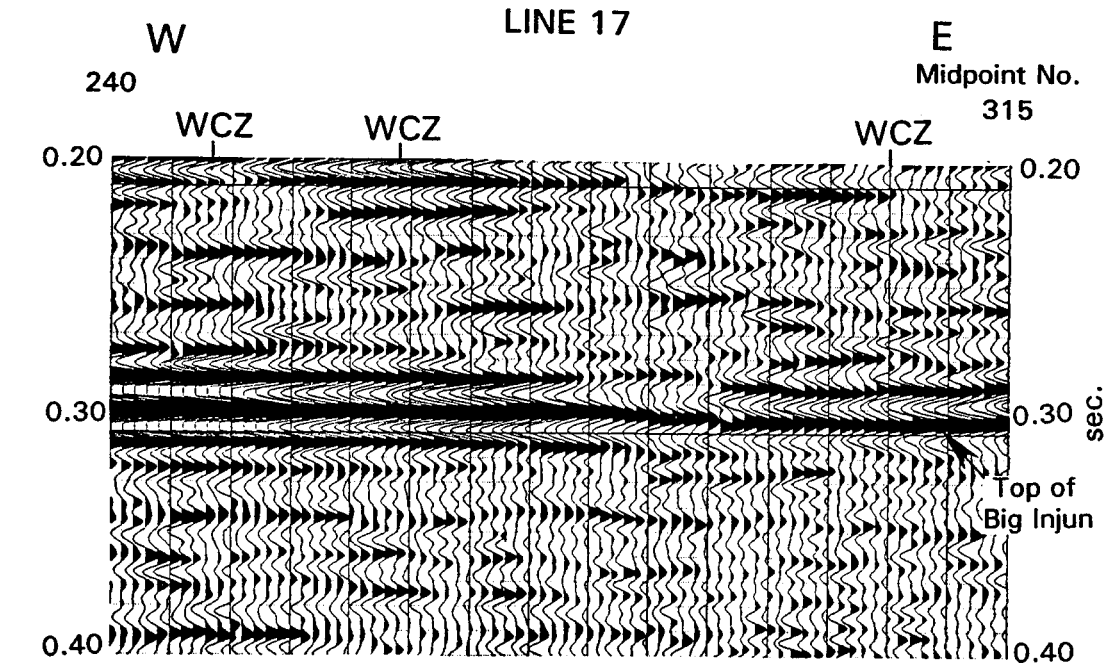

A. Weight Drop

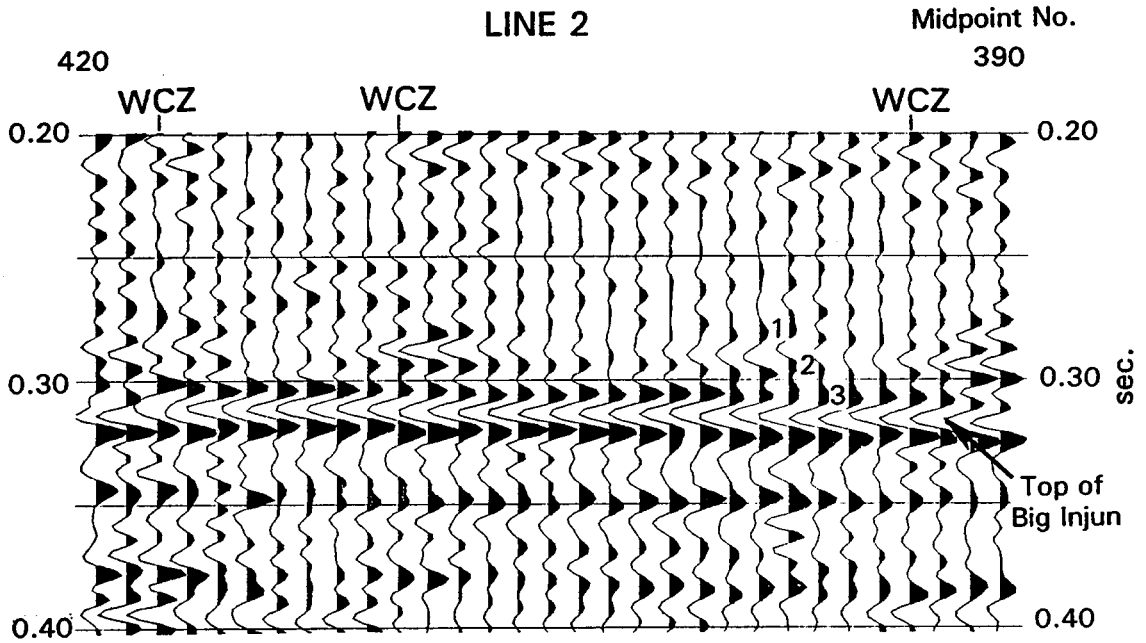

B. Vibroseis

FIGURE 42. Comparison of high resolution seismic data to reprocessed Vibroseis data near communicating wells (Figure 41). (a) High resolution data (midpoints 240 to 315) along Line 17; (b) Reprocessed Vibroseis data from Line 2 (midpoints 420 to 390). WCZ = Well Communication Zone.

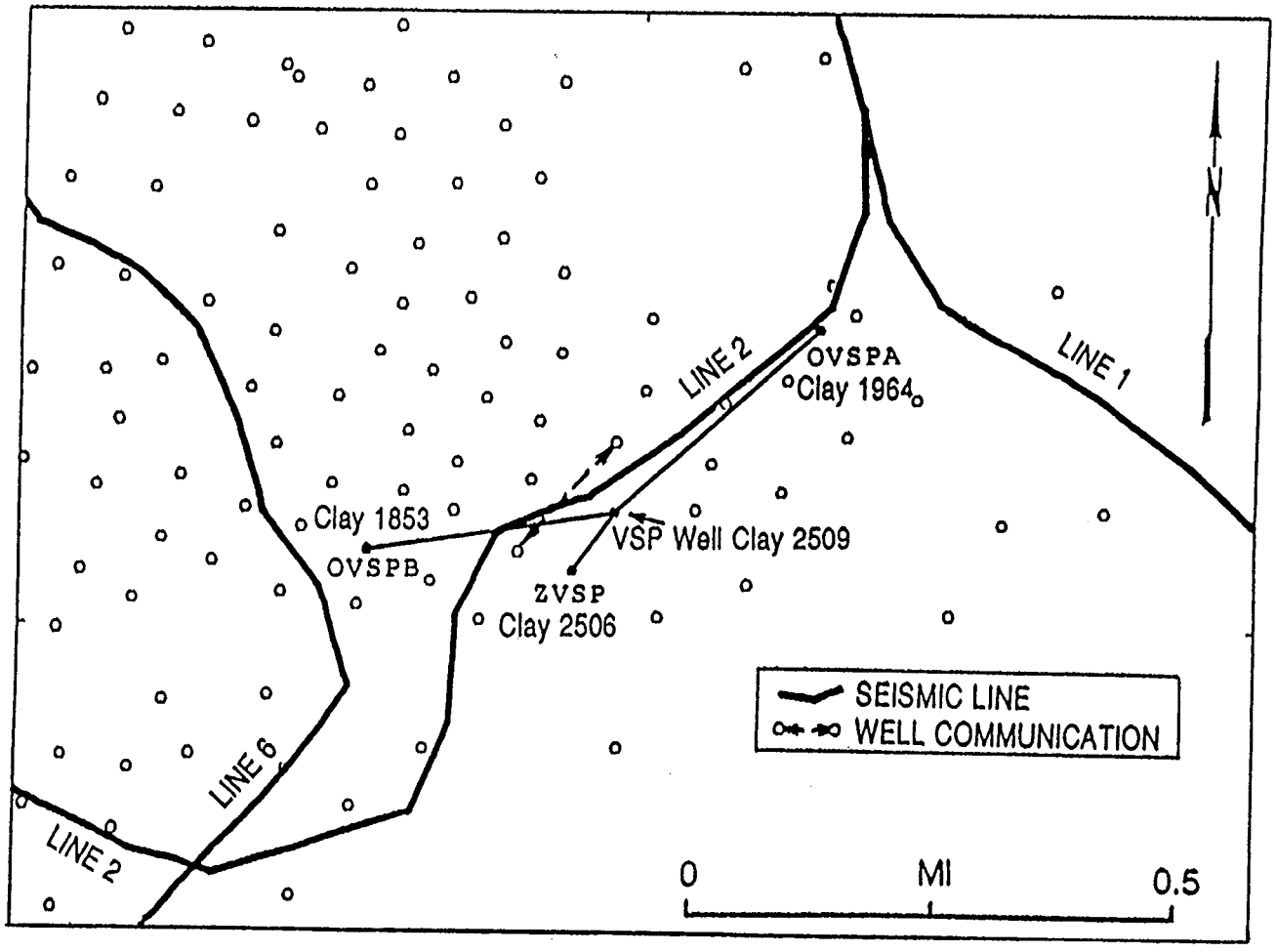

FIGURE 43. Location of three VSP offsets shot in Clay 2509 shown along with the location of two communicating wells.

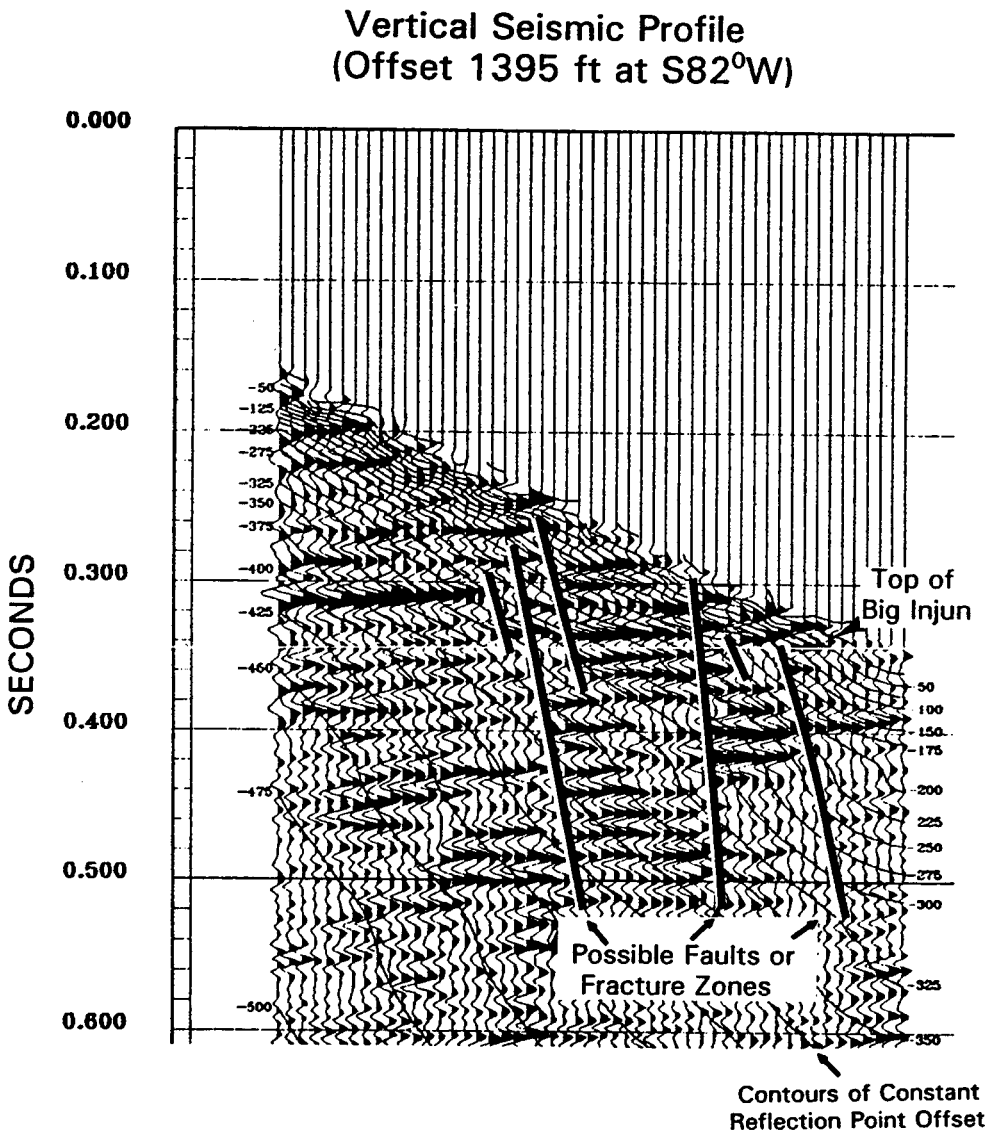

FIGURE 44. Western VSP offset (Figure 43) shown after moveout correction and waveshape deconvolution. Possible faults and fracture zones have been interpreted.

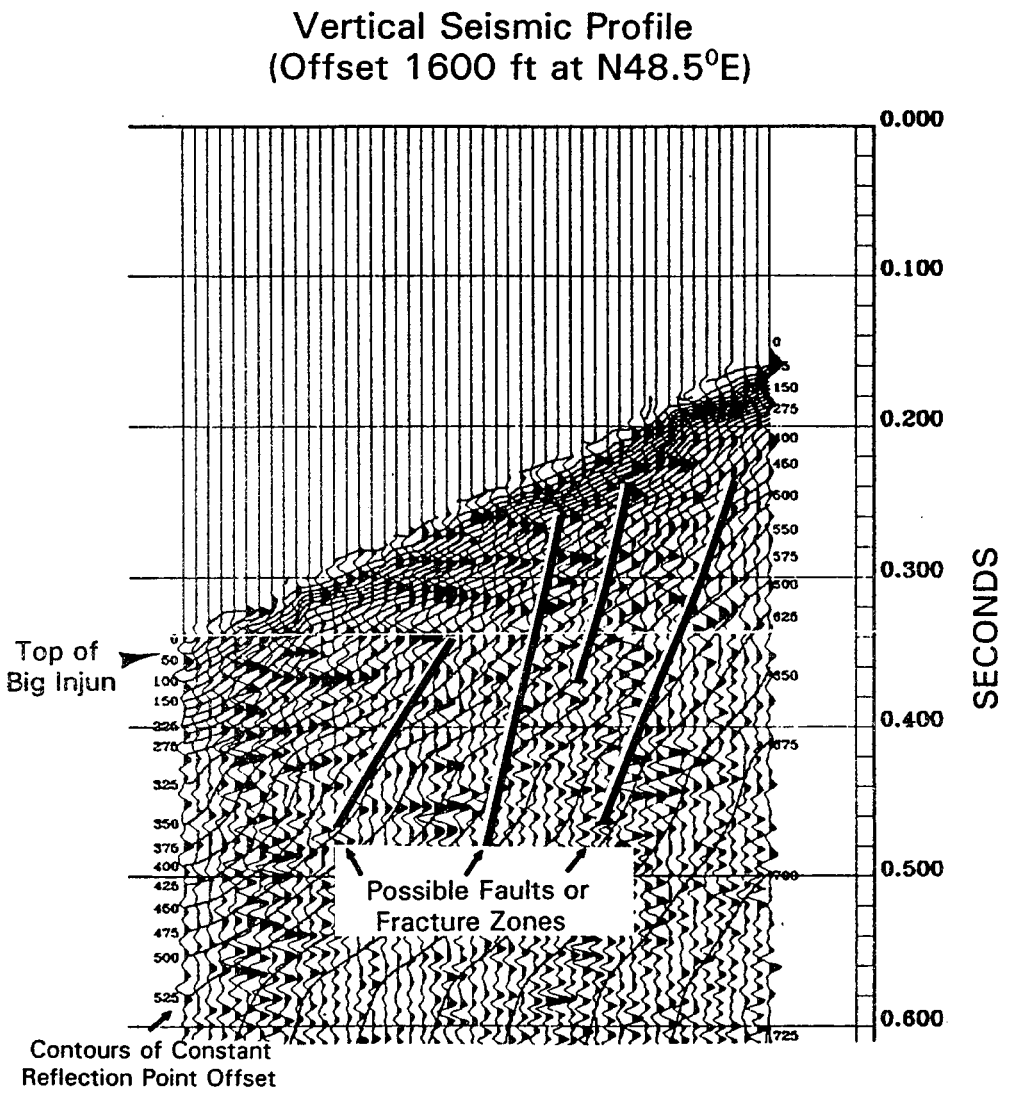

FIGURE 45. Northeastern VSP offset (Figure 43) shown after moveout correction and waveshape deconvolution. Possible faults and fracture zones have been interpreted.

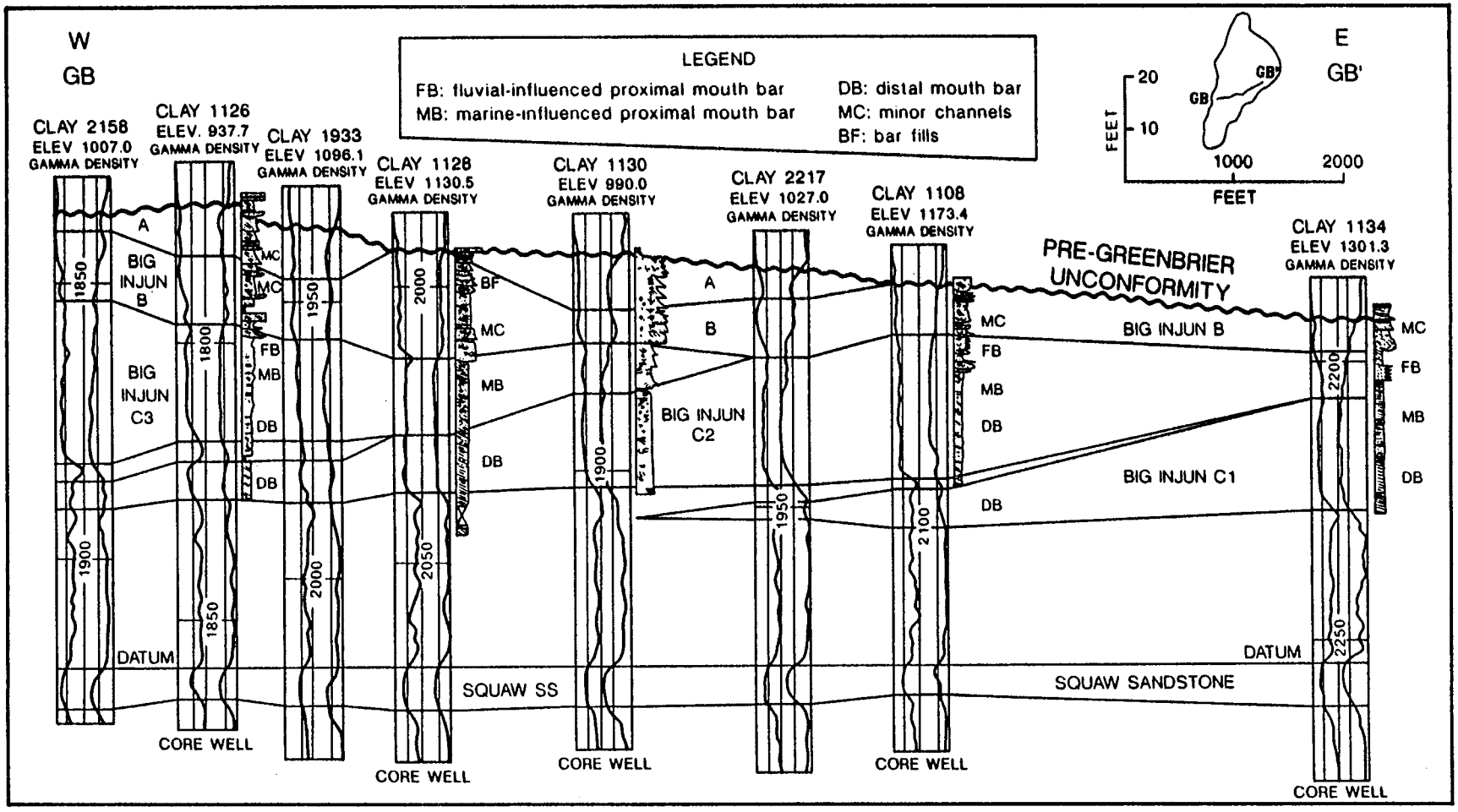

FIGURE 46. Stratigraphic cross section GB-GB' showing members, tongues, and subfacies of Pocono Big Injun. Datum is the top of the Squaw. Cored wells are shown adjacent to their gamma ray and bulk density log signatures. Informal members of the Big Injun (A, B, and C) are identified along with subunits (C1, C2, and C3) and subfacies.

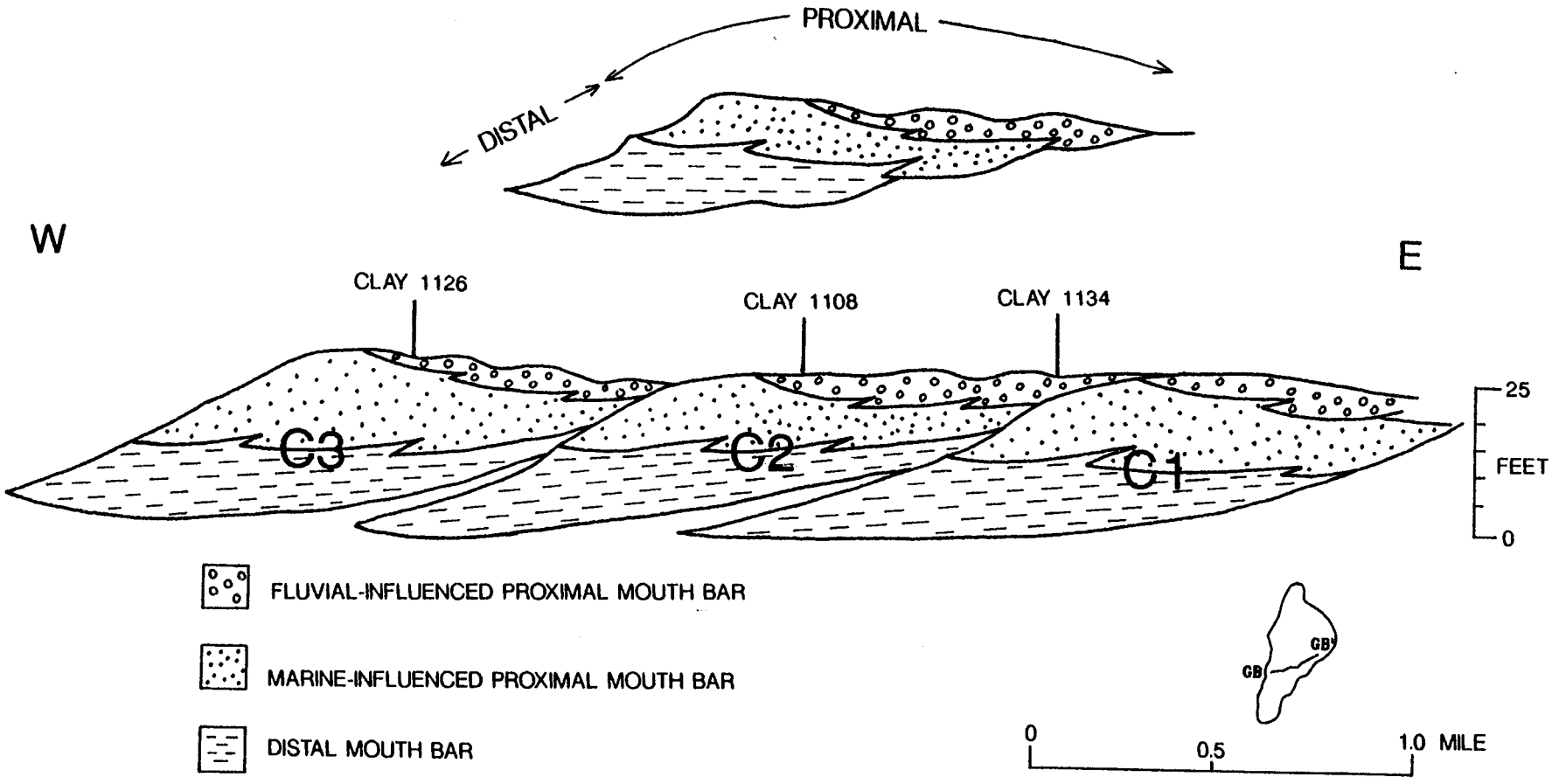

FIGURE 47. Diagrammatic reconstruction of delta-front facies of the C member of the Pocono Big Injun along profile GB-GB'.

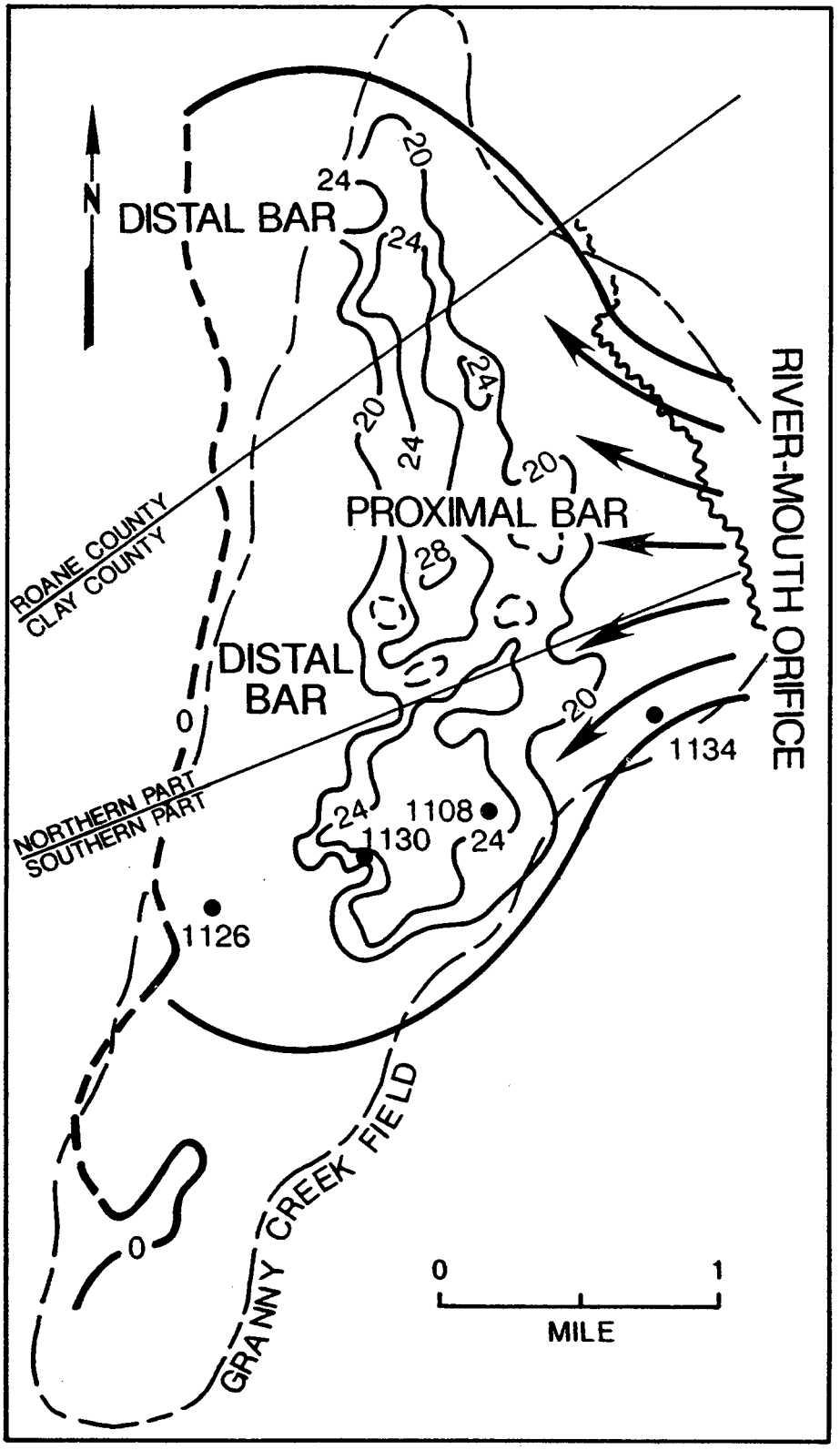

FIGURE 48. Isopach map of the C2 subunit showing interpreted depositional environments - the subfacies of a river-mouth bar. Locations of cored wells from profile GB-GB' (Figure 46) are also shown. Contour interval is 4 feet.

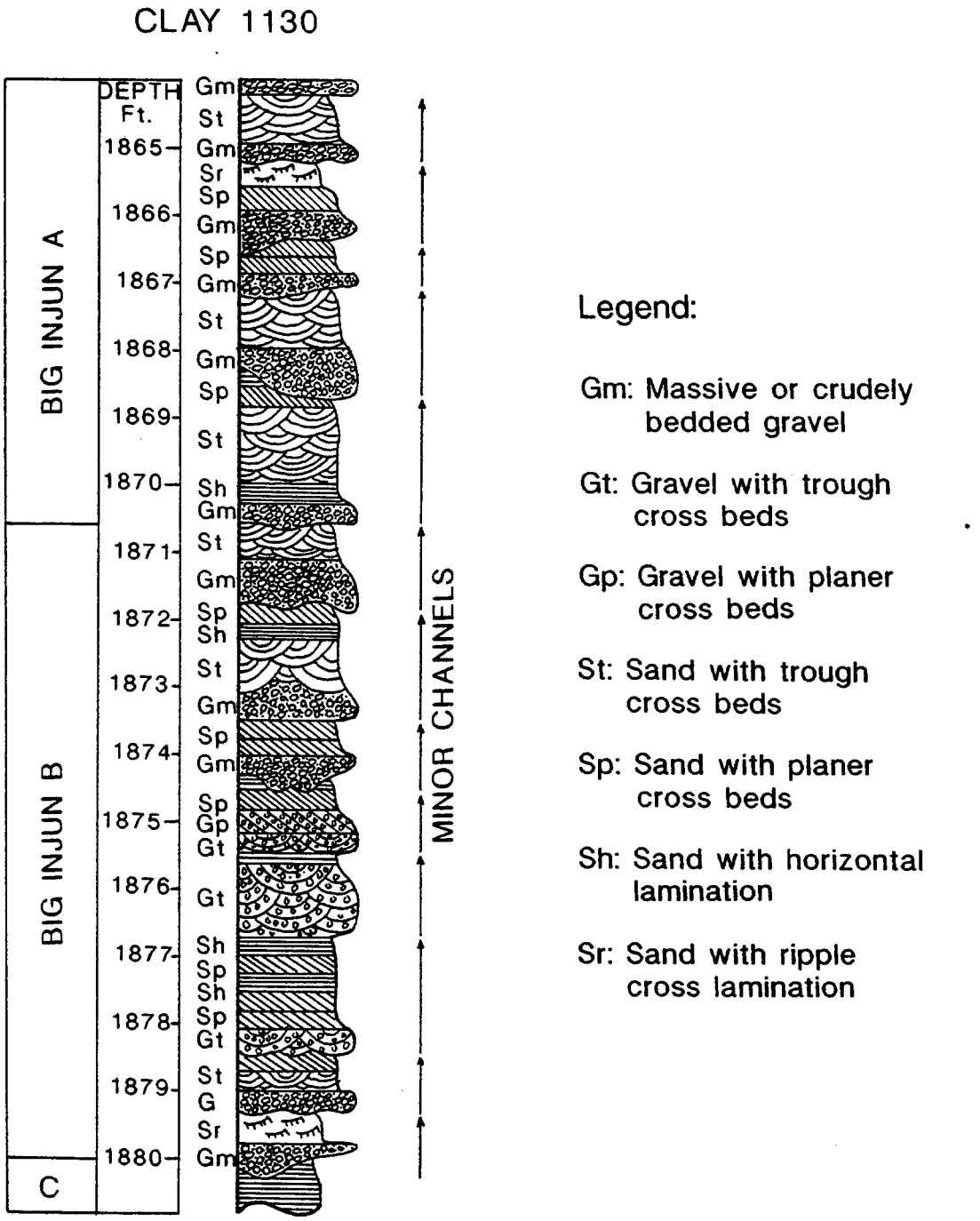

FIGURE 49. Vertical sequence of lithofacies for the Pocono Big Injun as interpreted from core for Clay 1130 (see Figure 48 for location). Lithofacies are coded and shown symbolically using the conventions of Miall (1977). Notice that the sequence suggests a bedload channel-fill deposit.

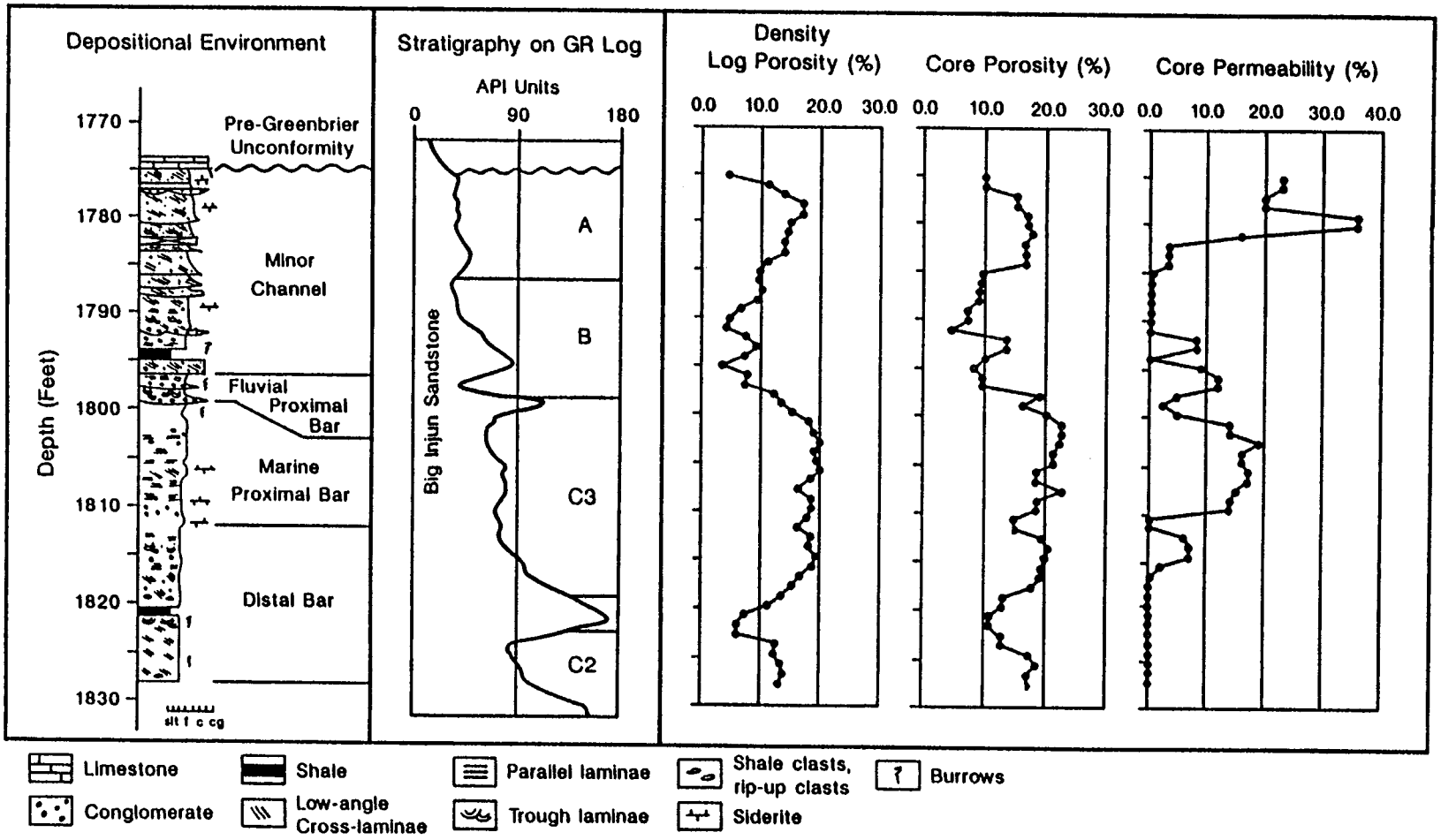

FIGURE 50. Depositional environments (subfacies) interpreted from textures, sedimentary structures, and fossils observed in core from Clay 1126 (see Figure 48 for location) and related to stratigraphic units of the Big Injun sandstone and their porosity and permeability values.

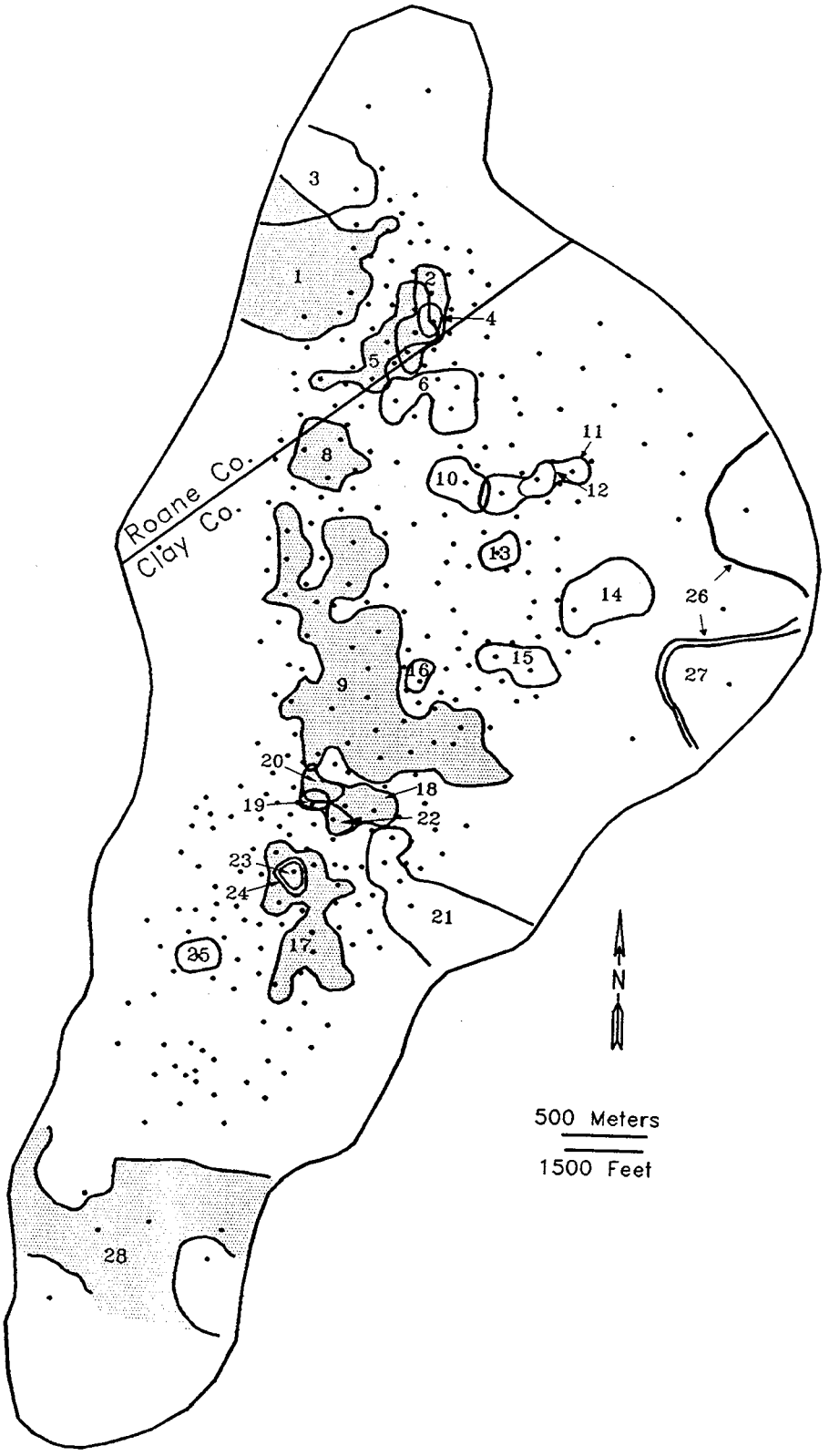

FIGURE 51. Map of Granny Creek showing the lateral extent of 28 density zones (identified by number) interpreted from logs from this field. The boundary of each zone is the zero thickness contour for the zone.

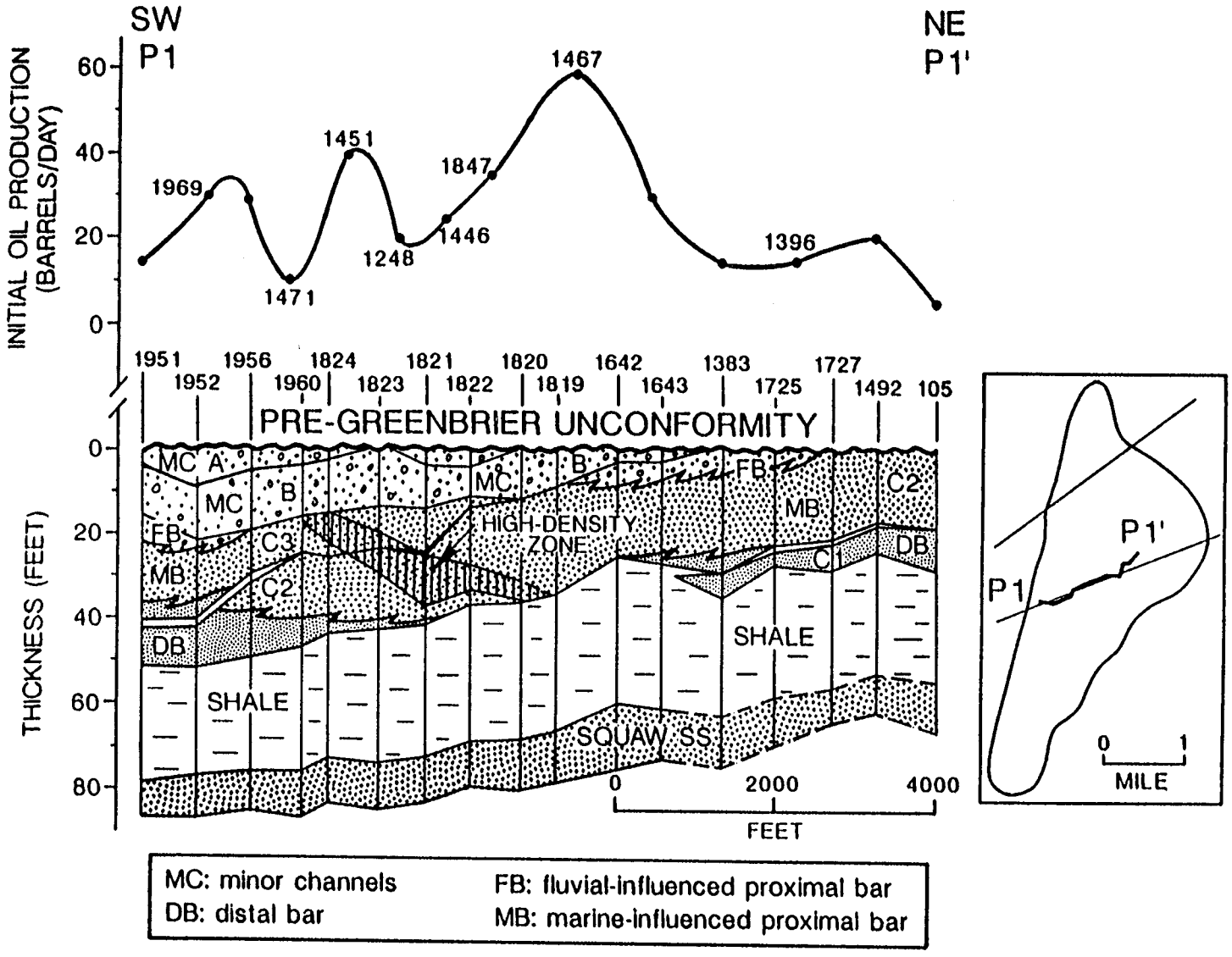

FIGURE 52. Initial oil production compared with stratigraphic cross section showing subfacies, high-density zone, relatively impermeable thin beds at boundary of tongues, and presence/absence of capping B member (potential seal over pay zone in C member). Profile P1-P1'. Initial oil production is plotted for wells on or adjacent to P1-P1'.

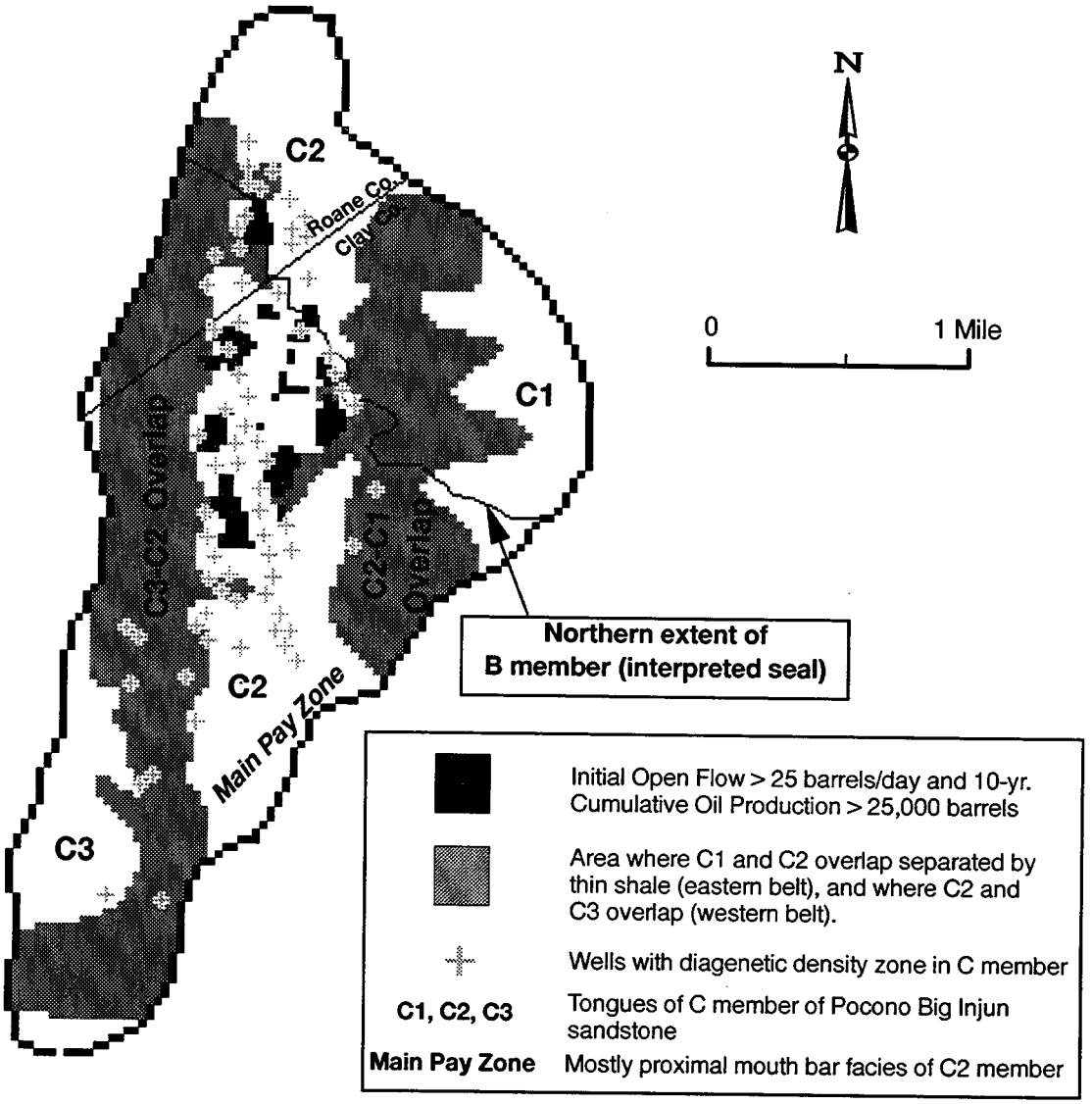

Four stratigraphic conditions that influence primary oil production are:

1. Presence of B zone seal (eroded by Pre-Greenbrier Unconformity)
2. North-south trend of pay zone, marine proximal mouth bar facies of C2
3. Depositional shale barrier
4. Diagenetic cementation/mineralization barrier

FIGURE 53. Geographic distribution of subunits of the C member (tongues C1, C2, and C3) of the Big Injun in Granny Creek field and its relationship to shale/diagenetic barriers and production.

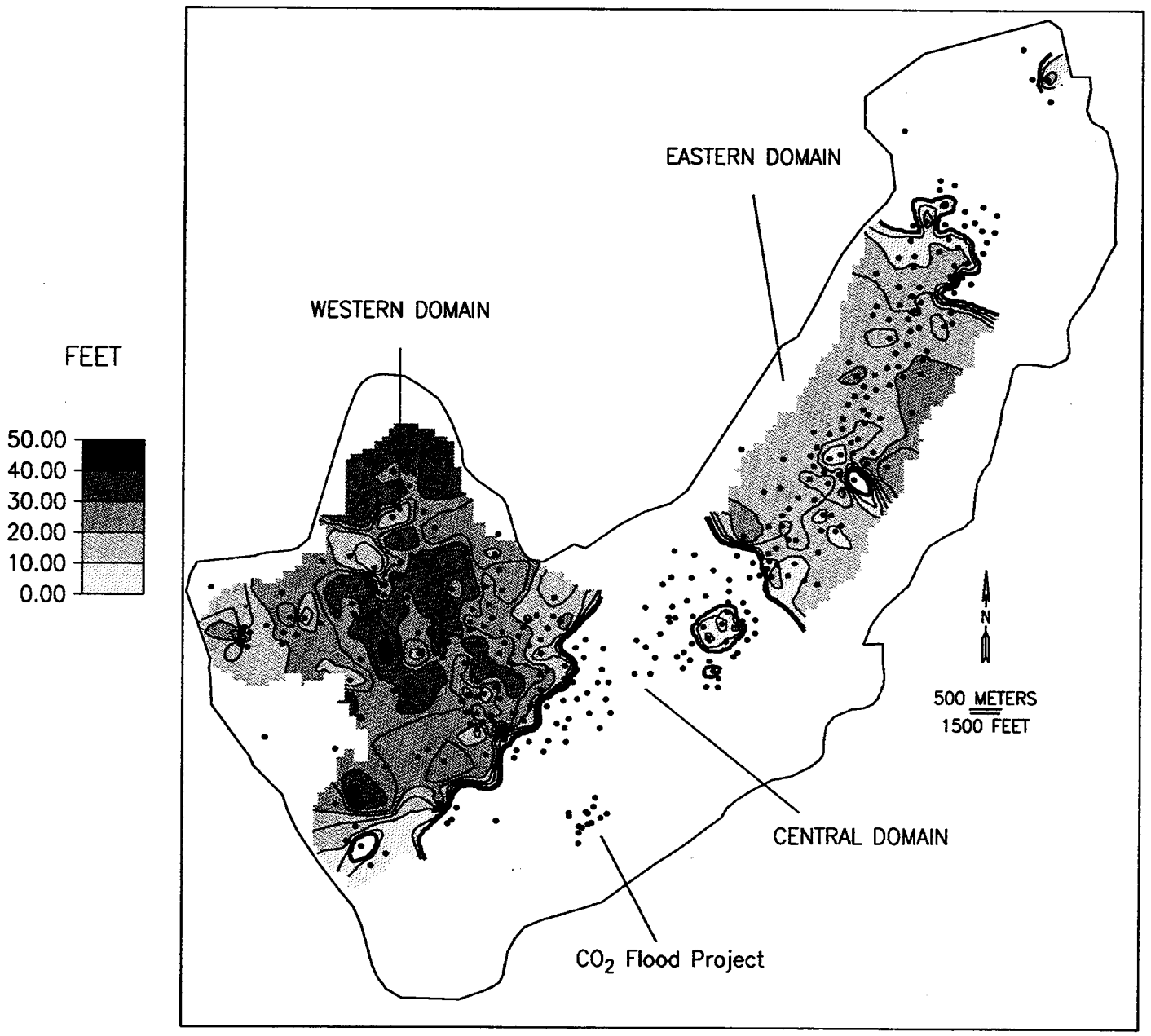

FIGURE 54. Isopach map of the porous unit at the base of the Greenbrier Limestone in Rock Creek field. The three domains discussed in text are shown along with the location of the CO_2 flood project. Contour interval is 10 feet.

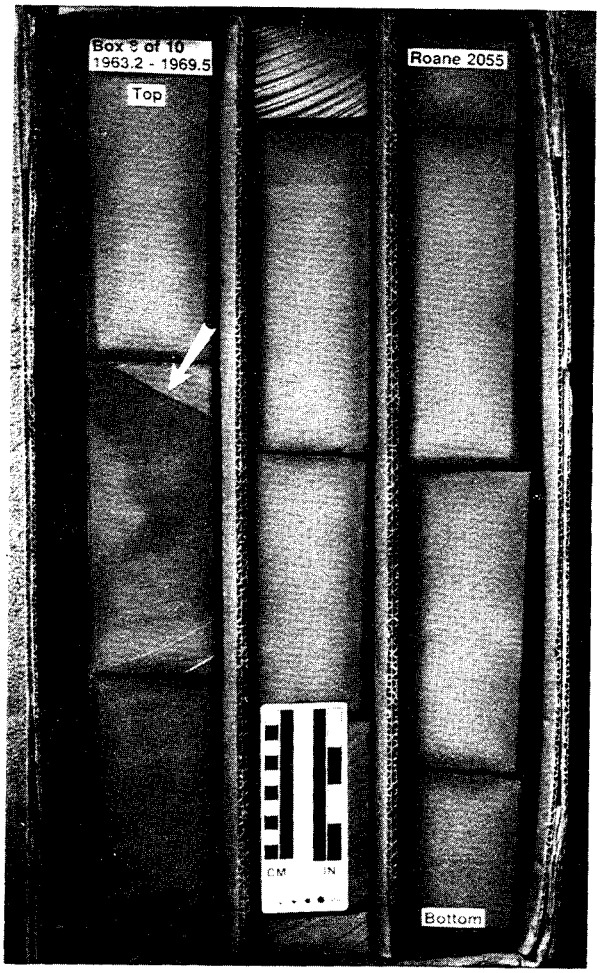

FIGURE 55. Photograph of core from Roane 2055 from the interval 1963.2' to 1969.5' showing the sharp boundary (arrow) between siderite cement zones and the rest of the core.

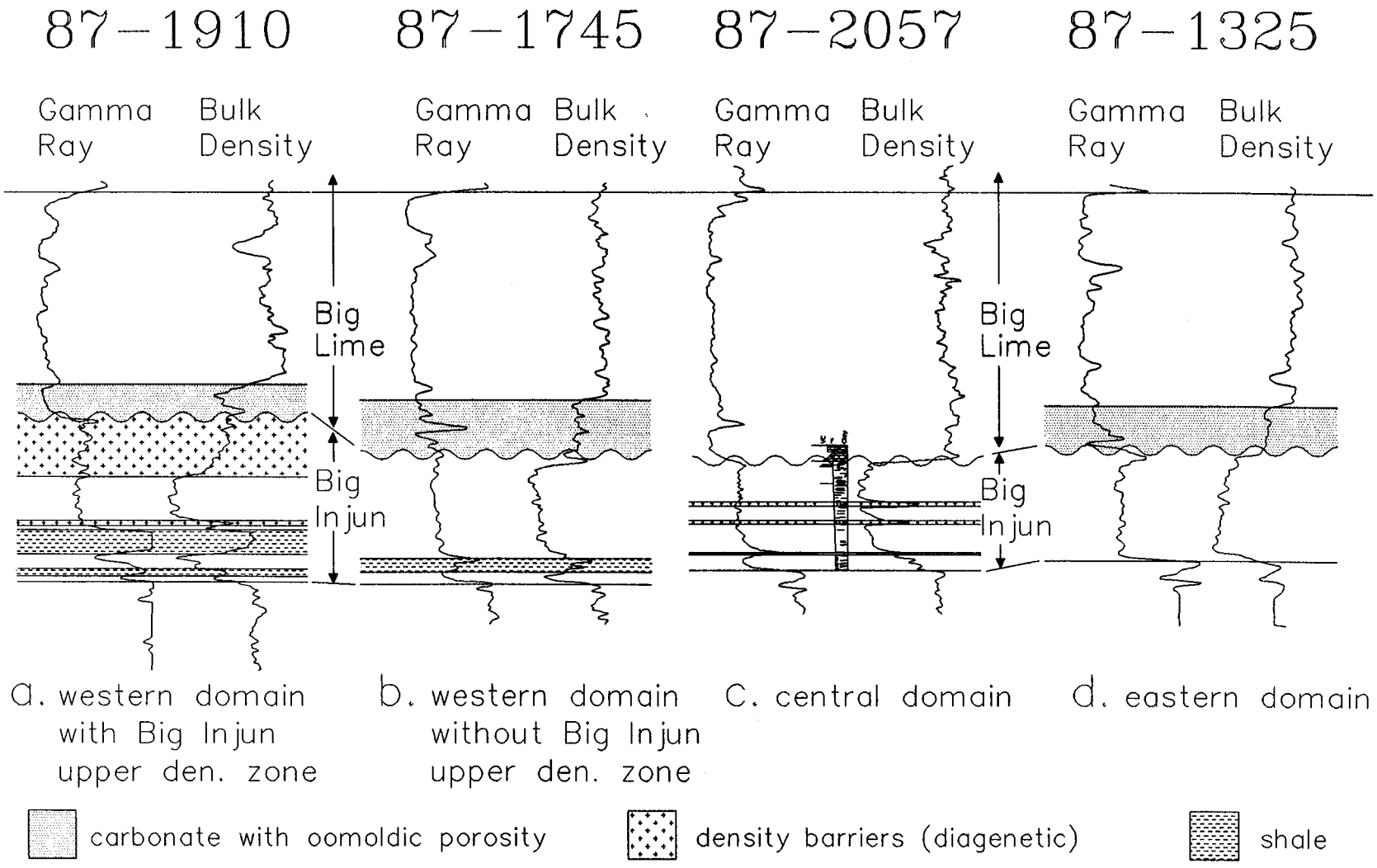

FIGURE 56. Typical log signatures for Rock Creek field. (a) and (b), from the western domain, show thick, porous Greenbrier overlying the Big Injun. Reservoir thickness in (a) is reduced by strongly cemented zones and inter-bedded shales; (c), from the central domain, show the absence of the porous basal Greenbrier - a diagrammatic core description is shown for comparison; (d), from the eastern domain, resembles (b) with a thinner porous Greenbrier. Core from Roane 1021 shows Greenbrier porosity to be oomoldic.

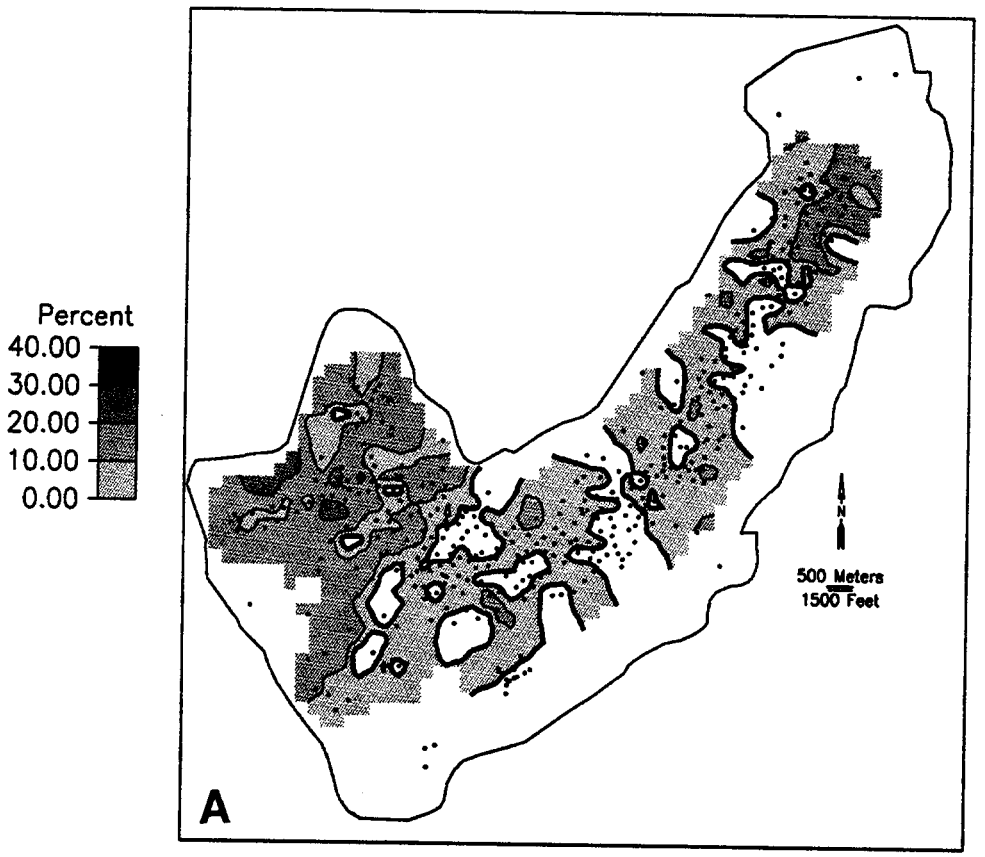

FIGURE 57. Isolith maps for the Big Injun interval in Rock Creek field. (a) Percentage of the interval composed of shale; (b) Percentage of the interval composed of strongly cemented sandstone. Contour interval for both maps is 10 percent.

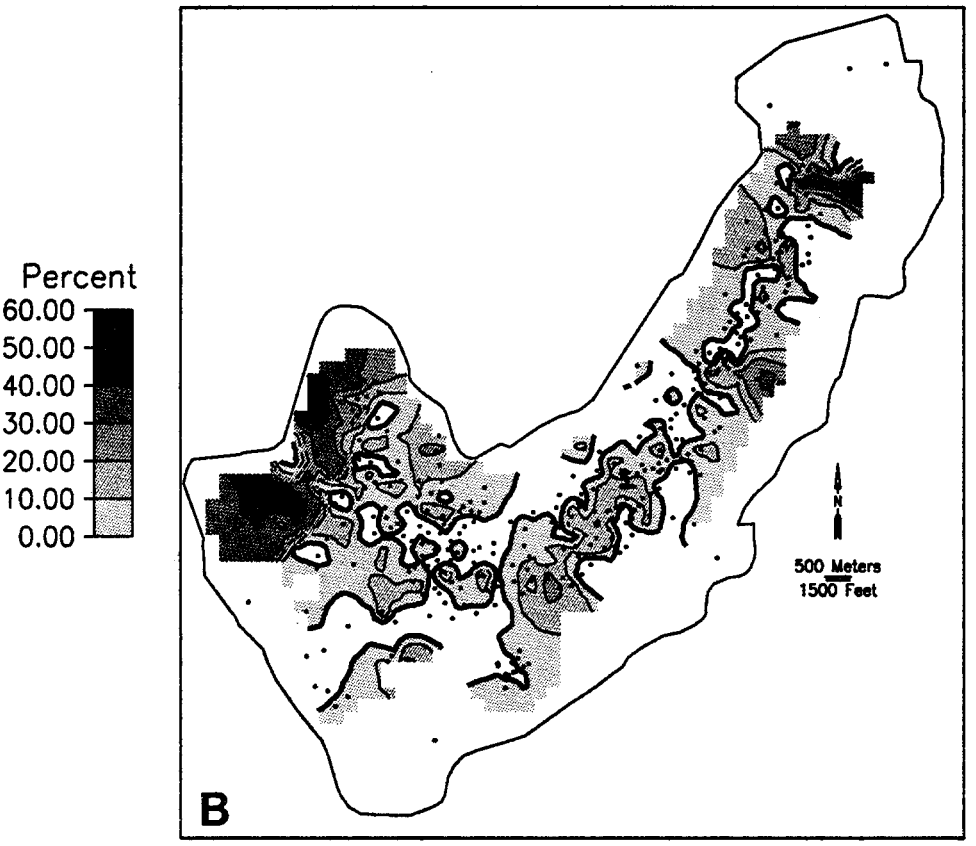

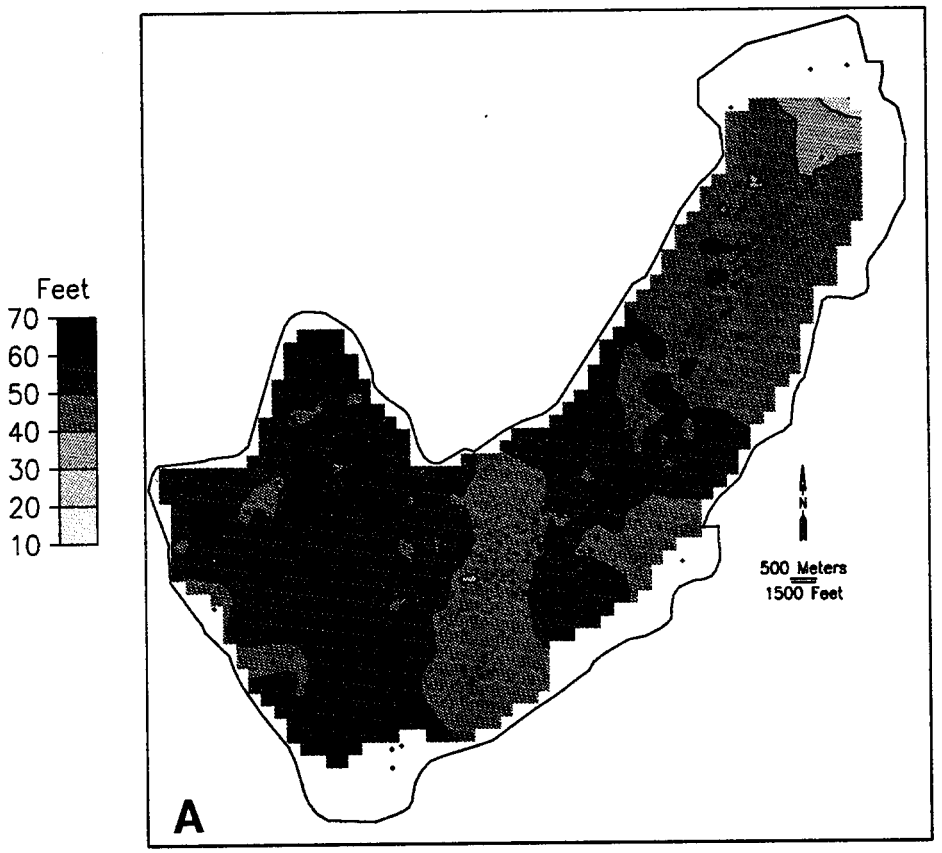

FIGURE 58. Isopach maps for the Big Injun interval in Rock Creek field. (a) Isopachs of the stratigraphic Big Injun based on drillers' log picks from the WVGES database and wireline log picks; (b) Isopachs of the reservoir Big Injun based on wireline logs. Contour interval for both maps is 10 feet.

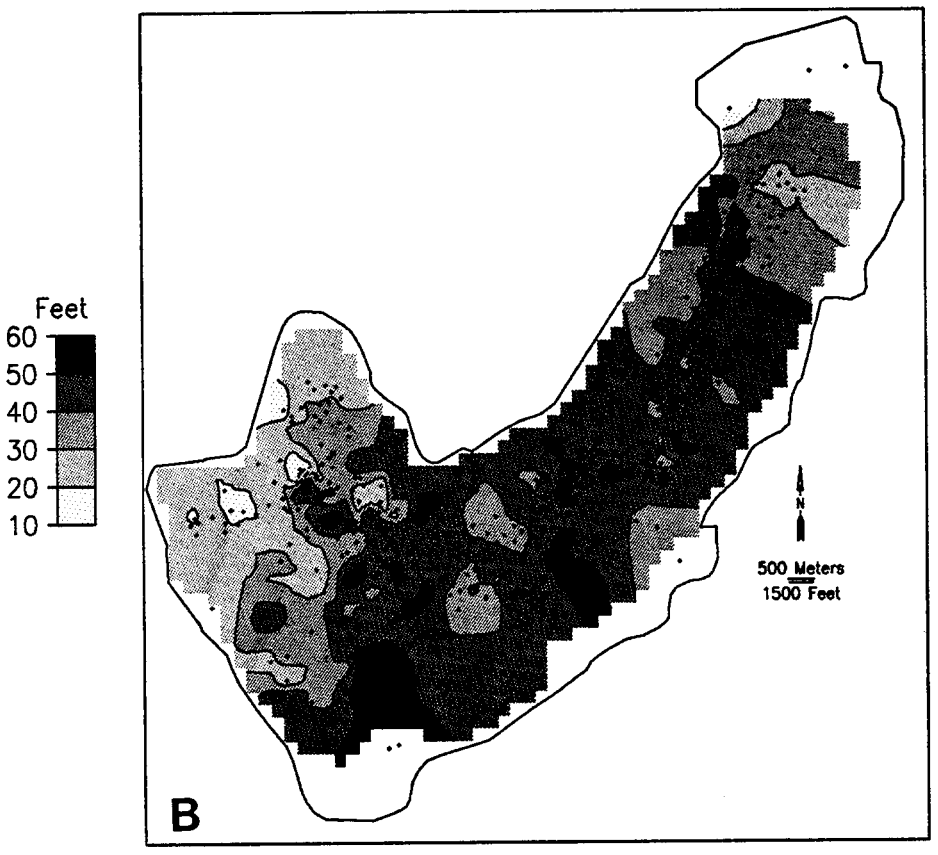

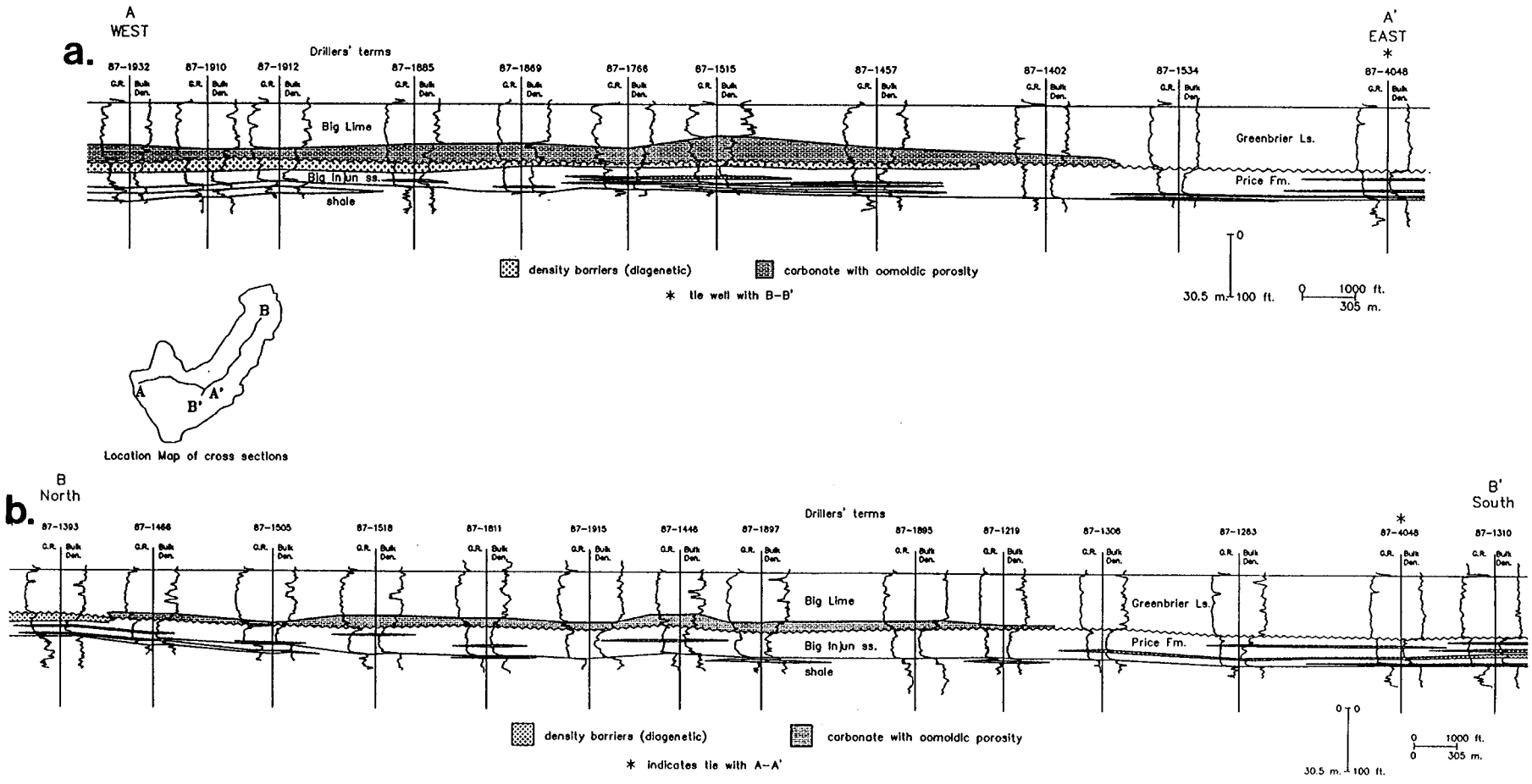

FIGURE 59. Two cross sections through the Big Injun interval from Rock Creek field. (a) Section A-A' shows the association of a thick cemented zone (density barrier) in the Big Injun with the presence of basal Greenbrier porosity. Reservoir thickness is reduced to the west by cemented zones and interbedded shale; (b) Section B-B' shows a thinner, basal porous unit in the Greenbrier and a few, thin cemented zones in the Big Injun. Few interbedded shales are present.

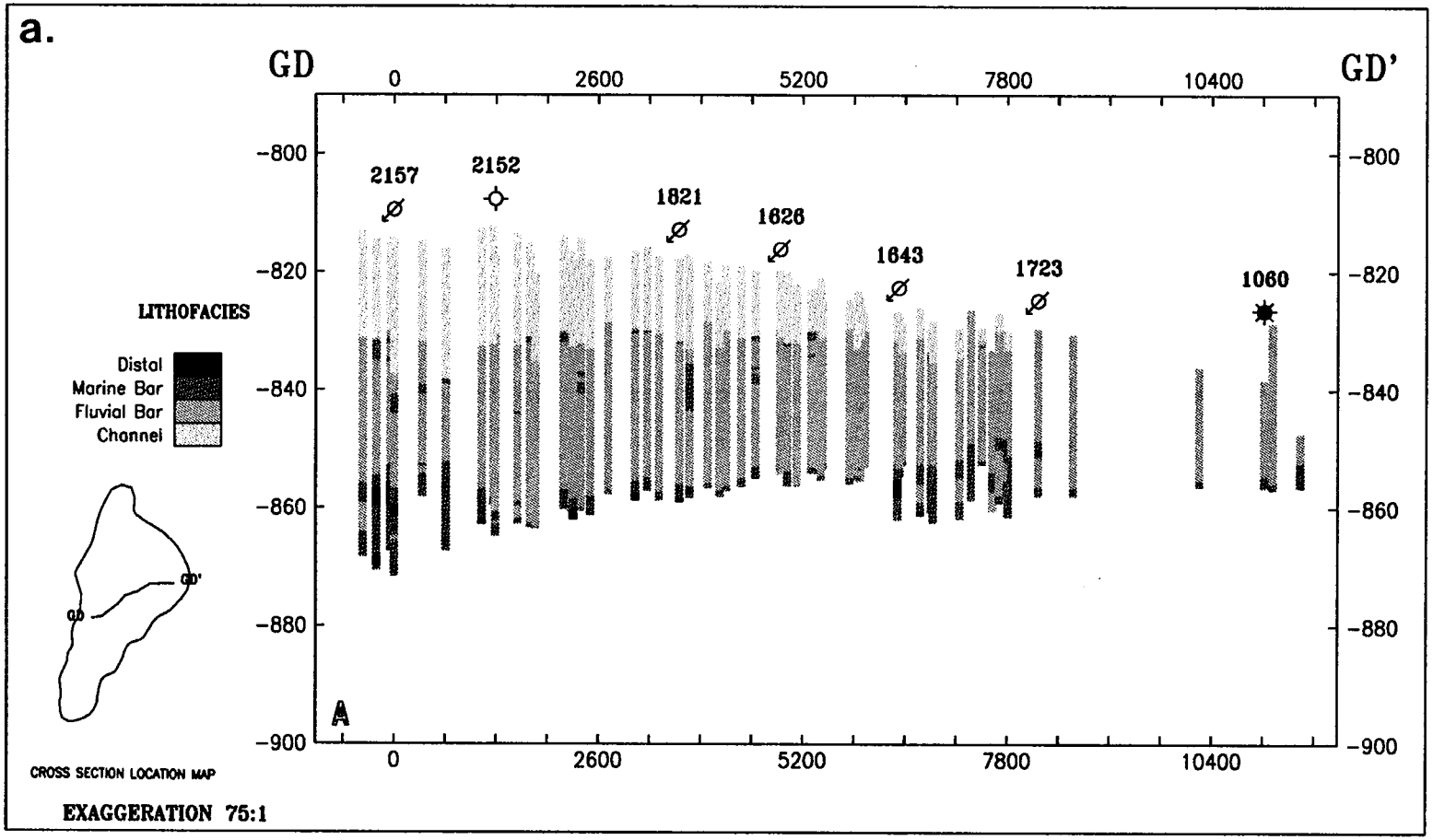

FIGURE 60a. Facies cross section GD-GD' for Granny Creek field. Four facies based on depositional environments are shown. Vertical exaggeration is 75:1.

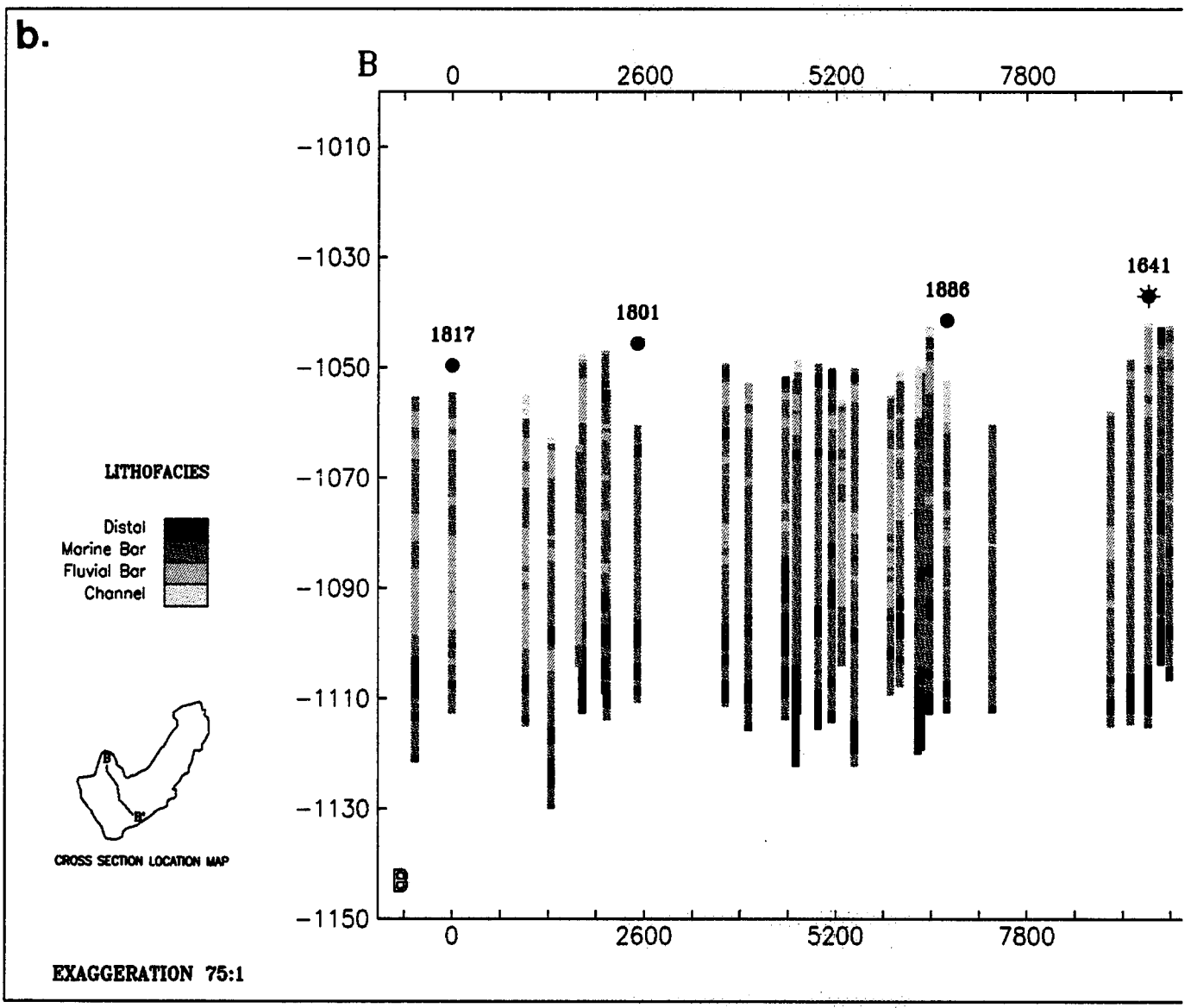

FIGURE 60b. Facies cross section B-B' for Rock Creek field. Four facies based on depositional environments are shown. Vertical exaggeration is 75:1.

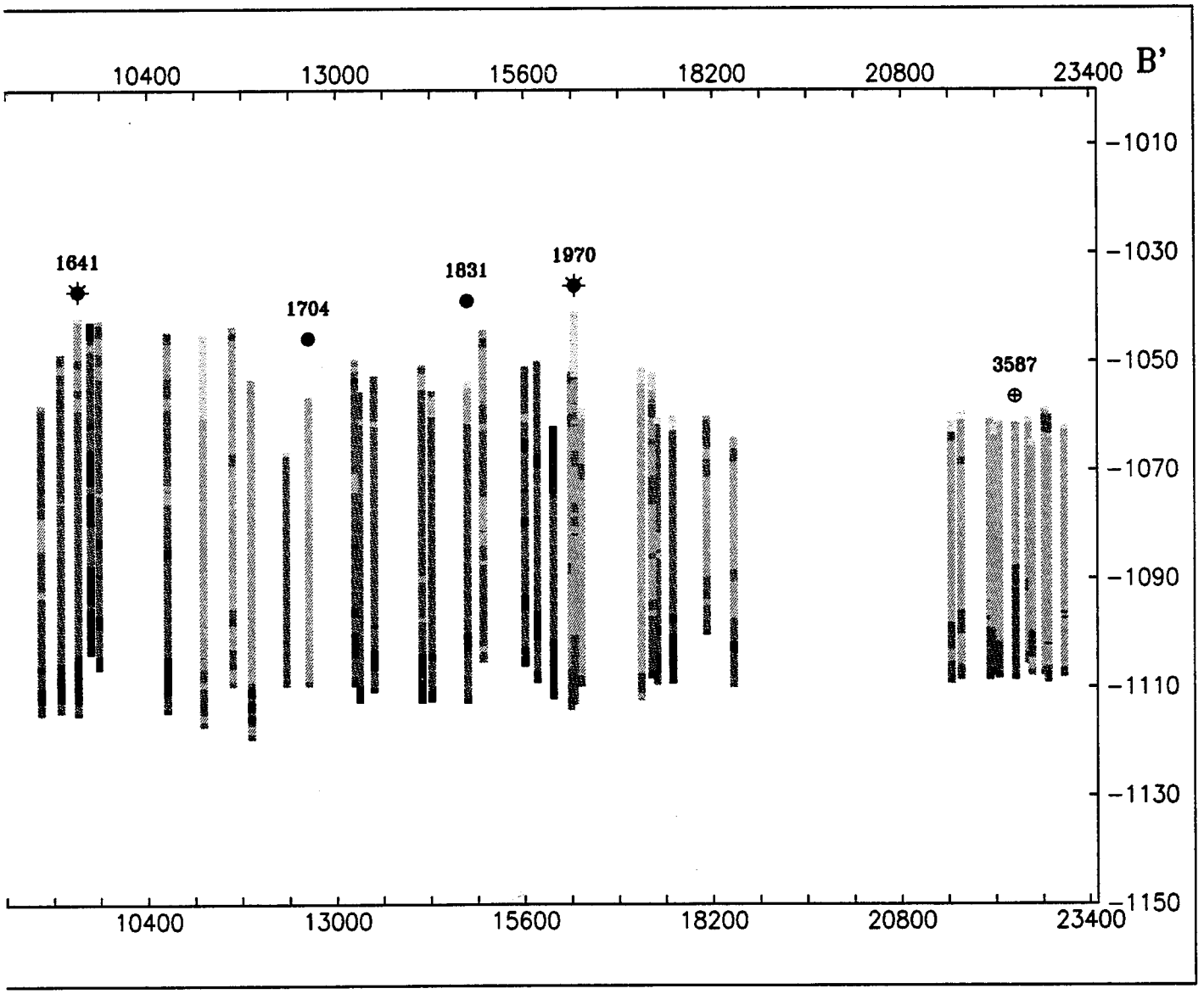
10400
13000
15600
18200
20800
23400
B'
-1010
-1030
-1050
-1070
-1090
-1110
-1130
-1150
1641
1704
1831
1970
3587

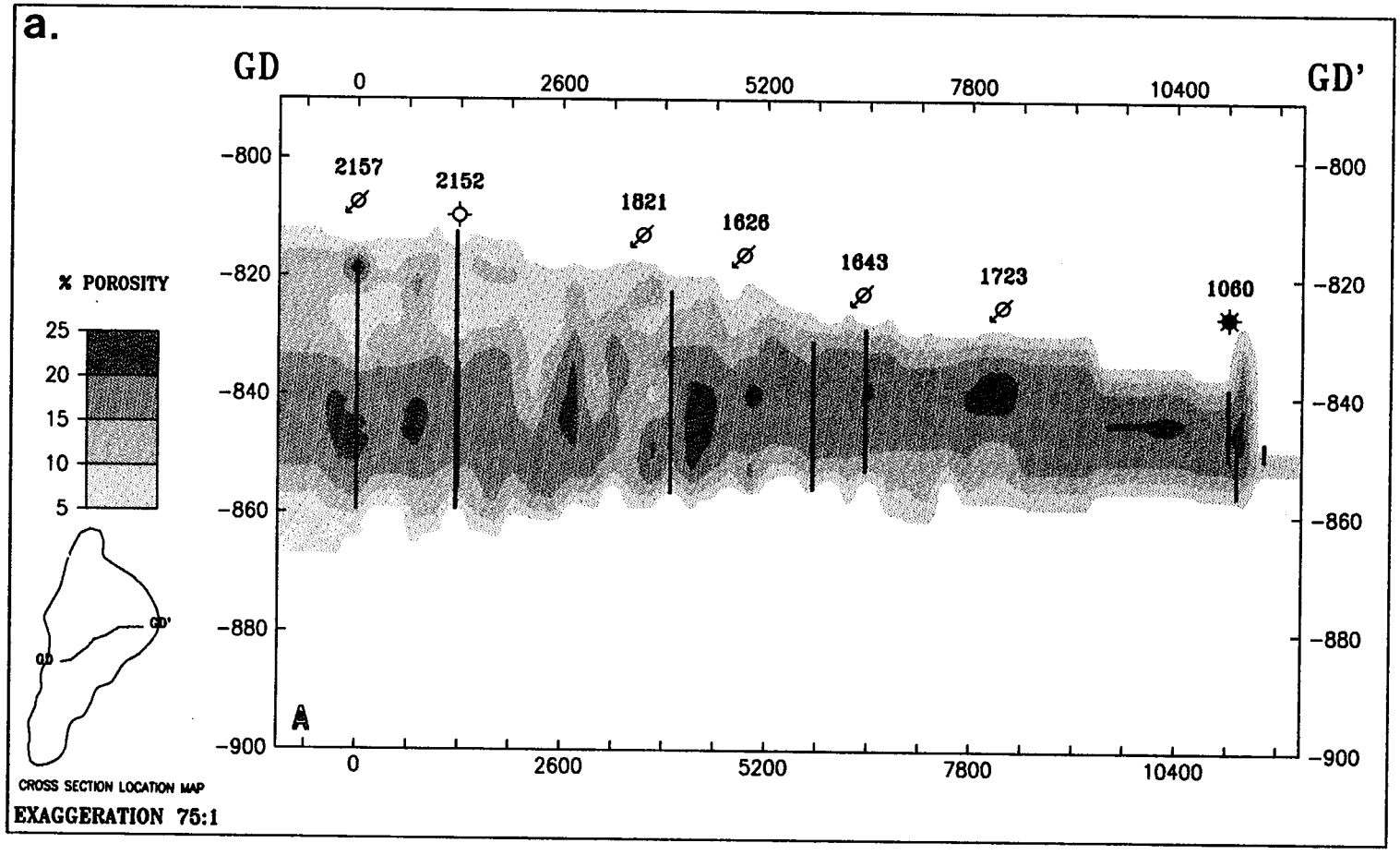

FIGURE 61a. Porosity cross section GD-GD' for Granny Creek field. Contour interval is 5 percent porosity; vertical exaggeration is 75:1. Reported producing intervals are shown as black vertical bars.

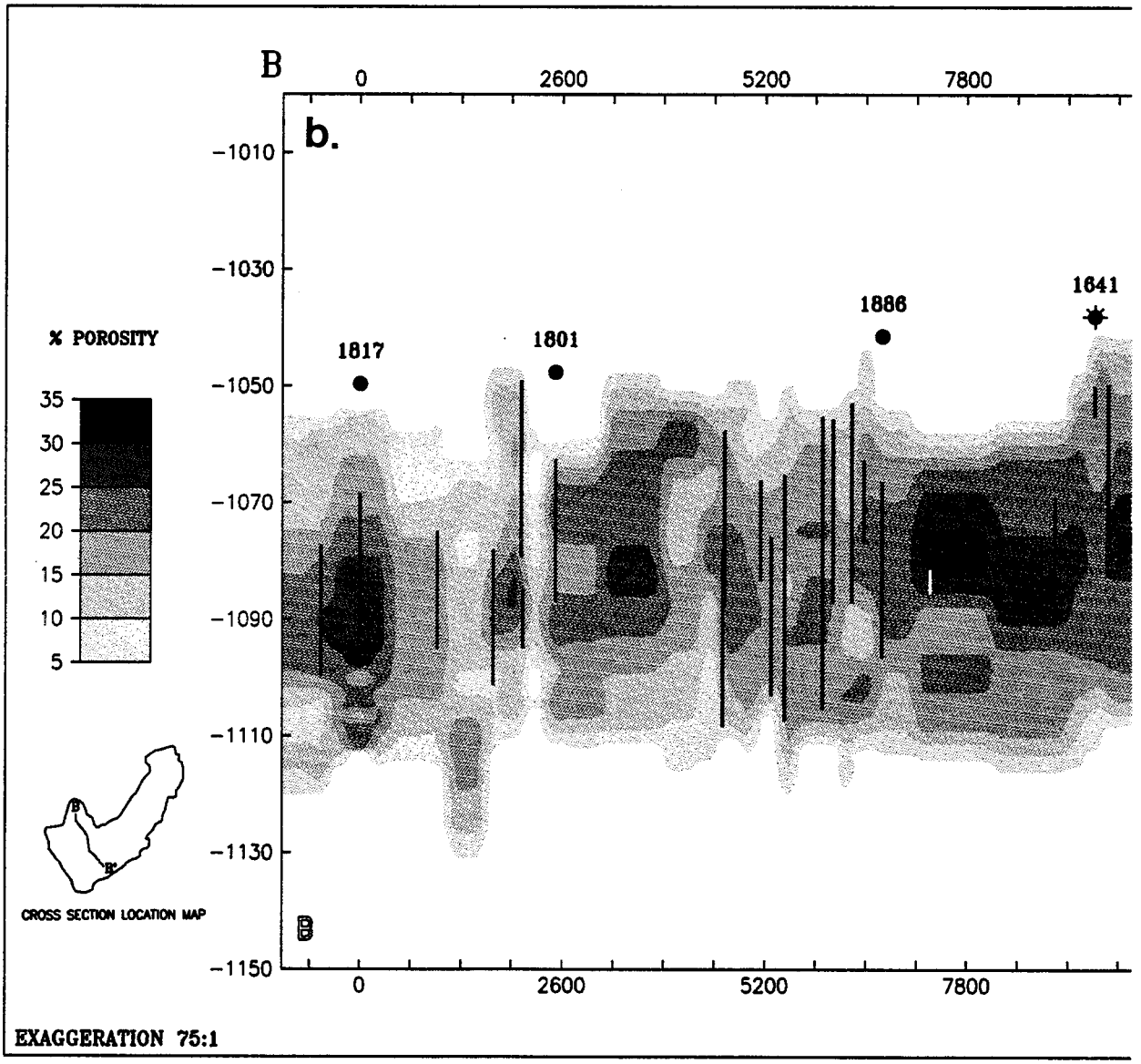

FIGURE 61b. Porosity cross section B-B' for Rock Creek field. Contour interval is 5 percent porosity; vertical exaggeration is 75:1. Reported producing intervals are shown as black or white vertical bars.

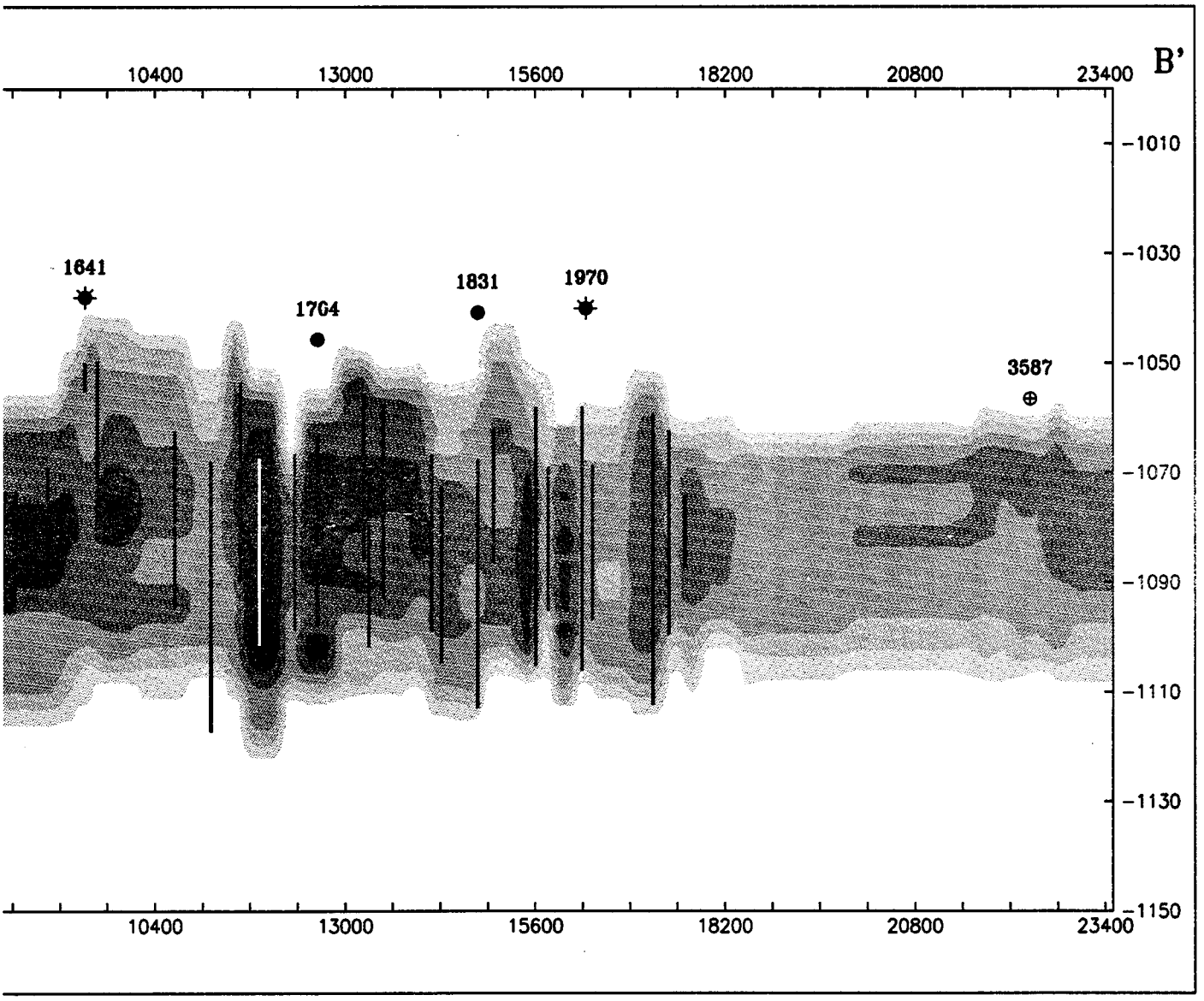
B'
10400
13000
15600
18200
20800
23400
-1010
-1030
-1050
-1070
-1090
-1110
-1130
-1150
1641
1704
1831
1970
3587

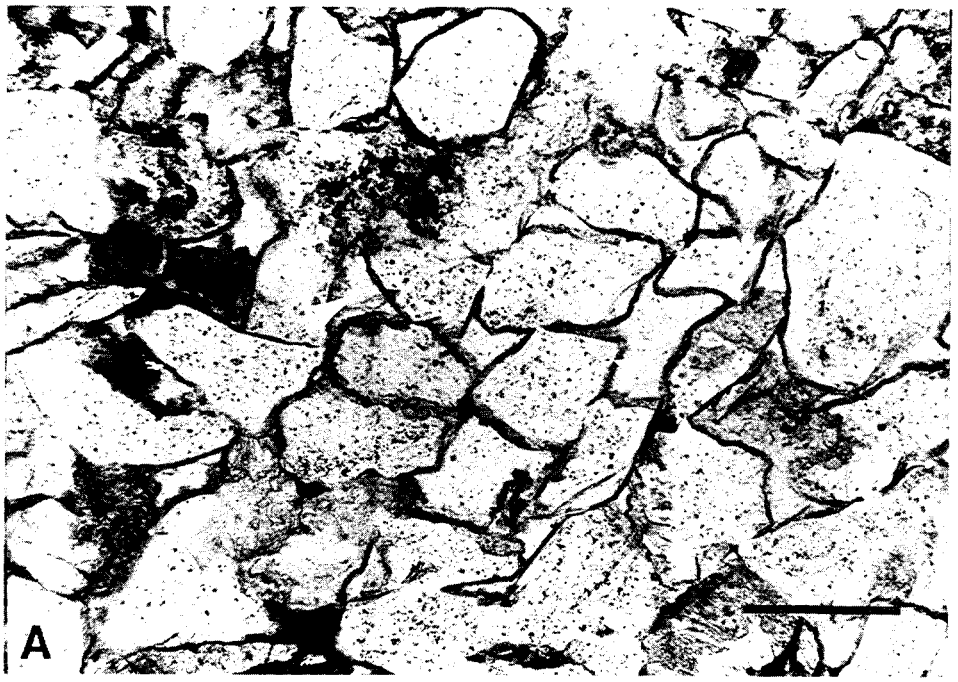

FIGURE 62. Photomicrographs of core material from Granny Creek field. (a) Clay 1132, 1972.3' - well developed chlorite coatings (arrows) which blocked nucleation sites for secondary quartz overgrowth. Bar scale is 0.05 mm long; (b) Clay 1107, 2127.4' - voids (V) resulting from leaching of feldspar grains. Most of the intergranular pores are filled with secondary quartz. Bar scale is 0.1 mm long. Both photomicrographs taken in plane polarized light.

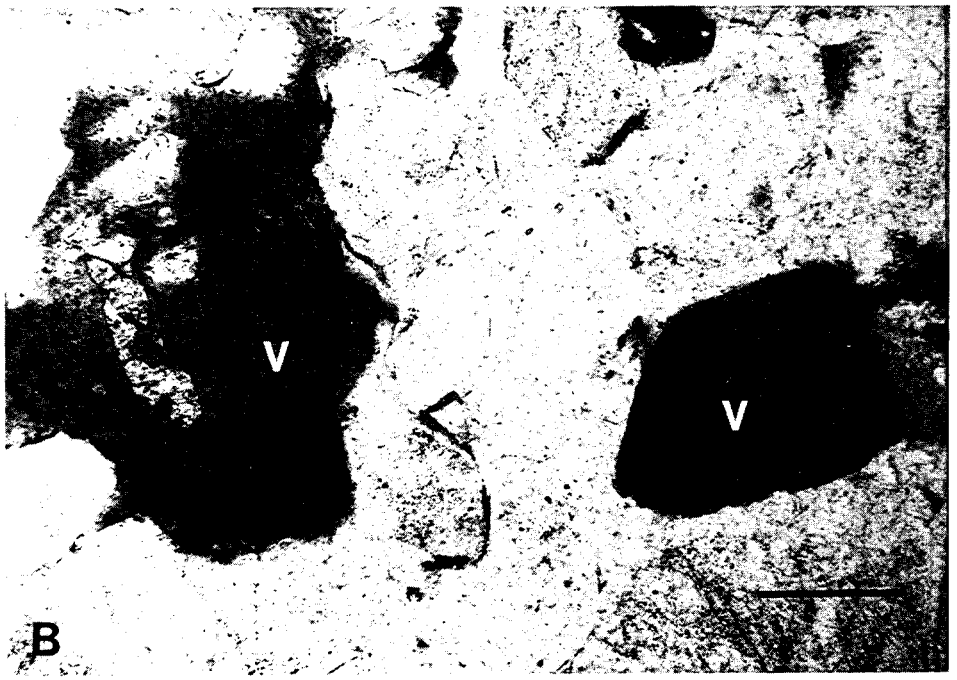

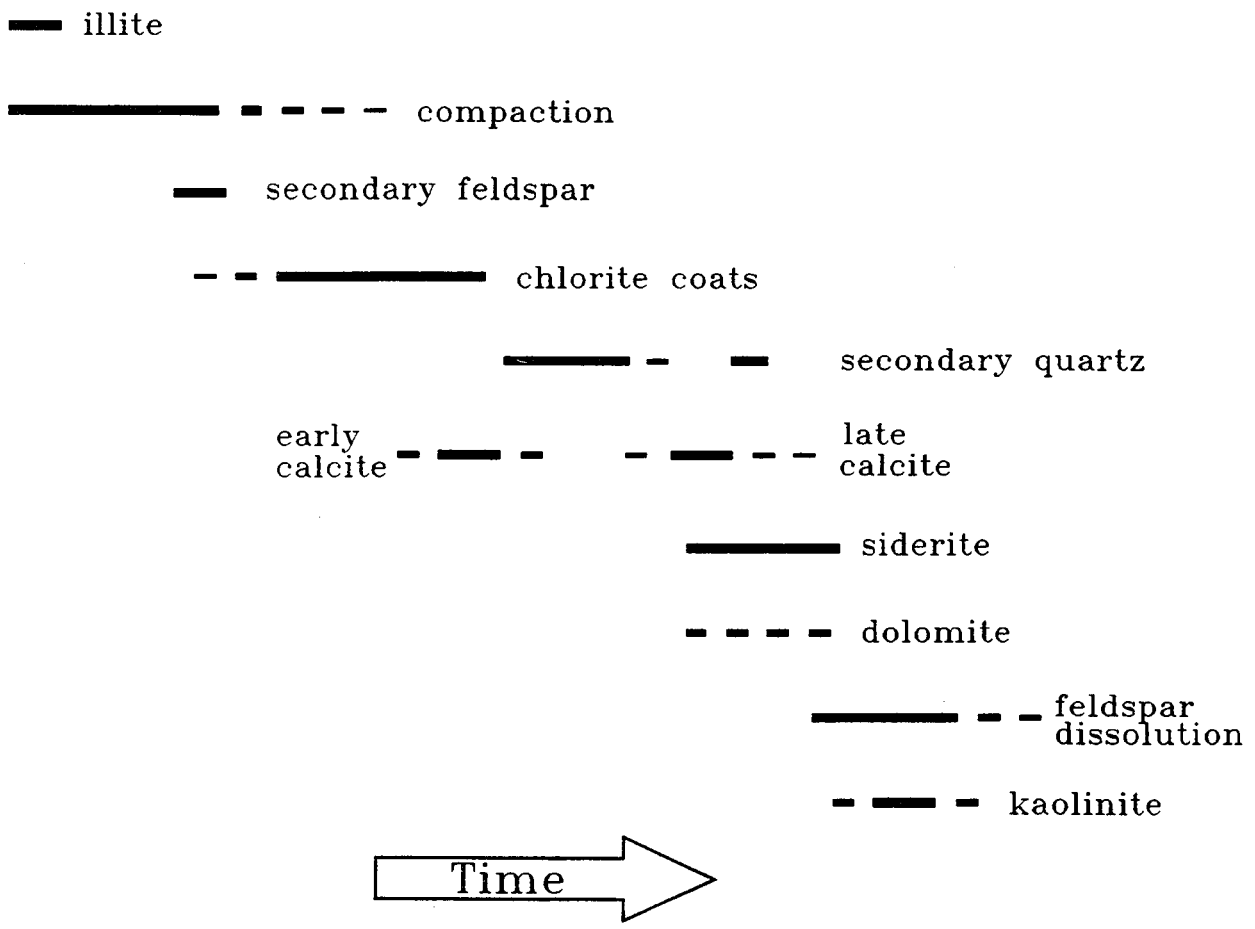

FIGURE 63. Paragenetic sequence for the Big Injun sandstone in Granny Creek and Rock Creek fields.

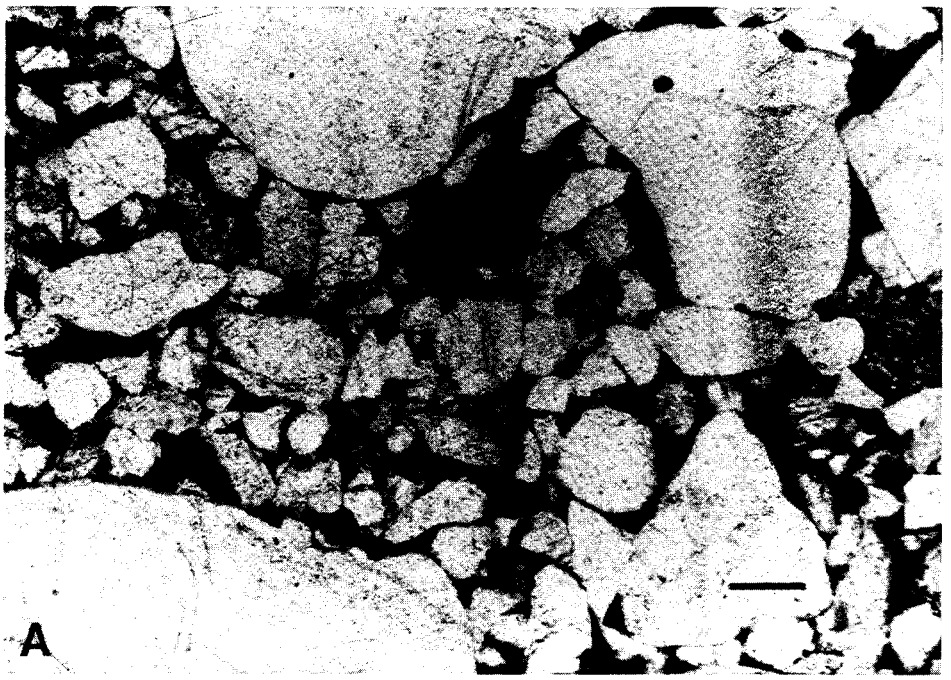

FIGURE 64. Photomicrographs of core material from Granny Creek field. (a) Clay 1107, 2132.5' - poor sorting in the B member of the fluvial channel sandstone resulting in a bimodal grain size distribution. Bar scale is 0.1 mm long; (b) Clay 1109, 1881.8' - intense pressure solution in an illite-bearing sandstone resulting in many sutured contacts (arrows). Bar scale is 0.1 mm long. Photomicrograph (a) taken in plane polarized light; (b) taken with crossed nicols.

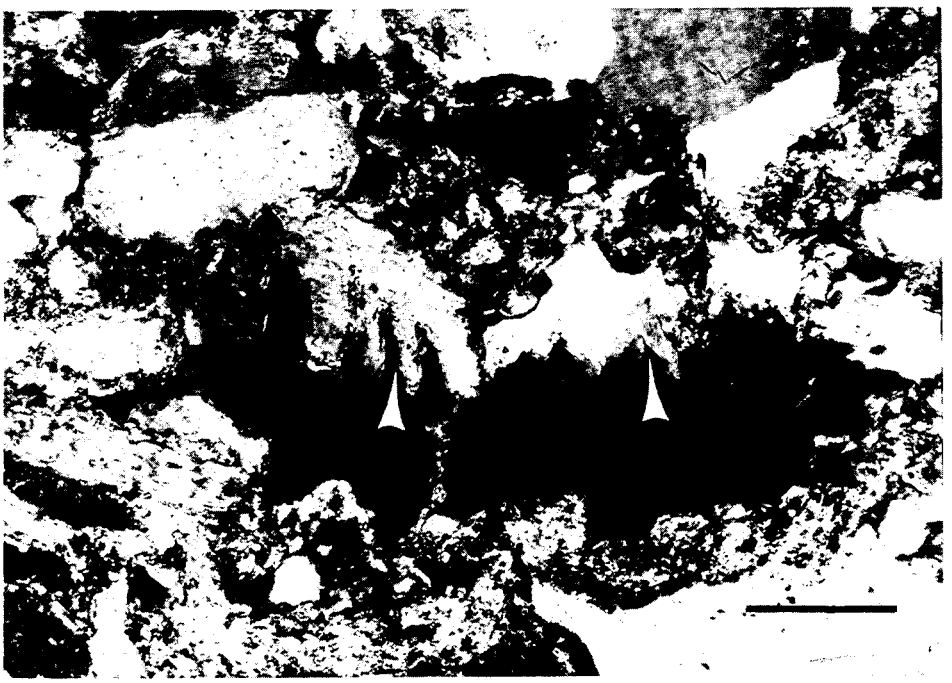

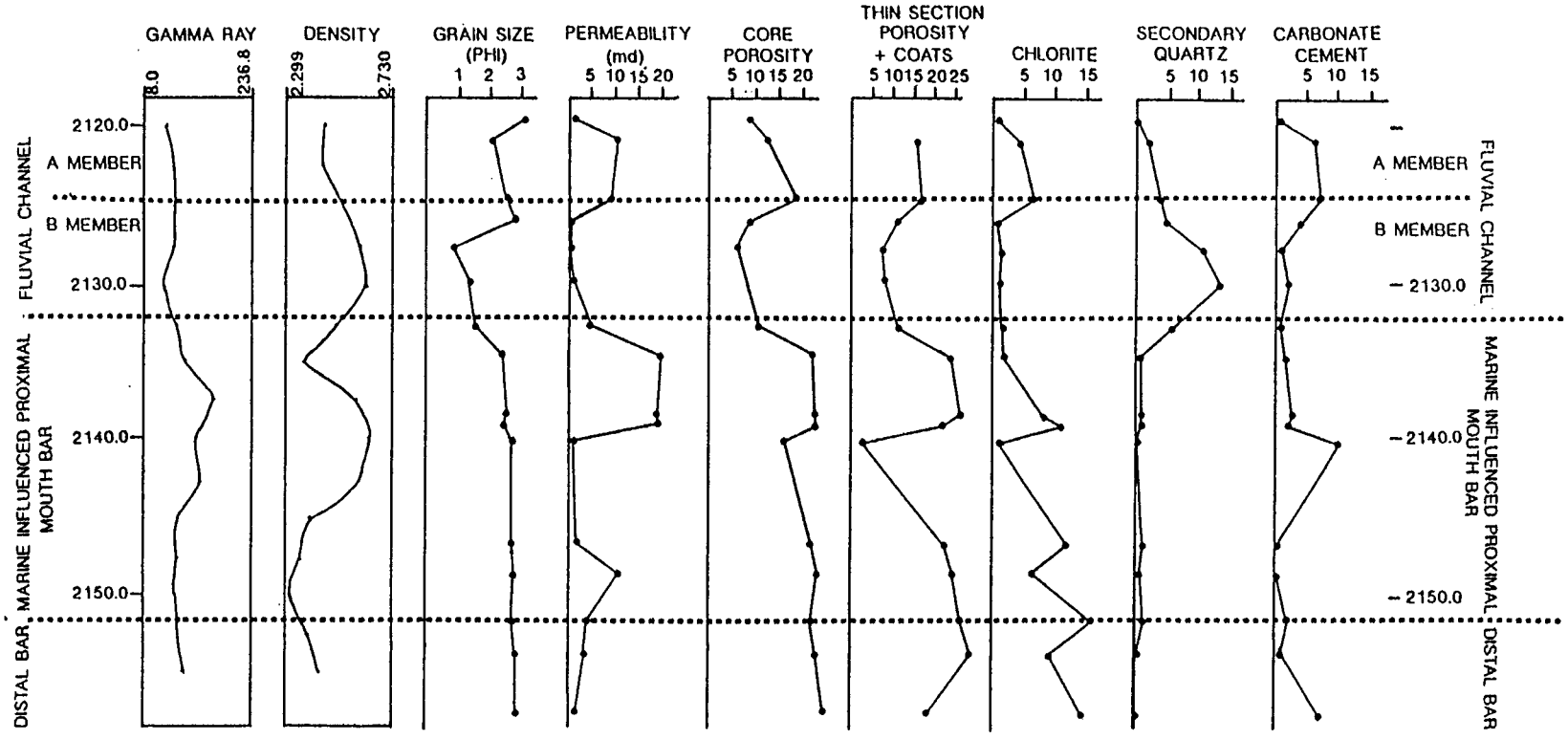

FIGURE 65. Comparison of wireline logs to pertinent characteristics of the Big Injun sandstone in Clay 1107.

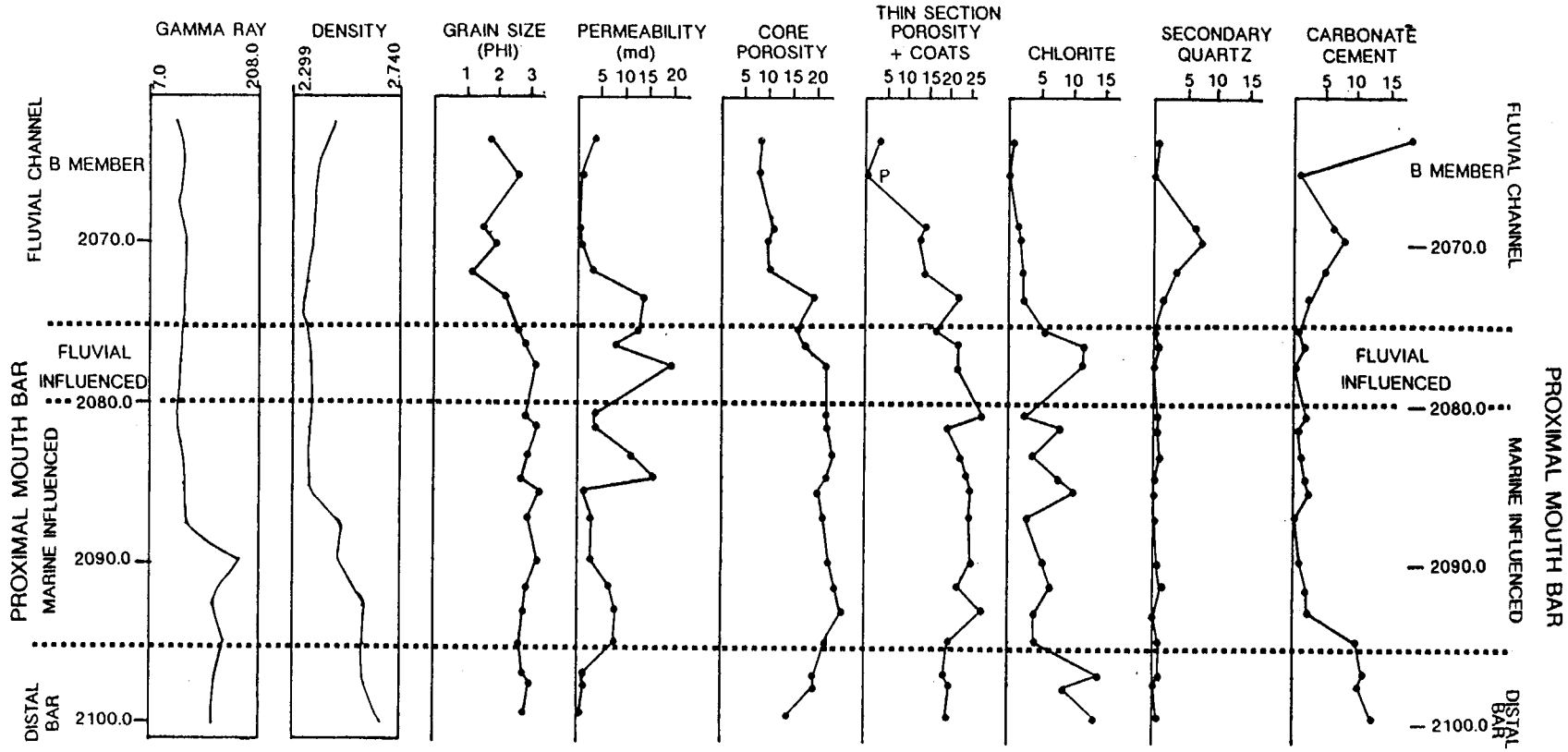

FIGURE 66. Comparison of wireline logs to pertinent characteristics of the Big Injun sandstone in Clay 1108. p = intense pressure solution.

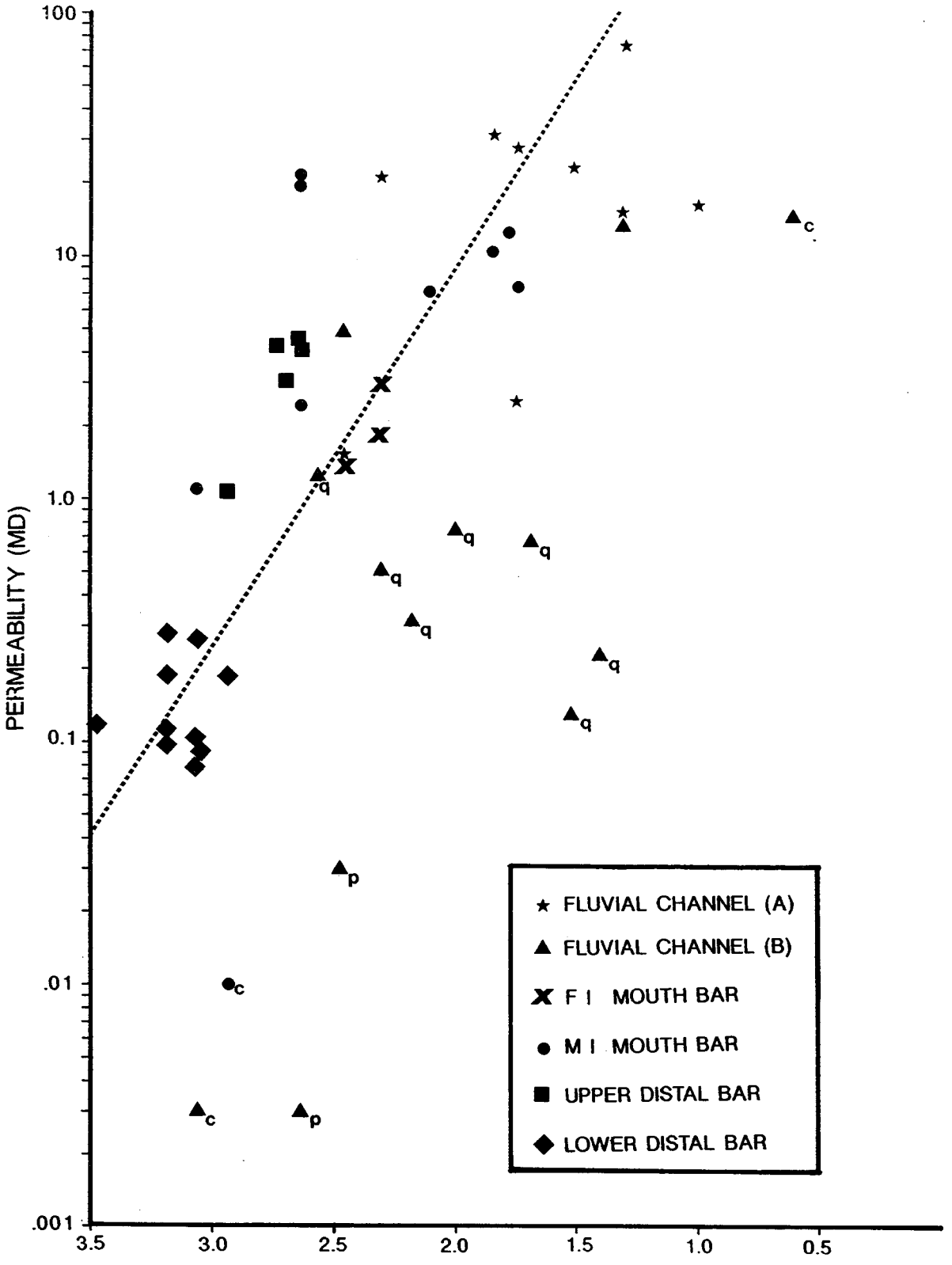

FIGURE 67. Graph showing the relationship between permeability and grain-size in Clay 1126. Lettered symbols indicate samples with large amounts of cement; these points were not used to determine the position of the best-fit line. q = quartz cement; c = carbonate cement; p = intense pressure solution; FI = fluvial influenced proximal mouth bar; MI = marine influenced proximal mouth bar.

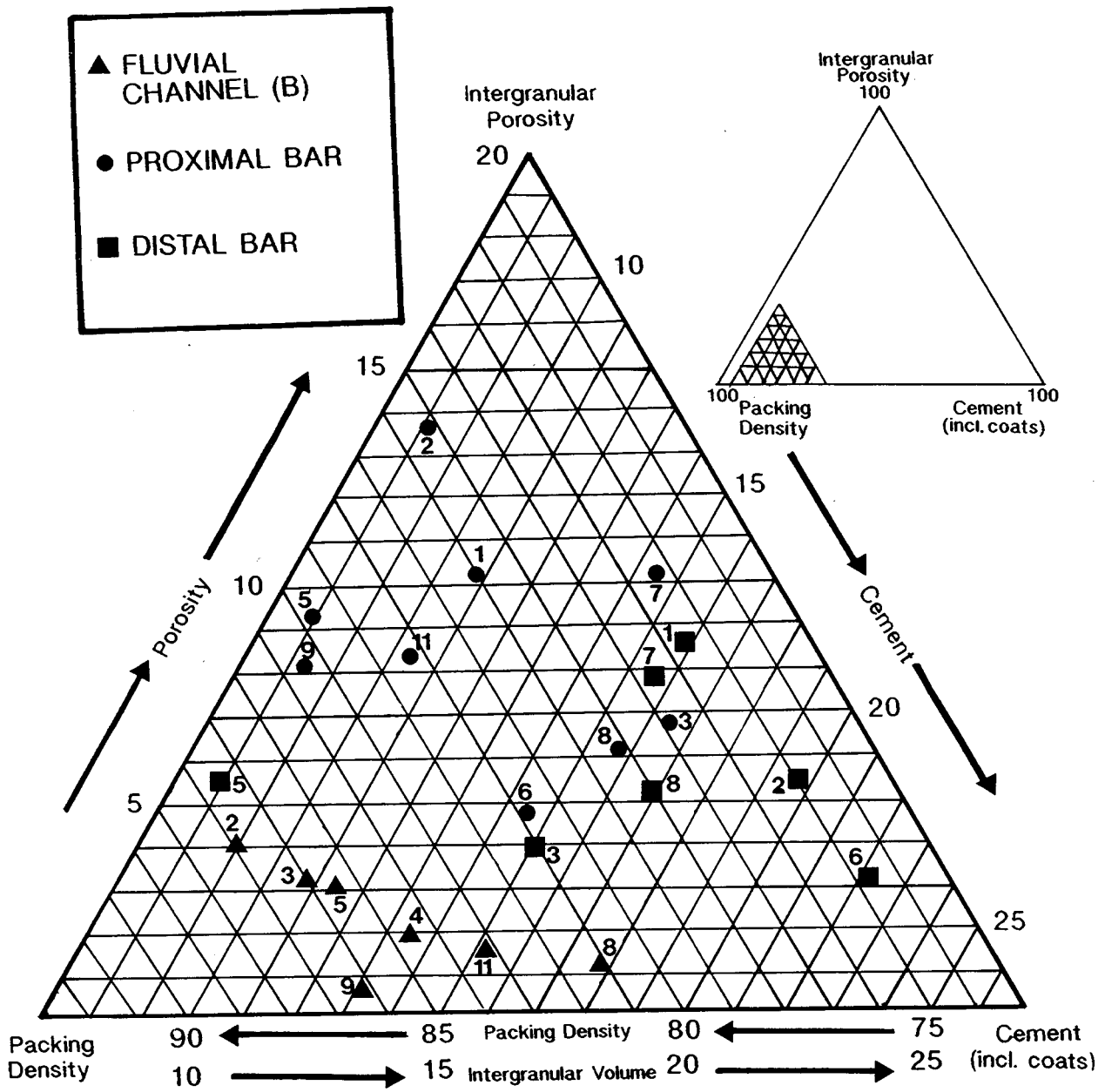

FIGURE 68. Enlarged portion of the triangular diagram showing the relationships between cement, packing, density, and intergranular volume for each Big Injun facies recognized in Granny Creek wells. Key to numbered symbols: 1 = Clay 1107; 2 = Clay 1108; 3 = Clay 1109; 4 = Clay 1110; 5 = Clay 1126; 6 = Clay 1128; 7 = Clay 1130; 8 = Clay 1132; 9 = Clay 1133; 11 = Roane 2410; 12 = Clay 1134.

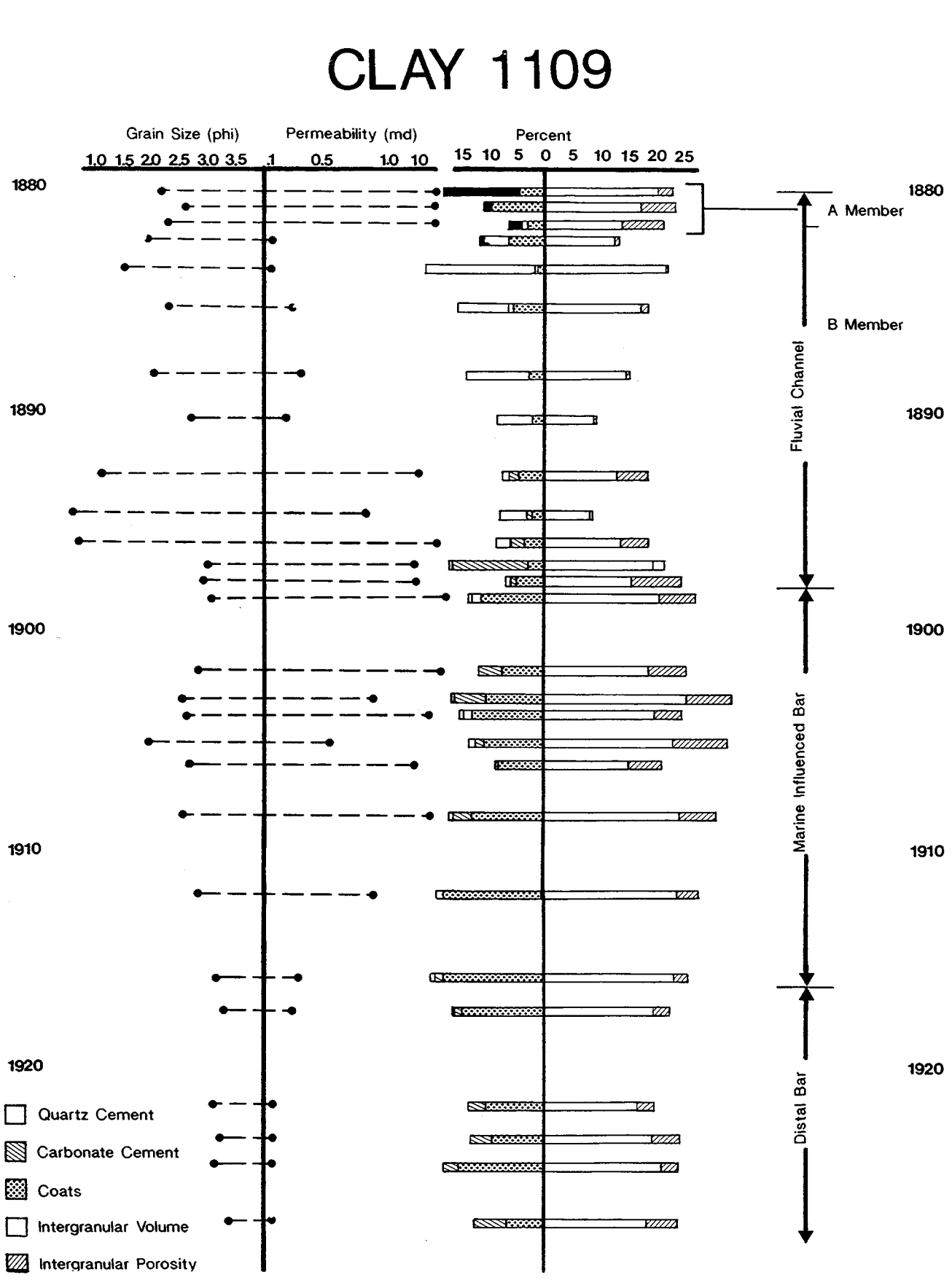

FIGURE 69. Relationships between permeability and grain size, cements, intergranular volume, and intergranular porosity for Big Injun facies recognized in Clay 1109.

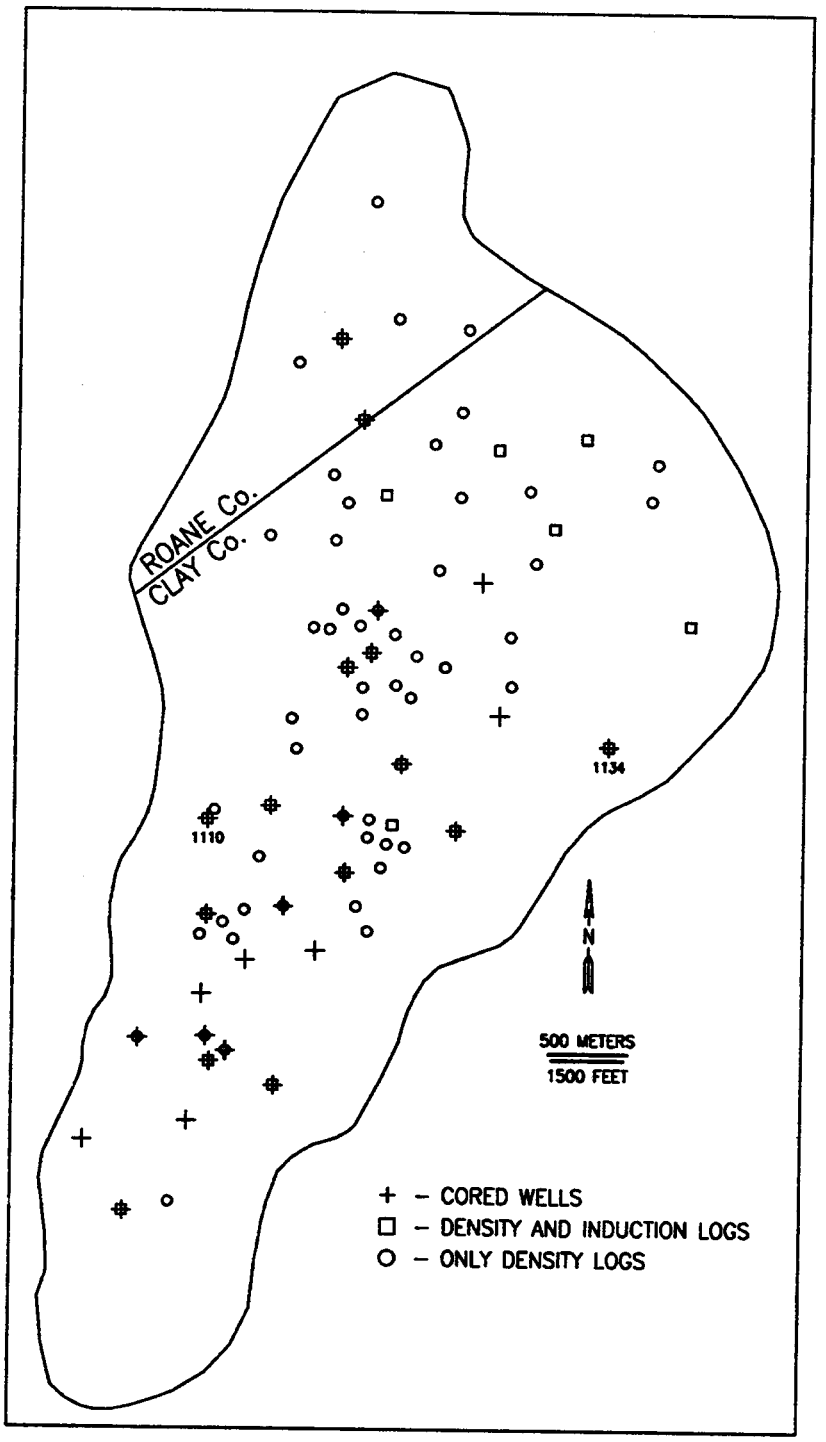

FIGURE 70. Location of cored wells in Granny Creek field. Also shown are the locations of selected wells used in a study of core porosity and permeability versus log porosity and permeability.

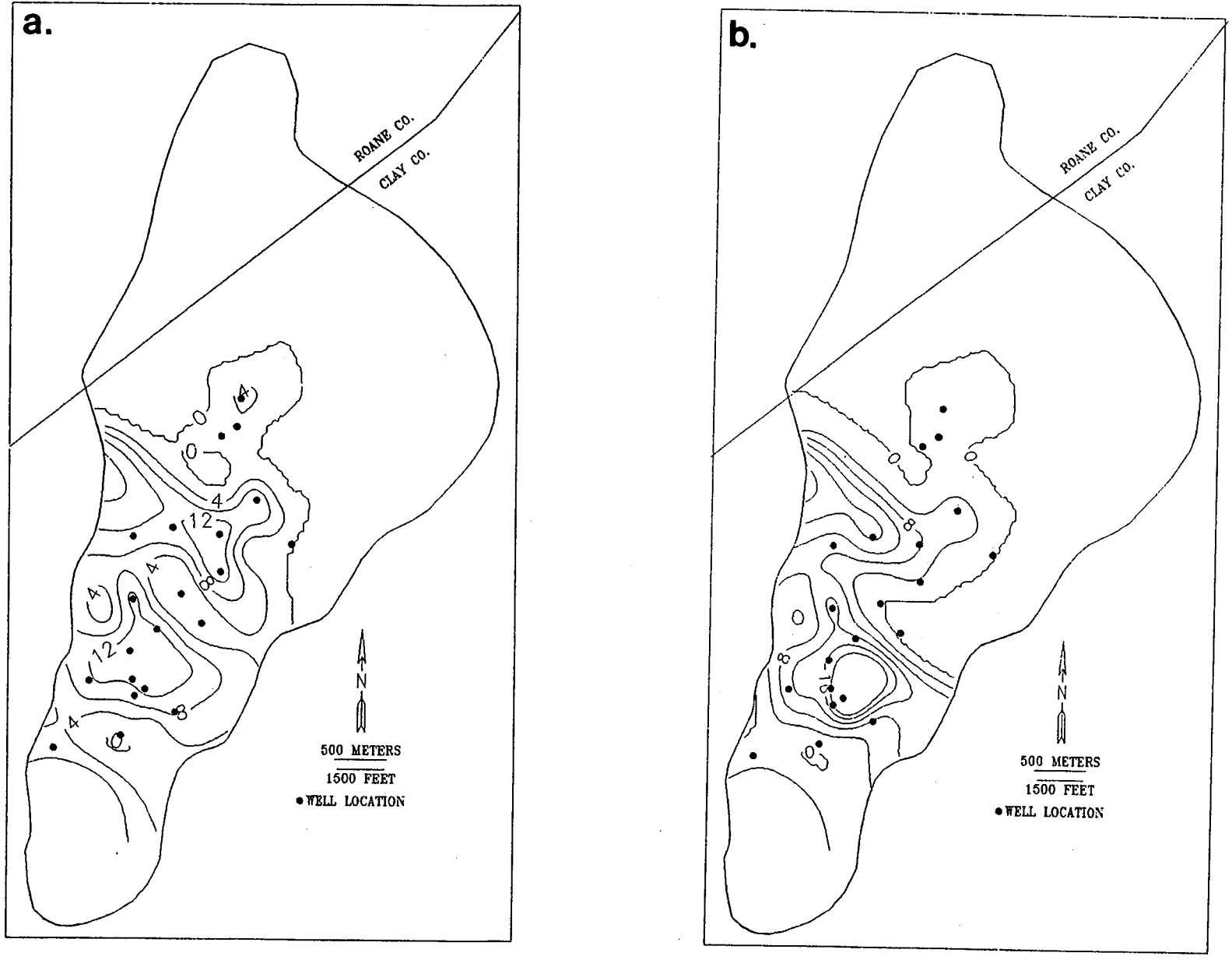

FIGURE 71. Distribution map of Big Injun porosity and permeability - zone A. (a) Average porosity derived from core analysis. Contour interval is 4 percent porosity; (b) Average permeability derived from core analysis. Contour interval is 4 millidarcies.

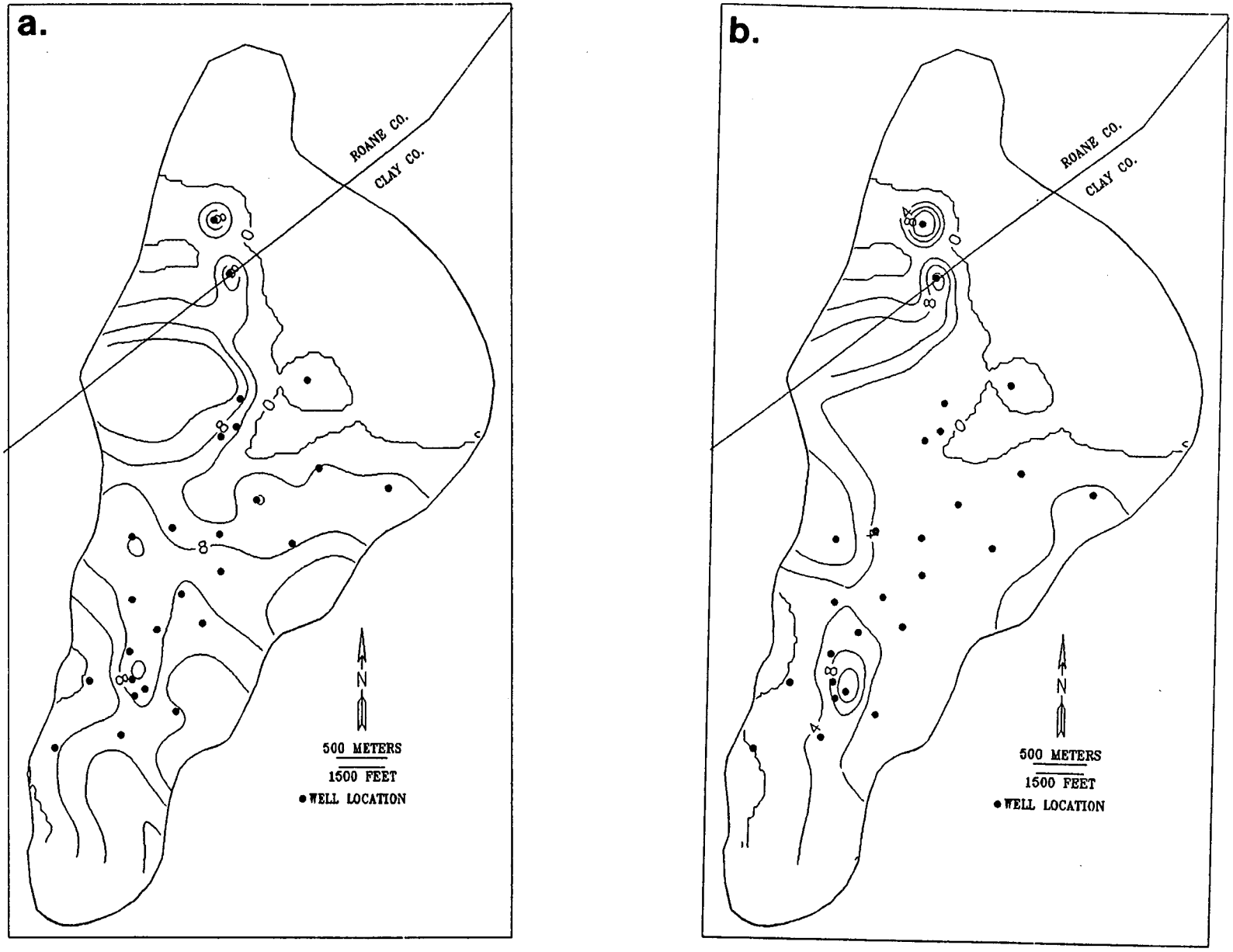

FIGURE 72. Distribution map of Big Injun porosity and permeability - zone B. (a) Average porosity derived from core analysis. Contour interval is 4 percent porosity; (b) Average permeability derived from core analysis. Contour interval is 4 millidarcies.

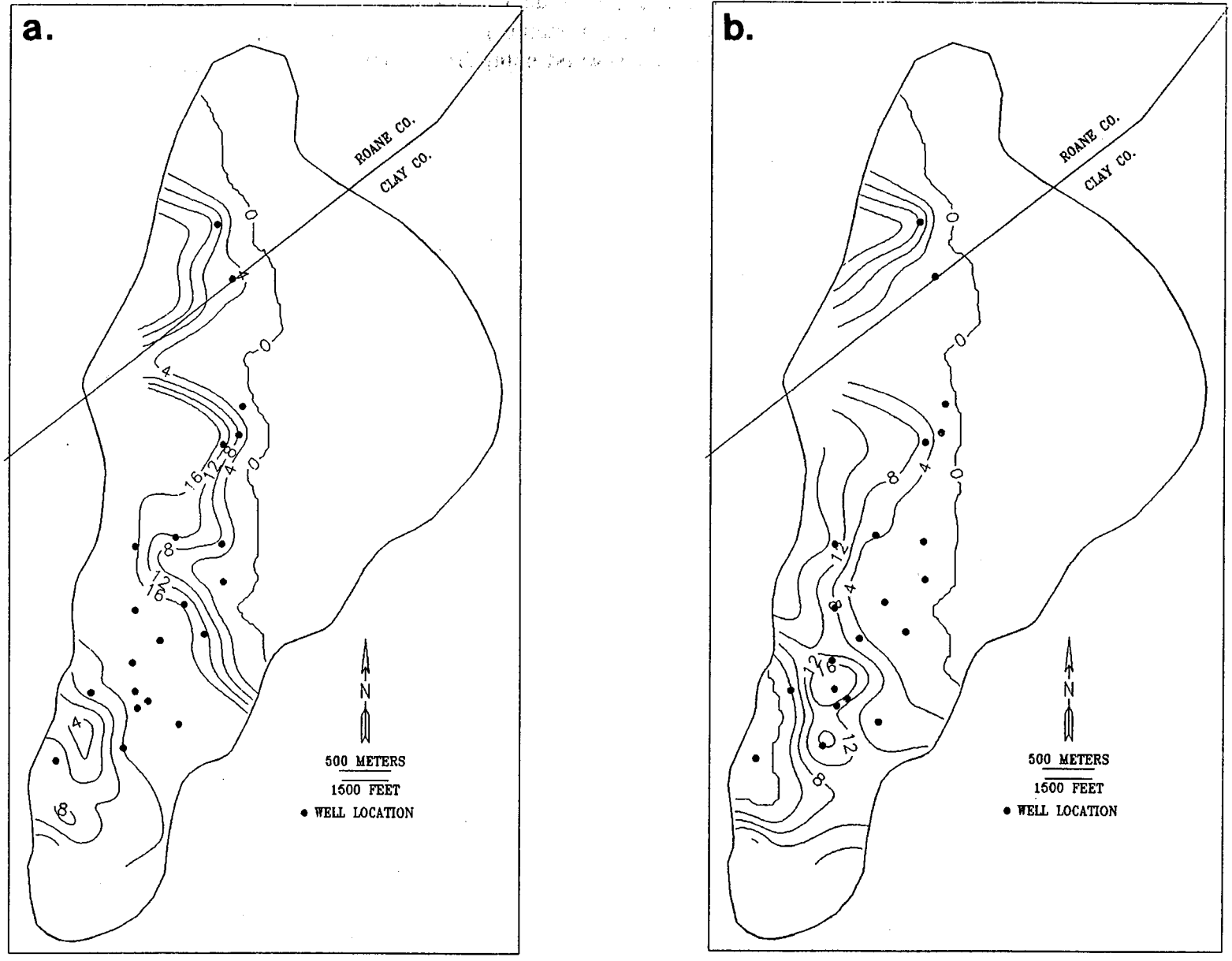

FIGURE 73. Distribution map of Big Injun porosity and permeability - zone C3. (a) Average porosity derived from core analysis. Contour interval is 4 percent porosity; (b) Average permeability derived from core analysis. Contour interval is 4 millidarcies.

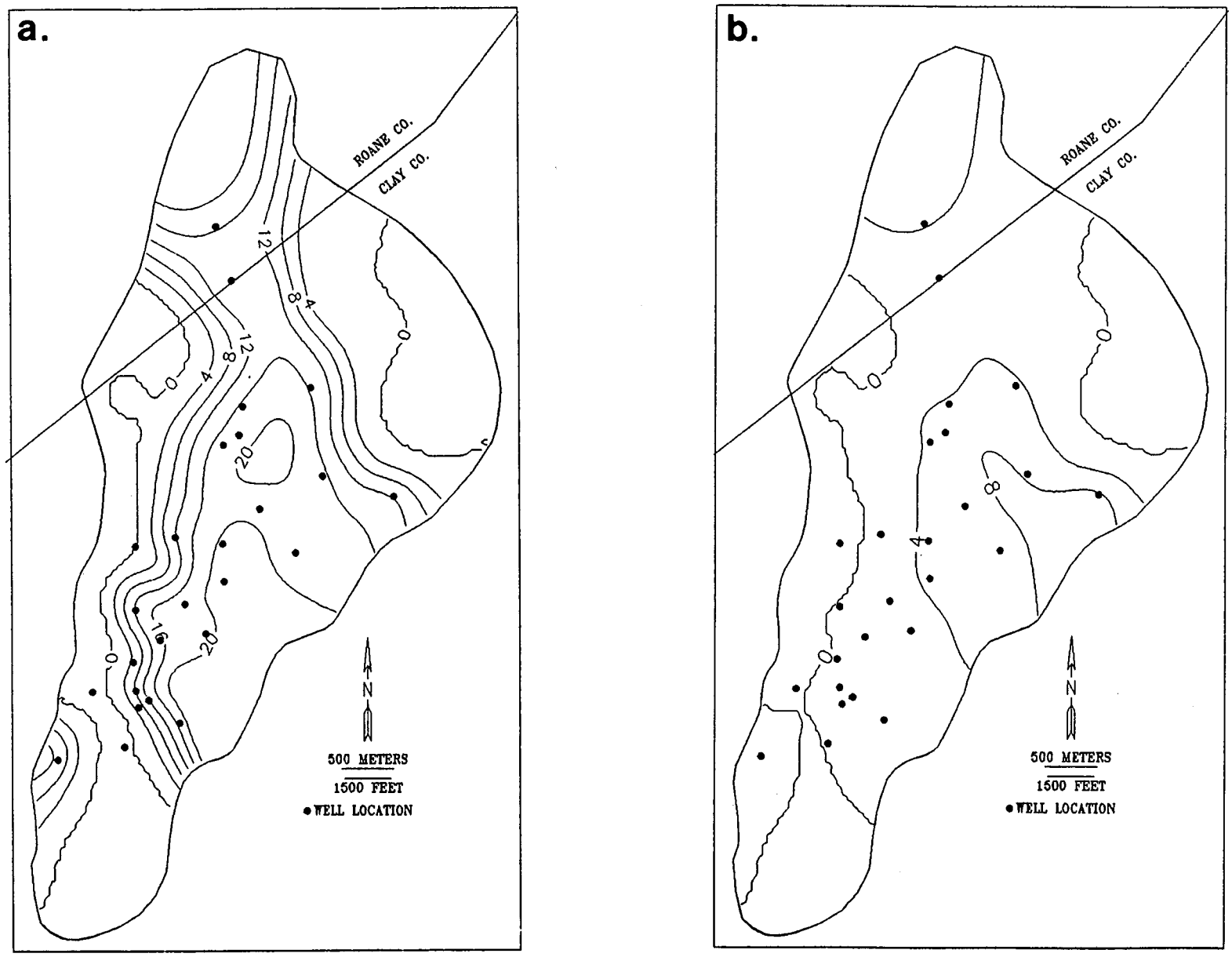

FIGURE 74. Distribution map of Big Injun porosity and permeability - zone C2. (a) Average porosity derived from core analysis. Contour interval is 4 percent porosity; (b) Average permeability derived from core analysis. Contour interval is 4 millidarcies.

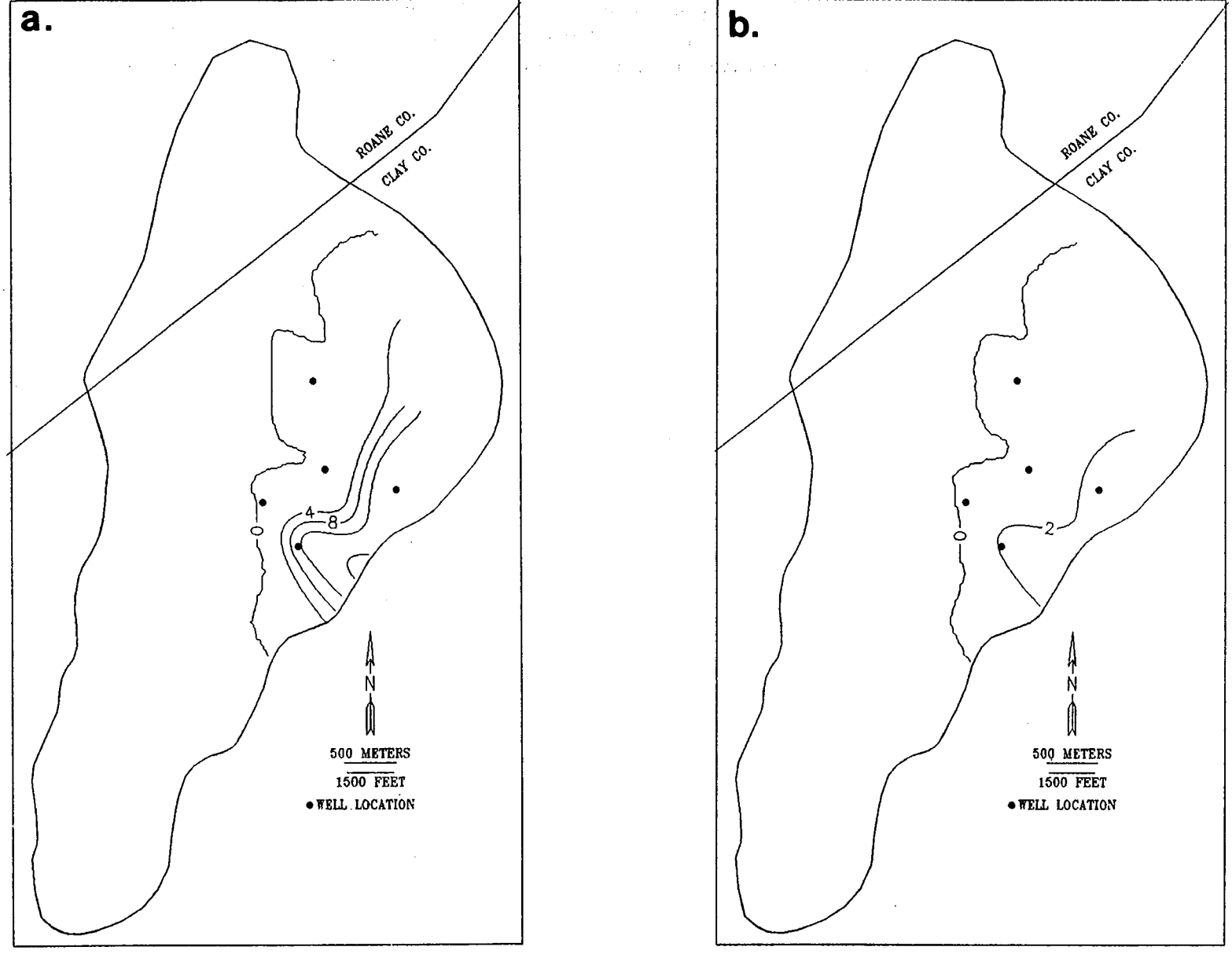

FIGURE 75. Distribution map of Big Injun porosity and permeability - zone C1. (a) Average porosity derived from core analysis. Contour interval is 4 percent porosity; (b) Average permeability derived from core analysis. Contour interval is 2 millidarcies.

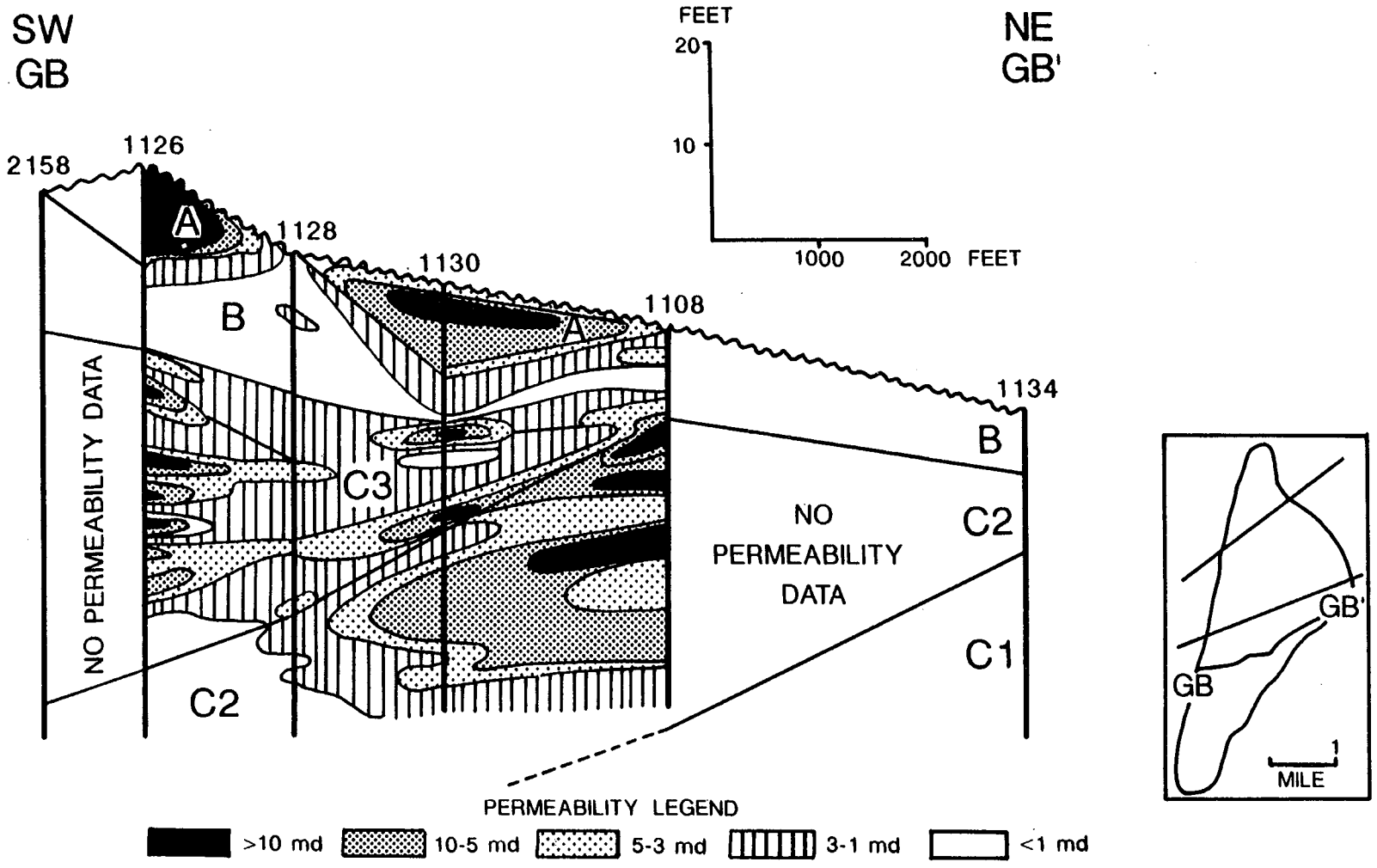

FIGURE 76. Permeability cross section GB-GB' for the Big Injun sandstone in Granny Creek field. Permeability values based on core analysis. Subdivisions of the Big Injun are superimposed on the cross section.

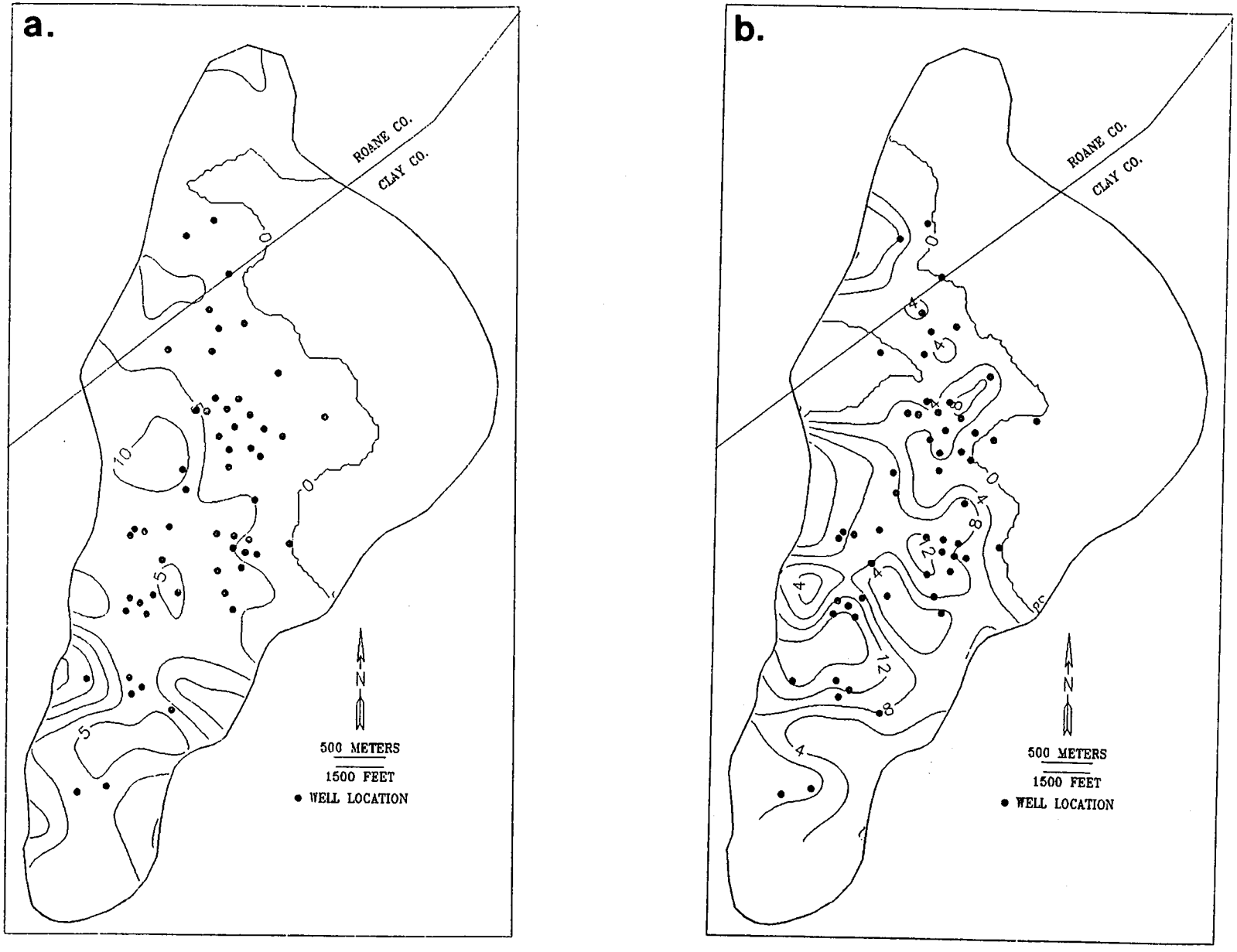

FIGURE 77. Distribution map of Big Injun thickness and porosity - zone A. (a) Thickness derived from well log interpretation. Contour interval is 5 feet; (b) Average porosity derived from well log interpretation. Contour interval is 4 percent porosity.

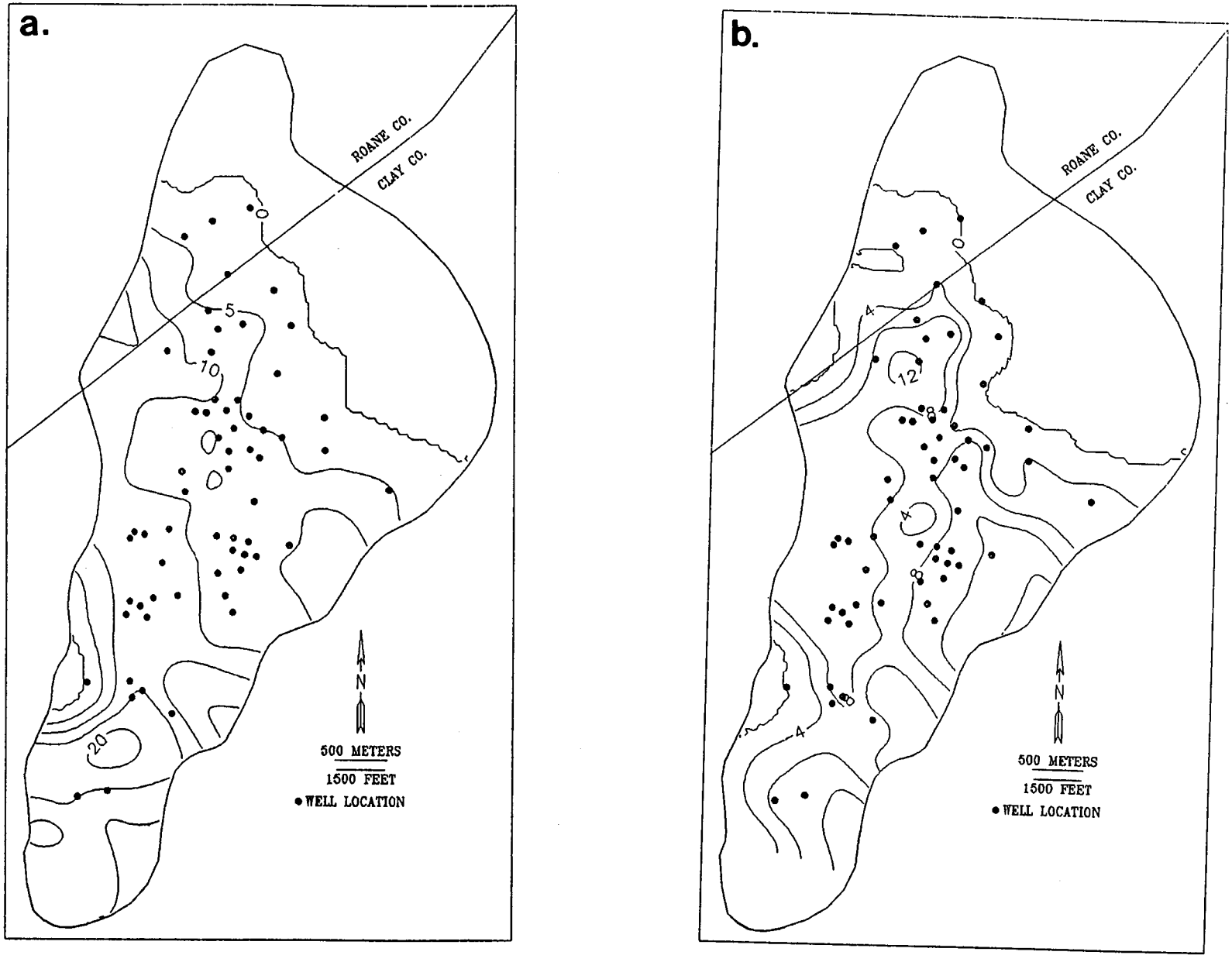

FIGURE 78. Distribution map of Big Injun thickness and porosity - zone B. (a) Thickness derived from well log interpretation. Contour interval is 5 feet; (b) Average porosity derived from well log interpretation. Contour interval is 4 percent porosity.

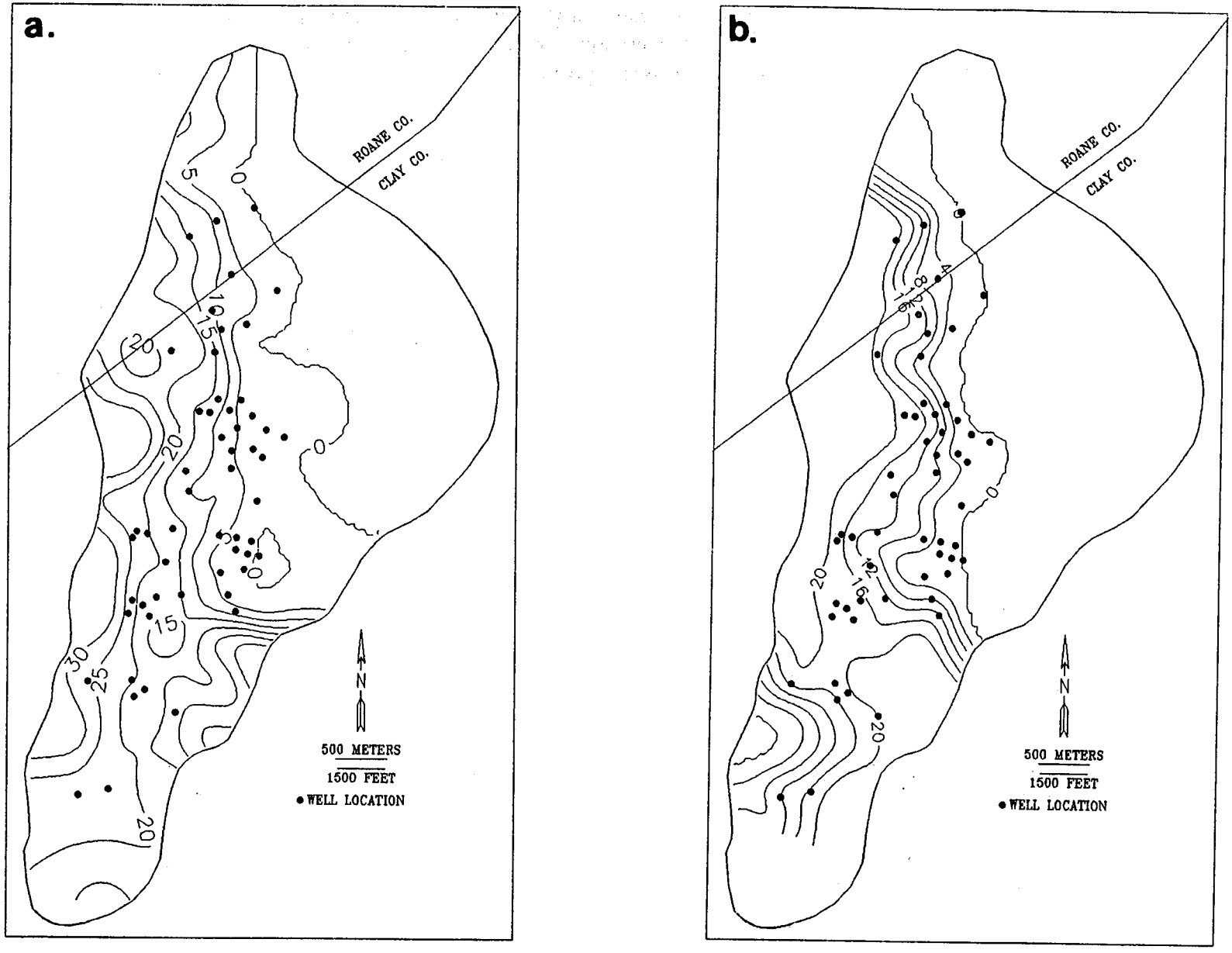

FIGURE 79. Distribution map of Big Injun thickness and porosity - zone C3. (a) Thickness derived from well log interpretation. Contour interval is 5 feet; (b) Average porosity derived from well log interpretation. Contour interval is 4 percent porosity.

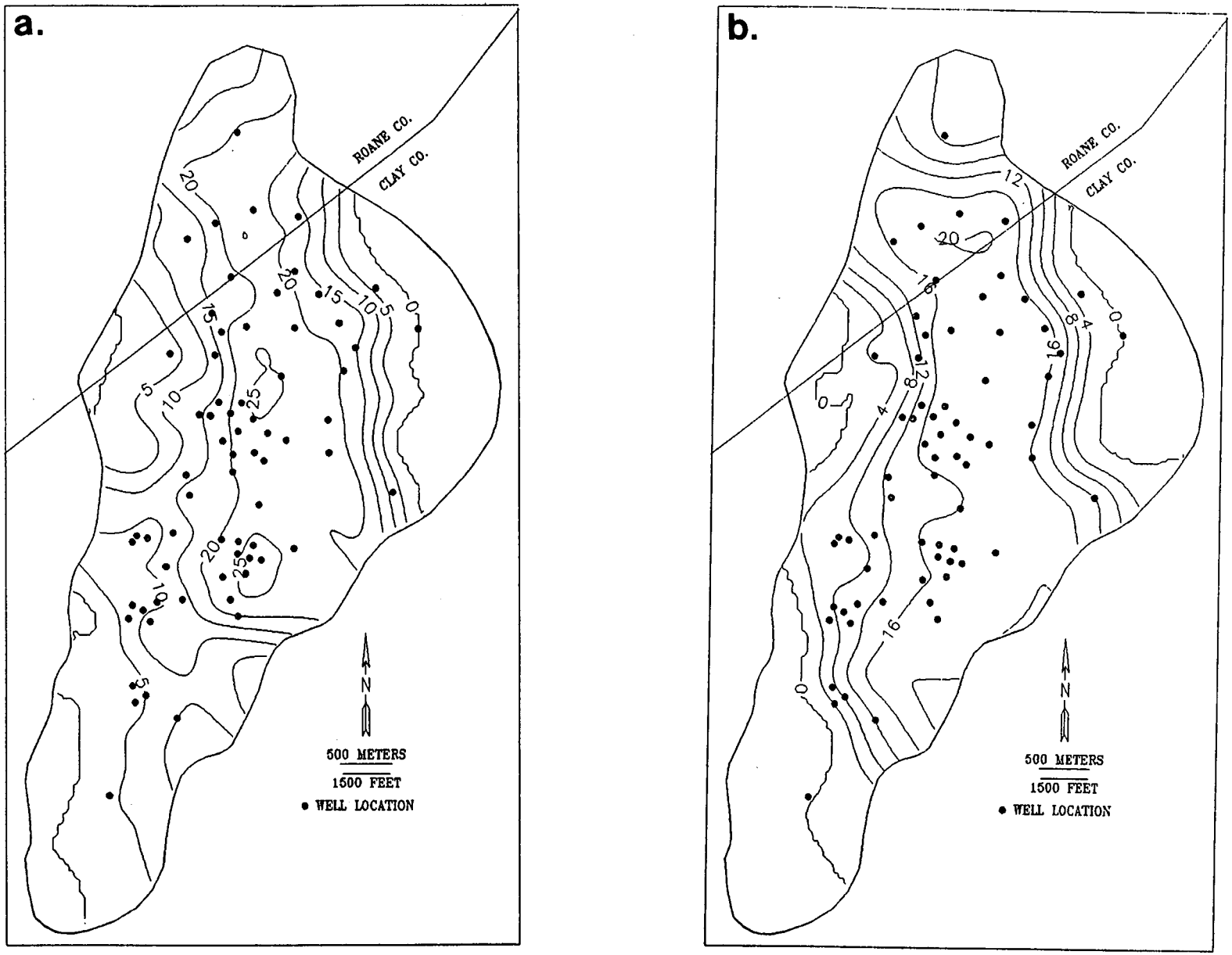

FIGURE 80. Distribution map of Big Injun thickness and porosity - zone C2. (a) Thickness derived from well log interpretation. Contour interval is 5 feet; (b) Average porosity derived from well log interpretation. Contour interval is 4 percent porosity.

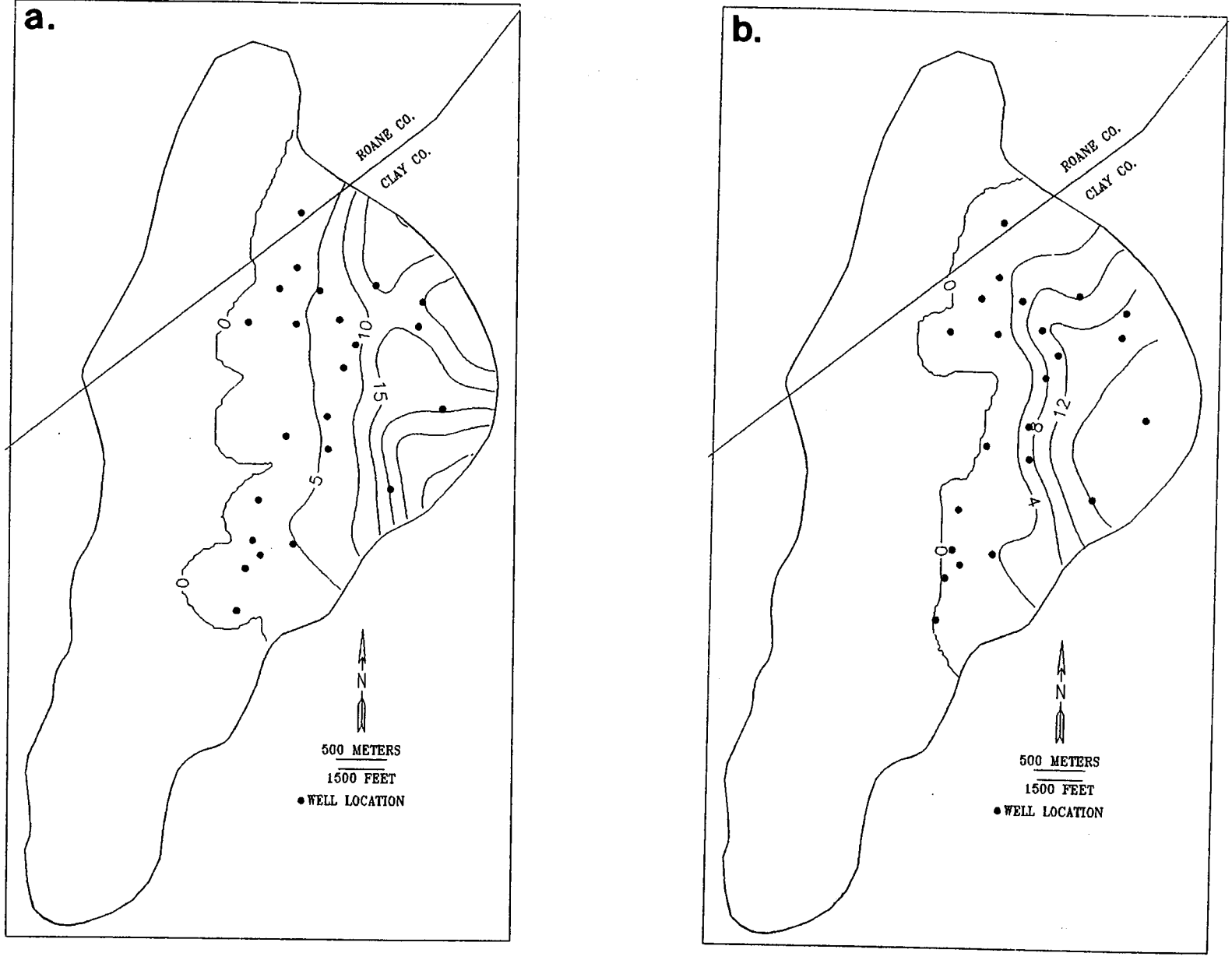

FIGURE 81. Distribution map of Big Injun thickness and porosity - zone C1. (a) Thickness derived from well log interpretation. Contour interval is 5 feet; (b) Average porosity derived from well log interpretation. Contour interval is 4 percent porosity.

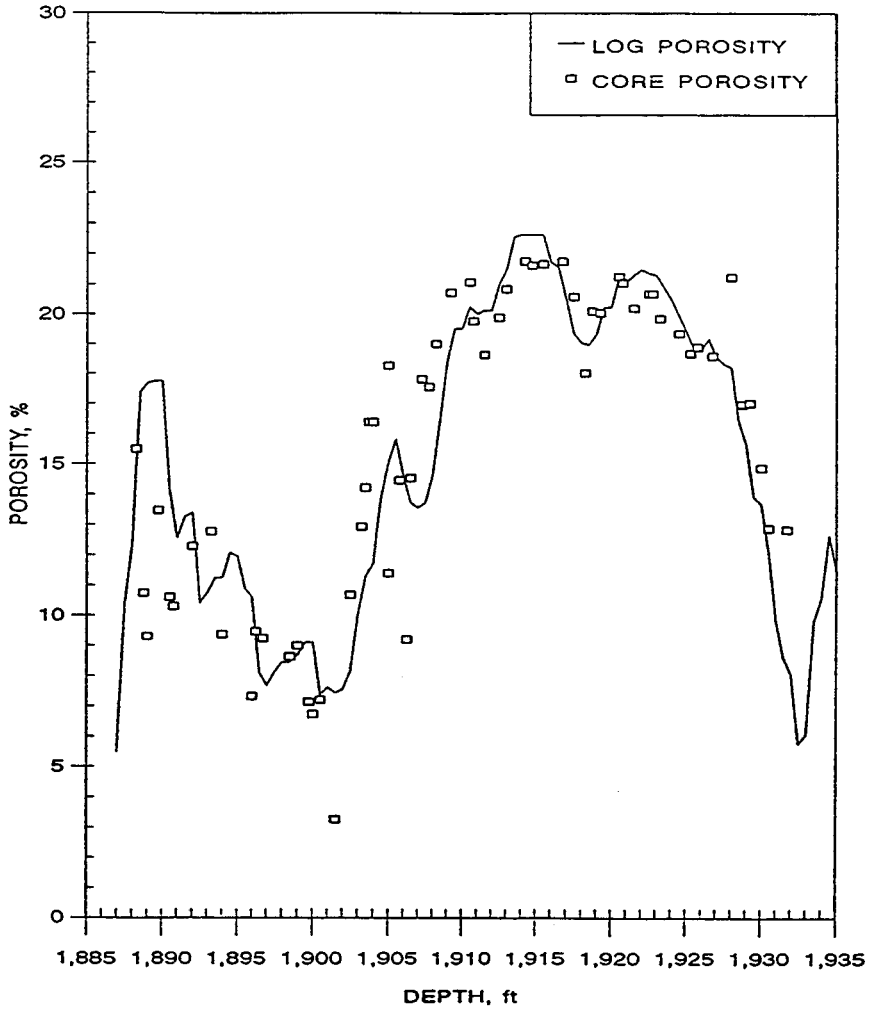

FIGURE 82. Comparison of core analysis and well log values for Clay 1110. (a) Core porosity versus log porosity; (b) Core permeability versus various geophysical log responses relative to depth.

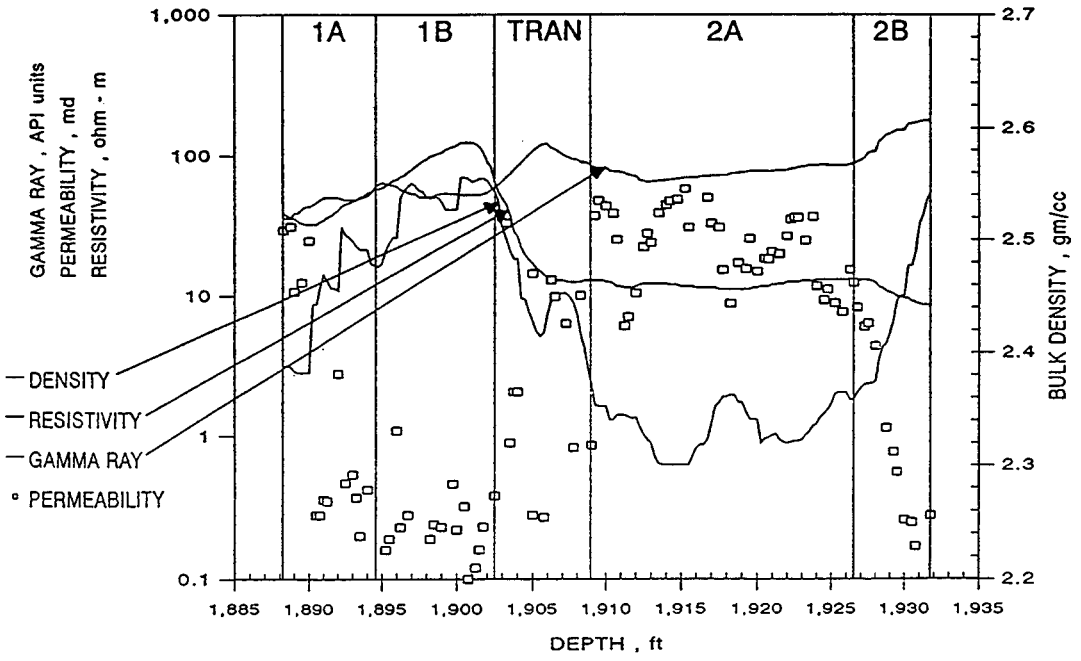

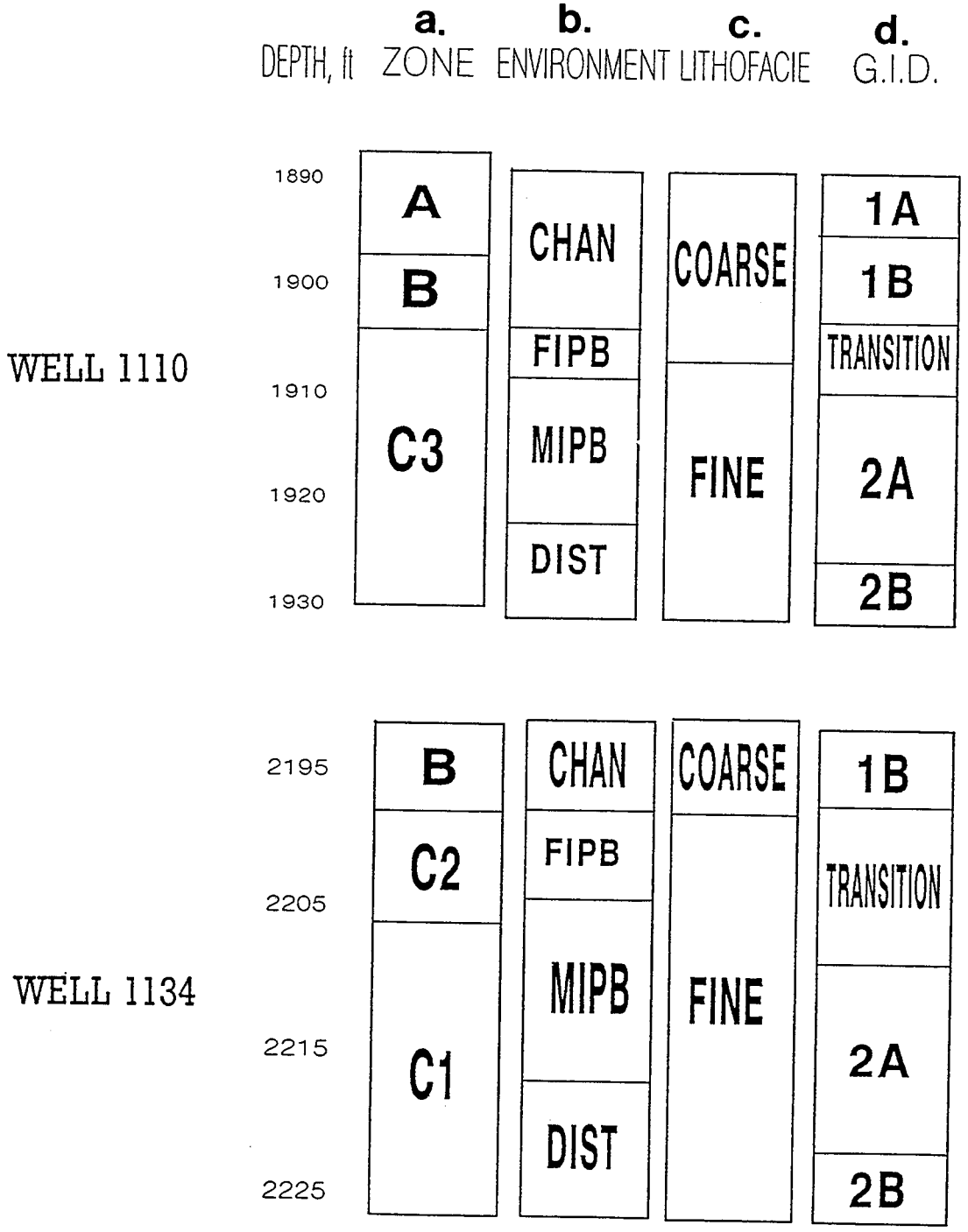

FIGURE 83. Subdivisions of the Big Injun sandstone for wells Clay 1110 and 1134. (a) Based density log response; (b) Based on depositional environment; (c) Based on grain size; (d) Based on Gamma Ray-Induction-Density (G.I.D.) log response.

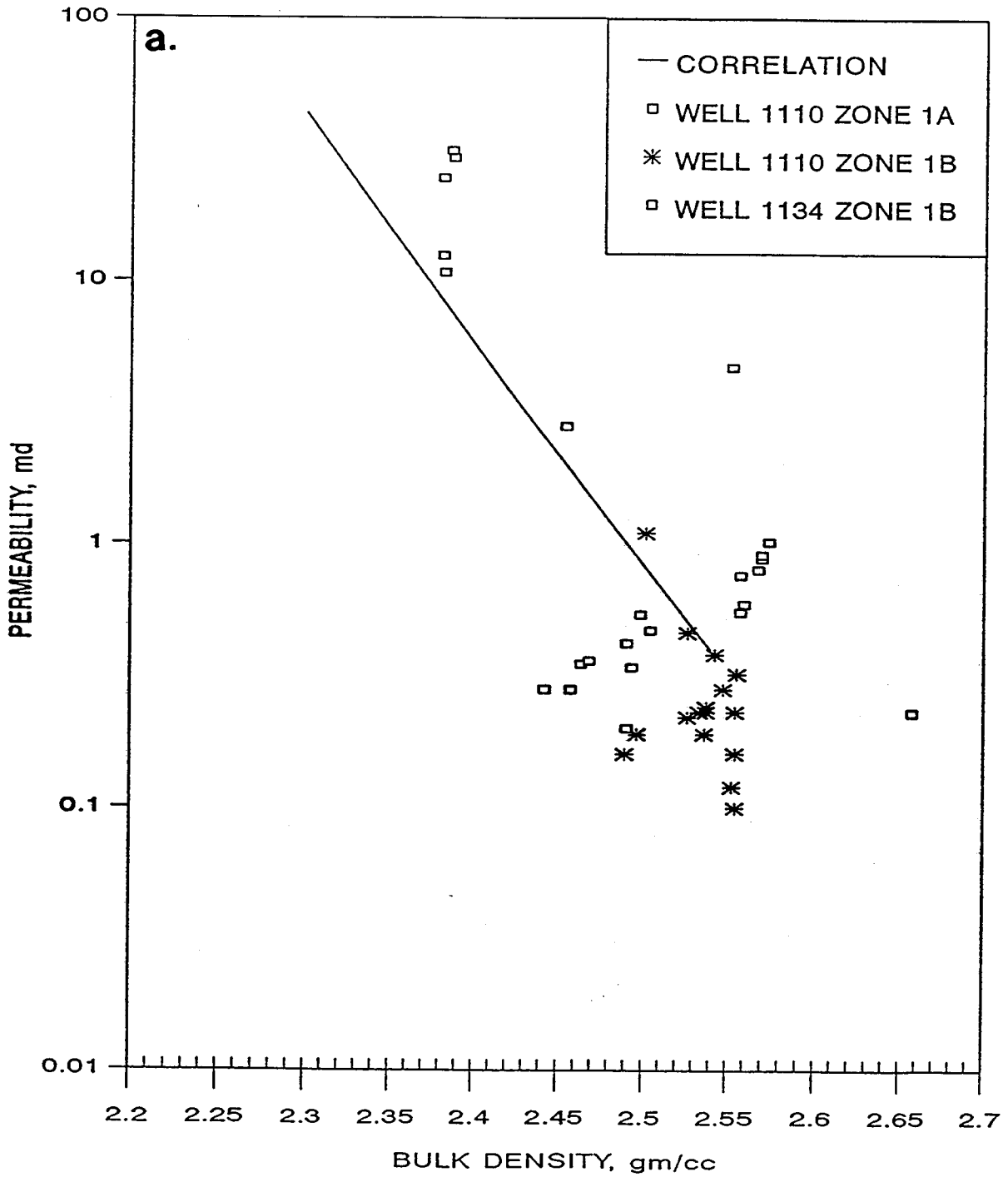

FIGURE 84a. Graph of core permeability versus log density for Gamma Ray-Induction-Density Zone 1 in Clay 1110 and 1134.

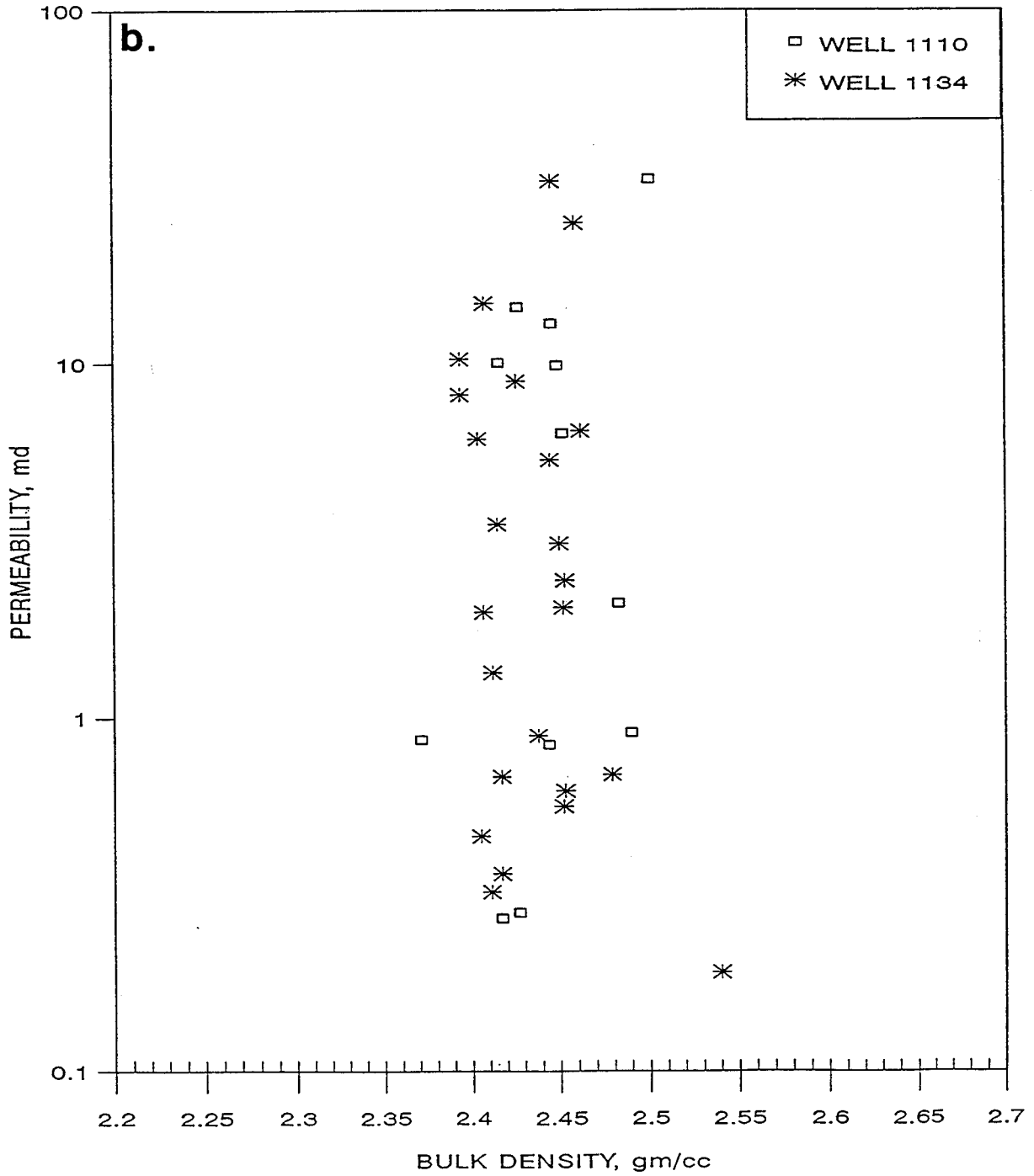

FIGURE 84b. Graph of core permeability versus log density for Gamma Ray-Induction-Density Transition Zone in Clay 1110 and 1134.

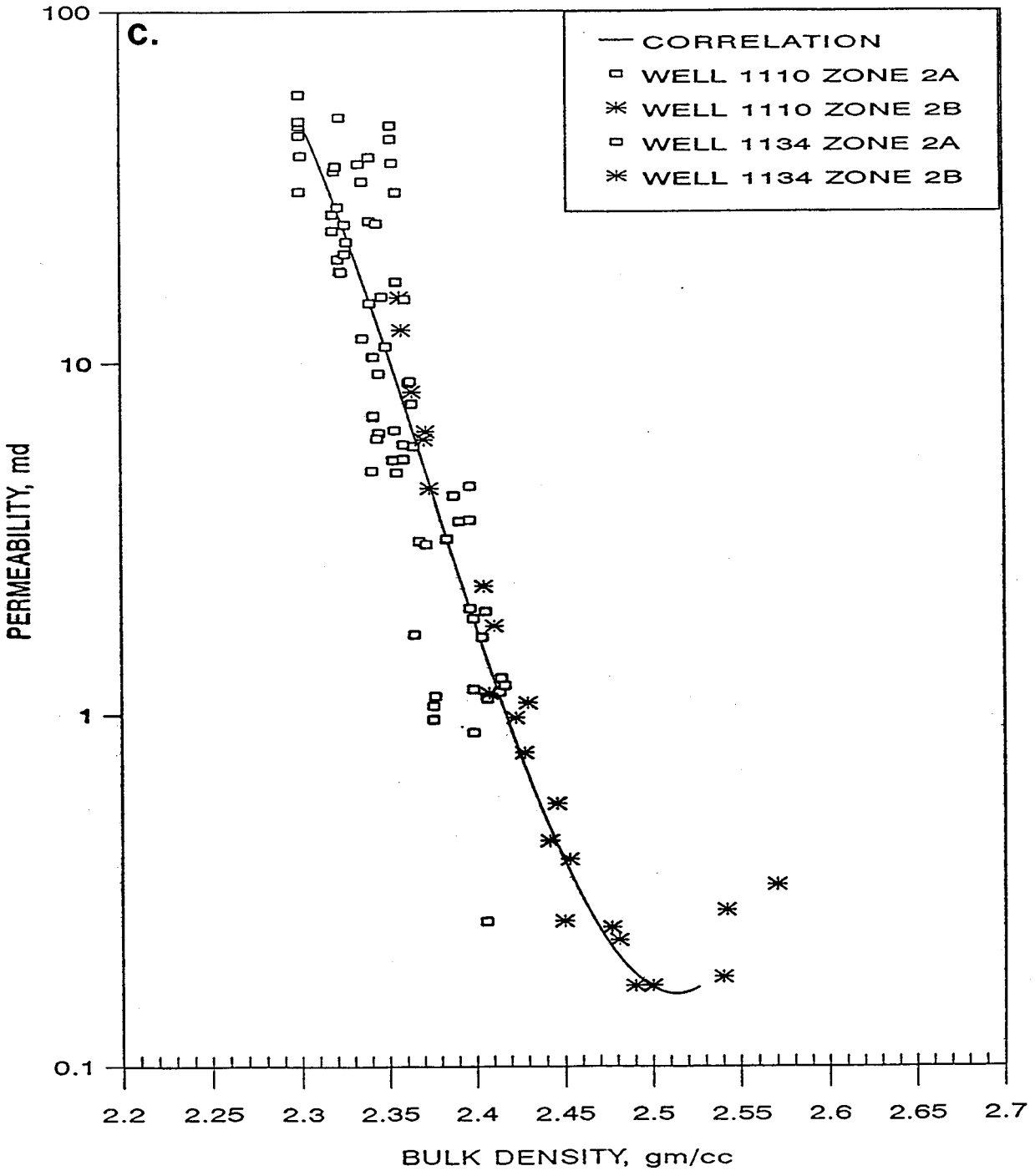

FIGURE 84c. Graph of core permeability versus log density for Gamma Ray-Induction-Density Zone 2 in Clay 1110 and 1134.

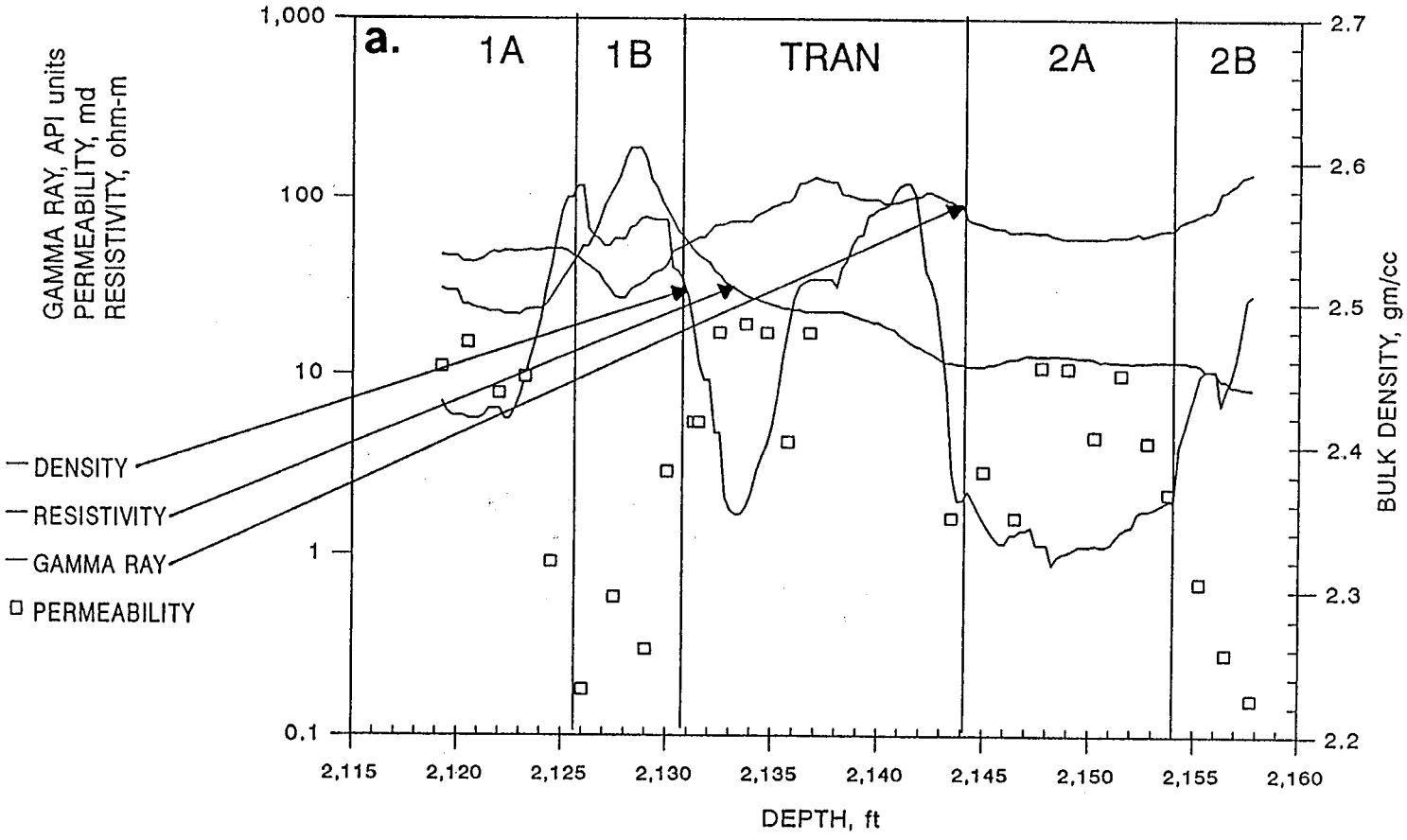

FIGURE 85a. Example of delineation of Gamma Ray-Induction-Density zones for Clay 1107.

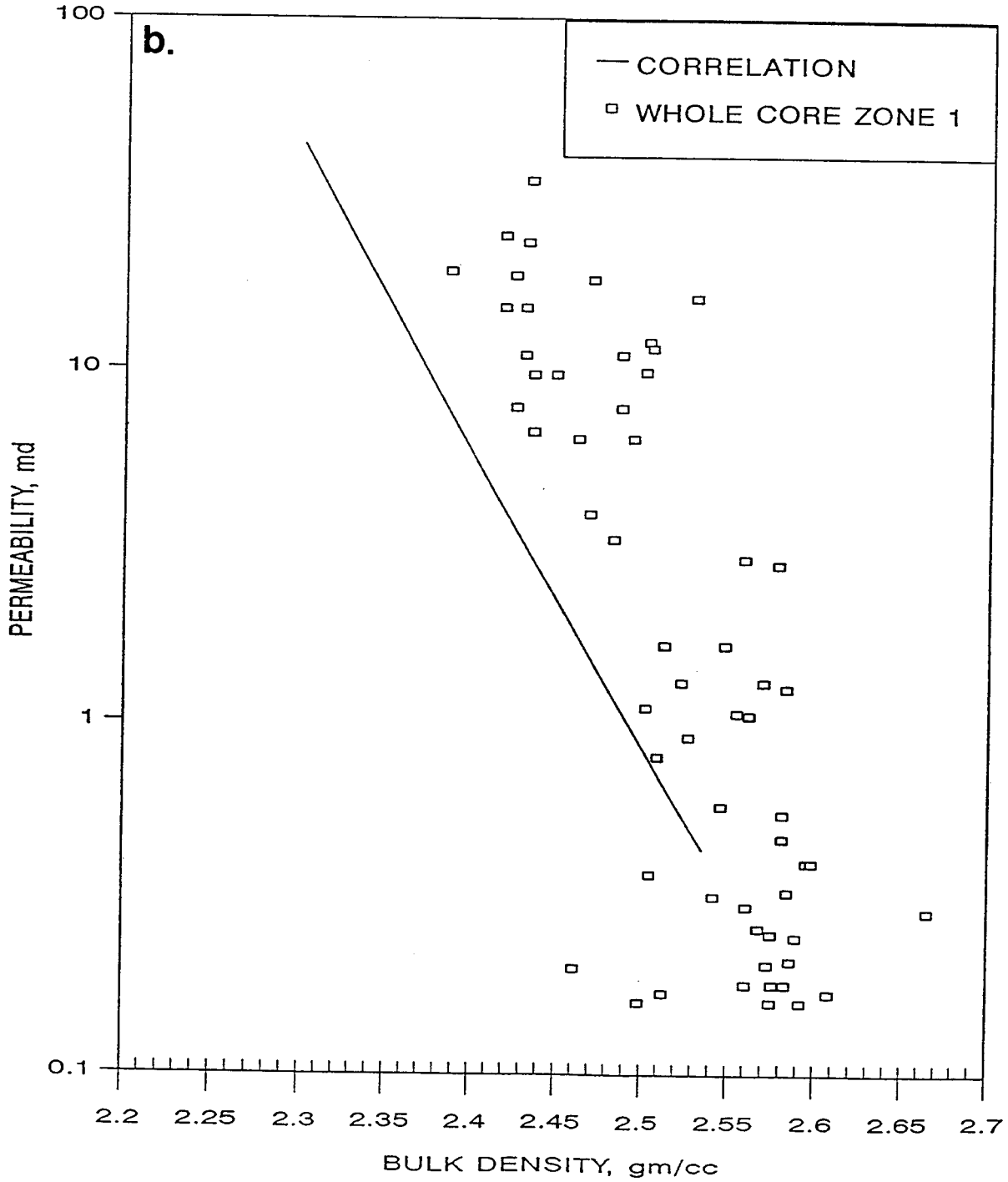

FIGURE 85b. Graph of core permeability versus log density for seven wells with core analysis - Gamma Ray-Induction-Density Zone 1. Curvilinear regression line based on data for Clay 1110 and 1134 is superimposed for comparison.

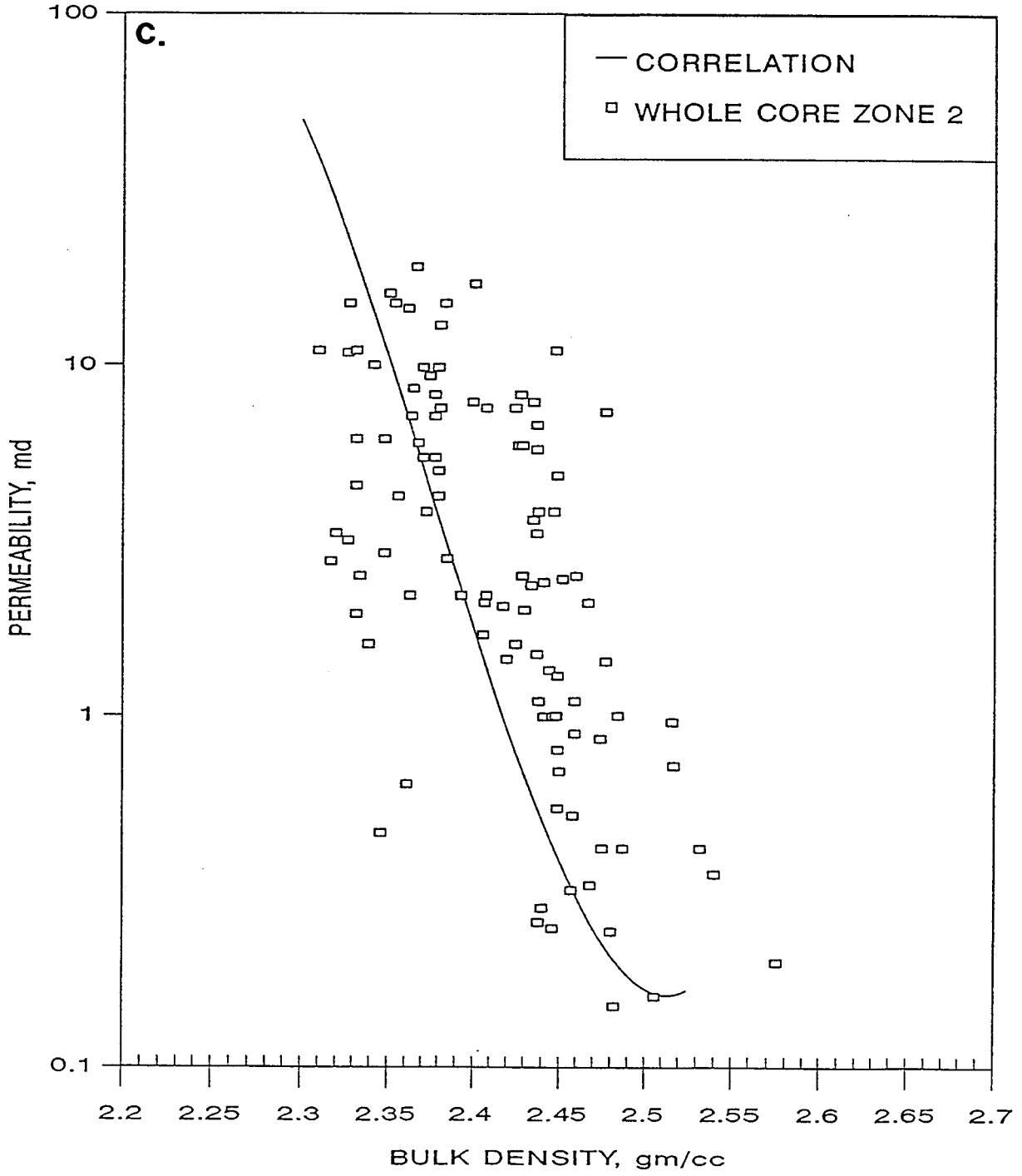

FIGURE 85c. Graph of core permeability versus log density for seven wells with core analysis - Gamma Ray-Induction-Density Zone 2. Curvilinear regression line based on data for Clay 1110 and 1134 is superimposed for comparison.

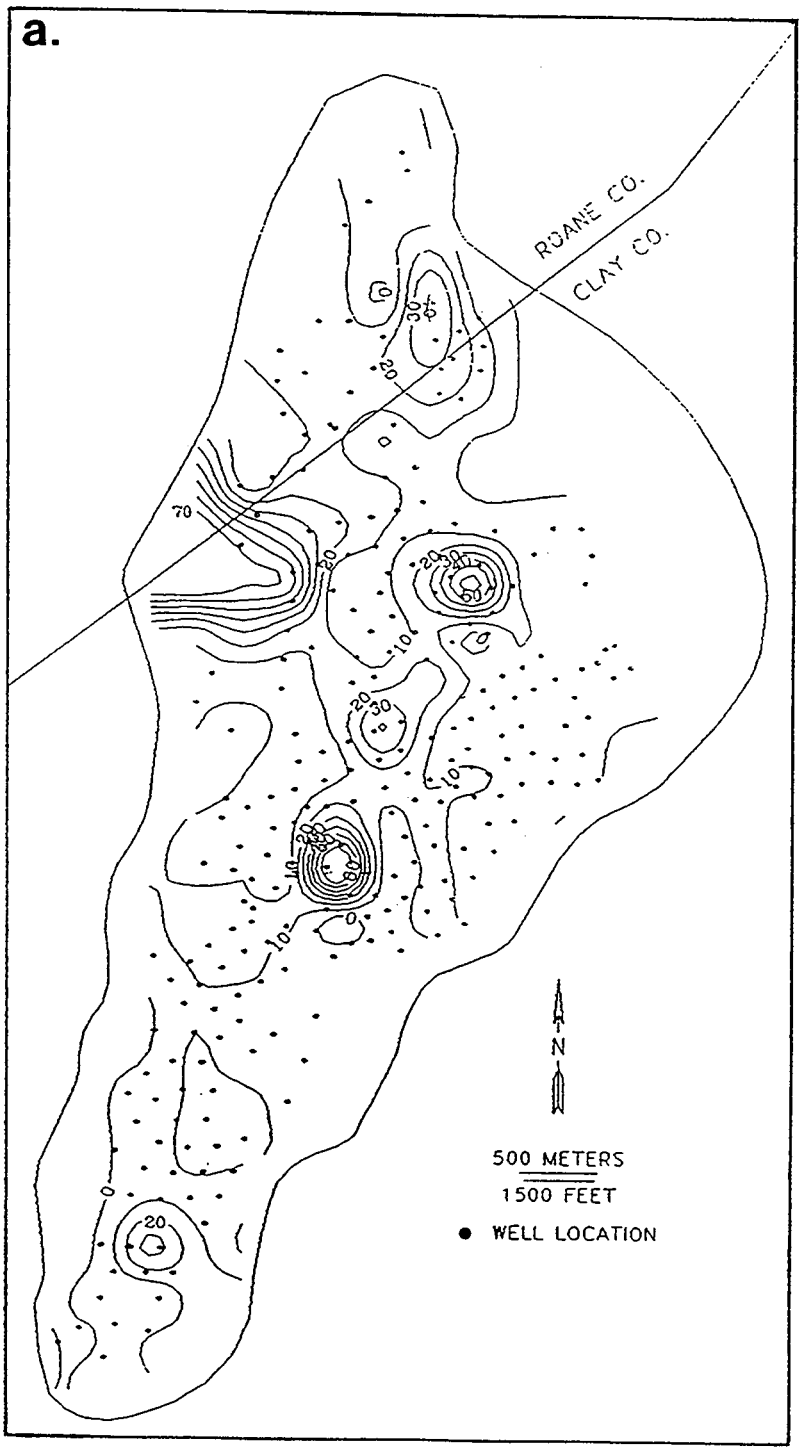

FIGURE 86a. Distribution of permeability based on Big Injun initial potential data from Granny Creek field. Contour interval is 10 millidarcies.

FIGURE 86b. Distribution of permeability based on Big Injun water injection data for Granny Creek field. Contour interval is 0.2 millidarcies.

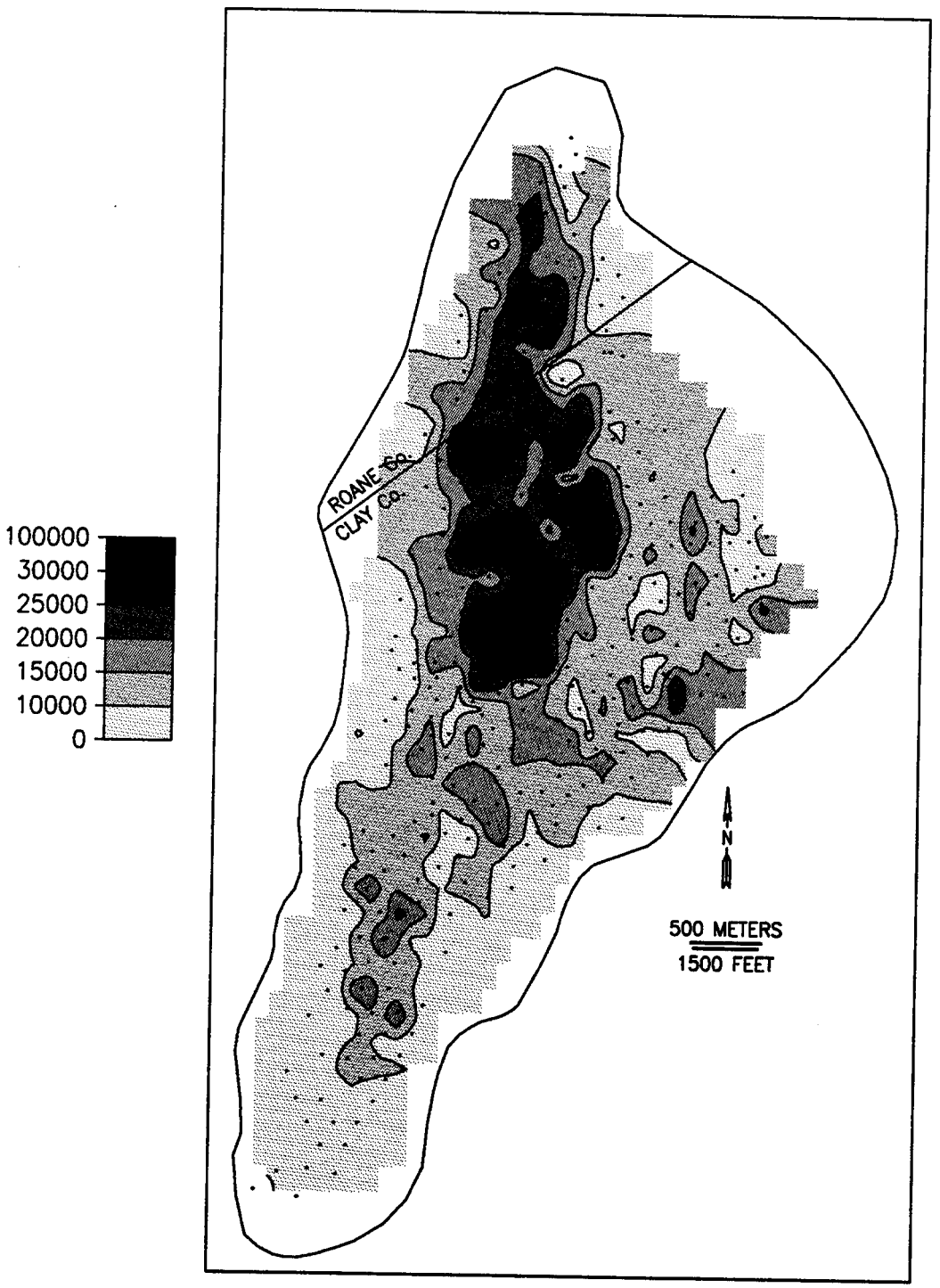

FIGURE 87. Contour map of cumulative oil production from uppermost Price Formation sandstone during first ten years of production in Granny Creek field. Units are barrels of oil.

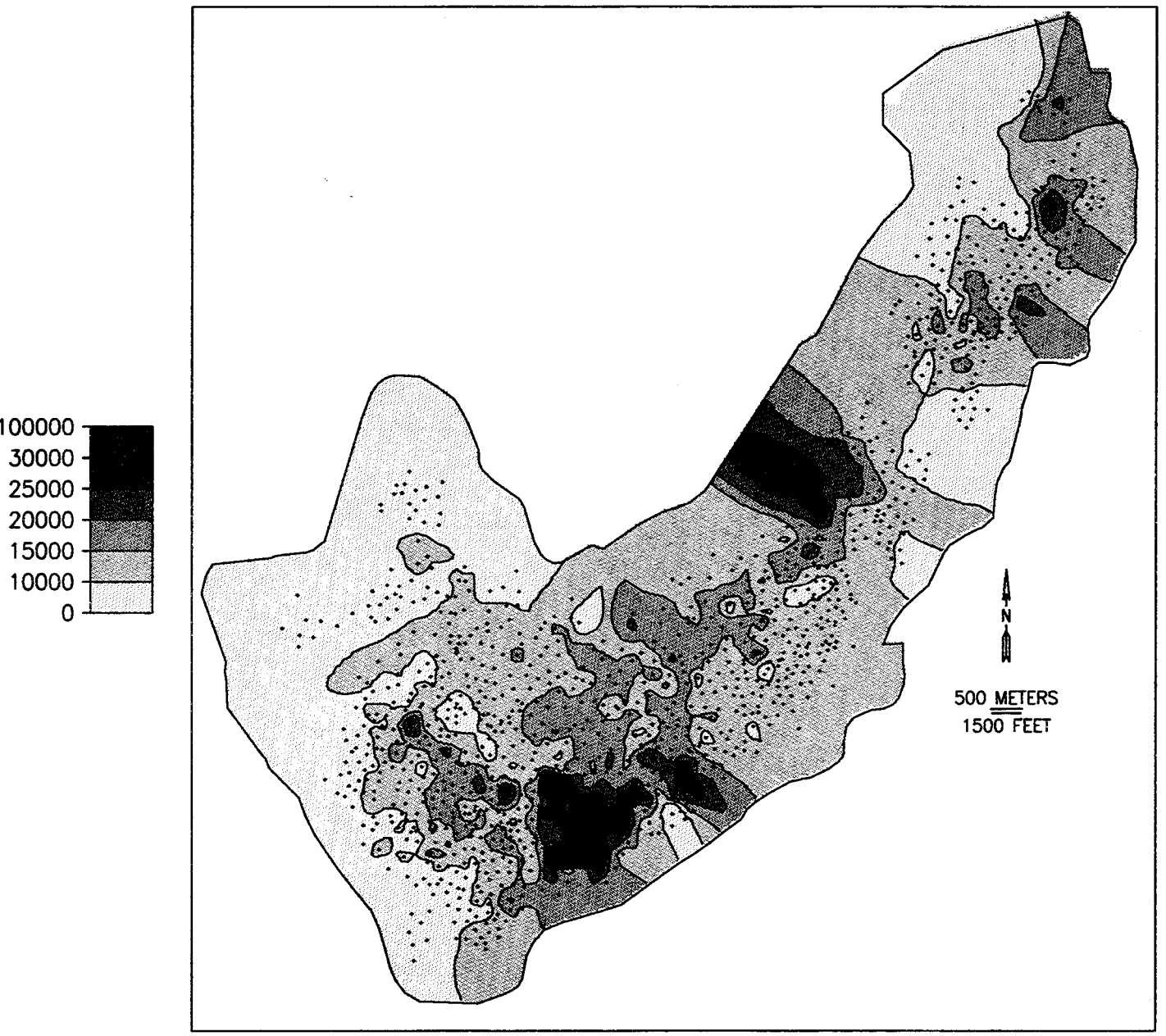

FIGURE 88. Contour map of cumulative oil production from uppermost Price Formation sandstone during first ten years of production in Rock Creek field. Units are barrels of oil.

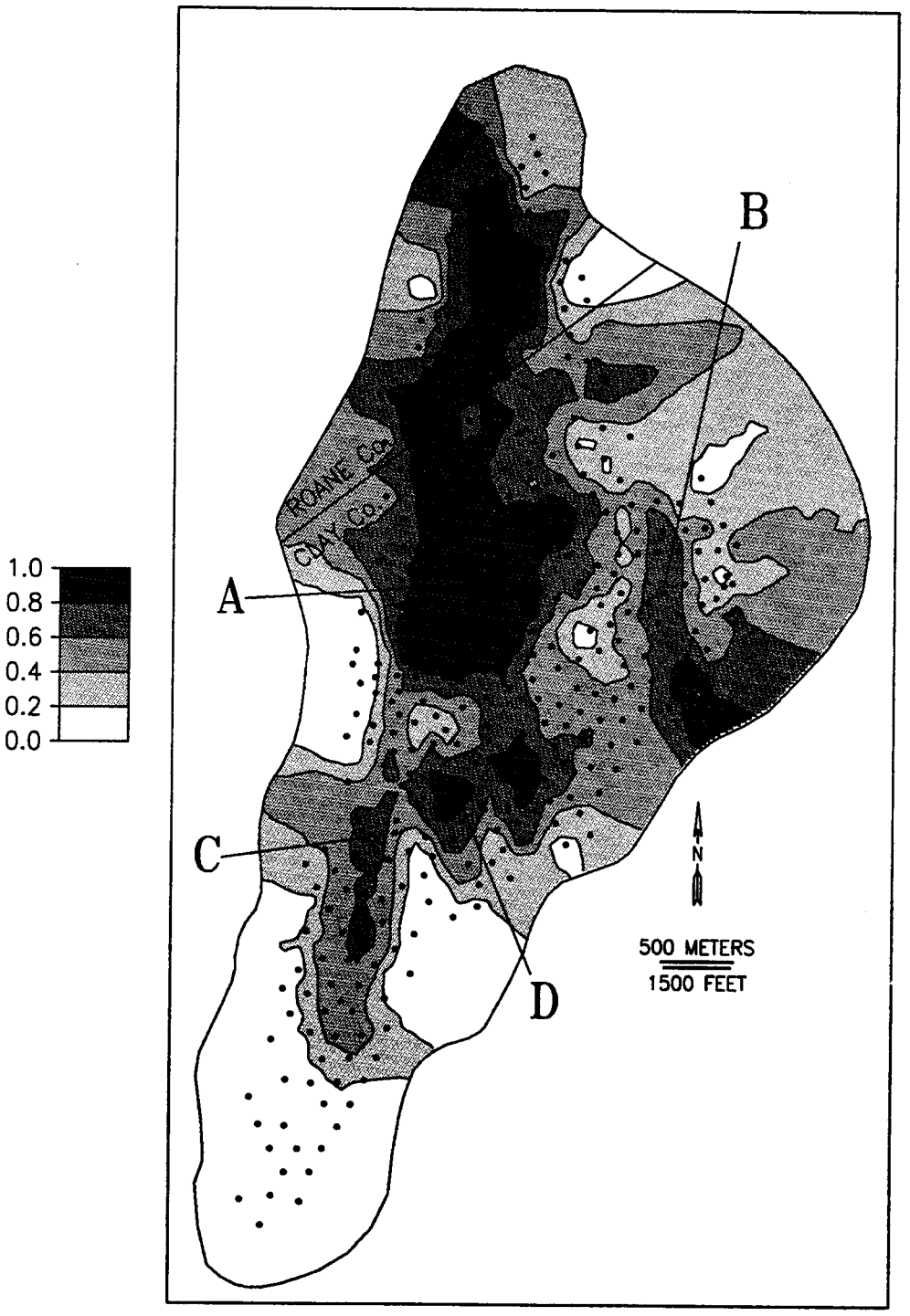

FIGURE 89. Contour map of probability of obtaining ten-year cumulative production exceeding 12,335 barrels of oil (50th percentile) in Granny Creek field.

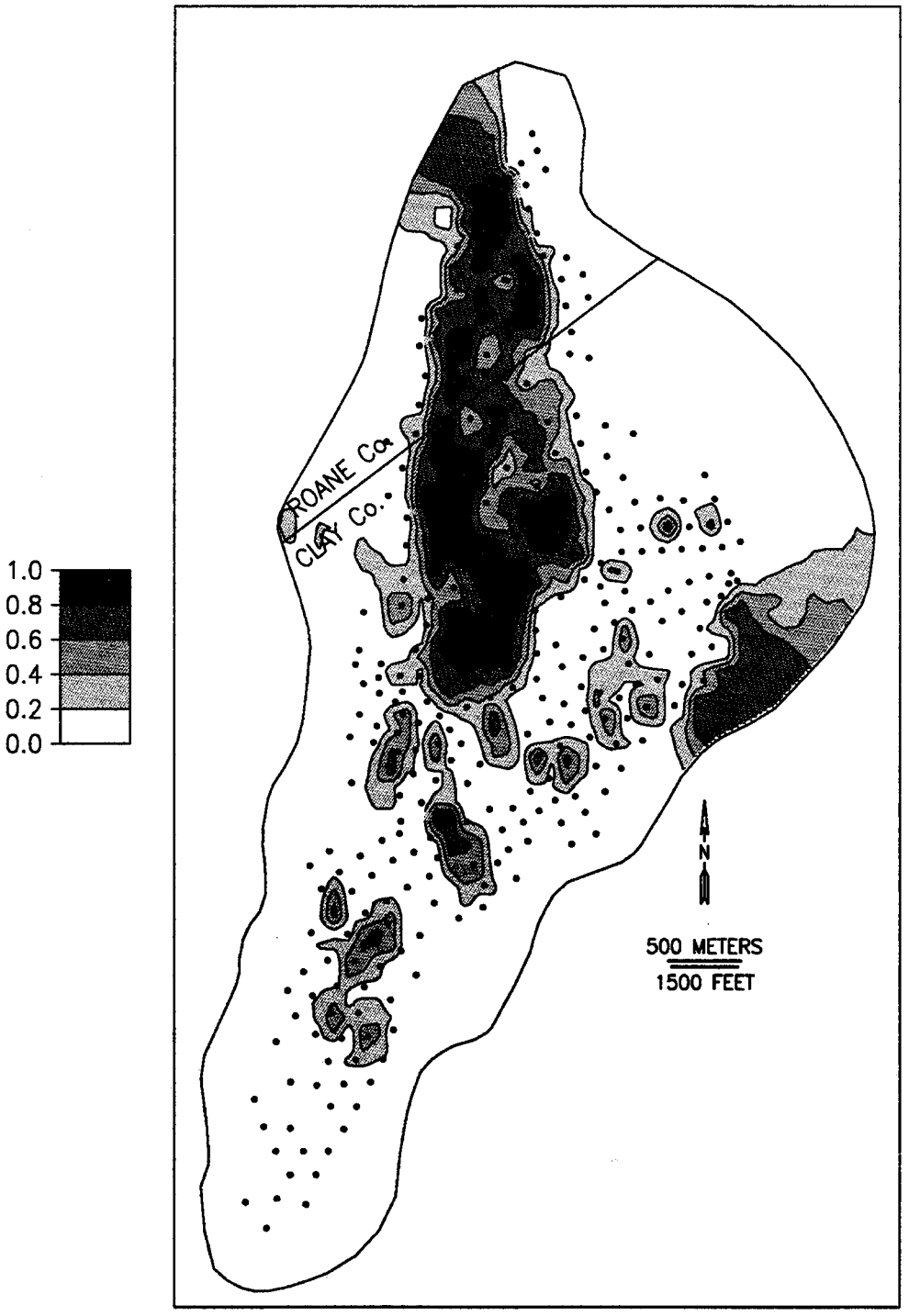

FIGURE 90. Contour map of probability of obtaining ten-year cumulative production exceeding 18,244 barrels of oil (75th percentile) in Granny Creek field.

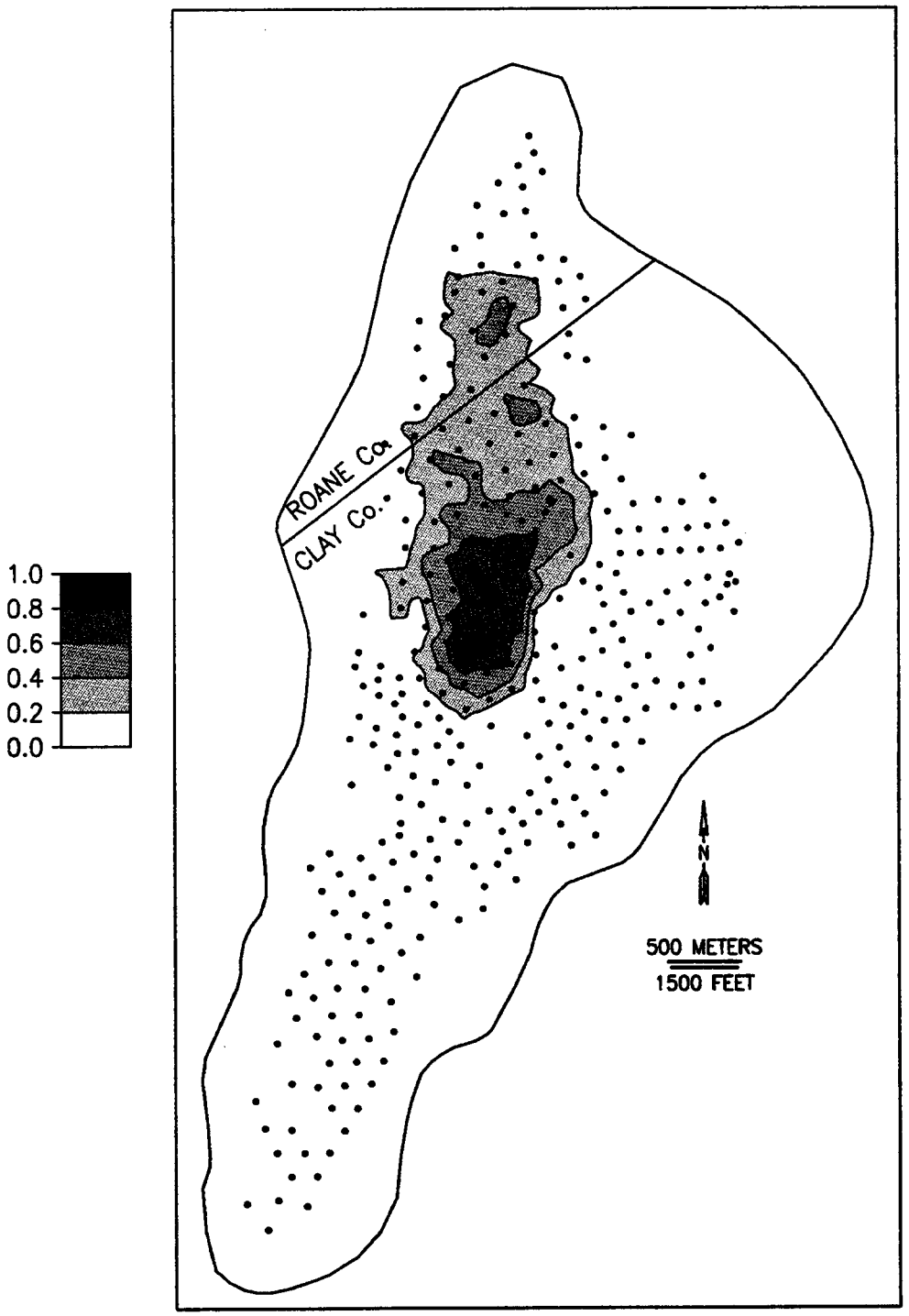

FIGURE 91. Contour map of probability of obtaining ten-year cumulative production exceeding 25,000 barrels of oil (90th percentile) in Granny Creek field.

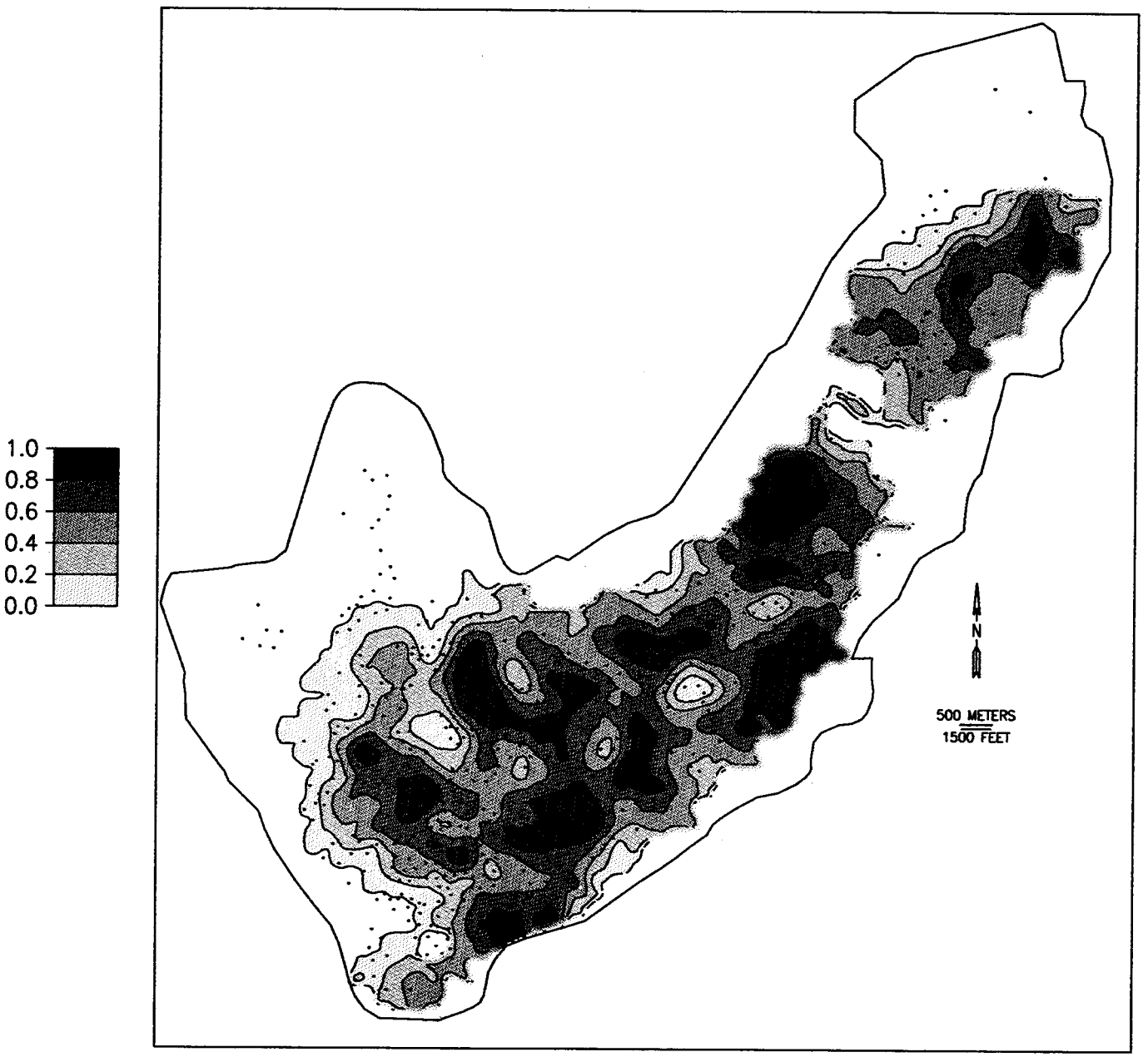

FIGURE 92. Contour map of probability of obtaining ten-year cumulative production exceeding 12,714 barrels of oil (50th percentile) in Rock Creek field.

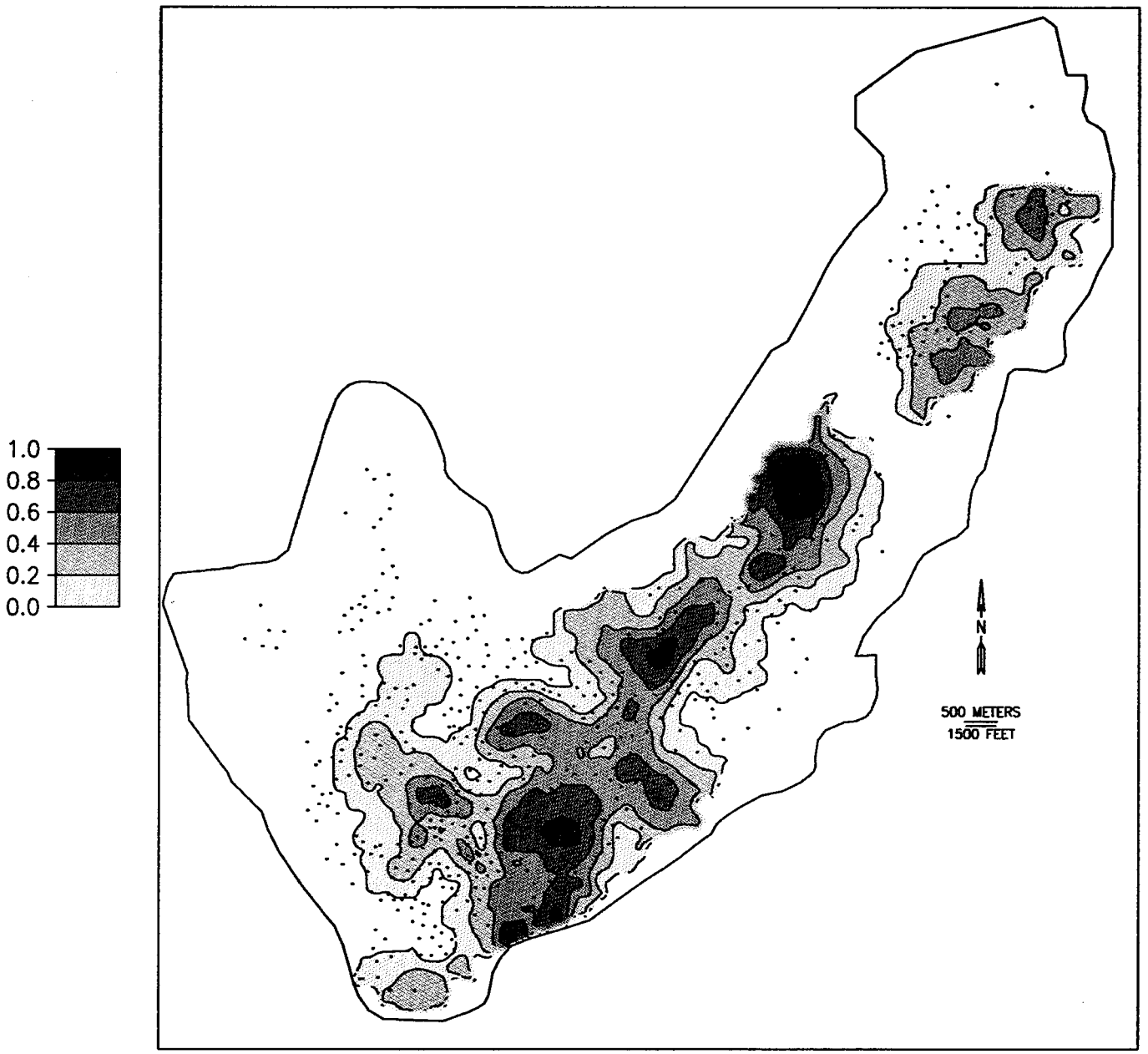

FIGURE 93. Contour map of probability of obtaining ten-year cumulative production exceeding 17,069 barrels of oil (75th percentile) in Rock Creek field.

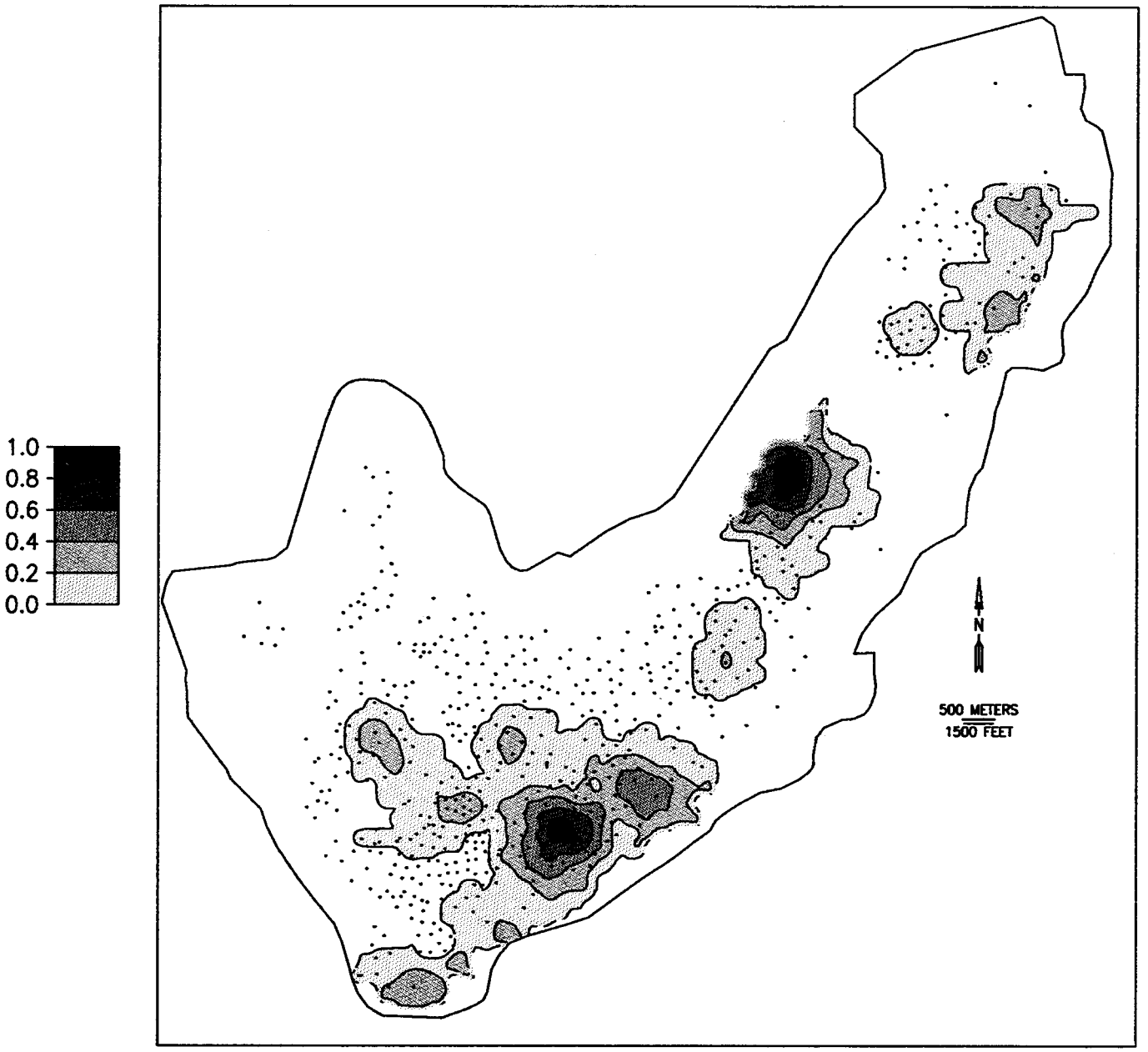

FIGURE 94. Contour map of probability of obtaining ten-year cumulative production exceeding 22,048 barrels of oil (90th percentile) in Rock Creek field.

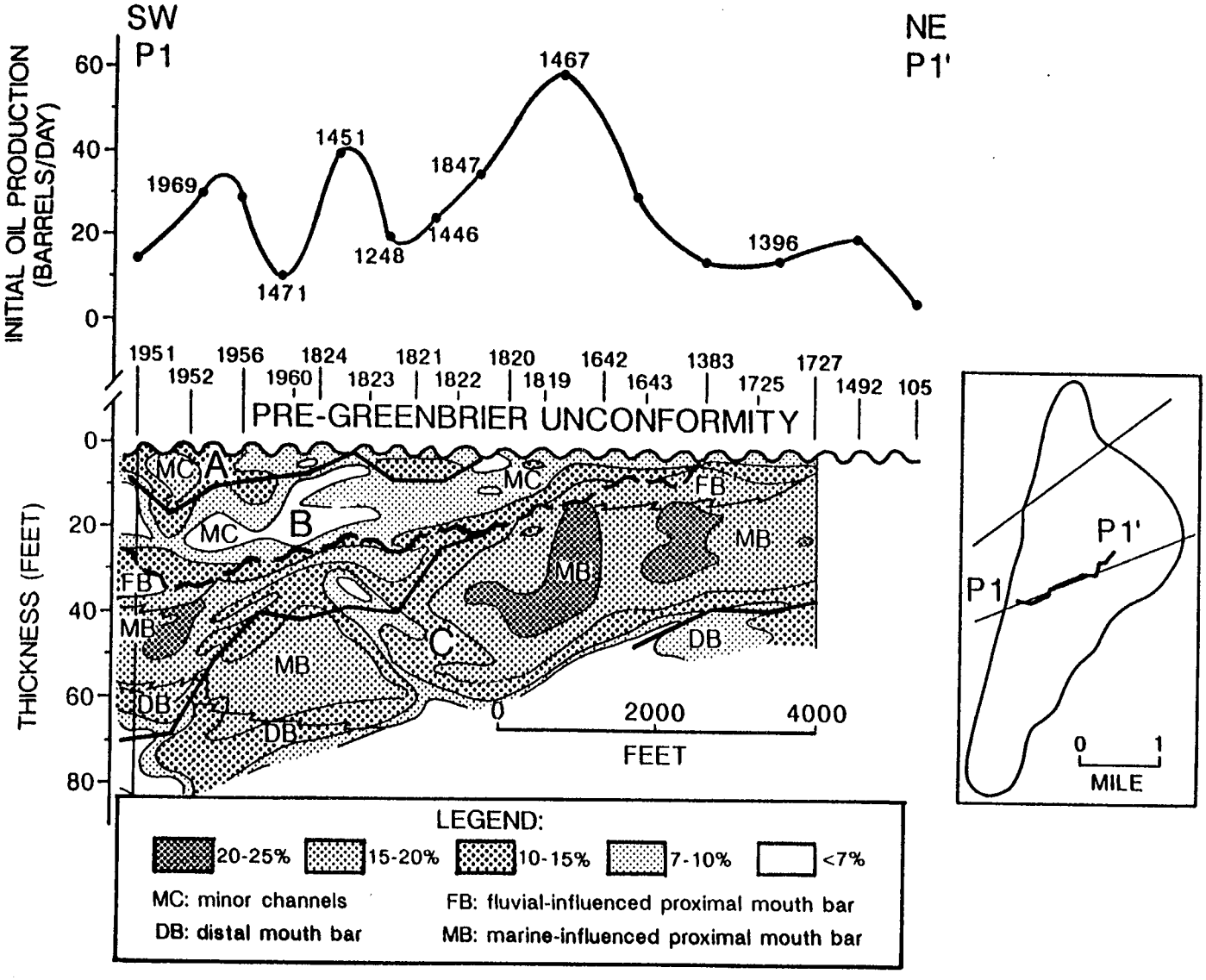

FIGURE 95. Interpreted log porosity facies superimposed on stratigraphic profile P1-P1' in Granny Creek field. Initial production for wells along the cross section is also show.

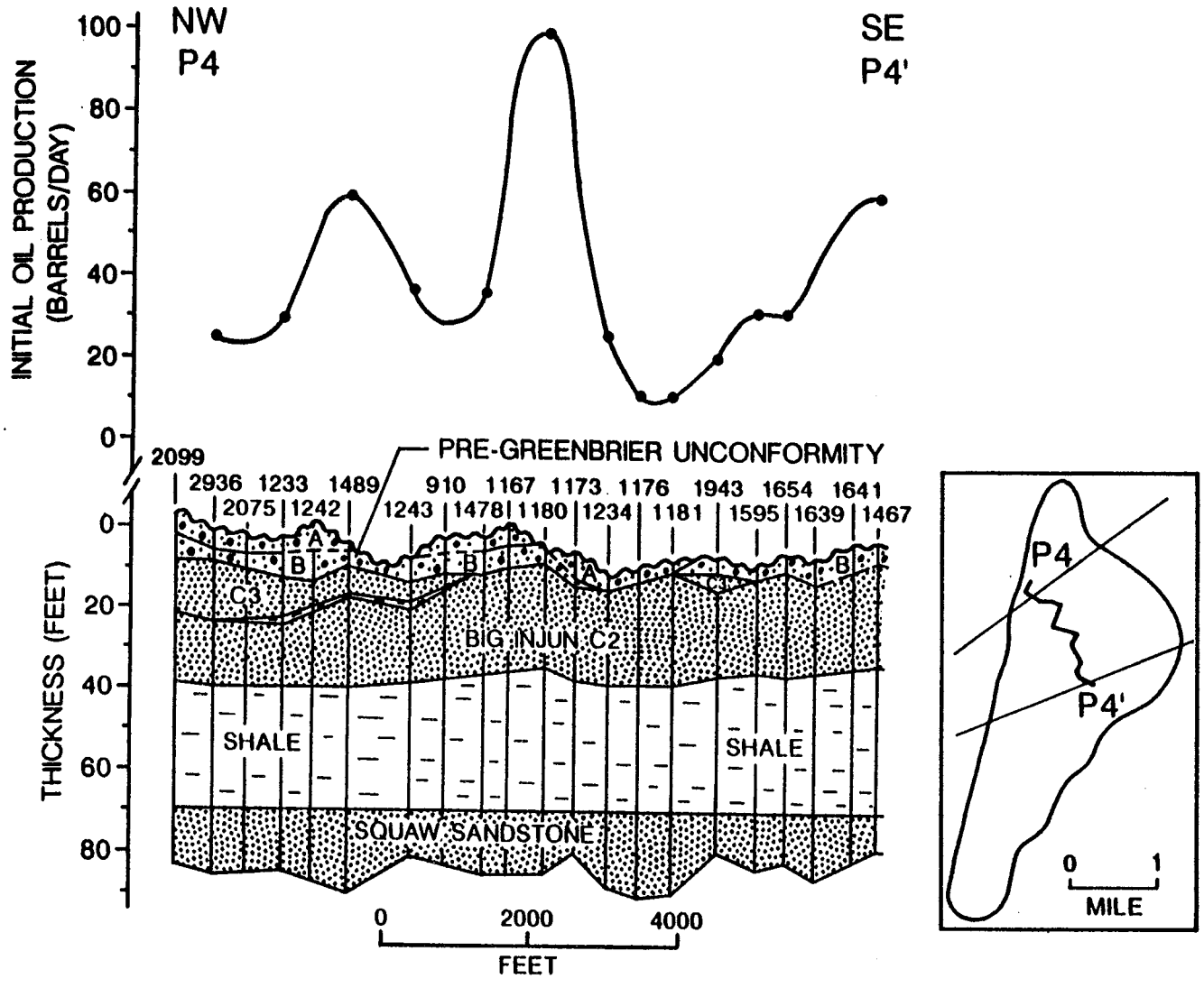

FIGURE 96. Stratigraphic cross section P4-P4' located parallel to and near the pinch-out margin of the B member of the Big Injun in Granny Creek field. Initial oil production for wells along the cross section is also shown.

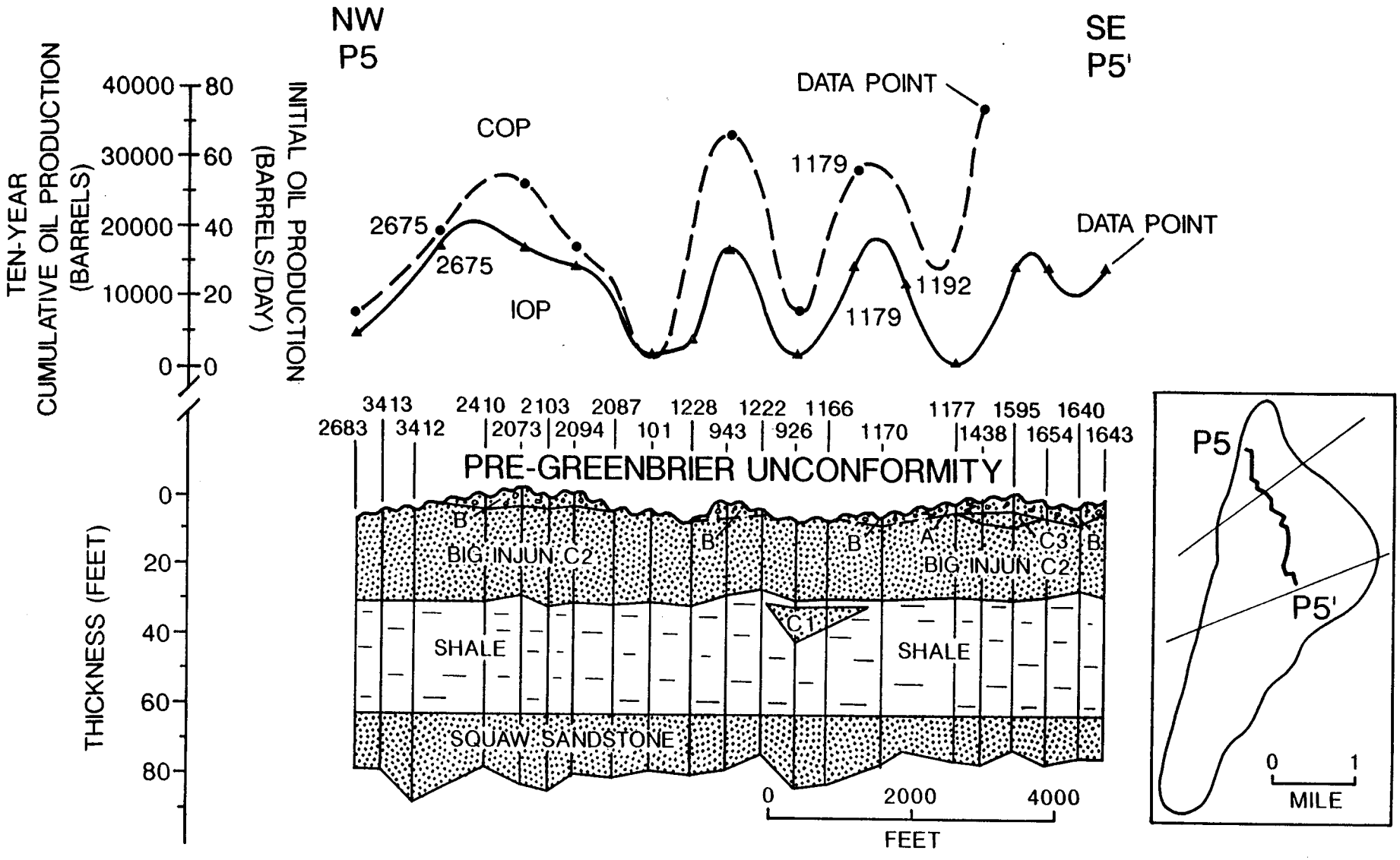

FIGURE 97. Stratigraphic cross section P5-P5' located parallel to and near the pinch-out margin of the B member of the Big Injun in Granny Creek field. Initial (IOP) and cumulative (COP) oil production is plotted for wells along the cross section.

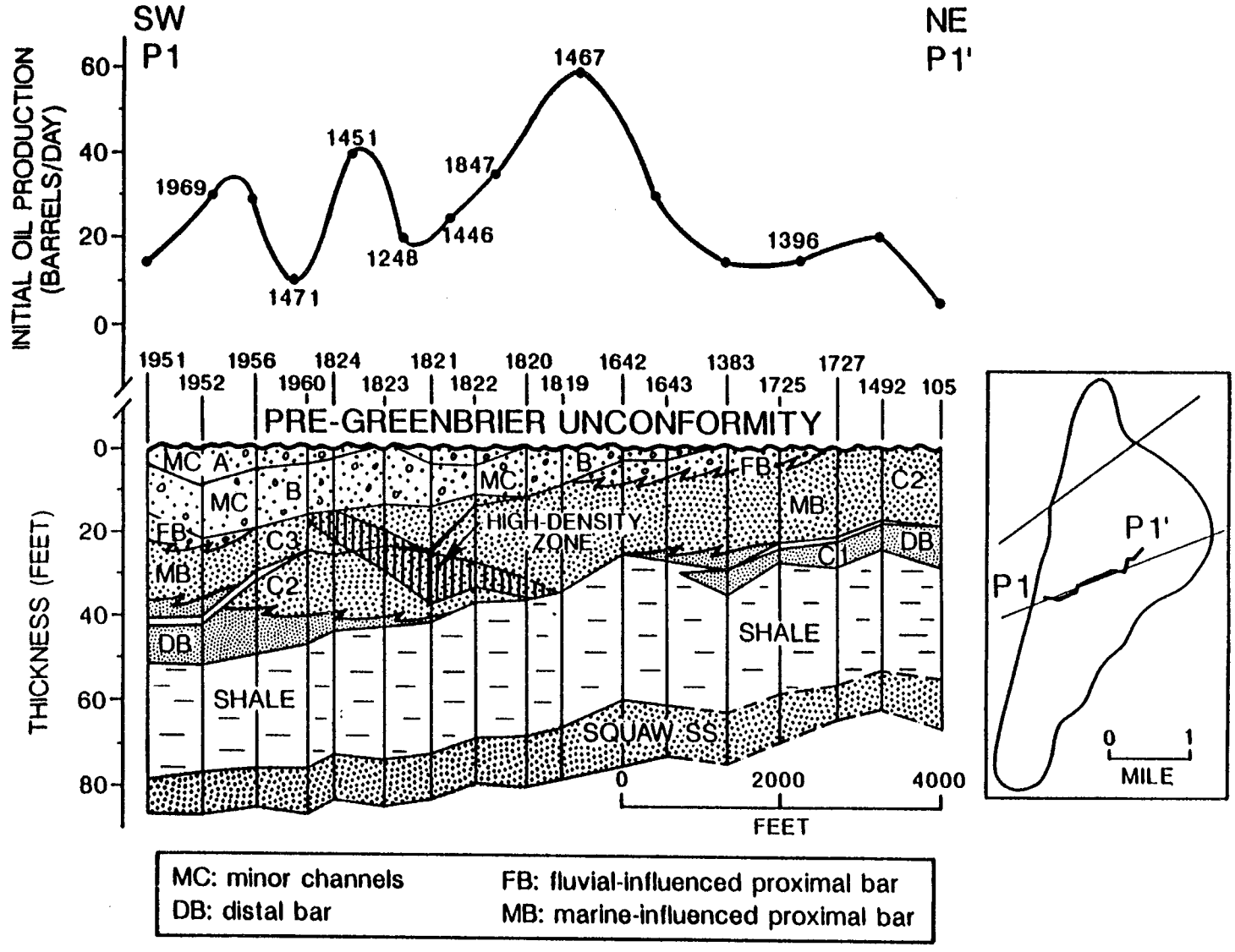

FIGURE 98. Stratigraphic cross section P1-P1' showing subfacies, high-density zone, relatively impermeable thin beds at margins of tongues, and the presence/absence of the B member (potential seal over pay zone in C member). Initial production for wells along the cross section is also shown.

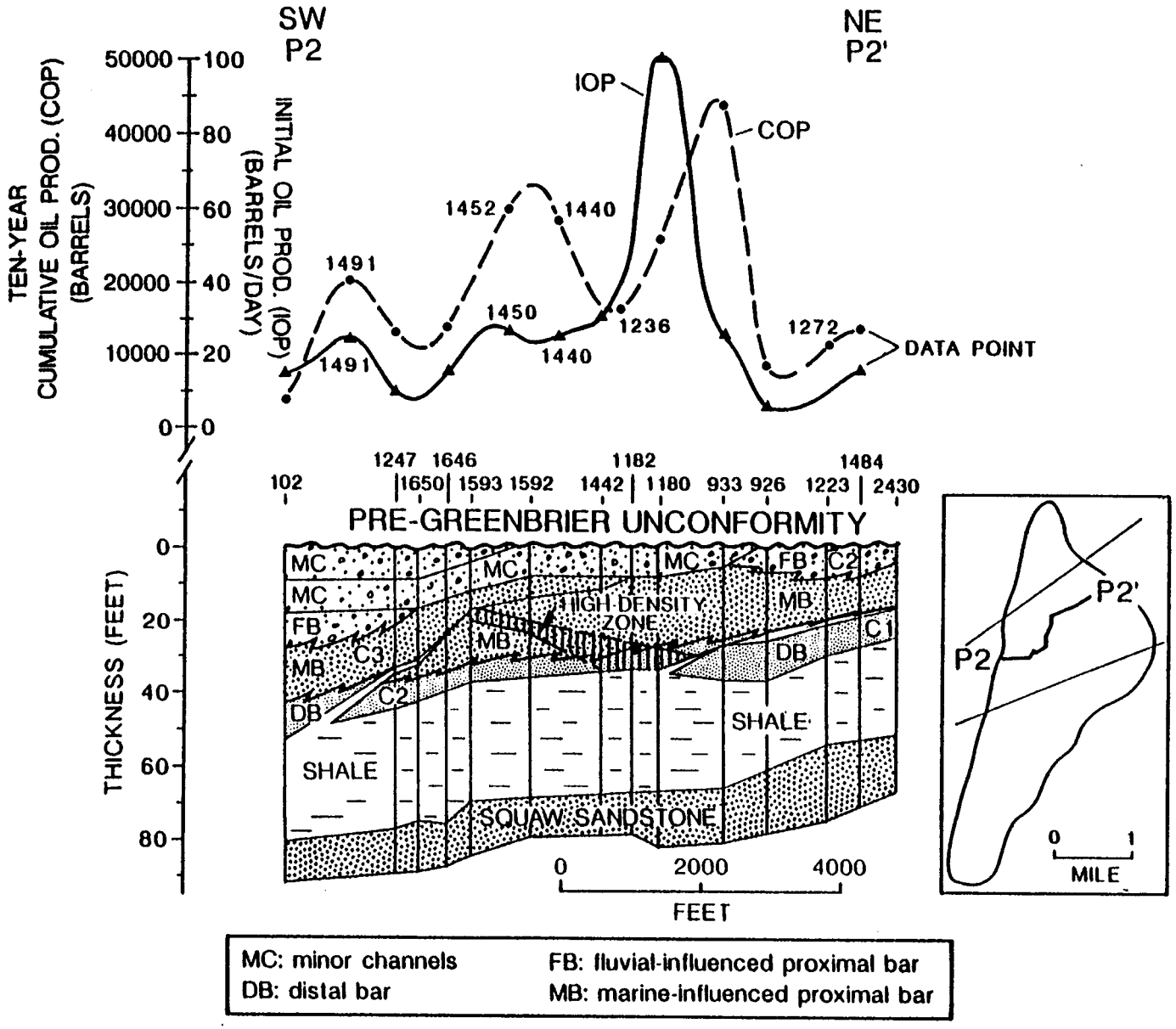

FIGURE 99. Stratigraphic cross section P2-P2' showing the relationship between permeable proximal mouth-bar facies and probable partial barriers to fluid flow (tongue margins and high density zone). Initial (IOP) and cumulative (COP) oil production for wells along the cross section are also shown.

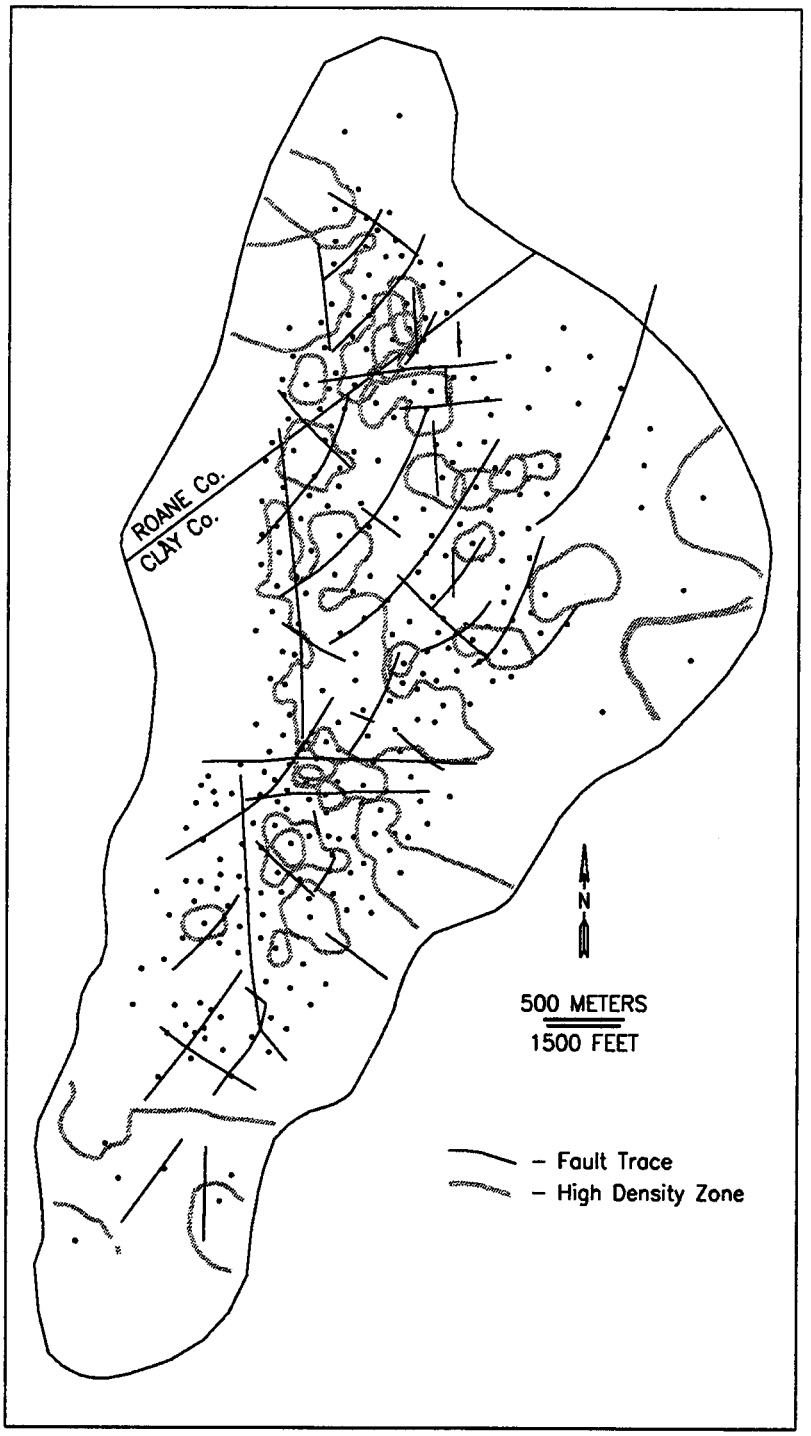

FIGURE 100. Map of Granny Creek field showing lateral extent of 28 density zones (denoted by their zero-thickness contour) in the fine-grained portion of the Big Injun. Faults inferred from seismic data and structure map for the Big Injun interval are superimposed.

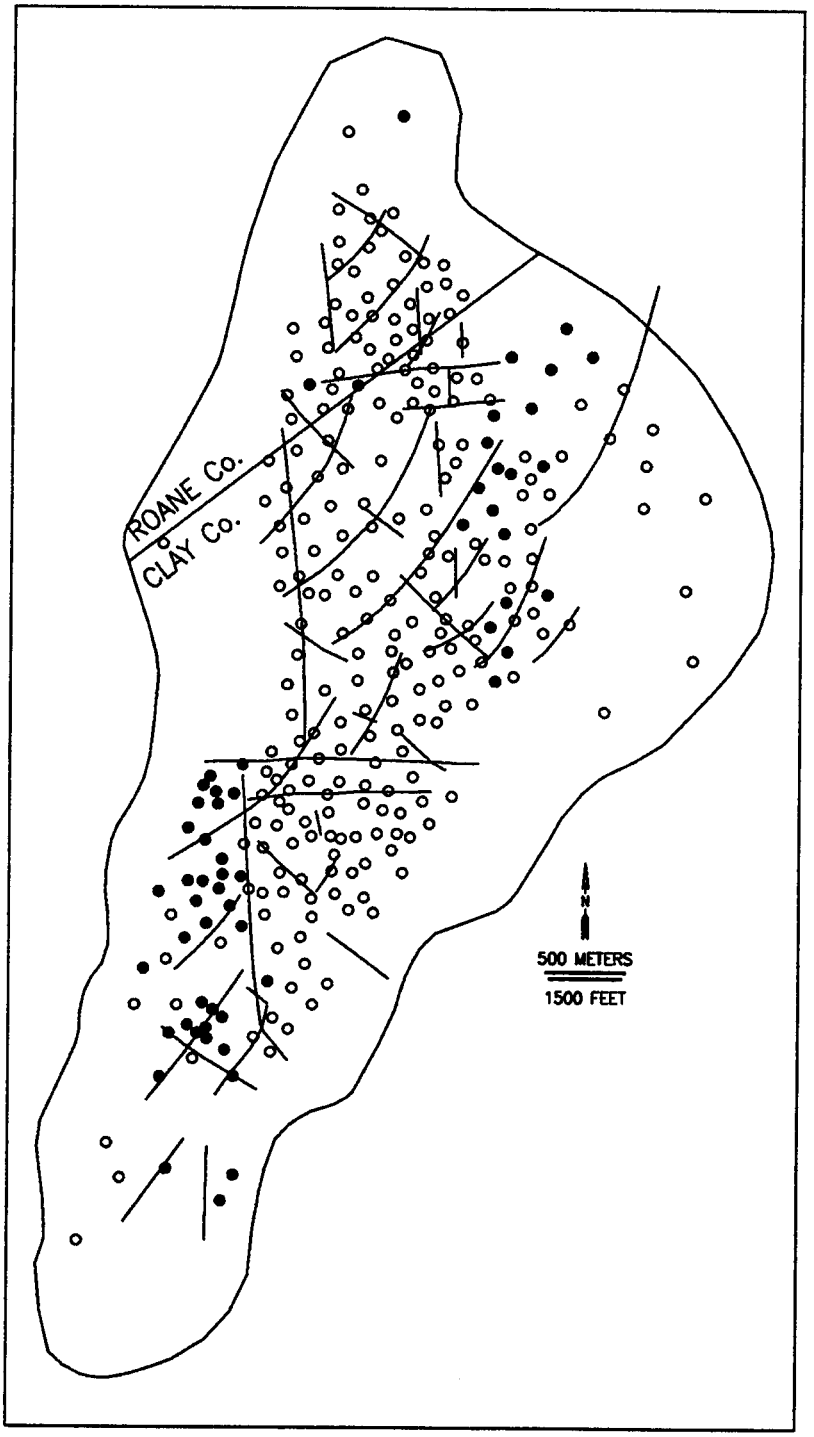

FIGURE 101. Map of Granny Creek field showing distribution of wells with shale/siltstone interbeds (filled circles) and without (open circles) in the fine-grained portion of the Big Injun. Faults from Figure 100 are superimposed.

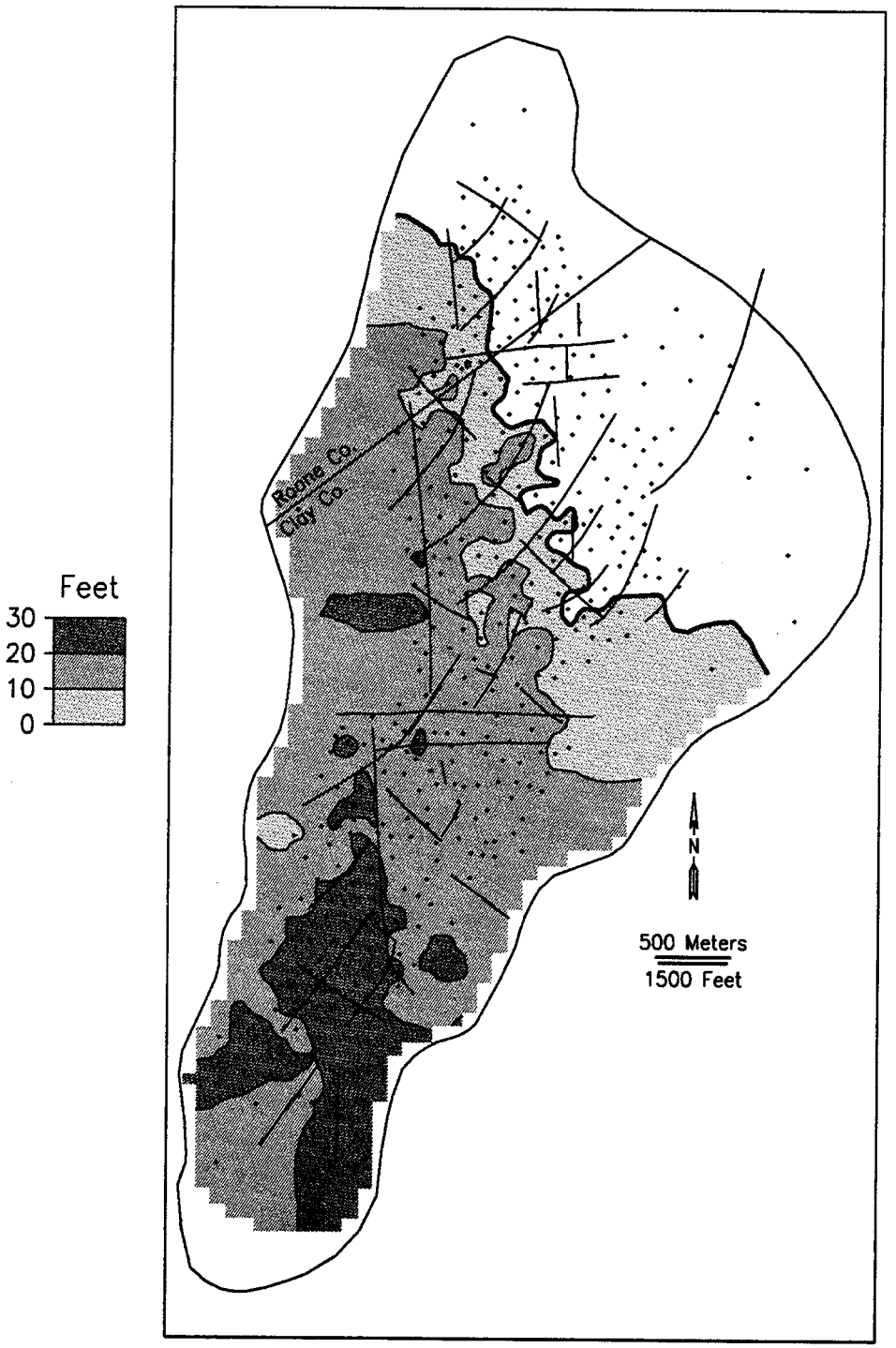

FIGURE 102. Isopach map of the coarse-grained portion of the Big Injun in Granny Creek field. Faults from Figure 100 are superimposed. Contour interval is 10 feet.

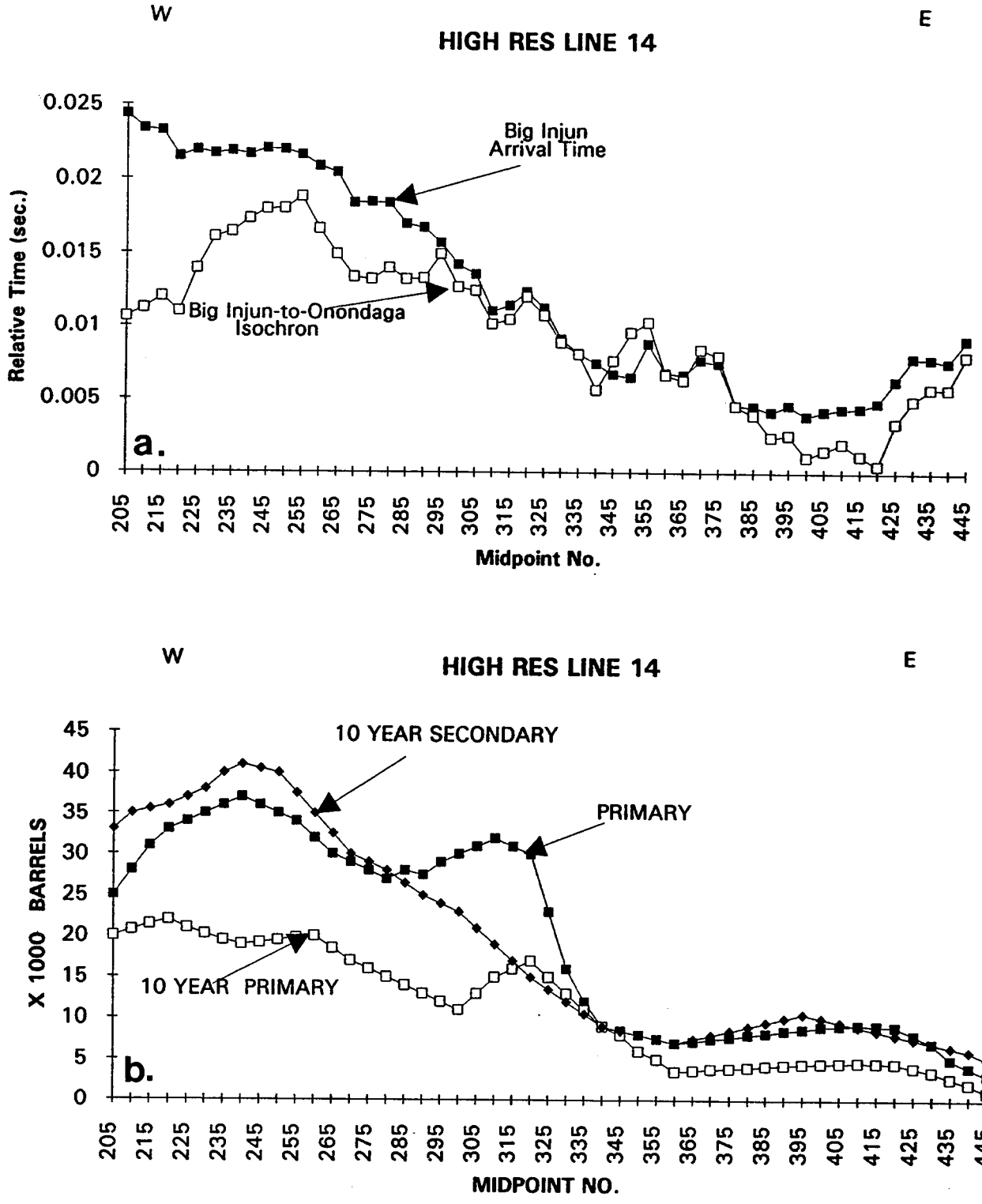

FIGURE 103. Seismic reflection timing and oil production along weight-drop Line 14. (a) Plot of Big Injun-to-Onondaga isochron and arrival times for the Big Injun reflection event; (b) 10-year primary, 10-year secondary, and primary production for wells along seismic line.

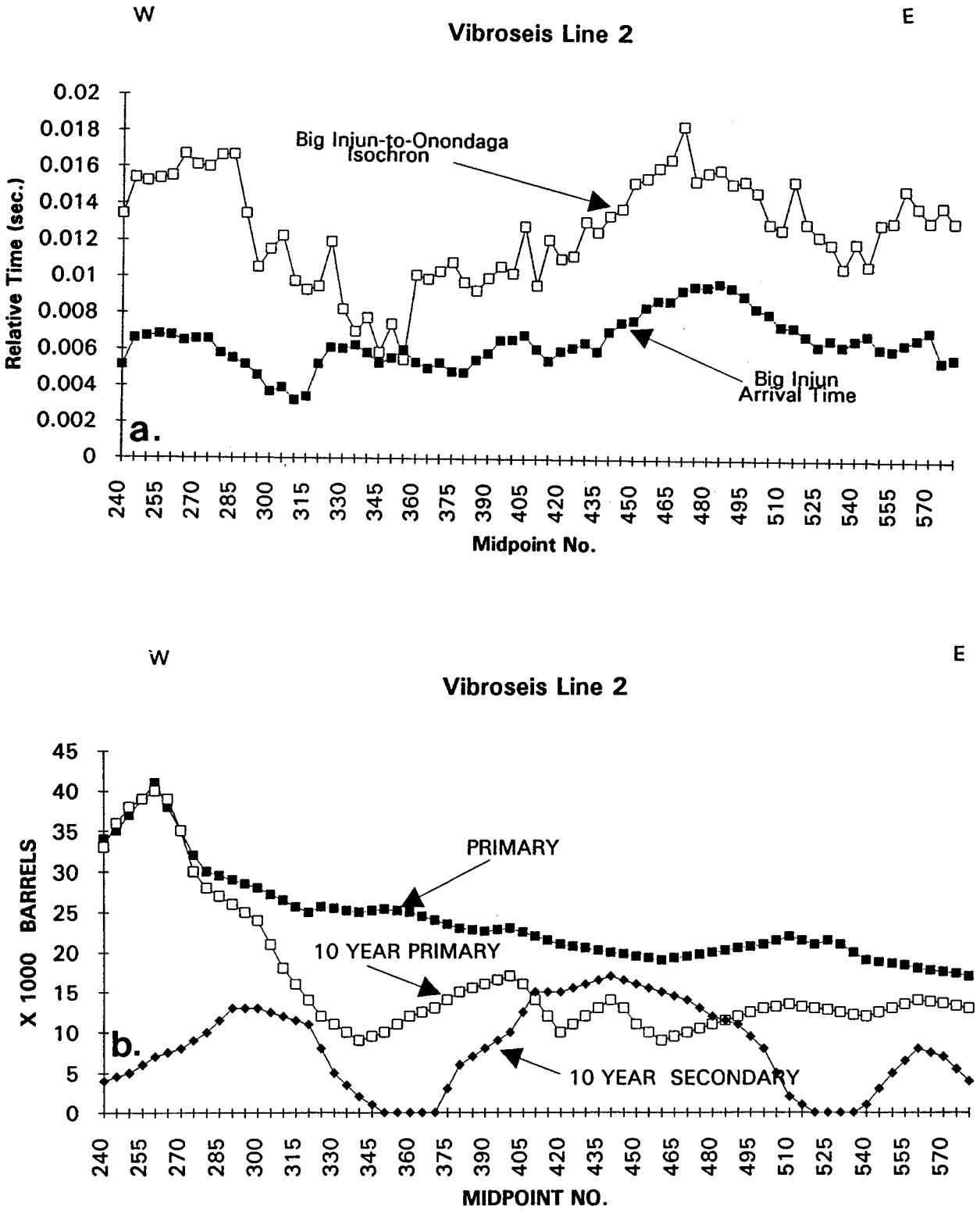

FIGURE 104. Seismic reflection timing and oil production along Vibroseis Line 2. (a) Plot of Big Injun-to-Onondaga isochron and arrival times for the Big Injun reflection event; (b) 10-year primary, 10-year secondary, and primary production for wells along seismic line.

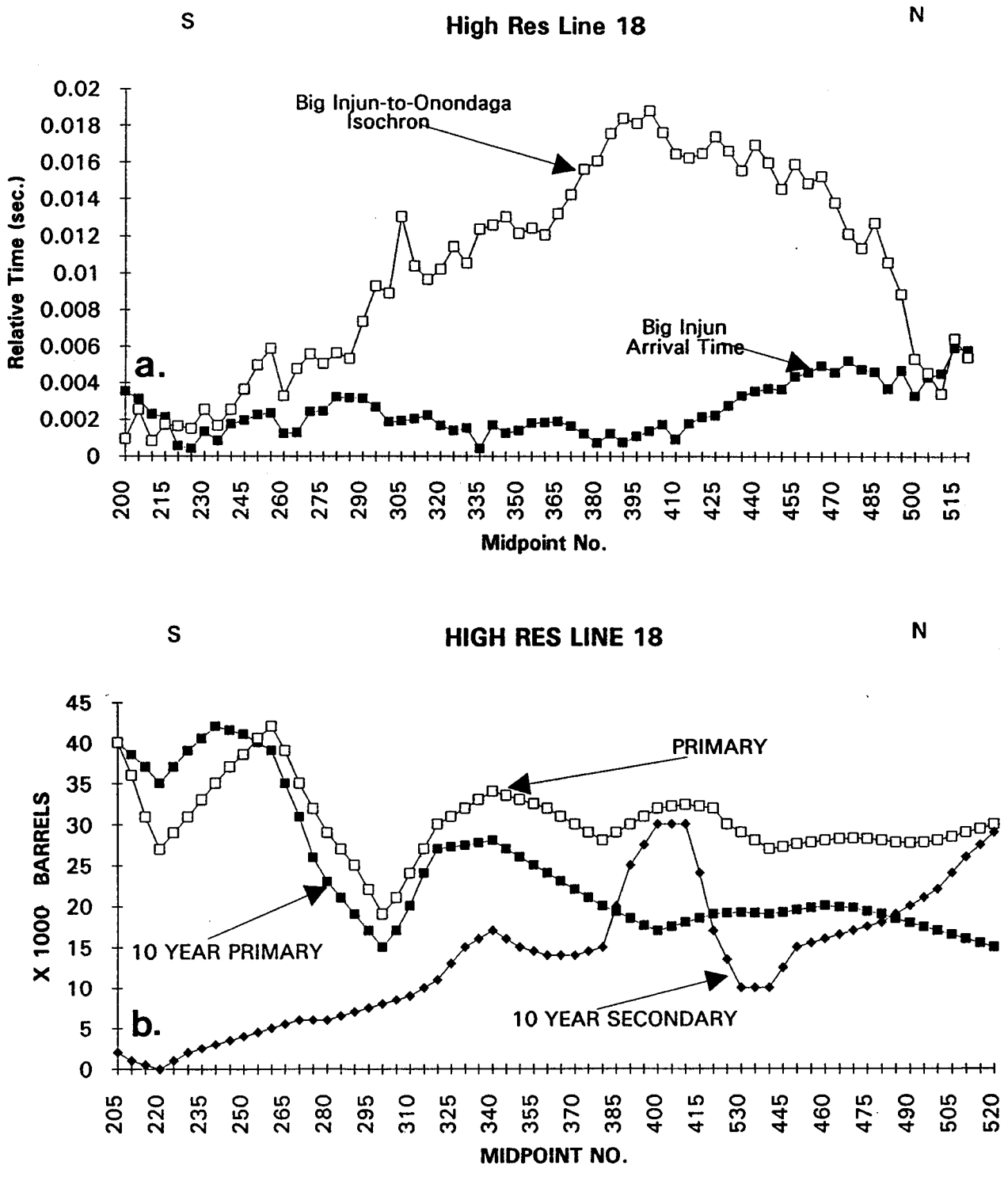

FIGURE 105. Seismic reflection timing and oil production along weight-drop Line 18. (a) Plot of Big Injun-to-Onondaga isochron and arrival times for the Big Injun reflection event; (b) 10-year primary, 10-year secondary, and primary production for wells along seismic line.

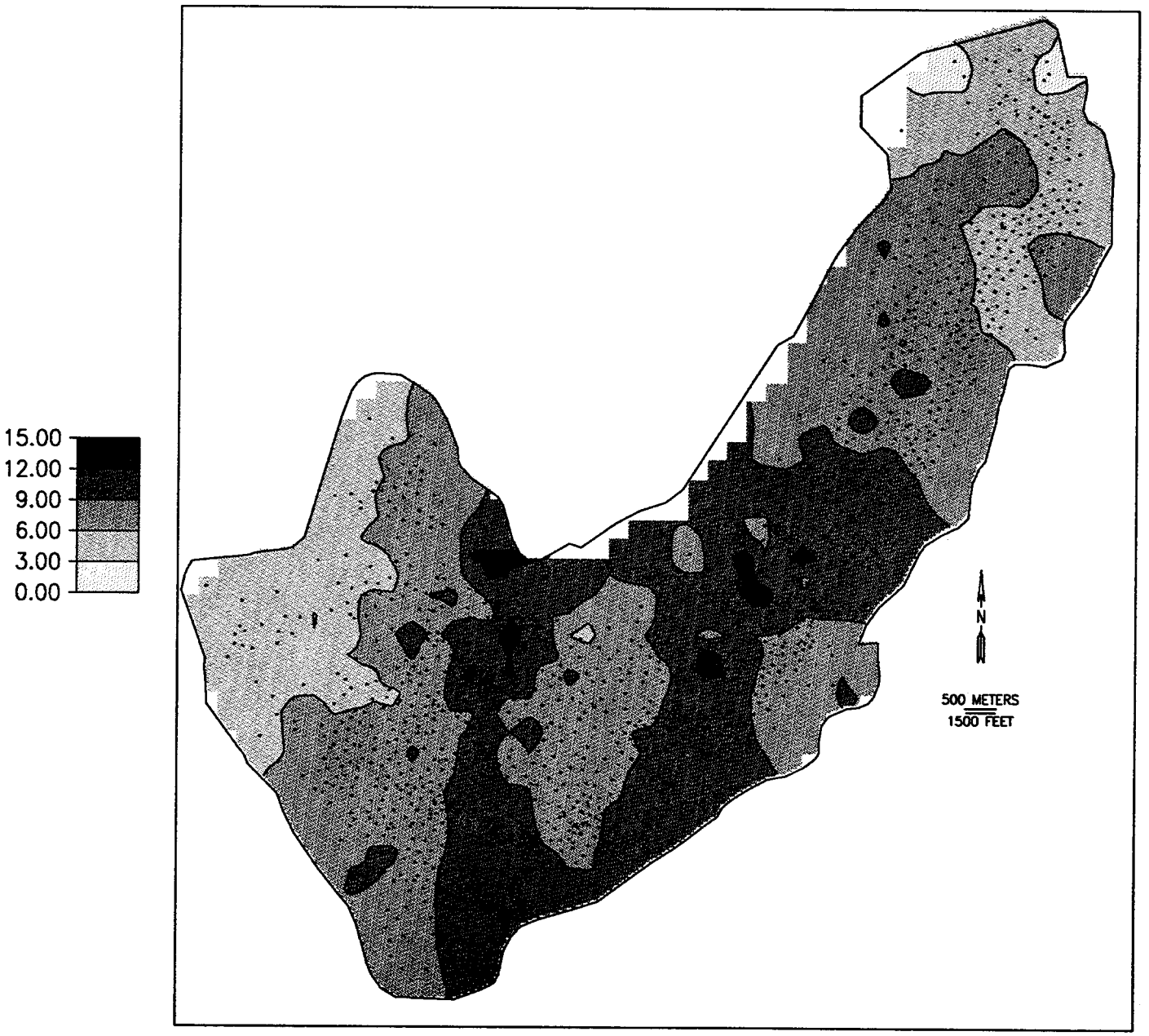

FIGURE 106. Contour map of porosity-feet for the Big Injun sandstone in Rock Creek field. Contour interval is 3 feet of porosity.

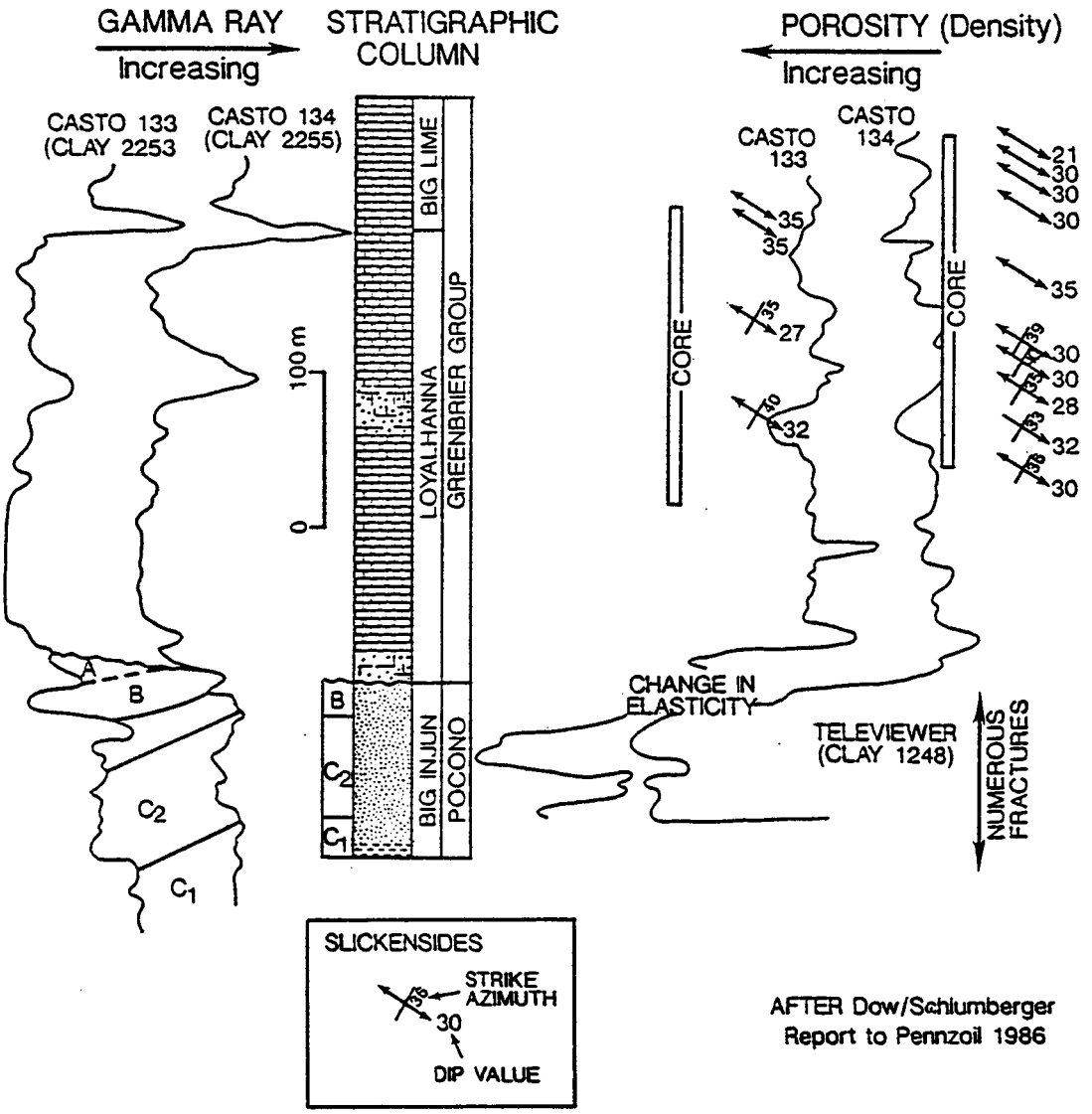

FIGURE 107. Orientation of slickensides in the Greenbrier interval from cores for Clay 2253 (Casto 133) and Clay 2255 (Casto 134).

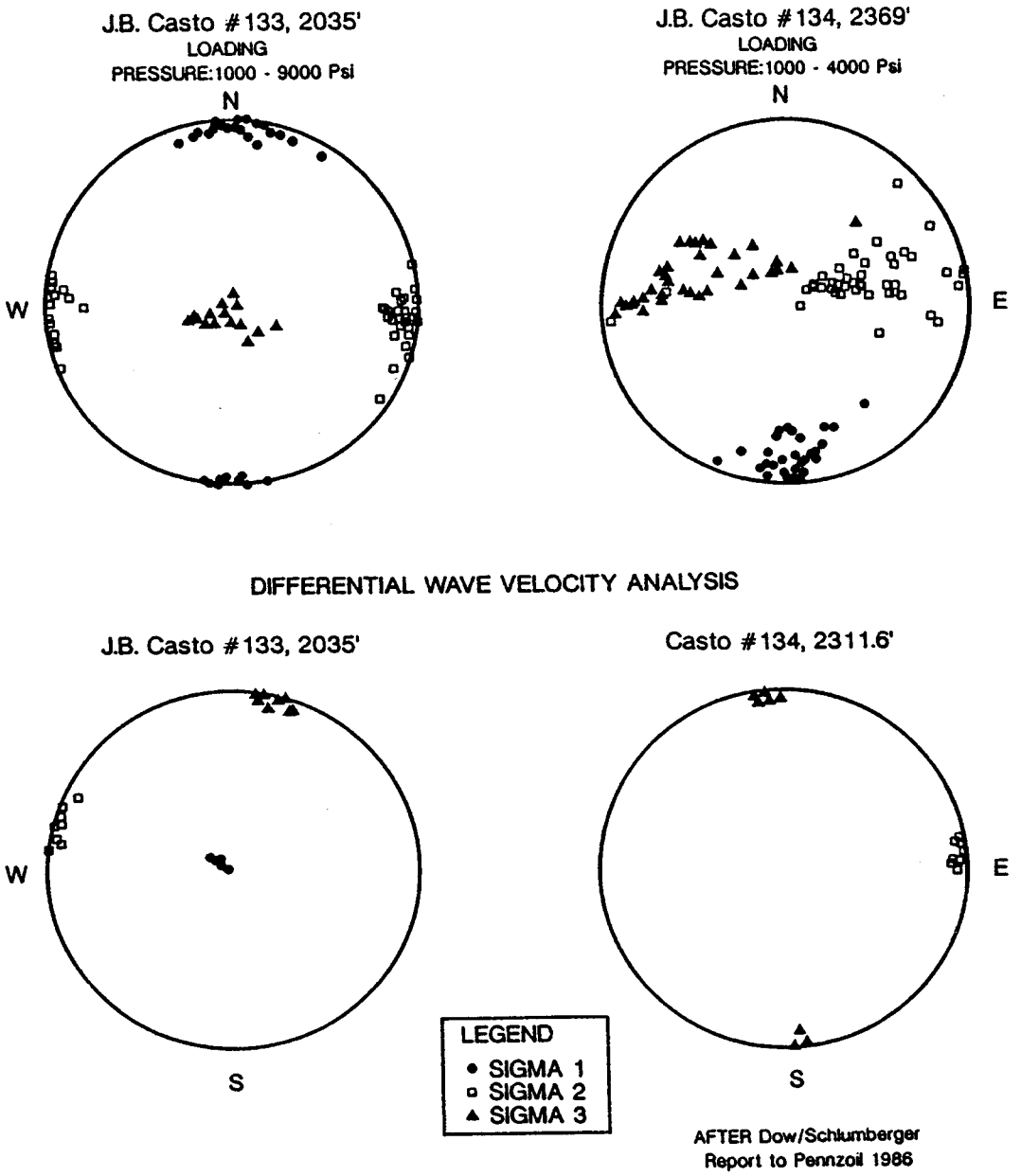

FIGURE 108. Polar plots of results of load and wave velocity analysis on core from Clay 2253 (Casto 133) and Clay 2255 (Casto 134) performed to determine the directions of *in situ* stress.

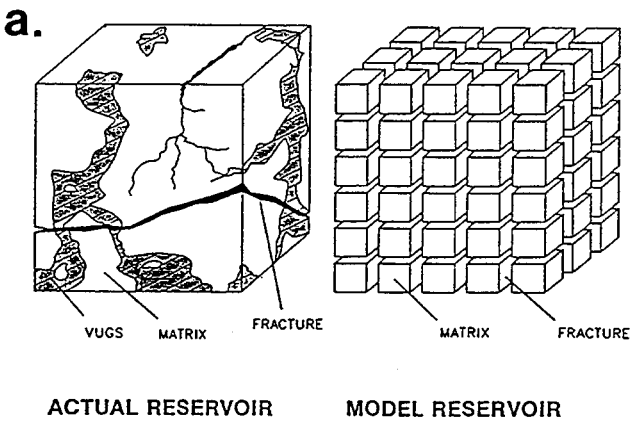

FIGURE A1. Model of reservoir porosity. (a) Idealization of a double porosity system; (b) Grid refinement.

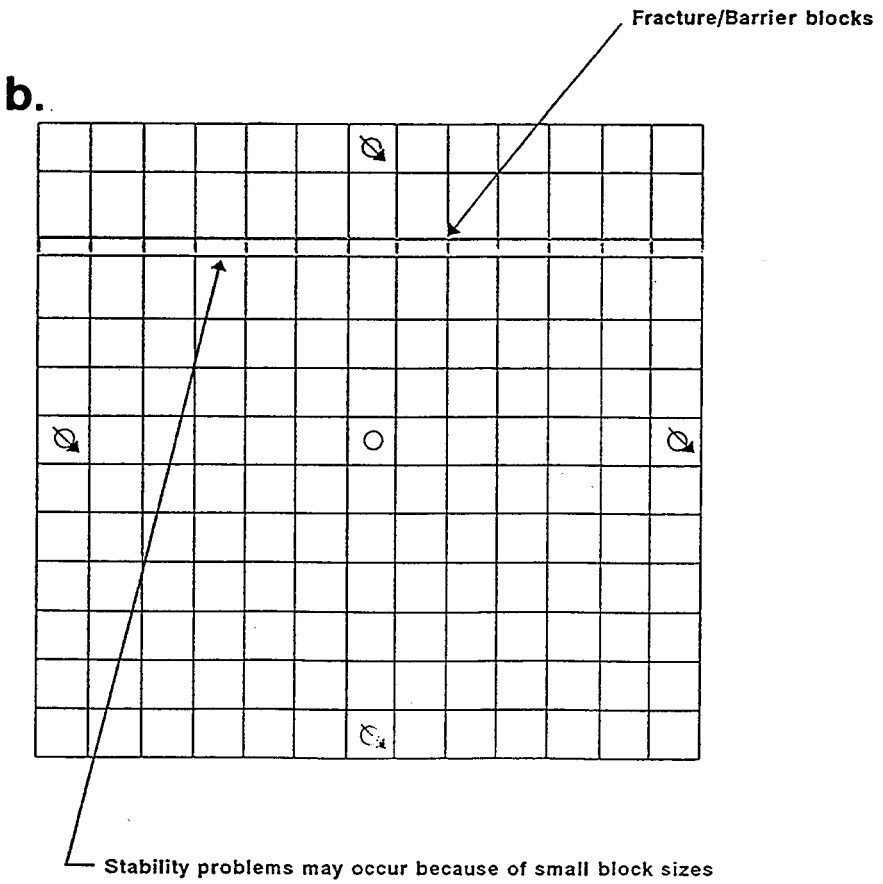

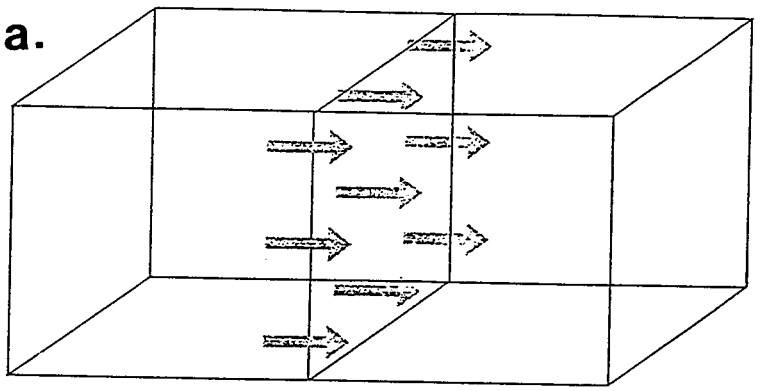

FIGURE A2. Flow path and heterogeneities in reservoir simulation. (a) Two adjacent block in numerical simulator; (b) Orientation of barriers and fractures.

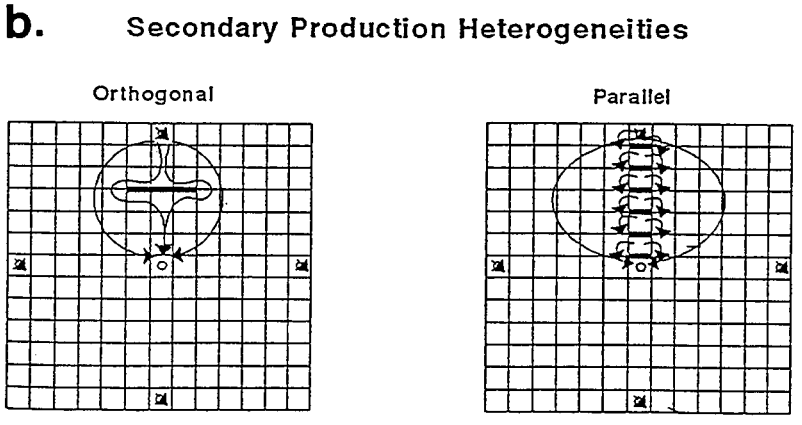

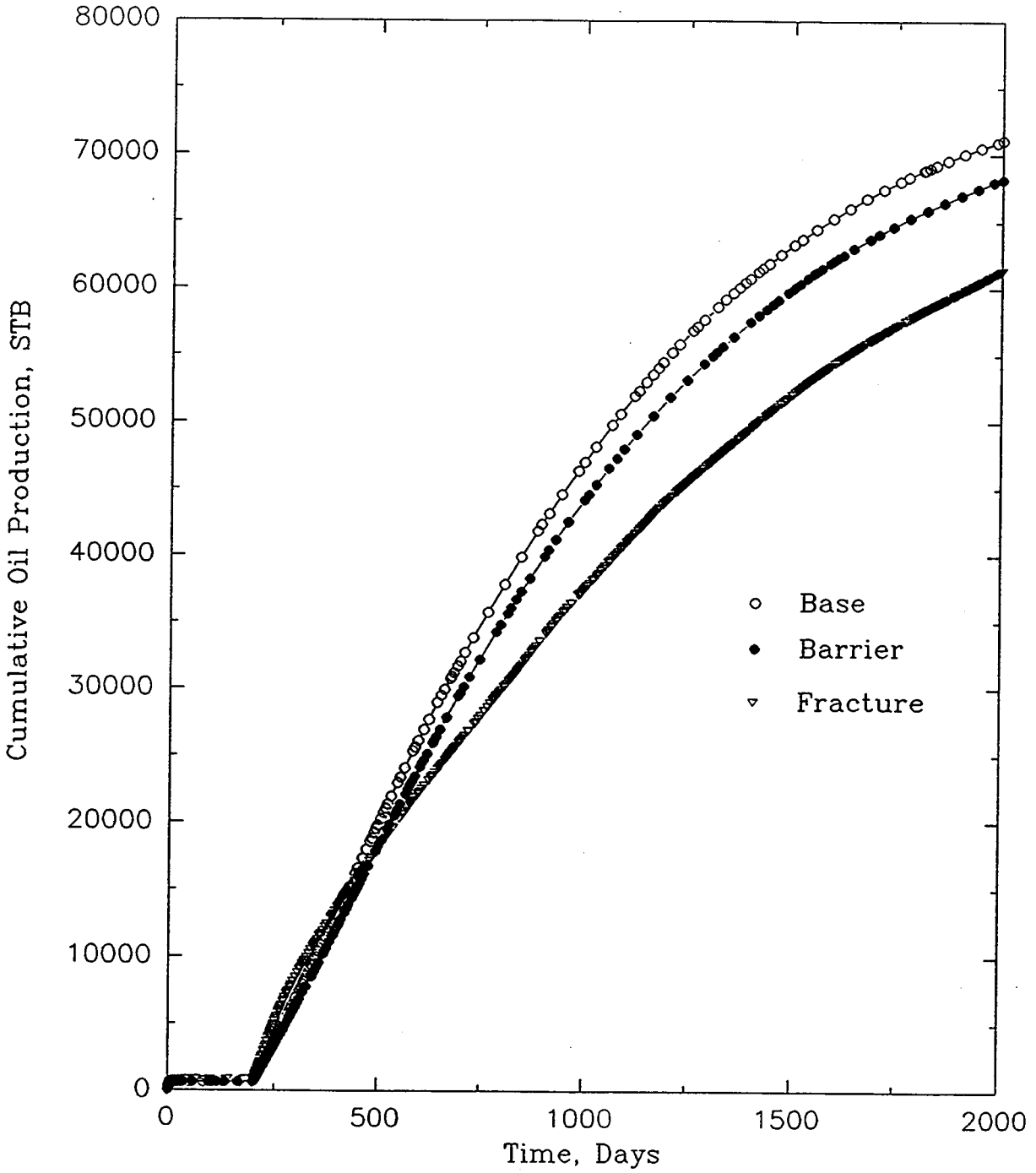

FIGURE A3. Graph of cumulative oil production versus time showing the effect of an isolated parallel fracture on secondary oil recovery.

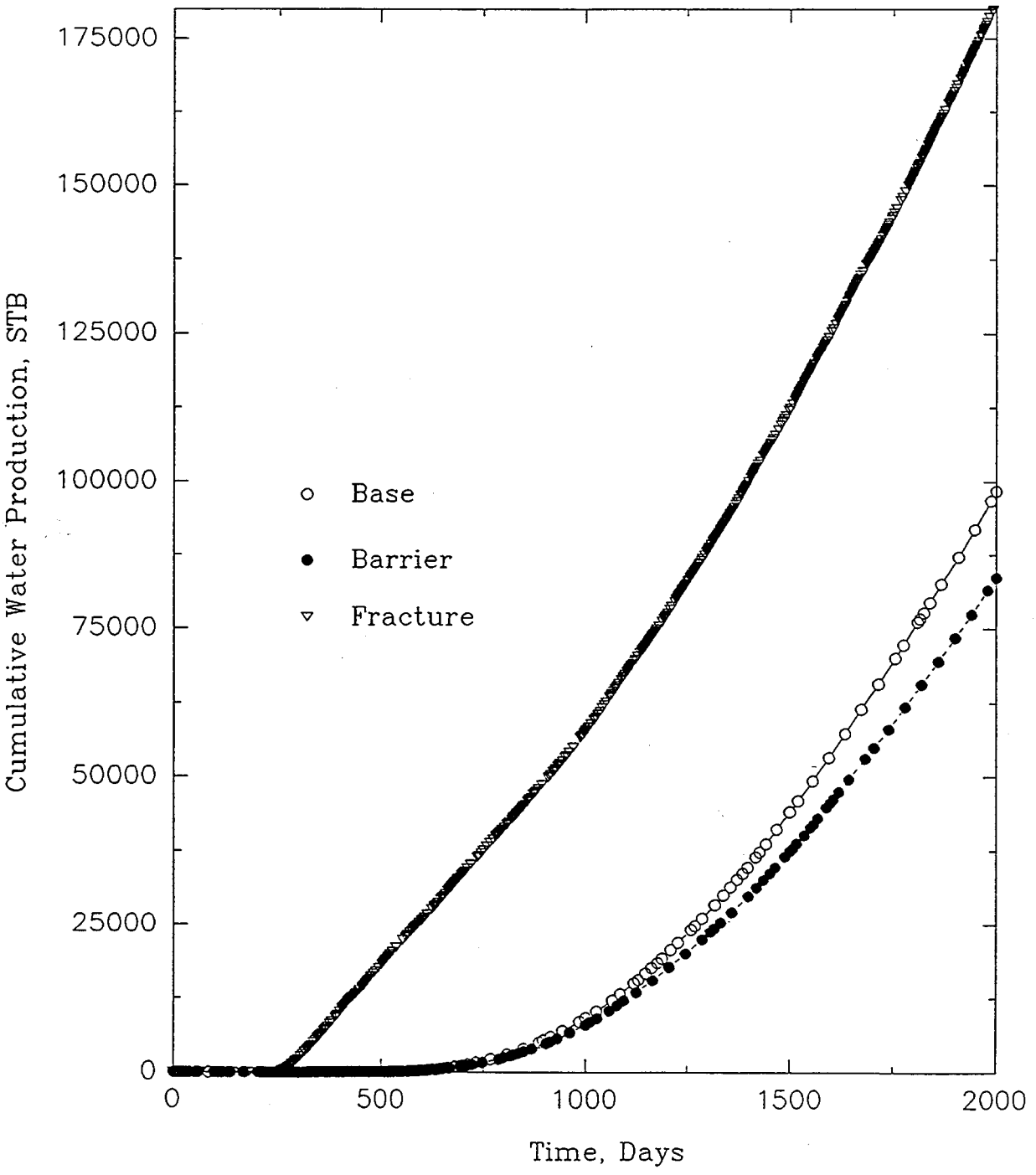

FIGURE A4. Graph of cumulative water production versus time showing the effect of an isolated parallel fracture on secondary water production.

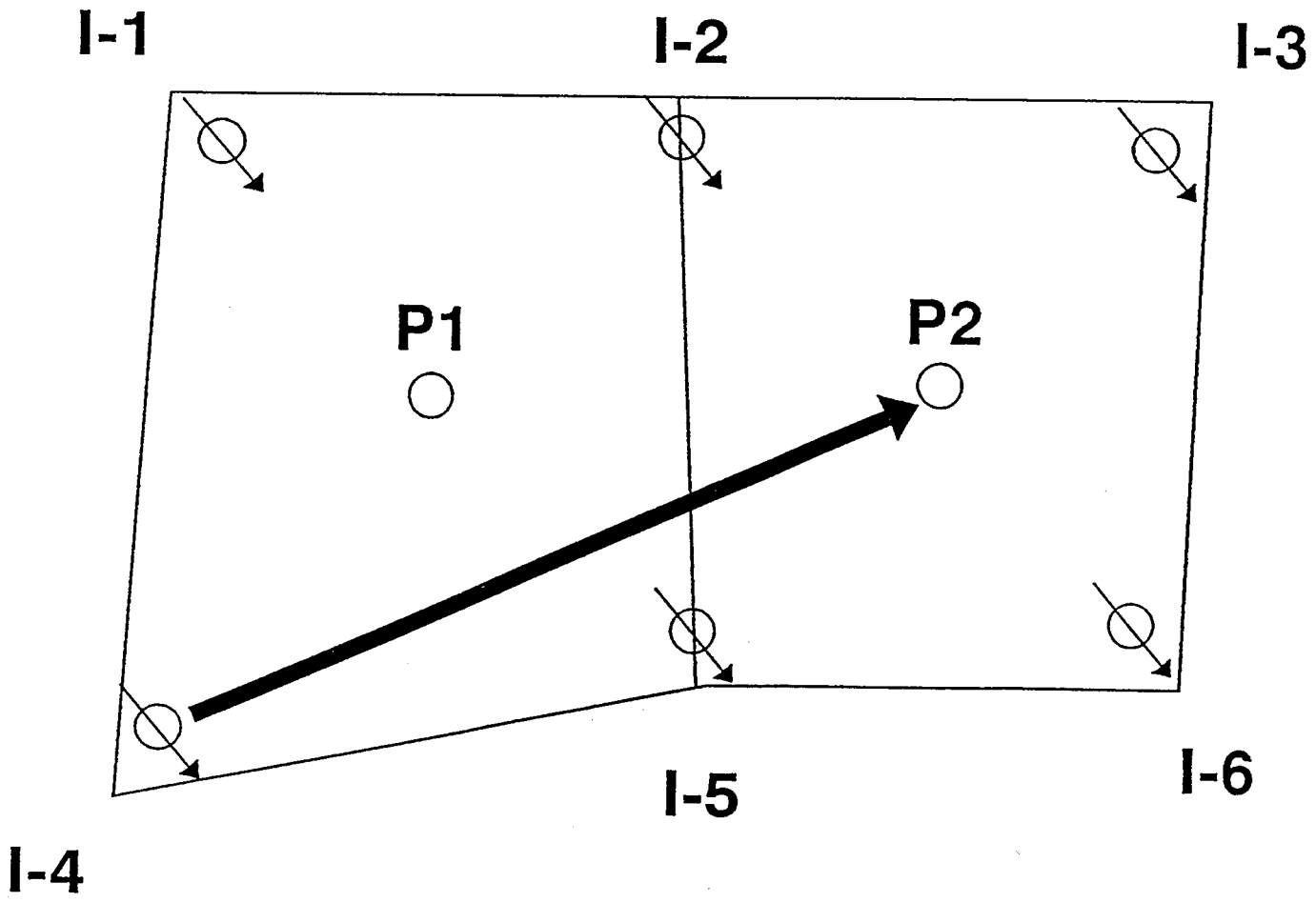

FIGURE A5. Diagrammatic representation of two adjacent five spots during simulation. See Figure 4 for location within Granny Creek field.

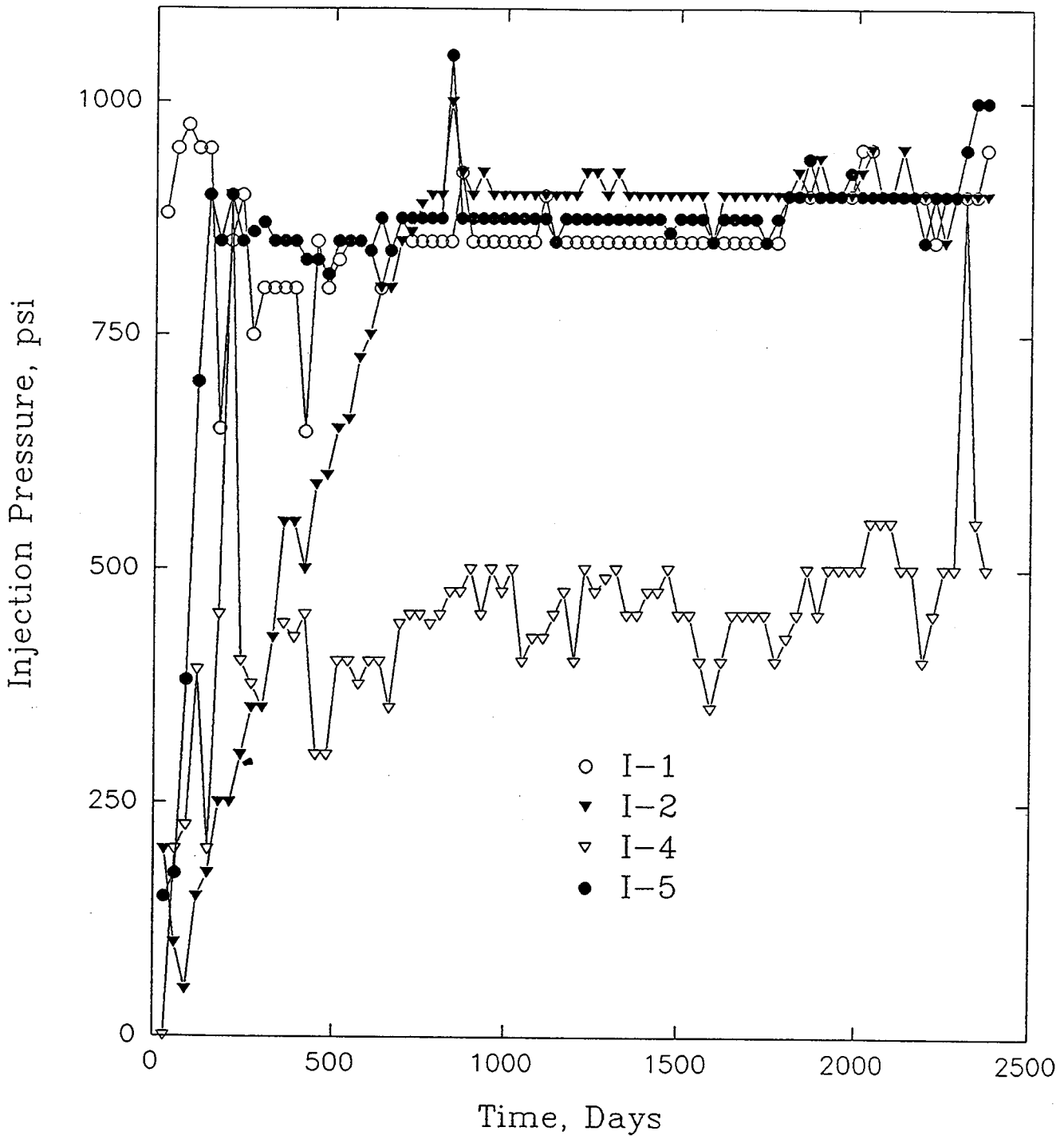

FIGURE A6. Graph of injection pressure versus time for four wells in five spot P1. See Figure A5 for location of wells.

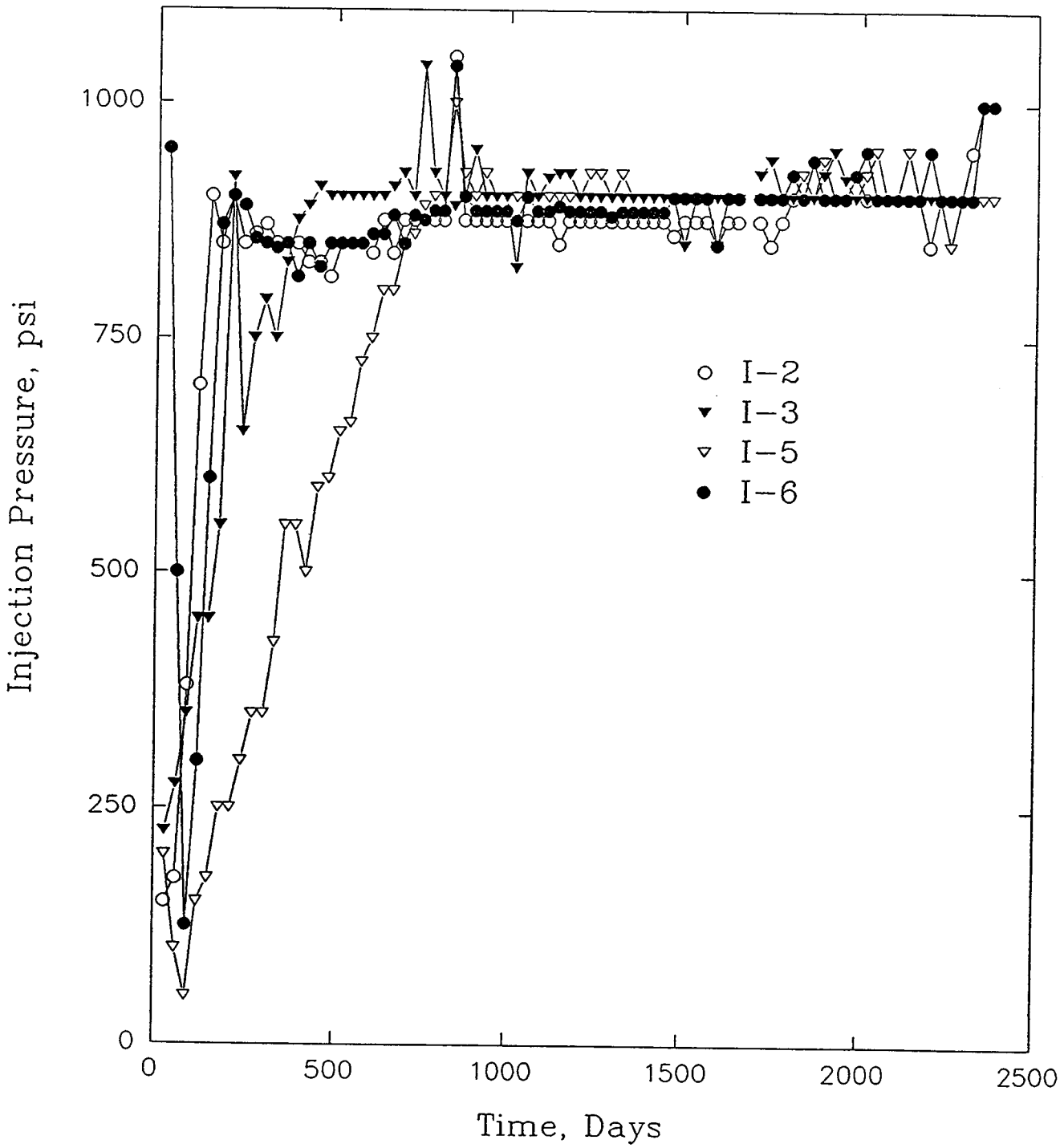

FIGURE A7. Graph of injection pressure versus time for four wells in five spot P2. See Figure A5 for location of wells.

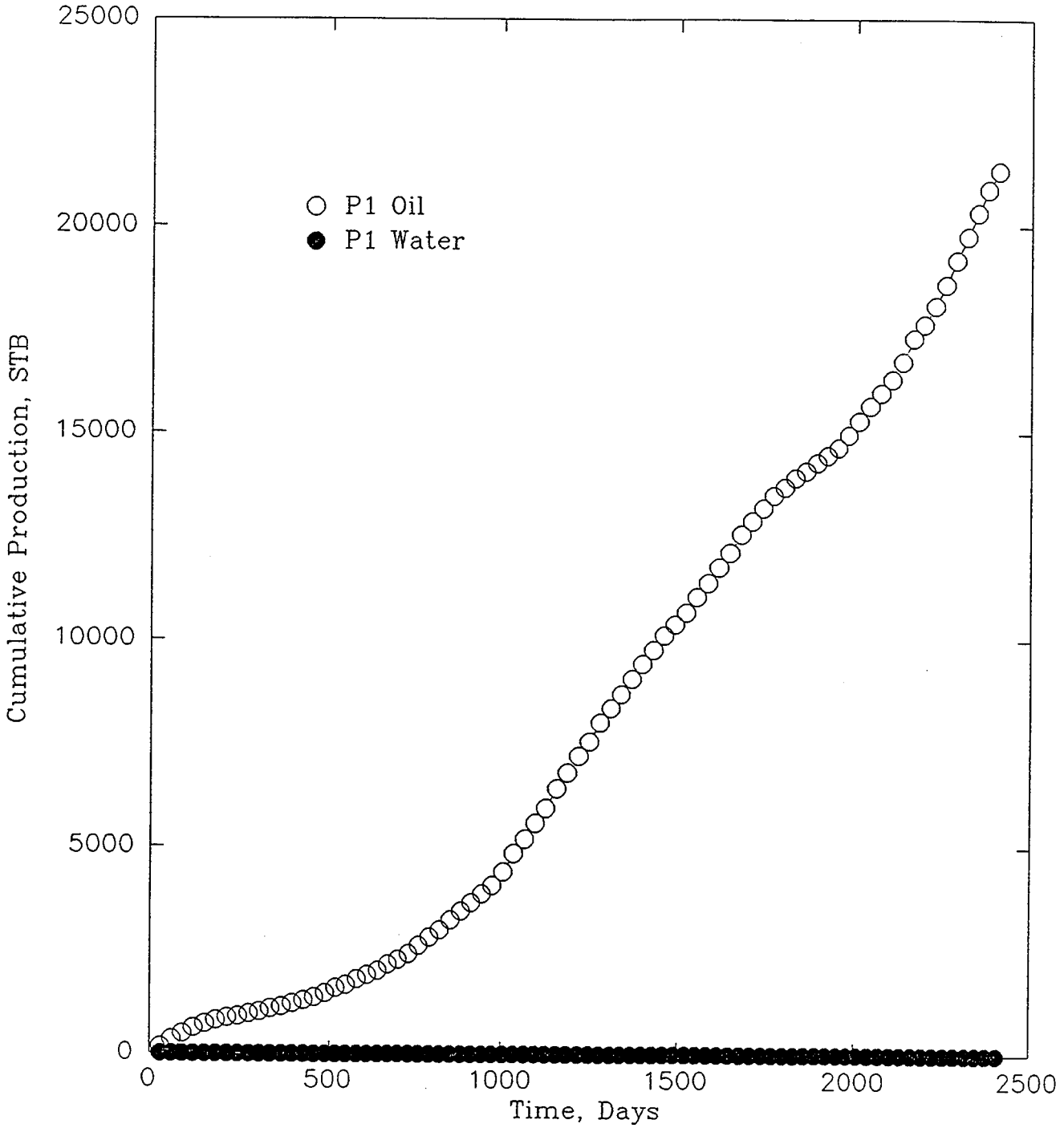

FIGURE A8. Graph of oil and water production versus time for five spot P1.

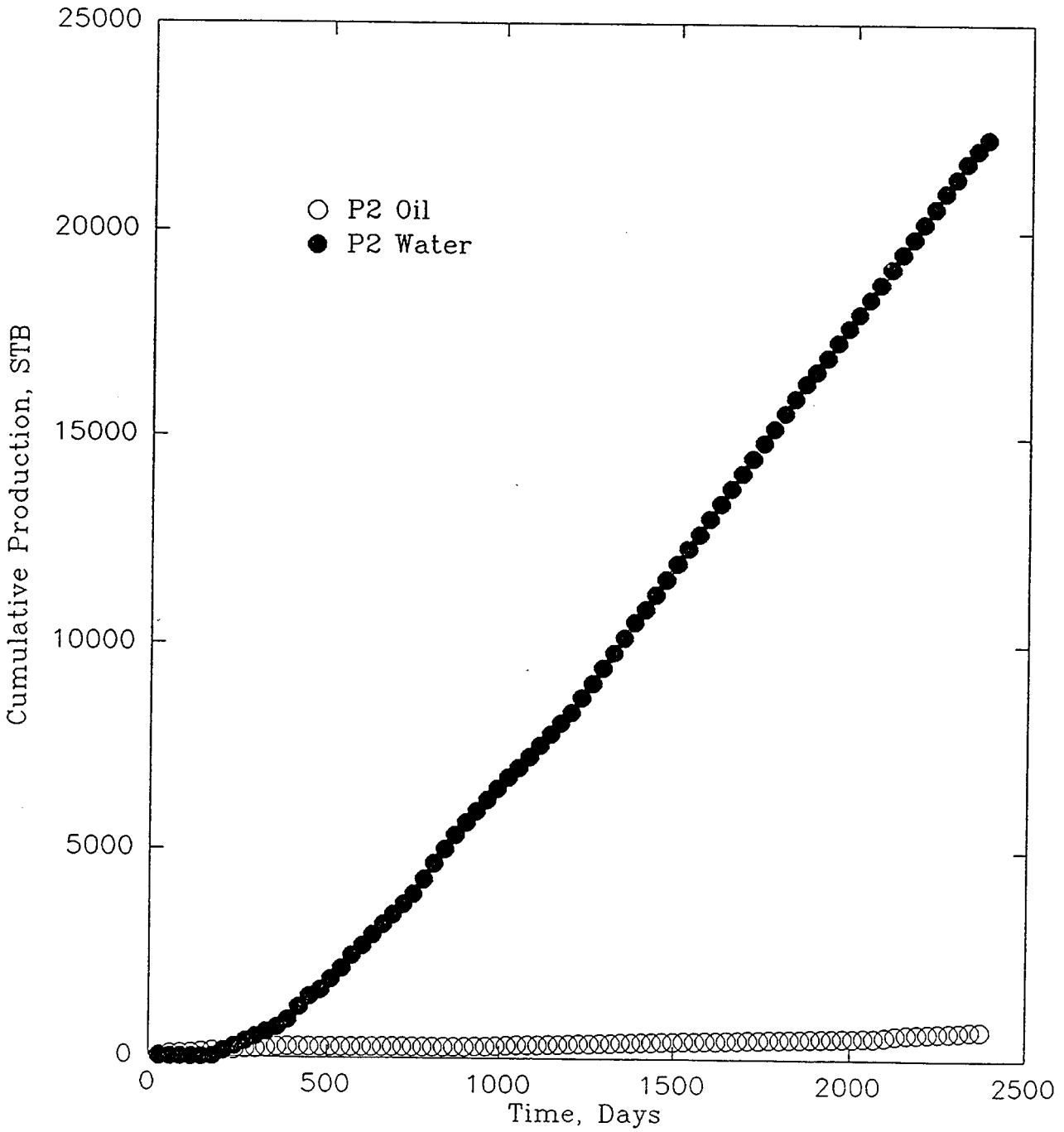

FIGURE A9. Graph of oil and water production versus time for five spot P2.

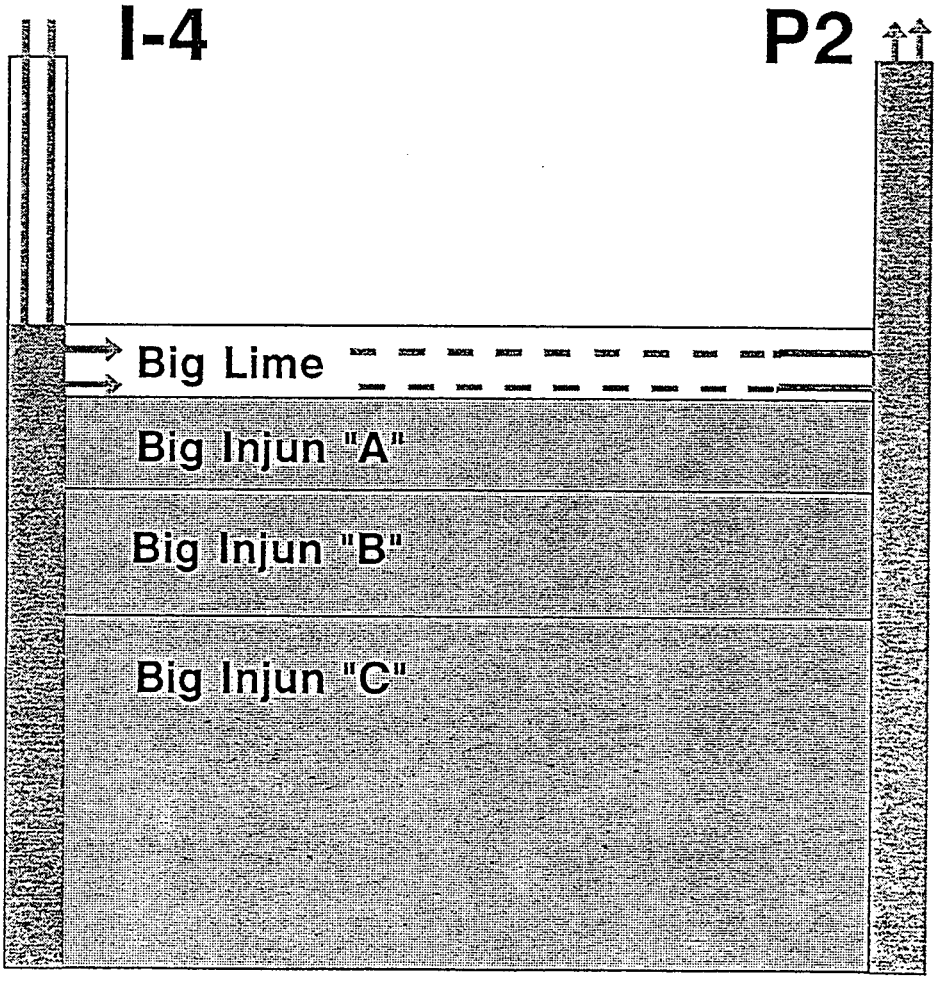

FIGURE A10. Diagrammatic representation of well communication through an isolated fracture in the Big Lime.

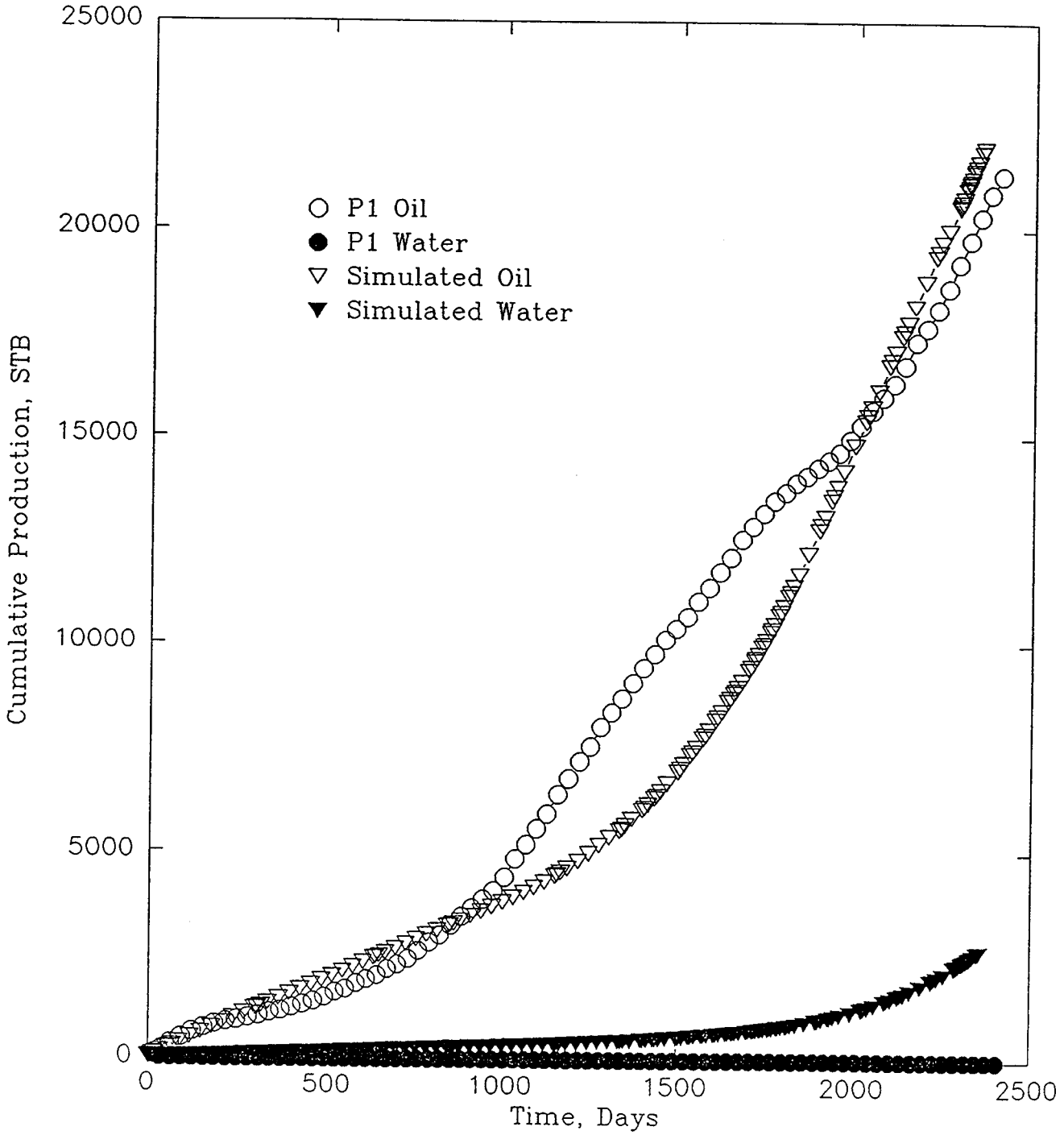

FIGURE A11. Graph of simulated production versus time for five spot P1.

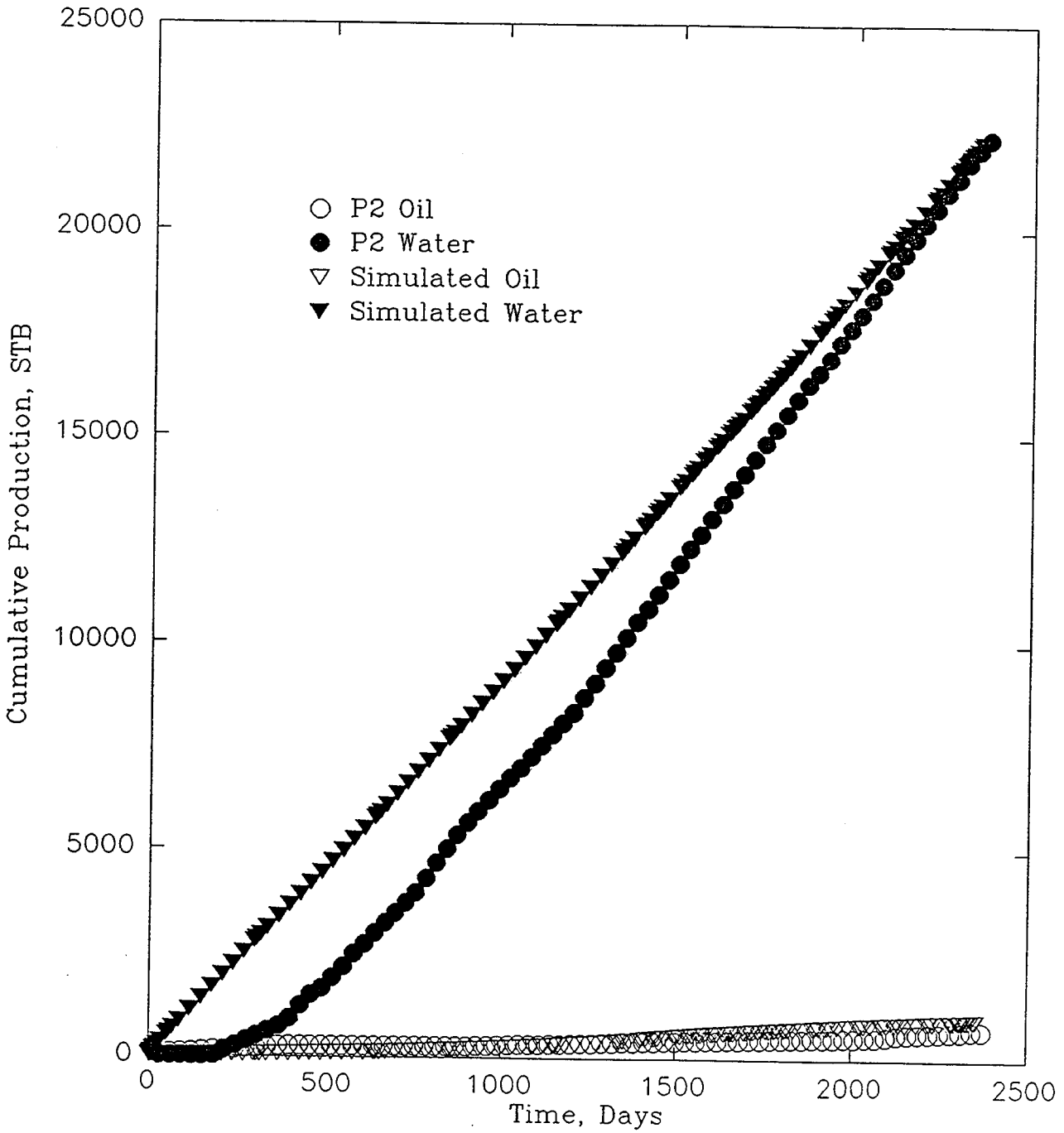

FIGURE A12. Graph of simulated production versus time for five spot P2.

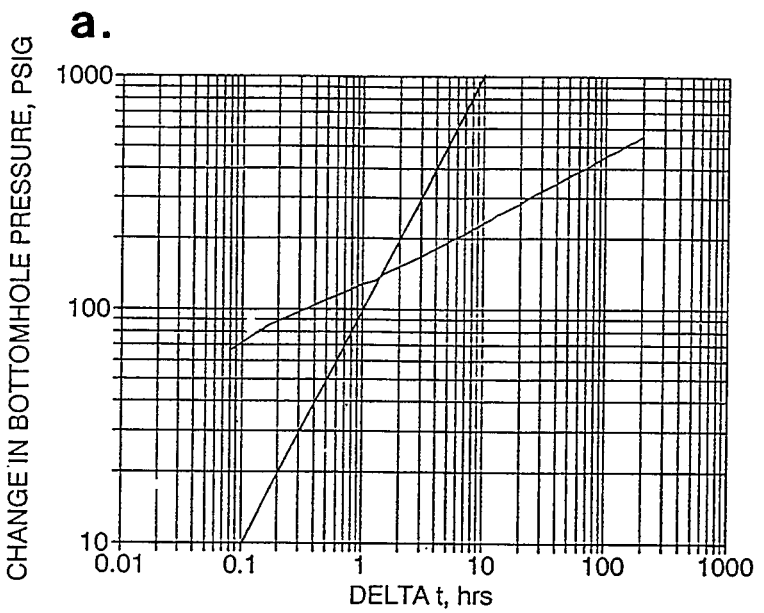

FIGURE B1. Log-Log plot of pressure fall-off to check for wellbore storage. (a) Clay 891; (b) Clay 2499.

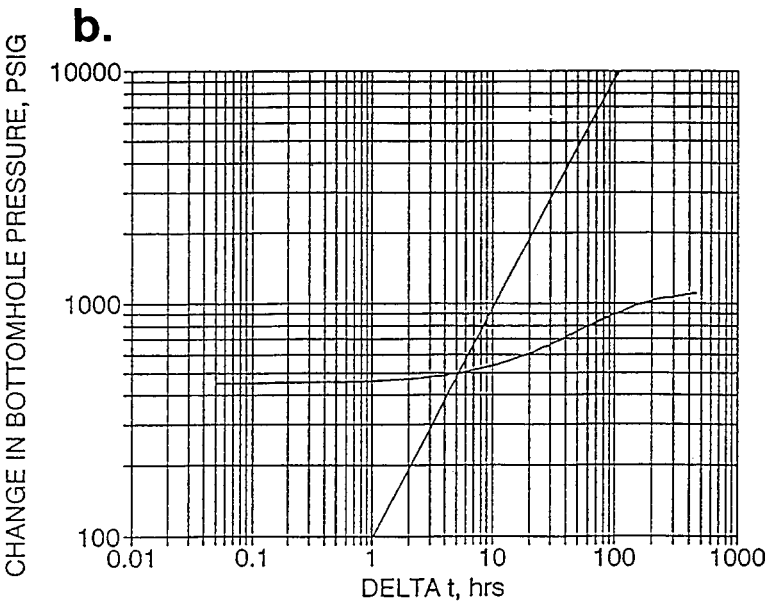

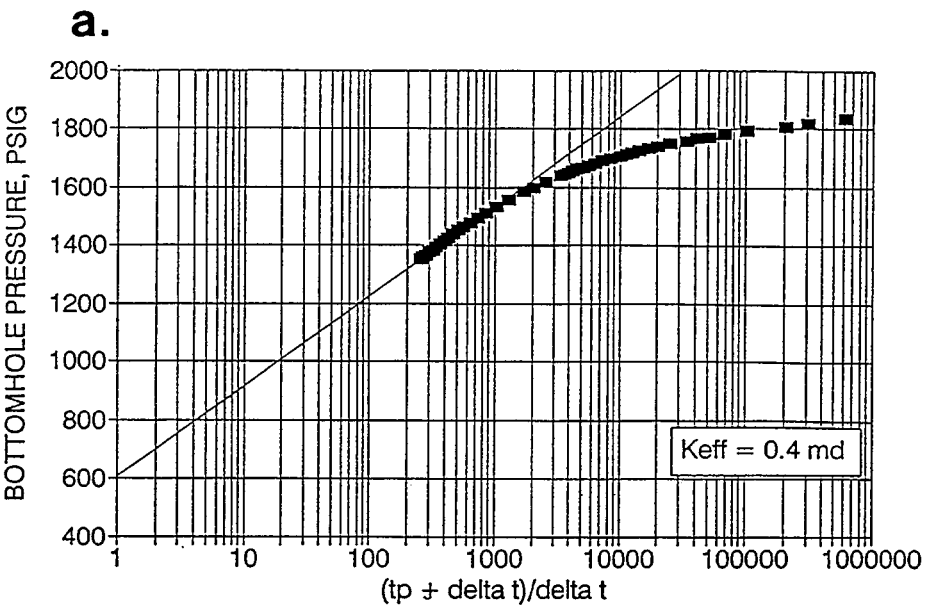

FIGURE B2. Semi-log plot of pressure fall-off. (a) Clay 891; (b) Clay 2499.

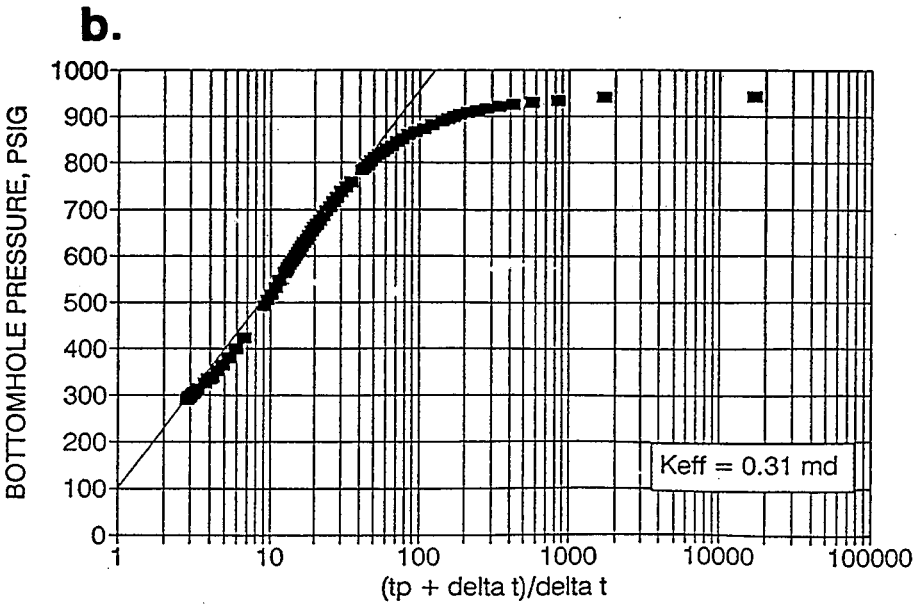

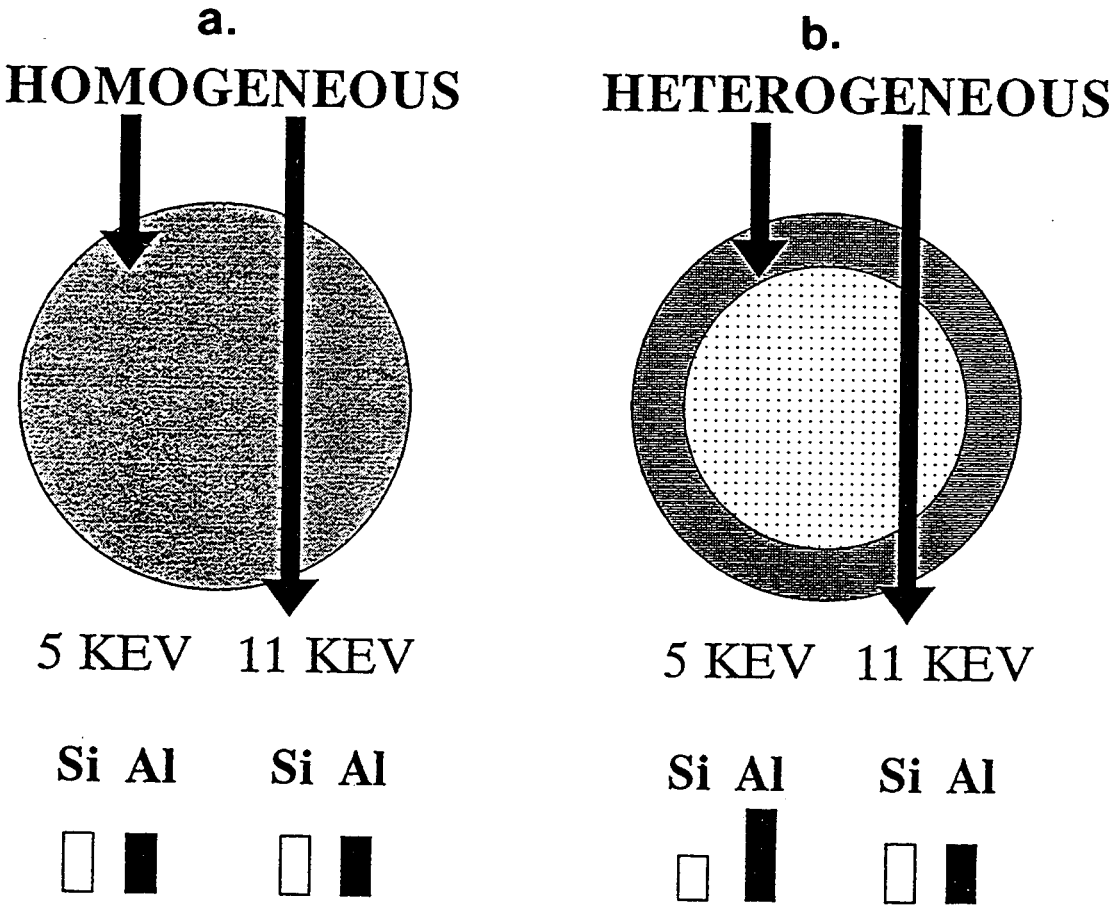

FIGURE C1. Characterization of pore wall mineralogy using SEM (KEVEX). (a) Elemental analysis - homogeneous mineralogy; (b) Elemental analysis - heterogeneous mineralogy.

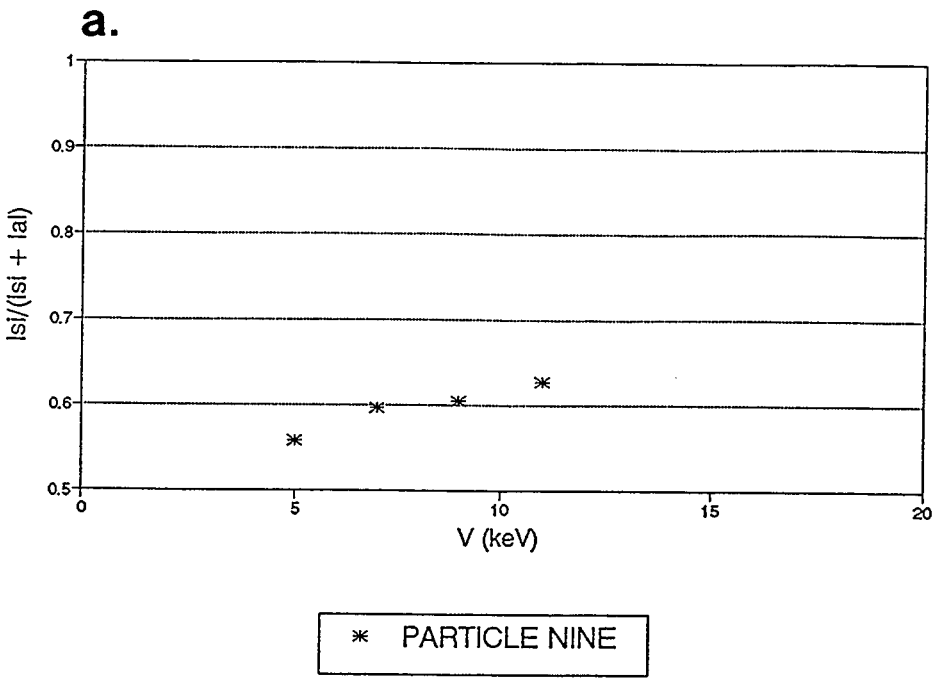

FIGURE C2. Silicon fraction plots. (a) Clay 1132; (b) Clay 1110.

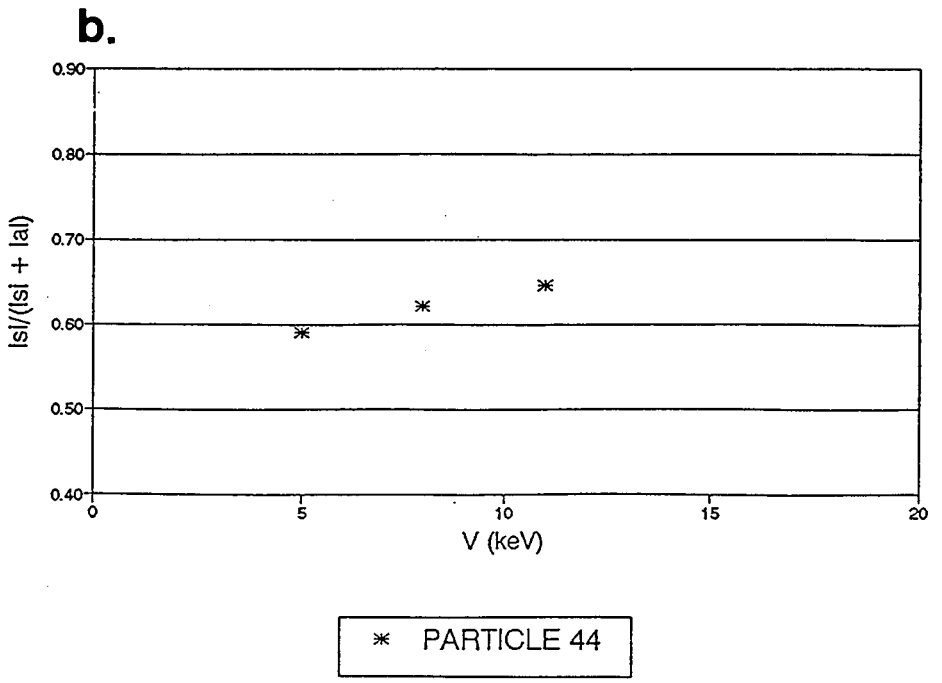

a.

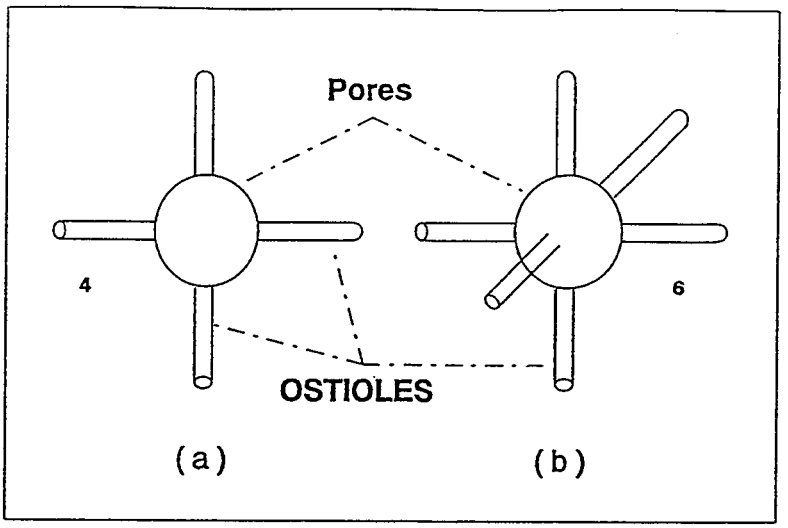

FIGURE D1. Diagrammatic representation of pores. (a) Pores with coordination numbers of 4 and 6; (b) Typical 3D array of pores with coordination number of 6. Each pore is connected to an identical plane in front and back.

b.

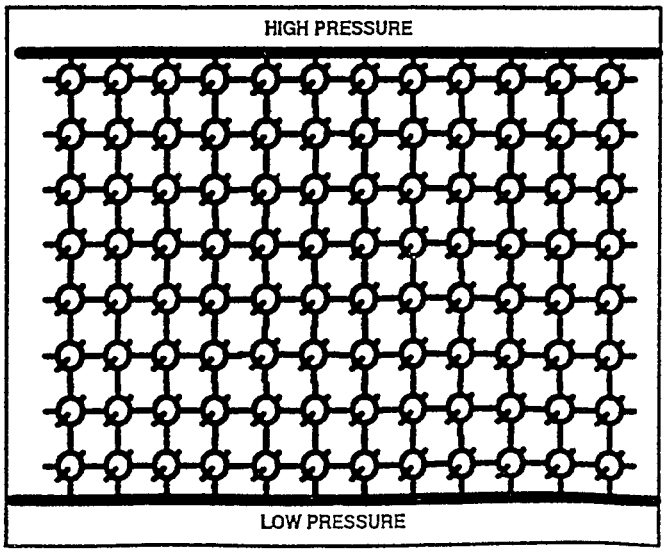

a.

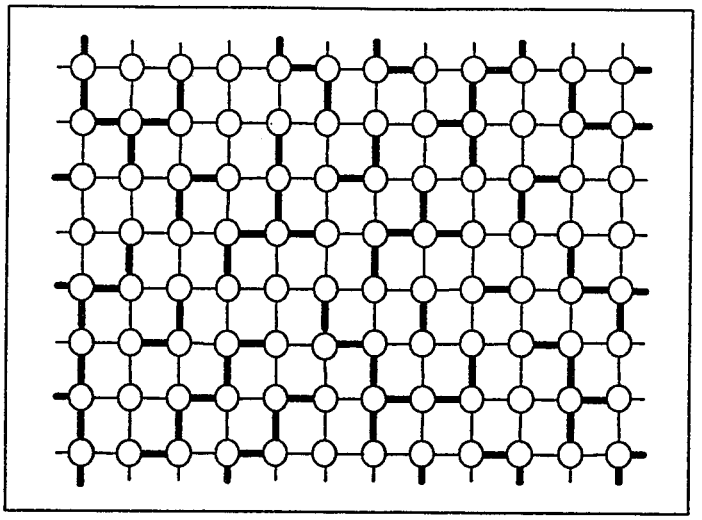

FIGURE D2. Diagrammatic representation of pore networks with different size ostioles (large ostioles shown as thick lines between pores). (a) Pore network with two ostiole sizes; (b) Effect of ostiole size on number of steps in simulation flow path.

b.

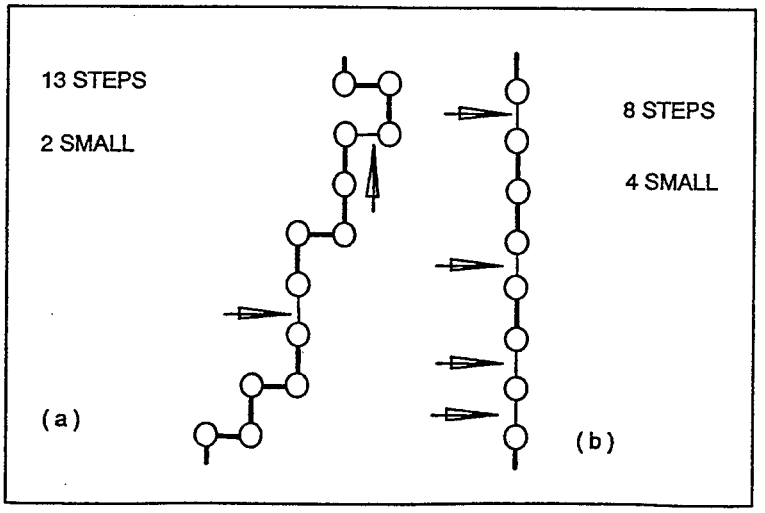

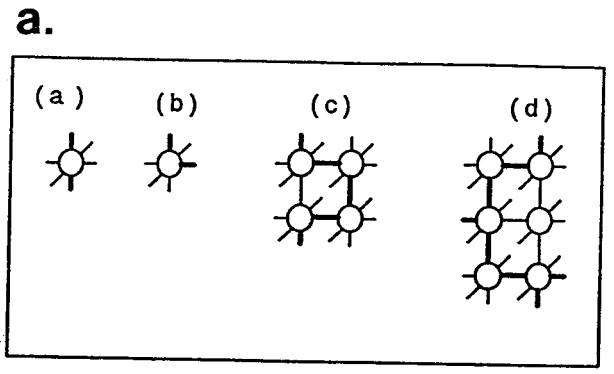

FIGURE D3. Ostiole size and flow path. (a) Path of flow through the large ostioles; (b) Difference in small ostioles in two paths (based on Equation 9).

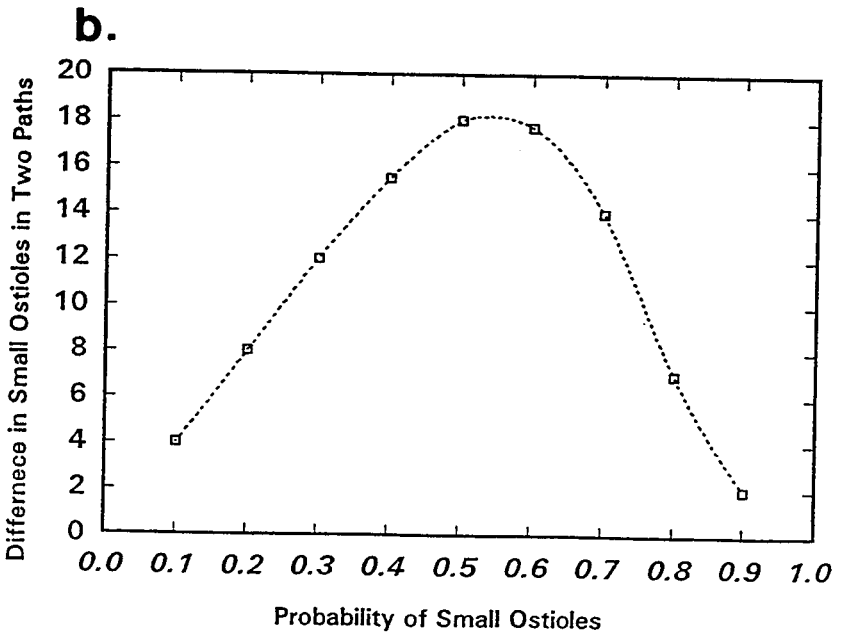

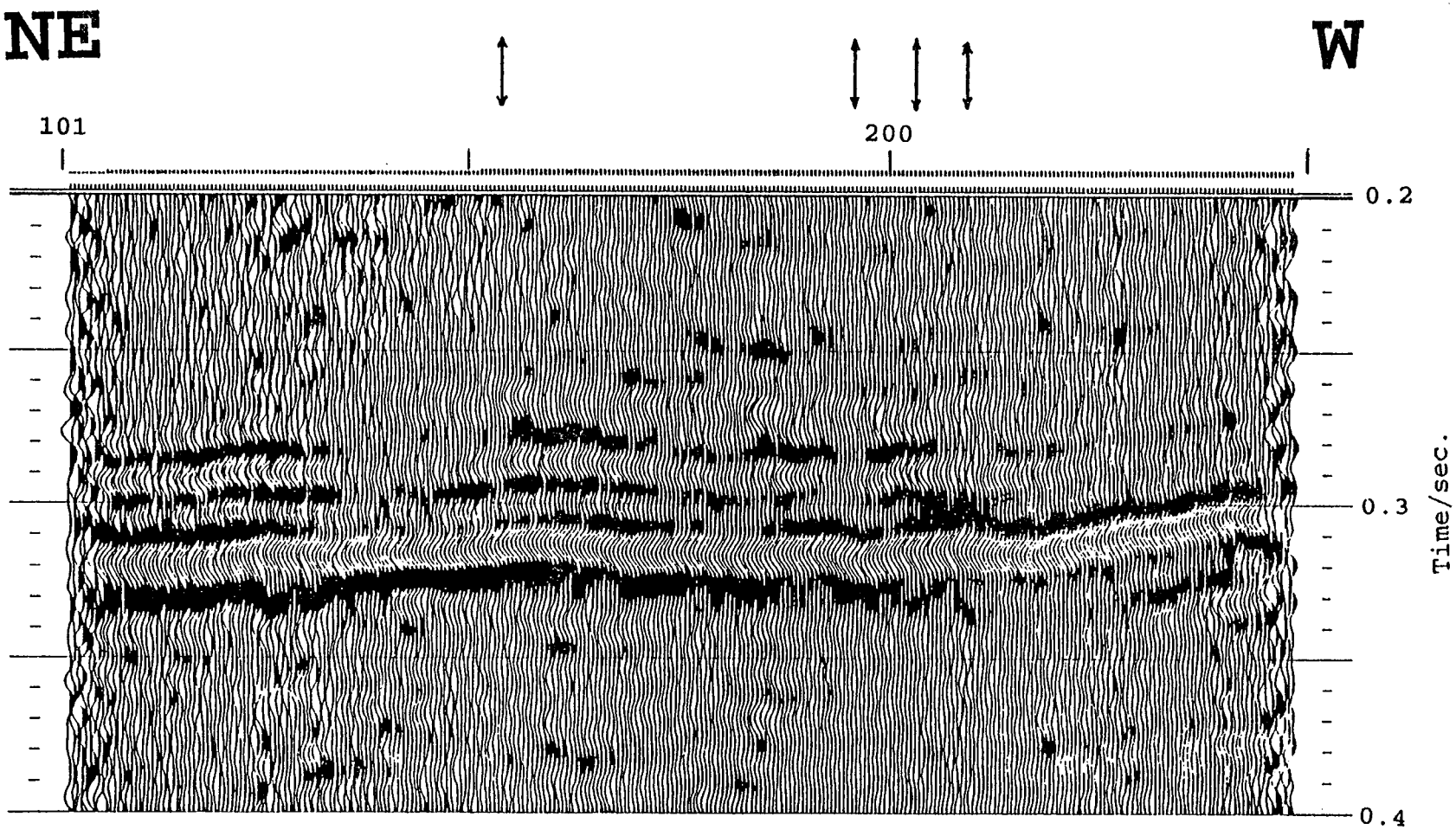

FIGURE E1. Line 2 after initial processing. Vertical arrows represent projected locations of communicating wells in the water-flood recovery operations. See Figure 25 for location of seismic lines in Granny Creek field.

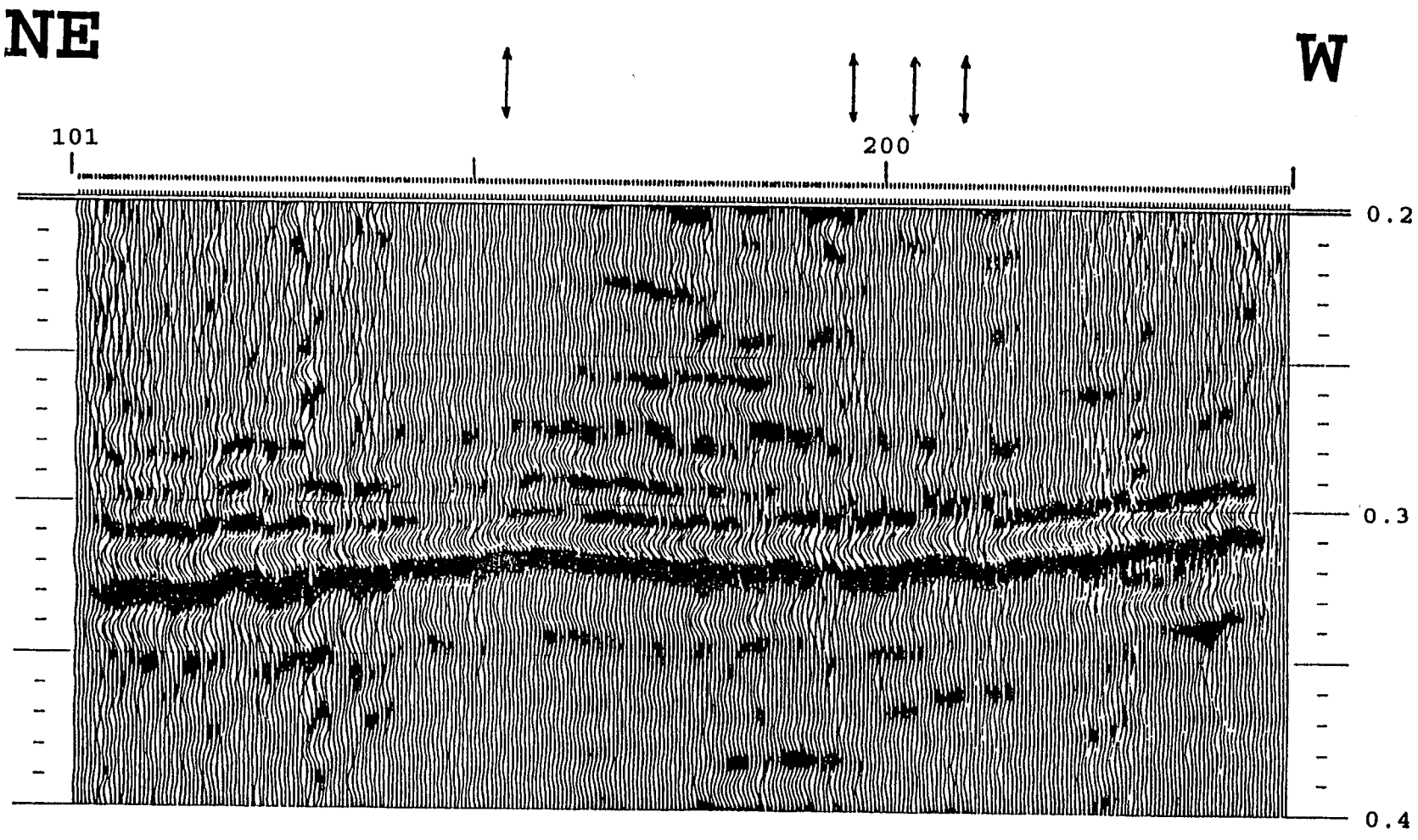

FIGURE E2. Line 2 reprocessed without deconvolution. Vertical arrows represent projected locations of communicating wells in the water-flood recovery operations.

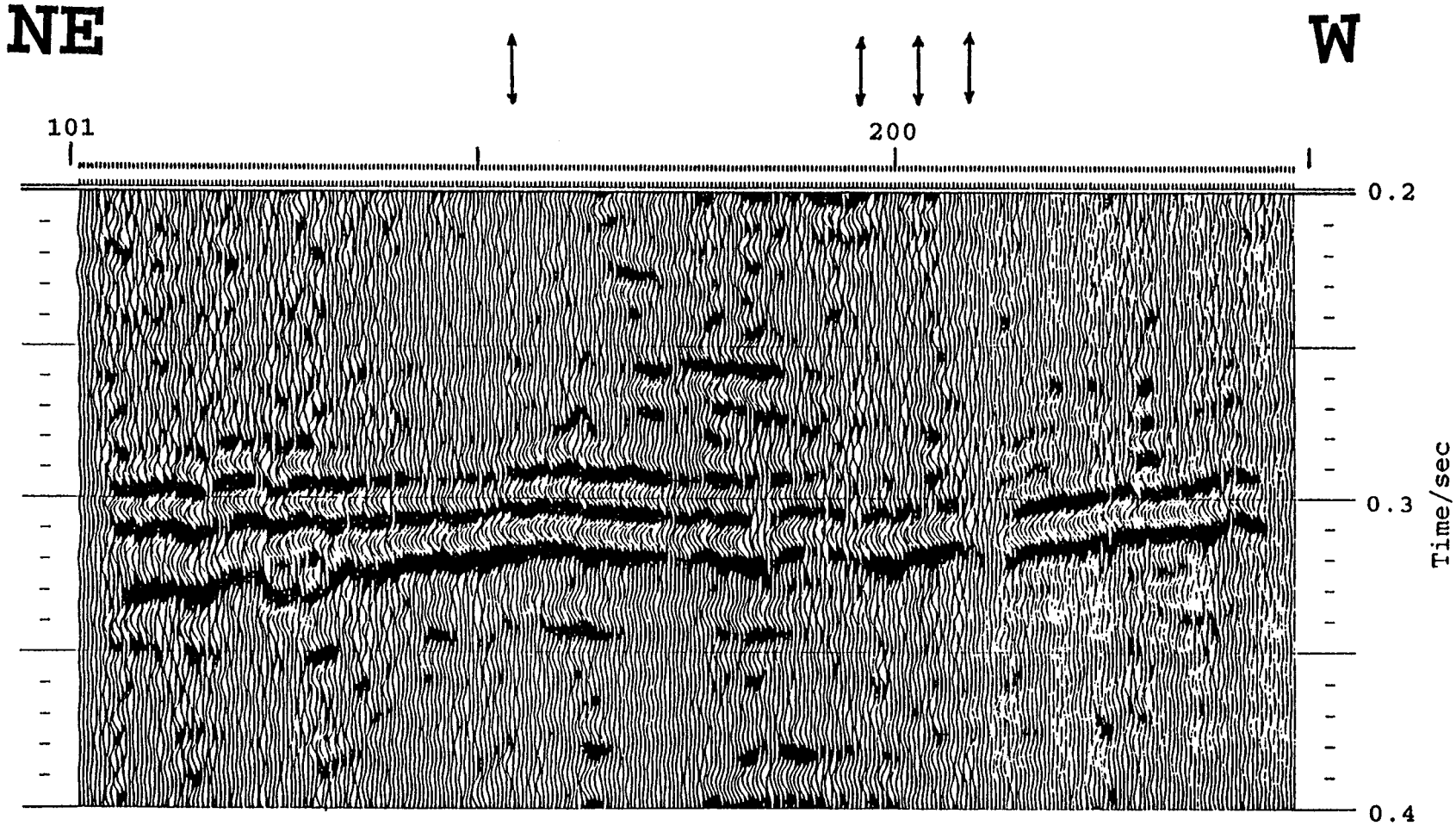

FIGURE E3. Line 2 after reprocessing using Berkhout deconvolution designed on the Klauder, revised stacking velocities and 20% stretch mute. Vertical arrows represent projected locations of communicating wells in the water-flood recovery operations.

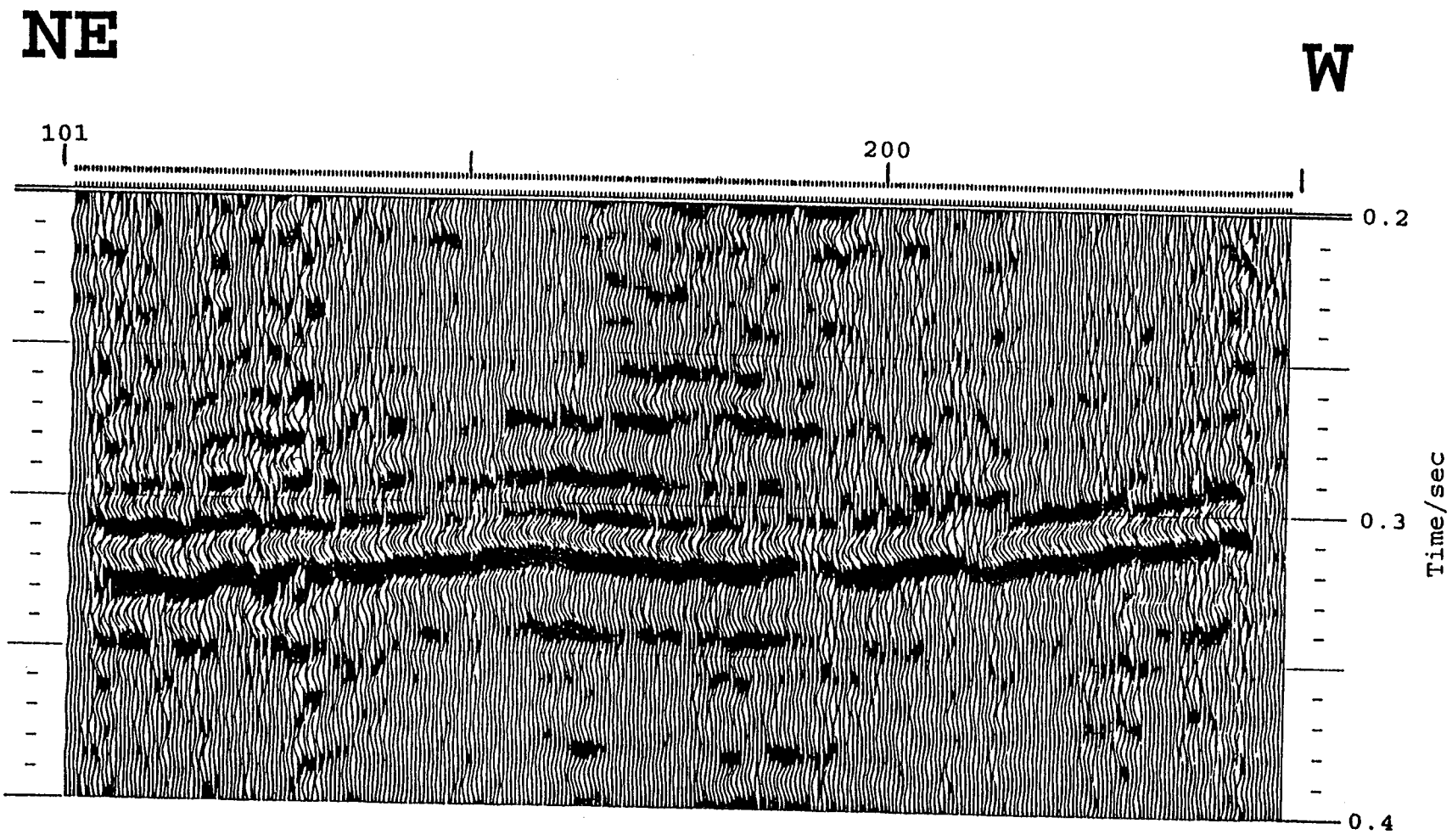

FIGURE E4. Line 2 after reprocessing using Berkhout deconvolution designed on the zero-phase equivalent of the wavelet measured in the VSP well.

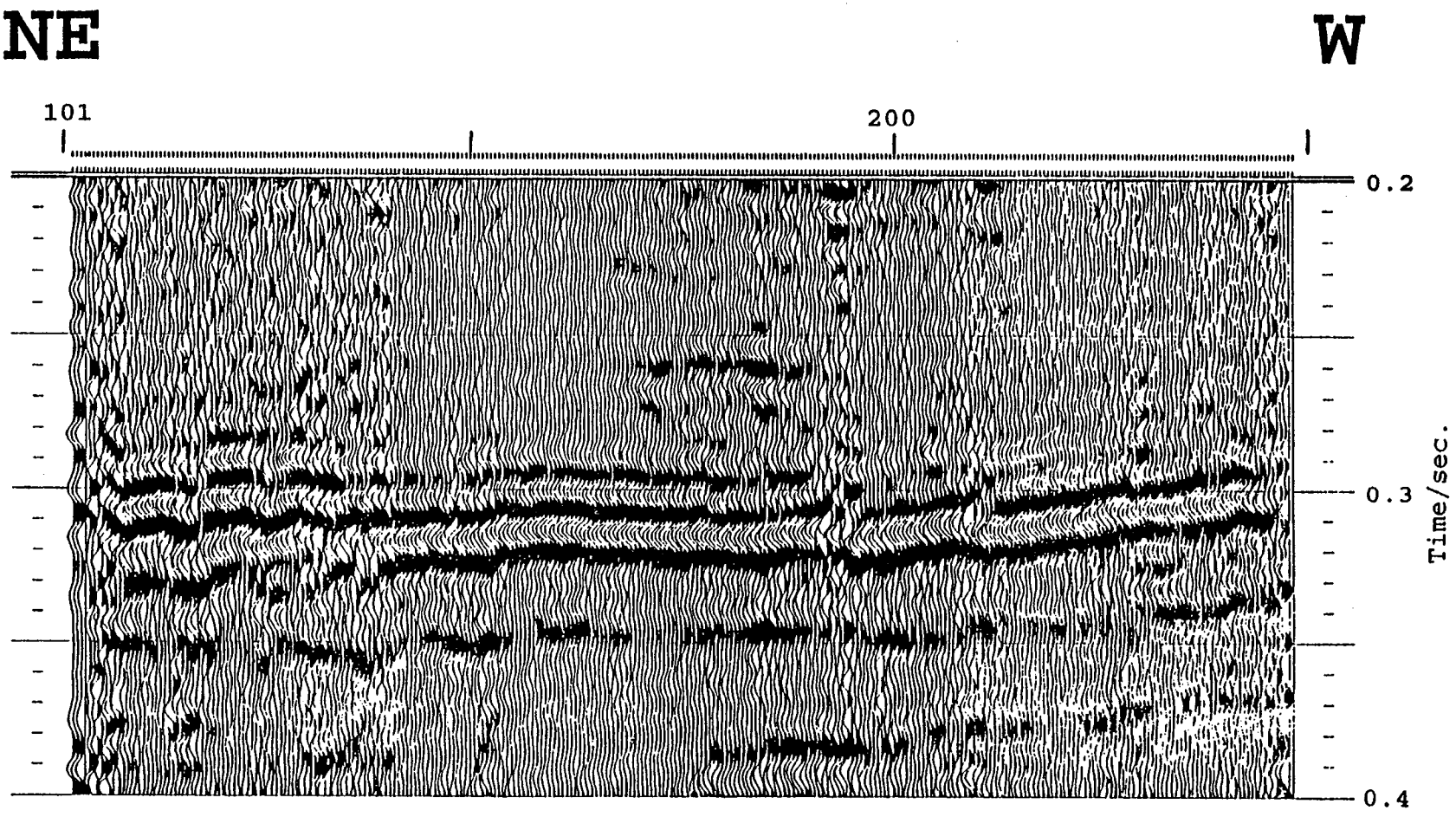

FIGURE E5. Line 2 reprocessed with deconvolution applied before gain recovery.

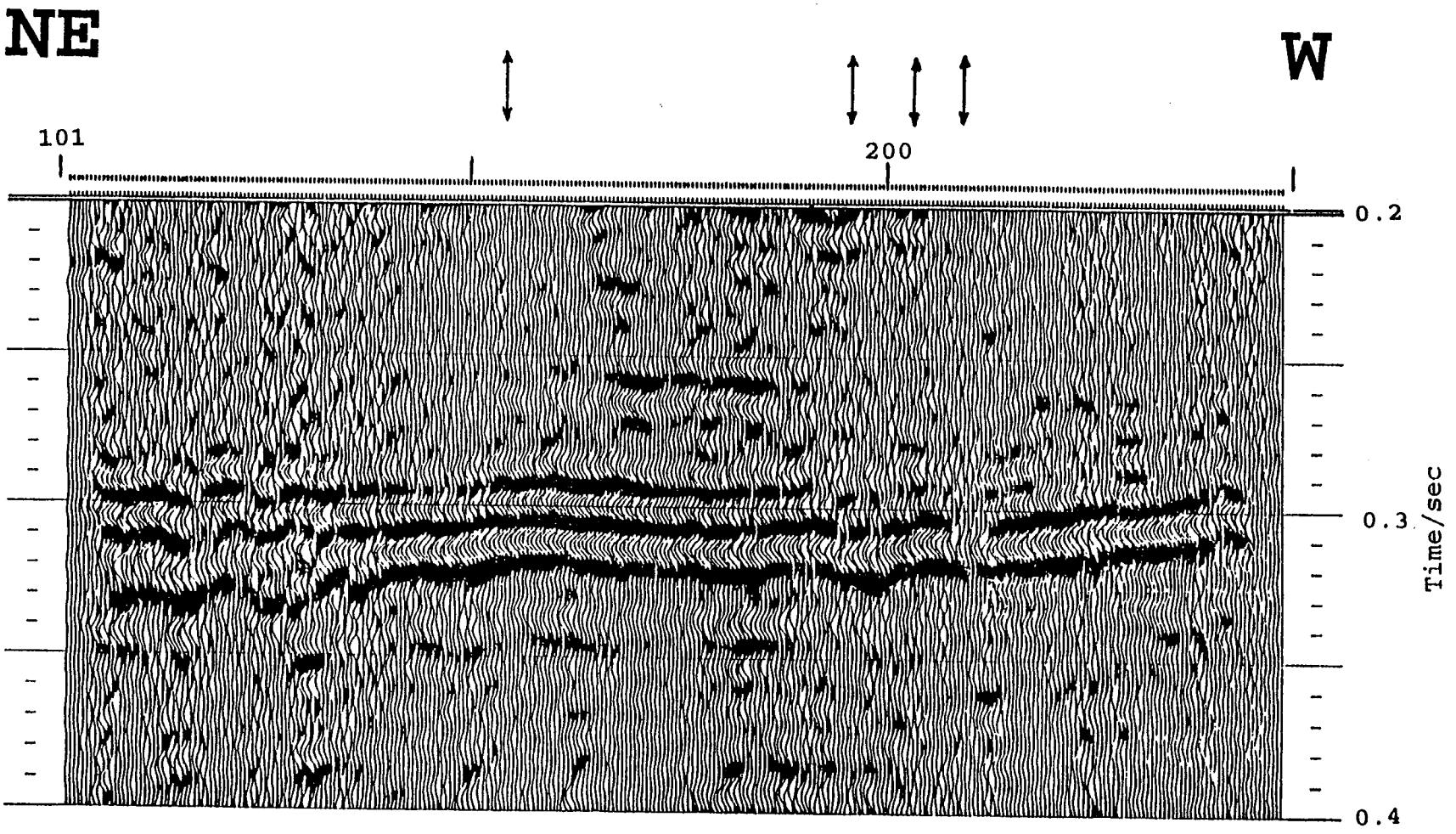

FIGURE E6. Line 2 reprocessed with stacking velocities increased by 400 feet/second above the optimal stacking velocity for the events at 0.3 seconds.

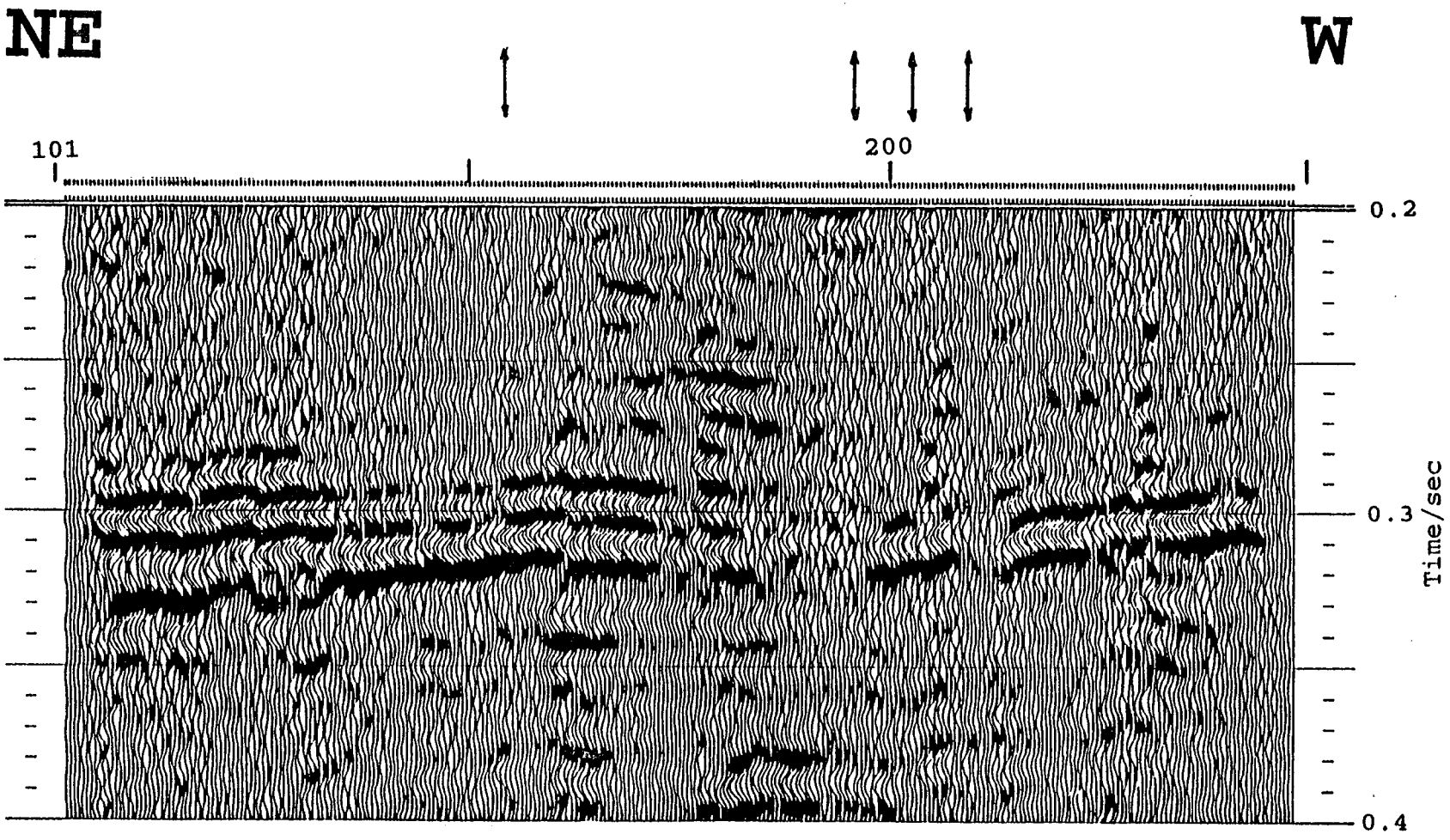

FIGURE E7. Line 2 reprocessed with stacking velocities decreased by 400 feet/second above the optimal stacking velocity for the events at 0.3 seconds.

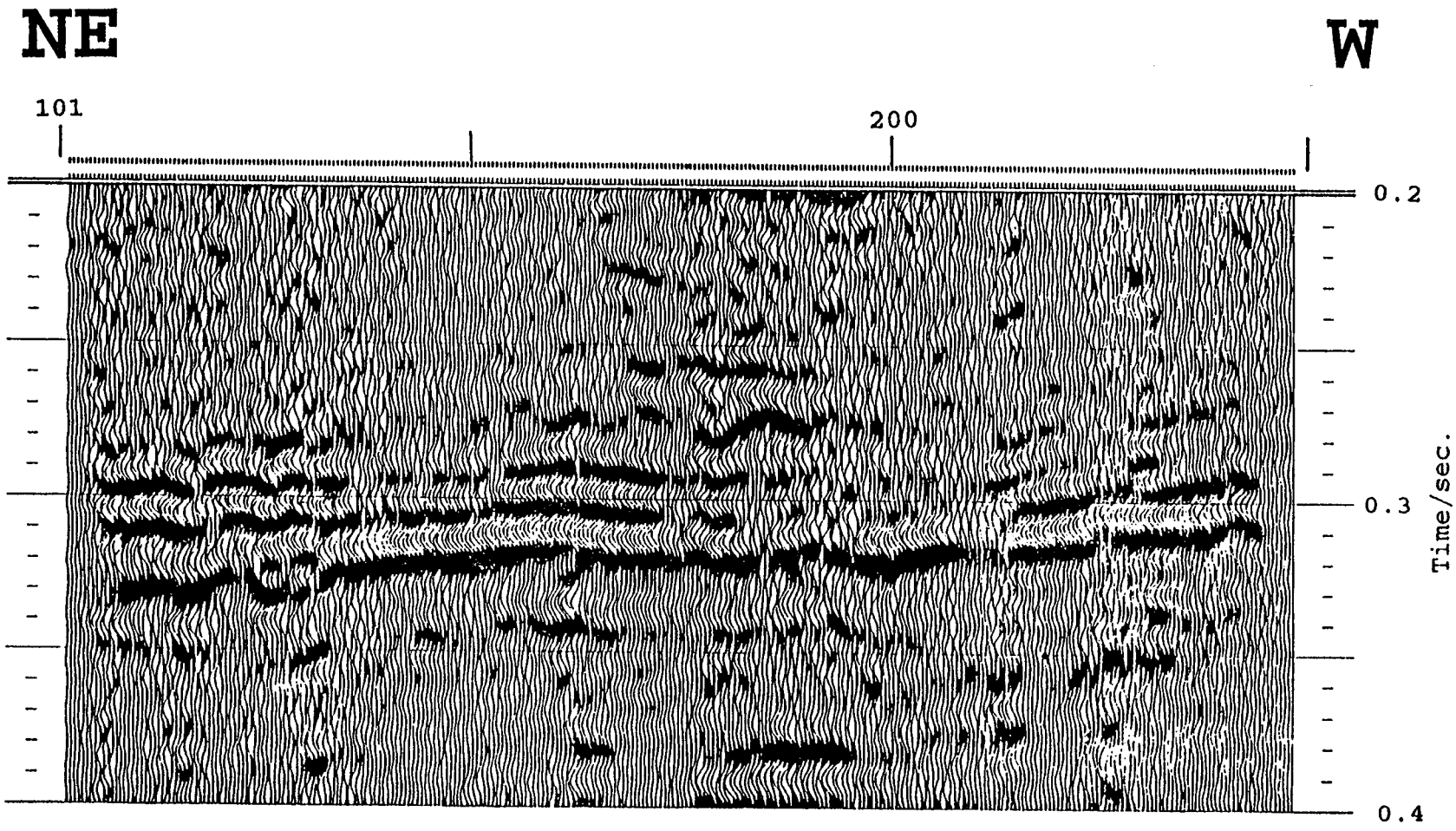

FIGURE E8. Line 2 reprocessed using a 30% stretch mute.

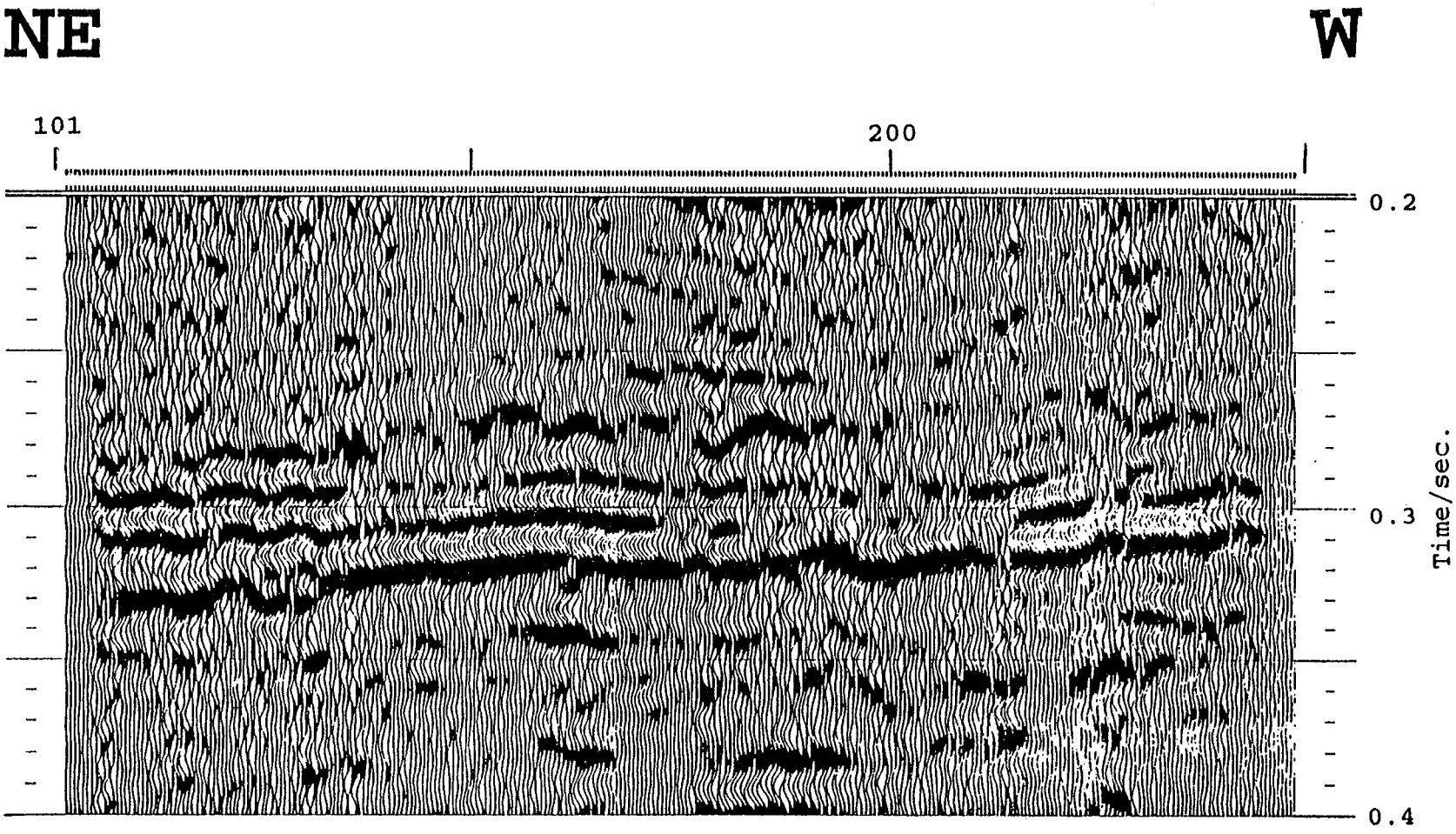

FIGURE E9. Line 2 reprocessed using a 40% stretch mute.

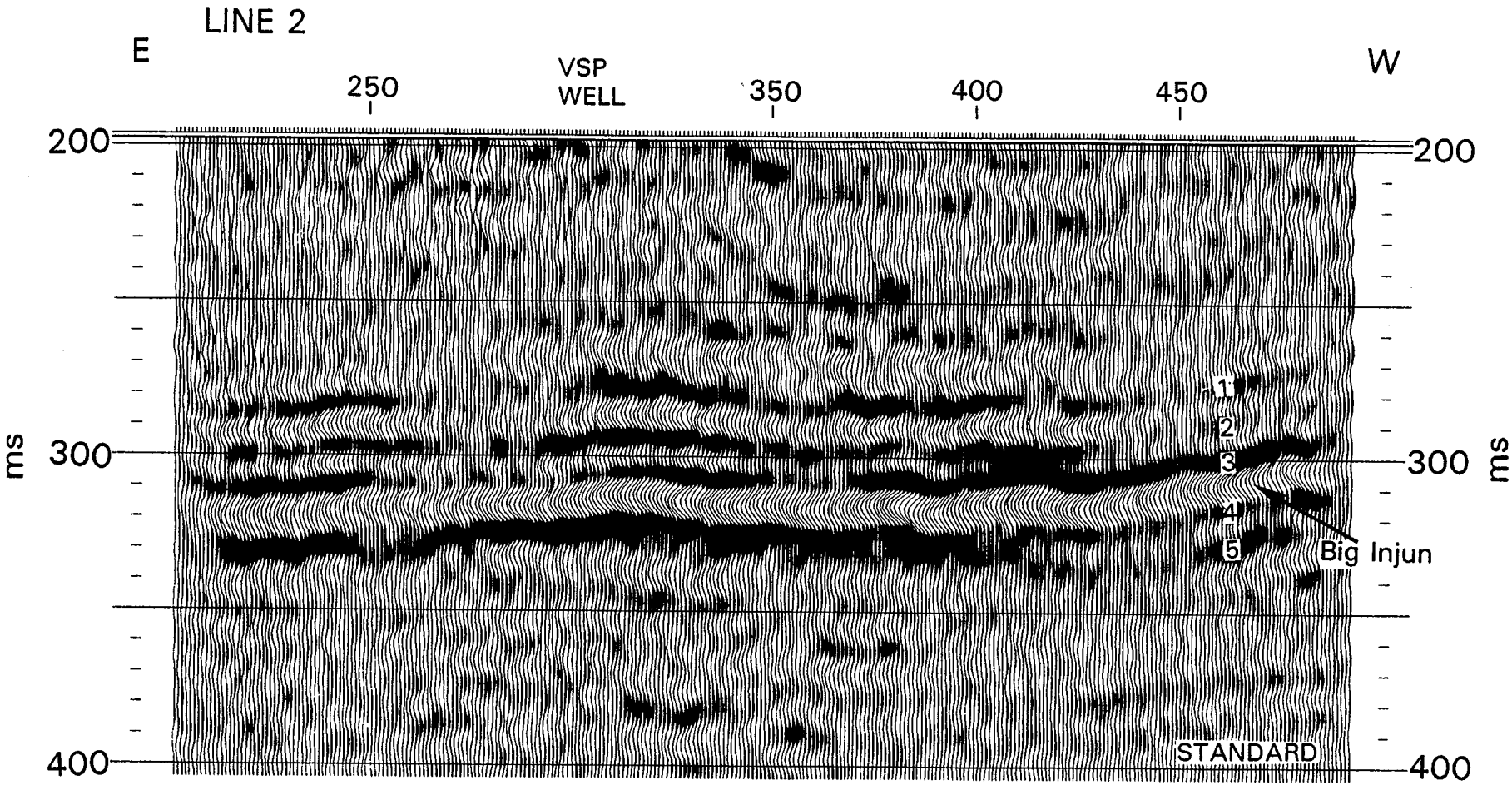

FIGURE F1. Seismic Line 2 from Granny Creek field. Projection of the VSP well onto the line is shown. The reflection associated with the Big Injun sandstone and events 1 through 5 are noted for reference. See Figure 25 for location of seismic lines in Granny Creek field.

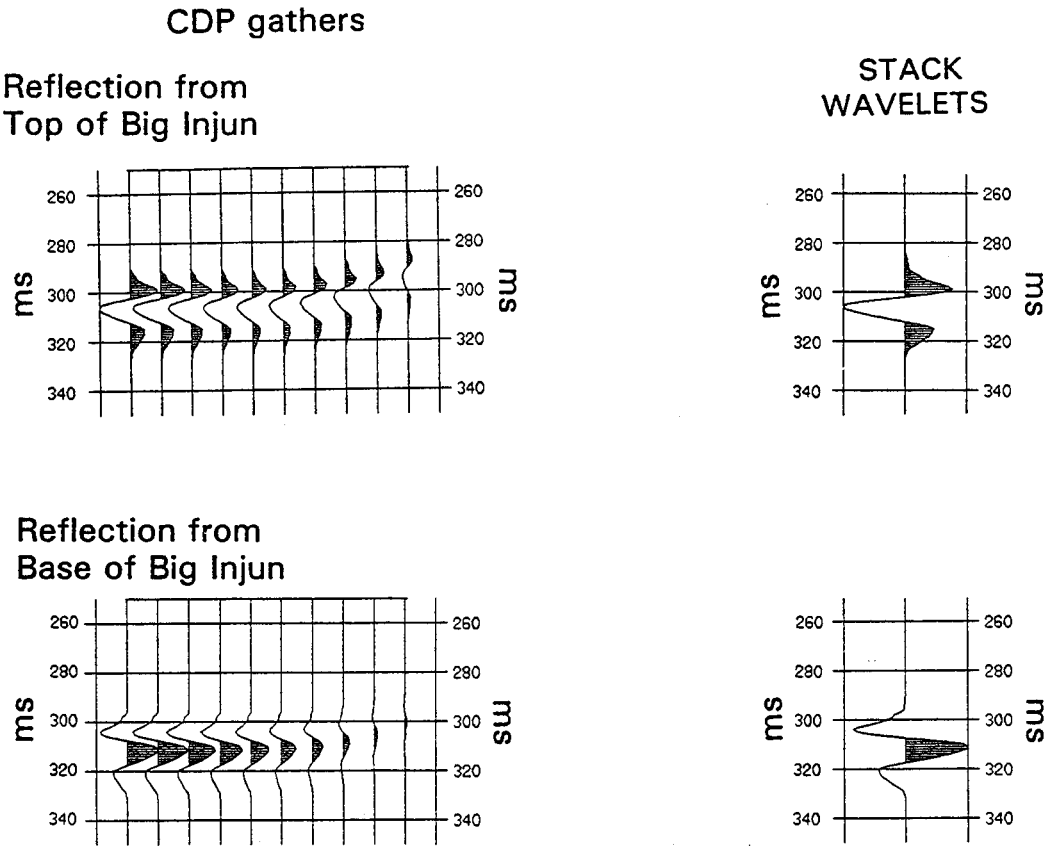

FIGURE F2. Reflection response of an isolated reflection from the top of the reservoir interval (Big Injun sandstone) is shown in a common midpoint gather after moveout correction. The stacked response or *stack wavelet* is shown on the right.

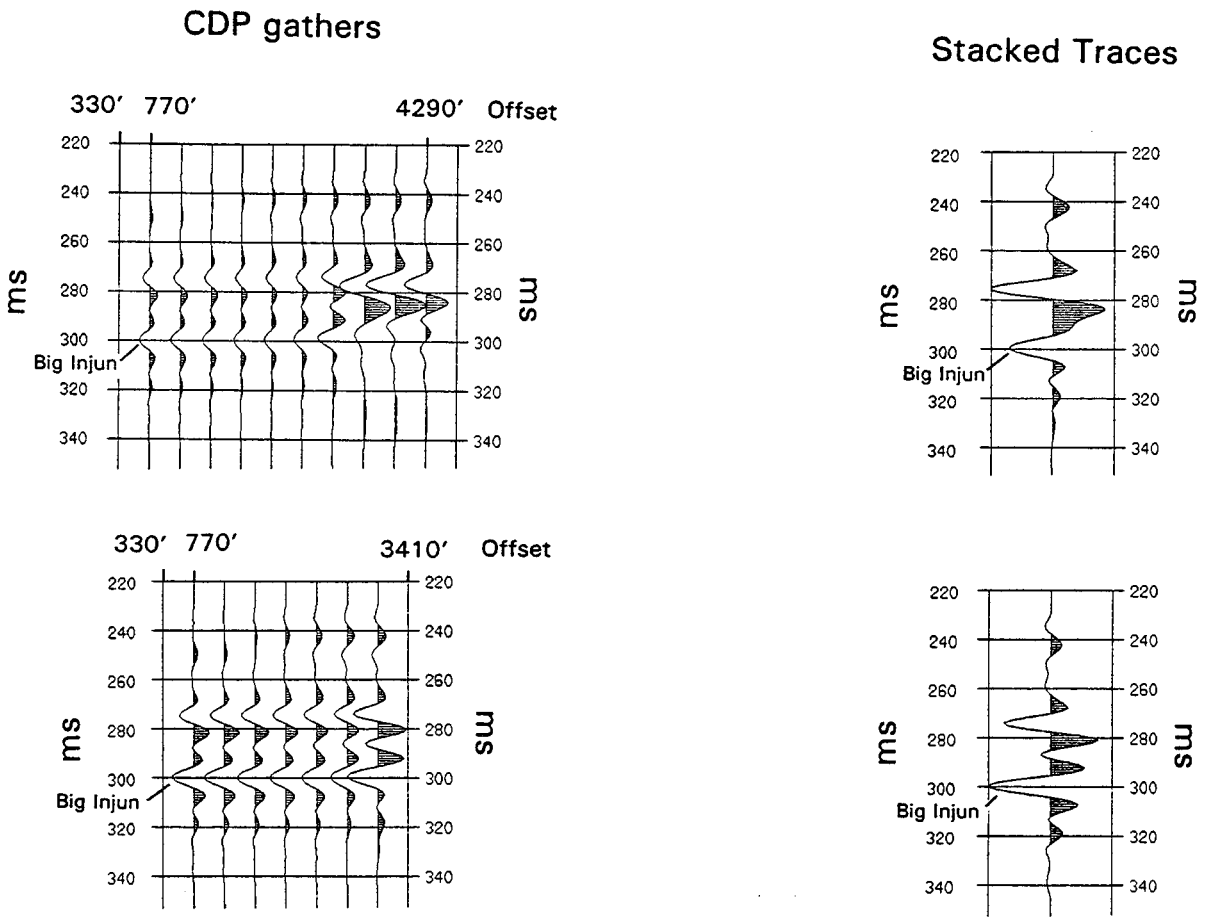

FIGURE F3. Offset reflection response for reflectors from the Mauch Chunk through Squaw intervals is shown on the right. The results of stacking different ranges of offsets are shown on the left.

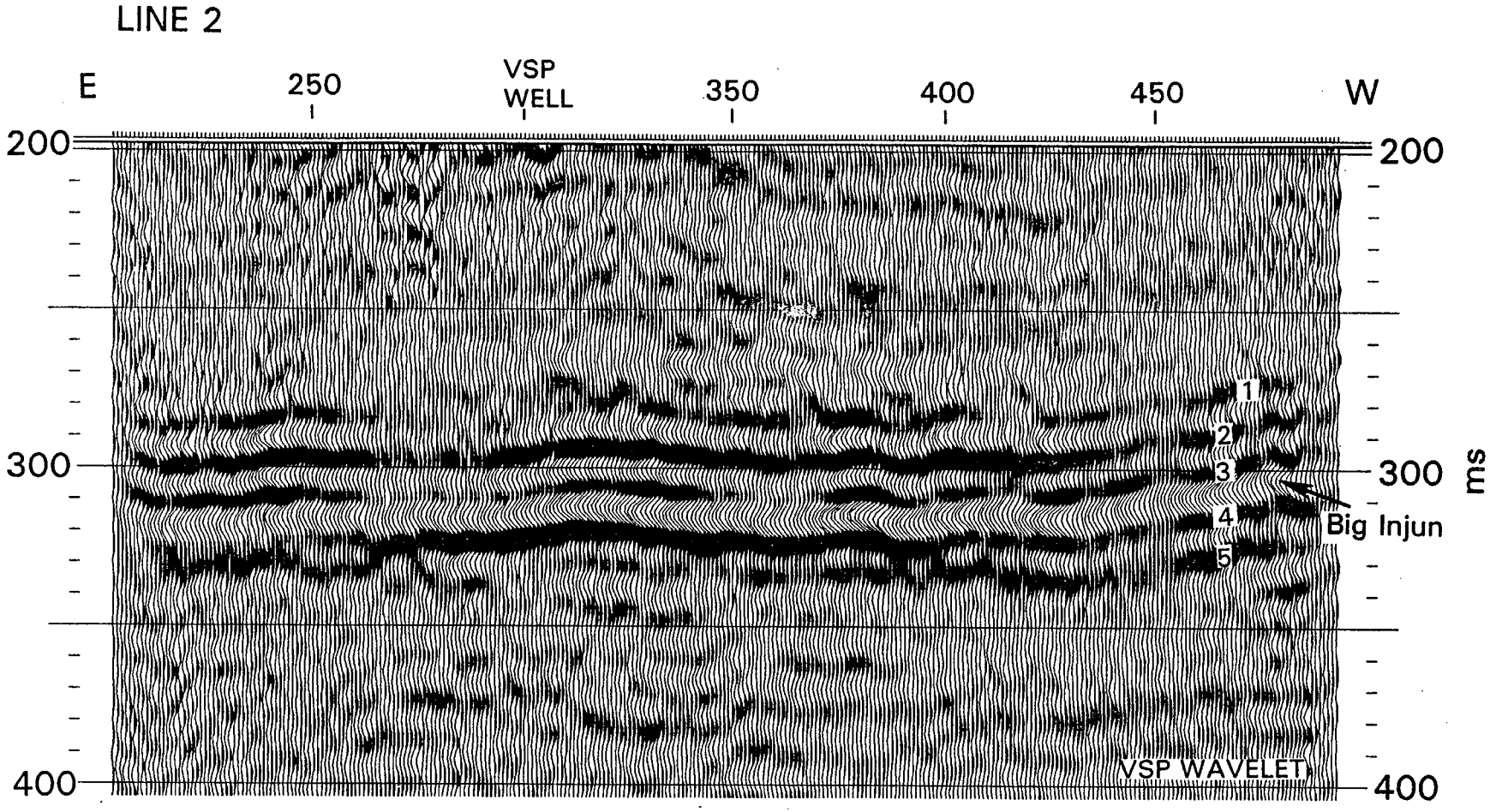

FIGURE F4. Post-stack wavelet deconvolution of the data shown in Figure F1. The filter was designed using the actual, mixed-phase wavelet measured in the VSP.

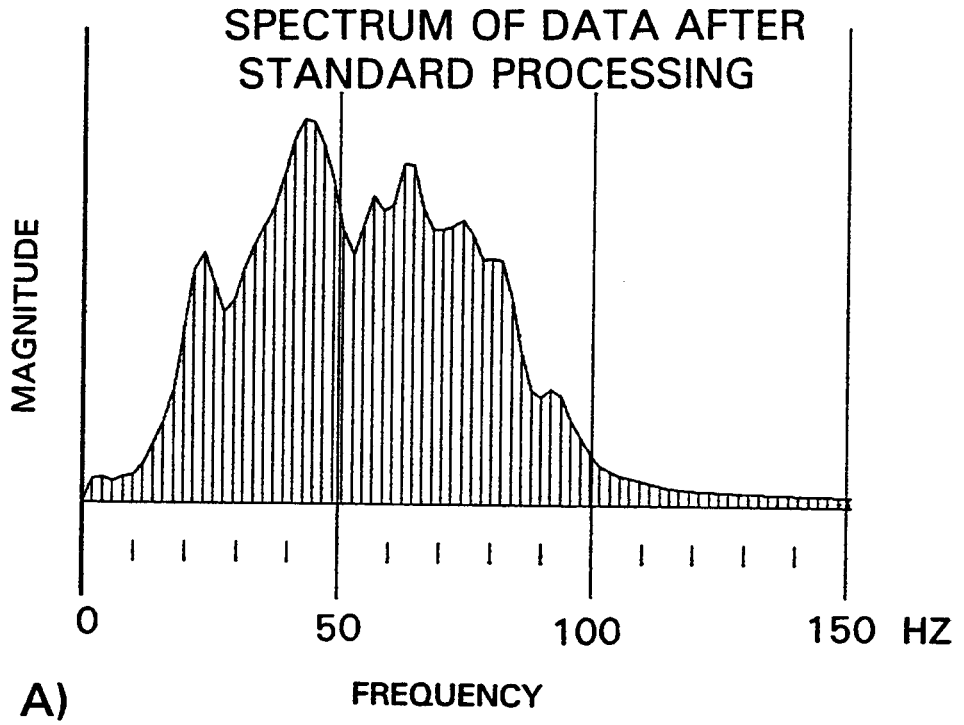

FIGURE F5. Amplitude spectra of the data. (a) Before frequency domain inversion; (b) After frequency domain inversion.

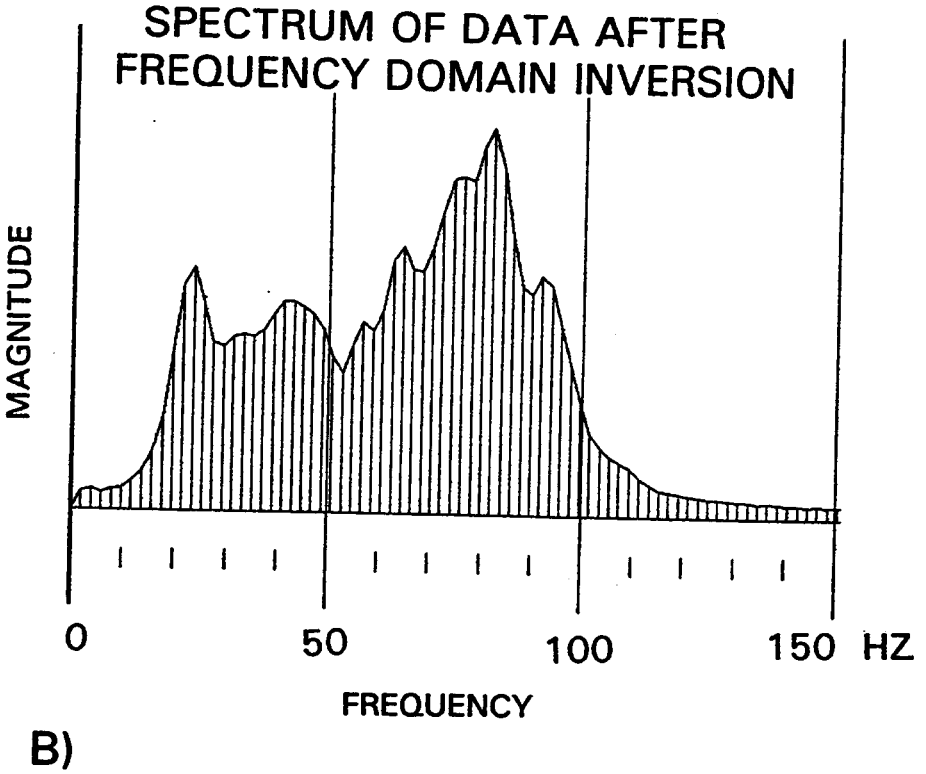

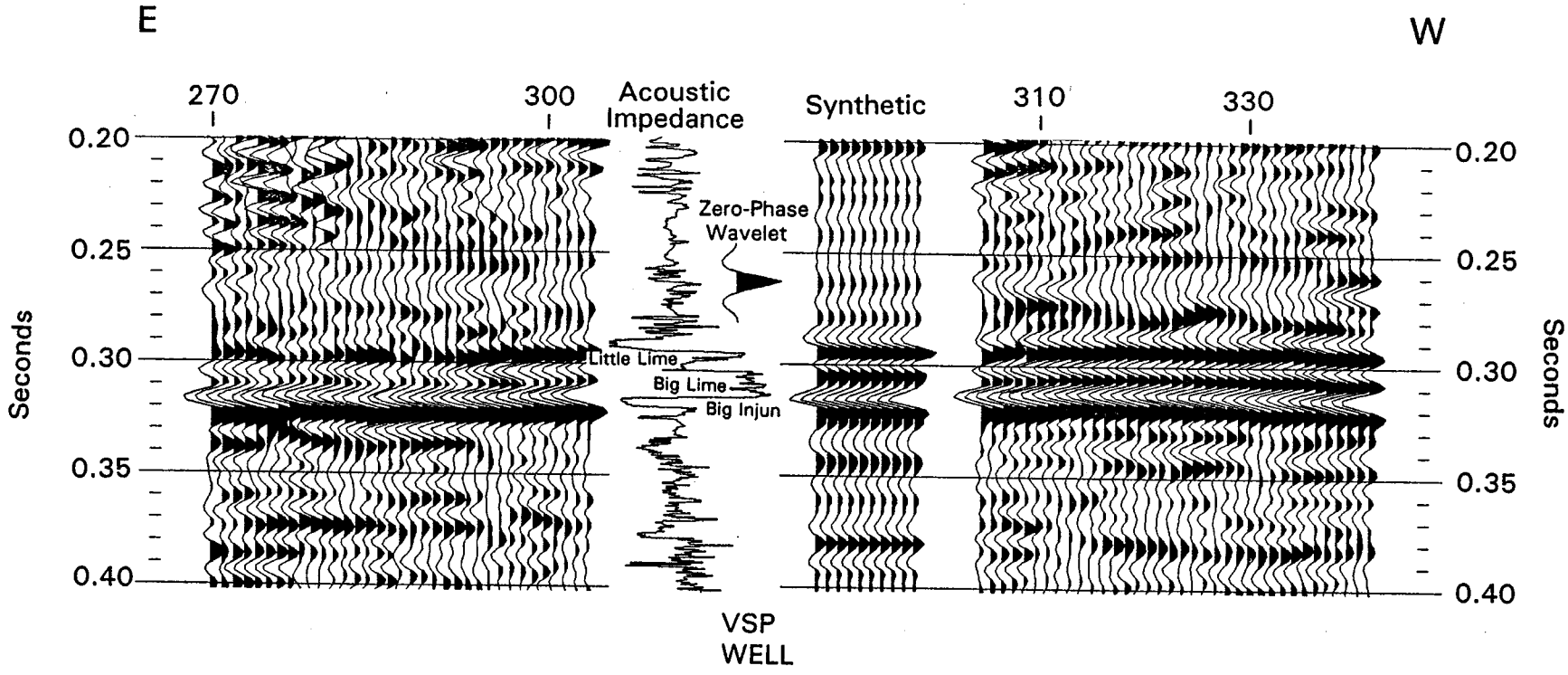

FIGURE F6. Synthetic seismic traces were computed using the zero-phase equivalent of the VSP wavelet. The synthetic traces are inserted into the data shown in Figure F3 near the VSP well.

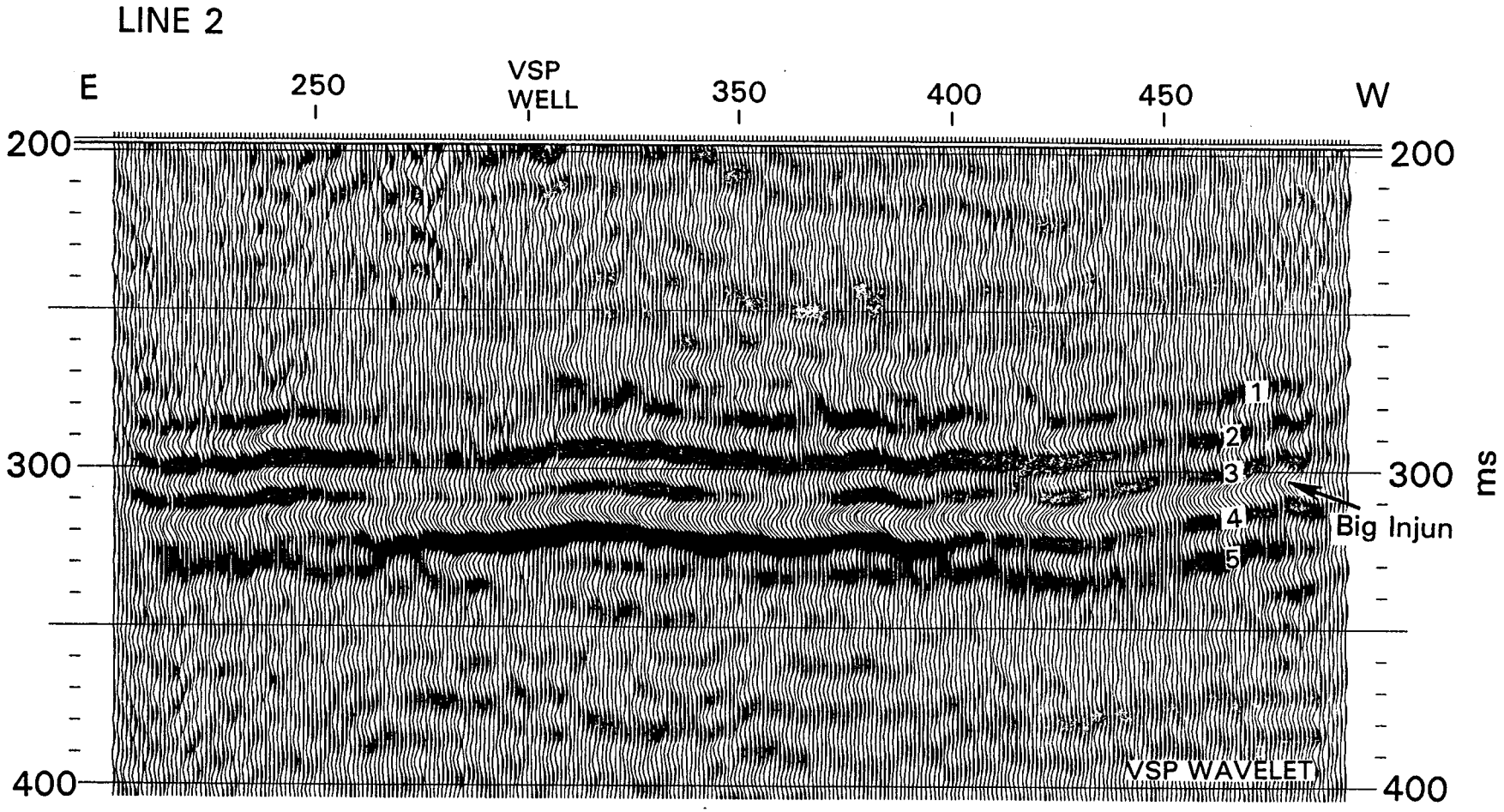

FIGURE G1. Vibroseis Line 2 after frequency domain inversion (Appendix F). See Figure 25 for location of seismic lines in Granny Creek field.

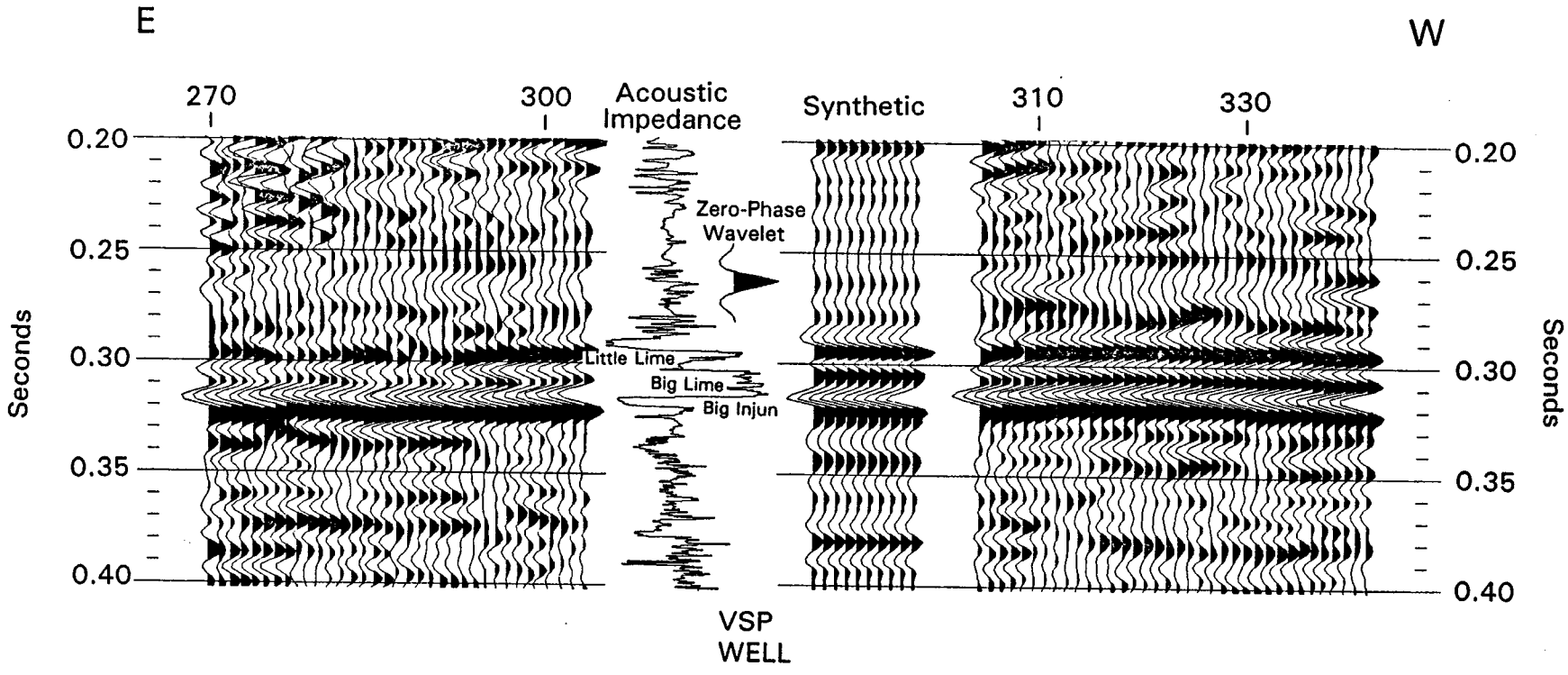

FIGURE G2. Comparison of synthetic seismic response to the data of Figure G1 near the VSP well. Acoustic impedance derived from the VSP well and the seismic wavelet used in the synthetic computations are also shown.

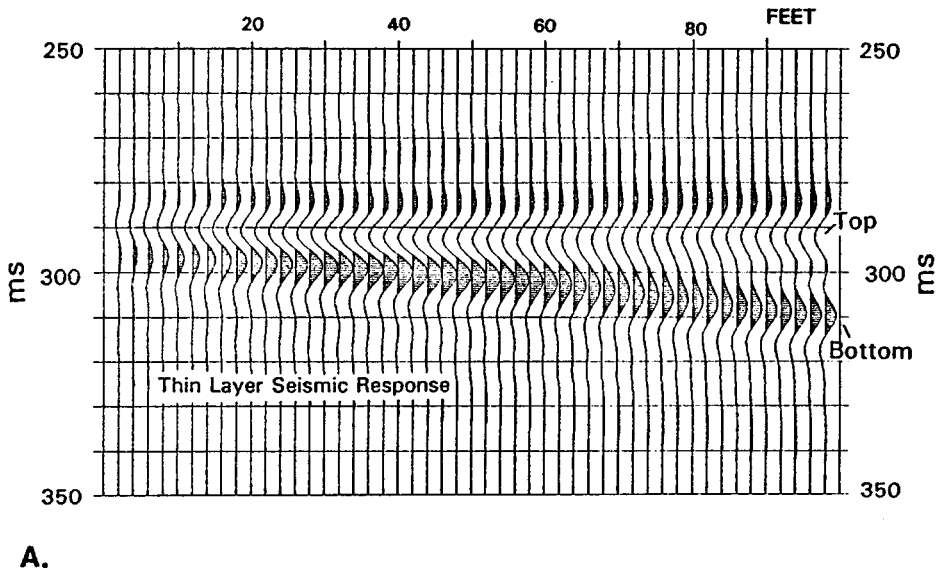

FIGURE G3. (a) Seismic response of a thin layer; (b) Reflection amplitude difference between the negative cycle from the top of the layer and the positive cycle at the base of the layer.

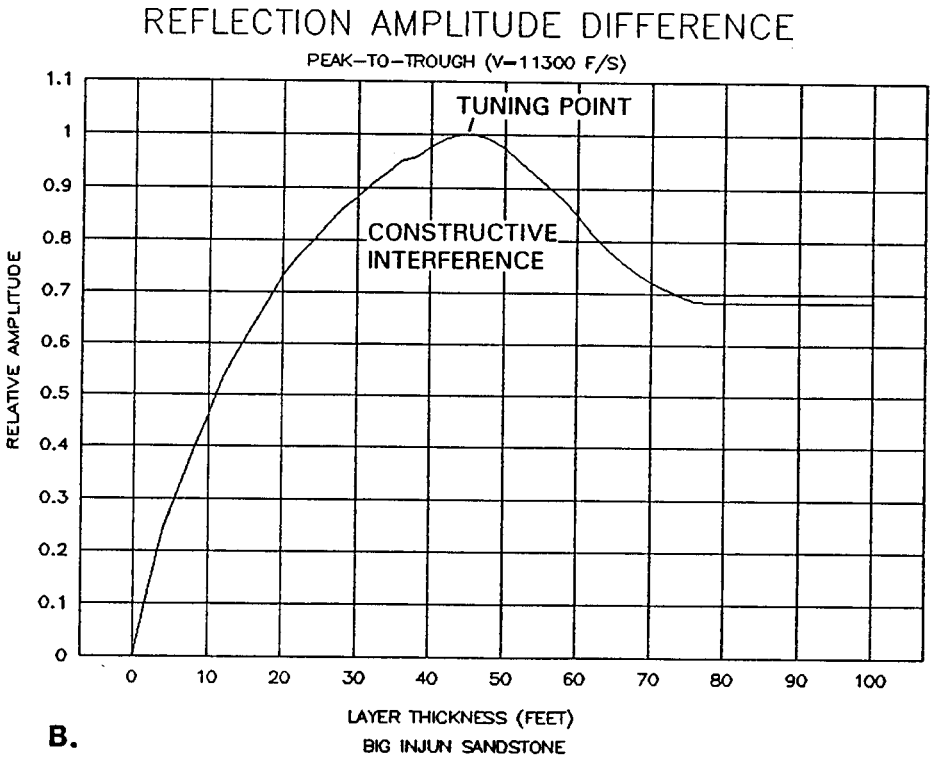

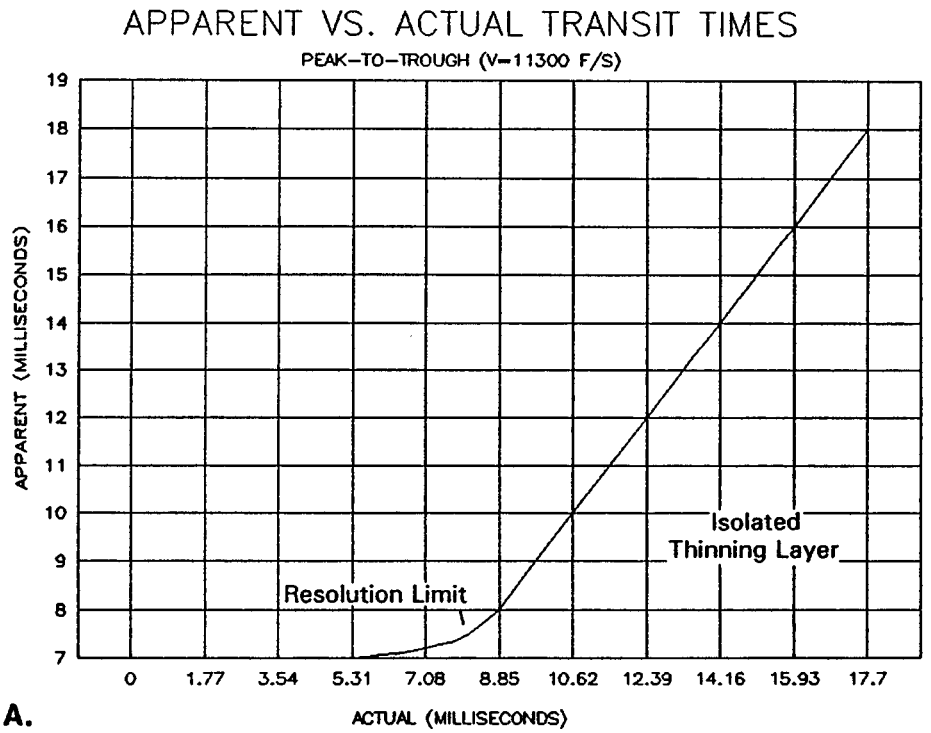

FIGURE G4. (a) Apparent travel times measured through the thinning layer plotted against actual travel times based on thickness; (b) Apparent travel times plotted against thickness.

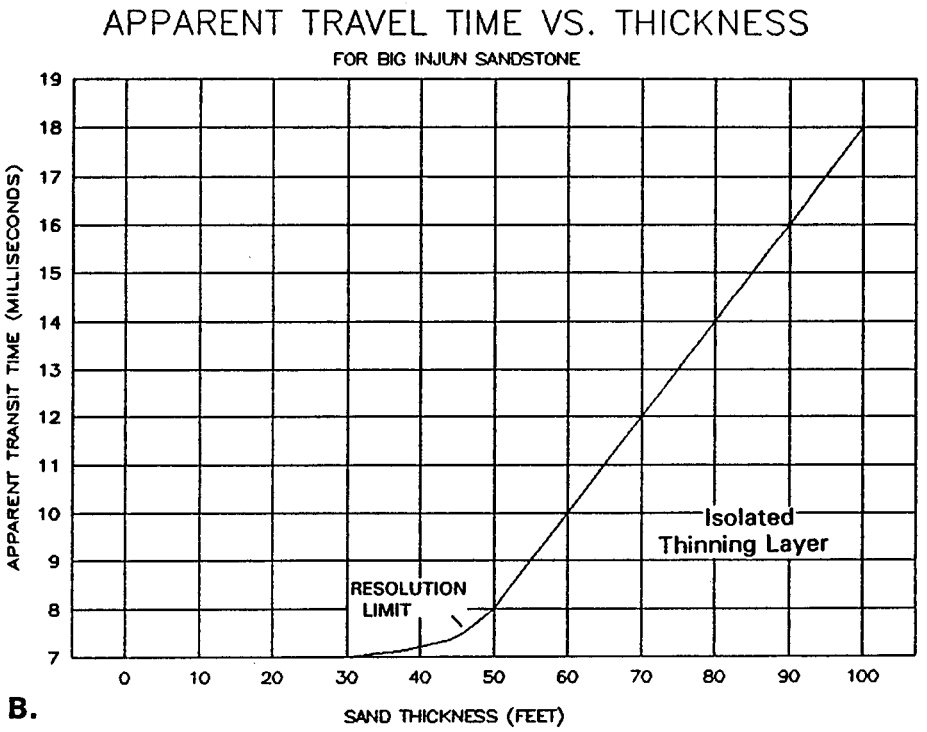

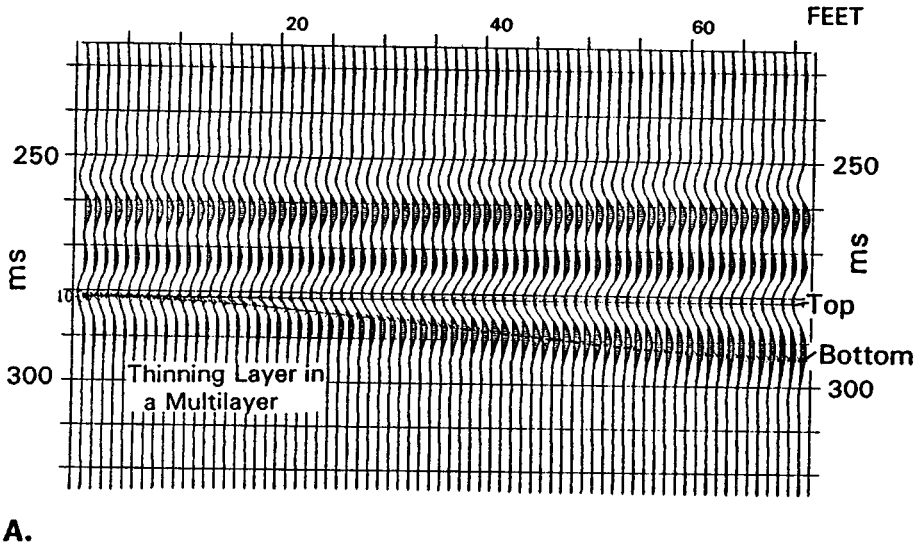

A.

FIGURE G5. (a) Seismic response of a thinning layer beneath a multilayer interval. Actual top and bottom of the layer are marked for reference; (b) Amplitude difference between the negative cycle associated with the top of the layer and the positive cycle at the base of the layer.

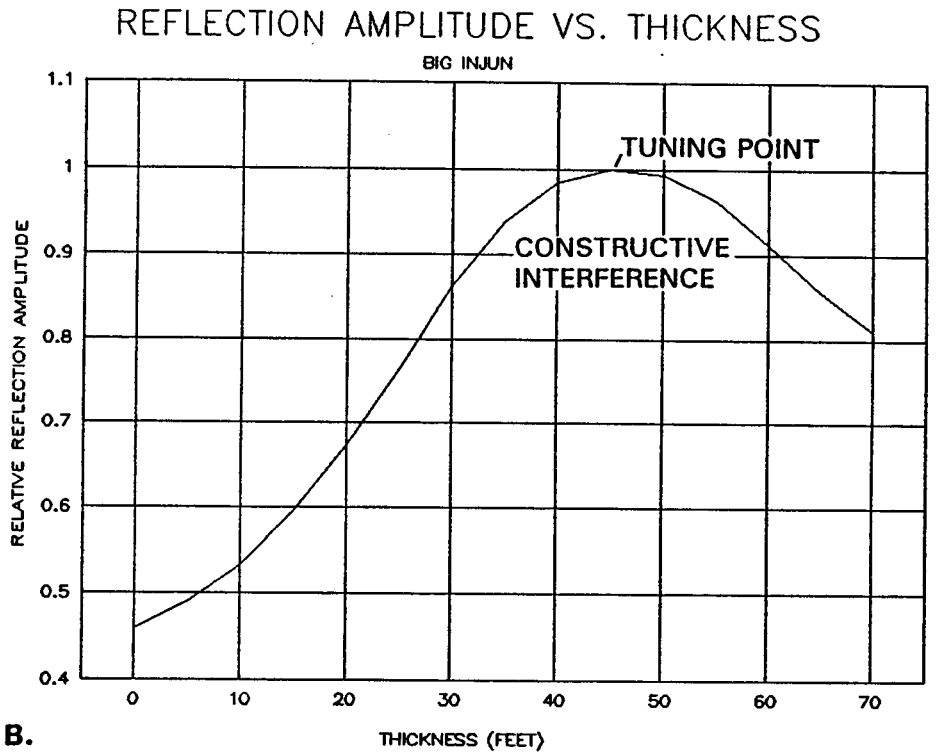

B.

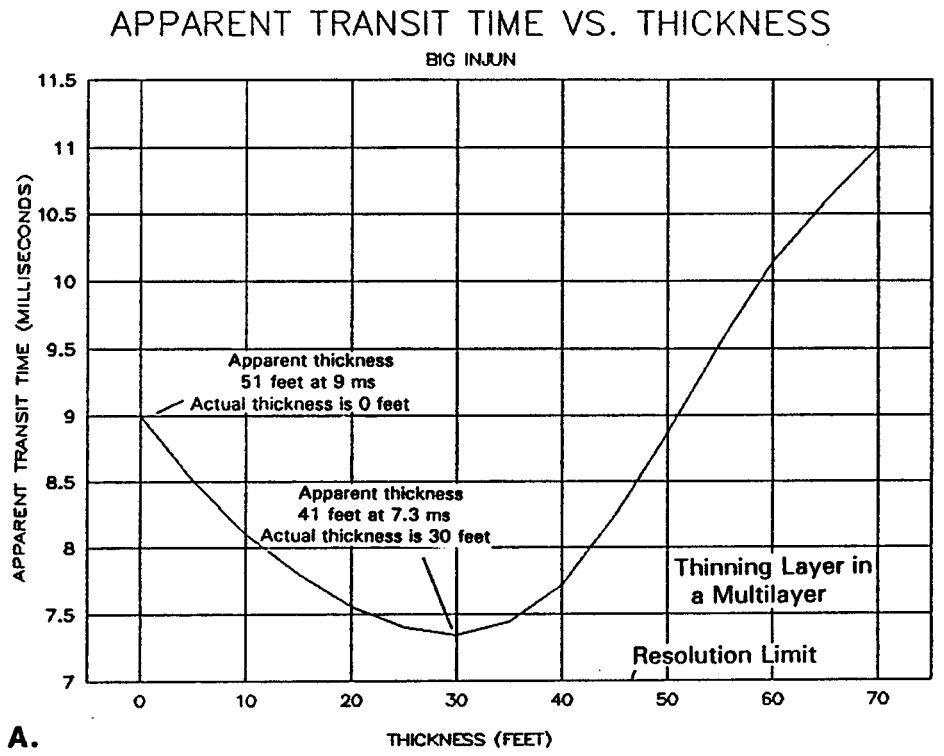

FIGURE G6. (a) Apparent travel times measured through the thinning layer plotted against actual travel times based on thickness; (b) Apparent travel times plotted against thickness.

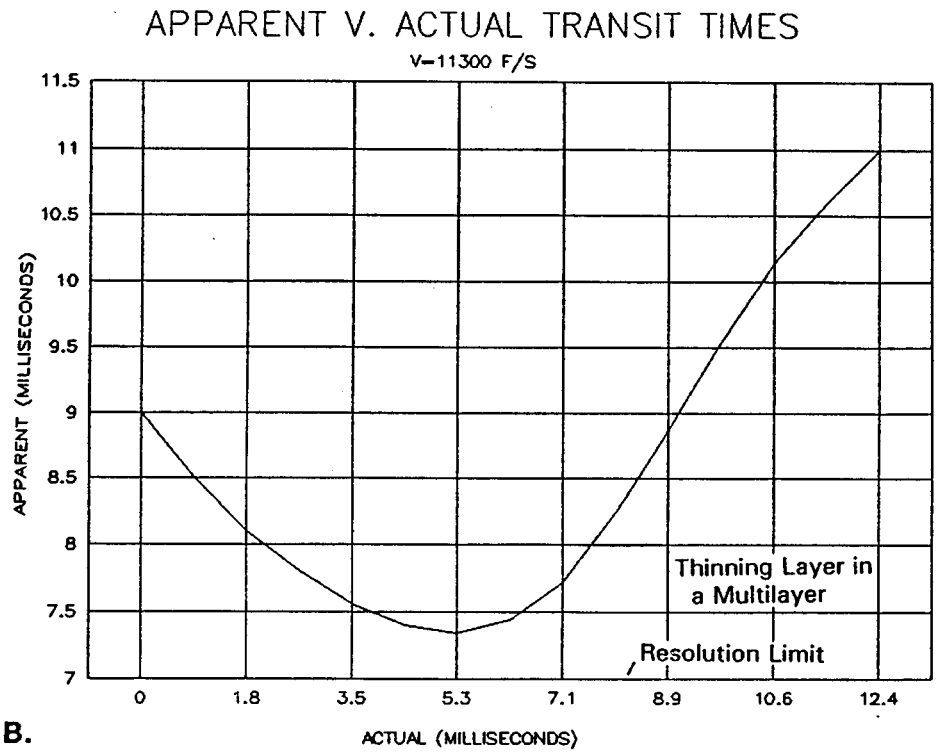

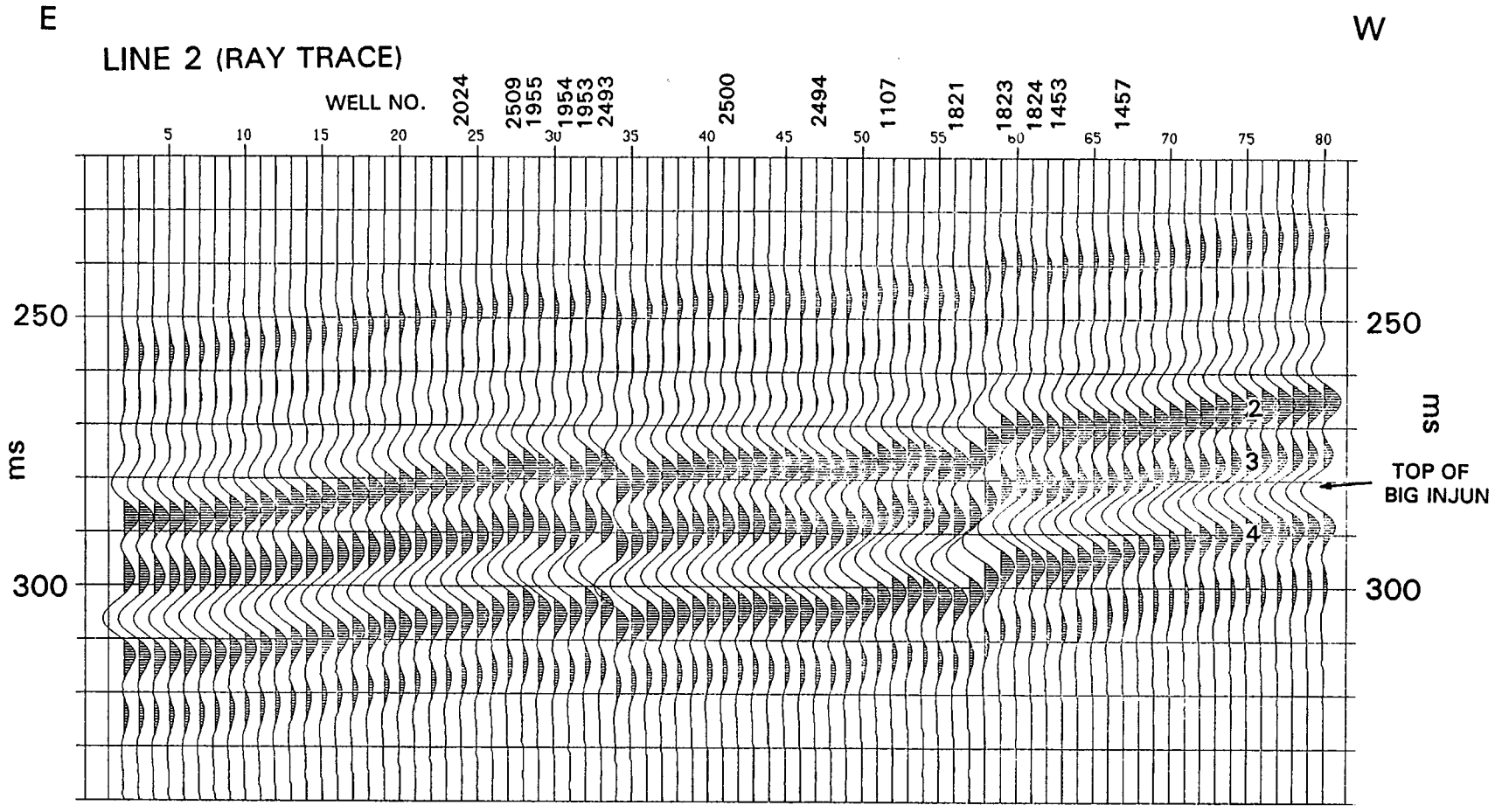

FIGURE G7. Synthetic seismic response along Vibroseis Line 2. Stratigraphic intervals were defined by gamma ray and density logs from several wells along the line (noted at the top). Velocities were assigned based on the sonic log from Clay 2509.

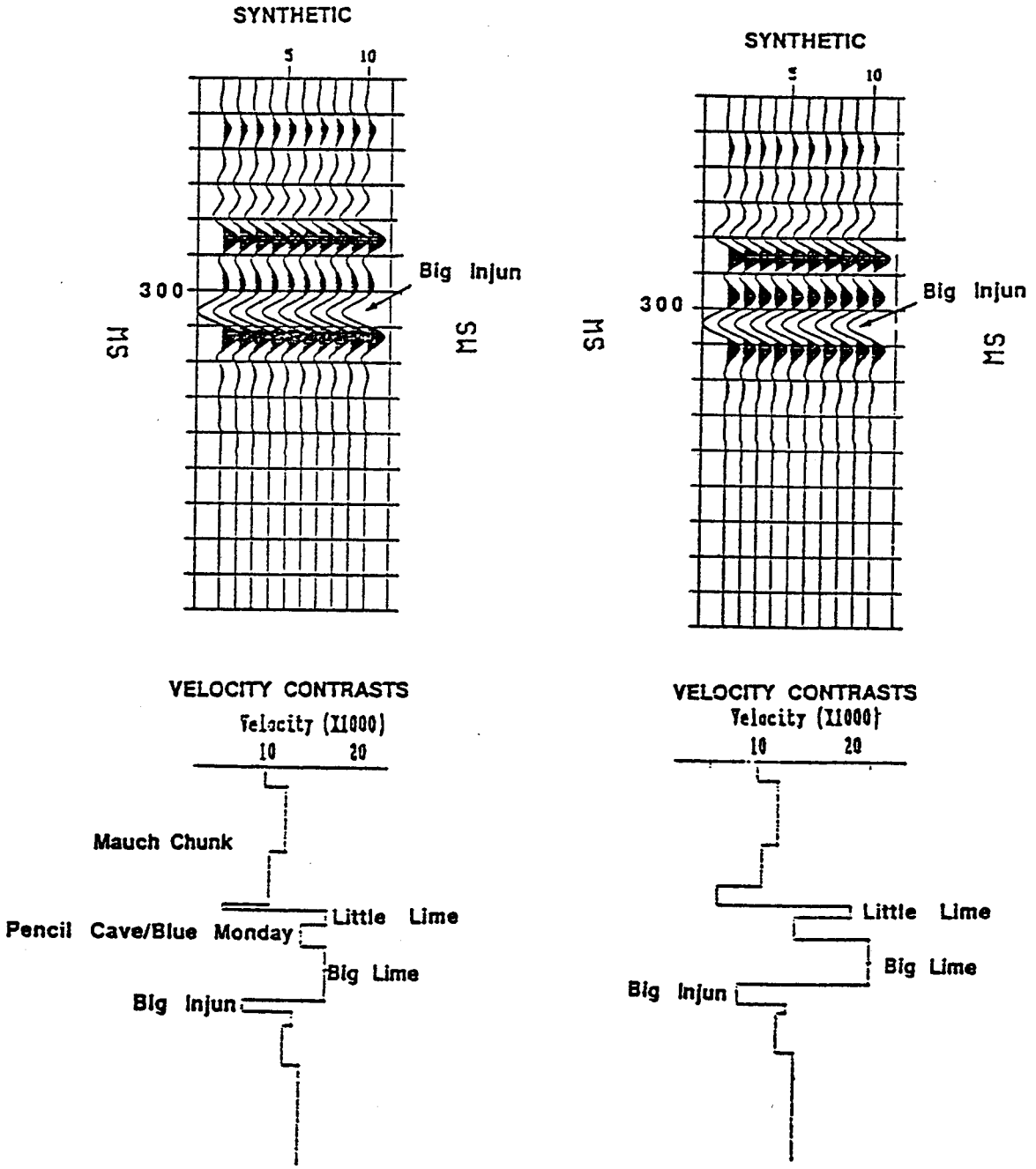

FIGURE G8. Synthetic seismograms and impedance variations derived to match some of the character changes observed in the seismic response of the Big Injun and adjacent intervals.

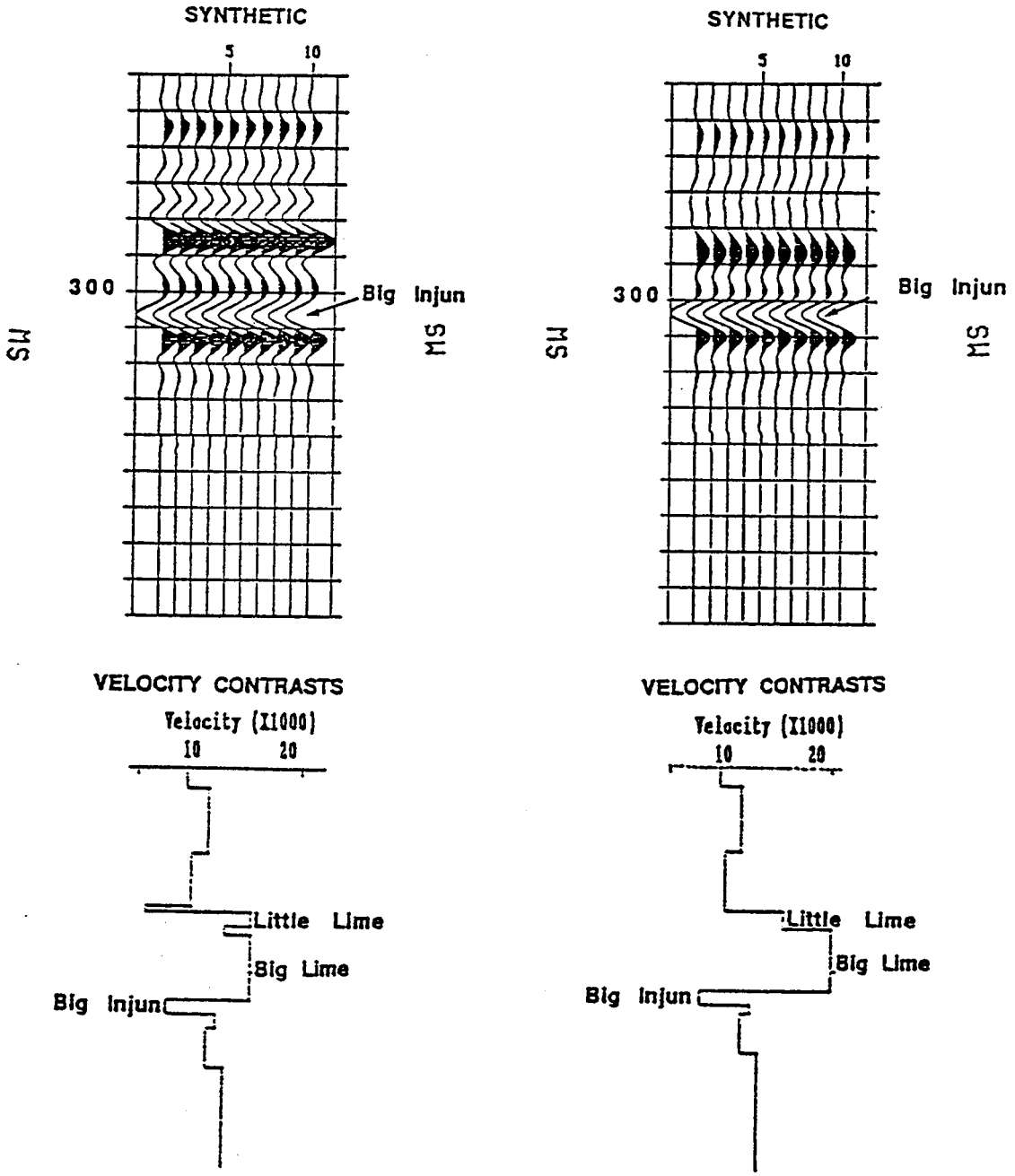

FIGURE G9. Synthetic seismograms and impedance variations derived to match some of the character changes observed in the seismic response of the Big Injun and adjacent intervals.

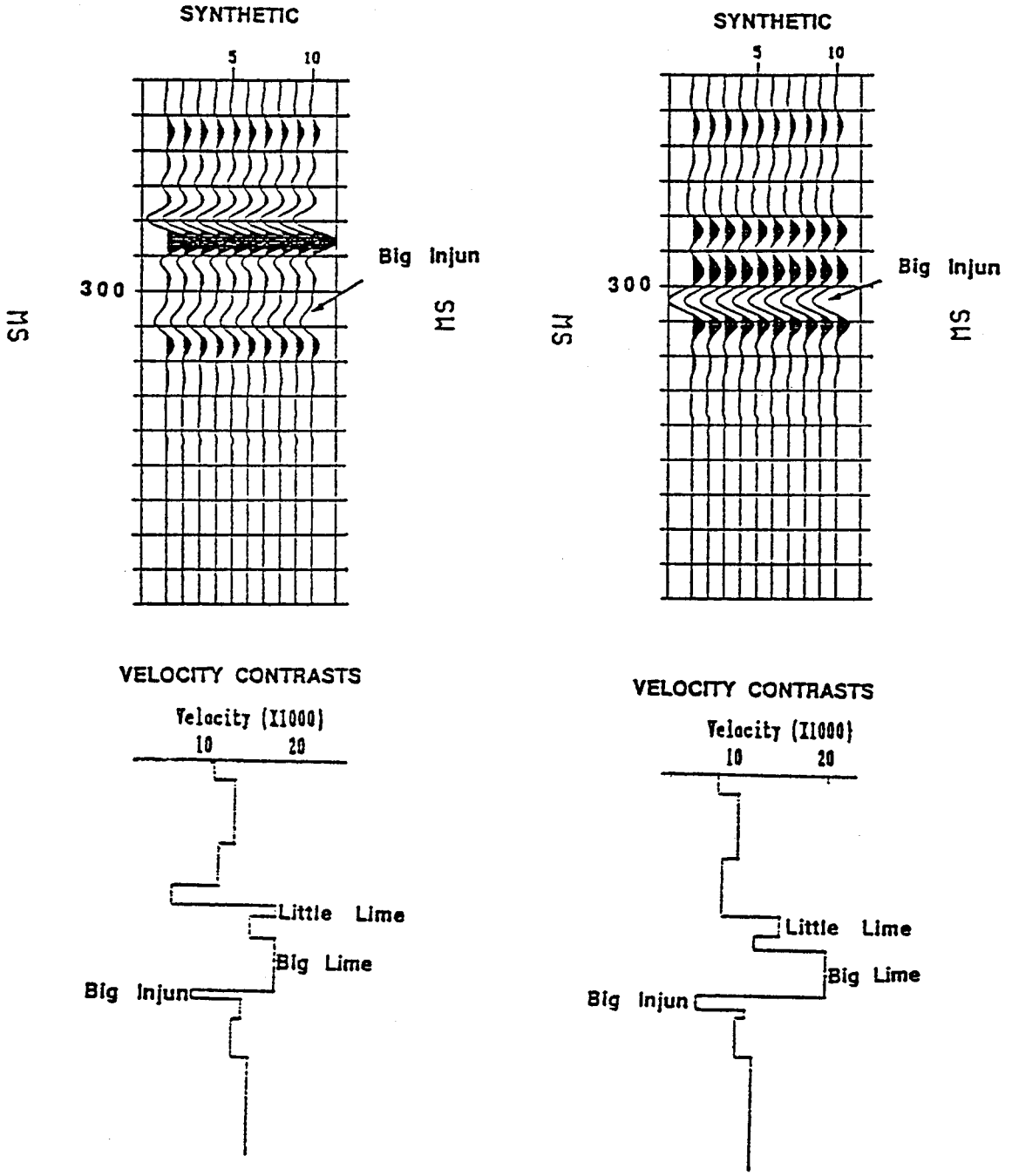

FIGURE G10. Synthetic seismograms and impedance variations derived to match some of the character changes observed in the seismic response of the Big Injun and adjacent intervals.

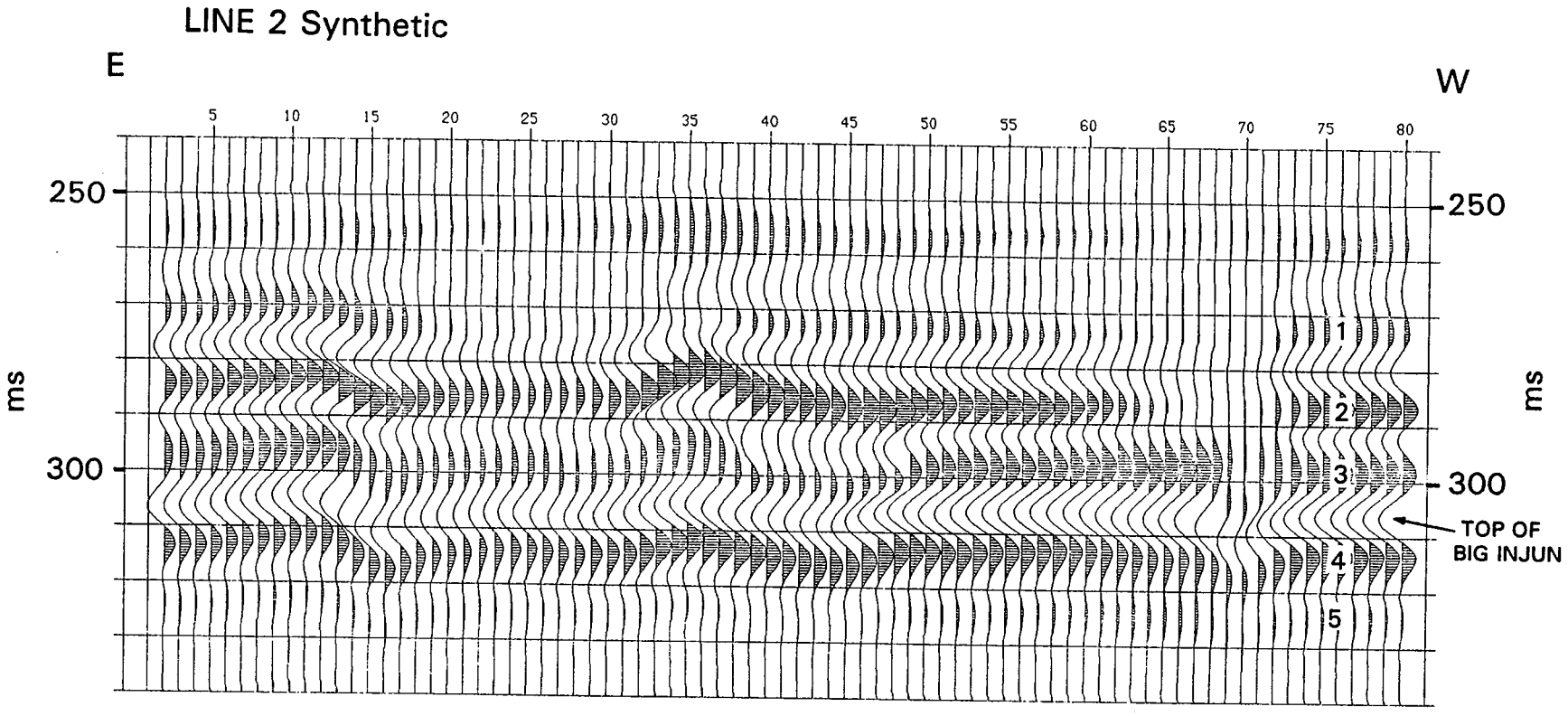

FIGURE G11. Synthetic seismic response along Vibroseis Line 2 modified to obtain a better match to the waveform variability observed along the line.

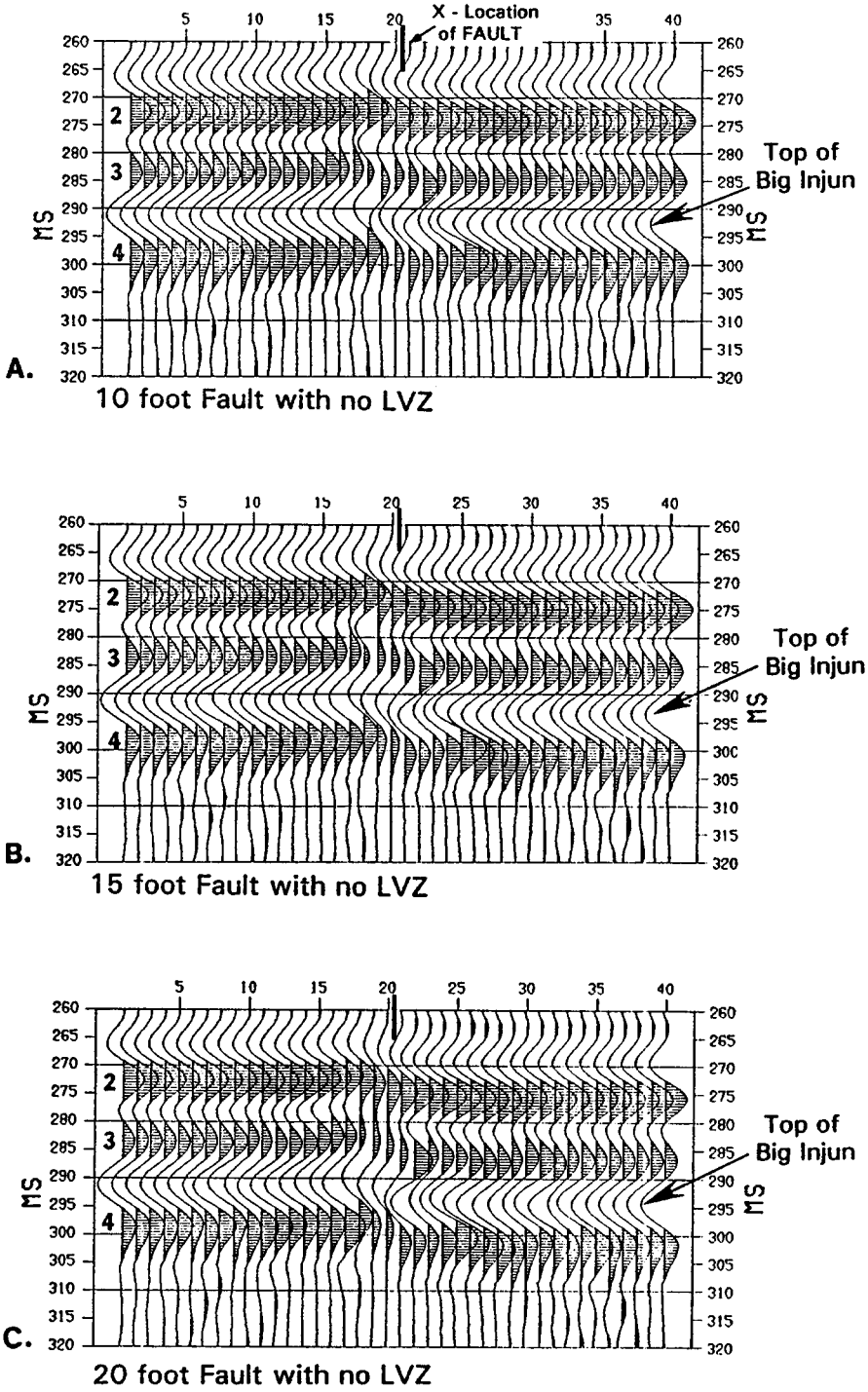

FIGURE G12. Synthetic seismic response of vertical faults. (a) 10 foot displacement; (b) 15 foot displacement; (c) 20 foot displacement.

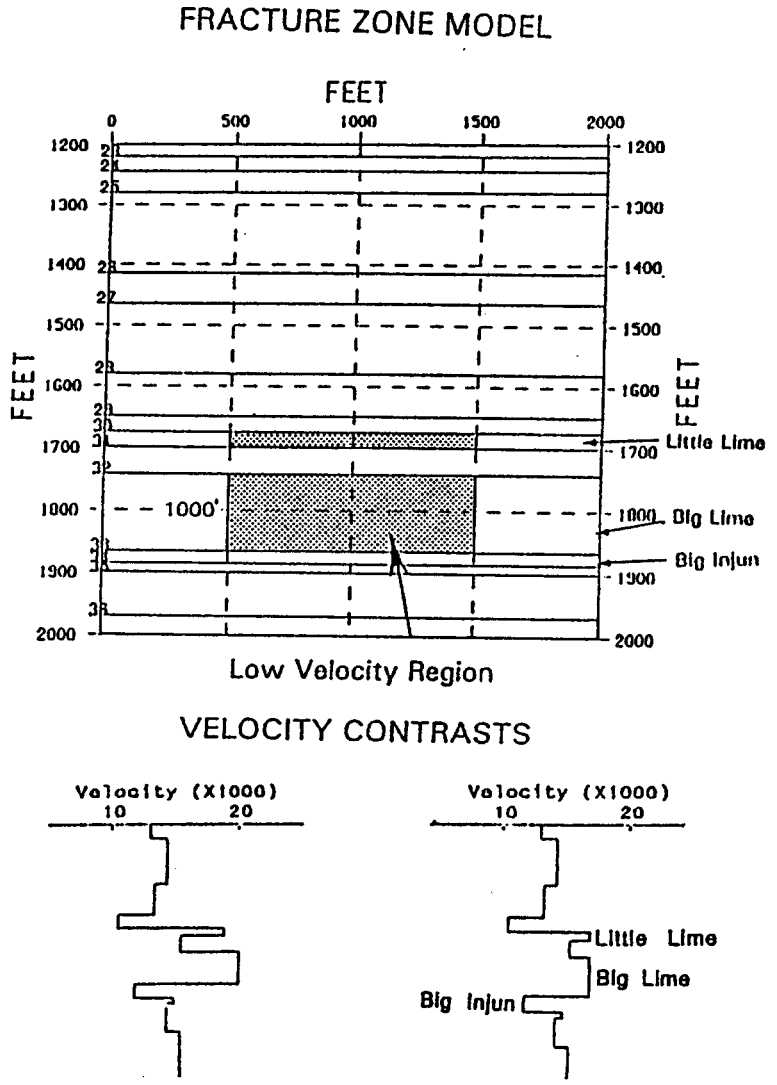

FIGURE G13. Cross section showing Big and Little Lime intervals. Velocity reduction of these two intervals as illustrated in the velocity plots below the cross section was used to simulate the effects of fracture zones.

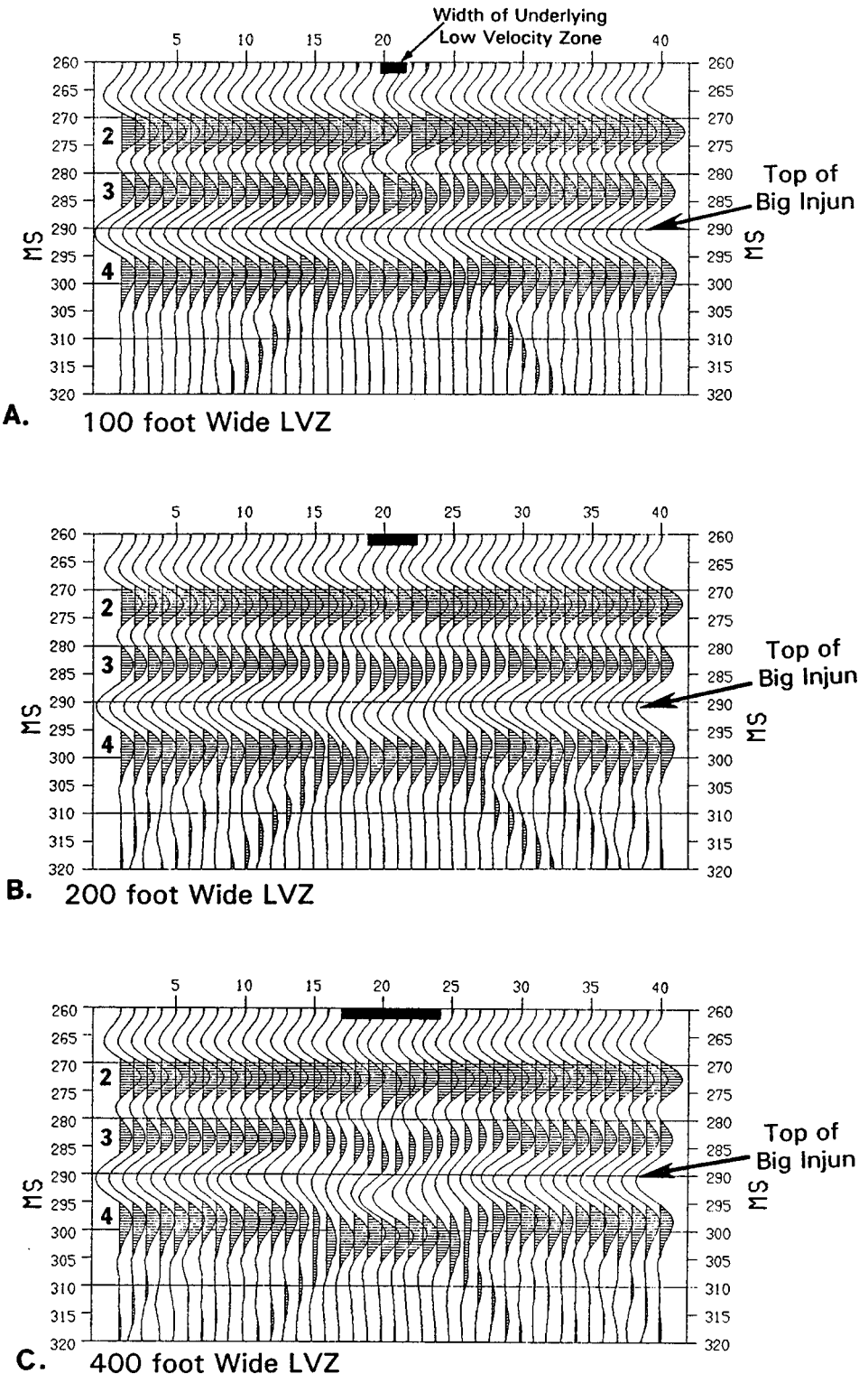

FIGURE G14. Response of low-velocity zones (fracture zones) of varying width. (a) 100 foot zone; (b) 200 foot zone; (c) 400 foot zone.

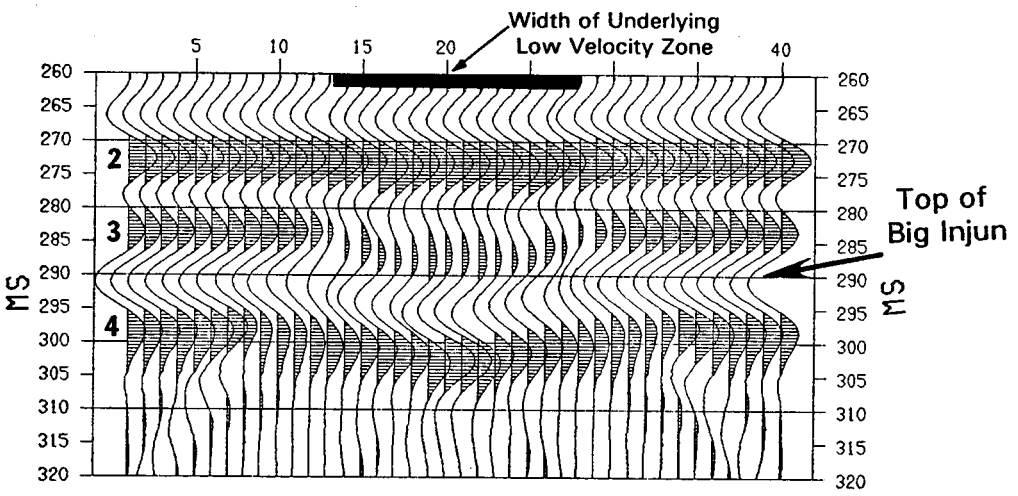

A. 800 foot Wide LVZ

FIGURE G15. Response of low-velocity zones (fracture zones) of varying width. (a) 800 foot zone; (b) 1000 foot zone.

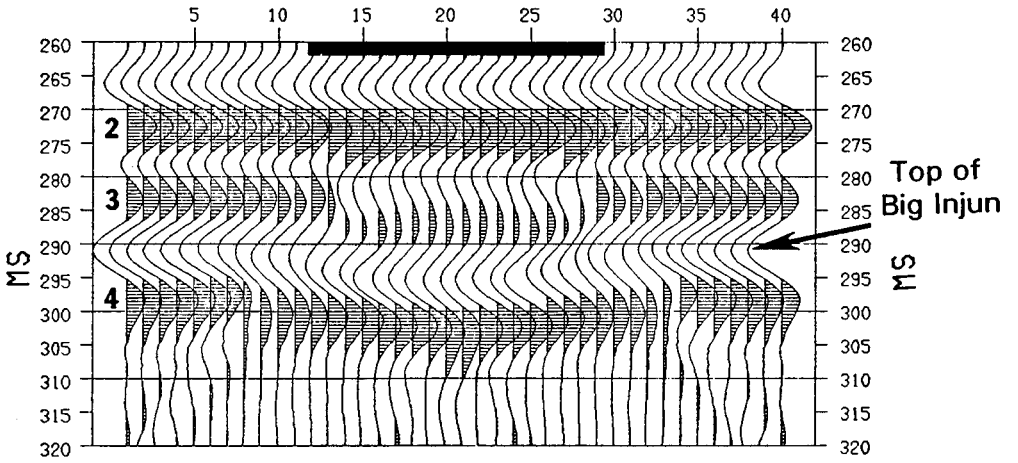

B. 1000 foot Wide LVZ

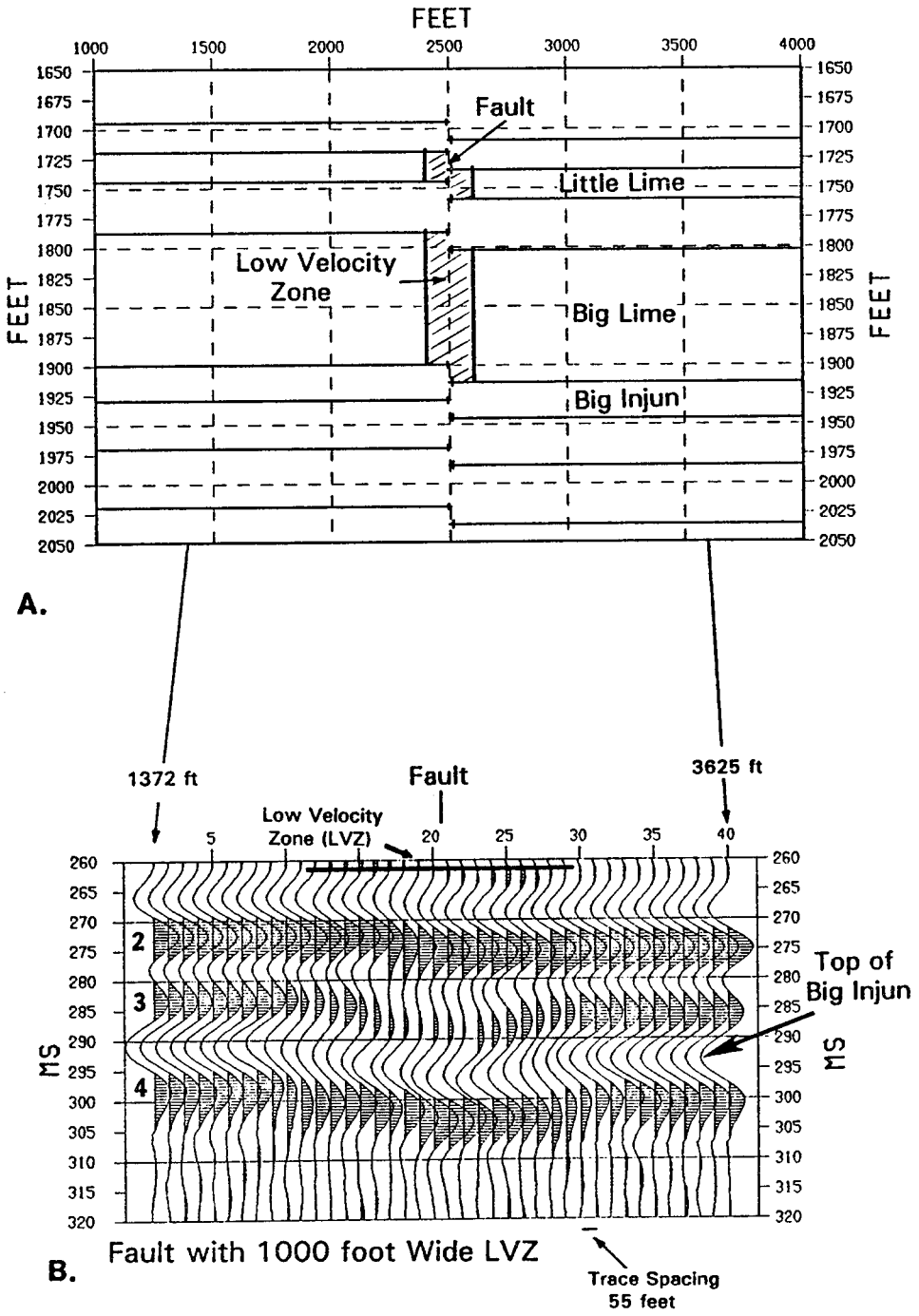

FIGURE G16. (a) Cross section showing 15 foot fault offset and bounding fracture zone; (b) Combined fault and fracture zone response for 15 foot offset and 1000 foot wide, low-velocity zone.

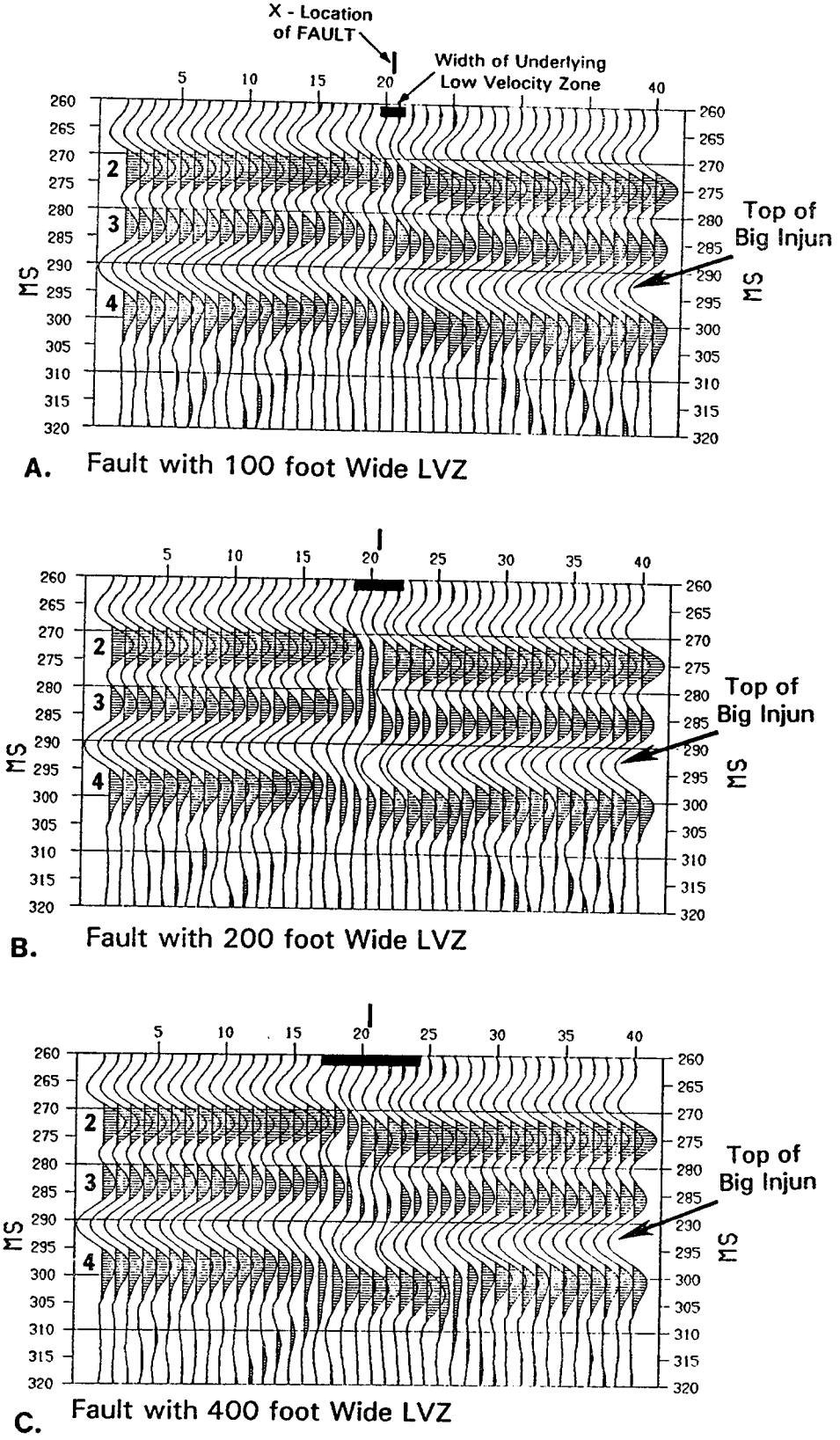

FIGURE G17. Combined fault and fracture zone response for 15 foot fault offset and low-velocity zones of varying width. (a) 100 foot zone; (b) 200 foot zone; (c) 400 foot zone.

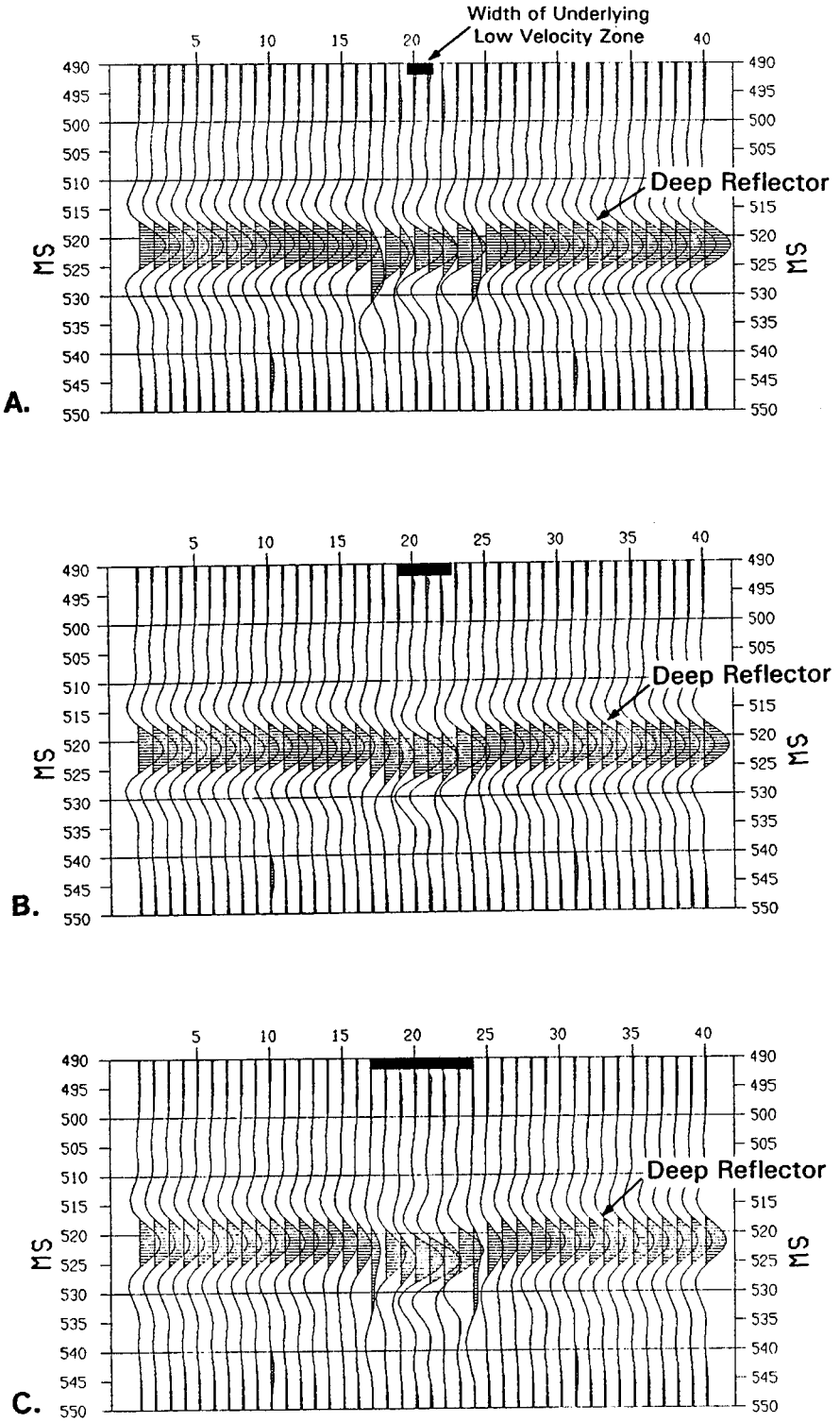

FIGURE G18. Wave-theory response of reflector beneath low-velocity zone of varying width. (a) 100 foot zone; (b) 200 foot zone; (c) 400 foot zone.

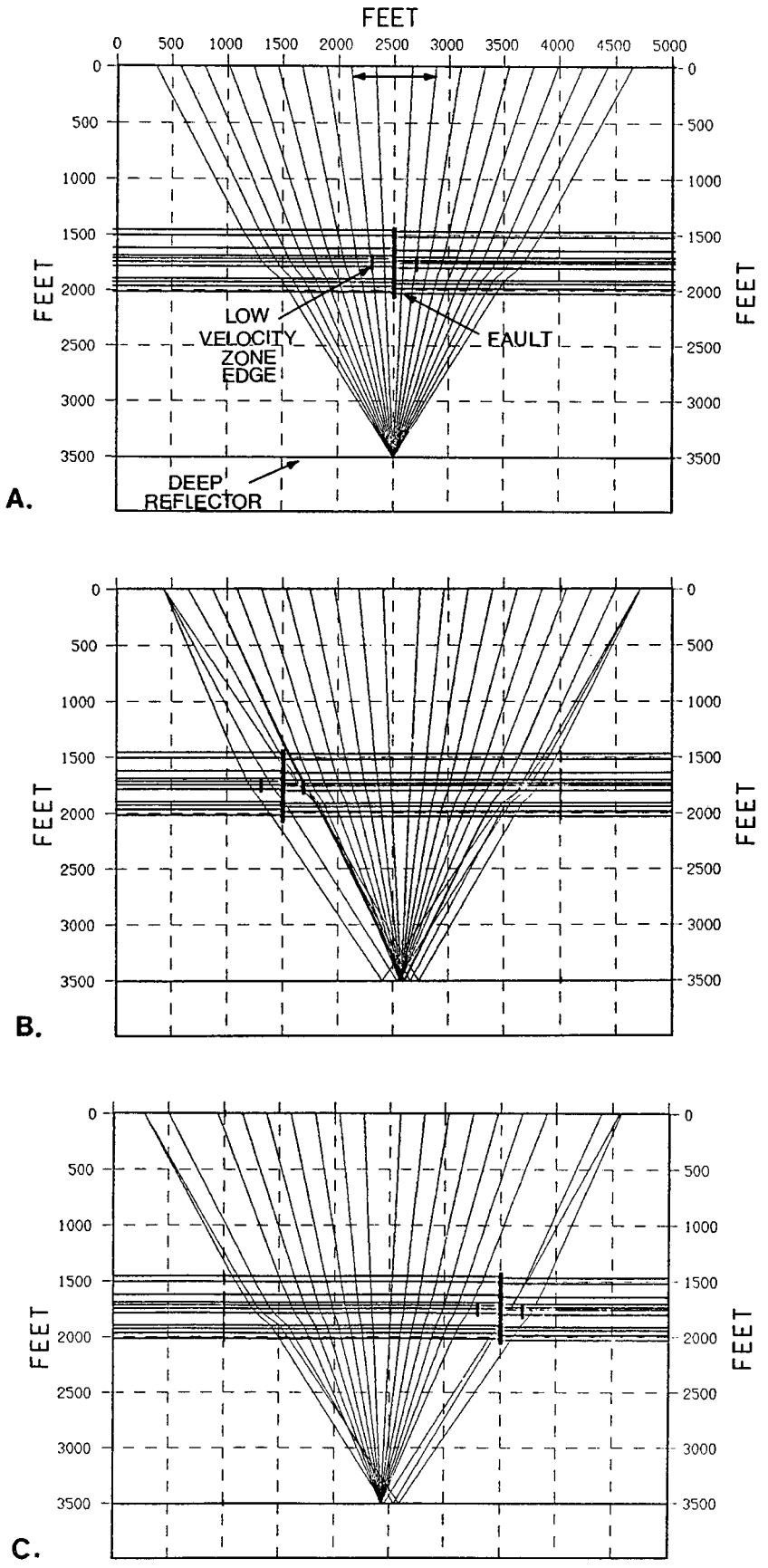

FIGURE G19. Plot of common midpoint raypaths to a deeper reflector. (a) Midpoint located directly over fault; (b) Midpoint 1100 feet to the left of the fault; (c) Midpoint 1100 feet to the right of the fault.

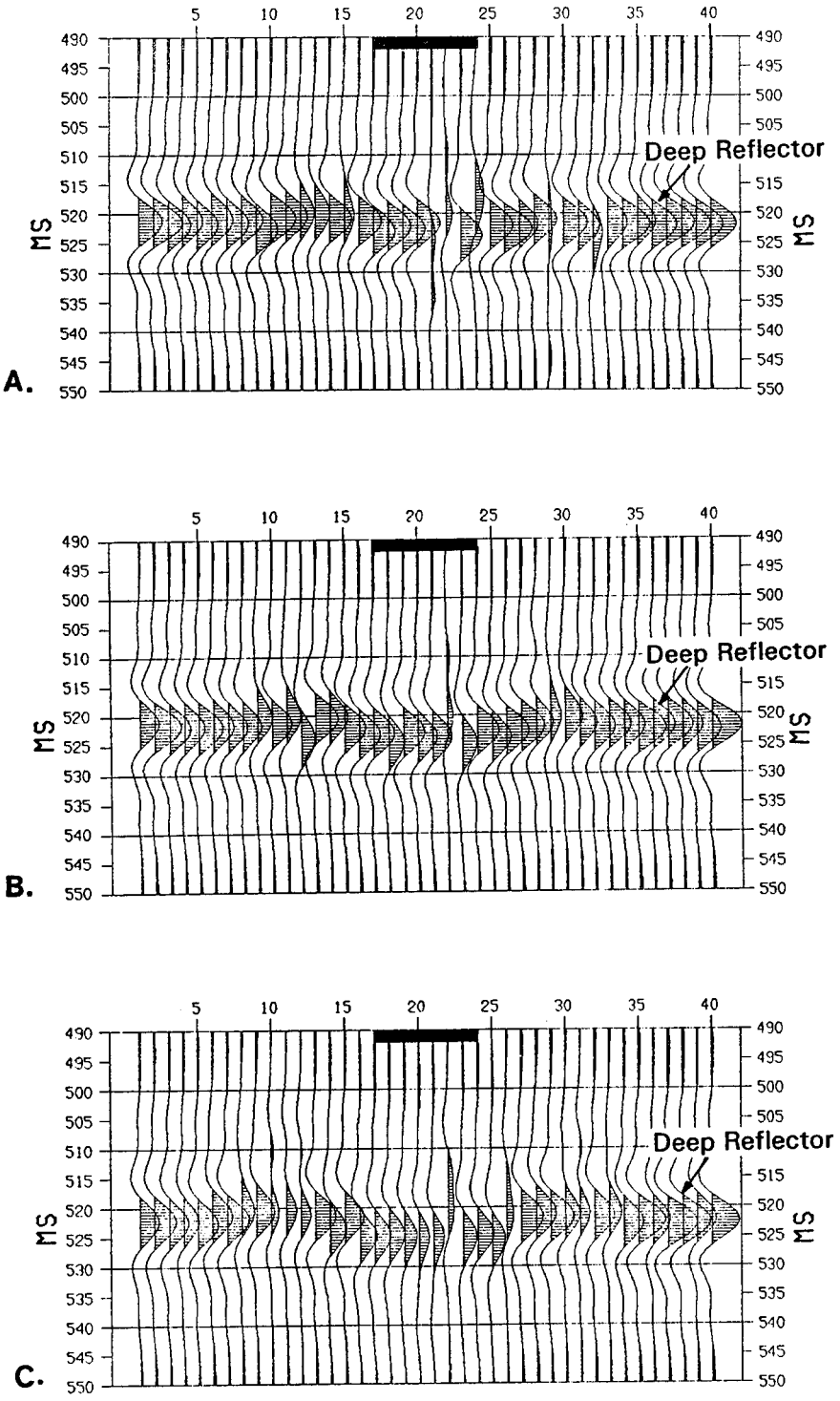

FIGURE G20. Synthetic seismic response computed summing traces in a synthetic common midpoint gather for low-velocity zones of varying width. (a) 100 foot zone; (b) 200 foot zone; (c) 400 foot zone.

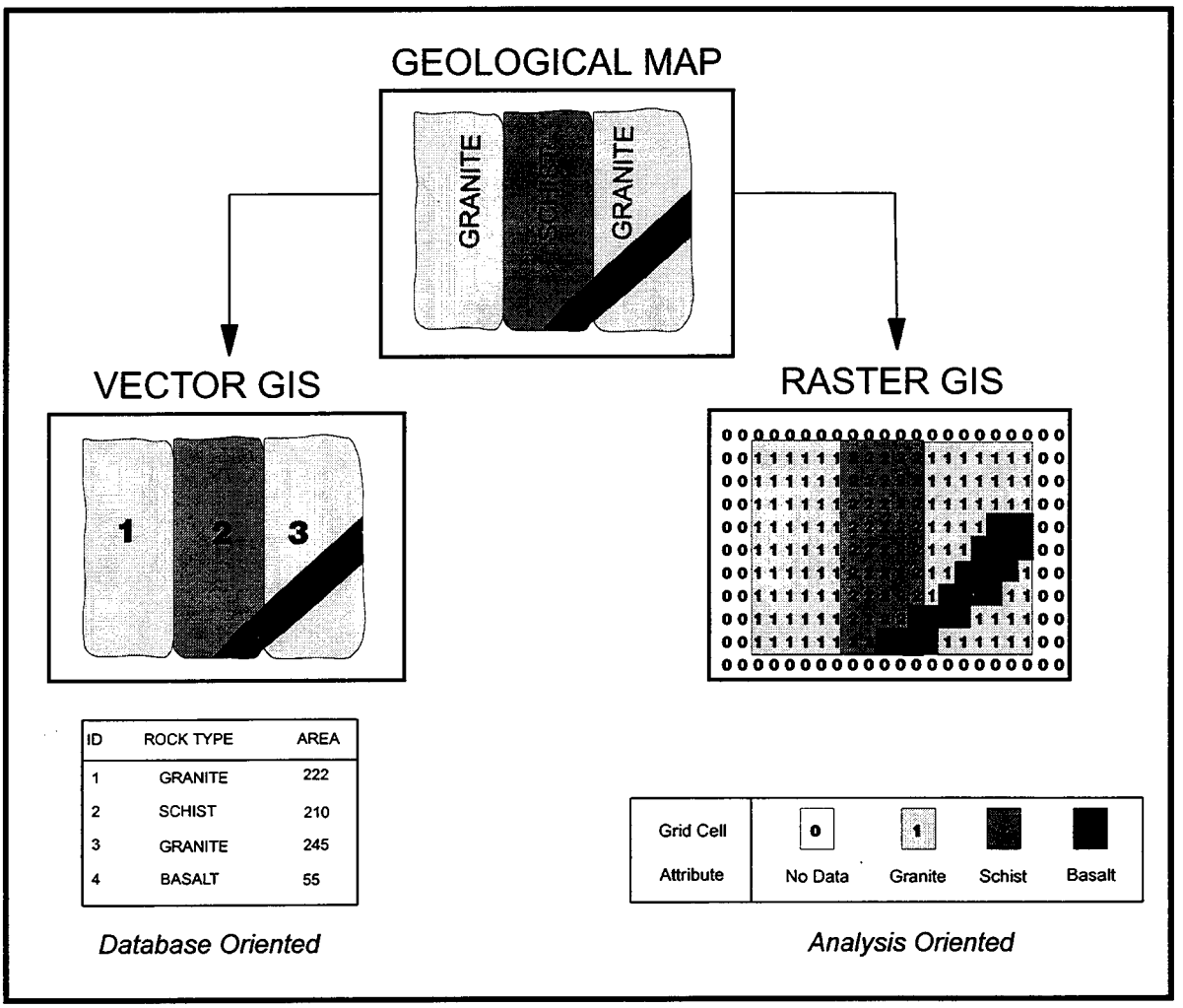

FIGURE I1. Raster versus vector GIS.

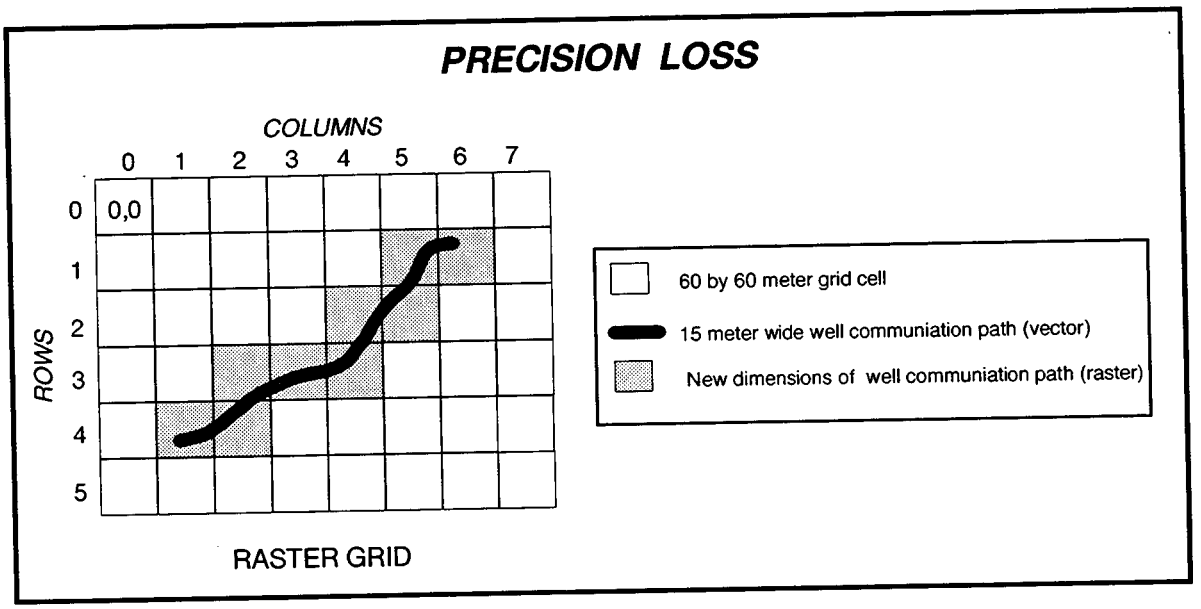

FIGURE I2. Precision loss from vector-to-raster conversion.

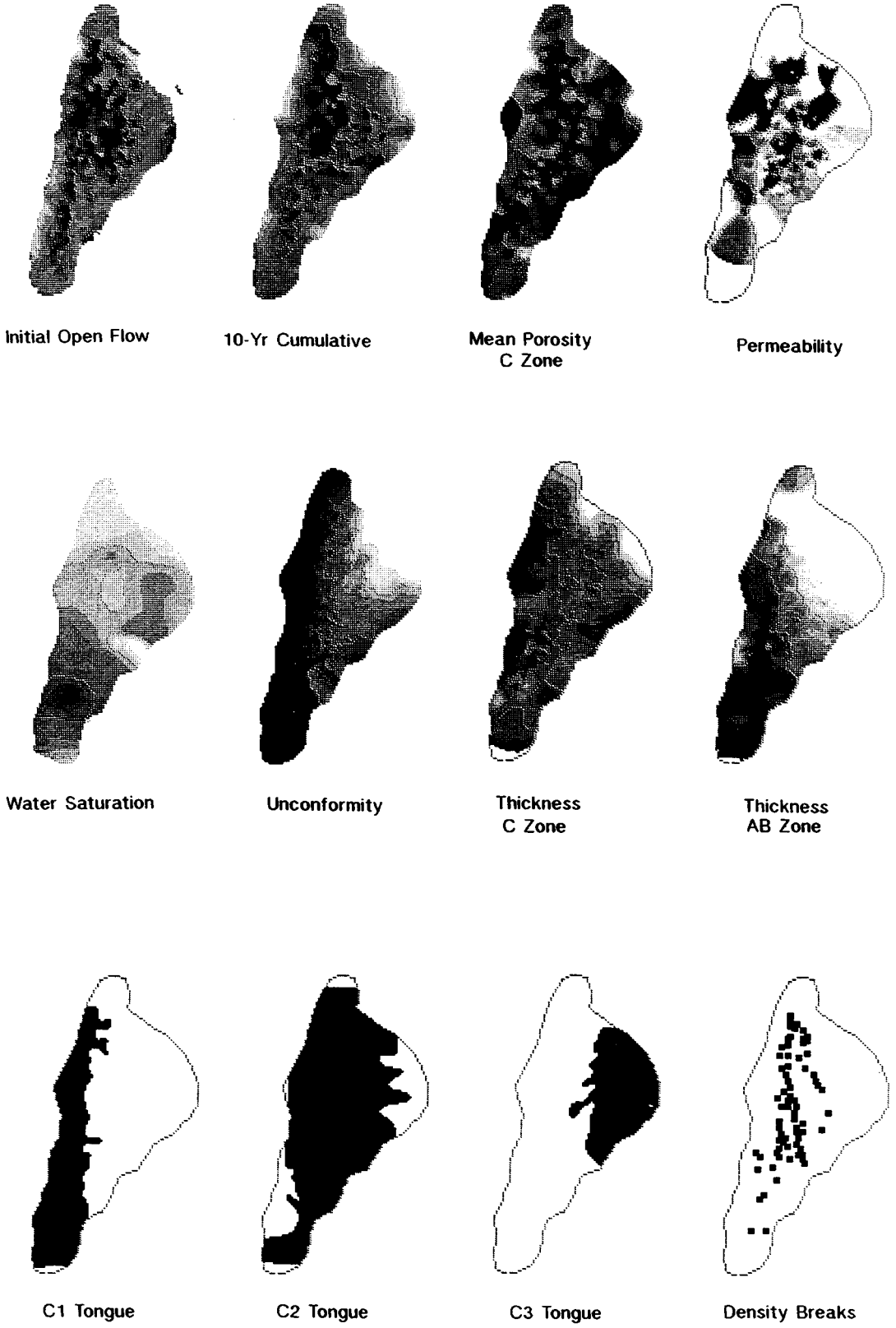

FIGURE I3. Types of raster images possible.

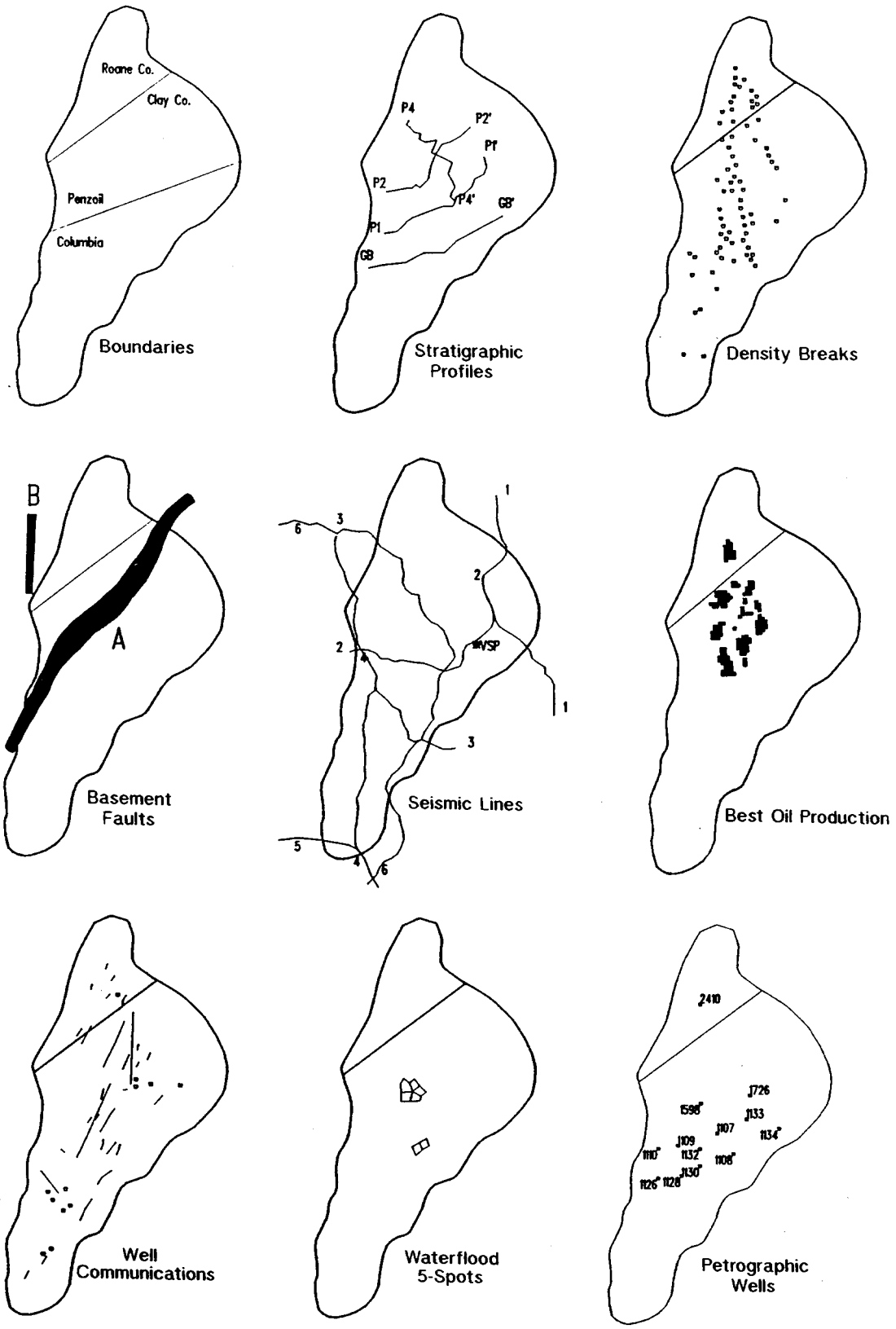

FIGURE I4. Types of vector images possible.

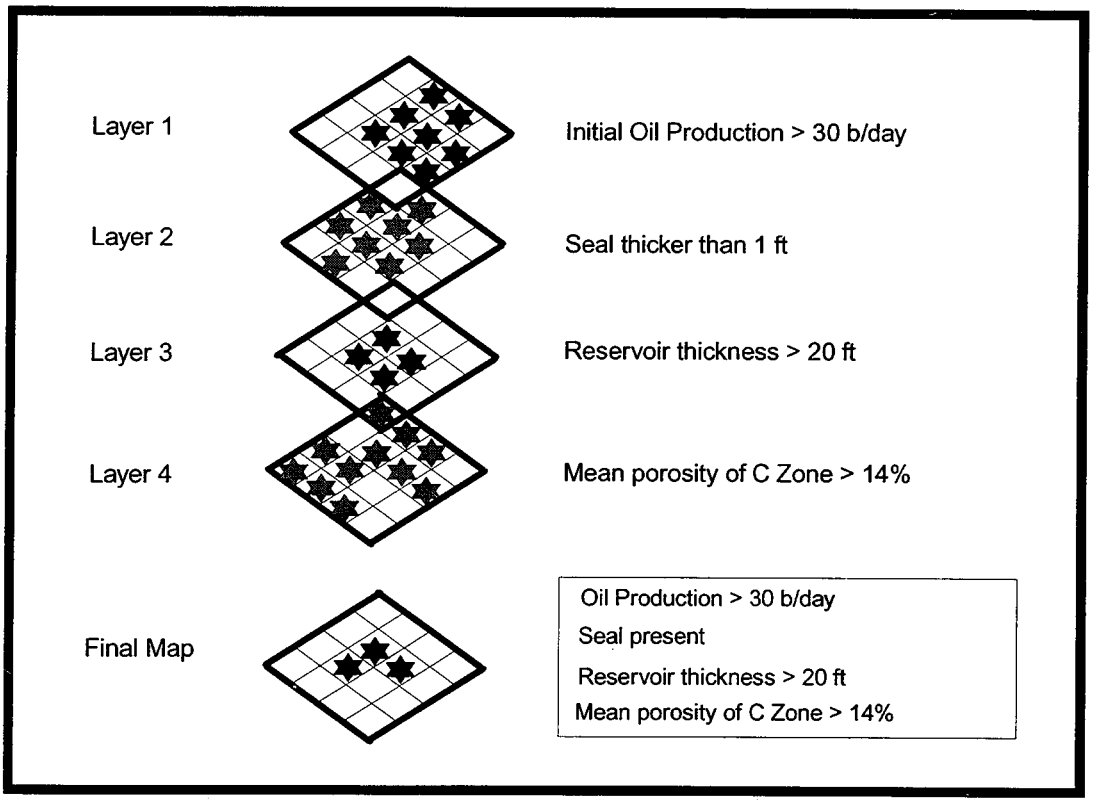

FIGURE I5. Example of a spatial query.

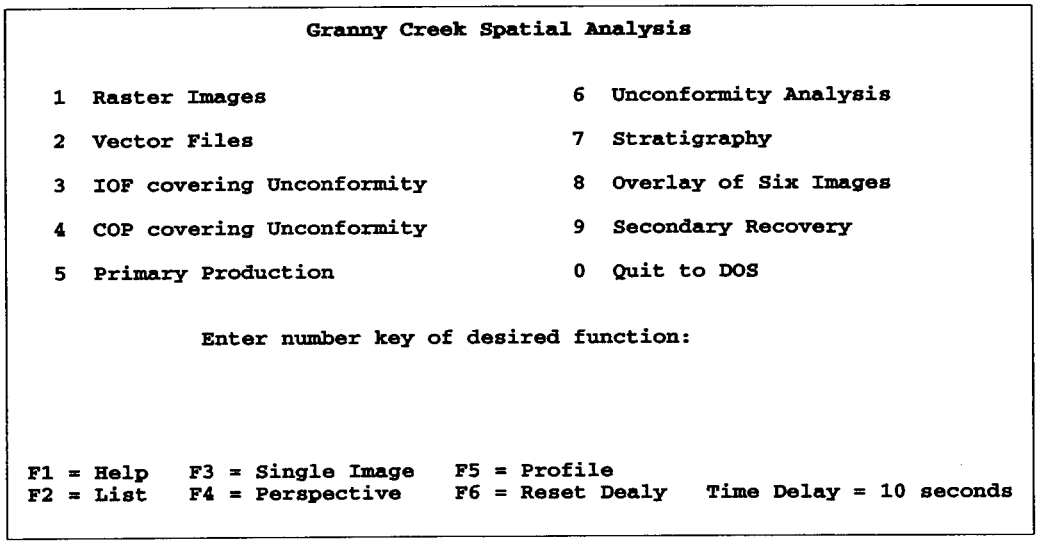

FIGURE I6 Menu for IDRISI video images

Image Enhancement

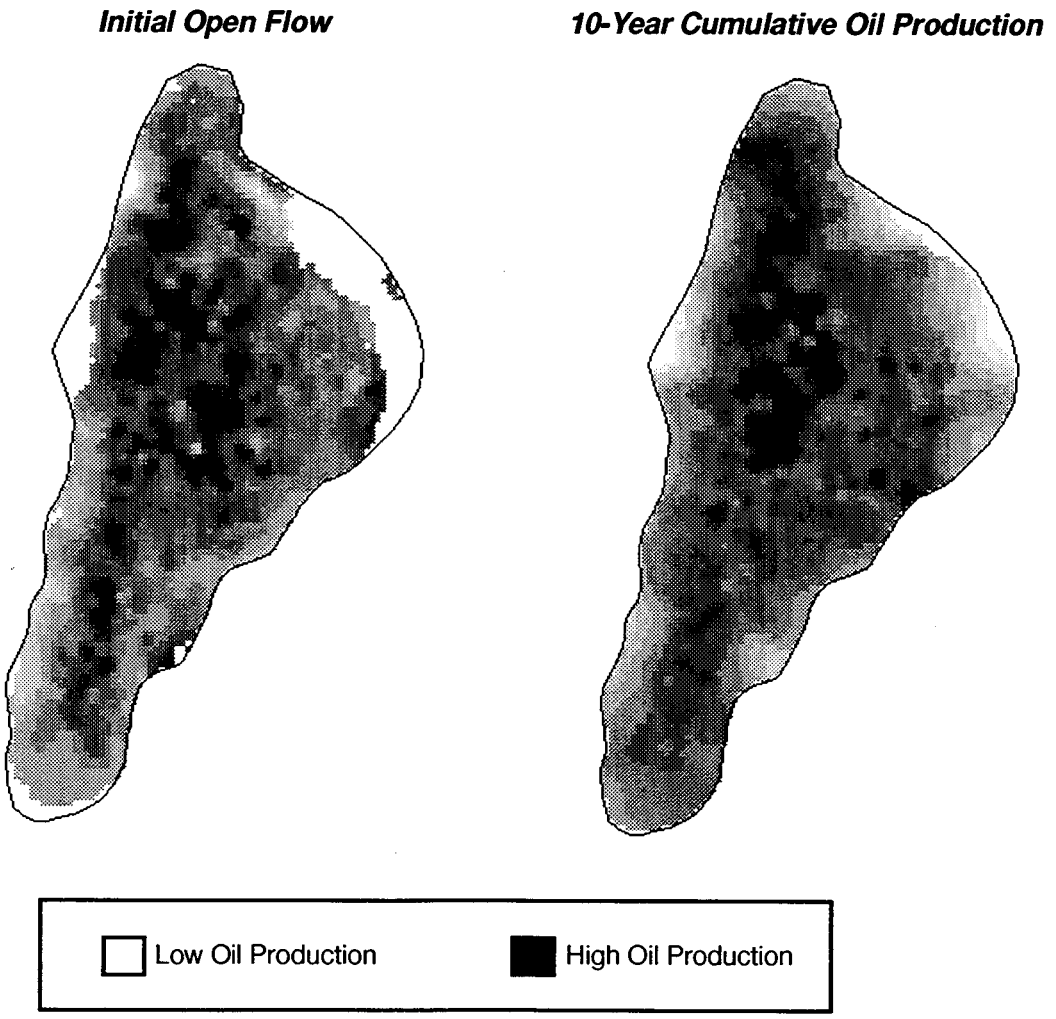

FIGURE I7. Image enhancement of two images: initial open flow and 10-year cumulative oil production.

a. Initial Open Flow (b/day)

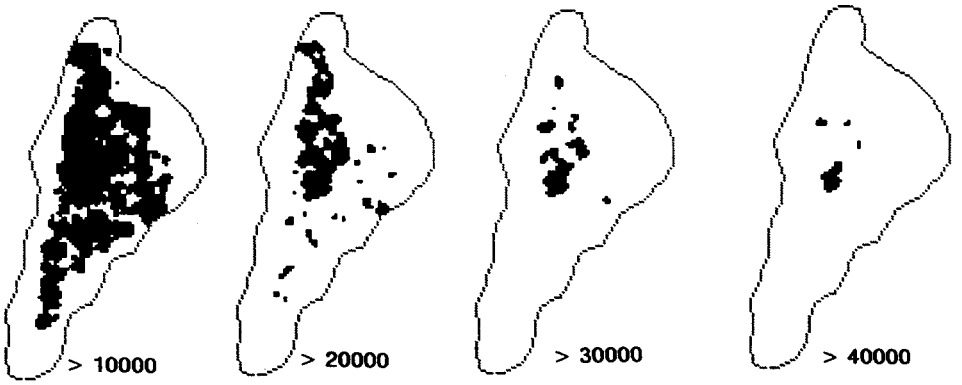

b. 10-year Cumulative Oil Production (barrels)

FIGURE I8. (a) Spatial distribution of initial open flow (IOF); (b) Spatial distribution of 10-year cumulative oil production (COP).

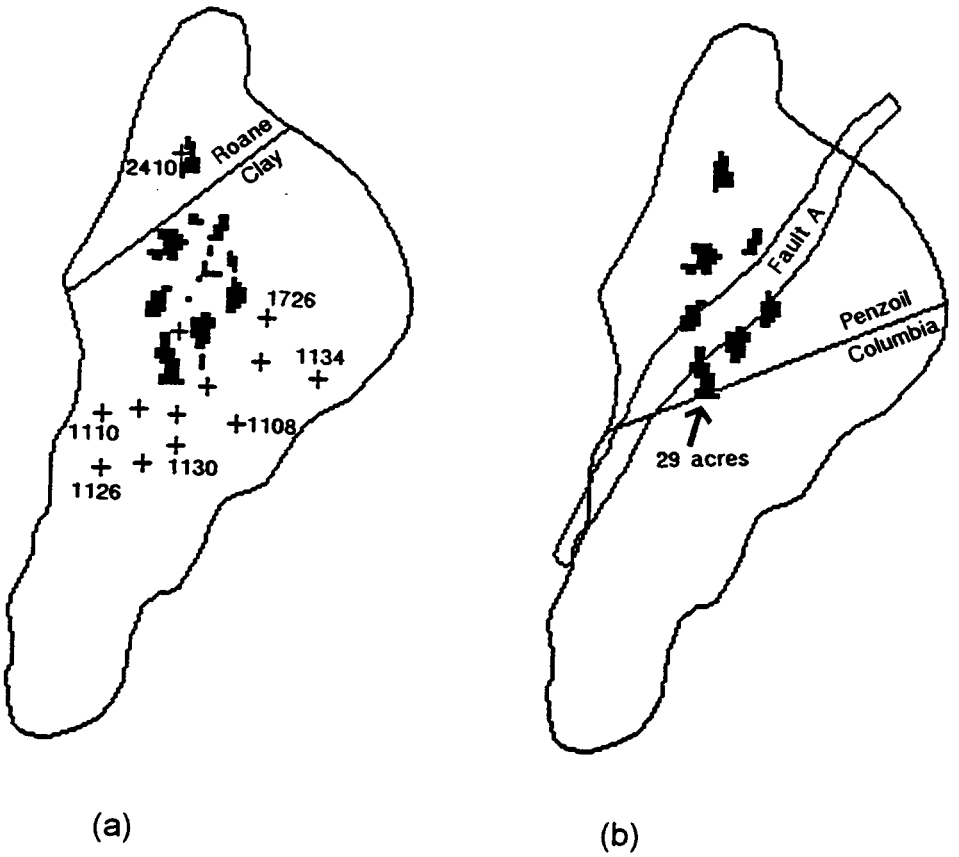

FIGURE I9. Spatial query of best oil production. (a) Best oil producing areas and petrographic well (+) locations; (b) Best oil producing areas greater than 10 acres, overlaid with basement fault "A" and company boundary.

Comparison of Northern and Southern Granny Creek Field

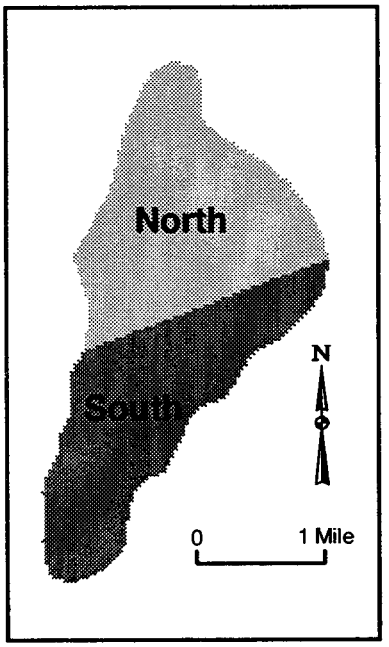

FIGURE I10. Map of Granny Creek field comparing the northern and southern regions.

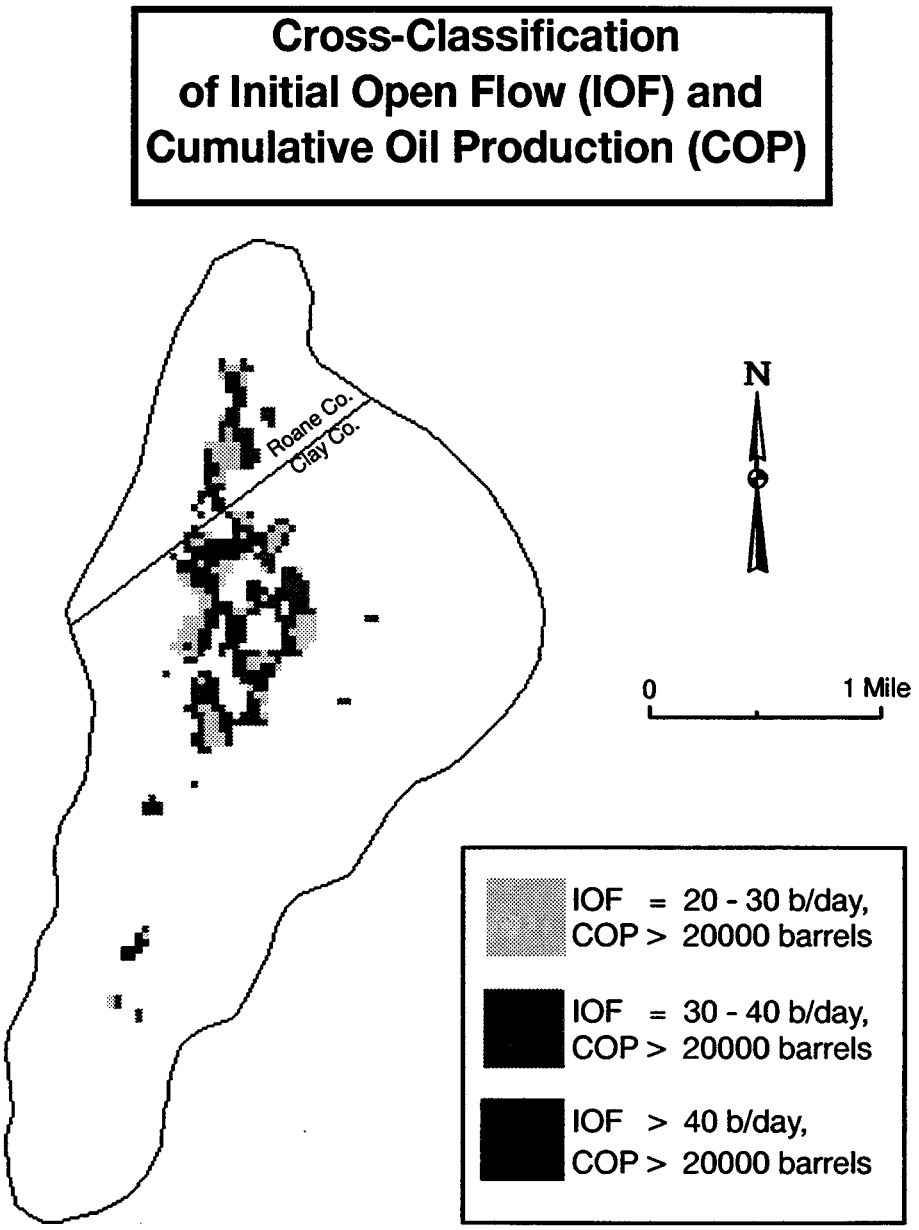

FIGURE I11. Reclassified cross-classification image of initial open flow and 10-year cumulative oil production.

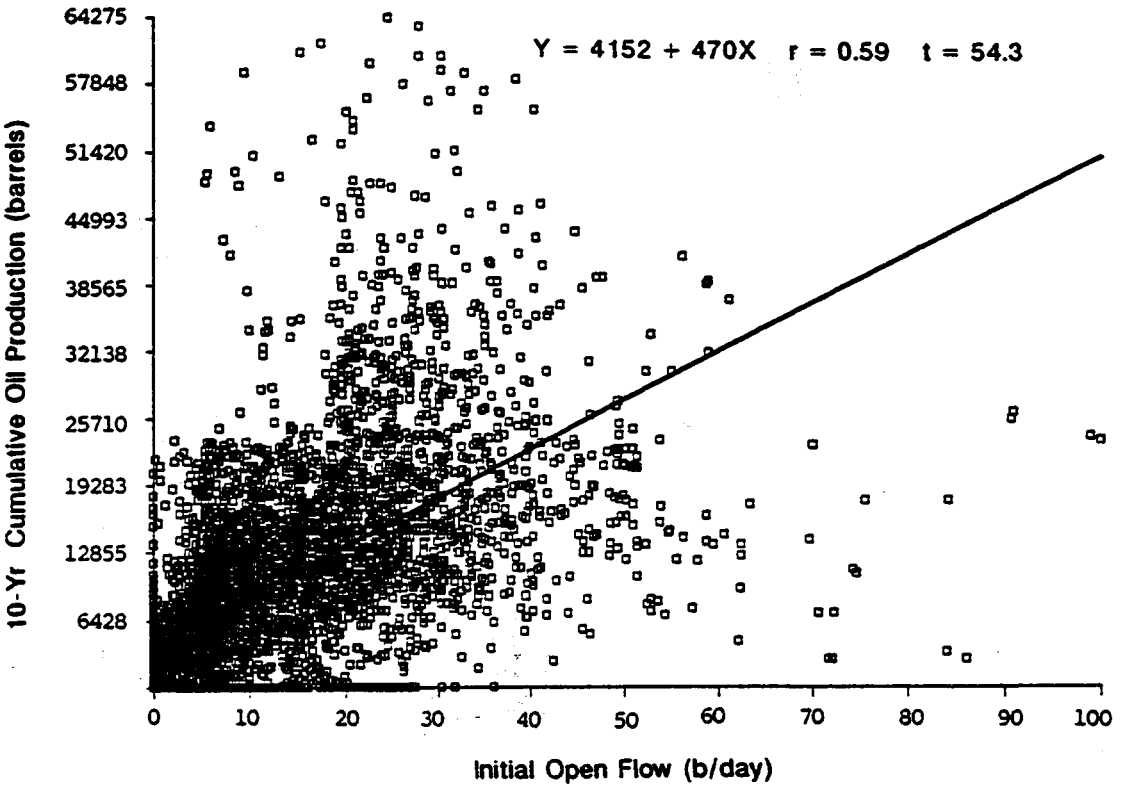

FIGURE I12. Linear Regression between two images: initial open flow and 10-year Cumulative Oil Production.

Step 1: Analyze Histograms

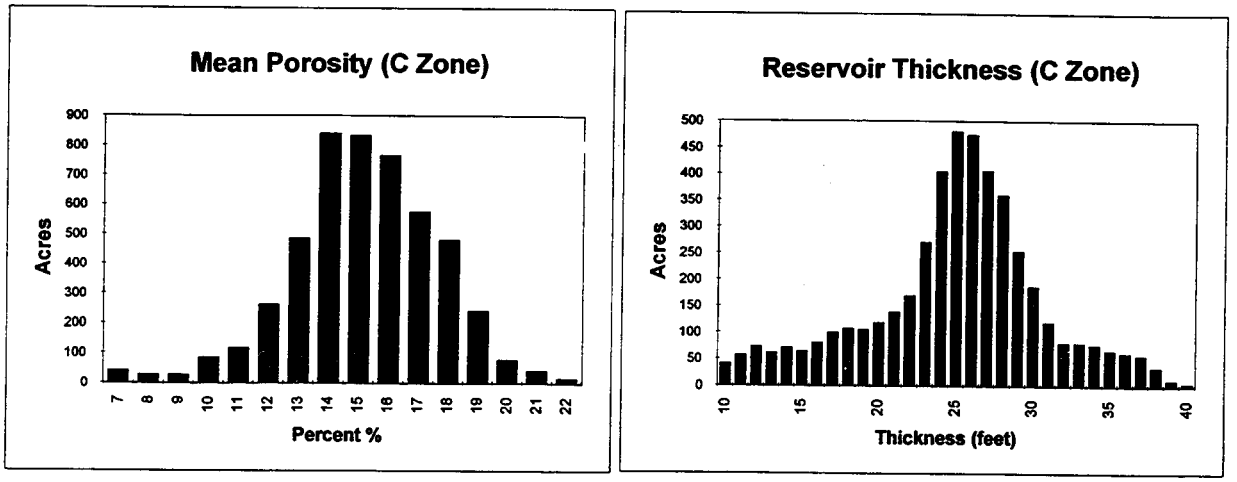

Step 2: Reclassify Each Parameter

Image 1 Seal - Thickness of Coarse Grain (Fluvial/A & B Zone) > 1 ft.
Image 2 Reservoir Thickness - Thickness of Fine Grain (C Zone) > 20 ft.
Image 3 Porosity - Mean Porosity of C Zone > 12%
Image 4 Water Saturation - Water Saturation of Fine Grain Zone < 50%
Image 5 Permeability - Mean Permeability of Big Injun > 5 md
Image 6 No Barriers - Not within 100 meters of Density Breaks

Step 3: Overlay

Optimal Production = (Seal x Reservoir Thickness x Porosity x Water Saturation x Permeability x No Barriers)

FIGURE I13. Spatial Query Steps: (1) Histogram Analysis (2) Reclassify Images (3) Overlay or Combine Images.

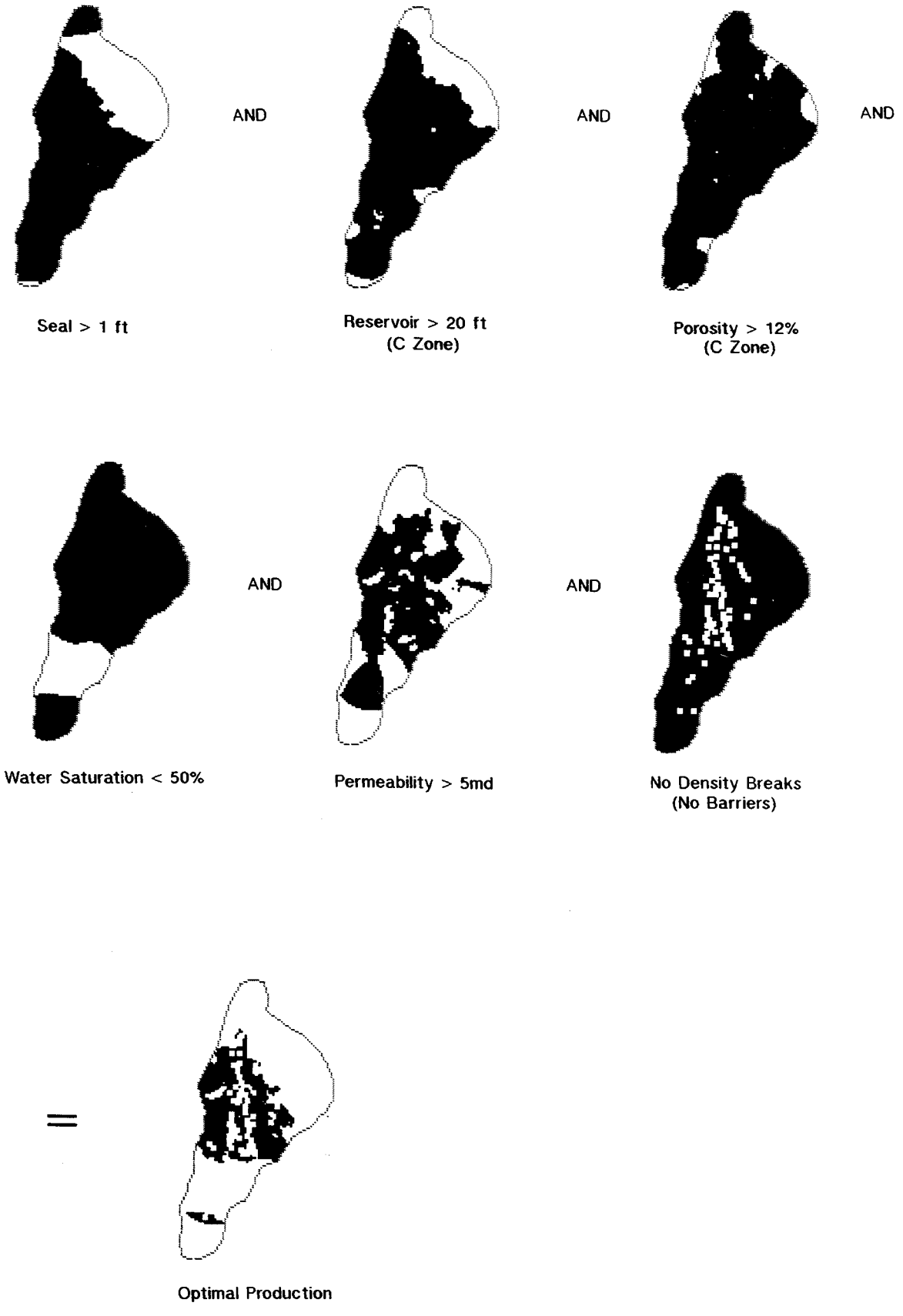

FIGURE I14. Spatial query of 6 geological and engineering variables to determine locations of optimal oil production. Solid black areas denote true conditions.

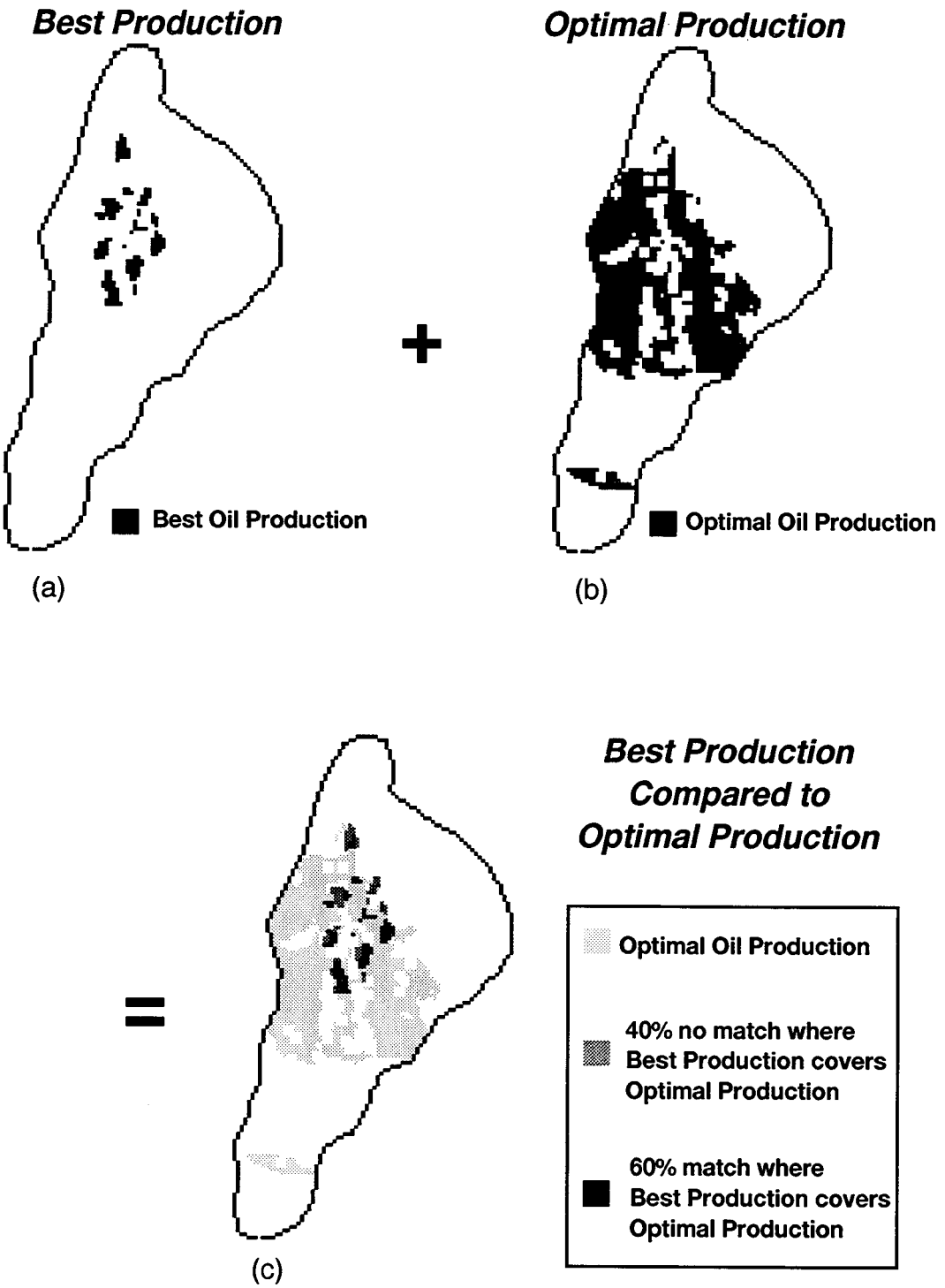

FIGURE I15. Best production compared to optimal production. (a) *Best Production* - initial open flow > 25 b/day AND 10-year cumulative production > 25,000 barrels. (b) *Optimal Production* - created from a spatial query of six geologic/engineering variables. (c) *Best Production* added to *Optimal Production* for comparative analysis.

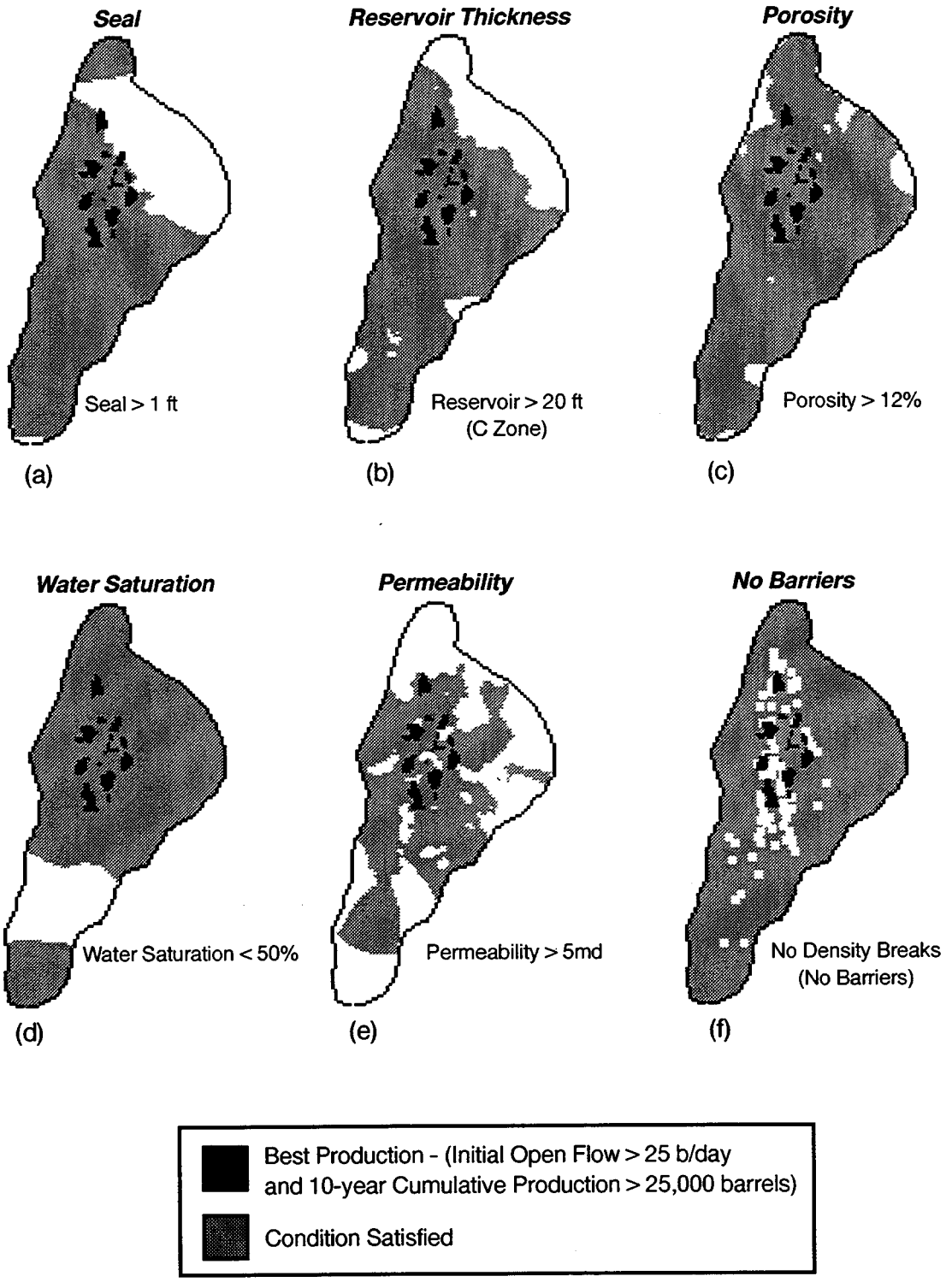

FIGURE I16. Reclassified images of spatial query compared to best oil production.

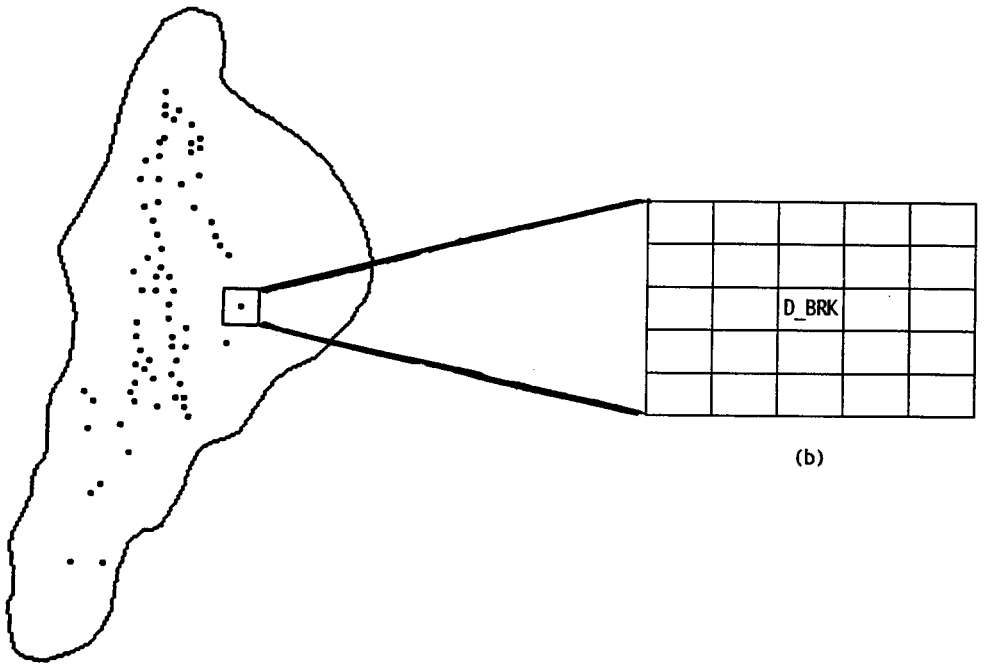

(a)

(b)

170	134	120	134	170
134	85	60	85	134
120	60	0	60	120
134	85	60	85	134
170	134	120	134	170

(c)

0	0	0	0	0
0	1	1	1	0
0	1	1	1	0
0	1	1	1	0
0	0	0	0	0

(d)

FIGURE I17. Possible errors from extending boundaries of wells with density breaks. (a) Locations of 71 wells with density breaks. (b) Raster grid for one density break (D_BRK) well location. (c) Euclidean distances computed between each grid cell and density break cell. (d) 100 meter buffer calculated around density break grid cell.

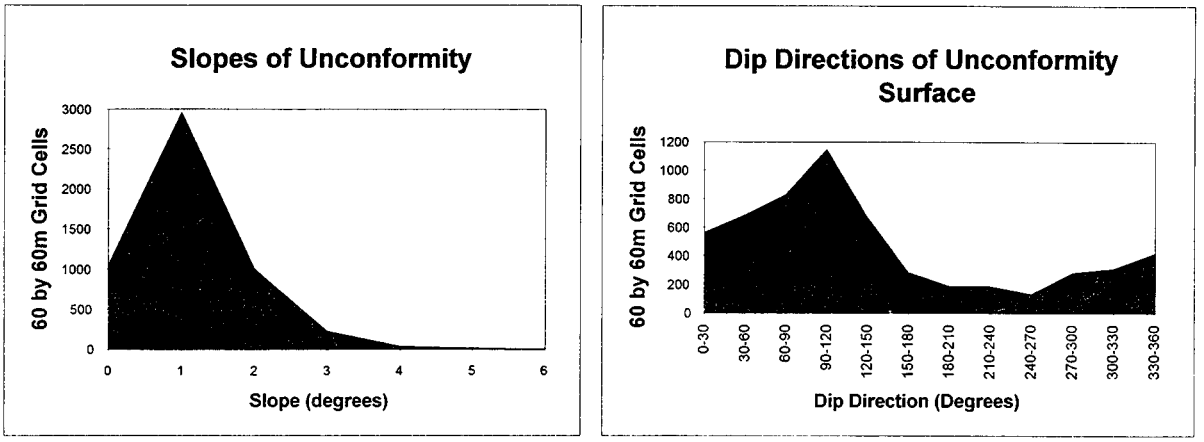

FIGURE I18. Slope and slope directions of Pre-Greenbrier unconformity surface.

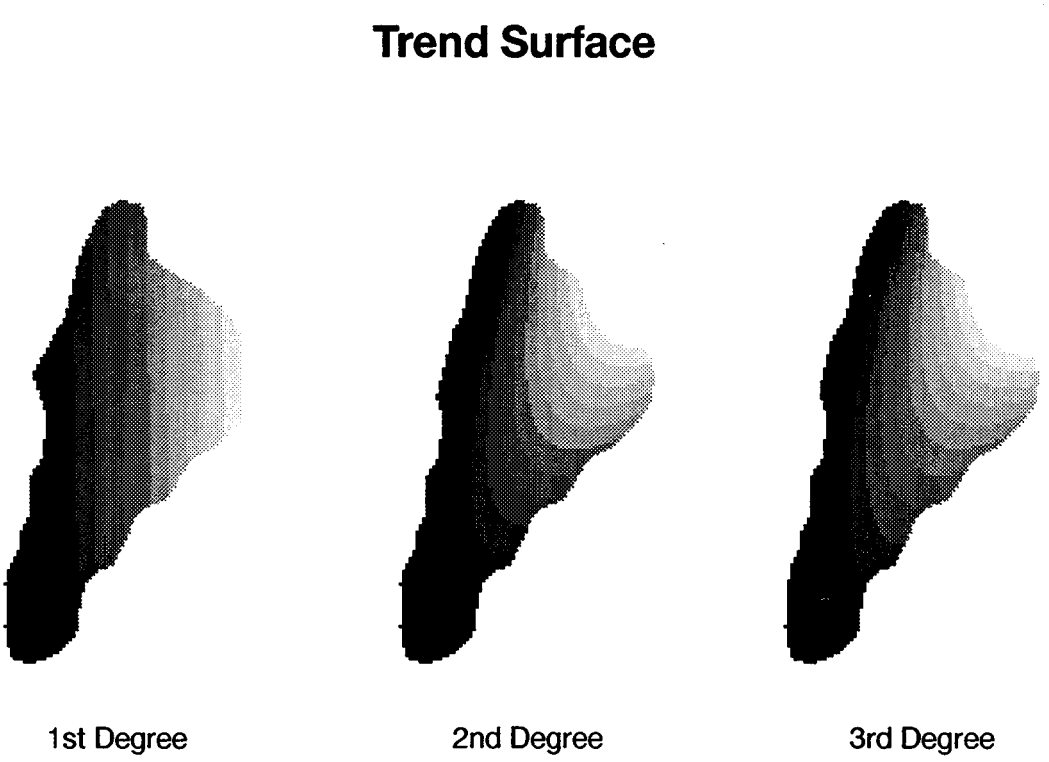

FIGURE I19. Trend surfaces of the elevation of Pre-Greenbrier unconformity surface.

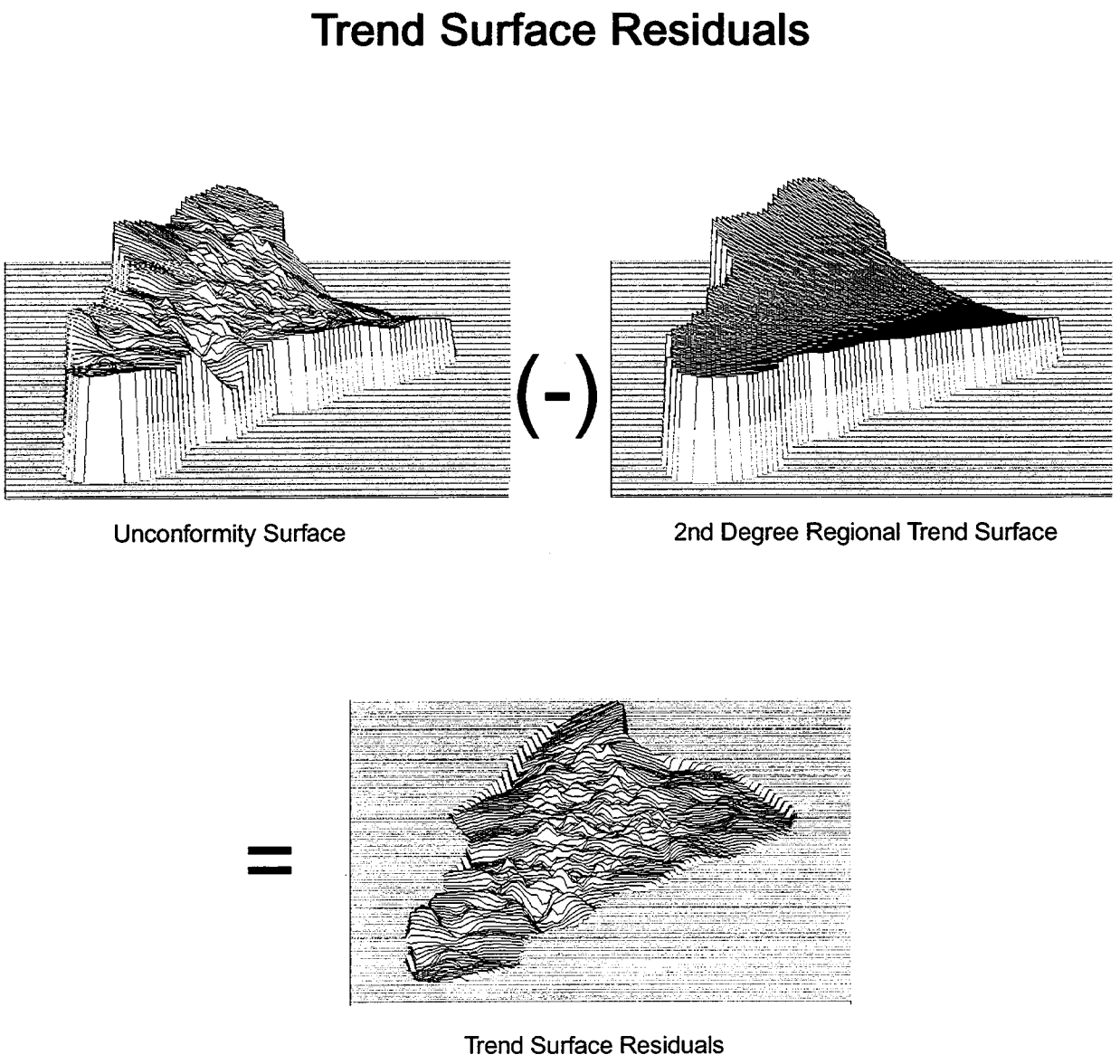

FIGURE I20. Trend surface residuals of the elevation of Pre-Greenbrier unconformity surface.

a.

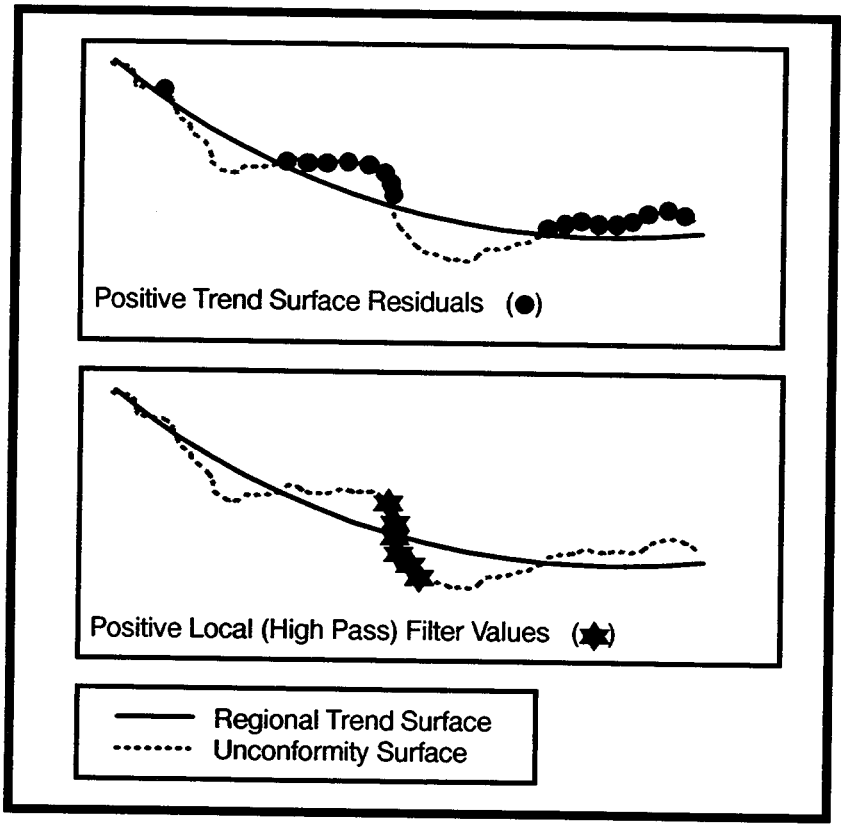

FIGURE I21. (a) Contrasting trend surface residuals to local high-pass filter values; (b) Details of local high-pass 3 by 3 filter.

b.

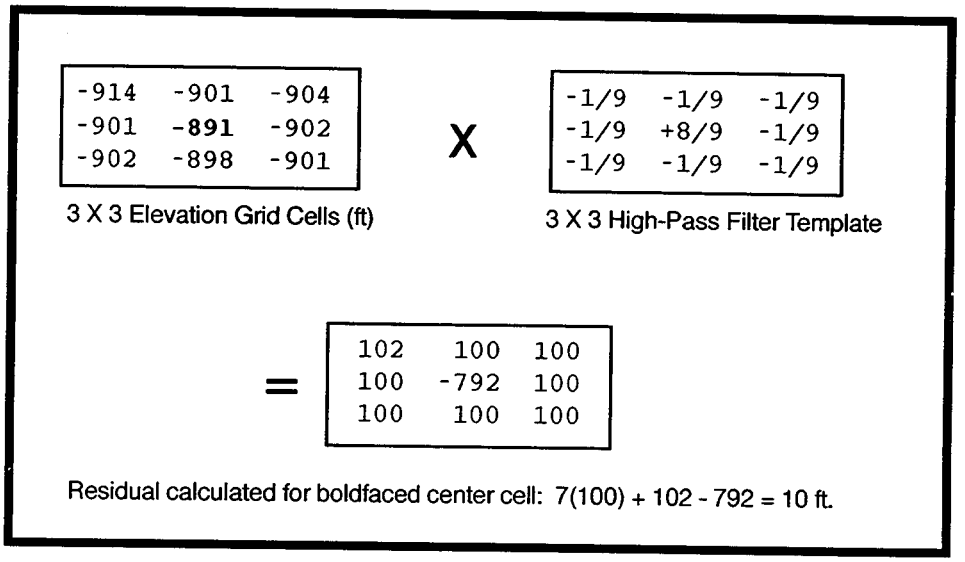

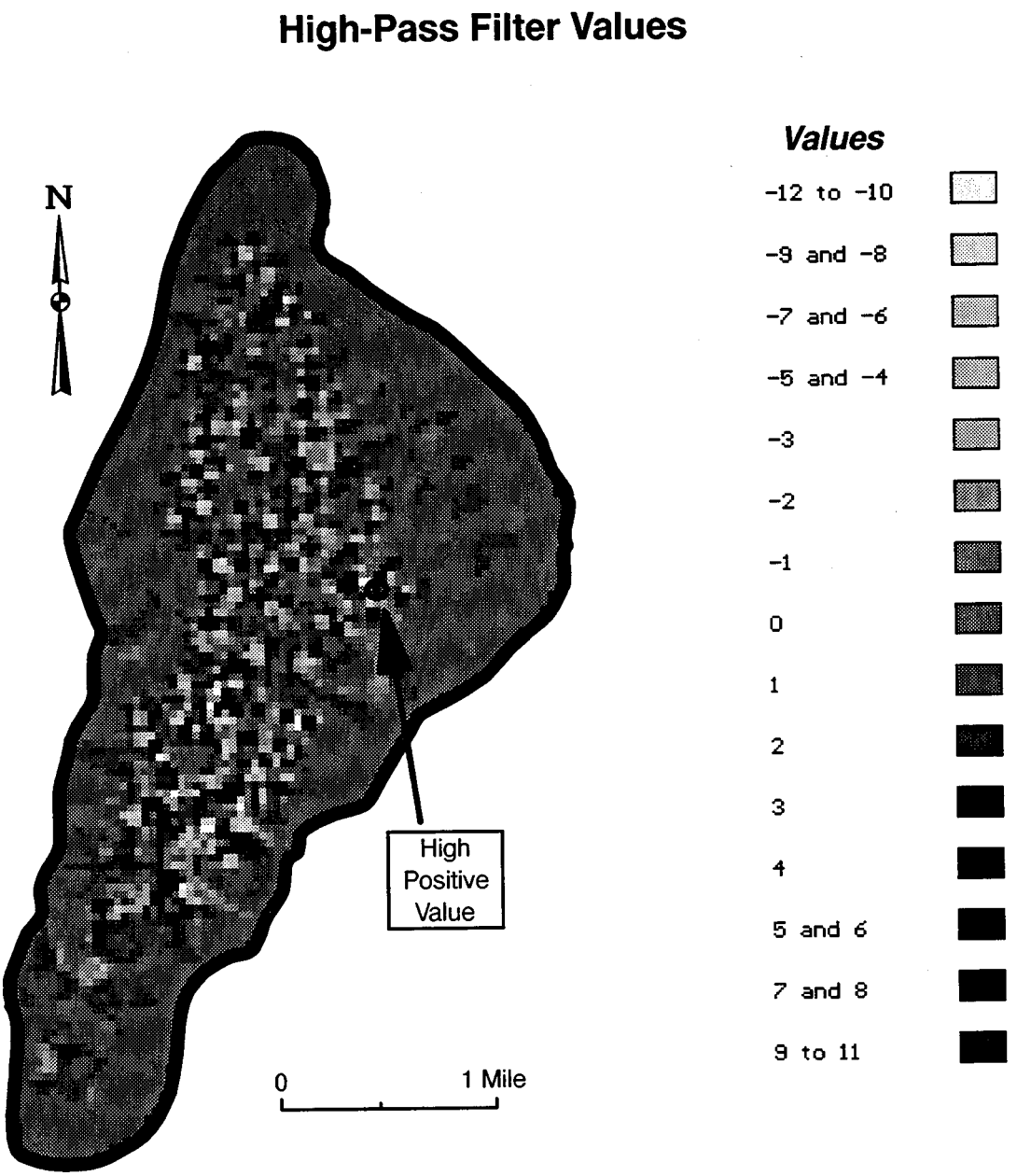

FIGURE I22. High-pass filter values for Pre-Greenbrier unconformity surface.

Best Oil Production Draped onto Unconformity Surface

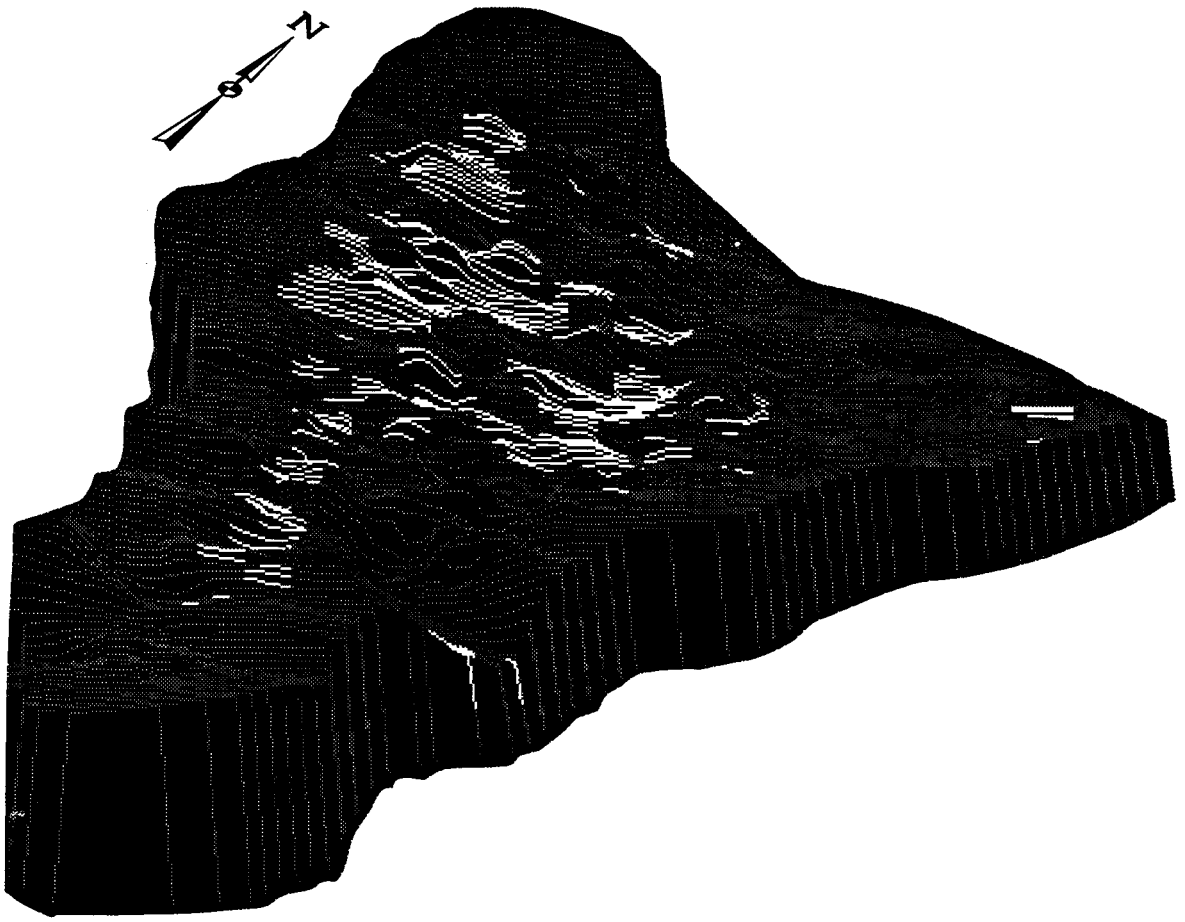

FIGURE I23. Initial open flow greater than 25 barrel/day (white lines) is draped onto the Pre-Greenbrier unconformity surface.

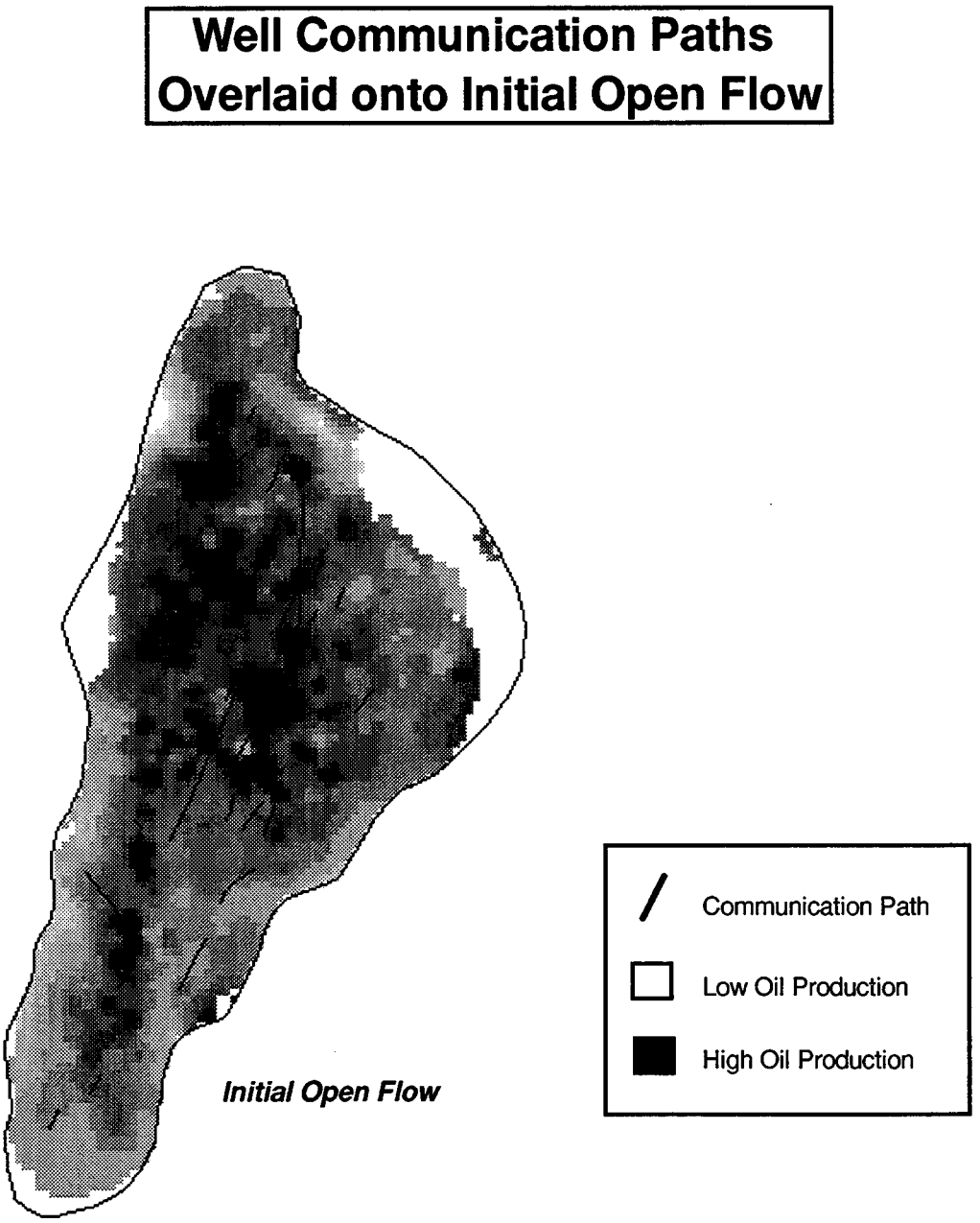

FIGURE I24. Communication paths compared to initial open flow.

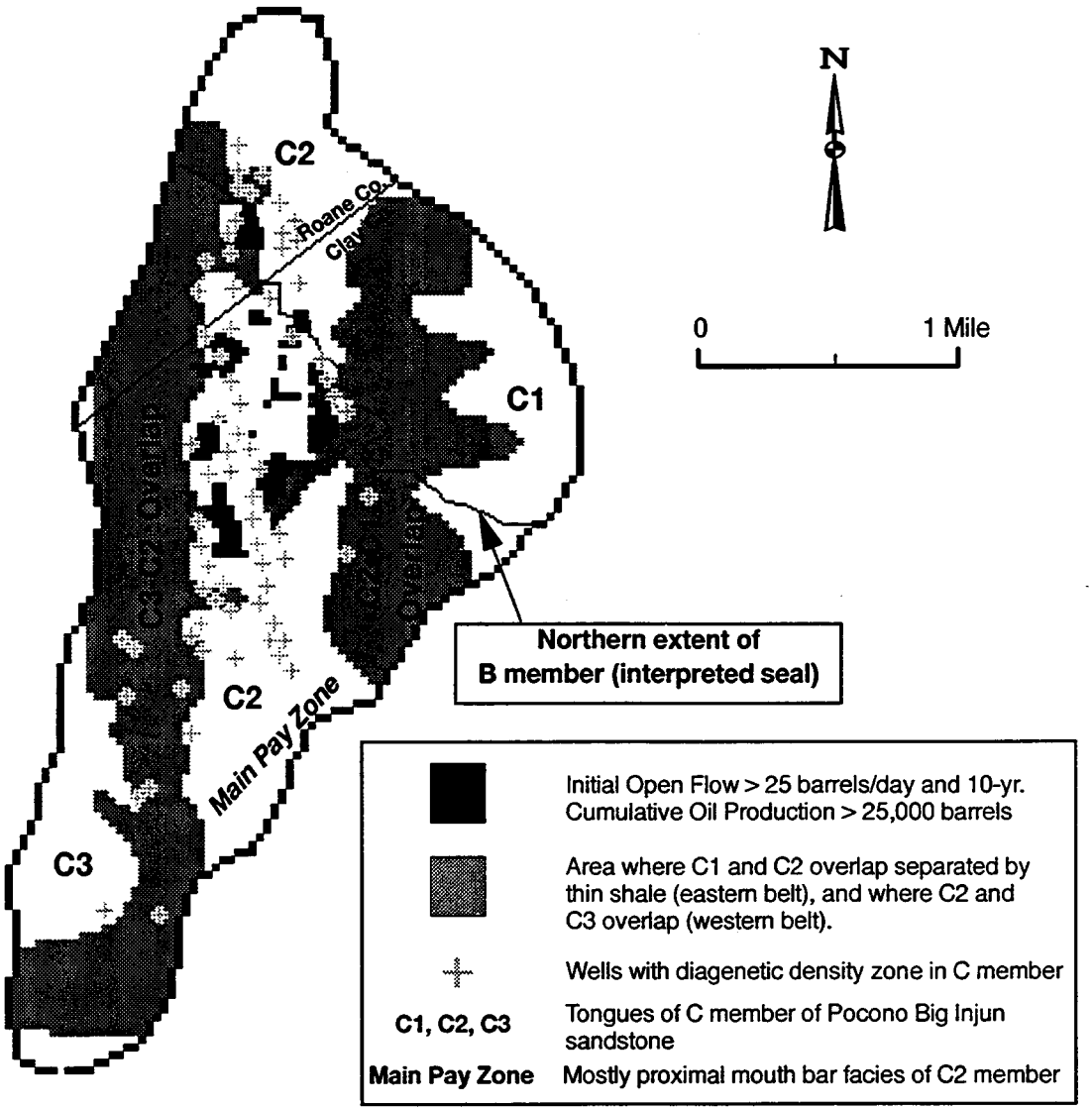

Four stratigraphic conditions that influence primary oil production are:

1. Presence of B zone seal (eroded by Pre-Greenbrier Unconformity)
2. North-south trend of pay zone, marine proximal mouth bar facies of C2
3. Depositional shale barrier
4. Diagenetic cementation/mineralization barrier

FIGURE I25. Spatial query of stratigraphy.

Cross-Classification of Two Stratigraphic Images

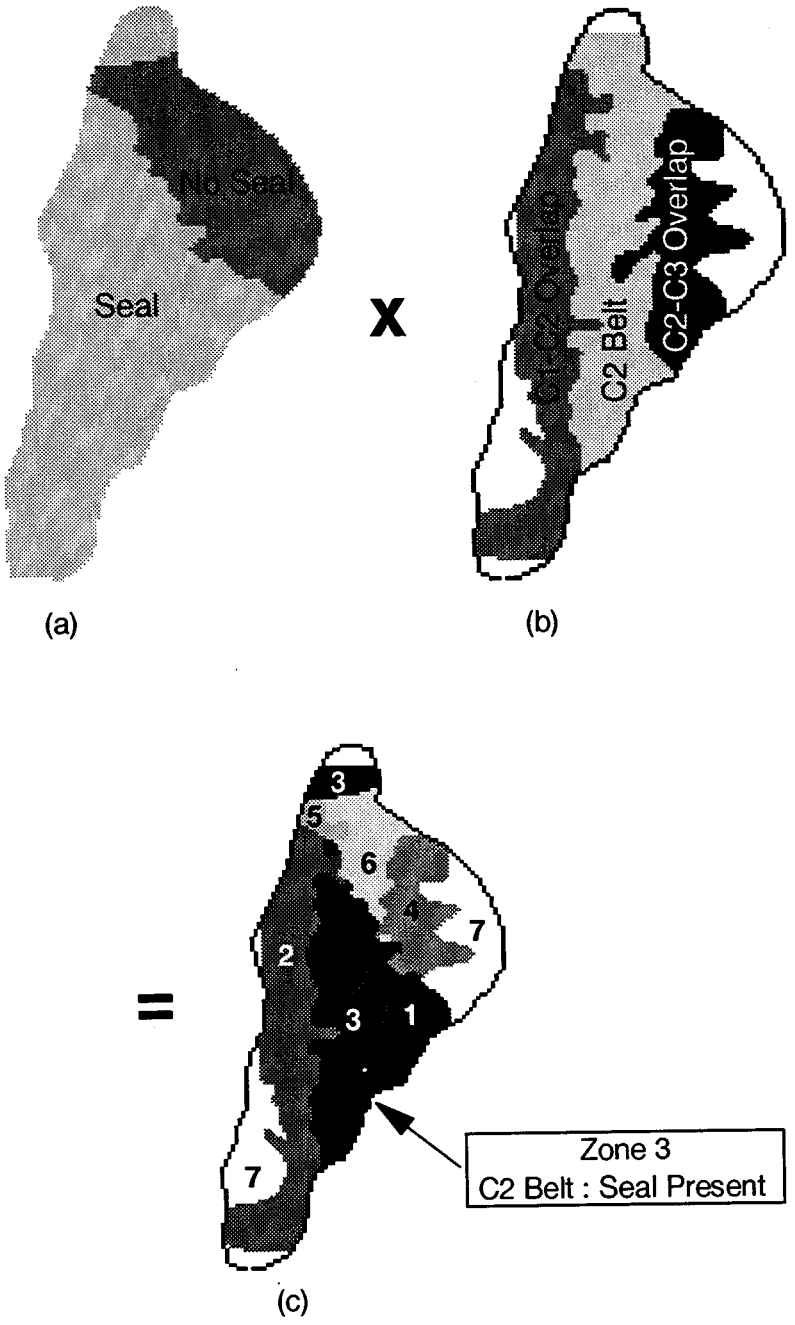

FIGURE I26. Cross-classification of diagenetic (seal) and depositional (mouth bar) images into seven zones. (a) Seal zones; (b) Mouth bar zones; (c) Seven cross-classified zones.

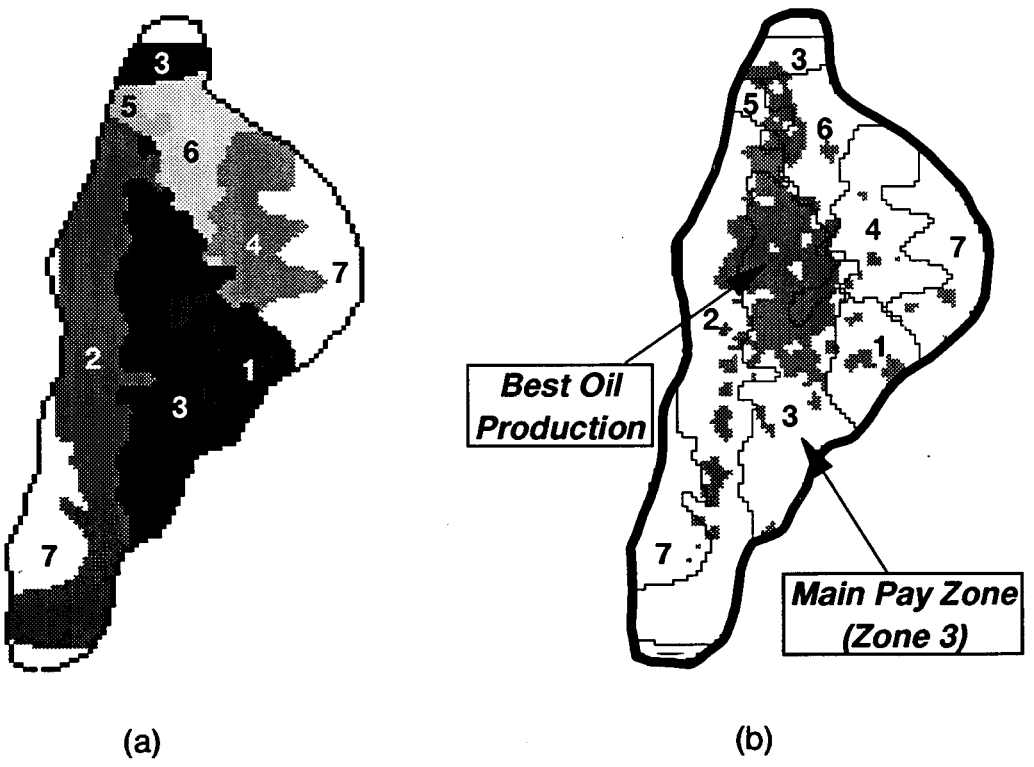

FIGURE I27. Cross-classified zones compared to best oil production. (a) Seven cross-classified zones created from two stratigraphic images; (b) Best oil production (initial open flow > 25 b/day OR 10-year cumulative production > 20,000 barrels) superimposed on cross-classified zones. In the main pay zone (C2 belt I seal present) the average initial open flow and average 10-year cumulative production are 19 b/day and 17,000 barrels respectively. This region encompasses 25% of the field.

Best Oil Production Draped onto a Stratigraphic Zone

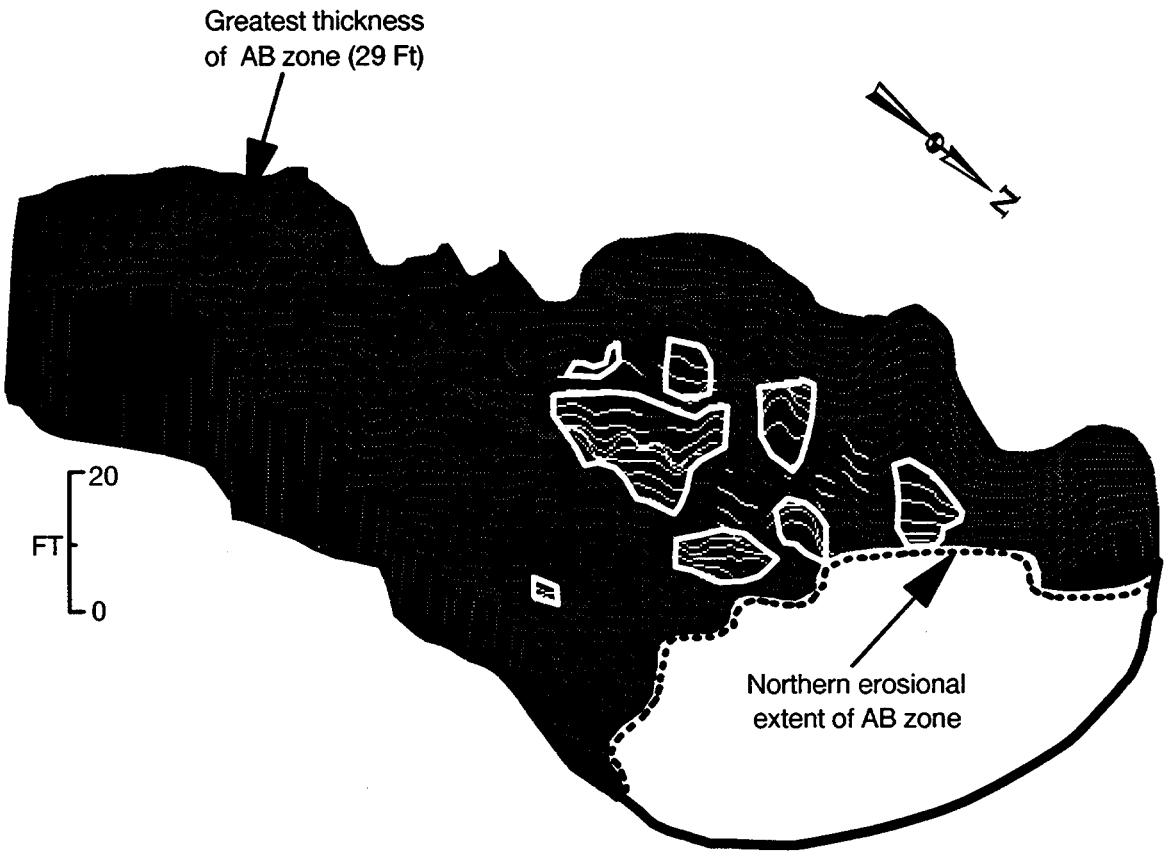

FIGURE I28. 10-year cumulative oil production > 25,000 barrels (white circles) superimposed on stratigraphic A & B zone (probable reservoir seal). Best production occurs where seal has not been eroded away.

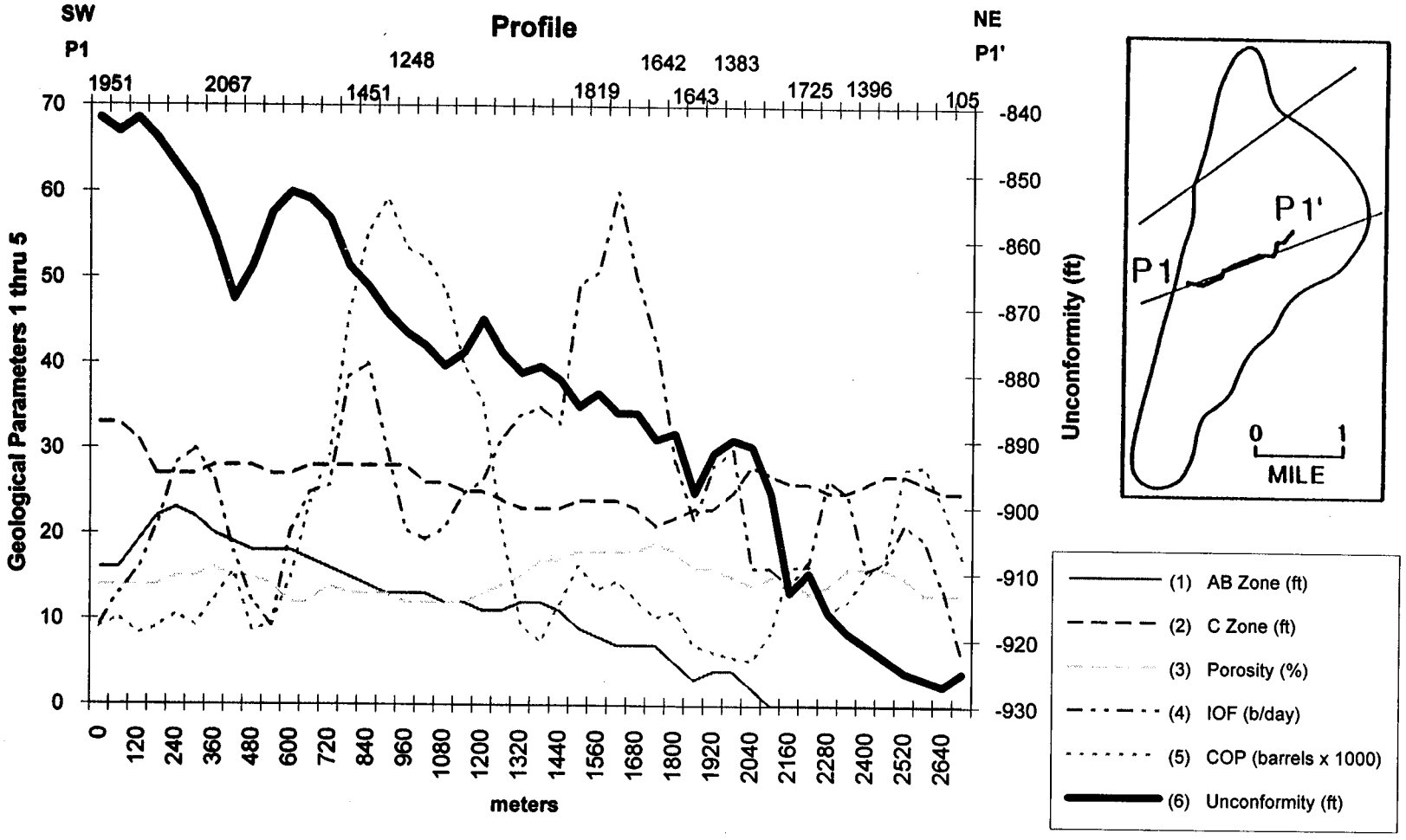

FIGURE I29. Profile P1-P1' taken across seven different raster images.

TABLE A1. Reservoir Parameters for Theoretical Simulation.

Parameter, unit	Value
Thickness (h), ft	20
Porosity (ϕ), %	18
Permeability (k), md	30
Initial Pressure (p), psi	2500
Initial Oil Saturation (S_o), %	68
Initial Water Saturation (S_w), %	32
Initial Gas Saturation (S_g), %	0
Bubble Point Pressure (P_b), psi	500

TABLE A2. Average Reservoir Parameters for Granny Creek Field at Time of Waterflood.

Parameter, unit	**Value**
Thickness (h), ft	40
Porosity (ϕ), %	16
Permeability (k), md	5-10
Initial Pressure (p), psi	175
Initial Oil Saturation (S_o), %	53
Initial Water Saturation (S_w), %	44
Initial Gas Saturation (S_g), %	3
Bubble Point Pressure (P_b), psi	500

TABLE B1. Pressure fall-off test data (Clay 891 and 2499).

WELL #	891	2499
THICKNESS	18 feet	16 feet
POROSITY	18.0 %	19.2 %
DEPTH	1766 feet	2194 feet
FLOW RATE	17.0 bpd	24.3 bpd
t_p	50704 hrs	840 hrs
VISCOSITY	0.8 cp	0.8 cp
B_w	1.0 bbl/stb	1.0 bbl/stb
C_t	9.9 E-6 psi^{-1}	9.9 E-6 psi^{-1}
r_w	0.328 feet	0.328 feet

TABLE B2. Data used for test analysis (Clay 891 and 2499).

STEP	PRESSURE,RATE psig,bpd	
	891	**2499**
0	552.1 0	369.4 0
1	1470.8 15	869.1 20
2	1540.6 25	882.9 40
3	1659.5 40	1305.2 60
4	1874.5 75	1438.8 70
5	1981.1 87	1475.8 80
6	2092.5 100	1506.8 90
7	-	1536.0 110
8	-	1574.5 130
MAX INJ RATE	120 bpd	69 bpd
MAX INJ PRESSURE	2300 psig	1455 psig

TABLE E1. Time-offsets and waveform changes in seismic data taken near communicating wells.

Well Line No.	Communication Station No.	Time Offset (ms)	Waveform Change
Line 2 (Vibroseis, Reprocessed)			
	152	2 ms	no
	195	4 ms	yes
	205	2 ms	no
	210	4 ms	yes
Line 2 (Vibroseis, Originally Processed)			
	152	0 ms	no
	195	2 ms	no
	205	0 ms	no
	210	2 ms	yes
Line 17 (Weight-drop Source, Overlapped with part of Line 2)			
	155=195/2	0 ms	yes
	135=205/2	0 ms	yes
	125=210/2	2 ms	yes
Line 3	221	2 ms	yes
	245	4 ms	yes
Line 6 (Vibroseis, Originally processed)			
	255=130-142/11	2 ms	yes
	295=265/11	0 ms	yes
	307=295/11	0 ms	no
	325=325/11	0 ms	no
	355=400/11	0 ms	yes
Line 11 (Weight-drop Source, overlapped with part of line 6)			
	130-142	0 ms	yes
	170	2 ms	yes
	295	2 ms	yes
	325	0 ms	yes
	400	4 ms	yes
Line 12	230	?	yes
	250	poor data	
Line 13	135	0 ms	yes
	152	0 ms	yes
	192	0 ms	yes
	302	2 ms	yes
Line 14	150	0 ms	yes
Line 15 (Brute stack)			
	227	4 ms	yes
	302	4-6 ms	yes
	338	4-6 ms	yes
Line 18	242	0 msu	?

TABLE E2. Stacking velocity and time delay.

Stacking Velocity	Time Delay	
	Station No. 155	Station No. 210
Final V +400'/s	0 ms	2 ms
Final V +200'/s	0 ms	4 ms
Final V	2 ms	6 ms
Final V -200'/s	4 ms	6 ms
Final V -400'/s	6 ms	8 ms

TABLE I1. Raster images.

10-Year Cumulative Production	Water Saturation
Initial Open Flow	Permeability
Big Injun Isolith	Mean Porosity of C Zone
Fluvial Channel Thickness (A & B Zone)	Porosity Feet
Mouth Bar Thickness (C Zone)	Density Breaks within C Zone
Mean Pressure (Southern Part of Field)	C1, C2, C3 Mouth Bar Tongues
Unconformity	

TABLE I2. Vector Files.

Type of Vector Data	Vector Entity
Granny Creek Boundary	Polygon
C-1, C-2, C-3 Mouth Bars	Polygon
Basement Faults	Polygon
Best Production	Polygon
County and Company Boundaries	Line
Northern Extent of B Member	Line
Seismic Lines	Line
Stratigraphic Profile Lines	Line
Well Communication Paths	Line
Waterflood 5-Spots	Line
Petrographic Wells	Point
VSP Well	Point
Wells with Density Breaks	Point

TABLE I3. Geographical and statistical analysis operations.

KEY WORD	OPERATION	SUMMARY DESCRIPTION
RECLASS	Query	Reclassifies grid cells for spatial query
OVERLAY	Query	Boolean AND and OR operations
	Map Algebra	Map algebra (multiply, add, subtract, cover) between two images
AREA	Query	Computes the area of cells belonging to the same class
DISTANCE	Distance	Calculates Euclidian distance between target cells
FILTER	Neighborhood	Filters change the values of cells according to the characteristics of neighboring values. High-pass filters extract areas of abrupt change versus those of gradual change.
SLOPE	Neighborhood	Calculates slope of strata from elevation data
ASPECT	Neighborhood	Calculates direction rocks are dipping
GROUP	Neighborhood	Classifies cells into contiguous groups
COLOR	Display	Produces color output or raster images
ORTHOGRAPH	Display	Produces 3D orthographic perspective plots of surface data
STRETCH	Image Enhancement	Visually enhances image
HISTOGRAM	Statistics	Provides a frequency histogram of cell values within an image. Also generates descriptive statistics of image.
REGRESSION	Statistics	Regression analysis of two images
CROSSTAB	Statistics	Produces a crosstabulation table which lists the frequency of two images' combined qualitative data. A cross-classification image is also generated.
Extract	Statistics	Extracts summary statistics from different regions
TREND	Statistics	Calculates trend surface images
PROFILE	Statistics	Creates a profile over space or time

TABLE I4. Overview of Granny Creek spatial analysis.

#	TOPIC	PRINCIPAL GIS OPERATION(S)	PROPERTY
1	Image Enhancement of Primary Production	Stretch	P
2	Reclassification of Oil Production	Reclassification	P
3	Spatial Query of Best Oil Production	Overlay	P
4	Comparison of Northern and Southern Granny Creek	Extract	P,E,S
5	Crosstabulation of Initial Open Flow (IOF) and Cumulative Oil Production (COP)	Crosstabulation	P
6	Linear Regression between IOF & COP Images	Linear Regression	P
7	Spatial Query using 6 Geologic/Engineering Variables	Overlay	P,E,S
8	Crosstabulation of Primary Production & Unconformity Surface	Crosstabulation	P, T
9	Dip Angles and Directions of Unconformity Surface	Slope, Aspect	T
10	Trend Surface of Unconformity	Trend Surface	T
11	Trend Surface Residuals	Overlay	P,T
12	Local High Pass Filter of Unconformity Surface	Filter	P,T
13	Oil Production Draped onto Unconformity Surface	Perspective	P,T
14	Communication Paths Compared to Initial Open Flow	Overlay	P,T
15	Spatial Query of Stratigraphy	Overlay	P,S
16	Cross-classification of Mouth Bars and Seal	Crosstabulation	P,E,S
17	Oil Production Draped onto a Stratigraphic Zone	Perspective	P,S
18	Spatial Query of Injection Pressure Rates	Overlay	P,E
19	Reservoir Volume	Scalar, Extract	T
20	Profile of Seven Raster Images	Profile	P,E,S,T

P = Production E = Engineering S = Stratigraphy T = Structure

TABLE I5. Summary statistics of the northern and southern regions of Granny Creek field. the first six properties are calculated mean values for each region; the last property (Best Production) represents total sum values.

#	PROPERTY	Penzoil (North)	Columbia (South)
1	C Zone Thickness (ft)	25.5	26.8
2	Total Big Injun Thickness (ft)	37.5	47.7
3	Average Log Density Porosity (%)	16.0	16.5
4	Average Permeability (md)	18.3	10.0
5	Initial Open Flow (b/day)	22.0	16.0
6	10-Year Cumulative Oil Production (barrels)	18401	12193
7	Best Production (acres) - Initial Open Flow > 25 b/day) AND (Cumulative Production > 25,000 barrels)	156	7

TABLE I6. Crosstabulation table of initial open flow and 10-year cumulative oil production categories. (Crosstabulated values in acres).

		INITIAL OPEN FLOW (b/day)					
		1-10	10-20	20-30	30-40	40-100	sum
CUMULATIVE	< 500 barrels	231	96	35	2	0	364
	500-10000	937	367	107	29	19	1459
	10000-20000	390	574	340	113	60	1477
	20000-30000	53	118	152	74	40	437
	30000-40000	2	22	70	29	15	138
	40000-50000	6	7	17	10	5	45
	50000-60000	2	6	11	7	0	26
	sum	1621	1190	732	264	139	3946

TABLE I7. Crosstabulation between primary production (10-year cumulative and initial open flow) and elevations of pre-Greenbrier unconformity. (Crosstabulated values in acres).

Elevation of Unconformity (feet)	Cumulative Production (barrels)							
	500 to 10,000	10,000 to 20,000	20,000 to 30,000	30,000 to 40,000	40,000 to 50,000	50,000 to 60,000	*COP > 20,000*	*COP > 500*
-955 to -935	80	14	0	0	0	0	0	94
-935 to -925	75	75	6	0	0	0	6	156
-925 to -915	45	73	3	1	0	0	4	122
-915 to -905	71	87	12	12	3	0	26	184
-905 to -895	110	114	24	17	0	0	41	265
-895 to -885	70	165	46	17	2	0	65	300
-885 to -875	112	190	70	15	6	2	93	396
-875 to -865	138	157	83	28	20	4	135	430
-865 to -855	93	114	66	28	7	2	103	310
-855 to -845	85	139	66	12	3	2	82	305
-845 to -835	181	176	39	4	3	0	45	402
-835 to -825	347	100	8	0	0	0	8	455
-825 to -815	291	42	4	0	0	0	4	336
-815 to -805	57	1	0	0	0	0	0	58
-805 to -785	10	0	0	0	0	0	0	10
Sum	1765	1446	426	133	43	10		

Elevation of Unconformity (feet)	Initial Open Flow (b/day)							
	1 to 10	10 to 20	20 to 30	30 to 40	40 to 50	> 50	*IOF > 20*	*IOF > 1*
-955 to -935	91	16	1	0	0	0	17	108
-935 to -925	129	30	10	0	0	0	40	169
-925 to -915	60	63	10	3	0	0	76	136
-915 to -905	56	67	37	15	1	3	123	179
-905 to -895	66	110	82	13	4	2	211	277
-895 to -885	117	90	85	23	13	15	227	344
-885 to -875	140	123	72	41	21	14	271	411
-875 to -865	168	139	98	30	6	7	280	448
-865 to -855	125	81	81	36	6	4	208	334
-855 to -845	78	105	72	45	10	3	235	313
-845 to -835	132	95	91	41	13	6	246	378
-835 to -825	202	153	49	6	6	0	214	416
-825 to -815	169	78	21	3	0	0	102	271
-815 to -805	36	2	0	0	0	0	2	38
-805 to -785	0	0	0	0	0	0	0	0
Sum	1570	1152	709	257	81	53		

> than 20 acres

TABLE I8. Trend surface statistics for the Pre-Greenbrier unconformity.

	Linear (1st Degree)	Quadratic (2nd Degree)	Cubic (3rd Degree)
Goodness of Fit (R2)	84.9%	90.8%	91.3%
Correlation Coefficient (R)	0.92	0.95	0.96
F ratio	1334	935	547
df (numerator)	2	5	9
df (denominator)	476	473	469

TABLE I9. Density breaks compared to worst oil production.

Oil Production	Conditions	Percentage of Density Breaks Matching Worst Production
Initial Open Flow	< 25 b/day	63%
Cumulative Oil Production	< 25000 barrels	80%
Worst Production	< 25 b/day AND < 25000 barrels	90%

TABLE I10. Summary statistics and crosstabulation between mouth bars and possible seal zones.

Mouth Bars	Acres	(%)
C1-C2 Overlap	898	18.5
C2-C3 Overlap	1401	28.8
C2 (Pay Zone)	1596	32.8
C3 or C1	967	19.9

Seal	Acres	(%)
Seal Present	3385	69.7
No Seal	1408	30.3

	Initial Open Flow (b/day)		10-yr. Cumulative Oil Production (barrels)		Acres	(%)
Cross-classification	Maximum	Average	Maximum	Average		
C1-C2 I Seal	52	14	43684	14409	382	7.8
C2-C3 I Seal	54	12	46048	7983	1310	27.0
C2 I Seal	99	19	64275	16311	1207	24.8
C1-C2 I No Seal	31	8	28077	8001	514	10.6
C2-C3 I No Seal	41	10	27779	13509	78	1.6
C2 I No Seal	85	13	36507	11328	383	7.9
Other					986	20.3

TABLE 1. Compilation of general trends of structure in the Granny Creek field area.

STRUCTURE	UNIT	GENERAL TREND
THIEF ZONES	BIG INJUN/BIG SHALE	NE
NATURAL FRACTURES	(SURFACE)	COMPLEX
NATURAL FRACTURES	DEVONIAN SHALE	NE
COAT CLEATS	(SURFACE)	E-W
INSITU STRESS	(BIG LIME)	E-W
FAULTS	BASEMENT	NE
SMALL THRUSTS	(SURFACE)	NE
SMALL FOLDS	(SURFACE)	NE
SMALL FOLDS	(BIG LIME)	NE-N-S

TABLE 2. Results of core analysis.

PERMIT No:	Zone A K	Zone A POROSITY	Zone B K	Zone B POROSITY	Zone C3 K	Zone C3 POROSITY	Zone C2 K	Zone C2 POROSITY	Zone C1 K	Zone C1 POROSITY
698	?	?	?	?	2.24	14.3	0.96	16.5	-	-
733	3.91	13.4	6.43	14.34	45.43	18.16	0.05	15.45	-	-
735	71.87	16.19	25.21	10.94	6.91	21.15	0.05	15.4	-	-
852	7.48	11.91	0.89	7.63	0.68	15.31	-	-	-	-
864	?	?	?	?	17.79	17.86	-	-	-	-
867	?	?	?	?	9.50	17.66	-	-	-	-
868	2.16	9.46	0.56	6.78	3.21	18.82	0.16	16.67	-	-
874	13.15	13.35	4.83	8.36	4.36	17.91	0.10	16.03	-	-
903	11.93	11.68	-	-	2.77	16.59	-	-	-	-
932	?	?	?	?	0.75	15.76	0.11	15.56	-	-
1059	3.53	7.73	5.56	8.49	6.25	17.14	0.30	4.6	-	-
1107	8.99	12.23	2.88	8.76	-	-	6.40	18.88	-	-
1108	-	-	1.27	6.97	-	-	6.53	17.04	3.91	17.33
1109	19.00	11.7	3.00	6.46	7.01	18.59	0.11	14.94	-	-
1110	8.44	11.19	12.12	12.26	16.76	18.52	?	?	-	-
1126	20.05	15.95	3.22	9.24	8.49	19.79	0.05	16.28	-	-
1128	-	-	0.43	7.26	1.56	17.17	1.20	19.23	-	-
1130	4.66	15.44	3.19	10.76	6.26	15.72	5.21	21.71	-	-
1132	9.63	15.7	3.95	7.5	2.95	12.85	5.08	21.05	-	-
1133	-	-	3.87	5.88	-	-	7.82	17	?	?
1134	-	-	4.71	5.42	-	-	9.76	13.59	2.38	15.89
1184	0.45	8	3.27	12.2	-	-	3.67	17.15	-	-
1309	-	-	23.97	17.97	3.43	15.56	3.82	16.12	-	-
1598	-	-	0.45	8.66	10.60	17.6	3.35	18.45	-	-
2253	0.12	7.2	?	?	0.71	13.7	8.15	17.05	-	-
2255	-	-	0.81	12.75	-	-	4.36	15.75	0.01	4.8
2410	-	-	41.75	21.63	19.46	18.28	4.23	16.78	-	-
Averages:	**12.90**	**12.51**	**6.07**	**9.14**	**9.79**	**17.50**	**4.05**	**17.17**	**2.10**	**13.60**

TABLE 3. Results of well log interpretation.

COUNTY No:	PERMIT No:	Zone A POROSITY	Zone A Sw	Zone A H	Zone B POROSITY	Zone B Sw	Zone B H	Zone C3 POROSITY	Zone C3 Sw	Zone C3 H	Zone C2 POROSITY	Zone C2 Sw	Zone C2 H	Zone C1 POROSITY	Zone C1 Sw	Zone C1 H
15	733	12.24	?	9	10.37	?	10	16.8	?	25	11.28	?	4	-	-	-
15	735	15.27	?	7	13.4	?	18	24	?	17	8.7	?	4	-	-	-
15	774	-	-	-	-	-	-	-	-	-	-	-	-	6.08	90.7	19
15	775	-	-	-	-	-	-	-	-	-	-	-	-	11.74	?	7
15	788	-	-	-	-	-	-	-	-	-	-	-	-	15.13	?	11
15	852	8.75	60.9	8	9.75	31.0	13	18.74	46.7	23	-	-	-	-	-	-
15	853	9.61	?	3	9.11	?	15	16.44	?	27	-	-	-	-	-	-
15	868	9.25	50.4	5	8.29	33.4	16	19.51	37.4	18	12.78	65.5	11	-	-	-
15	903	17.63	?	23	-	-	-	21.24	?	26	-	-	-	-	-	-
15	910	-	-	-	14.11	35.9	6	-	-	-	15.88	33.3	24	-	-	-
15	1059	9.13	53.3	6	3.5	83.5	17	12.41	71.2	19	7.22	69.6	3	-	-	-
15	1060	-	-	-	-	-	-	-	-	-	-	-	-	17.44	34.4	18
15	1107	11.78	37.9	7	9.49	29.4	9	-	-	-	15.18	40.6	25	-	-	-
15	1108	-	-	-	12.2	31.9	9	-	-	-	19.18	36.0	26	5.71	99.6	6
15	1109	10.8	44.5	5	7.76	30.3	15	17.04	35.6	19	12.07	66.5	9	-	-	-
15	1110	12.81	24.8	9	8.6	26.2	8	18.69	31.9	27	7.15	82.4	9	-	-	-
15	1126	14.58	24.7	9	8.03	39.2	13	17.16	33.9	22	12.3	60.0	6	-	-	-
15	1128	-	-	-	5.46	?	20	13.7	?	14	12.3	?	11	-	-	-
15	1130	12.06	34.2	9	8.81	32.4	6	13.27	47.3	7	15.41	49.4	9	-	-	-
15	1132	13.45	?	7	7.33	?	8	12.06	?	7	16.35	?	22	-	-	-
15	1134	-	-	-	6.49	35.7	6	-	-	-	14.15	38.4	8	16.28	36.6	21
15	1167	11.97	?	3	9.49	?	6	-	-	-	18.94	?	25	-	-	-
15	1176	13.41	?	4	-	-	-	-	-	-	18.29	?	23	-	-	-
15	1184	9.75	?	4	10.21	?	6	-	-	-	18.62	?	24	-	-	-
15	1185	13.91	?	7	-	-	-	-	-	-	20.1	?	27	-	-	-
15	1224	-	-	-	-	-	-	-	-	-	15.69	?	22	3.29	?	4
15	1225	-	-	-	-	-	-	-	-	-	16.33	?	23	-	-	-
15	1242	7.38	?	3	7.28	?	6	14.93	?	10	14.03	?	15	-	-	-
15	1243	-	-	-	9.09	?	5	15.22	?	7	18.2	?	22	-	-	-
15	1309	-	-	-	8.27	50.8	3	16.39	36.9	7	16.58	42.1	19	-	-	-
15	1591	8.7	?	5	7.33	?	9	18.28	?	11	13.46	?	17	-	-	-
15	1592	-	-	-	7.49	?	8	16.71	?	6	20.01	?	22	-	-	-
15	1596	-	-	-	9.65	?	11	18.96	?	16	14.25	?	10	-	-	-
15	1598	-	-	-	7.19	37.4	10	13.94	33.5	6	18.1	36.5	22	-	-	-
15	1601	-	-	-	10.41	?	9	-	-	-	18.83	?	25	-	-	-
15	1621	-	-	-	9.12	?	10	14.99	?	6	14.64	?	22	-	-	-
15	1626	-	-	-	12.62	?	10	16.12	?	3	18.35	?	19	-	-	-
15	1630	-	-	-	11.73	?	7	-	-	-	16.88	?	24	-	-	-
15	1639	-	-	-	9.44	?	5	-	-	-	16.41	?	26	-	-	-
15	1649	7.57	?	5	3.56	?	8	11.53	?	12	8.04	?	15	-	-	-
15	1726	-	-	-	-	-	-	-	-	-	18.81	?	21	8.22	?	6
15	1783	-	-	-	-	-	-	-	-	-	15.96	?	20	10.82	?	6
15	1933	15.36	?	9	12.01	?	13	17.52	?	19	10.26	?	9	-	-	-
15	1936	14.61	?	9	9.12	?	13	18.85	?	20	11.07	?	14	-	-	-
15	1941	16.18	?	8	13.54	?	14	18.06	?	22	7.84	?	8	-	-	-
15	1942	14.59	?	8	10.53	?	15	16.17	?	15	6.76	?	8	-	-	-
15	1951	12.8	?	4	10.63	?	11	17.68	?	26	7.79	?	8	-	-	-
15	1953	-	-	-	9.77	?	7	-	-	-	15.98	?	20	8.44	?	5
15	2001	8.49	?	9	8.48	?	7	12.37	?	7	11.81	?	20	-	-	-
15	2002	11.09	?	13	10.24	?	4	13.82	?	13	13.97	?	11	-	-	-
15	2133	-	-	-	11.01	?	14	16.89	?	3	19.02	?	25	-	-	-
15	2136	11.36	?	8	10.88	?	11	15.75	?	20	10.86	?	11	-	-	-
15	2150	11.76	?	9	9.23	?	6	16.33	?	4	17.96	?	25	-	-	-
15	2214	11.39	34.0	6	10.17	19.1	8	-	-	-	19.8	22.0	26	-	-	-
15	2215	8.55	?	3	11.18	?	8	-	-	-	17.92	?	25	-	-	-
15	2216	13.97	?	5	9.23	?	5	-	-	-	14.14	?	28	-	-	-
15	2222	8.36	?	4	9.33	?	10	-	-	-	16.69	?	25	-	-	-
15	2227	10.63	?	7	7.72	?	8	-	-	-	18.92	?	26	-	-	-
15	2229	-	-	-	9.73	?	11	-	-	-	16.87	?	25	-	-	-
15	2253	9.22	27.5	3	7.87	38.9	8	19.92	27.0	8	16.64	35.0	17	-	-	-
15	2297	-	-	-	-	-	-	-	-	-	19.64	?	17	14.62	?	7
15	2298	-	-	-	-	-	-	-	-	-	15.73	36.3	12	10.83	63.2	8
15	2301	-	-	-	8.8	?	17	17.08	?	21	12.49	?	6	-	-	-
15	2428	11.97	?	12	-	-	-	-	-	-	18.64	?	25	-	-	-
15	2430	-	-	-	-	-	-	-	-	-	17.23	34.2	17	5.5	98.9	6
15	2472	-	-	-	-	-	-	-	-	-	19.35	?	17	6.05	?	4
87	2102	14.44	?	7	-	-	-	20.68	?	9	16.5	?	19	-	-	-
87	2410	-	-	-	5.71	45.2	4	20.61	23.9	11	20.48	27.0	16	-	-	-
87	2411	-	-	-	-	-	-	-	-	-	16.68	?	24	-	-	-
87	2848	-	-	-	-	-	-	-	-	-	19.42	?	14	-	-	-
87	3415	-	-	-	-	-	-	-	-	-	2.48	?	21	-	-	-
Averages:		12.47	38.6	7.1	9.25	38.9	9.7	17.24	39.9	14.4	16.10	40.0	17.7	11.48	61.6	9.1

TABLE 4. Average porosity and permeability from core analysis.

ZONES	PERMEABILITY	POROSITY
ZONE A	12.90	12.51
ZONE B	6.07	9.14
ZONE C3	9.79	17.50
ZONE C2	4.05	17.17
ZONE C1	2.10	13.60

TABLE 5. Average porosity, thickness, and water saturation from log interpretation.

ZONES	POROSITY	THICKNESS	WATER SATURATION
ZONE A	12.47	7.1	38.6
ZONE B	9.25	9.7	38.9
ZONE C3	17.14	14.4	39.9
ZONE C2	16.10	17.7	40.0
ZONE C1	11.48	9.1	61.6

☆U.S. GOVERNMENT PRINTING OFFICE: 1994 - 560-030/00022